Spallings Release Positions Paper: Description and Evaluation of a Mechanistically Based Conceptual Model for Spall

1 May 1997

Prepared for

US Department of Energy
Carlsbad Area Office

By:
Sandia National Laboratories
and
Carlsbad Technical Assistance Contractor

For additional information about this documet, contact
M.K. Knowles or F.D. Hansen,
Repository Isolations Systems Department
Sandia National Laboratories
Albuquerque, NM 87185
505-848-0600

Contents

Contents (continued)

1.0 EXECUTIVE SUMMARY

This document describes a mechanistically based model that describes possible spallings events occurring as a result of an inadvertent human intrusion into the Waste Isolation Pilot Plant (WIPP). Development of this model was initiated in response to Conceptual Model Peer Review Panel (CMPRP) findings that the end-state erosional model used in the Compliance Certification Application (CCA) inadequately represented key physical elements of the spallings process. The strategy implemented to address panel concerns, and to form a basis for evaluating the volumes reported in the CCA, has been to evaluate the events and processes that are realistically expected to occur during a drilling intrusion, and to use this evaluation to develop a preliminary model that specifically addresses these events and processes. Whereas the model used in the CCA computes the expected total spall volumes by simulating only an end state of the spall process, the new model explicitly incorporates the entire response of the system from the time of the intrusion to the end of the event.

Three computational methods have been developed to quantify the mechanisms of the new conceptual model, and these have been used to calculate failed volumes of material. Consistency in the results obtained from these different computational approaches has provided internal validation of the assumptions used to implement the mechanistic conceptual model. Complementary efforts have been made to characterize the underground environment and waste forms to provide realistic parameters values and boundary conditions for the calculations. Corroboration of the physical processes, and of the calculated values for the failed volumes, is provided by analogous oil and gas production experience. The results obtained from the various computational models, using the parameters and boundary conditions provided by the characterization efforts and validated by a study of analogous situations, have led to a conclusion that, although the spallings model currently used in the CCA fails to capture the processes completely, the release volumes predicted by that model are a reasonable upper bound for the spalling process.

This conclusion is based on the comprehensive investigation described in this report and outlined in Figure 1-1. The basis for the conceptual model is a consideration of the probable state of the repository at the time of an intrusion, including the likely condition of the waste and the probability of potential spall drivers occurring, such as high gas pressures. In terms of the underground setting, it is noted that spall cannot occur if the gas pressures are not high enough to displace the drilling mud in the borehole, which requires pressures in excess of about 8 MPa. It is also clear from the results of these studies that the highest potential releases are associated with pressures close to lithostatic. The probability of these high pressures is low (of the order of 1 in 100), although they can still occur frequently enough to impact the final Complementary Cumulative Distribution Function (CCDF) for the repository.

An evaluation of the processes that will occur in the repository during spallling has guided characterization of the likely condition of the waste. This has enabled surrogate materials to be specified, and laboratory tests of these materials have provided estimates to be made of the salient mechanical and physical properties. Evaluation of waste states has emphasized that the probable nature of the waste will be as a mesoscopically heterogeneous material with some cohesion, as opposed to the cohesionless granular material assumed in the CCA. Evaluation has also emphasized that the brine saturation of the waste will be very low under the highest pressure scenarios, and the potential for blocky material with reasonable cementation will be high.
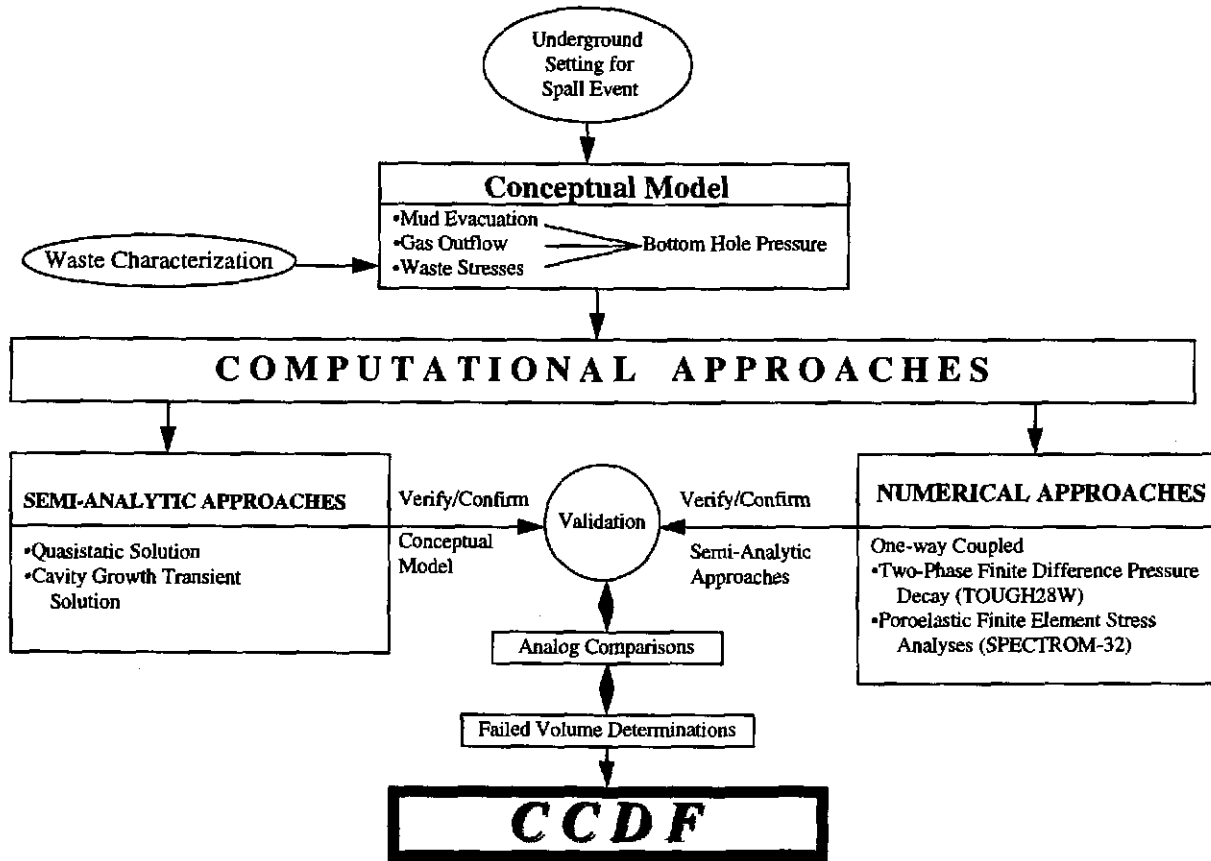
Figure 1-1. Spalling conceptual model: systems analysis.

Evaluation of the underground setting and of the waste characteristics provide input to the conceptual model, which is based on the physical and mechanical processes likely to accompany a drilling intrusion. These processes include initial mud ejection from the drillhole due to gas flow from the repository, the later flow of gas up the wellbore, and the associated change in the stress field near the intrusion. The basic assumption has been made that the waste will fracture, and spall will occur where the effective stresses are tensile and in excess of the tensile strength. The removal of fragmented material by the flow of high velocity gas during the later stages has been considered. These analyses show that at large fragmented volumes all the material will probably not be removed. However, the calculated volumes are small enough that it is conservatively assumed that all failed material is removed to the surface.

Having identified the governing physics of the spall event, the conceptual model was evaluated quantitatively using computational methods employing a semi-analytic solution technique and a full numerical approach. The primary semi-analytic approach is based on a transient solution for the gas flow in the repository, including cavity growth. Numerical calculations have been carried out by explicit coupling of a two-phase finite difference code for gas flow and a poroelastic finite element code for stress calculations. Comparisons of the computational results from the different methods have demonstrated quantitative agreement in the calculated values of failed volumes, which adds confidence to the various simplifications used in these approaches.

A better sense of validation for the computational results is usually derived by comparison of calculations to full scale experimental results. A study of analogs has provided this higher level of validation, with analogs from the petroleum production industry validating the methods used, while numerical values estimated from a study of the very similar analog from methane production demonstrate that the conceptual model for spallings represents the physics of the phenomena. Figure 1-1 shows how the several paths taken to evaluate spall events lead to reasonable approximations of spall release volumes. At the end of computational analyses of the spall event, the gas pressures, failed waste volumes, and probabilities of occurrence are collectively interpreted in terms of regulatory compliance.

The complete report of this systematic approach to potential spall events is extensive and includes detailed and rather complex arguments. Each of the evaluation paths shown schematically in Figure 1-1 represents large quantities of scientific work that comprise sections of the main report. Discussion of limiting conditions, conservatism, and the bounding nature of computations is found in the text itself and in completed records packages. These documents have received technical and Quality Assurance reviews and are available for reference.

1.1 Conclusions

A mechanistically based conceptual model for spalling release at the WIPP has been developed and evaluated. This model captures the expected form and characteristics of the waste as well as physical processes that would occur during a drilling intrusion. The physics underlying this model includes the important processes of the wellbore hydraulics as the borehole initially penetrates the waste panel, the coupled transient gas flow within the waste, and the mechanical response of the waste form to the gas transients. Possible failure mechanisms include tensile failure and shear-induced yield, while erosion at the end state will remove fractured material. Mechanisms of concern to the CMPRP, such as seepage forces and liquefaction, are included in these failure mechanisms.

Calculations have been based on an evaluation of the processes leading to potential spall conditions. These processes indicate that attainment of high pressures requires microbial action and incomplete corrosion of the waste drums. Probable conditions in the repository have been evaluated and probable degradation byproducts have been identified. Specimens of surrogate waste were fabricated using proportioned mixtures of degraded materials. Strength of degraded waste is expected to be a function of its saturation state. Repository pressure and saturation are also directly related: high gas pressures occur only when the waste is very dry. Tensile strength of saturated waste averages 0.074 MPa, and the average dry tensile strength increases to 0.151 MPa. In the saturated condition, surrogate specimens exhibit a cohesion of 0.13 MPa and a friction angle of 44°.

Spall volumes predicted by this modeling approach are extremely small for all gas pressures below lithostatic, with calculated solid release volumes significantly smaller than those used in the CCA. At any pressure below lithostatic, volumes of failed material available for transport to the surface are essentially very small for all values of waste strength. Very limited volumes are calculated even when conservative boundary conditions are used, including instantaneous blowout of wellbore mud. In extreme cases, where gas pressures approach or equal lithostatic, predicted spall volumes increase, but are still significantly lower than those used in the CCA.

The mechanistic conceptual model has been evaluated quantitatively using a semi-analytic approach and using numerical calculations that couple a finite difference fluid flow code and a finite element rock mechanics code. The semi-analytic approach, which is called the cavity growth method because it allows the region of tensile failure to grow progressively during a calculation, is used to determine the failed volumes listed in Table 1-1. The results from the cavity growth method are partly verified by comparison to the coupled numerical approach and by comparison to a simpler semi-analytic approach based on a quasi-steady approximation.

These calculations show that for repository gas pressures below 14 MPa there is no tensile failure predicted under realistic but conservative assumptions, and that predicted failed volumes are low at pressures above that. For example, solid volumes released for any single spall event when the initial repository effective stress is greater than 0.3 MPa are much smaller than values used in the CCA. The largest volumes occur when the repository gas pressure equals lithostatic (14.8 MPa), where additional levels of complexity occur. Consideration of several mitigating factors leads to the conclusion that release volumes are overpredicted by the numerical and analytical approaches. Realistic conditions of the waste form, including waste strength, particle size, waste plasticity, and heterogeneity, will readily mitigate releases, even at zero effective stress.

Table 1-1. Failure Radii and Uncompacted Volumes Calculated by the Cavity Growth Model

Initial Gas Pressure (MPa)	Tensile Strength (psi)	Tensile Radius (m)	Uncompacted Volume (m^3)
12		0.156	0
	10	0.156	0
	15	0.156	0
14	5	0.37	0.19
	10	0.21	0.02
	15	0.156	0
14.3	10	0.28	0.07
	15	0.20	0.02
	20	0.156	0
14.5	10	0.33	0.13
	15	0.23	0.03
	20	0.156	0
14.6	10	0.35	0.16
	15	0.24	0.04
	20	0.156	0
14.7	10	0.37	0.19
	15	0.26	0.06
	20	0.18	0.01
14.8	10	0.40	0.25
	15	0.27	0.07
	20	0.21	0.02

The suite of calculations used a tensile strength of 0.07 ±0.3 MPa (10 ±5 psi) for gas pressures below 14 MPa. This is very conservative because brine saturation is below 0.5 for any gas pressure above 8 MPa. As the strength data are based on saturated conditions, the average tensile strength inherently reflects the lowest expected strength conditions. At pressures between 14 MPa and lithostatic, a tensile strength of 15 ±5 psi is used, representing a very conservative strength distribution when the repository is dry.

These volumes are independently corroborated by directly analogous experience in coal seam methane production, where cavity development and physical models for the formation response to high gas pressures and intentionally introduced gradients have been examined in detail. Applying conditions closely paralleling the mechanistic conceptual model for spalling, industry experience and associated analytical calculations show cavity development to be very limited and conservatively approximated by the computational techniques used in the mechanistic spalling model.

The results presented in Table 1-1 indicate that release volumes presented in the CCA, which vary between 0.5 and 4 m^3, are conservative with respect to the releases predicted by the new mechanistically based spalling model. The volumes used in the CCA are conservative at all probabilities.

1.2 Summary of Text

Sections within this report include details from several complementary paths taken to evaluate spall phenomena. Investigation into the waste form, strength, and future states of the repository establish expected conditions in the underground. Analytical and numerical computational approaches have been used to implement the conceptual model. Computational results for the physical system are compared to and corroborated by analog experience. The predicted volumes for spall releases are compared to spall releases currently used in the CCA. The executive summary continues with a synopsis of major elements of this report.

1.2.1 Form and Strength of WIPP Waste

A number of potential future states of the repository are possible at the time of an intrusion. Those in which spall releases may occur are limited because, for spall to occur, gas pressure in the waste must be greater than 8 MPa, the pressure of the mud column. The state of the waste is such that a reasonable tensile strength and cohesion are anticipated for the waste, while the waste itself will consist of varying particulate sizes, including moderate to large pieces that will be difficult to remove through gas flow.

The conditions necessary for a large spall release include extremely high gas pressures, fine particle sizes, and absence of strength. High gas pressures require significant microbial degradation and some corrosion. However, even when biodegradation and corrosion occur, pressures near lithostatic are rarely developed in the performance assessment for the WIPP. Degradation processes would produce a layered, blocky structure comprising a substantial percentage of undegraded waste. Natural compression of degrading waste will produce a consolidated medium that is cemented to varying degrees by salt precipitate and corrosion reaction products. Taken separately, each of the primary driving influences for a large spall release is unlikely to develop. Simultaneous attainment of high gas pressure, fine particle sizes, and absence of strength is a low probability event.

Surrogate materials for mechanical properties determination were derived by logically tracing degradation processes and evolution of the underground setting from the CCA performance assessment. Beginning with a known inventory of materials placed in the WIPP, products of reactions were used to assemble relevant surrogates. Mechanical testing emphasized conservative, saturated conditions. Strength of degraded waste increases as saturation decreases because halite precipitation provides cement between particles. Brine saturation decreases as gas pressure in the repository increases. For example, pressures above 14 MPa always have saturations less than 0.25.

Permeability, failure strength, and elastic constants have been determined for saturated waste. Tensile strength of saturated samples averages 0.074 ±0.04 MPa. Unconfined compressive strength of saturated samples ranges from 0.32 to 1.4 MPa. The angle of internal friction is high (44.4°), indicating a pressure-sensitive material. Poisson's ratio is approximately 0.35, Young's modulus is approximately 300 MPa, and permeability is of the order of 4×10^{-15} m^2.

Any drying increases strength of the degraded waste surrogate material, as would be expected to occur in the repository when gas pressures are highest. Tensile strength, averaging 0.074 MPa in the saturated state, increases to an average of 0.151 MPa in the dry state. Conditions of high gas pressure in the repository favor increased strength because of precipitate cementation in the drier environments.

1.2.2 Computational Approaches

In response to concerns expressed by the CMPRP, the DOE has reevaluated the model used in the CCA and has proceeded to develop refined models that include realistic representation of the waste as well as a more comprehensive evaluation of the various mechanisms that might lead to a spall release. Given a borehole intrusion into the repository, the release of material through spalling is a possibility if the gas pressures are in excess of about 8 MPa. If gas pressures in the waste are less than 8 MPa, there is no mechanism to drive spalling, so drilling will continue, and waste could only be transported to the surface by the cuttings and cavings mechanisms.

When the wellbore intersects the disposal room at pressures above 8 MPa, gas will flow into the wellbore and eject the mud in the hole at a rate controlled by the wellbore hydraulics and the deliverability of the gas reservoir. Calculations show that evacuation of mud requires between about 50 and 100 seconds, with the bottomhole pressure falling relatively slowly during this unloading period. As the wellbore depressurizes, pressure gradients are created in the waste. If these gradients are steep enough, the combination of low wellbore pressures and higher near-wellbore pore pressures can lead to tensile effective stresses. Calculations show that because of the combination of relatively slow depressurization as the wellbore unloads and a relatively high permeability of the waste, significant tensile regions are only predicted for the very high initial gas pressures. Shear stresses in excess of a possible Mohr-Coulomb yield stress can also occur. These effects will likely induce localized fracture and increased permeability, rather than immediate material removal. Given the small volumes of fractured material computed, it is conservatively assumed that all material failed in tension is available for transport to the surface.

After these very early time mechanical effects, spalling may continue due to other mechanisms related to the drag effects from flowing gas. These mechanisms include erosion due to the flow of gas over surfaces with loosened materials; however, volumes produced by these mechanisms

Draft for Technical Review — 5/1/97

are found to be small unless the material is previously fractured and disaggregated. Under some realizations the effective stresses prior to intrusion are zero, which implies a potential for liquefaction. The computational approaches include liquefaction explicitly, but this condition does not persist near the borehole due to relatively high tangential stresses and waste cohesion.

Semi-analytic Calculations

A semi-analytic approach has been implemented to represent the borehole intrusion and waste response and to predict failed volumes. This approach simulates transient fluid flow with cavity growth. Wellbore unloading has been calculated through an analytical solution to slug flow, through coupled pipe flow, and through approximate transient gas reservoir flow solutions. Stresses have been calculated using spherical and cylindrical analytical solutions for a poroelastic material.

In the cavity growth method, the bottomhole pressure during mud ejection is calculated as a function of time by coupling the mass flux from the reservoir with the equations of motion for the mud. Pore pressure gradients in the waste (and mass flux from the waste) are calculated using a numerical solution for transient porous flow. These bottomhole pressures and pore pressure gradients are used to calculate radial effective stresses, using an analytical solution for spherical geometry, and hence to estimate failed volumes. Effective tension in excess of the tensile strength is assumed to result in failure and fragmentation of the waste.

Calculations using the cavity growth method show that for repository gas pressures below 14 MPa there is little or no tensile failure predicted under realistic but conservative assumptions. At gas pressures above 14 MPa, predicted volume of failed material increases. The cavity growth model is used as the primary calculational basis for failed volumes because it can dynamically couple the borehole hydraulics with a growing cavity in the waste. Calculated failed volumes are presented in the last section (1.2.5) of this summary, where they are compared graphically to those of the CCA.

1.2.3 Numerical Calculations

Numerical techniques, used to validate analytical methods, simulate the processes of two-phase pressure decay within the waste region following a drilling intrusion and the mechanical response of the waste formation to stresses induced by the changing pore pressure field. Numerical calculations simulate a waste panel conceptualized as a cylindrical volume. The radius of the cylinder is approximately 60 m, and its height is 2 m. A drill bit is assumed to penetrate at the center of the panel. The mesh for the cylinder is finely gridded (on the order of 1 cm radial and vertical extent) in the immediate vicinity of the drilling intrusion, with mesh size increasing in a regular manner with distance from the wellbore. Calculations have been made for gas pressures as high as lithostatic (14.8 MPa) and an initial wellbore pressure of 8 MPa. Each numerical simulation was run to highlight certain features controlling failure of degraded waste releases, as discussed below.

Fluid Flow Calculations

Pore pressure decay due to two-phase flow (brine and gas) was simulated using the TOUGH28W (Version 2.0) multiphase flow code. A "base case" model was developed to assess the depressurization process assuming a drill string instantaneously depressurizes the waste room.

This represents a conservative, upper bound of the resultant pore pressure gradients that could occur. The waste was assumed to consist of a homogeneous material with permeability and porosity consistent with realizations in the CCA. The drill string and annulus were assumed to have the same geometry as that used for the CCA intrusion scenarios.

In addition to these base case calculations, the influence of heterogeneity in the waste was considered. In the first set of heterogeneous calculations undertaken, an ordered variation in the waste properties was considered. Waste at the top of the room, comprising mechanically compressed, relatively undegraded waste, was assumed to have a high permeability and porosity. The lower regions of the room, consisting of degraded waste, degradation products that have migrated downward, and a higher brine saturation, were assumed to have a lower permeability and porosity. A fully random approach to waste heterogeneity was also evaluated. Five material types were ascribed to the waste, each having a different permeability. The grid elements were then randomly assigned to one of these material types. Evaluation of the effects of heterogeneity leads to the conclusion that results of the homogeneous models are highly conservative.

Mechanical Calculations

Mechanical response was evaluated using SPECTROM-32, Version 4.09 to calculate the poro-mechanical response of the simulated region, using pore pressure gradients supplied from the TOUGH28W calculations. In poromechanical simulations, the equilibrium equations are in terms of effective stresses, which are proportional to the forces acting on the waste matrix. Only changes in these forces can cause deformation (strain) of the waste. The two approaches used to calculate the effective stress states resulting from the given pore pressure field are as follows:

1. A poroelastic response (no plastic deformation) assumes that the material continues to accept load, regardless of the magnitude of the tensile stresses present. This approach therefore calculates the maximum volume within the domain that can be subjected to tensile stresses.

2. A limited tension response (incremental plasticity) tracks propagation of material failure that leads to fragmentation of the waste. This propagation of material failure causes redistribution of the stresses in the waste from the states predicted using the poroelastic model.

Two calculation sets have been completed using the base case pressure gradients provided by the TOUGH28W model. In the first set, a tensile failure criterion appropriate for the waste is assumed. The volume of material that experiences tensile failure depends on the chosen failure criterion and associated parameter values.

The second calculation considered the influence of inelastic material response on the mechanical response. For the extreme case of zero effective stress, the volume subjected to tensile failure for this limited tension model was approximately 10% of that predicted using the linear elastic model. This calculation demonstrates that failure volumes predicted using the linear elastic model are highly conservative.

Computational approaches that implement the mechanistic spall model vary in their relative sophistication and conservativeness. For example, the cavity growth model accounts for detailed wellbore hydraulics and cavity expansion, which lowers pressure gradients at the growing void surface. However, it is limited to one-dimensional cylindrical or spherical geometries. The full numerical calculations can model transient pressure gradients in nonspherical geometries and simultaneously allow inelastic deformation, thereby reducing stresses within the waste. In their

respective application to the spall model, each analysis technique provides insight to the governing phenomena. Using these calculations, the physics of the processes can establish trends under different conditions. The more basic calculations corroborate the cavity growth model, which by including fewer simplifications provides a more realistic evaluation of failed volumes. The fully coupled numerical simulations provide the ability to examine other important processes applicable to the conceptual model and are the most difficult of the three analysis techniques to implement.

1.2.4 Analogs

After evaluating published data from various engineering disciplines, several situations from the petroleum industry were selected for further evaluation as analogs to the spall of waste. These included wellbore stability during drilling, the production of formation particulates during depletion/production of the reservoir itself, the flowback of proppant from hydraulic fractures, and dynamic open hole cavitation of coalbed methane seams. Coalbed methane industry experience provides several similarities to the spall process, including material response to rapid pressure drop. Cavitation is most commonly attempted in the San Juan Basin of New Mexico and Colorado (it is successful only in parts of this basin because cohesion of coal in this area often prevents cavity growth). Material properties of this coal and the surrogate waste material for the WIPP site are remarkably similar. Material properties of the surrogate waste material possess strength properties sufficient to preclude cavity development and growth based on analogous industrial experience.

Cavitation of coalbed methane reservoirs, sometimes called dynamic open hole cavitation, employs a series of surging cycles to create a cavity across the coal zone. Two variations on the surging process are typically carried out: natural surging and injection surging. During natural surging, the well is shut-in (a valve is closed at the surface) before being abruptly opened for blowdown. During this blowdown period, gas, air, and sometimes solids are violently ejected. This process is repeated numerous times over a ten to fifteen day period. This analog has direct relationship to the WIPP because of the similarity in the material properties of coal to those for the WIPP surrogate materials and because of the similar pressure conditions and the fact that gas is the flowing fluid. Differences include the rapid, intentional depressurization of the coal seams compared to the somewhat slower depressurization expected at the WIPP because of mud blowout. Other differences include the fact that only one surging cycle is represented at the WIPP site, whereas multiple surging and shut-in cycles are imposed in coalbed methane cavitation situations.

Documented mechanical properties from coal are presented and compared with the WIPP site surrogate data. Public domain, numerical simulation data for single cycle (only one surge and instantaneous pressure reduction) are also presented. These published simulations were performed with one of the petroleum industry's most advanced, fully coupled flow and deformation models (originally developed for modeling unconsolidated oil sands in Alberta). Single phase, transient gas flow was represented. The model tracked changes in permeability resulting from changes in stress and/or volumetric strain, and allowed for the development of cavitation when tensile failure occurred. The input data and boundary conditions for these coalbed simulations are compared with the WIPP site conditions.

The published results for this analogous coalbed methane situation indicated no increase in the original wellbore dimensions as a consequence of instantaneous pressure reduction for cohesion greater than 0.1 MPa. The cohesion of the WIPP site surrogate material exceeds this limiting value, even in the saturated condition. This analog strongly suggests that the cohesive strength of WIPP degraded waste will prevent cavity growth and will prevent the creation of spalled material with depressurization of the wellbore.

A consideration of analogs from evaluations of sand production and wellbore stability have shown that the methods used in the semi-analytic studies are appropriate and have highlighted the relevance of several parameters, including cohesion and the effects of capillary tensions. In addition, these analogs have highlighted the essential conservatism of most analytic approaches based on continuum mechanics. As noted by Fairhurst (1990), these analytic models commonly underestimate the integrity of the formation and thus will tend to overestimate spall releases. As shown by many other studies, this is especially true when linear elastic methods are used and nonlinear effects and plasticity are ignored. An evaluation of various analogs from petroleum engineering has allowed the semi-analytic methods used to be validated.

1.2.5 Release Volumes

Current results, summarized earlier in Table 1-1, indicate that the spalling volumes from the mechanistic model are always less than the minimum volume for a CCA spalling event. The maximum spalling volume from the mechanistic model, 0.25 m^3, is a factor of 2 less than the minimum spalling volume in the CCA, 0.5 m^3. Comparing these volumes to the CCDF in the CCA requires consideration of the probability that these volumes are released. The impact to the CCDF is demonstrated in Figure 1-2.

A spalling CCDF depends not only on the consequence of spalling events but also on the probabilities of specific spall events occurring. The new spalling model differs from the CCA model in that low or zero volume release events are much more probable because they span a wide range of initial repository pressures from 8 MPa to 14 MPa. An analysis of the mean CCDF for pressure at first intrusion shows that the pressure exceeds 14 MPa with a probability of only 0.01. Furthermore, second and subsequent intrusions at high pressure are extremely unlikely.

Based on these analyses, the DOE has demonstrated that the releases used in the CCA due to a spalling event are, in fact, greater than those determined by a variety of other methods, and are therefore reasonable for the purposes of evaluating compliance to 40 CFR 191.

1.3 Reference

Fairhurst, C. 1990. "General Report: Deformation, Yield, Rupture and Stability of Excavations at Depth in Rock," in *Rock at Great Depth*, Maury, V. and Fourmaintraux, D., Balkema, Rotterdam: 1103-1114.
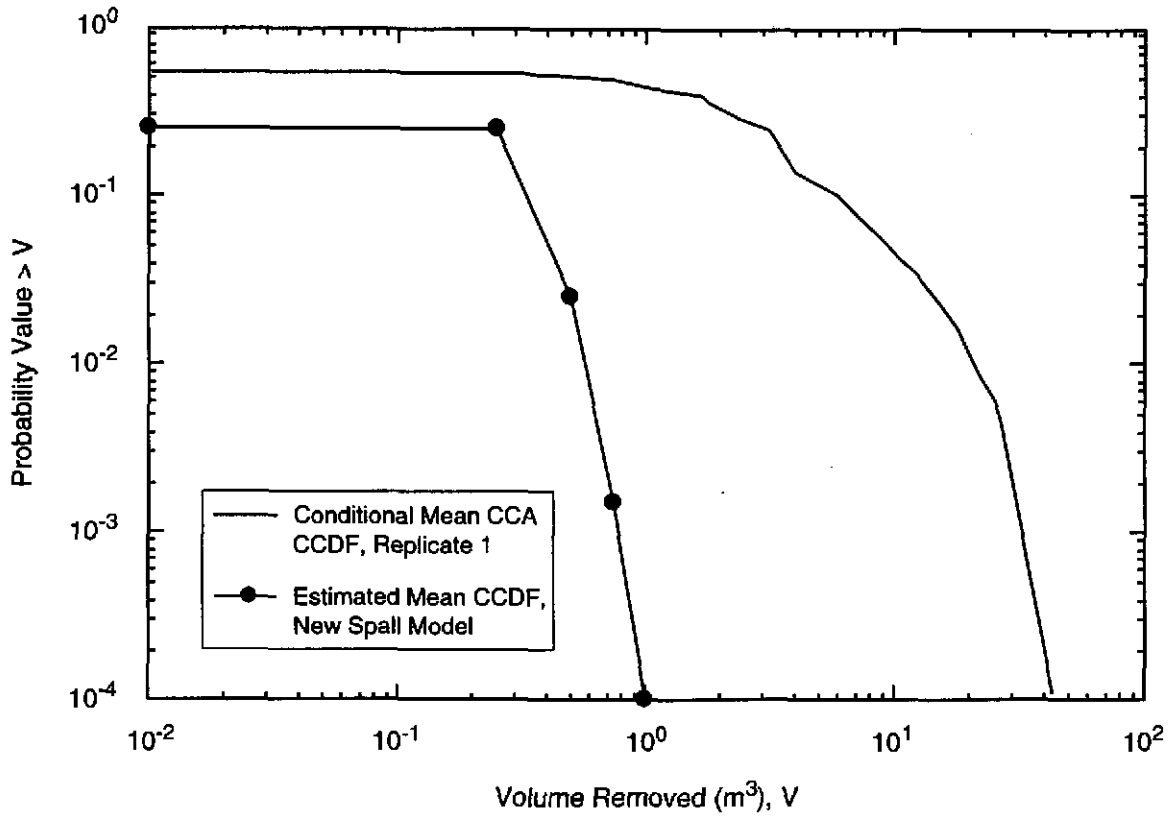
TRI-6121-436-0

Figure 1-2.   Comparison of effects of gas-pressure-dependent volumes from the new spalling model with the CCA conditional mean complementary cumulative distribution function.

Page intentionally blank

2.0 WASTE STRENGTH

This section discusses degraded waste strength, which greatly influences potential spall release. Evolution of the waste room and degradation of emplaced waste are discussed for the purpose of identifying suitable surrogate waste materials. A perspective from performance assessment (PA) regarding spall conditions is included. Utilizing the inventory of waste materials placed in the underground and following waste degradation through possible scenarios, recipes for surrogate products are determined. Specimens of representative degradation products have been fabricated and mechanically tested using standard laboratory procedures. Tests determine tensile strength, uniaxial and triaxial compressive strength, elastic constants, and brine permeability. Testing concentrates on the saturated state because it represents a conservatively low strength. Representative surrogate recipes derived from corrosion of 50% of the iron-based inventory comprise most test specimens because partial degradation is the expected condition. Sufficient experimental information has been collected for comparison between 50% and 100% degraded surrogate waste properties. Results from 38 tests are included in this report. For all tests on 50% degraded saturated surrogates, tensile strength ranges from 0.01 to 0.13 MPa, and unconfined compressive strength ranges from 0.32 to 1.4 MPa. Strengths of 100% degraded saturated surrogates are within these ranges. Poisson's ratio averages 0.35, Young's modulus is about 300 MPa, brine permeability is of the order of 4×10^{-15} m^2, and the angle of internal friction (ϕ) is approximately 45°. These results are used in semi-analytic and coupled numerical calculations of waste material response in the event of an inadvertent human intrusion at the WIPP.

2.1 Introduction

As noted by the Engineered Systems Data Qualification Panel, "degraded waste tensile strength can vary significantly." The Engineered Systems Panel recommended assigning distribution functions as a means of addressing strength uncertainties. We have chosen an empirical approach to reduce uncertainty in degraded waste strength. First the inventory of waste was surveyed and quantified. Degradation scenarios were evaluated to determine potential amounts of degraded product that would occur under the various predicted histories of the WIPP. Four evolutionary cases that capture the range of future states were developed. Based on these histories and operative degradation mechanisms, compositions of surrogate materials were defined. Experimental work emphasized conservative potential states, i.e., dominantly saturated conditions without MgO. Surrogate specimens were assembled by mixing degraded waste product and consolidating and saturating the mixture at pressures expected at the WIPP. Strength results were determined first because the new conceptual model for spall events is based on waste strength failure criteria.

Elements of these strength studies provide information on the range of potential forms of the waste (especially at the times and under the conditions at which spall events might occur) and are necessary to evaluate the resistance of degraded waste to spall release. The remainder of Section 2.0 presents results of several activities involved in determining surrogate degraded waste strength. First, salt creep is discussed because room closure greatly affects future states of the repository. Characteristics of the underground setting and the waste are described on the basis of room closure. Second, waste inventory and degradation history are used to develop surrogate combinations of materials for mechanical testing. Specimen preparation is discussed in some

detail. Testing techniques are recognized rock mechanics procedures and each technique is briefly summarized. A complete data summary is provided.

2.2 Waste States

The potential of solid material to discharge out the annulus of a drill string is governed by the evolution of the physical and mechanical properties of the emplaced waste materials. To examine a possible spalling event, estimation of waste degradation is necessary. Characterization of the setting over time begins with known initial conditions. Creep closure of the surrounding formation has been quantified through many *in situ* field-scale experiments, which validate the predictive capabilities of rock mechanics analyses. Mechanical response of waste drums as they are loaded by the creeping salt has been measured in the laboratory. Room closure and waste drum compression are relatively rapid processes. Over time, waste degradation and gas generation are postulated to occur. Characteristics of the underground setting can be followed logically to describe possible conditions that could exist at the time of a borehole intrusion. Characteristics of the waste (such as size, arrangement, strength, permeability, and porosity), coupled with gas pressure in the room, govern the potential for spalled waste volume release. The following subsections discuss evolution of the underground setting into which an inadvertent borehole could penetrate.

2.2.1 Amount of Compaction

The plastic flow qualities of salt are one of the primary reasons the National Academy of Sciences recommended bedded salt as a preferred medium for permanent storage of nuclear waste. Salt creeps readily into underground openings, thereby compressing and entombing waste emplaced in the excavations. Predictions of repository rock mechanics response benefit from several full-scale room closure experiments spanning periods greater than a decade. Rock mechanics models for salt creep have been validated against long-term field measurements to the extent that confidence in room closure expectations exists in the technical community. In a recent report the National Research Council WIPP committee notes that "as a result of an extensive rock mechanics research program, prediction of creep closure of repository excavations at WIPP is relatively straightforward" (NRC, 1996). On the basis of field measurements and validated constitutive models, prediction of room closure is understood and reliable.

Over the history of the WIPP studies, many calculations of room closure have been made. Several calculations of room closure performed with assorted materials placed in the rooms for longer times (Callahan and DeVries, 1994) show rapid closure for the first 50 years after excavation, then appreciable slowing after attaining closure of 50% or more, as illustrated in Figure 2-1. Compaction of room contents continues until the stress state reestablishes equilibrium. Waste compaction offers little resistance to creep closure for the first several decades, during which most closure occurs. Theoretically, gas generation could produce a backstress inhibiting closure, but the corrosion and microbial action necessary to produce gas proceed at rates that are slow compared to mechanical closure. In other words, waste and other materials placed in the repository disposal rooms will be compacted to a thickness of less than 2 m before gas pressures increase significantly.
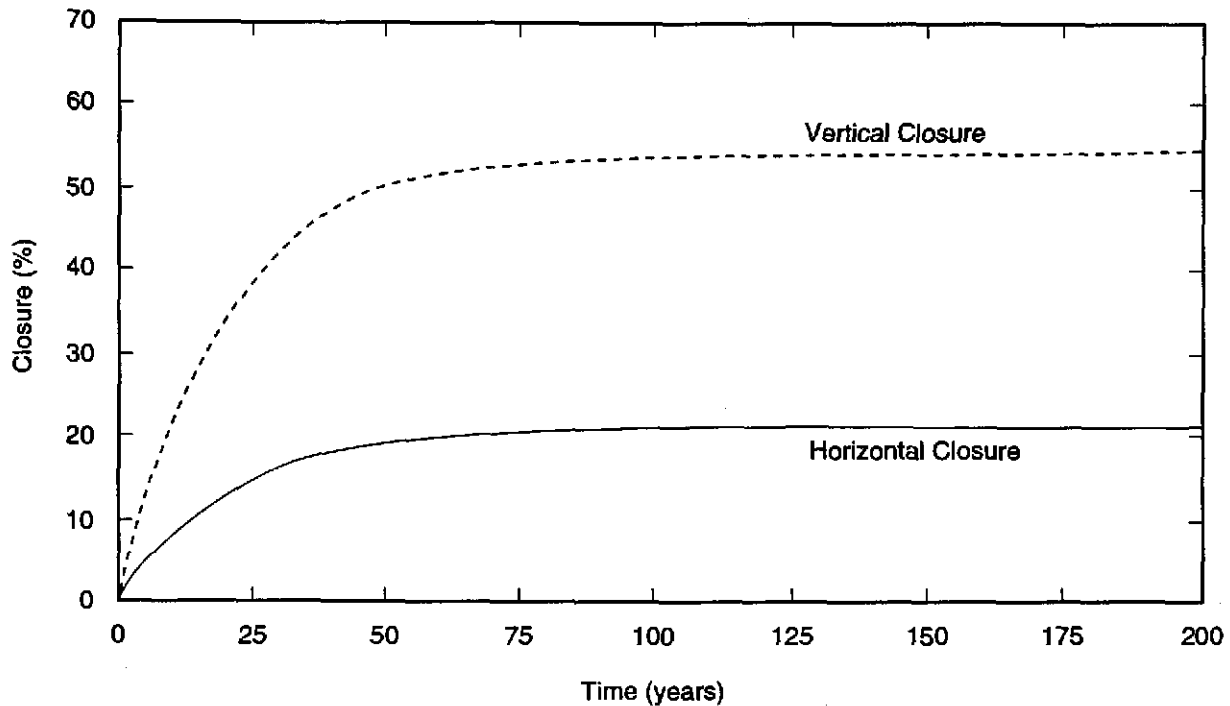
Figure 2-1. Room closure history of a disposal room filled with TRU waste and crushed salt (after Callahan and DeVries, 1994).

2.2.2 Waste Corrosion/Degradation

Conceptually, gas pressures in the WIPP are produced by corrosion of ferrous and nonferrous metals and by microbial degradation of cellulosic, plastic, and rubber waste constituents. A linkage can be developed between waste inventory and physical and chemical processes to quantify appropriate surrogate materials for degraded waste experiments. At the outset, it was decided not to specify the expected average waste condition but rather to emphasize extreme conditions in terms of degradation. Extreme conditions would be the most likely source for high pressure production and would also require ample brine. It was further recognized that more fully degraded waste leads to smaller average particulate sizes, most susceptible to gas transport in a spall event.

Salado brine will slowly enter the repository through brine seeps and DRZ drainage. In the presence of water, chemical degradation of the waste will occur. The corrosion of iron-bearing metals, aluminum, copper, and lead; the microbial-induced destruction of cellulosic materials; and the breakdown of solidification media lead to a decrease in the grain size of the initial waste constituents. The volume of metal-bearing solids in the repository will increase, however, as a result of corrosion reactions generating solid metal hydroxides, oxides, and carbonates.

Analysis of the vectors comprising the Compliance Certification Application (CCA) calculations shows that, in the undisturbed repository, corrosion of iron is limited by the availability of brine. In undisturbed cases, corrosion consumes up to a maximum of approximately 60 wt% of the iron present at the end of the 10,000-year performance period. The amounts of iron consumed at the time of the first spalling release are significantly less than 60 and 86 wt% for the undisturbed and disturbed cases, respectively. For the surrogate waste materials, we assume iron corrosion of 50 and 100 wt%.

2-3

Corrosion and microbial degradation of the waste are modeled in CCA calculations. Waste histories are expanded in a memorandum attached as Appendix A, which provides logic for surrogate mixtures. Initial repository inventory of waste materials is documented in the Baseline Inventory Report (BIR). Given the inventory, logical scenarios are followed through and a determination of the degraded and corroded residue is made. Representative surrogate materials are identified for the degraded waste residuals.

Waste emplacement at the WIPP is assumed to be a random distribution from the waste streams. Waste radionuclide content is considered homogeneous on that basis. However, in the analysis of possible spalling of materials, possible heterogeneous characteristics may have important implications. For example, heterogeneous layering of the waste is likely to result. A layered waste with less degraded material at the top represents one possible situation that would limit potential spall volumes because of large particle size. Layered heterogeneity is evaluated along with analyses of more fully degraded, uniformly weak degraded waste.

2.2.3 Surrogate Materials

Development of surrogate waste materials begins with definitions of waste categories and their degradation products for cases of metal corrosion, microbial degradation of cellulosics, and microbial degradation of plastic and rubber. The probabilities of these processes are sampled in CCA calculations. Surrogate mixtures are defined for four waste degradation and MgO backfill emplacement scenarios. Several mixtures representing the degraded waste are developed.

Degradation scenarios representing four representative cases are defined in Appendix A. They include:

1. A 50% case where half of the iron is corroded and half of the cellulosics, plastics, and rubber are degraded.
2. A 100% case where all of the iron is corroded and all cellulosics, plastics, and rubber are degraded.
3. A 50% case with MgO, which is identical to Number 1 above with an appropriate amount of MgO added.
4. A 100% case with MgO, which is identical to Number 2 above with an appropriate amount of MgO added.

The initial characteristics of WIPP waste are described in the TRU Waste Baseline Inventory Reports (US DOE, 1995; 1996). The following waste categories and descriptions in Table 2-1 are taken from the BIR.

The extent of corrosion of iron-bearing materials and steel waste containers is constrained by parameters used in the CCA calculations. It is likely that the extent of degradation of iron-bearing materials will be affected by their initial surface-to-volume ratio and the vertical position of the waste in the repository.

The saturation of the repository is uncertain, depending on location, time following closure, and the values of sampled parameters. The existence of a gas phase may limit the corrosion of the materials in the upper portions of the repository, but downslope areas of the repository tend to have higher brine saturations.

Table 2-1. Waste Concentrations

Waste Category	Inventory, average (kg/m³)	Inventory without MgO backfill (wt%)	Inventory with MgO backfill (wt%)
Iron-base metal, alloys	170	22	14
Steel container material	139	18	12
Aluminum-base metal, alloys	18	2	1
Other metal, alloys	67	9	6
Other inorganic materials	31	4	3
Vitrified	55	7	5
Cellulosics	54	7	4
Rubber	10	1	1
Plastics	34	4	3
Plastic container/liner material	26	3	2
Solidified inorganic material (including the cement)	54	7	4
Solidified organic material (not including the cement)	5.6	1%	0%
Solidification cement	50	7%	4%
Soils	44	6%	4%
MgO backfill	451	0%	37%

Table 2-2 is a summary of representative surrogate materials. Further discussion is provided in Appendix A. For degraded iron and small quantities of other corrodible metals, rusted metal and crushed limonite-goethite-rich rock samples are used. As iron corrodes to $Fe(OH)_2$ there is an increased volume, on a mole-per-mole Fe basis, of about 1.6, which is taken into account in developing waste mass distributions.

Many of the materials listed in the BIR categories "other inorganic materials" and "vitrified" are essentially inert at 20–25°C. In Cases 1 and 3—where one-half of the material is degraded—disaggregated paper, plastic, and rubber scraps are used. Degradation of cellulosics may be accompanied by the formation of humic materials, and peat is designated as an appropriate surrogate. Concrete and Environstone are simulated with pulverized dried concrete and gypsum board. The texture of sludge solidified in the case of the "solidified organic material" category is captured by the finer-grained component of the pulverized concrete and gypsum board. The soil component can accurately be represented with natural soil.

Table 2-3 is a summary of the constituents representing each case. Testing reported here includes only one surrogate specimen having an MgO constituent. Recipes from Case 1 and Case 2 are used for the greatest number of tests. A sufficient number of strength properties are developed for these surrogates to define a range of these conservative cases. In addition, testing was performed most frequently on saturated specimens.

Table 2-2. Degraded Waste Surrogate Materials

Waste Category	Example Waste Simulants
Iron-base metal, alloys; steel container material	strips of steel sheet metal, small nails (cut up), scraps of steel or iron
Corroded iron-base metal, alloys; steel container material	scrapings from rusted steel or iron; supplement with Fe(III)O.OH (goethite or limonite rock samples) crushed sand- to silt-sized particles
Corroded nonferrous metal and alloys	as above for corroded iron-base metal, etc.
Other inorganic materials; vitrified	broken labware, broken glassware
Cellulosics + rubber; plastics; plastic container/liner material	equal masses of (a) finely shredded paper, snipped cotton balls, sawdust, shredded plastic grocery bags, o-rings, rubber gloves, rubber bands, polyethylene sheet and bottles (all comminuted with a blender or other means) + (b) peat (no vermiculite)
Solidification cement	broken hydrated concrete and mortar, crumbled sheet-rock
Soils	natural soil
MgO backfill	commercial pellets

Table 2-3. Mass of Material in Test Specimens (kg)

Material	Case 1	Case 2	Case 3	Case 4
Iron, not corroded	1.9	0	1.2	0
Corroded iron and other metals	4.6	7.3	3.0	4.8
Glass	1.0	1.0	0.7	0.7
Cellulosics + plastics + rubber	0.7	0	0.5	0
Solidification cements	1.2	1.2	0.8	0.8
Soil	0.5	0.5	0.3	0.3
MgO backfill	0	0	3.5	3.4
Salt precipitate, corrosion-induced	0.47	0.90	0.30	0.60
Salt precipitate, MgO-induced	0	0	0.57	0.57
Total batch size	**10.4**	**10.9**	**10.9**	**11.2**

2.3 Specimen Preparation and Test Procedures

2.3.1 Specimen Preparation

A process for fabricating test specimens from a variety of waste surrogate constituent materials was developed. Constituents of surrogate specimens and fabrication processes were modified in response to development of degradation scenarios. A vast majority of tests were performed on the two most applicable "recipes" delineated in the rationale for waste surrogates discussed in Appendix A. These recipes include masses of materials listed in Table 2-3 for Case 1 and Case 2. The constitution of each test specimen is fully documented in the Quality Assurance scientific notebook.

Tables 2-4 and 2-5 itemize constituents of all recipes used for surrogate specimens. Tables 2-6 through 2-9 provide a complete summary for each specimen, including the recipe, consolidation history, and test conditions.

Table 2-4 Specimen Ingredients, Recipes 1 through 3

Batch Ingredient	Relative Weight Proportions for Recipes Specimen Identification Numbers			
	Recipe 1	Recipe 2		Recipe 3
	S1	S2 & S3	S4 &S5	S6 & S7
Iron				
Clean nails	3.00	0	0	0
Rusted	0	3.05	3.04	0
$FeCl_3$	2.00	0	0	0
Fe_2O_3	0	2.02	2.01	5.00
Glass	1.00	1.01	1.01	1.00
Cellulosics				
Cotton	0.10	0.10	0.09	0.10
Sawdust	0.90	0.90	0.77	0.90
Plastics/Rubber				
Plastic	0.81	0.96	1.01	1.00
Rubber bands	0.19	0	0	0
Crushed concrete	1.00	1.02	1.01	1.00
Soil	1.00	1.01	1.00	1.00
Crushed salt	2.00	2.04	2.00	2.00
Total Relative Batch Size	12.00	12.07	11.94	12.00

Table 2-5. Specimen Ingredients, Recipes 4 through 8*

Batch Ingredient	Relative Weight Proportions for Recipes Specimen Identification Numbers			
	Recipe 4	Recipe 5	Recipe 6	Recipe 8
	S8-S13, S19-S24	S14, S15, S17, S18, & S26	S16	S25
Scrap iron	1.90	0	1.20	0
Black Hills Bog iron	4.60	7.30	3.00	1.6 Fe(OH)$_2$
Glass	1.00	1.00	0.70	0
Cellulosics				
Paper	0.07	0	0.05	0
Cotton	0.07	0	0.05	0
Sawdust	0.07	0	0.05	0
Peat	0.07	0	0.05	1.67
Rubber bands	0.07	0	0.05	0
Rubber gloves	0.07	0	0.05	0
O-rings	0.07	0	0.05	0
Plastics				
- grocery bags	0.07	0	0.05	0
- sheeting	0.07	0	0.05	0
- bottles	0.07	0	0.05	0
Solidification cements				
Crushed concrete	0.60	0.60	0.40	0
Crushed gypsum	0.60	0.60	0.40	0
Soil	0.50	0.50	0.30	1.09
MgO backfill	0.00	0.00	3.50	0
Crushed salt precipitate	0.47	0.90	0.87	0.24
Total relative batch size	10.37	10.9	10.87	4.60

  * Note: Recipe #7 using MgO with 100% degraded waste has not been tested as of this writing. Recipe #8 represents a single drum of cellulosics and is not a surrogate defined in the original four degraded waste cases. It is included for completeness.

Table 2-6. Test Specimen Summary, S1 through S7

Specimen I.D.	Recipe Type	Prep. Date	Consolidation History						Test History		
			Machine No.	Duration [a] (hrs)	Length [b] (mm)		Diameter [c] (mm)		Date	Type [d]	Water Content @ Test (%)
					L_o	L_c	D_o	D_c			
S1	1	2/16/97	4	24.9	200	184	100	89	2/18/97	UCC	Wet
S2	2	2/18/97	4	17.4	200	184	100	82	2/19/97	UCC	Wet
S2-2 [e]					50	51	100	91	2/27/97	TWT	Air Dry
S3	2	2/19/97	4	18.4	200	193	100	87	3/4/97	UCC	Dry
S4/1	2	2/21/97	4	19.2	25	-	100	-	-	-	-
S4/2					50	52	100	86	2/25/97	BIT	Dry
S4/3					50	44	100	88	3/4/97	TWT	Dry
S4/4					50	49	100	93	3/4/97	TWT	Dry
S4/5					25	-	100	-	-	-	-
S5/1	2	2/21/97	3	14.3	25	-	100	-	-	-	-
S5/2					50	51	100	89	3/4/97	TWT	Dry
S5/3					50	46	100	88	3/4/97	TWT	Dry
S5/4					50	-	100	-	-	-	Defective
S5/5					25	-	100	-	-	-	-
S6	3	2/26/97	4	44.8	200	166	100	76	3/1/97	QS [f]	Wet
S7	3	2/27/97	3	26.5	200	192	100	70	3/5/97	UCC	Dry

(a) Consolidation stage performed at a hydrostatic stress of 15 MPa. (b) L_o = initial length, L_c = length after consolidation stage. (c) D_o = initial diameter, D_c = diameter after consolidation stage. (d) UCC = unconfined compression test, TWT = thick-walled hollow cylinder tension test, BIT = Brazilian indirect tension test. (e) Represents a thin disk cut from S2 after the UCC test was performed. (f) QS = quasistatic compression test performed at a confining pressure of 0.05 MPa and a pore pressure of 0.01 MPa.

Table 2-5. Test Specimen Summary, S8 through S14

Specimen I.D.	Recipe Type	Prep. Date	Consolidation History						Test History		
			Machine No.	Duration [a] (hrs)	Length [b] (mm)		Diameter [c] (mm)		Date	Type [d]	Water Content @ Test (%)
					L_o	L_c	D_o	D_c			
S8	4	3/2/97	4	20.2	200	188	100	80	3/5/97	UCC	Dry
S9/1	4	3/2/97	3	19.9	25	-	100	-	-	-	-
S9/2					50	56	100	97	3/7/97	BIT	Dry
S9/3					50	51	100	97	3/7/97	BIT	Dry
S9/4					50	43	100	97	3/7/97	BIT	Dry
S9/5					25	-	100	-	-	-	-
S10	4	3/3/97	4	15.0	200	172	100	87	3/4/97	UCC	Wet
S11	4	3/3/97	3	14.3	200	183	100	84	3/5/97	UCC	Moist
S12	4	3/4/97	4		200	171	100	86	3/5/97	UCC	Wet
S13/1	4	3/4/97	3	16.5	25	-	100	-	-	-	-
S13/2					50	-	100	-	-	-	Wet
S13/3					50	51	100	95	3/8/97	BIT	Wet
S13/4					50	47	100	91	3/8/97	BIT	Wet
S13/5					25	-	100	-	-	-	-
S14	5	3/5/97	4	16.7	200	165	100	92	3/7/97	Perm	Wet
					200	165	100	92	3/8/97	QS [e]	Wet

(a) Consolidation stage performed at a hydrostatic stress of 15 MPa for S1 through S11 and 5 MPa for S12 through S14. (b) L_o = initial length, L_c = length after consolidation stage. (c) D_o = initial diameter, D_c = diameter after consolidation stage. (d) UCC = unconfined compression test, TWT = thick-walled hollow cylinder tension test, BIT = Brazilian indirect tension test. (e) QS = quasistatic compression test at a confining pressure of 1 MPa and a pore pressure of 0.01 MPa.

Table 2-8. Test Specimen Summary, S15 through S20

Specimen I.D.	Recipe Type	Prep. Date	Consolidation History							Test History		
			Machine No.	Duration [a] (hrs)	Length[b] (mm)		Diameter[c] (mm)			Date	Type[d]	Water Content @ Test (%)
					L_o	L_c	D_o	D_c				
S15/1	5	3/5/97	3	15.7	25	-	100	-		-	-	-
S15/2					50	TBD[f]	100	TBD[f]		TBD[f]	TBD[f]	TBD[f]
S15/3					50	54	100	93		3/8/97	BIT	Wet
S15/4					50	42	100	92		3/7/97	BIT	Wet
S15/5					25	-	100	-		-	-	-
S16[e]	6	3/6/97	NA	NA	105	NA	52	NA		3/8/97	UCC	Wet
S17	5	3/6/97	4	13.9	200	180	100	73		3/8/97	UCC	Wet
S18/1	5	3/6/97	3	12.8	25	-	100	-		-	-	-
S18/2					50	TBD[f]	100	TBD[f]		TBD[f]	TBD[f]	TBD[f]
S18/3					50	42	100	92		3/8/97	BIT	Wet
S18/4					50	41	100	95		3/7/97	BIT	Wet
S18/5					25	-	100	-		-	-	-
S19/1	4	3/8/97	4	15.3	50	58	100	91		3/9/97	TWT	Wet
S19/2					50	51	100	93		3/9/97	TWT	Wet
S20	4	3/8/97	3	Leaked	-	-	-	-		-	-	-

(a) Consolidation stage performed at a hydrostatic stress of 5 MPa for S15 and S17 through S18. No consolidation stage for S16. (b) L_o = initial length, L_c = length after consolidation stage. (c) D_o = initial diameter, D_c = diameter after consolidation stage. (d) UCC = unconfined compression test, TWT = thick-walled hollow cylinder tension test, BIT = Brazilian indirect tension test. (e) Specimen was not subjected to a consolidation stage. (f) TBD = to be determined/designated.

Table 2-9. Test Specimen Summary, S21 through S26

Specimen I.D.	Recipe Type	Prep. Date	Consolidation History							Test History		
			Machine No.	Duration [a] (hrs)	Length[b] (mm)		Diameter[c] (mm)			Date	Type[d]	Water Content @ Test (%)
					L_o	L_c	D_o	D_c				
S21/1	4	3/9/97	4	19.2	50	53	100	94		3/11/97	TWT	Wet
S21/2					50	64	100	94		3/11/97	TWT	Wet
S22/1	4	3/9/97	3	18.4	50	51	100	94		3/11/97	TWT	Wet
S22/2					50	62	100	94		3/11/97	TWT	Wet
S23	4	3/10/97	4	14.7	200	190	100	93		3/12/97	QS[e]	Wet
S24	4	3/10/97	3	13.9	200	191	100	91		3/11/97	Perm	Wet
S25	8	3/11/97	4	16.3	200	158	100	81		3/12/97	UCC	Wet
S26	5	3/11/97	3	15.6	200	190	100	74		3/12/97	UCC	Wet

(a) Consolidation stage performed at a hydrostatic stress of 5 MPa for S15 and S17 through S18. No consolidation stage for S16. (b) L_o = initial length, L_c = length after consolidation stage. (c) D_o = initial diameter, D_c = diameter after consolidation stage. (d) UCC = unconfined compression test, TWT = thick-walled hollow cylinder tension test, BIT = Brazilian indirect tension test. (e) QS = quasi-static compression test performed at a confining pressure of 1 MPa and a pore pressure of 0.01 MPa.

Specimen preparation was limited to the preparation of surrogate waste specimens having solid cylindrical shapes, or thick-walled cylinders having a circular hole through the central axis of the cylinder. The process for preparing surrogate waste specimens required a number of sequential steps, including:

- preparation of raw materials
- weighing and mixing raw materials in proportions according to a prescribed recipe
- placement of the mixture in molds
- saturation of the mixture with brine
- consolidation of the mixture using hydrostatic stress
- extraction of the consolidated specimen from the mold
- trimming or machining (if necessary)
- specimen drying (if applicable).

Each step is described in further detail in the laboratory scientific notebook. The surrogate waste comprised raw materials including iron, glass, cellulosics, rubber, plastic, solidification cements, soil, and simulated precipitates of WIPP crushed salt. In general, each of these materials required some pretreatment to achieve particle or piece sizes appropriate for the finished specimen size. The iron constituent included simple iron (e.g., nails, rusted steel, scrap iron, etc.) and simulated decomposed iron (Fe_2O_3 and bog iron or goethite). The glass constituent comprised broken window pane glass approximately 2 to 3 mm thick that passed a 9.5-mm sieve. The cellulosics constituent included paper, cotton, sawdust, and peat. The sawdust and peat were used as received, while the cotton was separated into thin strands by hand. Paper was cut into squares measuring approximately 6 to 8 mm on a side. The rubber constituent, which included O-rings, rubber bands, and rubber gloves, was cut to produce pieces having no dimension that exceeded approximately 6 to 8 mm. The solidification cements comprising concrete and gypsum and crushed salt passed a 9.5-mm sieve. Laboratory-grade MgO product was added to one specimen.

Mixtures were placed in a mold configured appropriately for the type of specimens to be produced: i.e., (1) solid cylinders with length-to-diameter ratios (L:D) of 2; (2) solid cylinders with L:D of 0.5 and a nominal diameter of 100 mm; and (3) thick-walled hollow cylinders with an inside diameter of 30-mm, an outside diameter of 100 mm, and a length of 50 mm. The mold was formed by securing a two-component jacketing system including a 1.6-mm-thick lead inner jacket and a flexible Viton outer jacket sealed to metal endcaps. Porous felt metal was placed in the interface between the endcap and the surrogate mixture. After the raw constituents had been molded, the specimen was saturated with NaCl brine by connecting the vent of the bottom endcap to a brine reservoir with a hydraulic surface located at an elevation above the vent in the top endcap. Brine was permitted to flow from the reservoir through the specimen and out the top endcap. Saturation of the specimen was assumed when the brine effluent from the top vent ran freely with no entrapped air bubbles. The brine was produced by saturating distilled water with finely ground salt recovered from the WIPP.

All but one of the saturated specimen/mold assemblies was placed inside the pressure vessel of a standard triaxial compression machine and the annulus between the specimen mold and walls of the pressure vessel was filled with silicone oil. These specimens were consolidated (densified) under a hydrostatic stress of either 5 or 15 MPa. Initial tests consolidated the specimens to the approximate full lithostatic mean stress. Later, to be conservative, consolidation to a lower stress

of 5 MPa was implemented. One MgO specimen, S16, was not subjected to a consolidation stage. Instead this specimen remained at ambient pressure for a period of 48 hours to provide preliminary evidence of the strength contribution provided by MgO.

To evaluate effects of unsaturated specimens, some specimens having different water contents were prepared by drying the specimens for varying lengths of time either in an oven at approximately 40°C or at room temperature and humidity. Water contents at the time of mechanical properties testing were determined after the tests were completed by drying the specimens to constant mass in an oven at temperatures ranging from 40 to 95°C. The water contents were expressed as a weight percentage of the dry specimen weight.

2.3.2 Test Procedures

It is the goal of this effort to quantify surrogate waste material strength and deformational properties that can be implemented in the rock mechanics calculations of failed zones caused by inadvertent borehole intrusion. Testing approaches include tensile strength measurements, uniaxial compression, and triaxial compression tests leading to development of failure criteria. Test conditions emphasize the saturated state, although some tests are conducted in an unsaturated condition. The following text describes the test techniques employed.

2.3.2.1 Tensile Strength

The ideal test configuration for tensile strength is a "dog bone" specimen in uniaxial tension. We could not fabricate a dog-bone configuration in short order, so two alternative techniques were used: the Brazilian indirect method and thick-walled hollow cylinders. These sample geometries were conducive to our specimen preparation apparatus. The Brazilian technique applies a compressive state to induce a tensile field, assuming an elastic solution. The indirect technique is probably satisfactory for partially dry (stiffer) surrogate waste, but the saturated specimens were sufficiently ductile that tensile stress state predicted by elastic solutions might not be applicable. An alternative test technique using hollow cylinders was also used for saturated specimens. Further evaluation of test techniques may be appropriate to reduce uncertainty of reported results.

Indirect Tensile Tests. The Brazilian indirect tension test was one means used to assess the tensile strength of surrogate waste specimens. This method is termed an indirect method because a compressive line load is applied over the length of a cylindrical specimen having an L:D of approximately 0.5. The compressive load induces a tensile stress at the center of the specimen perpendicular to the applied line load. As the compressive line load increases, so does the tensile stress. When the tensile stress becomes equivalent to the tensile strength of the specimen, failure occurs. Failure is generally denoted by both a drop in the applied compressive line load and the simultaneous formation of a fracture parallel to the direction of the applied line load. The tensile strength is computed according to

$$T_o = \frac{2P}{\pi DL}$$

where:

T_o	=	Tensile strength, MPa
P	=	Line load at failure, MN

D	=	Specimen, diameter, m
L	=	Specimen length, m

Thick-Walled Tensile Tests. The thick-walled hollow cylinder tension test was one means used to assess the tensile strength of surrogate waste specimens. In this method, a pressure is applied to the surfaces of the inner diameter of a thick-walled hollow cylinder. The pressure produces a tensile hoop stress in the specimen that is highest immediately adjacent to the inner hole and decreases as the radial distance increases. The pressure is increased until the tensile hoop stress becomes equivalent to the tensile strength of the specimen, at which point the specimen fails. Failure is generally denoted either by the development of a fracture extending from the inner diameter to the outer diameter and a corresponding drop in the internal pressure, or by excessive radial deformation corresponding to a constant internal pressure. The tensile strength of the specimen is calculated from the specimen dimensions and the peak internal pressure using the following expression:

$$T_0 = -p_{max} \frac{\left(1 + \dfrac{R_i^2}{R_o^2}\right)}{\left(1 - \dfrac{R_i^2}{R_o^2}\right)}$$

where:

T_o	=	Tensile strength, MPa
p_{max}	=	Maximum internal pressure, MPa
R_i, R_o	=	Inner and outer radius, m

2.3.2.2 Uniaxial Compression Tests

The uniaxial compressive strength test was performed to determine unconfined compressive strengths of surrogate waste specimens. In this test, a solid cylindrical specimen having an L:D of approximately 2 is loaded with a compressive load in a direction parallel to the central axis of the cylinder, while the sides of the specimen remain unsupported; i.e., no confining pressures are applied. Loading continues until a peak compressive load is reached followed by a drop in load, at which point failure is assumed. The uniaxial compressive strength is then defined as:

$$C_o = \frac{F_{max}}{A}$$

where:

C_o	=	Uniaxial compressive strength, MPa
F_{max}	=	Peak force, MN
A	=	Cross-sectional area of the specimen, m^2

Owing to the ductile nature of some surrogate waste specimens, a failure defined as loss of load-bearing capacity was not always obtained. In such cases, the tests were terminated after large strain accumulation; the corresponding load is considered an approximation of its uniaxial strength.

Axial stress was calculated as the ratio of the current force to the current cross-sectional area of the specimen, while axial strain was calculated from the actuator displacement and the original specimen length. Because no radial strain measurements were made, the current cross-sectional area of the specimen was determined by assuming the radial strain was equivalent to $-v\varepsilon_1$ where v is Poisson's ratio and ε_1 is the axial strain. A value of $v = 0.5$ was assumed for the calculation. Based on these assumptions, the axial strain and axial stress were calculated as follows:

$$\varepsilon_1 = -\ln\left(1 - \frac{\Delta L}{L_0}\right)$$

$$\sigma_1 = \frac{F}{\frac{\pi}{4}\left[D_0\left(1 + v\varepsilon_1\right)\right]^2}$$

where L_0 and D_0 are the original specimen length and diameter, respectively.

2.3.2.3 Triaxial Compression Tests

The confined quasistatic compressive strength test was performed to determine the confined compressive strengths of surrogate waste specimens. In this test, a solid cylindrical specimen having an L:D of approximately 2 is loaded with a compressive load in a direction parallel to the central axis of the cylinder, while the sides of the specimen are subjected to a confining pressure. Loading continues until a peak compressive load is reached followed by a drop in load, at which point failure is assumed. The confined compressive strength is then defined as

$$\Delta\sigma^{max} = \sigma_1^{max} - \sigma_3$$

where:

$\Delta\sigma^{max}$	=	Confined compressive strength, MPa
σ_1^{max}	=	Maximum axial stress, MPa
σ_3	=	Confining pressure, MPa

The confined compressive strength tests can be used to determine elastic properties for the material, provided strains are recorded. In particular, Young's modulus (E) and Poisson's ratio (v) can be determined from the slopes of the axial stress difference versus axial strain curve (i.e., $\Delta\sigma-\varepsilon_1$) and axial stress difference versus radial strain curve (i.e., $\Delta\sigma-\varepsilon_3$) using the following expressions:

2-13

$$E = \frac{\Delta\sigma}{\Delta\varepsilon_1}$$

$$\nu = -\frac{E}{\frac{\Delta\sigma}{\Delta\varepsilon_3}}$$

The right side of the first equation and the denominator of the second equation represent the slopes of the stress difference versus axial strain curve and stress difference versus radial strain curve, respectively.

The test specimen was subjected to an axial load by advancing the axial loading ram of the test system with a hydraulic cylinder located in the base of the testing frame. Loading continued until a peak axial load or high magnitudes of strain had accumulated. During each test, several unload/reload cycles were performed to acquire data from which Young's modulus and Poisson's ratio could be calculated.

2.4 Results

Results from 38 tests are summarized in this document. These results provide sufficient basic information for calculational purposes. Ultimately, eight surrogate waste mixtures were used and are designated by "recipe" numbers. Nearly all tests were conducted on surrogate recipes for the 50% and 100% degraded waste cases. Different recipe numbers were assigned when any component of surrogate was changed. Most test results represent mechanical strength information. The 38 tests include 12 uniaxial compression stress tests, 21 tensile strength tests, and 3 triaxial compression tests. In addition to the strength tests, two brine permeability tests were performed. The test results from each of these types of tests and some preliminary data analyses are presented in the following paragraphs.

Mechanical strength test results are summarized in Table 2-10. The first column in the table uniquely identifies the test specimen. The second column contains the recipe used to fabricate the specimen. The third column indicates the level of hydrostatic consolidation. The fourth column presents the moisture content of the specimen at the time the specimen was tested. A designation of "wet" indicates the specimen was saturated but water content was not measured. The final three columns present strength data. Four types of tests were run, and the last column is a shorthand notation: UCC for a uniaxial stress test, BIT for a Brazilian indirect tension test, TWT for a thick-walled cylinder test, and TRX for a triaxial compression test. The results of each test are presented in terms of the minimum and maximum principal stresses where positive values indicate compression.

The ductile nature of the specimens during a triaxial compression test is illustrated in Figure 2-2, which plots axial stress difference versus axial and lateral strain for the triaxial compression test performed on specimen S14. The drained test was performed at room temperature using a constant confining pressure of 1 MPa. The load path incorporated two unload/reload cycles, which provided information for estimating the two elastic constants: Young's modulus and Poisson's ratio.

Table 2-10. Summary of Strength Tests on Surrogate Waste Specimens [a]

Specimen I.D.	Recipe No.	Compaction Pressure (MPa)	Water Content (%)	Strength (MPa)		
				σ_3	σ_1	Test [b]
S1	1	15	13.4	0	12	UCC
S2	2	15	8.7	0	1.35	UCC
S2-2	2	15	Wet	-0.07	0.06	TWT
S3	2	15	0	0	1.85	UCC
S4-2	2	15	0	-0.09	0.27	BIT
S4-3	2	15	0	-0.15	0.12	TWT
S4-4	2	15	0	-0.20	0.16	TWT
S5-2	2	15	0	-0.17	0.14	TWT
S5-3	2	15	0	-0.14	0.11	TWT
S6	3	15	17.5	0.05	2.25	TRX
S7	3	15	2.2	0	1.6	UCC
S8	4	15	4.8	0	1.4	UCC
S9-2	4	15	0	-0.06	0.17	BIT
S9-3	4	15	0	-0.11	0.33	BIT
S9-4	4	15	0	-0.11	0.33	BIT
S10	4	15	10.7	0	0.7	UCC
S11	4	15	6.1	0	0.32	UCC
S12	4	5	12.8	0	0.65	UCC
S13-3	4	5	11.9	-0.02	0.05	BIT
S13-4	4	5	12.8	-0.01	0.04	BIT
S19-1	4	5	13.8	-0.12	0.10	TWT
S19-2	4	5	13.7	-0.09	0.07	TWT
S21-1	4	5	13.7	-0.11	0.09	TWT
S21-2	4	5	13.6	-0.13	0.11	TWT
S22-1	4	5	12.4	-0.07	0.06	TWT
S22-2	4	5	12.2	-0.12	0.10	TWT
S23	4	5	13.9	1.0	5.8	TRX
S14	5	5	Wet	1.0	6.8	TRX
S15-3	5	5	12.0	-0.10	0.30	BIT
S15-4	5	5	14.2	-0.06	0.19	BIT
S17	5	5	17.1	0	0.15 [c]	UCC
S18-3	5	5	14.2	-0.03	0.09	BIT
S18-4	5	5	15.9	-0.03	0.09	BIT
S26	5	5	16.0	0	0.69	UCC
S16	6	0	22.9	0	0.85	UCC
S25	8	5	30.6	0	0.72	UCC

(a) S20: jacket leak; S24: permeability only. (b) UCC = unconfined compression test, TWT = thick-walled hollow cylinder tension test, BIT = Brazilian indirect tension test, TRX = triaxial compression test.
(c) Damaged specimen.
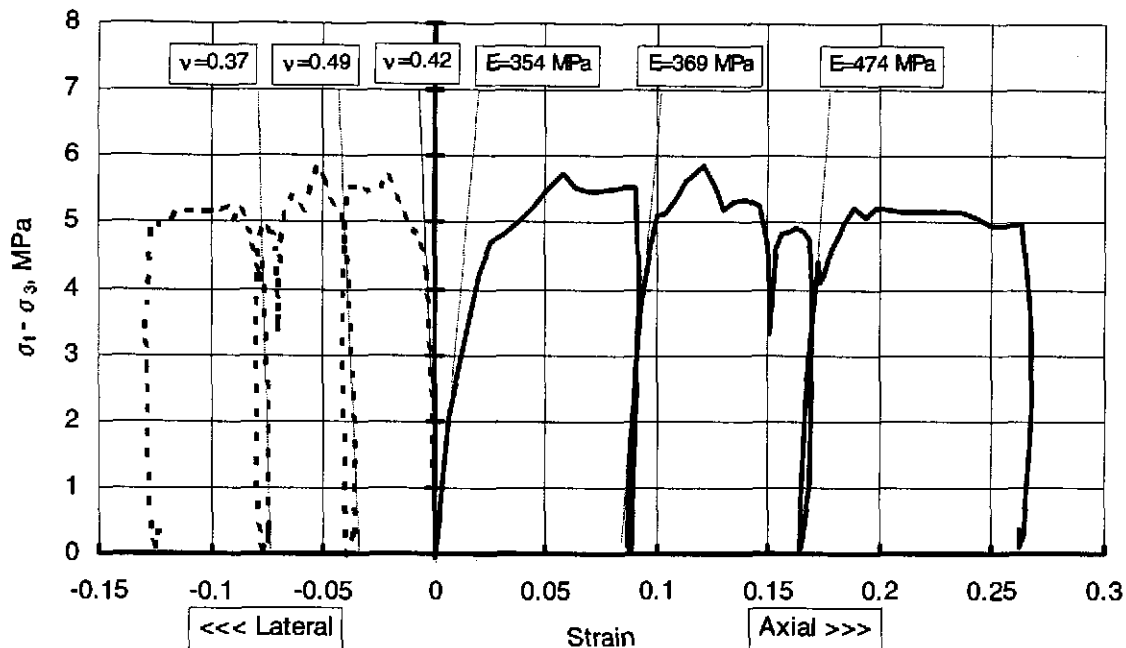
Figure 2-2. Triaxial compression test on Specimen S14.

Young's modulus was calculated from the slope of the axial stress difference versus axial strain data during the ascending load portions of the curve. Poisson's ratio was calculated by first calculating a similar slope for the axial stress difference versus lateral strain data during the ascending load portions of the curve. The ratio of Young's modulus to this lateral strain slope represented Poisson's ratio. Three sets of elastic constant estimates were obtained in this fashion and they are reported on Figure 2-2. The elastic constants for this test are also reported in Table 2-11, along with the elastic constants determined for triaxial tests on specimens S6 and S23.

The triaxial compression test on specimen S6 (Recipe #3, 100% degraded using Fe_2O_3 surrogate) was the first attempt at this type of loading on the test frame that was used, and there was considerable difficulty in controlling the load rate. These difficulties led to poor control of the confining pressure, which in turn led to poor determination of lateral strains because both values depend on proper dilatometer operation. Thus the values of Poisson's ratio for test S6 that are reported in Table 2-11 are considered unreliable compared to those determined during tests S14 and S23, where much better test system control was achieved.

Another test that has been rejected on experimental grounds is S17, which was a uniaxial stress test on material fabricated from Recipe 5. Its low strength is attributed to specimen fabrication. When the specimen was removed from the compaction vessel, one side was severely concave as a result of anomalous buckling of the protective lead jacket. Nevertheless, S17 was machined by hand to form an approximate cylinder suitable for uniaxial testing. Either the compaction anomaly or the machining may have damaged the specimen, leading to the anomalously low strength value.

Table 2-11. Elastic Constants Determined From Triaxial Compression Tests

Specimen I.D.	Cycle	Confining Pressure (MPa)	Elastic Constants	
			E (MPa)	v
S6	Initial		21	0.35
	1st Reload	0.05	72	0.09 [a]
	2nd Reload		73	0.07 [a]
S14	Initial		354	0.42
	1st Reload	1.0	369	0.49
	2nd Reload		474	0.37
S23	Initial		76	0.40
	1st Reload	1.0	366	0.29
	2nd Reload		220	0.36
	3rd Reload		219	0.36

(a) Test system control problems.

Two brine permeability tests were also performed on Recipes 4 and 5. The brine permeability tests were performed using a low confining pressure of 1 MPa to seal the elastomer jacket against the specimen (after the protective lead jacket used during compaction had been removed). A low confining pressure was used to minimize the possibility of any additional change in specimen density during the permeability test. The brine permeant was driven with a 0.35 MPa pressure at the specimen inlet while at the other end of the specimen a vented platen was connected to a burette to provide a measure of brine flow. Typical results of a permeability test are shown in Figure 2-3, which plots the brine flow in mL as a function of time for specimen S14.
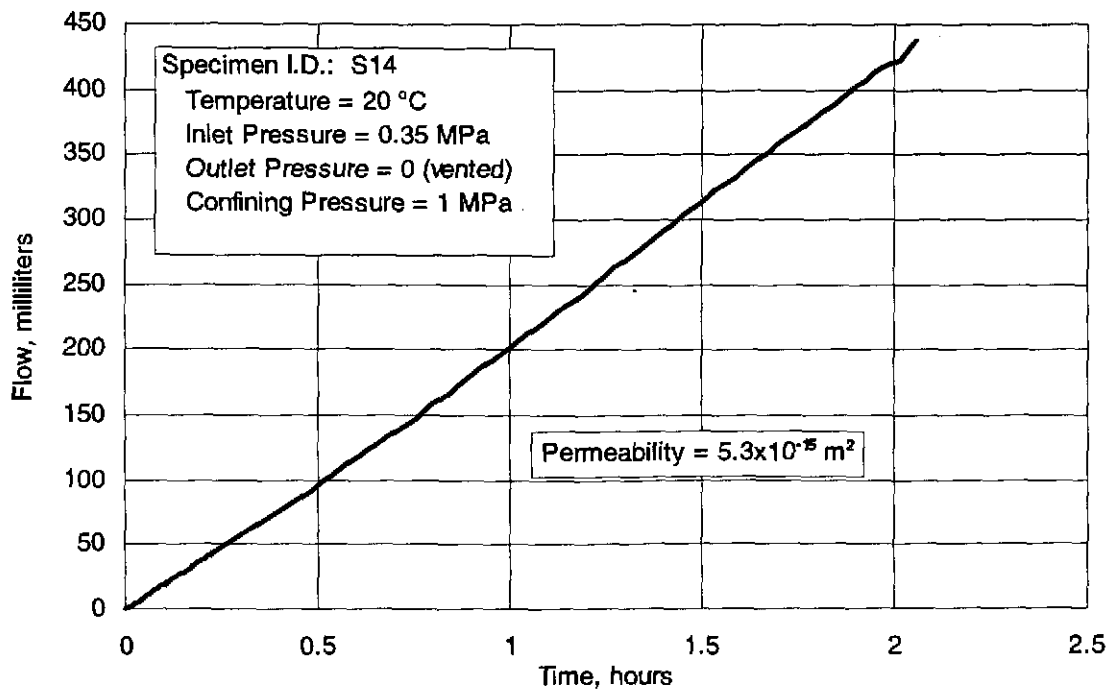
Figure 2-3. Permeability test on specimen S14.

As can be seen in the figure, the flow rate was linear, indicating a steady-state flow rate. The data in the figure were fitted to calculate the flow rate, which was then used to calculate a brine permeability value of 5.3×10^{-15} m^2. A second permeability test was performed on specimen S24 and yielded a value of 2.1×10^{-15} m^2.

2.5 Discussion

Test specimens were fabricated using fractions of surrogate materials appropriate for the degraded waste inventory. Initial dimensions of compression samples were approximately 100 mm in diameter and 200 mm in length. Compaction was applied hydrostatically in a drained, saturated state. Brine permeability, failure strengths, and elastic constants were measured. Tensile strength testing was accomplished using hollow cylinders and indirect tensile samples. Saturated surrogate samples are fairly weak and ductile. Tensile strength of saturated samples ranges from 0.01 to 0.13 MPa. Unconfined compressive strength of saturated samples ranges from 0.32 to 1.4 MPa. Poisson's ratio averages about 0.35, Young's modulus is approximately 300 MPa, permeability is of the order of 4×10^{-15} m^2, and $\phi \approx 45°$. Thirty-eight tests have been completed to date, and the records have been technically and QA reviewed and made part of the supporting data package.

Data collected thus far represent compelling quantitative measures of degraded waste strength. Although several "recipes" were used, most data have been acquired for surrogates representing Case 1 and Case 2, i.e., residuals from 50% degradation and 100% degradation, respectively. The greatest numbers of tests were completed for the 50% degraded case using Recipe #2 and Recipe #4. Recipe #2 is very similar to Recipe #4, except that Fe_2O_3 was used as the degraded Fe surrogate. In Recipe #4, comminuted Goethite (Black Hills Bog Iron) was used as degraded Fe surrogate. Both are probably acceptable surrogates for degraded iron, but it was felt that the uniform fine particle size of reagent grade Fe_2O_3 might be unrealistic. The entire data set for Recipe #2 and Recipe #4 includes dry, partially dry, and saturated specimens and consolidation pressures of 5 and 15 MPa. A sufficient number of tests has been completed to allow discussion of these test variations, as well as to quantify strength parameters for dry and saturated specimens.

Experimental variations allow evaluation of saturated, dry, and partially dry states for consolidation pressure effects between 5 and 15 MPa and for recipe variations. Initially, specimens were consolidated at 15 MPa, as that represented a nominal lithostatic pressure at the WIPP. To be conservative with regard to the pressure the waste actually experiences, a lower pressure of 5 MPa was used after the first several tests. Four saturated, unconfined compression tests were conducted on identical recipes. Three tests prepared at 15 MPa consolidation pressure provided unconfined strengths of 1.6, 0.32, and 0.70 MPa. The fourth test prepared at 5 MPa consolidation failed at an intermediate strength of 0.65 MPa. On this basis, no strength enhancement was found for consolidation to lithostatic pressures; however, further specimen preparation consolidation used a pressure of 5 MPa.

Tensile strength is thought to be the most significant with respect to failure and possible transport during a spall event. Therefore, several variations of test parameters were used in determining saturated and dry tensile strengths of surrogate recipes. Saturated tensile strength for the 50% (Recipe #4) degraded case averages 0.084 MPa (12 psi) and ranges from 0.01 to 0.13 MPa for the eight tests. A single saturated test using Recipe #2 had a tensile strength of 0.07 MPa. Saturated tensile strength of the 100% degraded case averages 0.055 MPa (8 psi) and ranged from 0.03 to

0.10 MPa for four tests. It appears that in the saturated state, the surrogates representing 50% degraded waste are stronger than those representing 100% degraded waste, although the range of strengths is larger.

Tensile strength of 13 saturated tests conducted on surrogates representing both the 50% and 100% degraded materials are treated statistically to quantify average values and standard deviations that may be appropriate for failed volume calculations. An average tensile strength using all 13 tests is 0.074 MPa, with a standard deviation of 0.04 MPa (10.7 ±5.8 psi). Therefore a suitable range for saturated tensile strength is considered to be 5 to 15 psi. These tensile strength values would be appropriate for repository conditions where significant saturations could occur. From the CCA, it can be demonstrated that gas pressure is inversely related to saturation: when saturation is relatively high, pressures are low (see Appendices D and E).

As discussed in the analog evaluations in Chapter 5 of this report, cohesion is a critical parameter for cavity calculations pertaining to methane production. Sufficient test data have been produced to allow determination of cohesion of surrogate materials. Table 2-12 summarizes a subset of data from Table 2-10 used for cohesion calculations. These data include all saturated tests (uniaxial, triaxial, and tension) run on the 50% and 100% degraded waste surrogates. Figure 2-4 is a plot of these data with a linear regression fit. Based on these data, an angle of internal friction (ϕ) of 44.4° and cohesion of 0.13 MPa are calculated.

Table 2-12. Summary of Data Used for Cohesion Calculations

Specimen I.D.	Recipe No.	Compaction Pressure (MPa)	Water Content (%)	Confining Pressure (MPa)	Strength (MPa)
S2-2	2	15	Wet	-0.07	0.06
S2	2	15	Wet	0	1.35
S21-2	4	5	Wet	-0.13	0.11
S19-1	4	5	Wet	-0.12	0.10
S22-2	4	5	Wet	-0.12	0.10
S21-1	4	5	Wet	-0.11	0.09
S19-2	4	5	Wet	-0.09	0.07
S22-1	4	5	Wet	-0.07	0.06
S13-3	4	5	Wet	-0.02	0.05
S13-4	4	5	Wet	-0.01	0.04
S8	4	15	Wet	0	1.4
S10	4	15	Wet	0	0.7
S11	4	15	Wet	0	0.32
S12	4	5	Wet	0	0.65
S23	4	5	Wet	1.0	5.8
S15-3	5	5	Wet	-0.10	0.30
S15-4	5	5	Wet	-0.06	0.19
S18-3	5	5	Wet	-0.03	0.09
S18-4	5	5	Wet	-0.03	0.09
S26	5	5	Wet	0	0.69
S14	5	5	Wet	1.0	6.8

$y = 5.659x + 0.6274$
$R^2 = 0.960$
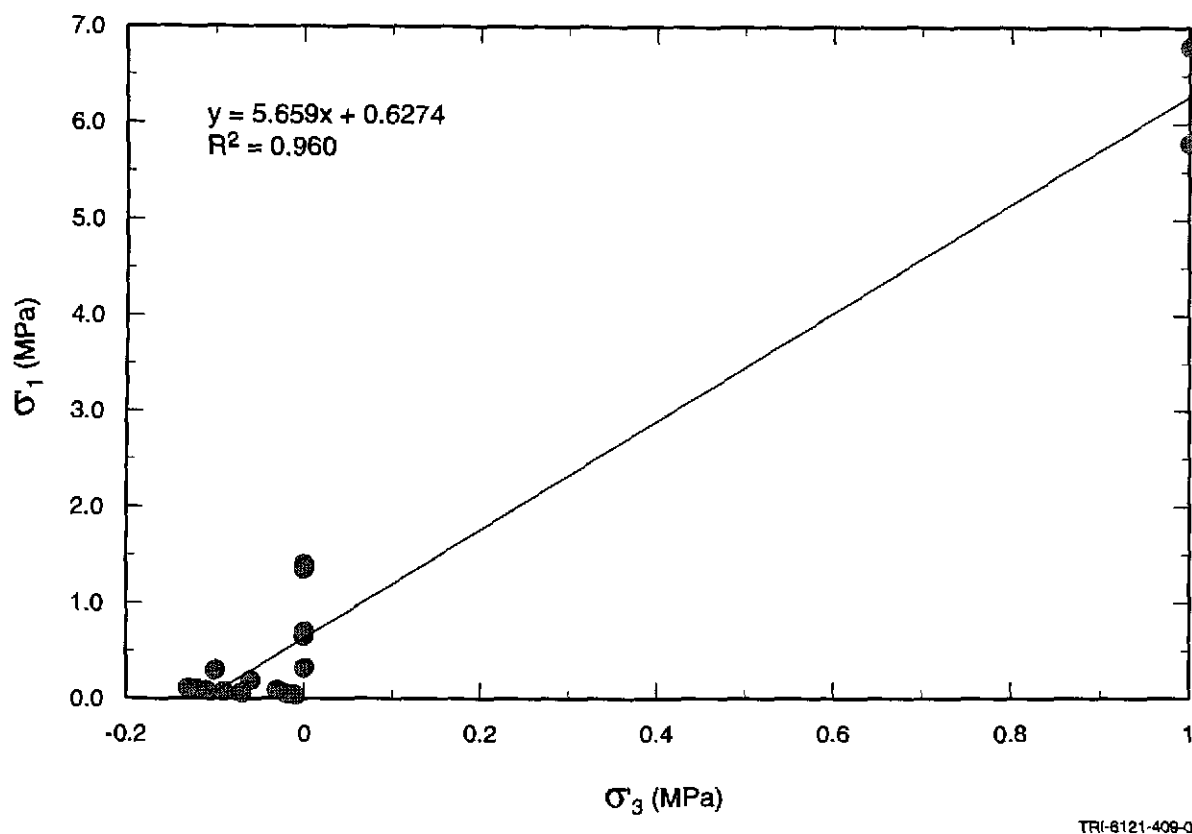
Figure 2-4. Plot of cohesion calculation data and linear regression fit.

Three dry tests on the 50% degraded surrogate (Recipe #4) yielded an average tensile strength of 0.093 MPa (13.5 psi). By comparison, five dry tests on the 50% degraded surrogate using Recipe #2 averaged 0.15 MPa (21.8 psi). Drying increases tensile strength by about a factor of two compared to the saturated condition. Significant increase above saturated strength would be appropriate for calculations of spall at high pressures because of the concomitant dry condition. Single uniaxial compressive strength tests are available to assess strength increases attributable to drying. Both specimens were of the same recipe and consolidation history. Dry specimen S3 has an unconfined compressive strength of 1.85 MPa, about 30% stronger than saturated specimen S2, with an unconfined compressive strength of 1.35 MPa.

Initially, it was thought that precipitated salt content would be a significant element of the surrogate mixtures. As it turns out, for saturated conditions, no significant influence is obvious for the quantity of salt added to the surrogates. Likely, precipitate strength would develop as degraded waste dried because crystallites of NaCl would bond grain boundaries. This is a likely physical process of strength increases noted for dry surrogate specimens.

The expected state of the waste at times when spall is most likely to occur comprises compacted drums of waste, encrusted along contact boundaries with minor degradation product. When expected states of the waste are considered with expected pressures in the repository of less than 12 MPa, the most likely conditions suggest that spalling would not be possible from the WIPP waste rooms. However, the expected states of the WIPP are not the most relevant to a spall event. Testing is being conducted to quantify the conditions that capture the "low end" of

possible mechanical strength created as a result of extensive degradation. These mechanical data are being used to calculate possible spall volumes when gas pressures are sufficiently high.

2.6 References

Callahan, G.D., and K.L. DeVries. 1991. *Analyses of Backfilled Transuranic Wastes Disposal Rooms*. SAND91-7052. Albuquerque, NM: Sandia National Laboratories.

US DOE (Department of Energy). 1995. *Waste Isolation Pilot Plant Transuranic Waste Baseline Inventory Report*. DOE/CAO-95-1121. Revision 2. December 1995. Carlsbad NM: United States Department of Energy, Carlsbad Area Office.

US DOE (Department of Energy). 1996. *Waste Isolation Pilot Plant Transuranic Waste Baseline Inventory Report*. DOE/CAO-95-1121. Revision 3. June 1996. Carlsbad NM: United States Department of Energy, Carlsbad Area Office.

NRC (National Research Council). 1996. *The Waste Isolation Pilot Plant: A Potential Solution for the Disposal of Transuranic Waste*. Committee on the Waste Isolation Pilot Plant, Board on Radioactive Waste Management. Washington, DC: National Academy Press.

Page intentionally blank

3.0 THE MECHANISTIC MODEL—SEMI-ANALYTIC COMPUTATIONS

This section describes a mechanistic model of the spalling process during the first stage of a borehole intrusion, when the drilling mud is being ejected by the high pressure gases in the repository, and during the second stage, when the gas is venting. The implementation of this model using semi-analytic techniques is also described. The results from these semi-analytic calculations define the failed volume as a function of repository pressure and tensile strength of the waste. The sensitivity of this volume to other parameters is also discussed in this section.

Tensile failure leads to waste fragmentation during the first stage of the borehole intrusion. Note that gas velocities are rather low while the mud is being ejected, and low gas velocity will significantly reduce the impacts of erosion and lofting on the spalling process. These other mechanisms are considered during the second stage of the blowdown process, which occurs when the mud has cleared the borehole and rapid gas movement can transport larger waste fragments directly to the surface. The total release volume depends on processes occurring for both stages of the blowout.

The conceptual model for the first stage of the blowdown process is based on three processes: the unsteady flow of mud to the surface, the flow of gas from the repository into the drilling annulus behind the mud, and the stress field in the waste as a function of the bottomhole pressure. The flow elements are coupled through the bottomhole pressure, which varies with the changing gas volume in the column. Coupling the motion of the drilling mud with the gas flow from the repository is essential for accurate calculation of this time-dependent process. The description of flow during the second stage also involves coupling gas flow from the waste to flow up the borehole.

A semi-analytic computational method has been implemented to simulate the first stage blowdown process. This method analyzes the flow of an ideal, isothermal gas in the repository during the blowdown, and couples the repository gas flow to the movement of the mud. This approach, called the cavity growth method, is based on a full numerical solution of the transient one-dimensional porous flow equations. The time-dependent output from this numerical solution is the bottomhole pressure and the pore pressure profile, which are incorporated into a closed-form analytical solution for the total stress/strain field near the borehole. This analytical solution for the stress field, with associated strength or failure criteria, defines the regions of tensile failure and shear yield surrounding the borehole. The material that fails in tension adjacent to the cavity is removed from the calculation and stresses are readjusted for the new location of the inner boundary. Removal of this failed material by erosion is considered in Stage 2. Although the indications are that not all of the material will be removed to the surface, the volumes calculated are small enough that it is assumed that all of the material is removed.

3.1 Introduction

Drilling intrusions through WIPP waste can produce a spalling event, which is defined as the direct release of solid material as a result of rapid gas movement toward and up a borehole at the time of intrusion. Spalling events are one of the major release mechanisms for the WIPP, based on the recent performance assessment for the Compliance Certification Application (CCA). The physical mechanism leading to a spalling release in the CCA is erosion and entrainment of solid waste particles due to rapid gas movement. The Conceptual Model Peer Review Panel (CMPRP)

has recommended that additional mechanisms beyond erosion, including tensile failure, lofting and liquefaction, should be considered in evaluating the volume of spalling releases.

The blowout process during a spalling event can be divided conceptually into two stages:

- Stage 1: Ejection of the drilling mud by high pressure gases in the repository, and waste response to pressure gradients during blowout.
- Stage 2: Rapid flow of gas, including any entrained solid material, from the high pressure repository.

Each stage may be important for spalling releases because the interaction of the flow toward the borehole with the compacted waste will differ with the rate of change of bottomhole pressure, the effective stress in the waste and the velocity of the gas. During the first stage, the initial depressurization and associated pressure gradients near the borehole will determine regions of tensile failure. Gas velocity is low during the first stage, while the mud is being expelled, the typical velocity at the drillhole being 5 m/s, as opposed to 100 m/s during Stage 2. Most entrainment of larger particulates will therefore take place during this second stage.

For the simplest tensile failure model, with a brittle failure criterion, the volume that fails in tension is assumed to fragment to a particulate consistency. More sophisticated failure models, which involve stress relaxation from plasticity or an equivalent mechanism, will not necessarily fragment the waste into small particles. However, the initial depressurization during mud blowout largely determines the volume of fragmented material that is available for entrainment and transport later in the process. Calculations have been made of the removal of this failed material by erosion. However, the volumes calculated to have failed are small enough that is has been assumed, for the conditions considered here, that any material which fails under simple (brittle) tensile failure will be transported to the surface at some time in the blowdown process.

A mathematical model of the Stage 1 blowout process has been developed to assist in predicting the regions of tensile failure surrounding a borehole. The mathematical model is currently designed for a hemispherical geometry, which is appropriate when a borehole first intersects a high pressure room. The hemispherical geometry is appropriate because the maximum region of tensile failure directly adjacent to the borehole occurs within the first few seconds after an intrusion, when changes in pore pressure are still localized around the borehole, and because the rate of advance of the drill bit is very slow relative to the time scale for tensile failure during Stage 1, and following a blowout further drilling will stop.

A key element of the Stage 1 model is coupling of gas flow from the repository to the acceleration and displacement of the mud in the borehole. The Stage 1 model determines the motion of the mud and the bottomhole pressure as a function of time, basing the bottomhole pressure on the net mass influx from the repository and the free volume available for the gas.

Transport of any brine that might be contained in the region of tensile failure is not considered. The WIPP performance assessment already includes a contribution from dissolved actinides in brine. This contribution is computed in the direct brine release model and automatically included in the Complementary Cumulative Distribution Function (CCDF) for total releases from the repository. The computational results presented in this section show that the volume of waste that fails in tension is relatively small in comparison to the maximum release volumes predicted for direct brine release. For example, the volume of waste that has failed in tension during Stage

1 is usually much less than 2 m^3 (of uncompacted waste). The entrained brine in this volume is limited by porosity and by brine saturation. The entrained brine will be at most 70% of the total spall volume, or about 1.43 m^3 of brine, because the porosity of the waste is often 70% for higher pressure spalling events. In most cases where spall may occur, brine saturations are very low so the available volumes of brine will be even less. This entrained volume (less than 1.4 m^3) can be compared to the maximum volume of down-dip direct brine release, which is 55 m^3 of brine, or the maximum volume of up-dip brine releases, which is 32 m^3 of brine (Analysis Package for Direct Brine Release Calculations, 1996.). These data show that the volume of entrained brine in a region of tensile failure during Stage 1 is substantially less than the volume of brine released through brine blowout and should therefore have a negligible impact on performance.

Stage 2 will start after the mud has been ejected from the drillhole, a process which is expected to take on the order of 50 to 100 s. Calculations indicate that the bottomhole pressure (BHP) will reduce from values of about 7 to 8 MPa at the end of Stage 1 to about 0.5 to 1 MPa in Stage 2, with the final pressure drop occurring in a few seconds. The BHP will stay at this value until a panel is depleted, which will take several days, or until the well is shut-in.

During Stage 2 additional tensile failure may occur due to the new, lower, wellbore pressure. This pressure may cause renewed tension to be applied to the walls of the borehole cavity. This mechanism is considered in Section 3.5, where it is shown that the effects will be minor. During Stage 2, higher gas velocities may occur, of the order of 1 to 50 m/s depending on the cavity size. For smaller cavities, these velocities will be lower, as will the proportion of material removed. Since most failed cavities calculated for the conditions considered here are quite small, it is assumed that all material is removed.

3.2 Conceptual Model, Mathematical Models and Numerical Methods

3.2.1 Conceptual Model

The conceptual model for Stage 1 has three major elements,

1. motion of the column of mud;
2. gas flow within and from the repository; and
3. stresses in the waste.

All three elements are dynamically coupled through a single variable, the bottomhole pressure. The conceptual models for these three major elements and the calculation of bottomhole pressure are detailed below. The second two elements will also occur in Stage 2.

3.2.1.1 Motion of the Column of Mud

The motion of the column of drilling mud is based on transient pipe flow for an annulus of constant cross-sectional area. Note that the conditions are never sufficiently severe to eject the drill string, and that mud blow is assumed to be restricted to the annulus due to the resistance to flow offered by the nozzles in the bit. The equation of motion for the mud column considers the pressure differential across the mud column, the viscous drag from the pipe walls and the hydrostatic weight of the mud. The pressure differential is calculated from the transient bottomhole pressure and atmospheric pressure. The viscous drag force is based on a Fanning

friction factor for a fully rough pipe. The hydrostatic weight of the mud column varies with time because the length of the mud column decreases as the mud is ejected.

The mud column is assumed to accelerate uniformly. This assumption will be valid because the time scale for mud blowout, on the order of 50 to 100 s, as demonstrated later, is much greater than the acoustic transit time through the mud, which is on the order of 0.5 s (or less as the column is ejected). In other words, the Mach number of the flow is close to zero and an incompressible model with uniform properties for the mud column will be an excellent approximation. This same argument also shows that pressure will be very close to uniform in the gas column behind the mud during Stage 1.

The interface between the mud and gas is assumed to remain in an ideal, one dimensional configuration throughout the mud blowout process. In reality, experimental data (Santos, 1990) demonstrate that gas will penetrate the interface, resulting in a region of mixed, two phase flow separating the mud and gas columns. This two phase region has been ignored here because maximum tensile stresses surrounding the borehole occur at very early times, typically 1 to 3 seconds, before a substantial two phase region can form. In addition, the early time drop in pressure is determined primarily by the change in volume due to displacement of the mud column, rather than by formation of bubbles across an interface. Thus a simple one dimensional model will adequately represent the pressure drop accurately at early times, when tensions in the waste are greatest.

3.2.1.2 Gas Flow Within and From the Repository

The gas flow rate from the repository is based on the pseudopressure approach to calculating compressible flow in a porous medium (Chan et al., 1993). The cited reference includes transient solutions for a constant cavity (bottomhole) pressure as well as approximate solutions based on steady state profiles in the porous medium. Solutions are represented for one-dimensional flow of an ideal, isothermal gas in planar, cylindrical, and spherical symmetry.

The conceptual model assumes one dimensional, spherically symmetric flow in the porous medium. This assumption is reasonably accurate from the time when a borehole first intersects a high pressure room until the resulting pressure disturbance reaches the floor of the repository. Since maximum tensile stresses in Stage 1 occur at early times, before the pressure disturbance has propagated to the floor of the repository, a spherically symmetric model has been chosen for these calculations. Note that the calculations with TOUGH28W and SPECTROM-32, as presented in Section 4.0 of this report, generally confirm the spherical symmetry of the pressure disturbance at early times, even though the borehole is represented as a disk at the top of the room.

At later times, if a drillbit fully penetrates a room, a cylindrical geometry is more appropriate. This geometry may be more appropriate for cuttings/cavings releases, but the high pressure gradients necessary for tensile failure occur at early times, before the drillbit has completely penetrated the repository horizon. In this sense the cylindrical geometry is an end state that can easily be considered with the semi-analytic approach for spalling, if that is appropriate.

3.2.1.3 Calculation of Bottomhole Pressure

The motion of the drilling mud, the gas flow from the repository and the stress distribution in the waste are directly coupled through the bottomhole pressure. The bottomhole pressure is based on

3-4

the ideal gas law for hydrogen, with a time dependent volume for the gas column and the net mass influx into the borehole.

The gas column is assumed to have uniform pressure and temperature in Stage 1. This is an excellent approximation because the flow velocities are low, typically less than 10 m/s, resulting in a Mach number (in hydrogen) of less than 0.01. Compressibility effects are negligible for a Mach number close to 0, and a uniform pressure and temperature in the gas column will be valid.

Friction with the pipe walls and the hydrostatic weight of the gas column will also generate pressure gradients between the top and bottom of the gas column, but these changes are minor compared to the average pressure of the gas column. The standard formula for pressure drop along a pipe with gas flowing at 10 m/s and a length of 655 meters gives a change of about 0.08 MPa. Similarly, the maximum hydrostatic weight of the gas column is only 0.08 MPa. These small changes in gas pressure have been ignored in this analysis because they are much less than typical values for bottomhole pressure during mud blowout, which are several MPa or greater.

After the mud has been ejected, the pressure in the borehole will fall rapidly, and gas flow out of the waste will be controlled by the friction in the wellbore and the deliverability of the waste. It is estimated that the pressure at the bottom of the hole will fall to about 0.5 to 1 MPa in about 1 to 2 s, based on an estimated acoustic transit time of about 0.5 s.

3.2.1.4 Stress and Failure in the Waste

The calculation of the total stress in the waste is based on the static response of a hollow elastic sphere that is subject to both mechanical loading and to pore pressure effects. The elastic response of a hollow sphere under mechanical loading is given by Timoshenko and Goodier (1970). The inner surface is subject to the bottomhole pressure. The outer surface is subject to the far field pressure, which is the repository pressure at the time of intrusion.

The simple elastic response is modified in the presence of pore pressure. When pore pressure is present, additional strains and stresses are generated that are analogous to the standard (elastic) formulation for strains and stresses from thermal expansion (e.g., Stagg and Zienkiewicz, 1975). Timoshenko and Goodier also provide an appropriate solution for thermally generated stresses in a hollow sphere. In addition, the material response is governed by the effective stress, that is, the initial stress minus the pore pressure.

The failure model is based on a combination of brittle tensile failure and Mohr-Coulomb shear failure using the effective stress in the waste. The cavity growth model allows failed material to be removed from the calculation, with conservation of mass and energy for the gases and solids. Stresses will redistribute when the material is removed from the inner wall, but not when material fails in an inner region.

All material that fails in brittle tension is assumed to be highly fragmented. Although erosion has been considered in Stage 2, and calculations indicate that for larger cavities this ability to remove all failed material may be limited, it is assumed that all fragmented material will eventually be released directly to the accessible environment. That is, transport to the surface is assumed, independent of the flow rates of gases or the size of particulates. This is demonstrably a conservative assumption. Material that fails in shear will not necessarily fragment. However, the region of shear failure is generally less than or equal to the region of tensile failure with the cavity

growth model, so it has not been necessary (to date) to evaluate the degree of fragmentation under shear failure.

3.2.2 Mathematical Models

The conceptual model which is described in the preceding section has been implemented in two ways: one using "semi-analytic" techniques and a second using a full numerical implementation of both the pressure and stress fields. The fully numerical methods are discussed in Section 4.0; the semi-analytic method, called the cavity growth method, is discussed here.

The cavity growth model couples the ejection of the mud during Stage 1 to the flow of gas from the repository, calculates bottomhole pressures and pore pressure profiles, and uses these values to compute stresses using closed form spherically symmetrical solutions. The cavity growth method is based on a full numerical solution of the one-dimensional gas diffusion equation and allows the cavity to grow as spall occurs.

The mathematical basis for this method, and the computational scheme, is discussed in the remainder of this section.

3.2.2.1 Motion of the Column of Mud

The equations of motion for the mud column are based on the forces accelerating the mud. The force balance for the acceleration of the mud column is given by:

$$m\frac{dv}{dt} = F_p - F_f - F_w \tag{1}$$

where m is the mass and v is the velocity of the mud column, F_p is the pressure force across the mud, F_f is the frictional force retarding the motion of the mud, and F_w is the hydrostatic weight of the mud column. The equations for these quantities are:

$$m = \rho_m(L-x)A \tag{2}$$

$$F_p = (P_{bh} - P_{atm})A \tag{3}$$

$$F_f = \frac{f(L-x)\rho_m v^2 A}{2d_e} \tag{4}$$

and
$$F_w = \rho_m(L-x)Ag \tag{5}$$

where:

P_{bh}	=	the bottomhole pressure,
P_{atm}	=	atmospheric pressure,
f	=	the Fanning friction factor,
ρ_m	=	the density of the drilling mud,
g	=	the acceleration of gravity,
L	=	the initial length of the mud column,
d_e	=	the effective hydraulic diameter of the annulus,

3-6

x	=	the displacement of the mud column, assumed positive upward,
v	=	the velocity of the mud column, and
A	=	the cross-sectional area of the borehole,
t	=	the time since the borehole first intersected the repository.

Substituting into Equation 1, the equations of motion for the mud velocity and displacement are given by:

$$\frac{dv}{dt} = \frac{P_{bh} - P_{atm} - f[(L-x)d_e]\rho_m v^2 / 2 - \rho_m g(L-x)}{[\rho_m(L-x)]} \qquad (6)$$

and

$$\frac{dx}{dt} = v \qquad (7)$$

The effective hydraulic diameter for an annulus is given by the difference between the outer and inner diameters of the annuli. The value for f, the Fanning friction factor, is taken to be a constant value, independent of Reynolds number, because the borehole will have high roughness and because the Reynolds number is relatively high. For example, the Reynolds number for the mud is about 70,000 for a typical flow velocity of 5 m/s during Stage 1. The value for f becomes almost constant in this range of Reynolds number, with a strong dependence on roughness but a very weak dependence on flow velocity or mud viscosity. The range of values for f in this study has been between 0.01 and 0.06, based on the estimated roughness of the borehole as a concrete pipe and the drill collar as structural steel.

The initial conditions for solving Equations 6 and 7 are that displacement and velocity equal zero at time zero, when the borehole first intersects a room.

3.2.2.2 Gas Flow Within and From the Repository

The governing equations for flow of a compressible gas in a porous medium are adapted from Chan et al. (1993). Chan's results are originally written using pseudopressure as the independent variable but, as shown in this reference, the combination of the continuity equation and Darcy's law reduce to the following equation for an isothermal, ideal gas:

$$\frac{\partial p}{\partial t} = \frac{k}{2\phi\mu}\nabla^2(p^2) \qquad (8)$$

where p is pore pressure, t is time, k is permeability, ϕ is porosity, and μ is viscosity. The gas equation of state for isothermal flow is

$$\rho = Ap \qquad (9)$$

where ρ is density and A is a constant. For an ideal gas, A is given by $1/(R_0 T)$ where R_0 is the gas constant (for hydrogen in this case) and T is the (constant) temperature. Darcy's law is given by

$$q = \frac{k}{\mu}\nabla p \qquad (10)$$

where q is the volume flux.

The cavity growth method solves the pseudopressure diffusion equation numerically. In Equation 8, ∇^2 takes its appropriate form for one-dimensional flow in planar, cylindrical, or spherical symmetry. The spherical case has been used for these analyses, corresponding to initial response to drillbit penetration into the top of the waste. Equation 8 ignores the wave dynamics of the fluid flow in the porous medium, which is appropriate for all but the earliest times (less than a millisecond or so). This assumption is discussed in more detail in Section 3.2.3.1.

The boundary condition for Equation 8 at the inner boundary, which is the inner face of the waste, is a hybrid flow/pressure boundary condition. The mass flowing out of the waste and the amount of expanding mass of gas in the wellbore are balanced using a time-iterative method. This leads to a time-dependent pressure in the wellbore, which is used as the inner boundary condition at the current face of the waste and as the pressure at the base of the mud column. The boundary condition for Equation 8 at the outer boundary is a no-flow condition.

The initial conditions for Equation 8 are the specified gas pressure in the waste, prior to intrusion, and the hydrostatic weight of the mud column.

3.2.2.3 Calculation of Bottomhole Pressure

The pressure in the gas column is calculated with the ideal gas law,

$$p = \rho R_0 T \tag{11}$$

and

$$p = \frac{M_0 + M(t)}{V(t)} \tag{12}$$

where

ρ	=	the density of the gas,
R_0	=	the gas constant for the gas,
T	=	the temperature of the gas,
M_0	=	the initial mass in the hemispherical cavity,
M	=	the cumulative mass influx to the gas column, with $M(0)=0$, and
V	=	the total volume of the gas column and hemispherical cavity.

The temperature of the gas, hydrogen in this case, is assumed to be constant at 300K. The total volume of the gas column includes the free volume created by displacement of the mud and the volume of any cavity that results from tensile failure of the waste. The initial volume of this cavity is taken to be 100% of the pore volume of the first computational zone adjacent to the wall. This volume is 0.001 m^3. The total mass in the gas column includes the initial mass in the hemispherical cavity and the cumulative mass influx from the porous medium, including any mass released during tensile failure and fragmentation of the waste.

3.2.2.4 Stress and Failure in the Waste

The basic equations for the elastic response of a hollow sphere are given in Timoshenko and Goodier, (1970). These equations, which are usually written in terms of effective stress when pore pressure is present, are given by:

$$\sigma_r' = \sigma_{sr} + \sigma_0\left[1 - \frac{1}{(n-1)}\left(\frac{r_w}{r}\right)^n\right] + p_w\left(\frac{r_w}{r}\right)^n - \beta p(r) \tag{13}$$

$$\sigma_\theta' = \sigma_{s\theta} + \sigma_0\left[1 + \frac{1}{(n-1)}\left(\frac{r_w}{r}\right)^n\right] - \frac{p_w}{(n-1)}\left(\frac{r_w}{r}\right)^n - \beta p(r) \tag{14}$$

where σ_r' and σ_θ' are the radial and tangential effective stresses, respectively; n is 2 or 3 for cylindrical or spherical symmetry, respectively; and σ_0 is the far-field stress. A compressive stress is assumed to be positive. σ_{sr} and $\sigma_{s\theta}$ are the pore pressure stresses, given by

$$\sigma_{sr} = (n-1)\beta\left(\frac{1-2\upsilon}{1-\upsilon}\right)\frac{1}{r^n}\int_{r_w}^{r} p' r^{n-1} dr \tag{15}$$

$$\sigma_{s\theta} = -\beta\left(\frac{1-2\upsilon}{1-\upsilon}\right)\left(\frac{1}{r^n}\int_{r_w}^{r} p' r^{n-1} dr - p'\right) \tag{16}$$

In these equations, β is the Biot constant, given by $1-C_r/C_b$, where C_r and C_b are the matrix and bulk compressibility. For slightly consolidated or high porosity materials, β is typically close to 1. υ is Poisson's ratio, and

$$p' = p - p_0 \tag{17}$$

where p_0 is the far-field pressure. Detailed derivations of these equations are presented in Appendix B.

Two types of failure modes have been considered for the waste: tensile failure and shear failure. For tensile failure, the radial effective stress is compared with a tensile strength, T_0. If the tensile strength is exceeded, the material is assumed to no longer be capable of carrying tensile stresses (or strains). This always occurs first at the wellbore face. For the transient numerical calculations, the tensile-failed material is removed from the calculation. That is, the inner face is moved into the material to the first nontensile failed position beyond the failed position and the gas mass previously occupying the pore space in the tensile-failed zone is intermingled with the gas in the wellbore. This is equivalent to assuming a zero elastic modulus and an infinite permeability for tensile-failed material. In the case where a tensile-failed zone forms in the interior of the transient model, as happens at later times, the material is assumed to be protected by the inner compression zone and is not removed.

For shear failure, a Mohr-Coulomb criterion is used:

$$|\tau| = S_0 + \mu\sigma_n' \tag{18}$$

where $|\tau|$ is the shear stress, S_0 is the cohesion, μ is the internal friction coefficient, and σ_n' is the normal effective stress.

For the hemispherical geometry, this can be written as (Jaeger and Cook):

$$\sigma_\theta' \left[\left(1 + \mu^2 \right)^{1/2} - \mu \right] - \sigma_r' \left[\left(1 + \mu^2 \right)^{1/2} + \mu \right] = 2 S_0 \qquad (19)$$

No adjustment is made to stresses or strains as a result of shear failure, in part because the material will probably yield in shear, rather than showing brittle failure. Such an adjustment could be made (by restricting stresses and allowing larger strains), but this should only reduce the outer bound of the shear failure. Thus the current simpler technique is probably conservative with regard to the maximum extent of shear failure. It is worth noting that, in general, the extent of the shear zone is either similar to, or less than, that of the tensile failure zone for these calculations.

3.2.2.5 Bottom Hole Pressure and Stress State During Stage 2

Gas will continue to flow from the repository after the mud has cleared the borehole (assuming that the driller has failed to control the blowout). The bottomhole pressure is determined by the capacity of the repository as a gas reservoir and the flow of compressible gas up the cleared borehole. The compressible flow up the borehole under isothermal conditions with pipe friction is given by (Binder, 1958):

$$\frac{fL}{d_e} = \frac{1}{\gamma M_1^2} \left[1 - \left(\frac{P_{atm}}{P_{bh}} \right)^2 \right] - 2 \ln \left(\frac{P_{bh}}{P_{atm}} \right) \qquad (20)$$

where

γ = the isotropic exponent of the gas, and
M_1 = the inlet Mach number.

The value for d_e is the effective hydraulic diameter of the annulus. The annulus is defined by the borehole diameter and the drill collar diameter, ignoring the change in the cross-sectional area for the drill pipe.

The capacity of the repository as a gas reservoir is computed with a quasi-static model to simplify the calculations. The details of this model are presented in Section 3.4. Since the capacity (mass flow rate) varies with the bottomhole pressure, multiple calculations must be performed to define the response of the reservoir.

The bottomhole pressure is determined by a consistent solution of Equation 20 and the mass flow rate from the repository as a function of bottomhole pressure. Typical values of bottomhole pressure during Stage 2 are 0.5 to 1 MPa.

The stress state and failure criteria for Stage 2 are identical to those in Section 3.2.2.4 for the Stage 1 calculations.

3.2.2.6 Erosion

Erosion occurs due to solid materials being removed by the viscous drag of flowing fluids, and in the present context includes the possibility of removal of material from the solid waste or of already failed material by the flow of gas. Erosion could occur due to the radial flow of gas into a sub-spherical cavity around the borehole, or due to gas flow into and along channels in a layered or otherwise heterogeneous waste.

Material which fails in tension is assumed to be removed to form a hemispherical cavity beneath the drill bit. Gas will flow radially into this cavity. The mechanism of erosion from the solid surface during either Stage 1 or Stage 2 is included in the poroelastic formulation of the stresses discussed in Section 3.2.2.4, so failures due to this mechanism are included in the volumes given in Section 3.3.1.4. Calculations of the erosion of the fractured material have been made, based on classical treatments of the erosion of particulates by flowing fluids. For large cavities these calculations suggest that the removal of materials will be limited to channels, and that the material removed will be smaller than the total amount of material that is available. For smaller cavities this effect is reduced, and under the current set of conditions all the failed material is included in the volumes shown in Section 3.3.2 (Table 3-2) and is assumed to be carried to the surface, so the mechanism of erosion of failed material is included.

3.2.3 Numerical Method

A fully implicit finite difference scheme (Press et al., 1989) that is unconditionally stable is used to solve Equation 8 by directly inverting the associated tridiagonal matrix. Zone sizes and time steps are chosen to maintain physically realistic gradient definitions. The zone size for this study is 1 cm and the time step is initialized at 0.0001 s and never exceeds 0.01 s.

As noted previously, the motion of the mud is coupled to the pressure in the gas column at each time step of the calculation. The specific steps in coupling gas inflow with mud acceleration are as follows:

1. Calculate the new mass of gas in the gas column using Darcy's law at the inner face of the waste, including any additional gas released through tensile failure.
2. Reduce the time step and recalculate if the change in gas mass is greater than 1% (this value is based on numerical experiments).
3. Calculate acceleration, velocity increment and displacement of mud.
4. Calculate new volume of gas column resulting from mud displacement and removal of material due to tensile failure.
5. Calculate new pressure in gas column from ideal gas law.

One additional numerical feature is required for physically realistic failure initiation at very early times. All of the equations used here are quasi-static with respect to wave dynamics. As a result, at very small times, the borehole stress reduction caused by penetration of the drillbit is computed to propagate instantaneously through the waste, while the accompanying gas pressure reduction only propagates at the rate allowed by Equation 8. It is likely that the rate of stress propagation will be on the order of the compressional wave speed in the waste, which is estimated to be 500 to 1000 m/s. For a perfectly elastic material, this artifact leads to the result of negative radial effective stresses everywhere at zero time. Since the waste is not a perfectly elastic material, this result is not physically realistic. To eliminate this physically unrealistic result without having to add the unnecessary complexity of wave propagation to the calculations, we introduce a "maximum tensile failure velocity." This velocity, which would be expected to be of the same order of magnitude as the compressional waste velocity, is used to limit the rate of tensile failure propagation into the waste. Test calculations show that almost any finite value of this velocity eliminates the non-physical result at early times. Thus the actual value of the velocity parameter becomes unimportant, as is desired for a numerical parameter.

The numerical solution for the transient flow case is contained in a computer program called GasOut. GasOut is written in Borland Delphi® Version 2. This programming language is Borland's extension of the standard Pascal language to object-orientation and the Microsoft Windows 95® and Windows NT® operating systems. GasOut is a 32-bit Windows executable running under Windows 95 or Windows NT. A listing of GasOut is provided in Appendix C.

3.3 Results and Discussion for Cavity Growth Model

3.3.1 Typical Response During Mud Blowout

3.3.1.1 Pressure Response

Figures 3-1 through 3-7 present the response of the mud column and repository, using typical values of the blowout parameters. Figures 3-1 through 3-3 present the displacement, velocity, and acceleration of the mud column, respectively, for the first 5 s of the blowout process. Figures 3-4 and 3-5 present the bottomhole pressure and the cumulative mass influx into the gas column. Finally, Figures 3-6 and 3-7 present pore pressure profiles in the waste and the growth of the region of tensile failure for the first 5 s of the transient response.

The parameter values for this calculation are typical of the blowdown process. The repository pressure is 14.5 MPa and the tensile strength of the waste is 15 psi. Other parameter values are based on Appendix PAR(ameters) of the Compliance Certification Application (CCA), on an estimate for the Fanning friction factor for the borehole, and on typical values for porosity in a spalling event. These values are summarized in Table 3-1. Values for the waste pressures and mechanical parameters are discussed in Section 3.3.1.2.
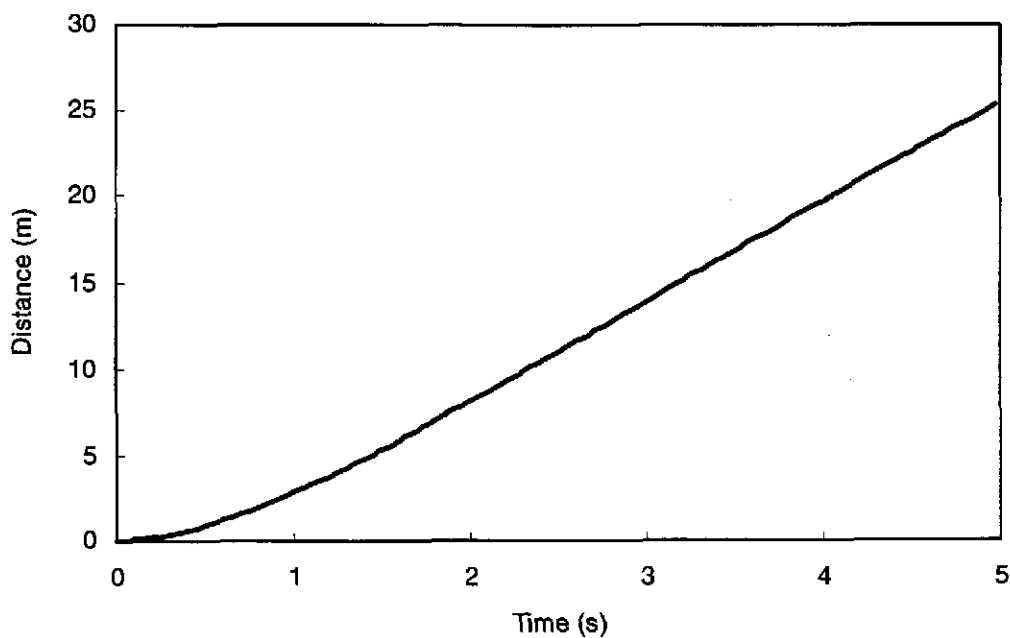
Figure 3-1. Mud displacement for typical blowout parameters.
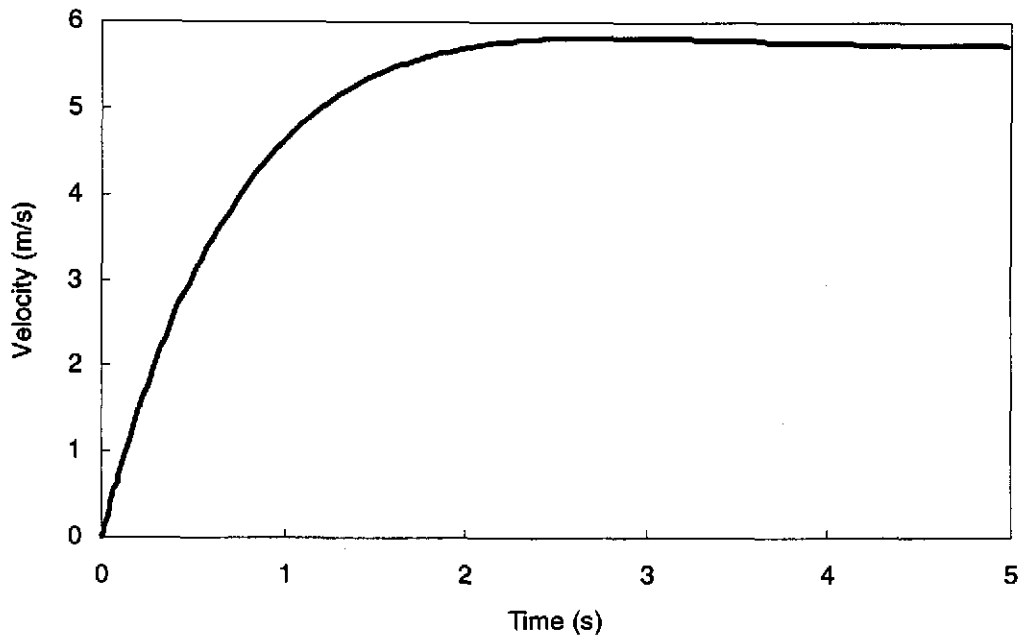
Figure 3-2. Mud velocity for typical blowout parameters.
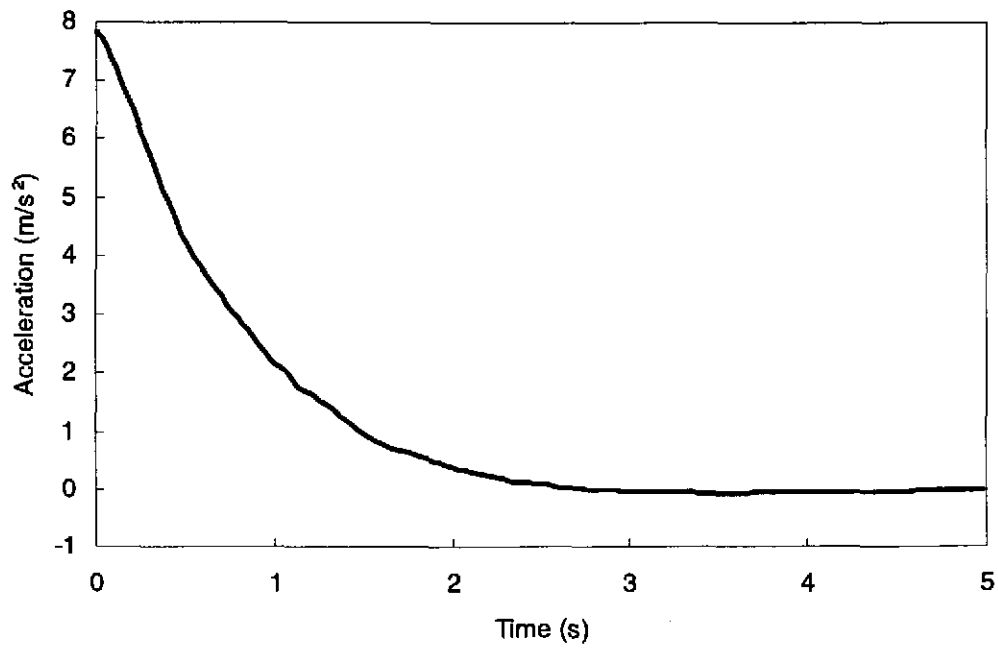
Figure 3-3. Mud acceleration for typical blowout parameters.

3-13
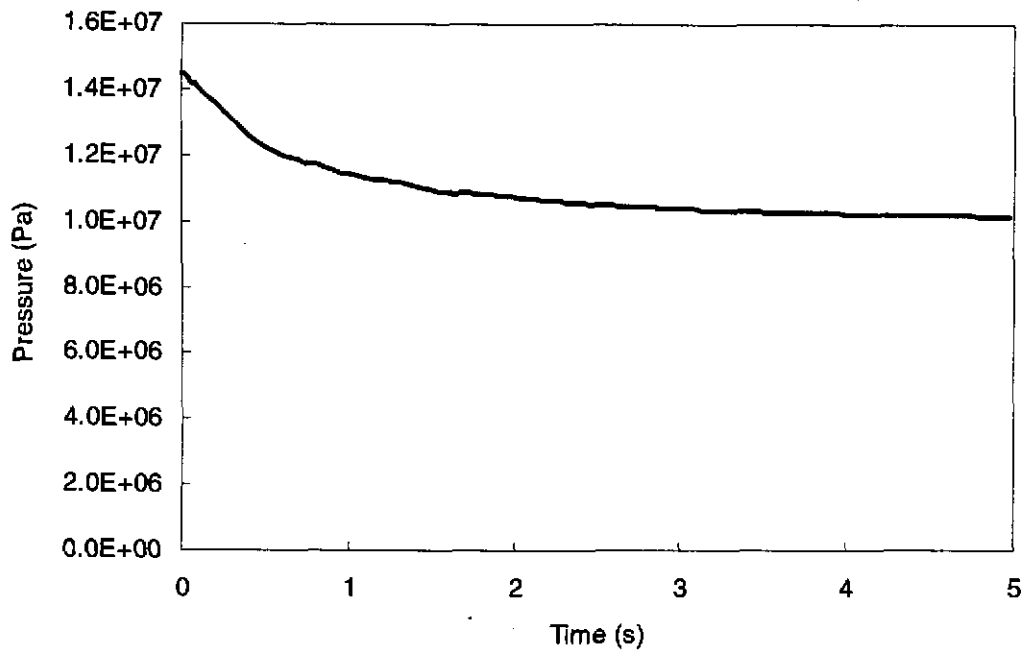
Figure 3-4. Bottomhole pressure during the blowout process.
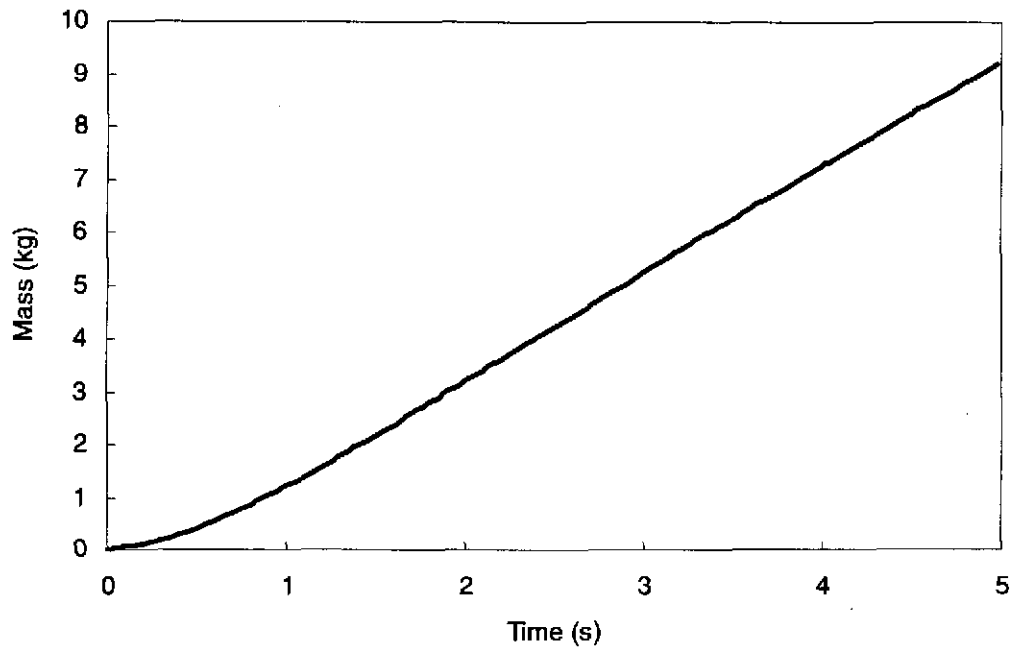
Figure 3-5. Cumulative mass influx into the gas column from the repository.
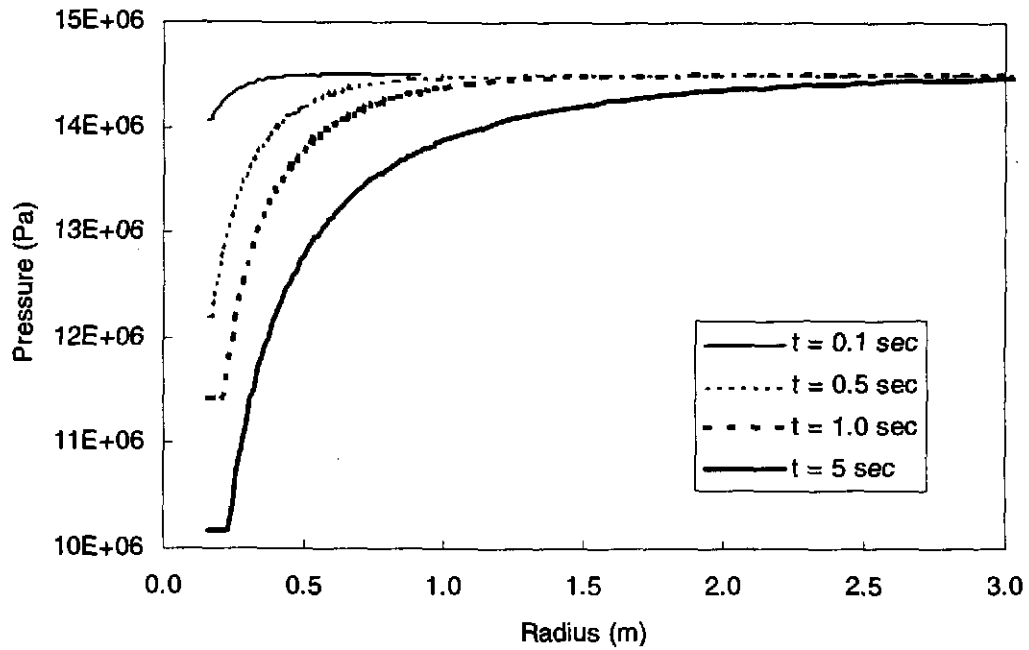
Figure 3-6. Pore pressure profiles in the waste.
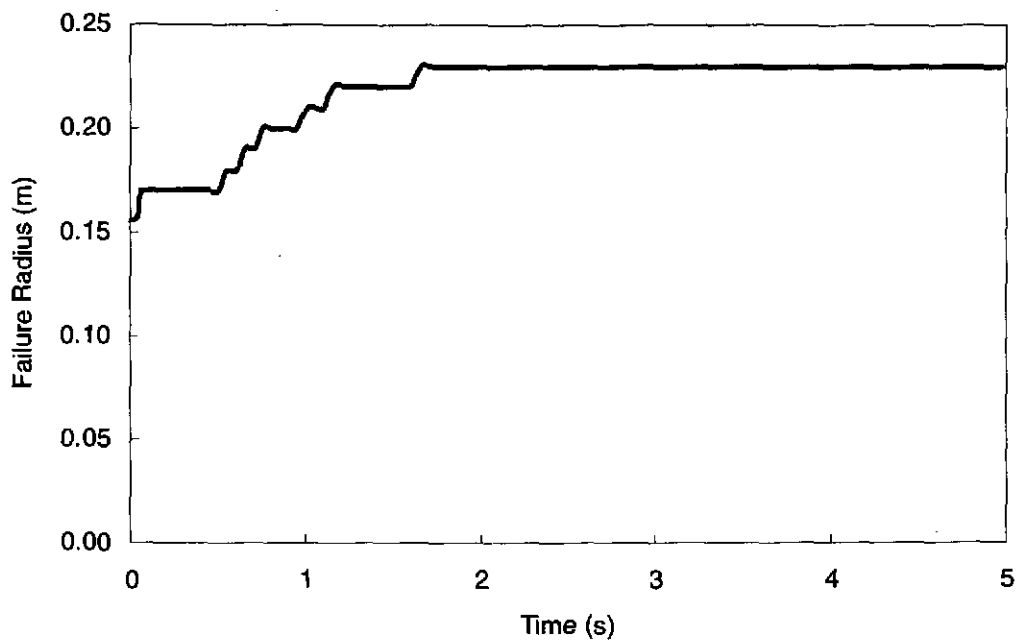
Figure 3-7. Region of tensile failure for the first 5 s of transient response.

Table 3-1. Parameter Values for the Typical Mud Blowout Calculation

Parameter	Value
Repository Pressure (Pa)	14.5×10^6
Waste Permeability (m^2)	1.7×10^{-13}
Waste Porosity (-)	0.70
Gas* Density (kg/m^3)	11.33
Gas Temperature (K)	300
Gas Isentropic Exponent	1.41
Gas Constant, R_0 ($N \cdot m/kg/^\circ K$)	4116.
Gas Viscosity (Pa-s)	9.2×10^{-6}
Mud Density (kg/m^3)	1211.
Mud Viscosity (Pa-s)	0.00917
Fanning Friction Factor (-)	0.01
Length of Borehole (m)	655.
Diameter of Borehole (m)	0.3112
Diameter of Inner Annulus (m)	0.2032
Effective Hydraulic Diameter (m)	0.108
Atmospheric Pressure (Pa)	89465.

* The gas is hydrogen for all calculations, as in the CCA.

The Fanning friction factor, f, has been estimated based on the flow in a pipe of comparable roughness to the borehole. As noted previously, the Reynolds number of the mud at a typical blowout velocity of 5m/s is high enough that f is almost independent of Reynolds number (and hence of flow velocity and mud viscosity). The borehole will have a rough outer surface and a smoother inner surface (the drill collar) for the uncased section below the Salado. Moody (1994) recommends friction factors between 0.027 and 0.05 for concrete pipe and 0.016 for structural steel. The value selected for this calculation, 0.01, is representative of the lower end of these ranges.

At the start of the blowout process there is a large difference between the repository pressure, 14.5 MPa, and the hydrostatic pressure of approximately 8 MPa. This pressure differential produces rapid acceleration of the mud column over the first second or two of the blowout process (see Figure 3-3). This "spike" of acceleration produces a step change in velocity at early times, as shown in Figure 3-2. The rapid acceleration and associated displacement of the mud column slowly reduces the bottomhole pressure, as shown in Figure 3-4. Note that the pressure does not drop immediately to 8 MPa, the hydrostatic weight of the column of mud, because of gas inflow from the repository into the free volume beneath the mud.

3.3.1.2 Stress Response

The typical Stage 1 stress responses from the cavity growth model are shown in Figures 3-8 and 3-9. Figure 3-8 shows the effective radial stress profiles in the waste as a function of time. The effective radial stress is the sum of the non-pore pressure and pore pressure stresses, minus the pore pressure. The early time stress profiles show the development of a tensile zone, which grows with time during the initial depressurization. After about 1 s, an inner compressive zone starts to develop, shielding the outer regions from the borehole cavity. Figure 3-9 shows the effective tangential stresses, which are compressive at all times and radii.
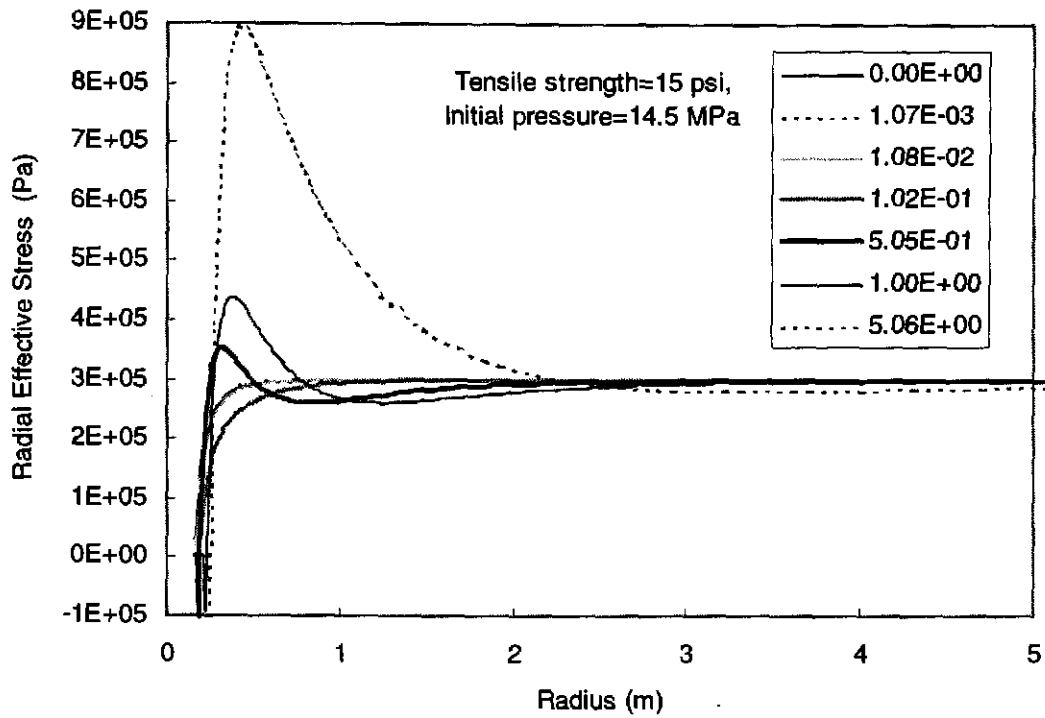
Figure 3-8. Effective radial stress profiles as a function of time.
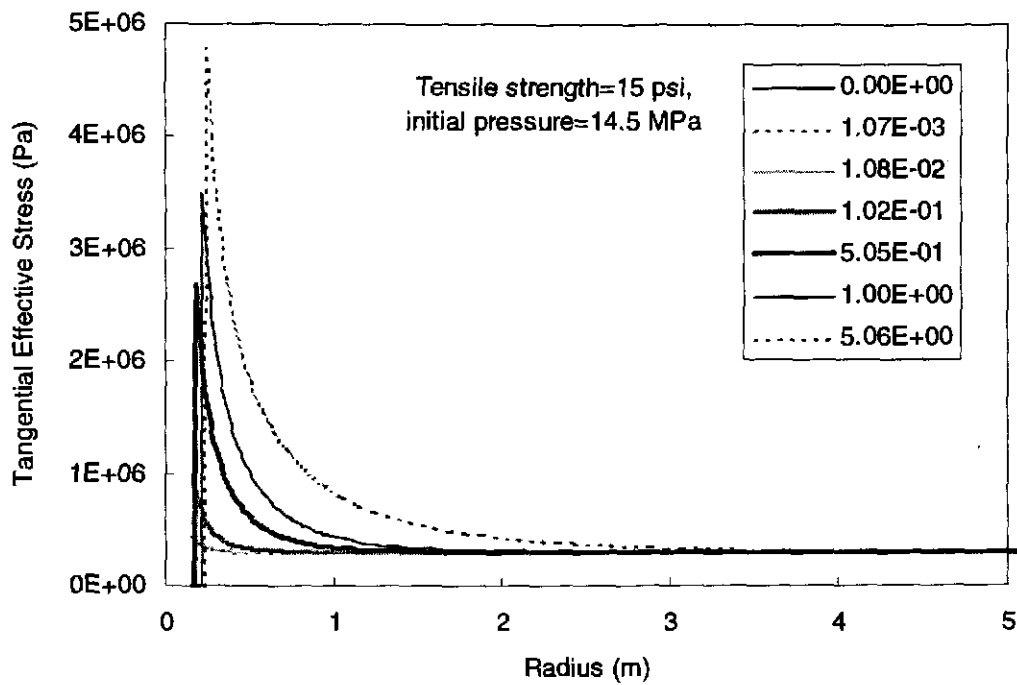
Figure 3-9. Effective tangential stresses.

3.3.1.3 Effect of Cavity Growth

The cavity growth model includes the capability to dynamically modify the size and properties of a failed region adjacent to the borehole. This central failed region is referred to as the cavity in this discussion. The calculation of material failure and growth of the cavity is described in detail here.

At each time step, each finite difference zone is checked for the presence of an effective radial tensile stress that exceeds the assigned tensile strength of the material. If that is the case, and if the zone is adjacent to the cavity, the material in that zone is assumed to be disrupted, and the cavity boundary is allowed to advance to the next zone boundary. This process is allowed to proceed, in space and time, until tensile failure adjacent to the current cavity no longer occurs. To avoid excessively discontinuous behavior in space and time, the time step is dynamically adjusted so that generally no more than one zone can fail per time step.

To maintain mass balance, the solid mass of the new boundary-failed zone is assumed to be mixed into the cavity as a solid volume, but with no associated mechanical effects. The gas mass contained in the porosity of the failed solid is assumed to be mixed with the cavity gas. Since the pressure within the solid is usually greater than the pressure within the cavity, the gas mass added to the cavity should produce a higher cavity pressure than without cavity growth. In the remaining waste, pore pressures are assumed to be those that existed before the tensile failure, but with a new inner boundary condition to reflect the changed cavity boundary and pressure. Subsequent stresses are calculated with these new boundary conditions. Since the solid stress state is assumed to be quasi-static, and the transient porous fluid flow is included in the existing calculation, this method of accounting for failure induced cavity growth appears to be a reasonable first approximation without adding the complexity of full nonelastic strain calculation.

Figures 3-10 through 3-12 show the effect of adding tensile-induced cavity growth for calculations with the parameters given in Table 3-1. Both the mud velocity and the bottomhole pressures are higher with cavity growth, as shown in Figures 3-10 and 3-11. This is the expected response because tensile failure adds high pressure gas to the cavity, increasing the bottomhole pressure and acceleration of the mud.

For a tensile strength of 15 psi, the cavity grows to 0.23 m in about 2 s, as shown in Figure 3-12. The comparable calculation without cavity growth fails out to 0.17 m, equivalent to one zone width.

The "stair-step" appearance of the cavity growth case in Figure 3-12 is not caused by overly large time steps or zone sizes. The time represented in the figure corresponds to more than 300 steps, and each failure "event" corresponds to one zone failing over many time steps. Instead, there is a tendency for each tensile failure event to cause a relaxation of tension near the boundary of the remaining solid. Tensile stresses subsequently build and another tensile failure ensues, and so forth. While this behavior is qualitatively reasonable, the quantitative effects of alternate failure models may be substantial. For example, the effects of nonelastic strain relaxation in possibly mitigating the stair-steps have not been calculated.
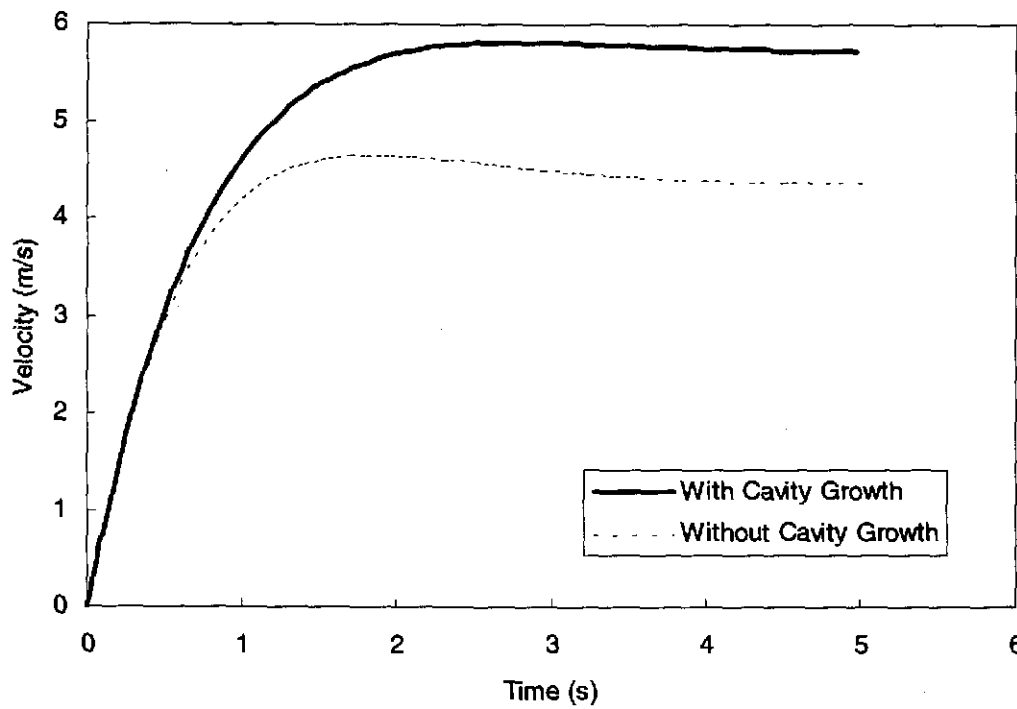
Figure 3-10. Effect of adding tensile-induced cavity growth.
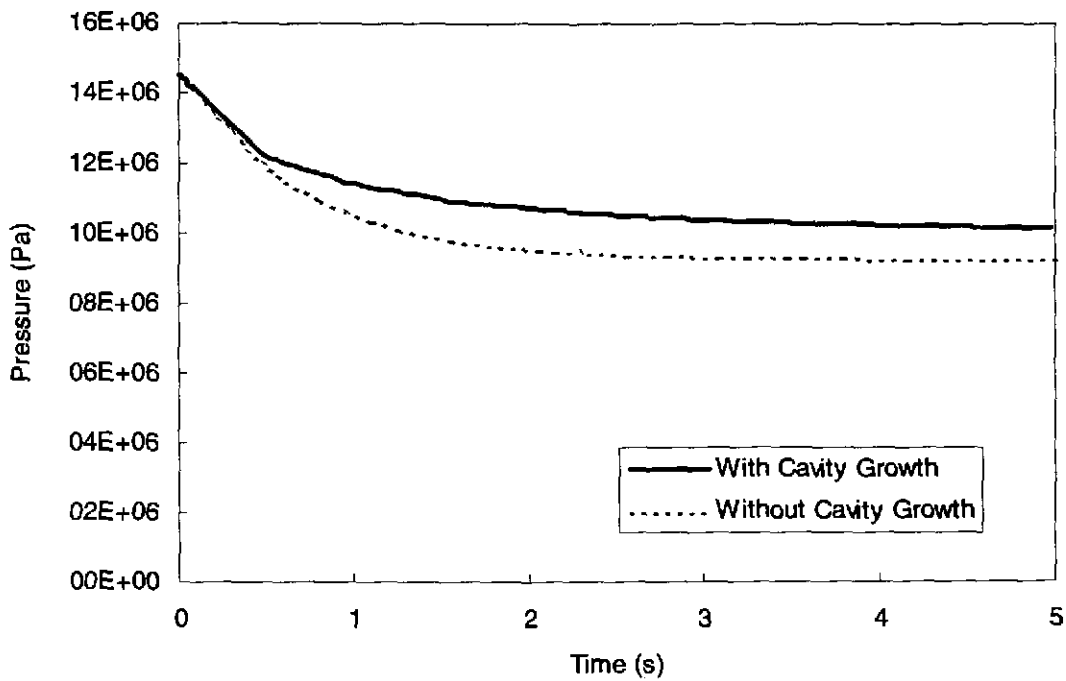
Figure 3-11. Effect of adding tensile-induced cavity growth.
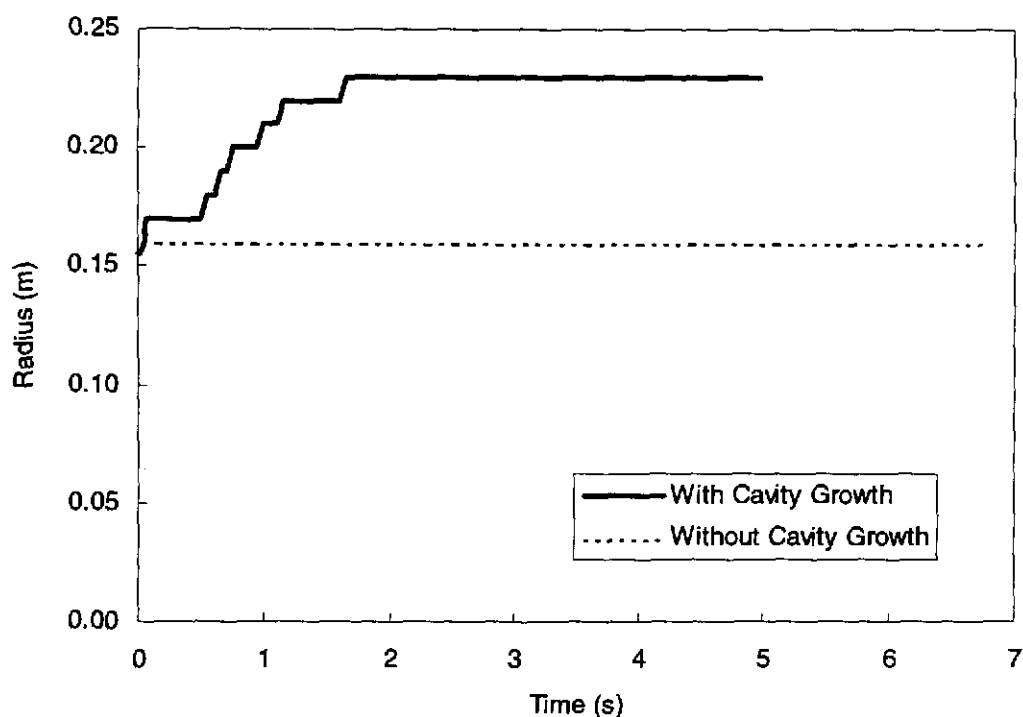
Figure 3-12. Effect of adding tensile-induced cavity growth.

Figures 3-13 and 3-14 present the effective stress profiles at various times without cavity growth. These profiles can be compared to the corresponding plots in Figures 3-8 and 3-9 with cavity growth. The results for radial effective stress are generally similar, with the radial stress at the inner boundary remaining near -15 psi (-0.1 MPa), the tensile strength, with or without cavity growth. In addition, the radial effective stress becomes compressive after 1 s with or without cavity growth. The tangential effective stress with and without cavity growth also exhibits similar behavior in that it is always positive and compressive.

While this simple comparison may make it appear that removal of failed material is unimportant, computational testing has shown that the response at 14.8 MPa, with initial conditions of zero effective stress, will be much more sensitive to the failure mechanisms, including stress redistribution and changes in permeability of the waste.

3.3.2 Tensile Failure Volumes during Stage 1

Potential spall volumes are calculated using the following assumptions:

1. Material which is at a tensile radial effective stress in excess of the tensile strength is considered to have failed. Failure in this sense means the development of discrete fractures. Based on the experimental data presented in Section 2, the tensile strength is 0.07 MPa ±0.035 MPa (10 psi ±5 psi) below 14 MPa initial pressure, and 0.105 MPa ±0.035 MPa (15 psi ±5 psi) above that.
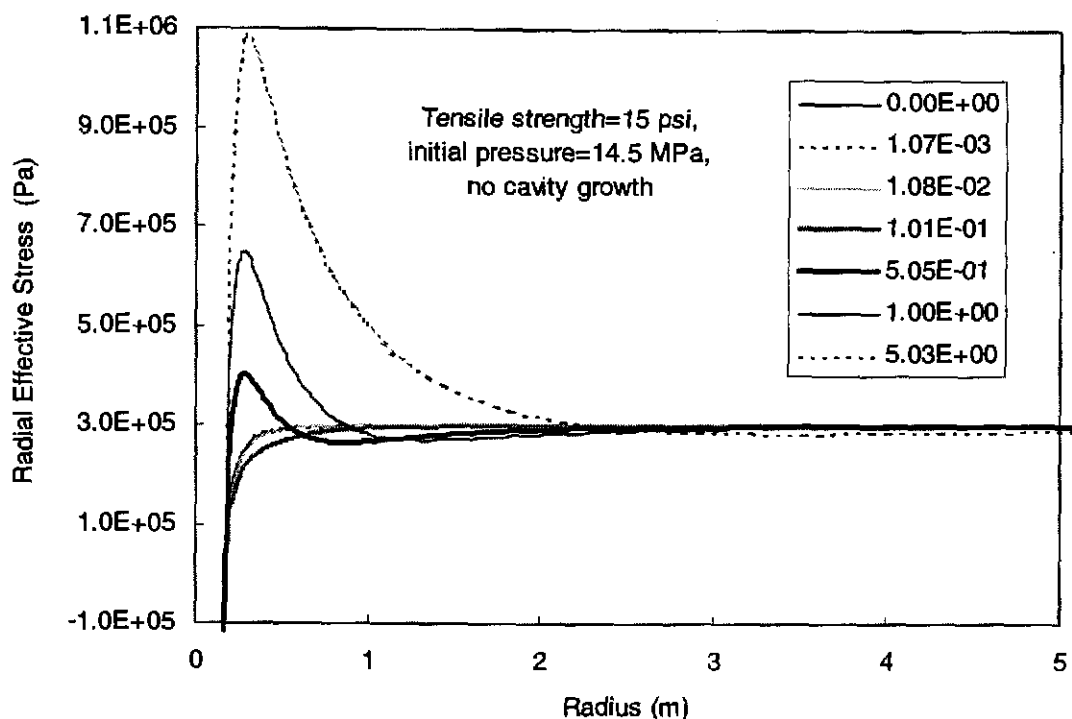
Figure 3-13. Effective stress profiles without cavity growth
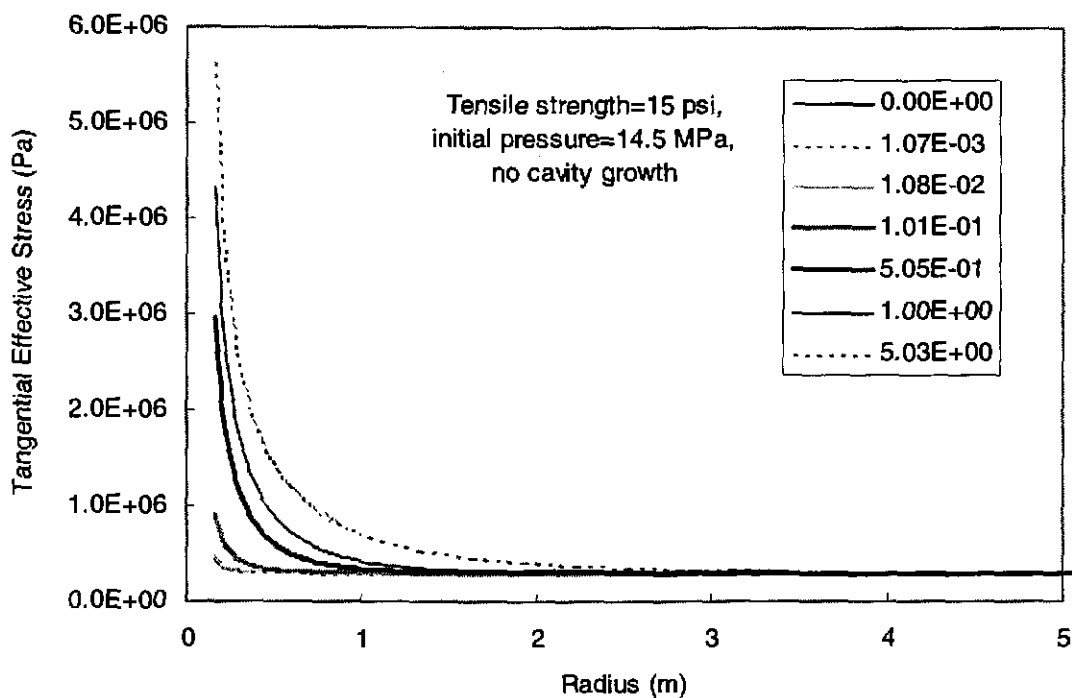
Figure 3-14. Effective stress profiles without cavity growth.

2. If the tensile failed material is in contact with the borehole cavity, then it is assumed that the failed material will contribute to the spall volume. "Borehole cavity" is taken here to mean the initial cavity volume plus any new cavity created by spalling. Conversely, if the borehole cavity is separated from the failed zone by material which has not failed, and which has not been removed earlier, then the failed zone is not considered to contribute to the spall volume.

3. For the conditions considered here, it is assumed that any material that is spalled will be carried to the surface.

4. Material where the stresses exceed the appropriate yield criterion do not contribute to the spall volume. The expected response under shear failure will be yield and plastic deformation. Under these conditions the stresses will be modified and discrete failure with multiple fracturing is not expected. In addition, the calculated yield zones are, in general, of the same approximate size, or smaller than, the tensile zones. Hence shear failure is not a major contributor to spall volume.

Volumes calculated by the cavity growth model using the above assumptions are reported in Table 3-2. Note that the radius of the unimpeded tensile zone is given. This quantity is the maximum radius of the zone in which the radial tensile stress exceeds the strength and which is contiguous with the borehole cavity. The uncompacted spalling volume is also reported. This volume is directly equivalent to the volumes reported in the CCA. The uncompacted spalling volume is calculated as follows:

$$V_0 = \frac{1-\varphi}{(1-\varphi_0)} V$$

$$V = \frac{2}{3} \pi r^3$$

where:

V	=	compacted spalling volume
V_0	=	uncompacted spalling volume
r	=	the radius of the unimpeded tensile zone,
φ	=	the compacted porosity of the waste, taken here as 0.7
φ_0	=	the initial uncompacted porosity, or 0.848

It will be noted from Table 3-2 that: below 14.3 MPa repository pressure there is essentially no spall predicted, while above that the volumes are not large.

3.4 Sensitivity Studies

The spall volumes computed with the cavity growth model are sensitive to a number of physical parameters, including tensile strength, Poisson's ratio, waste permeability, pipe friction factor, and the geometry of the annular flow path in the borehole. In addition, the late time response during Stage 1 and Stage 2 is potentially important for estimating the condition of the waste when the mud clears the wellbore.

Table 3-2. Failure radii and Uncompacted Volumes Calculated by the Cavity Growth Model

Initial Gas Pressure (MPa)	Tensile Strength (psi)	Tensile Radius (m)	Uncompacted Volume (m³)
12		0.156	0
	10	0.156	0
	15	0.156	0
14	5	0.37	0.19
	10	0.21	0.02
	15	0.156	0
14.3	10	0.28	0.07
	15	0.20	0.02
	20	0.156	0
14.5	10	0.33	0.13
	15	0.23	0.03
	20	0.156	0
14.6	10	0.35	0.16
	15	0.24	0.04
	20	0.156	0
14.7	10	0.37	0.19
	15	0.26	0.06
	20	0.18	0.01
14.8	10	0.40	0.25
	15	0.27	0.07
	20	0.21	0.02

One parameter, tensile strength, has been evaluated directly with the cavity growth model, as shown in Table 3-2. Other parameters have been evaluated with a quasi-static model that provides an approximate solution to the porous flow equations. The quasi-static model was initially developed because it provides physical insights into the response of the mud and waste during the complete Stage 1 blowdown process. It also provides a partial verification of the volumes predicted by the cavity growth model for non-zero effective stress. Finally, it is very computationally efficient because it runs on two Excel spreadsheets.

A brief description of the quasi-static model is presented in this section, followed by a discussion of the late time response and sensitivity of spalling volume to selected parameters.

3.4.1 Quasi-Static Model and Numerical Solution

The conceptual and mathematical models for the quasi-static model are identical to those for the cavity growth model, except that the gas flow in the porous medium is approximated by a sequence of steady-state profiles and the size of the cavity does not change after tensile failure. The mathematical formulations for the motion of the mud column, for the calculation of bottomhole pressure, and for the calculations of stress and failure in the waste are as described in Sections 3.2.2.1, 3.2.2.3 and 3.2.2.4, respectively, for the quasi-static model.

An approximate solution to the one-dimensional equations for gas flow in a porous medium are given in Chan et al., 1993. This approximate solution assumes that the pressure profile in the porous medium is given by the steady state profile between the inner wall, at pressure p_0, and an outer boundary at the far field pressure, p_1. This outer boundary is located at a distance R whose

location changes with time. The cited reference derives ordinary differential equations in planar, cylindrical and spherical symmetries for R and for M, the cumulative mass influx through the inner boundary. The appropriate equations for one dimensional, spherically symmetric flow of an ideal, isothermal gas are given by:

$$\Psi(p) = \frac{R\Psi(p_1) - a\Psi(p_0)}{R-a} - \frac{aR[\Psi(p_1) - \Psi(p_0)]}{r(R-a)} \qquad (21)$$

$$\frac{dR}{dt} = \frac{ak(p_1^2 - p_0^2)}{2\mu\phi p_1 R(R-a)} \qquad (22)$$

and

$$\frac{dM}{dt} = \frac{kAR(p_1^2 - p_0^2)\pi a^2}{\mu a(R-a)} \qquad (23)$$

where

$\Psi(p)$	=	the pseudopressure, which equals p^2/μ for an ideal gas,
$R(t)$	=	the outer radius of the steady state pressure distribution,
$M(t)$	=	the cumulative mass influx through the inner boundary (inward is positive),
a	=	the radius of the inner wall,
p_0	=	the pressure in the gas column, which is also the bottomhole pressure,
p_1	=	the far-field repository pressure,
m	=	the viscosity of the gas,
f	=	the porosity of the waste,
A	=	a constant, equal to $1/(R_0 T)$, and
k	=	the permeability of the waste.

Equation 21 is the steady-state pseudopressure profile in the porous medium. The inner boundary for these equations is a hemispherical cavity of radius a, directly underneath the borehole. The value of a is taken to be equal to the radius of the borehole for computational purposes.

The boundary conditions for Equation 21 are:

$$p(a) = p_0$$

and

$$p(R) = p_1$$

The initial conditions for Equations 21, 22, and 23 are:

$$p_0(0) = p_1$$

$$R(0) = a$$

and

$$M = \text{initial mass in cavity}.$$

The approximate solution in Equations 21 through 23 assumes that pressure is constant at the inner wall. However, it has been applied to the mud blowout process where the bottomhole pressure will vary with time. In this case, the quasi-static model passes through a sequence of steady state profiles where both R and p_0 will vary with time. This quasi-static approximation is partly validated by comparison of results from the quasi-static model to the results from the cavity growth model for the full transient solution for Equation 8.

The numerical solution technique for solving Equations 6, 7, 11, 12, 21, 22, and 23 is based on a second order Runge Kutta integration scheme for a system of first order ordinary differential equations (Abramovitz and Stegun, 1970). This is a straightforward process, except at time zero when the values of dR/dt and dM/dt are indeterminate, with both numerator and denominator going to zero.

To avoid the indeterminate values for dR/dt and dM/dt at time zero, the differential equations for R and M can be integrated and expanded to yield approximations for $R(t)$ and $M(t)$ as $t \rightarrow 0$:

$$R(t) \rightarrow \sqrt{a + \frac{k\left(p_1^2 - p_0^2\right)t}{\mu \phi p_1}} \tag{24}$$

$$M(t) = \sqrt{\frac{2\pi a^2 kA\left(p_1^2 - p_0^2\right)\phi \rho t}{\mu}} \tag{25}$$

Equation 25 can now be combined with Equations 14 and 15 into a quadratic equation for the cavity pressure at time, t, close to zero:

$$\left(V^2 + \beta\right)p_0^2 - \left(2 M_0 V R_0 T\right)p_0 + \left[\left(M_0 R_0 T\right)^2 - \beta p_1^2\right] = 0 \tag{26}$$

with

$$\beta = \frac{4\pi^2 a^4 k p_1 \phi t}{\mu} \tag{27}$$

Equation 26 is solved for the value of p_0 at a small, initial non-zero time. (A typical value for this initial time is 0.01 s). The values of R and M at this time are then determined from Equations 24 and 25, respectively. After this initial step, the standard Runge Kutta procedure is used for all subsequent time steps.

The time step for the Runge Kutta procedure varies during the calculation. The choice of time step is motivated by a need for better numerical accuracy during the initial transient and during the rapid acceleration as the mud clears the borehole at the end of the calculation. The time step is 0.01 s for the first second and then 0.1 s from 1 to 5 s. By 5 s the acceleration of the mud is very small and the time step is increased to 0.5 s. The time step remains at 0.5 s until late in the blowout process, when the mud acceleration again increases as the mud column becomes very short. The time step is reduced to 0.2 s when the mud acceleration increases to 0.1 m/s^2 and subsequently to 0.1 s when the mud acceleration increases to 1 m/s^2. The time step remains at 0.1 s until the mud clears. There are a total of 400 to 500 time steps in a typical calculation.

The numerical integration of the blowout equations is performed in a spreadsheet for Microsoft Excel for Windows 95, Version 7.0a. The output data from the blowout calculation includes the values of p_0 and $R(t)$ for calculating the quasi-static pore pressure profiles surrounding the borehole (see Equation 21). A second Excel spreadsheet calculates the stress distributions and failure volumes for these pressure profiles, using Equations 13 through 19. Note that these stress distributions are static, so a numerical integration is not required for this part of the problem.

3.4.2 Late Time Response

Figures 3-15 through 3-18 present the response of the mud column and waste with the quasi-static model using typical values of the blowout parameters in Table 3-1. Figures 3-15 through 3-17 present the acceleration, velocity and displacement of the mud column, respectively, for the duration of the blowout process. Figure 3-18 presents the bottomhole pressure. Note that the Fanning friction factor for the quasi-static calculation is 0.02, rather than 0.01; however, this change results in only a small difference in the response of the mud column or bottomhole pressure, as discussed in Section 3.4.3.

At the start of the blowout process, there is a large difference between the repository pressure (14.5 MPa) and the hydrostatic pressure of approximately 8 MPa. This pressure differential produces a rapid acceleration of the mud column and a "step" change in velocity over the first few seconds of the blowout process, as shown in Figures 3-15 and 3-16. The resulting displacement of the mud column (see Figure 3-17) reduces the bottomhole pressure, as shown in Figure 3-18.

After the initial acceleration, the velocity of the mud column is approximately 5 m/s for the next 50 s. This velocity represents a balance between the pressure differential across the mud column, the frictional drag from the walls, the weight of the mud column, and the gas inflow from the repository. The gas column behind the mud will also have this velocity, which is equivalent to 11 miles/hour. Within the repository, the high porosity (0.7) and large cross-sectional area for flow will reduce the pore velocity further. The conclusion is that there will be relatively little lofting and erosion of larger particulates for most of the mud blowout process. Note that this conclusion must be reexamined after the mud is expelled from the borehole because gas velocity will increase substantially without the confinement from the mud.

Velocity and acceleration increase near the end of the blowout process because the bottomhole pressure remains substantial while the length and mass of the mud column decrease to zero. While the rapid increase in velocity and acceleration are correct in a qualitative sense, the quantitative values for velocity are just an approximation. The Stage 1 model has an ideal mud/gas interface that is only an approximation to the late-time response, where the two-phase (mud/gas) flow regime will have a major impact on final gas and mud velocities. In addition, the time step in the Runge Kutta integration scheme must be decreased for better accuracy, but this is a minor concern compared to the representation of the two-phase flow.

After the mud has been ejected, the pressure in the borehole will fall rapidly, and gas flow out of the waste will be controlled by the friction in the wellbore and the gas deliverability of the waste. It is estimated that the pressure at the bottom of the hole will fall to about 0.5 MPa in about 1 to 2 s, this time being based on one-way acoustic transit time of about 0.5 s in the borehole.
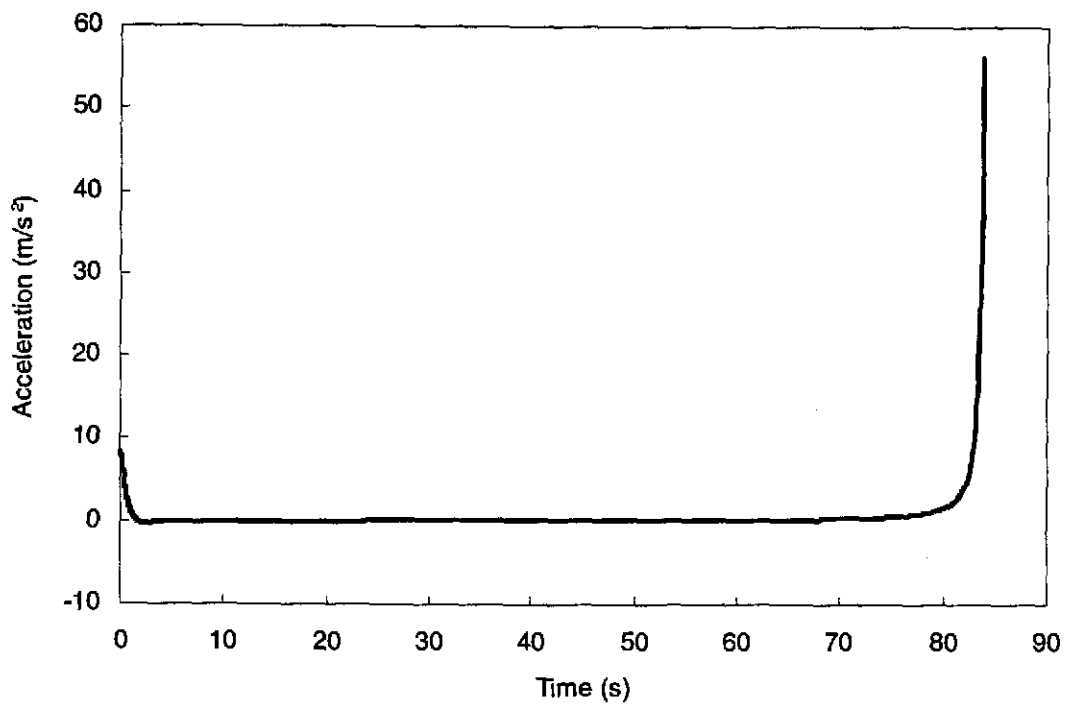
Figure 3-15. Mud acceleration.
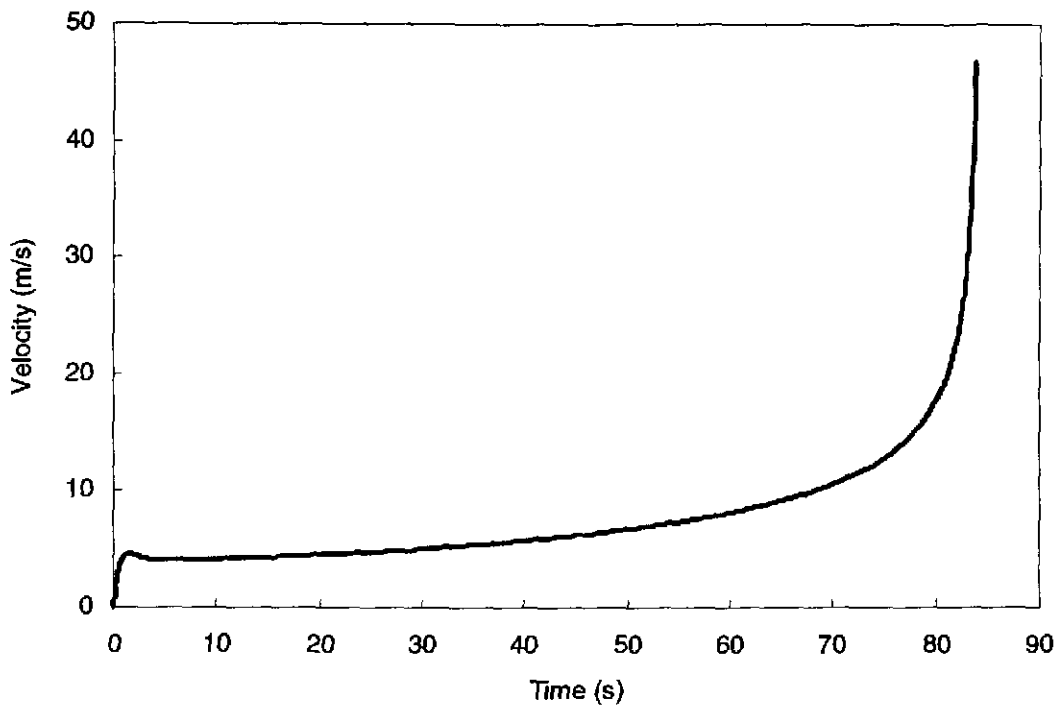
Figure 3-16. Mud velocity.
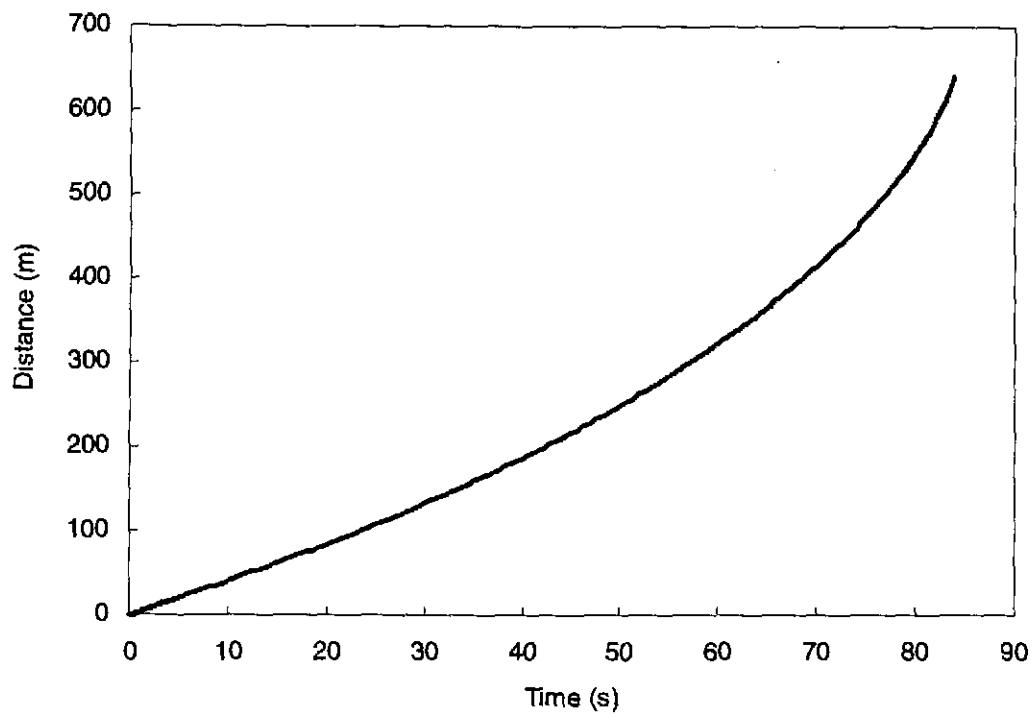
Figure 3-17. Mud displacement.
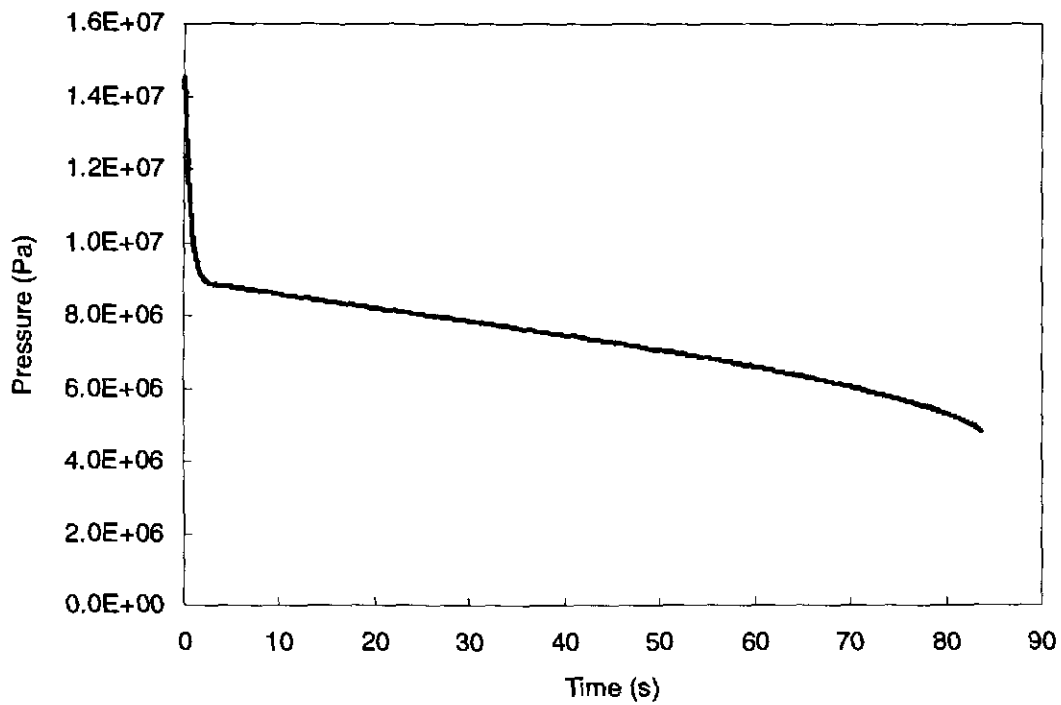
Figure 3-18. Borehole pressure.

From that time on, the pressures at the bottom of the wellbore will remain fairly constant until the panel is depleted or the well is shut in. The bottomhole pressure of 0.5 MPa is appropriate when the bottomhole cavity has the same radius as the borehole, 0.1556 m. For a larger bottomhole cavity, the greater surface area increases the deliverability of the waste, leading to somewhat higher bottomhole pressures.

3.4.3 Comparison of Quasi-Static and Cavity Growth Models for a Constant Cavity Size

Parallel calculations were performed with the quasi-static model and the cavity growth model to provide a partial verification/benchmarking of both methods. Since removal of material from the inner cavity substantially alters the bottomhole pressure and pore pressure profiles in the waste, this feature of GasOut was turned off for this comparison. The initial repository pressure is 14.5 MPa for both calculations. The Fanning friction factor is 0.01 and 0.02 for the cavity growth model and the quasi-static model, respectively. All other parameters are as shown in Table 3-1.

Figures 3-19 through 3-21 compare the displacement, velocity, and acceleration of the mud column for the first 5 s for both models. There is clearly excellent agreement between the calculations for the motion of the mud. Figures 3-22 and 3-23 compare the bottomhole pressure, cumulative gas inflow, and gas inflow rates for the first 5 s. Again, there is close agreement between the two models. Figures 3-24 and 3-25 compare the pore pressure profiles in the waste at 0.1 seconds and at 5 seconds.
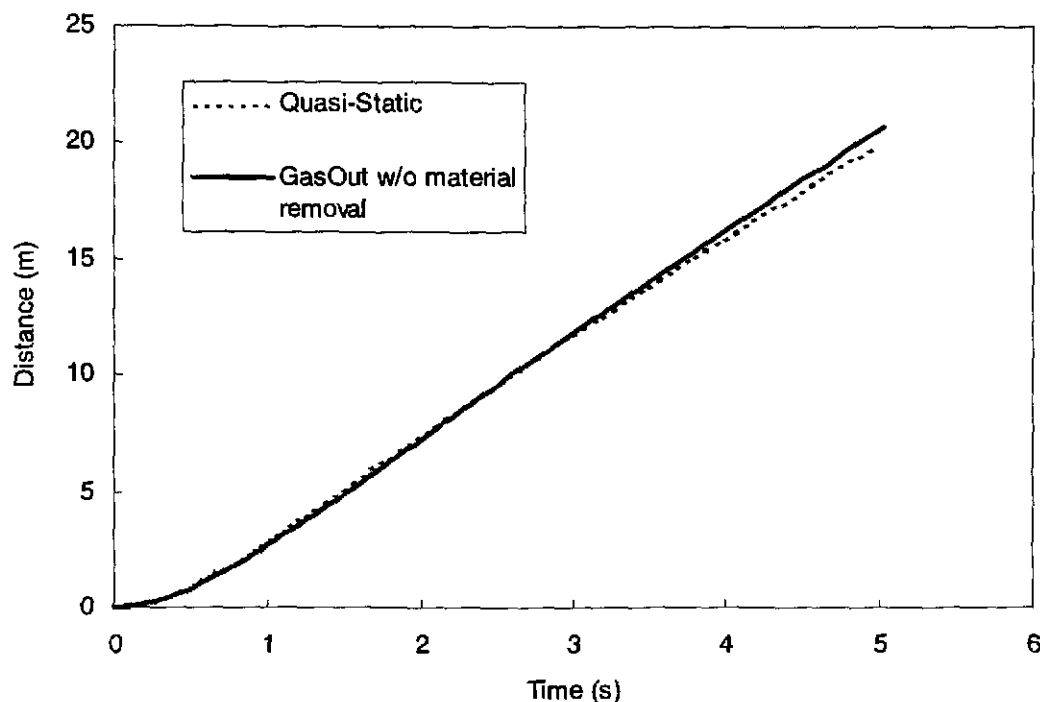
Figure 3-19. Displacement of the mud column for the first 5 s for both models.
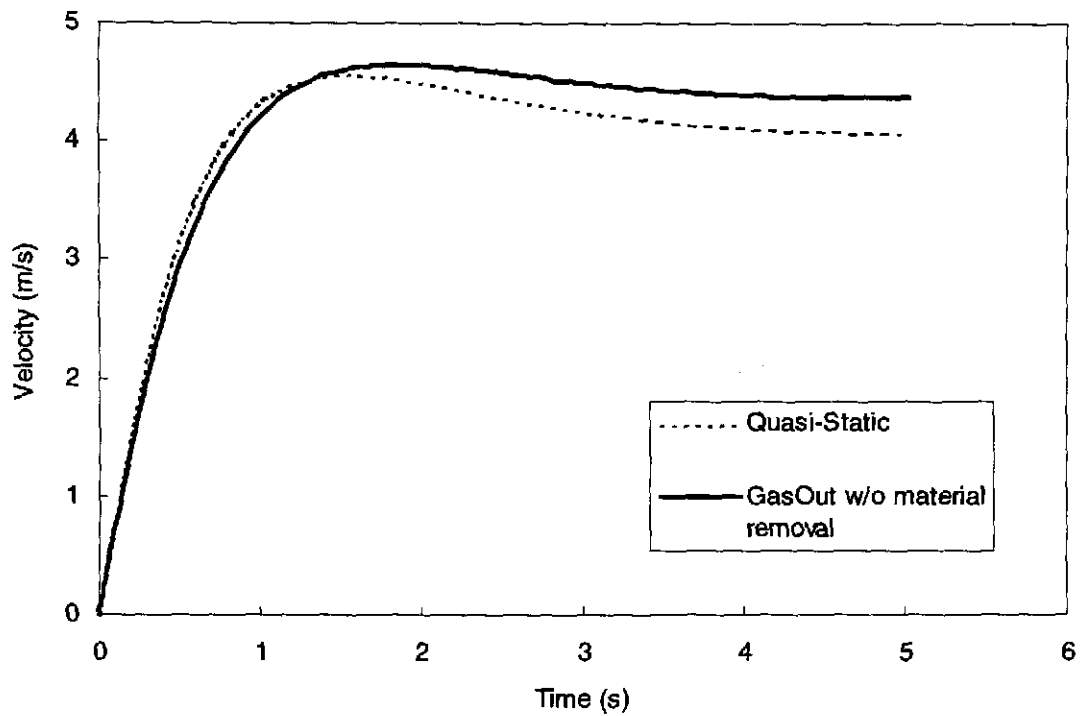
Figure 3-20. Velocity of the mud column for the first 5 s for both models.
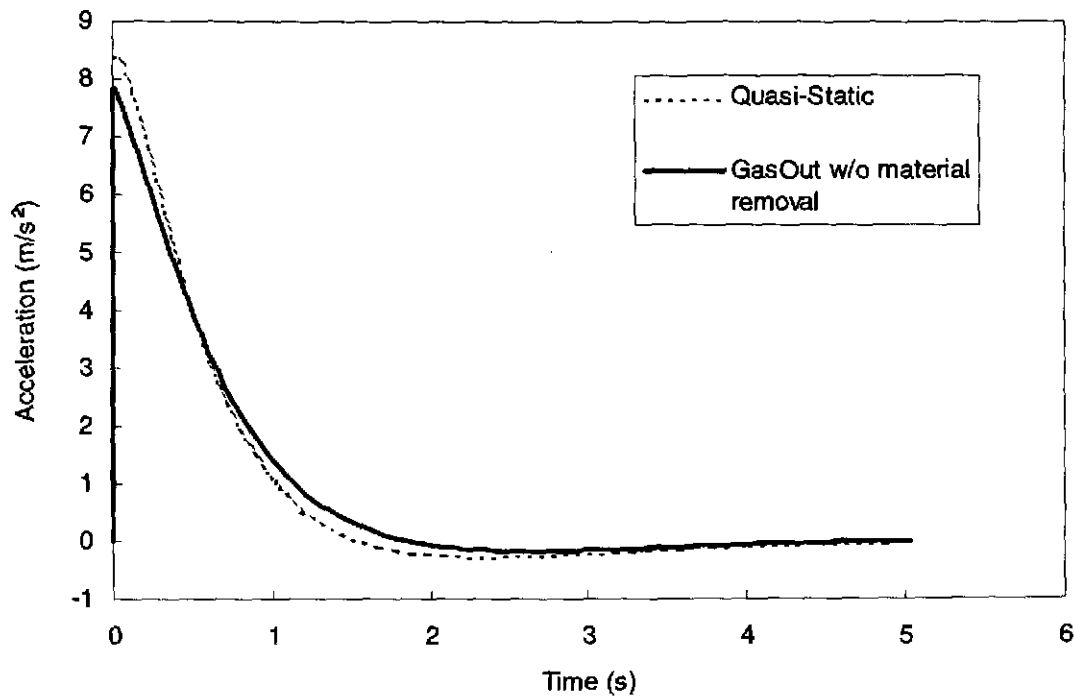
Figure 3-21. Acceleration of the mud column for the first 5 s for both models.
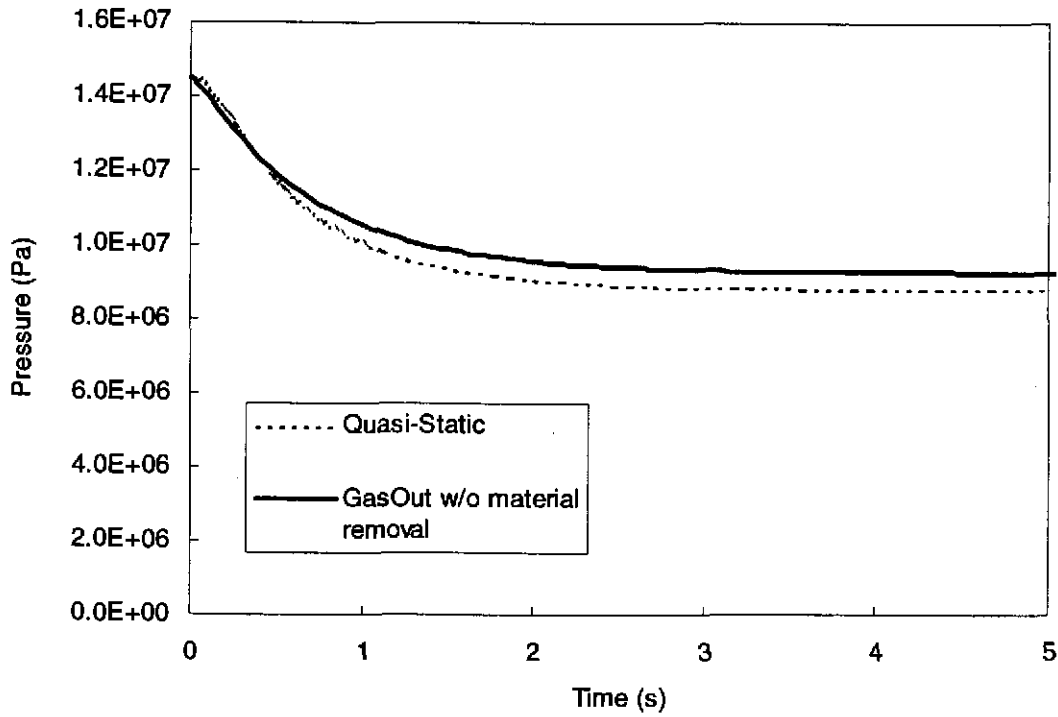
Figure 3-22. Bottomhole pressure, cumulative gas inflow, and gas inflow rates for the first 5 s.
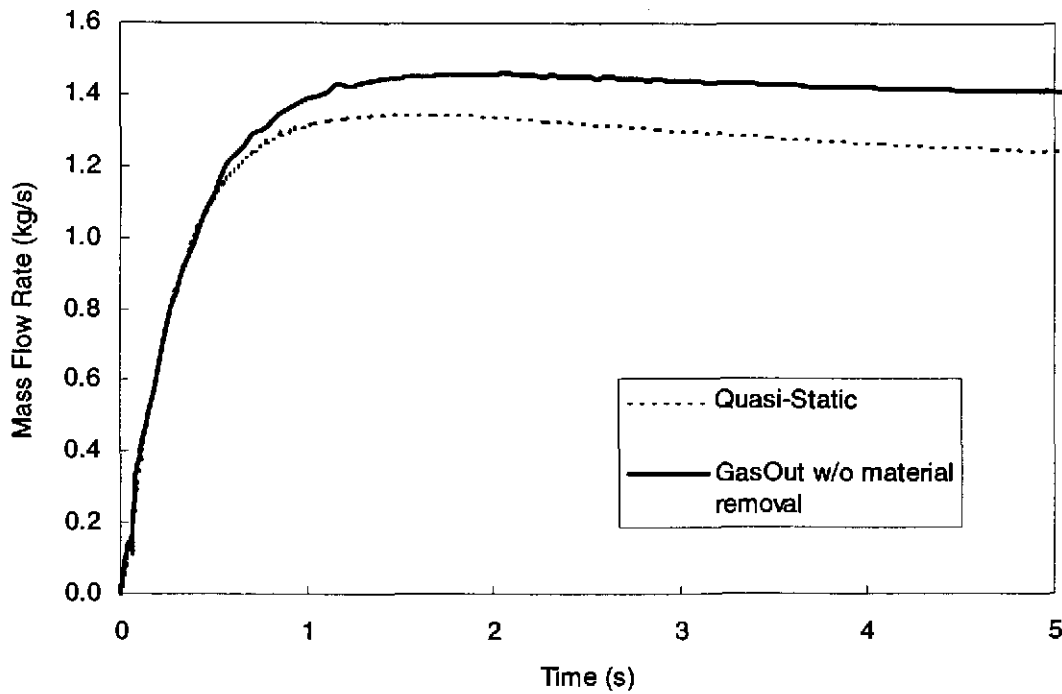
Figure 3-23. Bottomhole pressure, cumulative gas inflow, and gas inflow rates for the first 5 s.
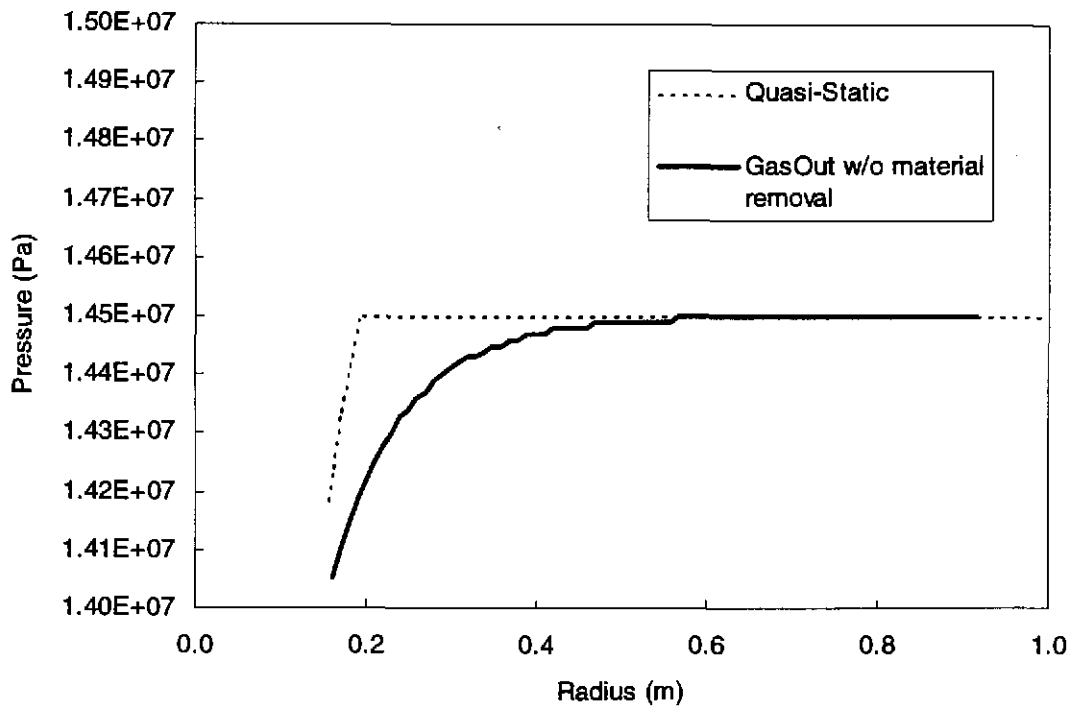
Figure 3-24. Pore pressure profiles in the waste at 0.1 seconds.
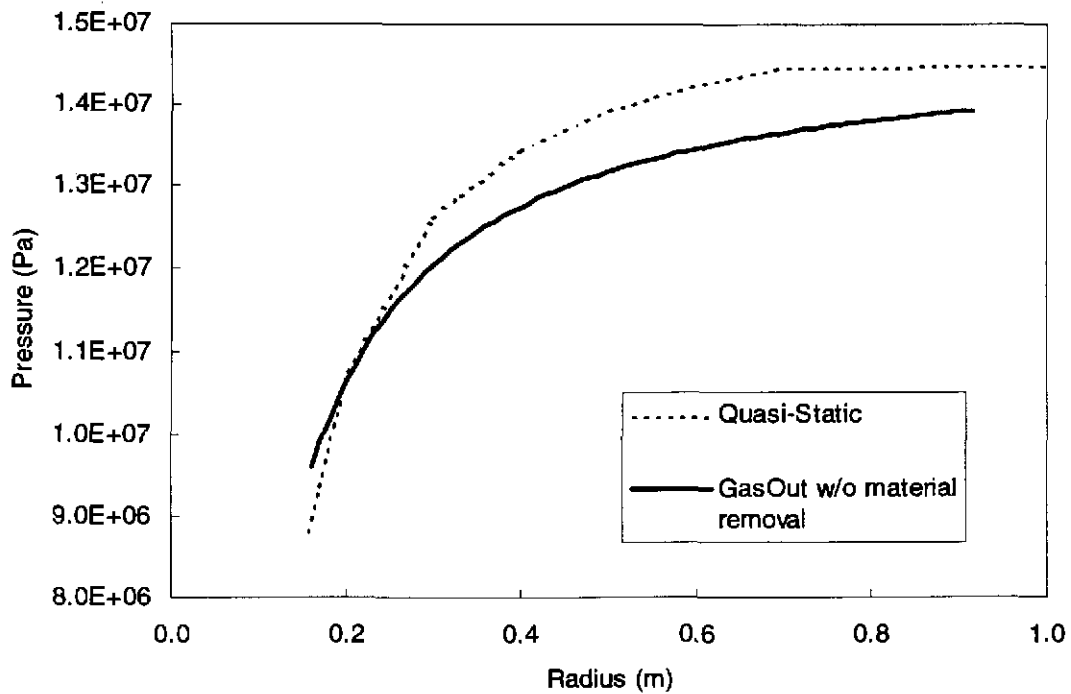
Figure 3-25. Pore pressure profiles in the waste at 5 seconds.

There are two important facts to note in these comparisons:

1. The pressure profile from the quasi-static model is much steeper at early times in the sense that the pressure change is more localized around the cavity.

2. At the cavity wall, the pressure gradients are very similar for both models. This similarity explains the agreement of bottomhole pressure and mass influx, which is driven by the pore pressure gradient at the wall.

The failure radii and spalling volumes computed by the two models for non-zero effective stress are very similar. Table 3-3 presents a comparison of these numerical values, which are quite close considering the differences in pore pressure profiles and in the removal or retention of failed material at the cavity wall. In most cases, the cavity-growth model produces somewhat less tensile failure than the quasi-static model. Exceptions are the lowest initial pressures combined with lowest initial strengths and the highest initial pressure and lowest strength.

Table 3-3. Volumes Calculated by Quasi-Static and Cavity Growth Models

Initial Gas Pressure (MPa)	Tensile Strength (psi)	Tensile Radius (m) QS Model	CG Model	Uncompacted Volume (m^3) QS Model	CG Model
12	10	0.156	0.156	0	0
14	10	0.156	0.21	0	0.02
14.3	15	0.156	0.20	0	0.02
14.5	15	0.44	0.23	0.34	0.03
14.6	15	0.49	0.24	0.47	0.04
14.7	15	0.66	0.26	1.17	0.06

3.4.4 Sensitivity to Parameters

The sensitivity of the results to a number of parameters has been determined using the quasi-static model. Parameters investigated include the tensile strength, Poisson's ratio, waste permeability, pipe friction factor, and the geometry of the annular space.

3.4.4.1 Strength

Variations in strength affect the potential spall volume through calculation of the extent of the zone in which tensile stresses exceed the strength. Data presented in Section 2 indicate that reasonable values for strength of the waste are 0.07 MPa (10 psi) for 14 MPa initial pressure and below, and 0.105 MPa (15 psi) above that pressure, with an uncertainty of ±0.035 MPa (5 psi) for both cases. As shown in Table 3-2 and Figures 3-26 and 3-27, an increase in strength can decrease the potential spall volume.

3.4.4.2 Poisson's Ratio

Poisson's ratio enters into the calculation of pore pressure stresses and as such can have an effect on the stress distributions. The pore pressure stresses reduce to zero at a Poisson's ratio of 0.5 because the stress calculation includes a factor of $(1-2v)$. Conversely, the pore pressure stresses increases as the Poisson's ratio decreases. As noted in Section 2, the measured Poisson's ratio for the surrogate materials was 0.35, and this value has been used in calculations. However, given the nature of the materials, it would seem likely that Poisson's ratio would be larger rather than smaller, so that the use of 0.35 for this parameter is conservative.
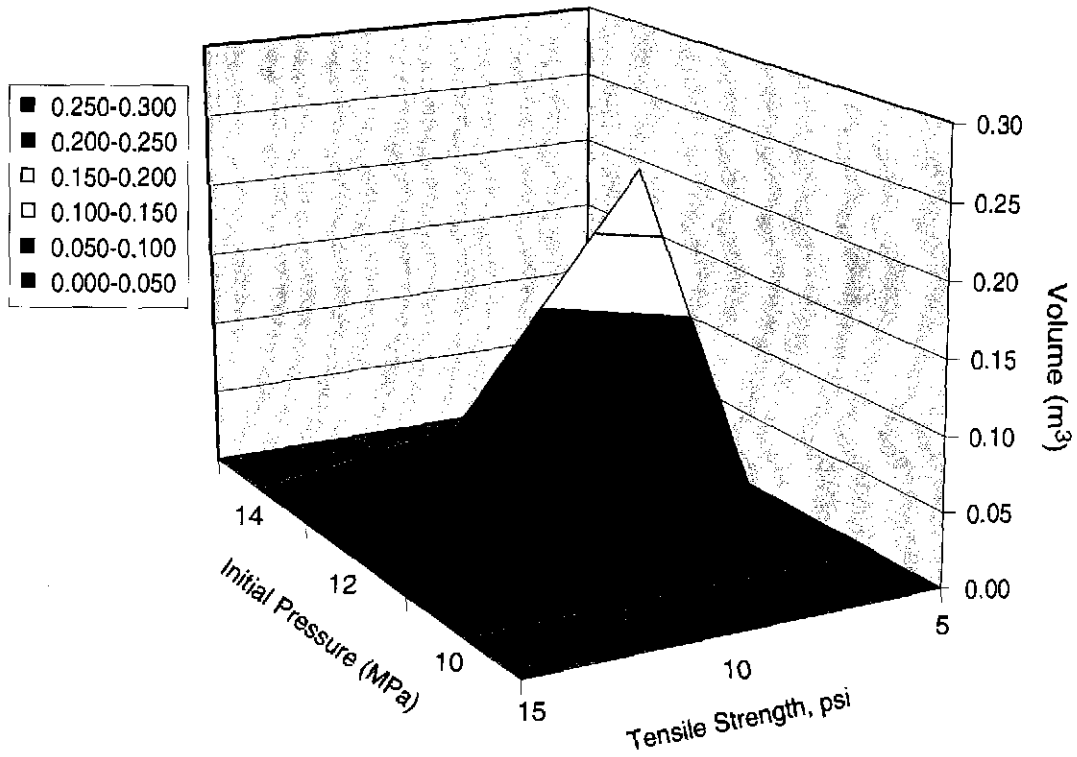
Figure 3-26. Decrease in potential spall volume resulting from strength increase (<14 MPa).
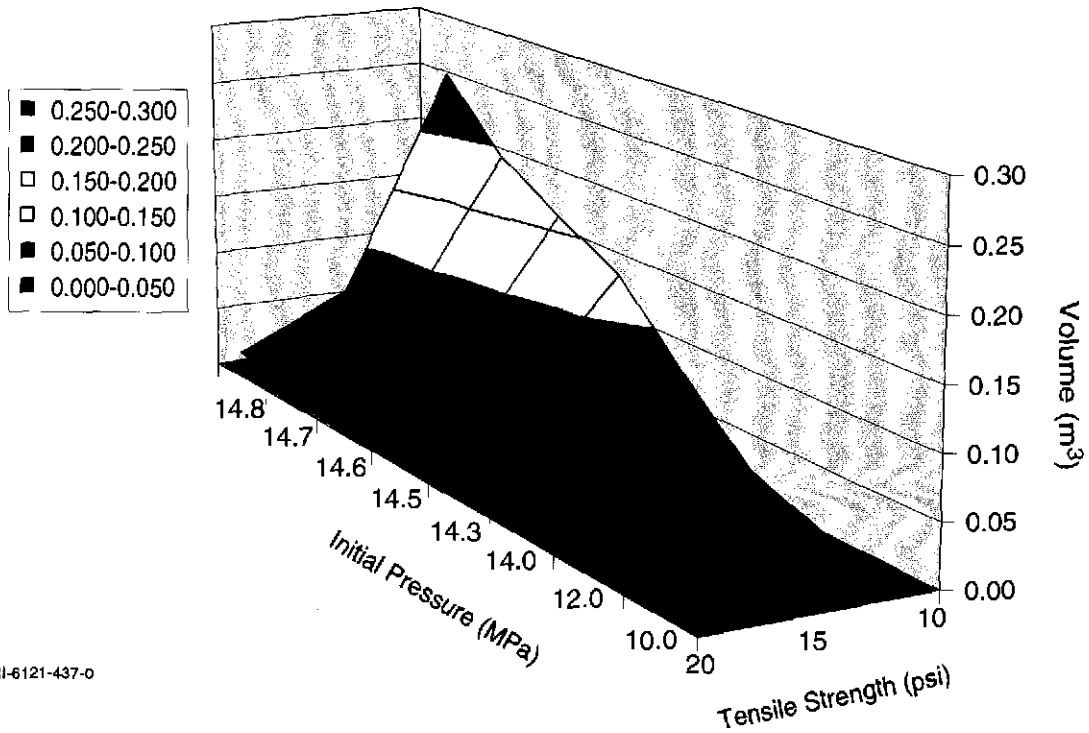

TRI-6121-437-0

Figure 3-27. Decrease in potential spall volume resulting from strength increase (>14 MPa).

3-34

3.4.4.3 Waste Permeability

Mud blowout calculations have been made for waste permeability of 10^{-14}, 10^{-15} and 10^{-12} m^2. The waste permeability is a key parameter because it directly controls the gas influx to the borehole. The CCA value for waste permeability is 1.7×10^{-13}. A reduction in waste permeability will significantly alter the mud blowout process. At lower permeabilities, the mud flows extremely slowly out of the borehole so that there is really no rapid blowout event. However, tensile failure volumes are much less sensitive to permeability because the region with high pore pressure gradients is confined to a small region around the hemispherical cavity. Time histories for mud velocity and bottomhole pressure are presented in Figures 3-28 through 3-33 for waste permeabilities of 10^{-14}, 10^{-15} and 10^{-12}.

The response for a waste permeability of 10^{-14} m^2 (Figures 3-28 and 3-29) show that the mud velocity accelerates rapidly and then oscillates about 0.3 m/s while the pressure drops rapidly and then oscillates about 7.7 MPa, the hydrostatic pressure. This is a reasonable response because the lower permeability room will provide less gas influx than for the standard repository permeability. The initial acceleration of the mud column still occurs because there is a substantial pressure differential on the column at time zero, but the pressure in the gas column will tend toward hydrostatic because the formation cannot provide enough gas influx to drive pressure significantly above hydrostatic pressure. In effect, the gas/mud acts like a spring/mass system with the spring initially extended from its equilibrium position.

There is a small residual velocity (0.3 m/s in comparison to about 5 m/s for the base case) because of the smaller gas influx from the formation. The displacement of the mud column at 160 s is only 50 m and the displacement at 340 s, the end of the calculation, is 114 m. Both values are much less than the length of the borehole, 655 m. The gas influx is sufficiently low that a driller might not even know that the rig has penetrated the repository.

With an additional decrease in waste permeability to 10^{-15} m^2, the gas influx becomes so small that the residual velocity oscillates near zero and the pressure oscillates around hydrostatic pressure (Figures 3-30 and 3-31). The mud displacement is only 3.5 m at 70 s and 4.5 m at 100 s. In effect, there is no blowout event and hence no spalling.

As an aside, the pipe friction factor for the low permeability cases is based on the assumption that the Reynolds number is high enough to transition to fully turbulent flow. The mud velocities with low waste permeabilities, around 0.3 m/s, result in peak Reynolds numbers of about 5,000. This value for Reynolds number is an order of magnitude less than the typical case because the flow velocity has dropped by an order of magnitude. This value of Reynolds number is tending toward the transition region in Moody's diagram, but should be sufficiently accurate for this modeling study. In any case, changes in friction factor will tend to change the rate of damping of the oscillations, rather than the basic response of the system.

Finally, an increase in permeability to 10^{-12} m^2 produces a more rapid mud blowout process. The mud clears the borehole in 51 s, as opposed to 88 s for the base case. Bottomhole pressure remains about 2.5 MPa higher than for the base case. This is reasonable because the mass flow rate from the repository is greater than for the base case. Time histories for mud velocity and bottomhole pressure are presented in Figures 3-32 and 3-33.
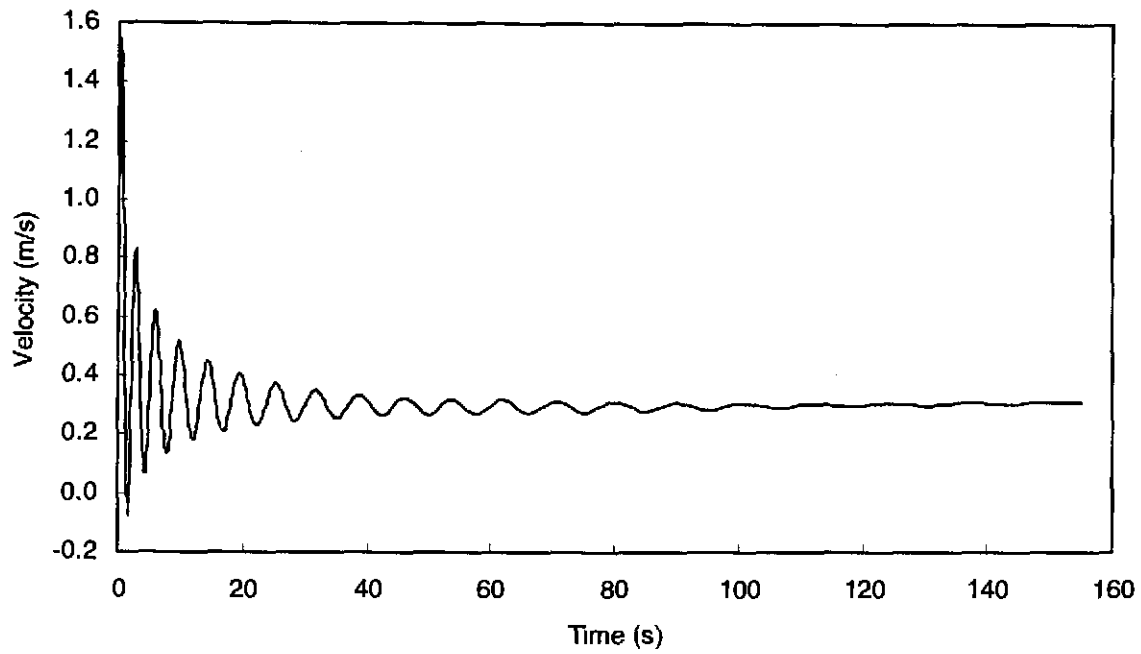
Figure 3-28. Mud velocity for a waste permeability of 1×10^{-14} m^2.
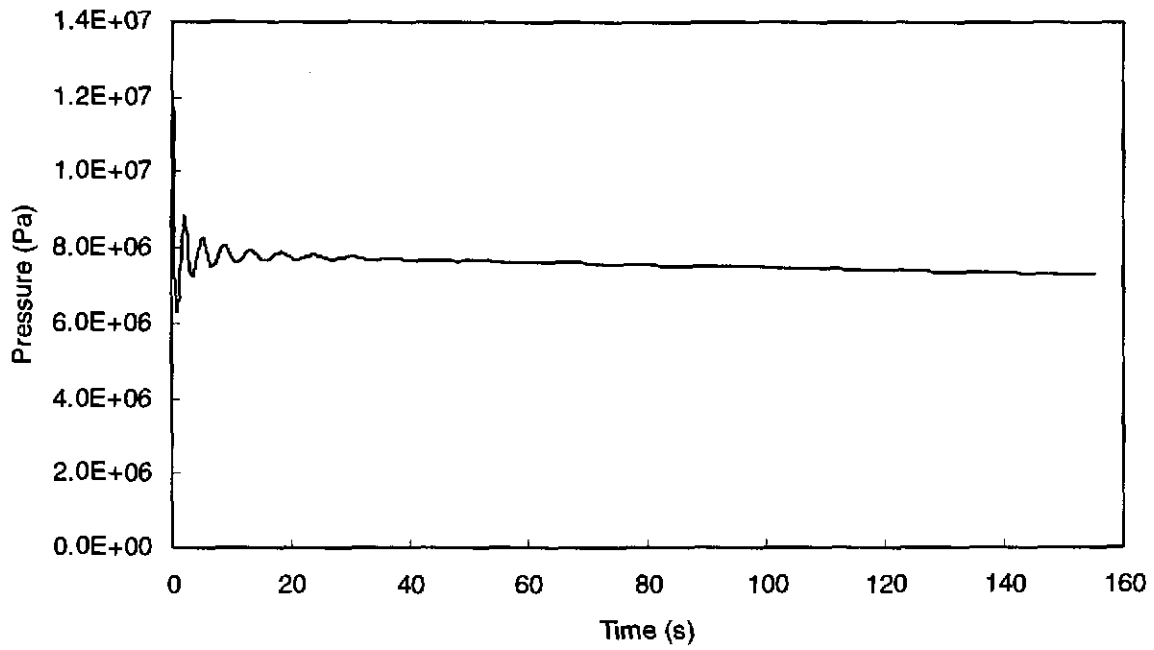
Figure 3-29. Bottomhole pressure for a waste permeability of 1×10^{-14} m^2.
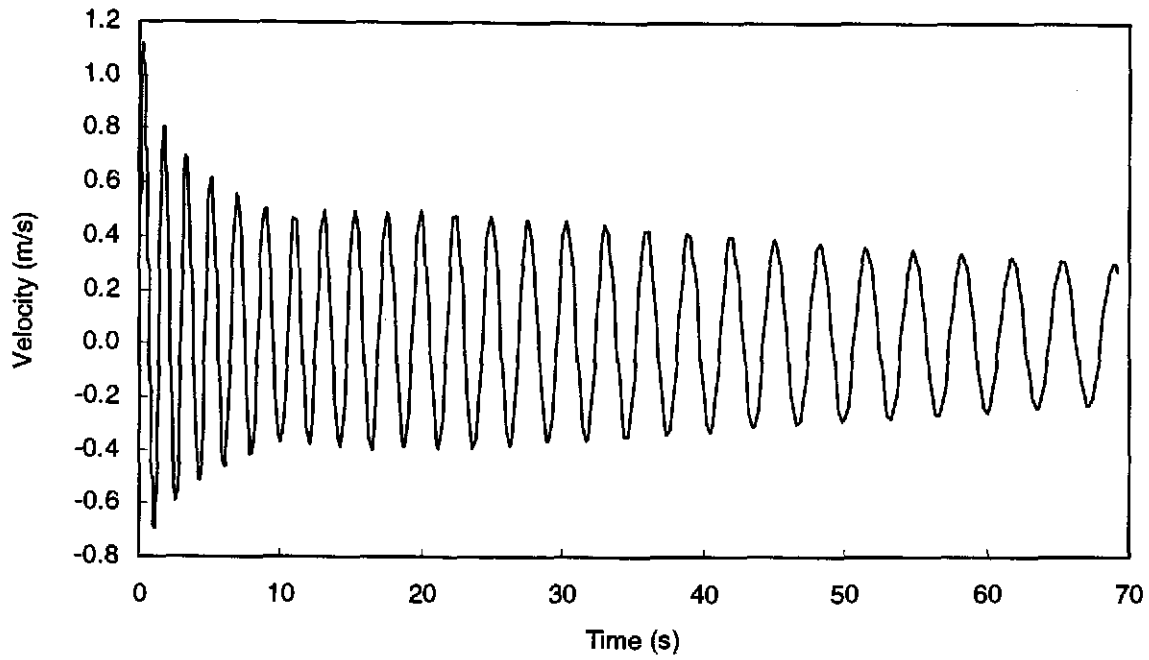
Figure 3-30. Mud velocity for a waste permeability of 1×10^{-15} m^2.
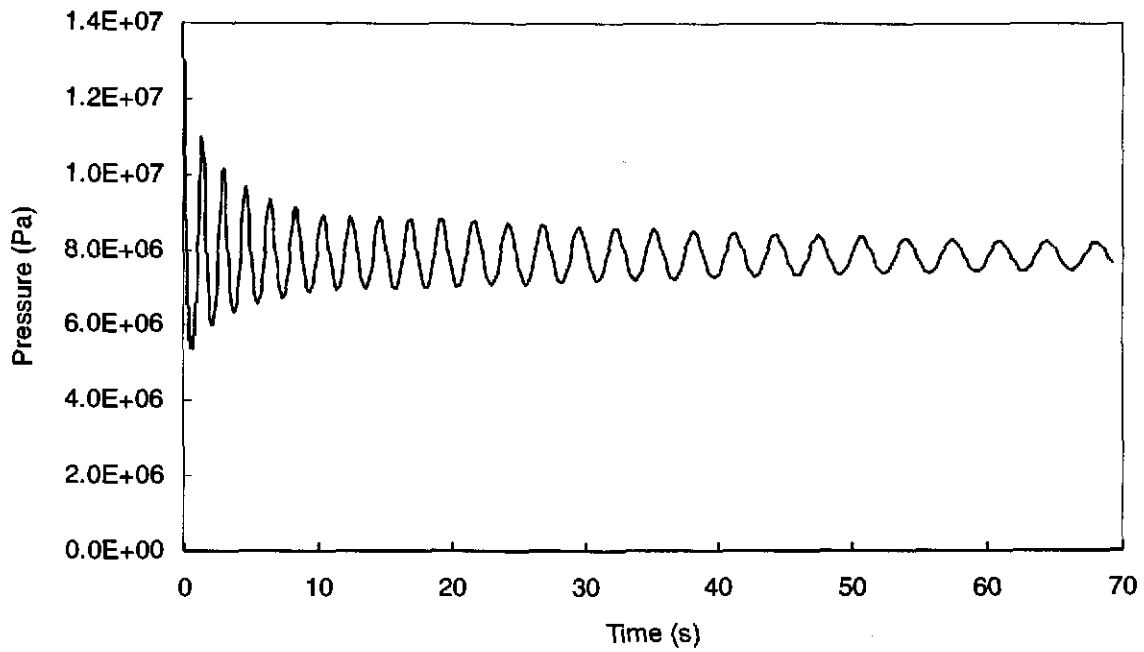

Figure 3-31. Bottomhole pressure for a waste permeability of 1×10^{-15} m^2.
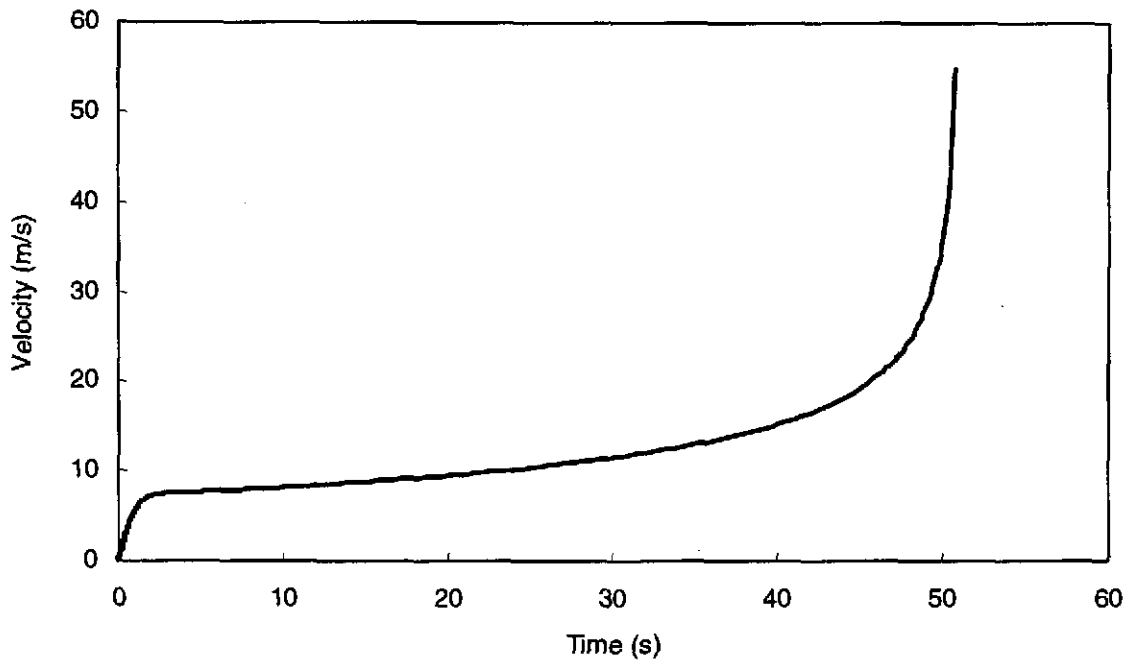
Figure 3-32. Mud velocity for a waste permeability of 1×10^{-12} m^2.
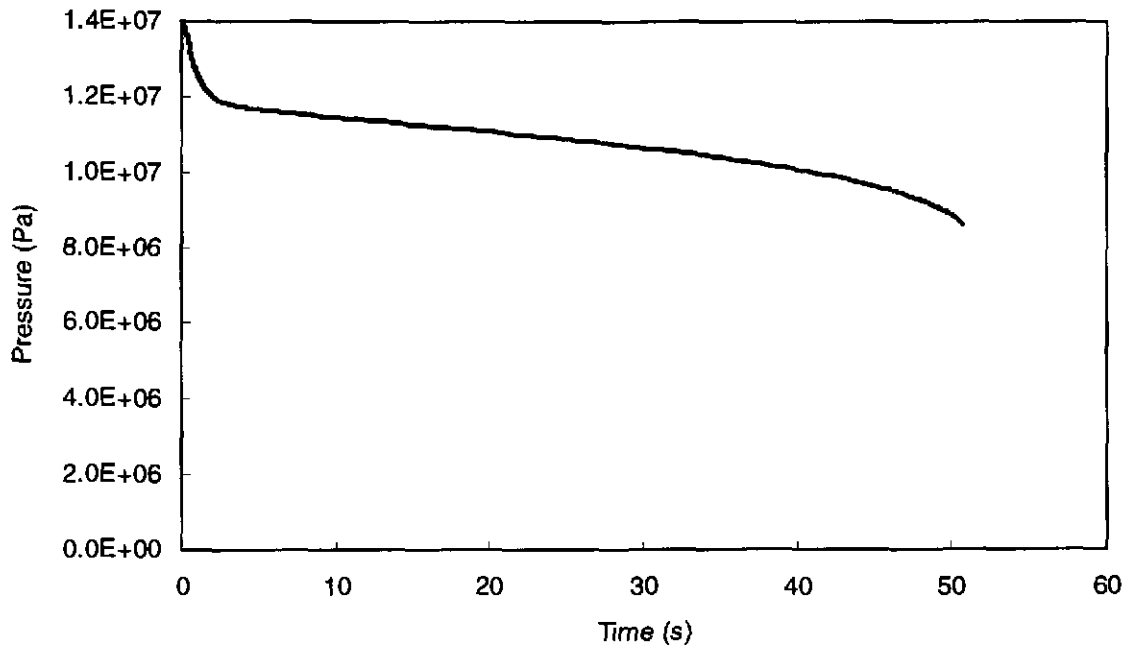
Figure 3-33. Bottomhole pressure for a waste permeability of 1×10^{-12} m^2.

3.4.4.4 Fanning Friction Factor

The borehole will have a rough outer wall and a much smooth inner wall (the drill collar) for the uncased section, below the Salado. Moody recommends friction factors between 0.028 and 0.058 for concrete pipe and 0.016 to 0.021 for structural steel (Moody, 1944. The standard value selected for the quasi-static model, 0.02, is midway between these ranges, while the high value of 0.0642 is greater than the maximum value for concrete, as discussed below.

For a concrete pipe with a 0.108-m effective hydraulic diameter, Moody has a range of relative roughness of 0.003 to 0.03. At a Reynolds number of 70,000 the friction factor is 0.028 to 0.058 for relative roughness of 0.003 to 0.03, respectively. At infinite Reynolds number, the friction factor is 0.026 to 0.057, respectively. The conclusion here is that the friction factor is very insensitive to the Reynolds number, and hence to mud velocity and mud viscosity, for a rough concrete pipe with mud moving at 5 m/s.

For a smoother commercial steel pipe, the relative roughness is 0.0004. The corresponding friction factor is 0.021 at a Reynolds number of 70,000 and 0.016 at infinite Reynolds number.

Previous work estimated an absolute roughness of 0.04 to 0.01 m for the borehole (Butcher et al., 1995, Table 5, page 71). These values are certainly too high for the cased section of the borehole (above the Salado). A value of 0.004 m for absolute roughness was selected as a compromise because both the cased and uncased sections have a relatively smooth inner wall. This absolute roughness corresponds to a value of the friction factor of 0.0624 for a fully rough pipe at infinite Reynolds number.

The increase in friction factor from 0.02 to 0.064 produces a slower blowdown process, with slower velocities and with higher down-hole pressures. The blowdown process requires 122 s, as opposed to 88 s for the base case. The mud velocity at 10 s is 2.97 m/s, as opposed to 3.68 m/s for the lower friction factor. Finally, the bottomhole pressure falls to 5.7 MPa at 122 s, as opposed to 4.6 MPa for the base case. Each of these changes is consistent with the increased friction for mud flow in the borehole.

Although the time for the blowout is substantially longer, the early time response is quite similar for either value of the friction factor. Figure 3-34 compares mud velocities, and Figure 3-35 compares bottomhole pressure for both values of the friction factor over the first 5 s of the blowout process. The response is quite similar for the first second or so, which is expected while the mud velocity and associated frictional pressure loss in the borehole are still small. This fact is important because the largest tensile failure regions occur at early times, when the response is similar. The conclusion here is that the change in friction factor will have only a minor impact on the tensile failure volume.

3.4.4.5 Annular Geometry

The computational model for Stage 1 ignores the change in cross-sectional area at the juncture between the drill collar and drill pipe. The drill collar, which is 183 m long and has a diameter of 0.2032 m (8 in.), is directly adjacent to the repository. The drill pipe, which is 0.1143 m (4 in.) in diameter, extends 472 m down from the surface. The standard value for the inner diameter of the annulus is based on the drill collar diameter along the total depth of the borehole (655 m).
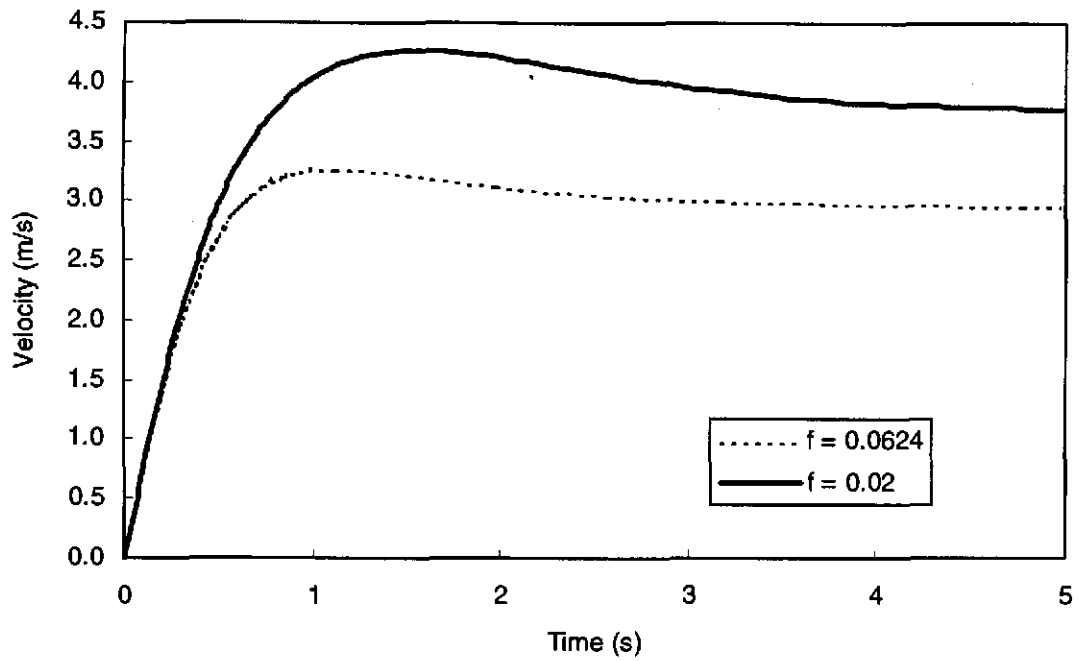
Figure 3-34. Comparison of mud velocities for calculations with Fanning friction factor.
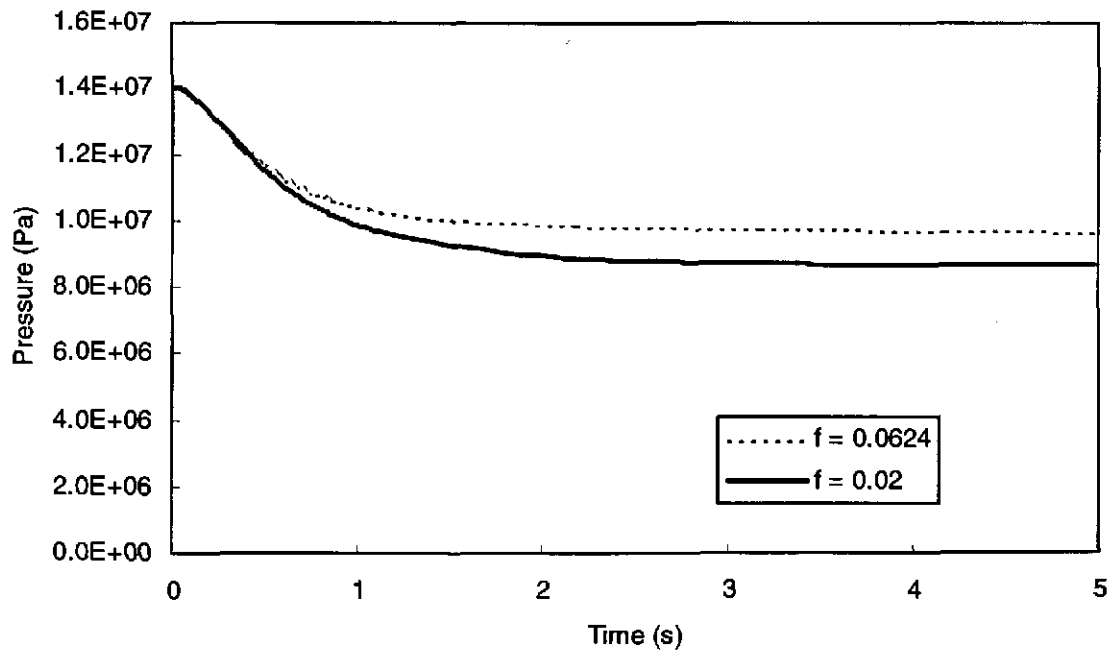

Figure 3-35. Comparison of bottomhole pressure for calculations with Fanning friction factor.

A calculation with a larger annular geometry, based on the drill pipe rather than the drill collar, was performed to bound the response with a change in cross-sectional area between the drill collar and the drill pipe. The effective hydraulic diameter changes to 0.1969 for this case. The annulus based on the drill pipe results in a slower blowout process because there is more volume and hence lower bottomhole pressure than for the annulus based on the drill collar. For example, the duration of the blowout process is 98 s for a drill pipe annulus versus 88 s for a drill collar annulus. Also, the bottomhole pressure is 3.65 MPa at the end of the blowout, lower than the value of 5.7 MPa for the calculation with a drill collar annulus.

In spite of the late time differences, mud velocity and bottomhole pressure are similar for the first second or so, when the region of tensile failure surrounding the borehole is greatest. This similarity occurs because displacement of the mud column is small in the first second. Since the annular geometry based on the drill collar is more accurate for early times in the blowout process and since there are not major differences at early times, when tensile failure is greatest, the calculations with a constant annular region, based on the drill collar, are being used as the basis for this study.

3.5 Other Mechanisms

Consideration has been given to the probable contribution of liquefaction, seepage forces and erosion during the Stage 1 events. These are briefly discussed here:

3.5.1 Liquefaction

Liquefaction occurs if a material looses its shear strength, which effectively causes the material to behave like a liquid. This situation often occurs in soils, where a granular, cohesionless material may experience liquefaction in undrained and drained states. These granular, cohesionless materials tend to compact when subjected to vibrations. If the material is saturated with liquid and the permeability is low enough to prohibit drainage, pore pressure increases as the pore volume decreases without significant drainage. Dynamic conditions such as earthquake vibrations are often sufficient to create pore pressures equal to the total stress, which results in effective stresses of zero. Thus, the material looses its shear strength, behaves similar to a liquid, and liquefaction has occurred (e.g., Seed and Idriss, 1982).

Liquefaction may also occur in granular, cohesionless materials as a result of fluid flow (draining material) when the pore pressures are relatively high and the resulting pore pressure gradients are significant. When a fluid flows through a porous medium, a drag force occurs along the solid-fluid interfaces. The drag force of the fluid on the solid manifests itself as a pressure decay creating gradients through the material. If the pressure gradient is large enough, the resulting seepage forces can create states of stress that exceed the strength of the material and create a liquefied condition. Thus, liquefaction induced by pore pressure gradients does not require dynamic or other vibratory compacting events to reach the liquefied state. For example, artesian springs flowing through soils may result in liquefaction, which is commonly called a *quick condition*.

These processes are potentially applicable to repository waste during a spalling event. Gas generation in the repository provides pore pressure increases similar to the pore pressure increases caused by compaction assisted by vibrations. A significant rate difference exists between these analogous events since the vibration-induced pore pressure increases occur much more rapidly

than the gas pressure increase in the repository. The slow build up of pressures in the repository dictates that the pressure will not exceed the lithostatic state of stress (14.8 MPa). Since the pore pressure increase caused by gas generation will not exceed the lithostatic state of stress (i.e., a maximum effective stress of 0) the waste form will not liquefy during the pore pressure build up (gas generation period) because the saturated waste cohesion (0.13 MPa) is sufficient to suppress liquefaction. Thus, before intrusion occurs, the waste will not be in a liquefied state. In addition, the attainment of high gas pressures (>14 MPa) is only possible for waste saturations less than 25%, where waste strength would be greater than the saturated state (see Appendix D). While the drilling intrusion scenario is a dynamic event, the associated dynamic vibratory loads are insufficient to cause liquefaction of the waste.

After drillhole intrusion into the repository occurs, gas will flow through the repository and eventually up the drill string. Flow through the waste is accompanied by pressure gradients through the waste, which may create seepage forces sufficient to exceed the cohesion of the material. If the cohesion of the waste is exceeded, liquefaction of the waste will occur. The analytical and numerical models used to evaluate the spalling events include this type of liquefaction explicitly in the calculations. That is the seepage forces, which are proportional to the pressure gradients, are included in the models. If the seepage forces are sufficient to exceed the waste strength, a state of liquefaction is predicted.

However, liquefaction is not expected to effect the behavior of the waste during a potential spall event, because the mean effective stress at the borehole is compressive throughout the event, which increases shear strength. The only occasions that zero mean effective stress occurs in the repository are before penetration and after penetration only at locations far removed from the wellbore. Both of these conditions require that the initial state be prescribed such that the pore pressure equals the total stress. During a blowout with a potential accompanying spall, the wellbore pressures will be less than the far-field pressure. Under these conditions the radial effective stress will be zero at the wellbore, but the tangential effective stress will be compressive because of the stress concentration around the wellbore (e.g., Figures 3-13 and 3-14). The net result is that the mean effective stress will be compressive at all times (e.g., Figures 3-16 and 3-17), which prevents liquefaction from occurring.

3.5.2 Seepage Forces

Seepage forces occur due to the viscous drag of fluids flowing through a porous medium (e.g. Taylor, 1948; Bear, 1972). These forces are included in the elastic stresses used in the calculations through the pore pressure stresses given in Equations 13 through 16.

3.5.3 Erosion

Erosion occurs due to solid materials being removed by the viscous drag of flowing fluids, and in the present context includes the possibility of removal of material from the solid waste or of already failed material by the flow of gas. Erosion could occur due to the radial flow of gas into a sub-spherical cavity around the borehole, or due to gas flow into and along channels in a layered or otherwise heterogeneous waste. Erosion has been considered further in Section 3.2.2.6.

3.6 References

Abramowitz, M. and Stegun, I., 1970. *Handbook of Mathematical Functions with Formulas, Graphs, and Mathematical Tables,* National Bureau of Standards, Applied Mathematics Series 55, Ninth Printing, Washington, D.C.

Analysis Package for Direct Brine Release Calculations (Task 4), 1996. SWCF-A:1.2.07.4.1:PA:QA:Analyses:AP-029:BRAGFLO Direct Brine Release Calculations (Task 4).

Apostol, Tom. M., 1962. *Calculus, Volume I Introduction, with Vectors and Analytic Geometry,* Blaisdell Publishing Company, New York, New York.

Bear, J., 1972. *Dynamics of Flow in Porous Media,*

Binder, R.C. 1958. *Advanced Fluid Mechanics,* Volume 1. Englewood Cliffs, NJ: Prentice Hall, pg. 63.

Butcher, B.M., Webb, S.W., Berglund, J.W., and Paul R. Johnson, 1995. *Systems Prioritization Method - Iteration 2 Baseline Position Paper: Disposal Room and Cuttings Models, Volume I,* Sandia National Laboratories, Albuquerque, New Mexico, March 28, 1995.

Chan, D.Y.C., Hughes, B.D. and L. Patterson, 1993. *Transient Gas Flow Around Boreholes,* Transport in Porous Media, 10, 137-152.

Jaeger, J.C. and N.G.W. Cook, 1969. *Fundamentals of Rock Mechanics,* Chapman and Hall Ltd., London, England.

Moody, L.F., 1944. *Friction Factors for Pipe Flow,* Transactions of the ASME, 66, 8, pp. 671-684, November, 1944.

Press, W.H., Flanery, B.P., Teukolsky, S.A. and W.T. Vetterling, 1989. *Numerical Recipes in Pascal,* Cambridge University Press, pp. 48-49 and 693-698.

Sabersky, R.H. and A.J. Acosta, 1964. *Fluid Flow,* MacMillan and Company, New York, pp. 148-153.

Santos, O.L.A., 1989. *A Dynamic Model of Diverter Operations for Handling Shallow Gas Hazards in Oil and Gas Exploratory Drilling,* Ph.D. dissertation submitted to the Department of Petroleum Engineering, Louisiana State University and Agricultural and Mechanical College, May, 1989.

Seed, H. B. and I. M. Idriss, 1982. *Gound Motion and Liquefaction During Earthquakes,* prepared for the Earthquake Engineering Research Institute, Berkeley, CA.

Stagg, K.G. and O.C. Zienkiewicz (eds.), 1975. *Rock Mechanics in Engineering Practice,* John Wiley & Sons, London, England.

Taylor, D.W., 1948. *Fundamentals of Soil Mechanics,* John Wiley and Sons, New York.

Timoshenko, S.P. and J.N. Goodier, 1970. *Theory of Elasticity,* Third Edition, McGraw-Hill Book Company, New York, NY.

Page intentionally blank

4.0 NUMERICAL CALCULATIONS

The entry of a drill string into a waste disposal room initiates several transient events, as discussed in Section 3. If the gas pressure in the waste exceeds that of the drilling fluid, then gas will flow from the porous waste to the intrusion borehole. The resultant effects include reduction in pore pressures in the waste, alteration of the stress field of the waste forms, and possible ejection of the drilling mud and a quantity of the waste material to the surface. Numerical methods have been developed to simulate the following processes of the conceptual model:

1. one-way coupling of the two-phase pressure decay and stress response within the waste region following a drilling intrusion;

2. gas flow from the waste region to the wellbore, resulting in expulsion to the surface of drilling mud, gas, and particulate matter through the annular volume of the drill string; and

3. decoupled two-phase pressure response within a simulated waste region.

Coupled fluid/stress numerical calculations have been conducted to quantify the effects of the first process. These calculations are presented in Section 4.1 A numerical fluid flow and mass flux model of the drill string and waste disposal region were developed to assess the result of the second process. This approach is discussed in Section 4.2. Calculations of gas flow through the porous waste regions were conducted to evaluate the influence of model assumptions on the predicted two-phase pressure response of the disposal rooms during a drilling intrusion. These calculations are presented in Section 4.3. A comparison of numerical calculation results to the semi-analytic results in Section 3 is presented in Section 4.4. The influence of model assumptions on calculations of volumetric releases is presented in Section 4.5.

4.1 Coupled Fluid/Stress Calculations

In poromechanical simulations, the equilibrium equations are written in terms of effective stresses, which are proportional to the forces acting on the waste matrix. Only changes in these forces can cause deformation (strain) of the waste. The depressurization process created by a borehole intrusion results in a change in the borehole pressure and in the pore pressure field in the formation, which leads to changes in the stress distributions and to the development of seepage forces. The presence of pore pressure distributions can produce tensile effective stresses on the material, which may result in failure of the waste material. The coupled numerical calculations presented in this section estimate the volume of the waste that could experience tensile stresses as a result of a drilling intrusion. This type of failure may result in fragmentation of the waste, thus producing a volume of material available for transport to the surface. The material could also experience fracturing, resulting in alteration of both flow and mechanical properties. Both these possibilities are explored within this section.

4.1.1 Numerical Model

Calculations performed to date using the coupled fluid pressure/stress method employ two approaches to simulate the pressure drawdown resulting from the drilling intrusion. The first (constant boundary) method assumes that the waste region is instantaneously exposed to a drilling intrusion having a brine pressure of 8 MPa at time t=0. This pressure condition is held constant in the wellbore for the first set of calculations. By imposing the maximum pressure reduction on

the wellbore, this bounding base-case configuration provides estimates of the maximum spatial extent of any tensile failure effects.

In the second (transient boundary condition) method the pressure drawdown in the waste was also simulated to evaluate transient effects that occur in the first few seconds following a drilling intrusion. This represents a more complicated analysis that simulates more realistic conditions than the bounding base-case configuration. A poroelastic material model was assumed for calculation of the resulting stress fields. Results of these calculations are compared to those derived from the more conservative constant boundary condition.

Estimation of the mechanical response of the waste requires application of a material model to the waste. Bounding calculations assume a poroelastic response in the waste form. These poroelastic analyses allow quantification of the possible magnitudes, extents, and durations of stresses developed in the waste immediately after a borehole intrusion. However, propagation of failure cannot be simulated in poroelastic simulations because, by definition, inelastic deformation leading to waste fragmentation is not included in them. Limited tension simulations associated with the constant boundary condition method were conducted to assess the progressive nature of failure and its stabilization under the same conditions as used in the poroelastic simulations. The limited tension analyses include the transfer of loads from the material exceeding the specified tensile strength (failed material) to the remainder of the formation.

Fluid flow/waste pressure response was calculated using the TOUGH28W, Version 2.0 multiphase flow code (Pruess, 1991). Poromechanical effects of stress and strain were calculated using the SPECTROM-32, Version 4.09 code (Callahan, 1994). Fluid flow/wellbore hydraulics response was calculated using a new code, COMBO2, developed for this application.

4.1.2 Geometry

All calculations simulate a waste panel, conceptualized as a cylindrical volume. The radius of the cylinder is approximately 60 m and its height is 2 m. A drillbit is assumed to penetrate at the center of the panel. The drillhole has a radius of 0.1556 m (12.25 in. diameter), and the collars have a radius of 0.1016 m (8 in. diameter). The geometry of the bit is not included in these calculations. The extent of the drilling intrusion is limited to the upper boundary of the model for these calculations. Continued drilling is not realistic if the CCA value of permeability is used since, as discussed in Section 3.3, gas flow to the wellbore results in mud ejection.

Layers of the axisymmetric TOUGH28W grid are presented in Table 4-1. The uppermost layer is assigned halite properties to simulate the effect of overlying layers. Note that the layers start at a thickness of 0.01 m (1 cm) at the top (387.393 m) of the waste-filled room, and increase at a rate of 1.1 for layers 2 – 13, then increase at a rate of 1.4 until the bottom of the modeled region is reached. The discretization provides necessary refinement in regions where detail is desired. Increasing element size permits the overall grid to be of sufficient size such that outer boundary effects are minimal. The lower boundary is impermeable.

Columns of the grid are presented in Table 4-2. The drill string is simulated as a single column with a radius of 0.1016 m. The annulus is simulated as two radial elements of equal incremental radius. Similar to the layering scheme, radial thicknesses start at 0.01 m beyond the edge of the drillhole, increase at a rate of 1.1 for the first 15 radii, then increase at a rate of 1.4 thereafter. The actual radius of the grid is larger than the 48 m needed to simulate an equivalent panel. This

is, however, not significant because pressure decay never reaches this boundary during the simulated times.

The TOUGH28W grid used in these analyses was compared to the grid developed for scoping studies presented to the CMPRP in January 1997. Results for similar conditions were visually compared to those obtained with the previous grid, and it was concluded that the current grid provides a more definitive resolution for the processes of interest than the grid used in January.

The axisymmetric finite-element mesh used for all SPECTROM-32 simulations is finely gridded in the vicinity of the wellbore, consistent with the TOUGH28W mesh. Elements adjacent to the borehole have a thickness of 0.01 m, with progressively increasing thicknesses at increasing distances from the borehole surface. Sensitivity of results to size of the SPECTROM-32 mesh was evaluated. Mesh size and gradation were sufficient to resolve the processes of interest. Detailed results of this sensitivity analysis are available in the analysis package prepared for this report. The SPECTROM-32 finite element mesh is shown in Figure 4-1.

Table 4-1. TOUGH28W Grid Layers

Element Center (m)	Δz (m)	Element Center (m)	Δz (m)	Element Center (m)	Δz (m)
387.4030	0.1000E-01	387.2934	0.1949E-01	387.0349	0.4550E-01
387.3930	0.100E-01	387.2730	0.2040E-01	386.9710	0.6390E-01
387.3825	0.1100E-01	387.2505	0.2250E-01	386.8817	0.8930E-01
387.3710	0.1210E-01	387.2257	0.2480E-01	386.7567	0.1250E+00
387.3583	0.1331E-01	387.1985	0.2728E-01	386.5816	0.1751E+00
387.3443	0.1464E-01	387.1686	0.3001E-01	386.3365	0.2451E+00
387.3289	0.1611E-01	387.1356	0.3301E-01	385.9933	0.3432E+00
387.3120	0.1772E-01	387.0804	0.5520E-01	385.5129	0.4806E+00

Table 4-2. TOUGH28W Grid Columns

| Element Center (m)	Δr (m)	Element Center (m)	Δr (m)	Element Center (m)	Δr (m)
0.0508E+00	0.5080E-01	0.3032E+00	0.2249E-01	0.2039E+01	0.5052E+00
0.1143E+00	0.2540E-01	0.3279E+00	0.2474E-01	0.2746E+01	0.7072E+00
0.1413E+00	0.2860E-01	0.3552E+00	0.2730E-01	0.3737E+01	0.9901E+00
0.1606E+00	0.1000E-01	0.3894E+00	0.3420E-01	0.5124E+01	0.1386E+01
0.1711E+00	0.1100E-01	0.4374E+00	0.4800E-01	0.7065E+01	0.1941E+01
0.1827E+00	0.1160E-01	0.5045E+00	0.6710E-01	0.9784E+01	0.2717E+01
0.1954E+00	0.1270E-01	0.5985E+00	0.9400E-01	0.1359E+02	0.3804E+01
0.2093E+00	0.1397E-01	0.7300E+00	0.1315E+00	0.1892E+02	0.5326E+01
0.2247E+00	0.1537E-01	0.9142E+00	0.1841E+00	0.2638E+02	0.7457E+01
0.2416E+00	0.1690E-01	0.1172E+01	0.2577E+00	0.3682E+02	0.1004E+02
0.2602E+00	0.1859E-01	0.1533E+01	0.3608E+00	0.5144E+02	0.1461E+02
0.2807E+00	0.2045E-01				
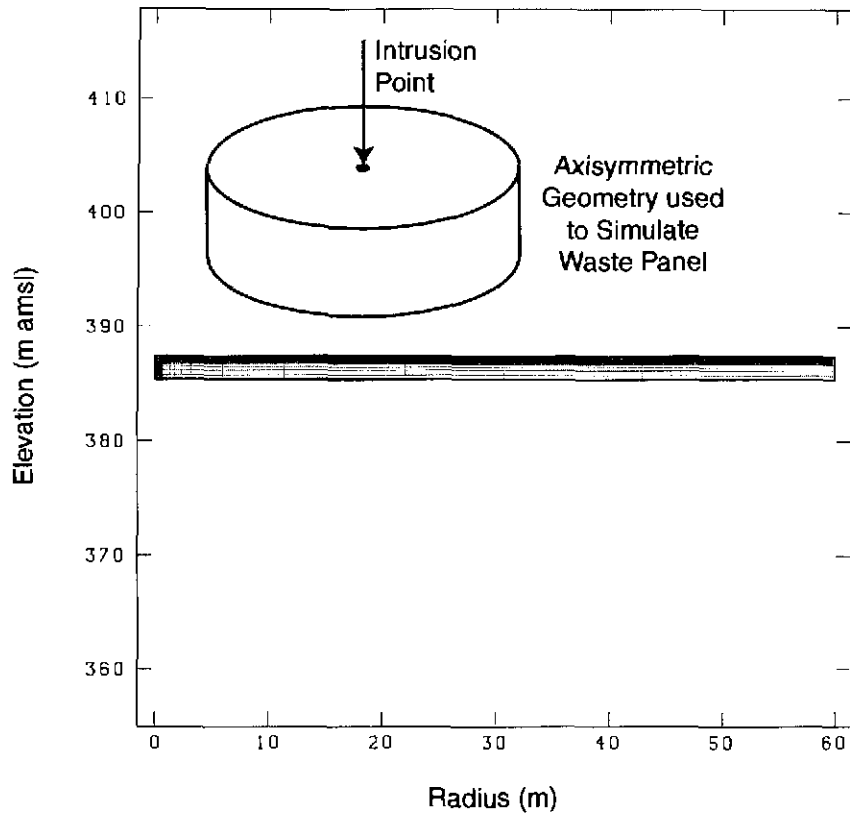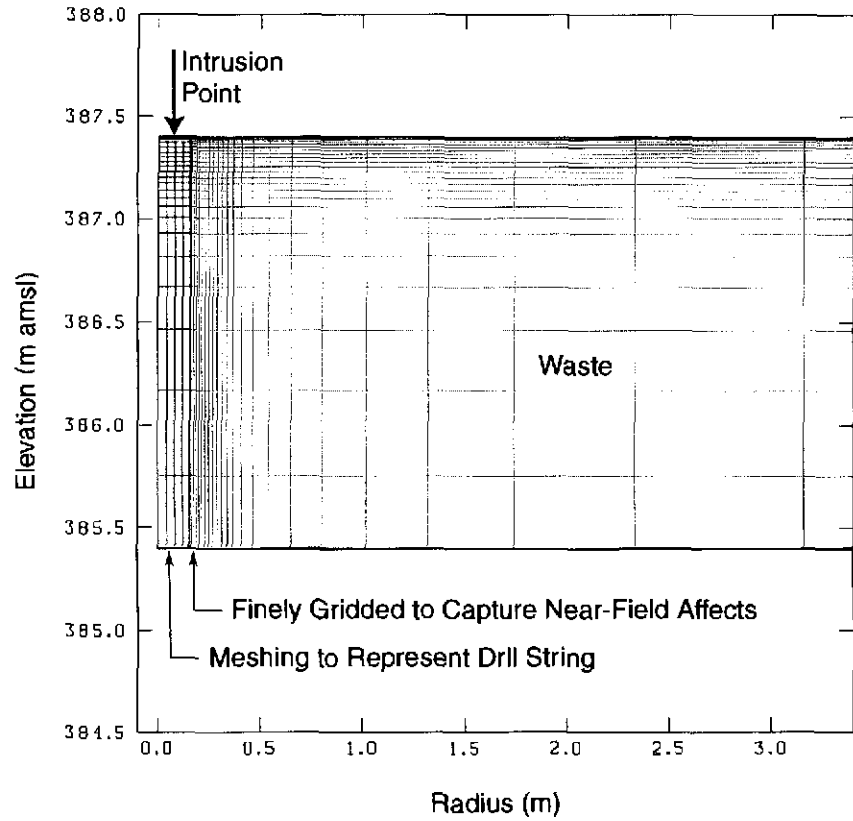
Figure 4-1. a) SPECTROM-32 finite element mesh. b) Zoom plot of near-field SPECTROM-32 mesh.

TRI-6121-423-0

4.1.3 Material Properties

Consistent with the assumptions in the CCA, the numerical model characterizes the waste as a homogeneous material with high permeability and porosity. Waste porosity is calculated in the CCA and is a function of the gas pressure in the waste; it varies from a minimum of 0.46 for low pressure realizations to 0.6 for a gas pressure of 14.8 MPa. Relevant fluid flow properties used for the waste, drill string, annular volume, and the overlying halite are presented in Table 4-3. The relative permeability and capillary pressure relationships and associated parameters were selected to simulate the expected two-phase behavior of the system and are consistent with those used in the CCA. As discussed in Section 2, the waste will consist of materials having various sizes and properties. The waste character, coupled with a very high porosity relative to geologic materials, is consistent with the assumption that two-phase effects will not restrict the gas flow through the disposal regions. The selected value for porosity differs slightly from that used for the semi-analytic calculations discussed in Section 3. This difference will result in slight changes to the specific response of the model, but the general character will not be affected.

The assumed mechanical properties of the waste are also summarized in Table 4-3. Calculations were under way in parallel with waste characterization, so conservative values were used to initiate calculations. As seen in Table 4-3, the elastic modulus and Poisson's ratio differ from those derived for surrogate waste. Sensitivity of the numerical results to these parameters has been evaluated. Section 3.3.3 shows that the selected values for these properties produce a conservative result. The assumed value for initial brine saturation of the waste corresponds to the residual brine saturation state specified for the waste in the CCA. Actual saturation conditions necessary to produce high pressures are below 0.25. This results in a maximum gas volume available for the blowout.

Table 4-3. Parameter Definitions

Parameter	Halite	Waste	Drill Pipe	Annulus
Permeability (m^2)	3.16E-23	1.7E-13	3.16E-23	1.0E-10
Porosity	0.01	0.60	0.01	0.99
Brooks-Corey	0.7	2.89	0.7	—
Compressibility of Rock (1/Pa)*	9.75E-11	0	0	8.05E-9
Threshold Pressure (Pa)	1.0E8	0	1.0E8	0
Residual Brine Saturation	0.3	0.075	0.3	0
Residual Gas Saturation	0.2	0	0	0
Relative Permeability Model	van Genuchten	Brooks-Corey	Completely Permeable	Linear
Capillary-Pressure Model	van Genuchten	Brooks-Corey	Linear	Linear
Elastic Modulus (MPa)	n/a	31000	n/a	n/a
Poisson's Ratio	n/a	0.25	n/a	n/a
Tensile Strength (MPa)	n/a	0.025 – 0.10	n/a	n/a

  * Zero compressibility selected to prevent implementation of the TOUGH28W pressure-dependent porosity feature. Scoping calculations demonstrated that results are insensitive to this parameter.

4.1.4 Boundary Conditions

All flow calculations assumed no-flow conditions at the outermost radius of the cylinder. Modeling a waste panel as a cylinder permits gas to flow freely between disposal rooms, thus representing a conservative approximation of the panel geometry because gas flow will be

restricted between rooms. The presence of an overlying halite layer with a no-flow upper boundary prevents gas flow through the disturbed rock zone (DRZ) that is present in the CCA model of the repository. This assumption adds additional conservatism to the calculation because a DRZ above the panel would allow bleed-down of pressure before the drill bit enters the waste. A no-flow boundary is assumed for the lower boundary of the model.

The boundary condition applied at the point of drilling intrusion is of considerable importance to the response of the waste formation. For comparative purposes, a "base case" boundary condition was devised. This condition consists of a fixed wellbore pressure and is described in Section 4.1.5. Transient conditions that model the wellbore hydraulic response are also applied, and results are compared to the base case. This approach permits both qualitative and quantitative comparisons of numerical results presented in this section and semi-analytic results presented in Section 3. The base case configuration also represents an upper bound on depressurization effects.

The mechanical model consists of the waste-filled room without any of the host salt formation included. Analytical solutions for pressurized boreholes show that the stress field is perturbed by less than 5% at radii greater than five times the borehole radius. Although the stress field within five radii is changed significantly, particularly at the borehole surface, the impact of the stress changes in the salt has a negligible impact on the waste. The most important aspect of the borehole is the stress reduction in the vicinity of the intrusion, which is included explicitly in the mechanical model. In addition, the host salt is assumed to be significantly stiffer than the degraded waste. Although the host salt formation is a viscoplastic material, the short time durations required for analysis of any spall event preclude significant time-dependent deformation in the salt. Thus these assumptions permit exclusion of the host salt formation from the mechanical model. By virtue of the kinematic boundary conditions imposed, the host salt formation is represented as a rigid surface that imposes no shear resistance to movement of the waste.

Kinematic boundary conditions applied around the exterior of the mechanical finite-element model (SPECTROM-32) constrain displacements normal to the surfaces to zero, except at the base of the borehole (top of the waste) where a compressive normal traction is applied, representative of pressure from the weight of the mud or drawdown pressures resulting from mud ejection. This condition is consistent with the initial effective stress state for a specified pore pressure. For example, at an initial pore pressure of 14.8 MPa, a compressive normal traction of 14.8 MPa is applied at the borehole to maintain zero effective stress at time zero.

4.1.5 Constant Boundary Condition Method

Initial Conditions

By the time of a borehole intrusion (at least 100 years after repository closure), creep of the salt surrounding the waste reduces stresses to negligible values compared to the deviatoric stresses that were originally induced in the salt by excavation of the waste disposal regions. A lithostatic stress state of 14.8 MPa, based on the weight of the overburden at the disposal horizon, is assumed in the surrounding salt at the time of intrusion. This stress must be supported by the contents of the disposal rooms (degraded waste and gas), so the initial total stress state is assumed to be isotropic and uniform at 14.8 MPa.

A portion of the total stress exerted by the surrounding salt is supported by the gas pressure in the disposal rooms, and the remainder is supported by the effective stresses acting through the matrix of the waste. The mechanical response of a porous medium (deformation and failure) is governed by the effective stress. The effective stress in the waste is initialized in a manner consistent with the application of the specified pore pressure in the gas. The minimum initial effective stress is assumed to be zero, which occurs when the initial pore pressure is 14.8 MPa.

The boundary traction condition at the borehole is instantaneously reduced at time $t=0^+$ to 8 MPa, representing removal of salt at the time of the intrusion. For the flow calculations, this condition is imposed through specification of the pressure in a simulated borehole. An arbitrarily large volume is assigned to the borehole, ensuring that the imposed pressure remaines constant throughout the simulated period. This instantaneous depressurization is simulated in the SPECTROM-32 model by reducing the normal traction at the borehole to 8 MPa.

For a spall event to occur, the initial gas pressure in the waste must exceed the hydrostatic pressure (8 MPa) in the drilling fluid. Predictions of waste gas pressure in the CCA range from less than 8 MPa to approximately lithostatic (14.8 MPa). Instantaneous depressurization calculations were conducted for initial waste gas pressures of 10, 14, and 14.8 MPa to assess the impact of gas pressure on waste fragmentation. Table 4-4 summarizes the calculations and also provides an identifier for each subset of the calculations. These identifiers will facilitate discussion of the results of the analyses.

Table 4-4. Base Case Configuration: Instantaneous Wellbore Depressurization

Descriptor	Initial Waste Gas Pressure (MPa)
IPNL	14.8
EPNL	10
XPNL	14
IPNL-LT	14.8; limited tension material model

Procedure

The two codes used in the coupled calculations solve the fluid flow and poromechanical equations separately. Explicit coupling of the processes was accomplished via a "hand-off" process. Each computational model was initialized using the appropriate conditions. A borehole intrusion was then simulated in the TOUGH28W model, and pore pressure profiles were generated for discrete points in time. The pore pressure fields were read from an external file for each pore pressure distribution into the SPECTROM-32 computational model, and equilibrium stress states were calculated. Details of the process are summarized here:

1. Model elements are initialized at the specified gas pressure and gas saturation.
2. Gas saturations in the halite elements are re-set to approximate minimal gas migration from the waste to the halite. This reflects the conservative assumption that no bleed-off in pressure will occur prior to the intrusion event.
3. Pressure at the intrusion point (drill string and annulus) is set to 8 MPa.
4. Gas saturation in the annulus and drill string is set to minimal value.
5. Pore pressure fields are saved at 0.001, 0.01, 0.1, 1, and 10 s for hand-off to SPECTROM-32.

Failure of the waste form could occur if stresses induced by the drilling intrusion exceed the strength of the material. Laboratory studies of surrogate materials (Section 2) demonstrate the waste is weakest in tension. Therefore, it is assumed that a tensile failure criterion is appropriate for the waste.

Results and Discussion: Base Case

Pore pressure results for all cases show that the maximum spatial extent of the depressurized zone is small for the first several seconds following a borehole intrusion. Gas flow to the wellbore results in rapid repressurization of the artificially imposed wellbore pressure. High pressure gradients exist only within the first 0.5 to 1 m in either the vertical or horizontal direction, and these gradients are approximately hemispherical in form. Calculations also show that the stress fields are approximately spherical for the first fractions of a second following intrusion.

The TOUGH28W results for waste gas pressures of 14.8, 14, and 10 MPa are shown in Figures 4-2, 4-3, and 4-4, respectively. Tensile and shear stresses for an initial waste gas pressure of 10 MPa are shown in Figures 4-5 and 4-6. A tensile zone is predicted only within the immediate vicinity of the wellbore, but still represents a very small volume of material that could experience tensile failure (less than 0.01 m^3). This zone is a direct consequence of the imposition of a constant pressure boundary of 8 MPa at the wellbore. The influence of the imposed condition dissipates rapidly as the pore pressure decays (Figure 4-4). The effective stress state of the waste formation is compressive prior to the drilling intrusion; the low pressure drilling intrusion therefore has only a limited effect on the resultant stress field.

For an initial gas pressure of 14 MPa, the effective stress state is also compressive before a drilling intrusion. As a result, the response of the material (Figures 4-7 and 4-8) is similar to that seen for a waste gas pressure of 10 MPa: tension is predicted only in the immediate vicinity of the wellbore. As the pore pressure decays, the tensile zone shrinks to within an even smaller radius of the imposed boundary condition. The zone of maximum shear stress falls within the zone of tensile stresses.

The case of zero initial effective stress at the time of a hypothetical drilling intrusion produces a different result than that predicted for stress states exhibited for initial gas pressures of 10 and 14 MPa. As seen in Figure 4-7, the pore pressure decay will behave in a manner similar to that displayed by the lower initial gas pressures if the waste material does not experience fragmentation. Figure 4-9 shows that the predicted stress response differs from those shown previously. The contour levels shown in this figure depict maximum tensile stresses greater than 0.025 MPa (3.75 psi). If the material was in fact a perfectly elastic medium, tension would be predicted throughout the simulated waste formation.

Prediction and interpretation of the waste response for a pore pressure of 14.8 MPa requires consideration of several additional points. These are:

1. the waste is not a perfectly elastic material;
2. pressure drawdown in the wellbore is neither instantaneous nor constant, as simulated here;
3. the waste region is not homogeneous.
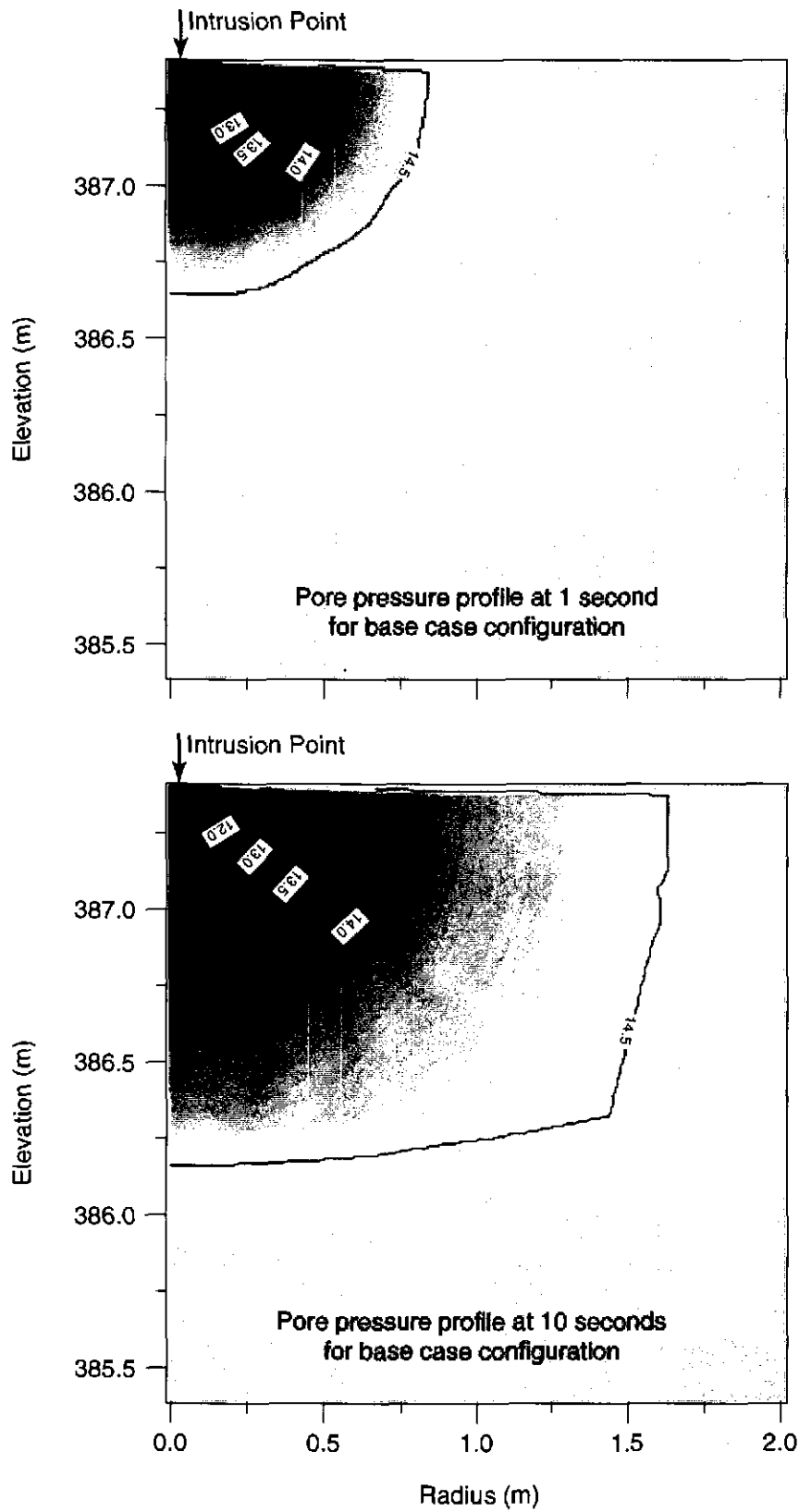
Figure 4-2. TOUGH28W results for waste gas pressure of 14.8 MPa constant boundary condition of 8 MPa at the wellbore. Contours are in MPa.
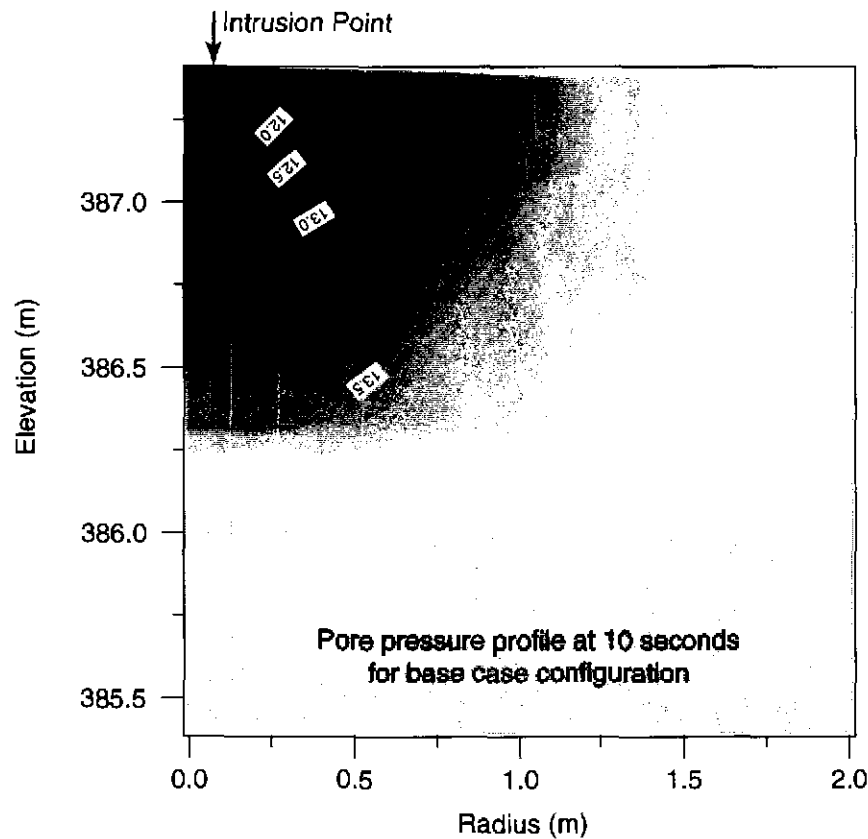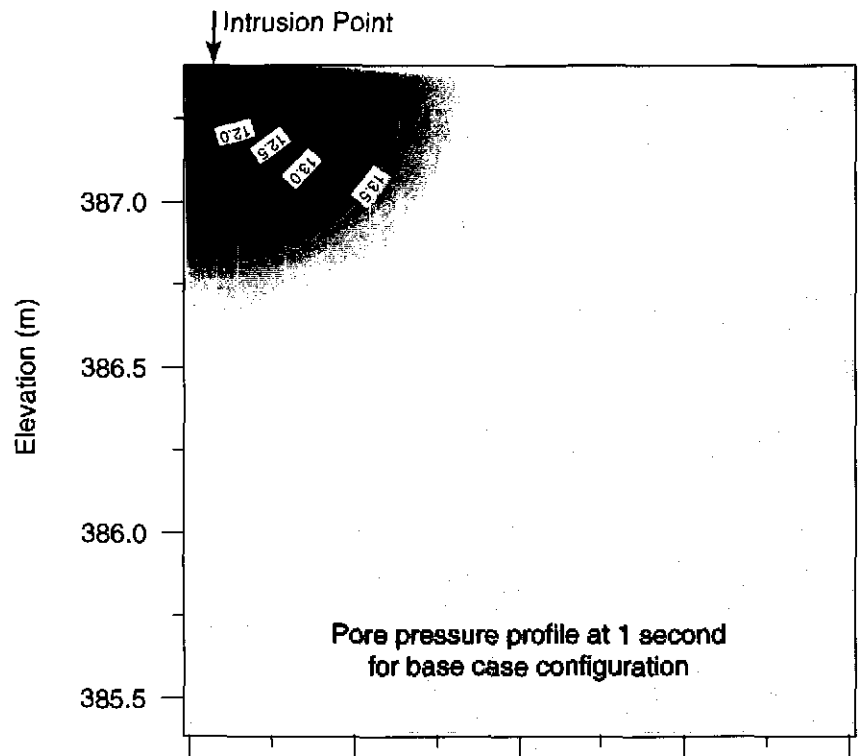
Figure 4-3. TOUGH28W results for waste gas pressure of 14 MPa constant boundary condition of 8 MPa at the wellbore. Contours are in MPa.
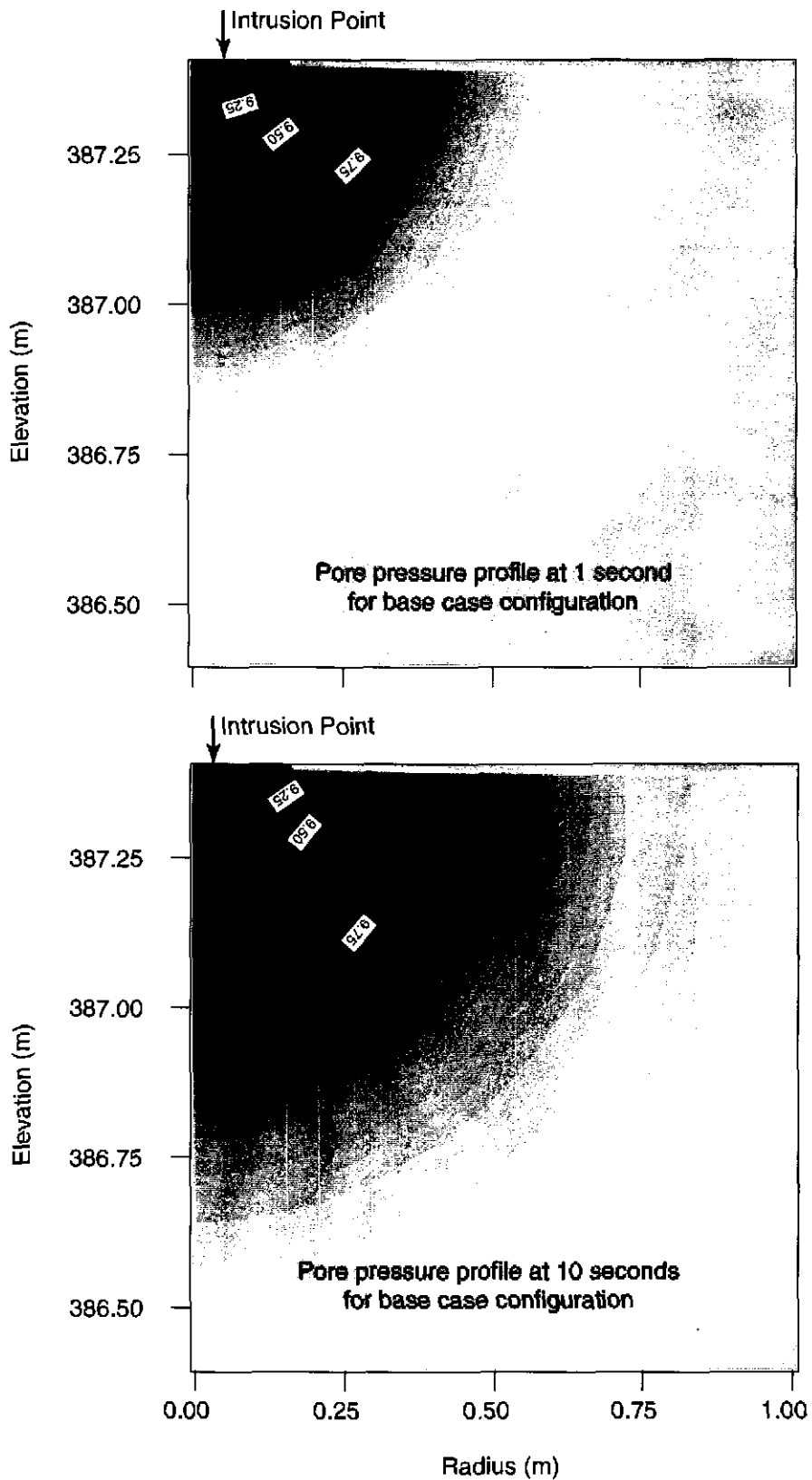
Figure 4-4. TOUGH28W results for waste gas pressure of 10 MPa; constant boundary condition of 8 MPa at the wellbore. Contours are in MPa.

SPECTROM-32 results for waste gas pressure of 10 MPa
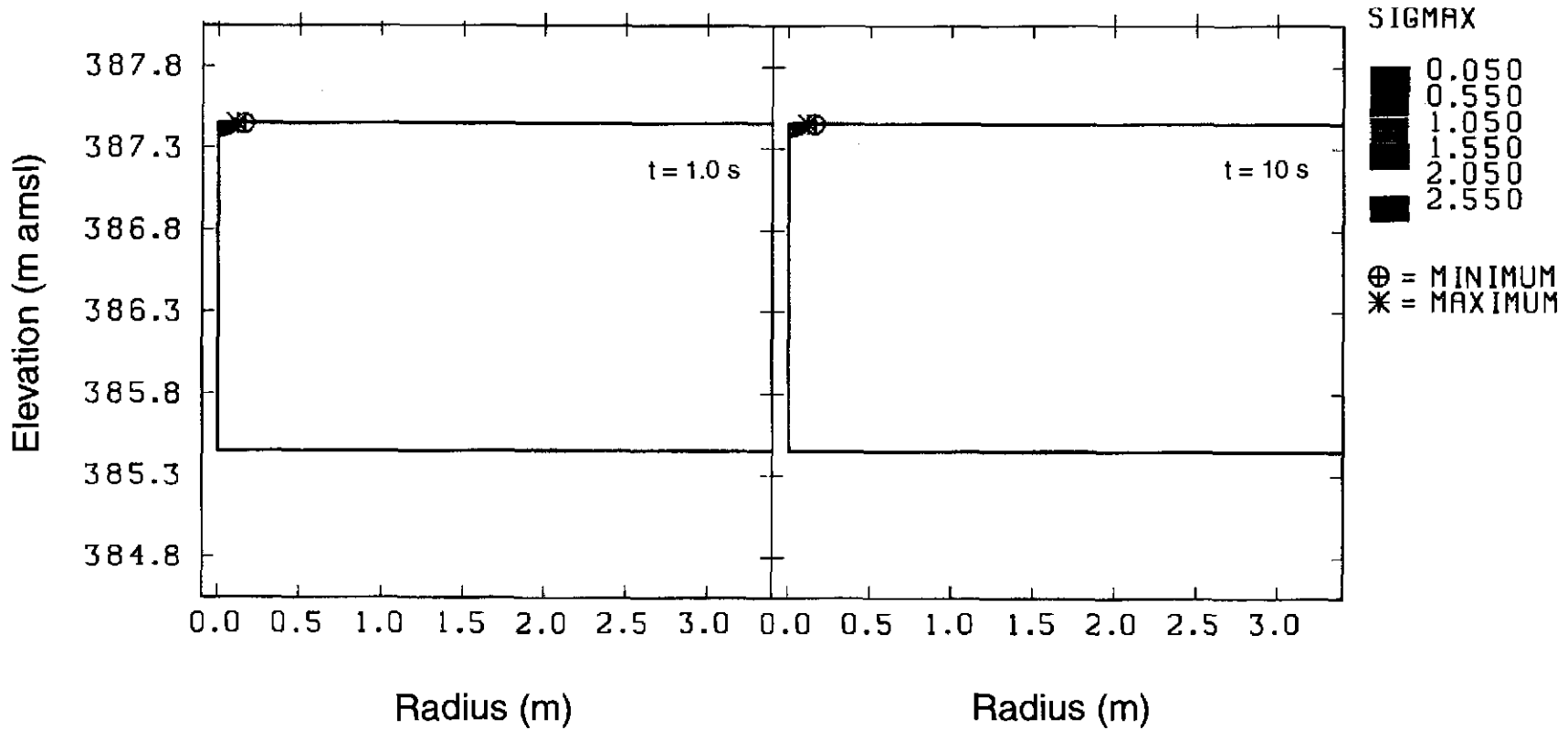
Figure 4-5. Contours of maximum tensile stress at 1 second and 10 seconds after intrusion. Waste gas pressure is 10 MPa prior to intrusion. Drilling wellbore pressure is set at the upper left corner of each plot to a constant value of 8 MPa. Contours are in MPa.
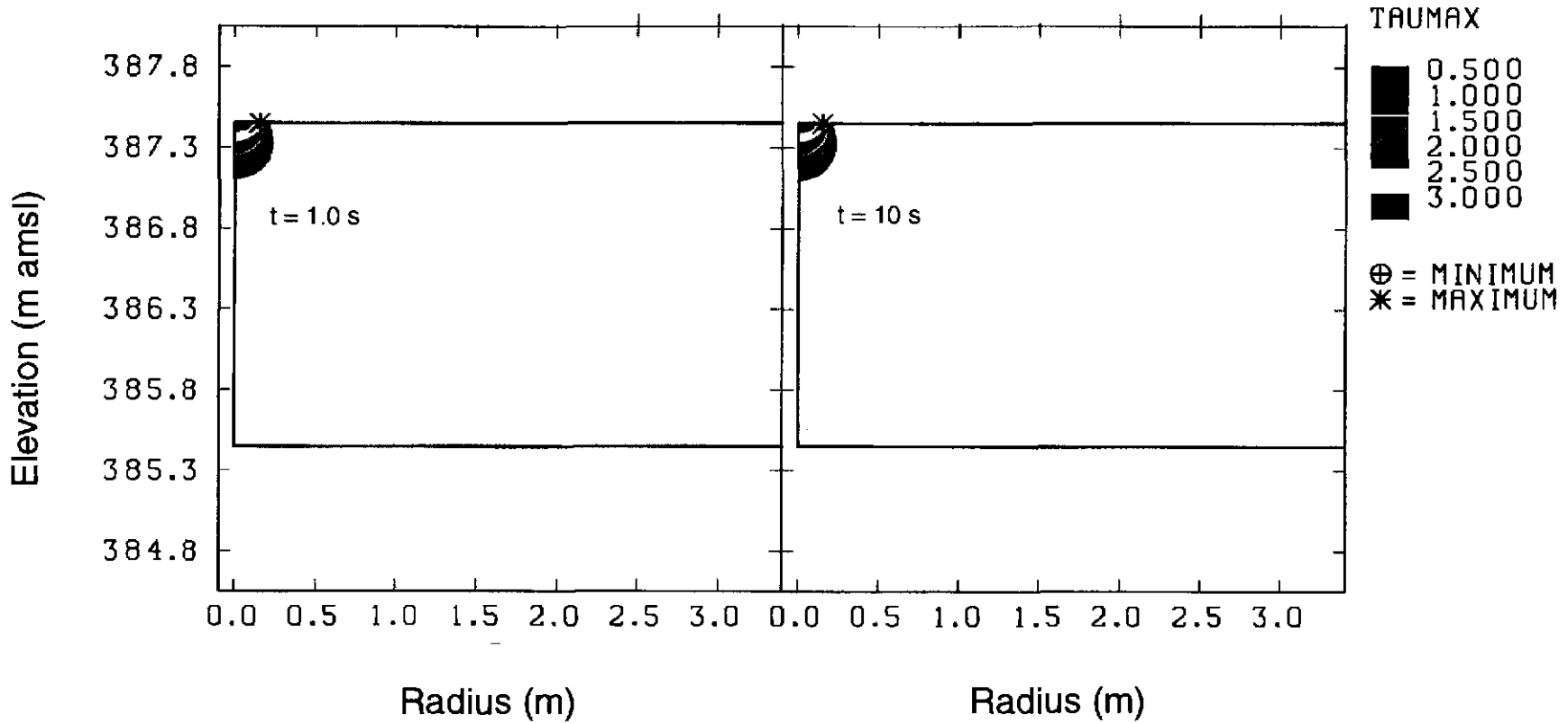
TRI-6121-417-0

Figure 4-6. Contours of maximum shear stress at 1 second and 10 seconds after intrusion. Waste gas pressure is 10 MPa prior to intrusion. Drilling wellbore pressure is set at the upper left corner of each plot to a constant value of 8 MPa. Contours are in MPa.

SPECTROM-32 results for waste gas pressure of 14 MPa
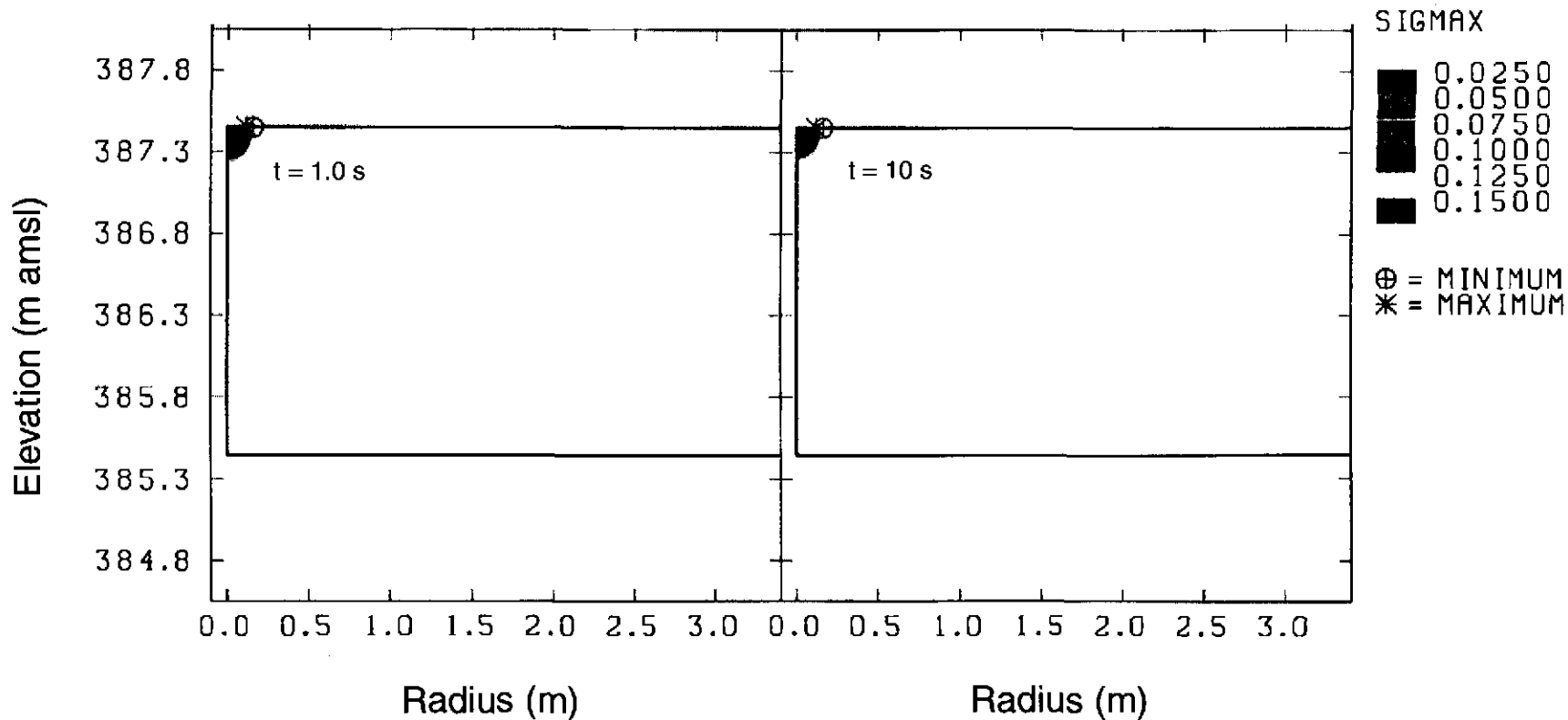
Figure 4-7. Contours of maximum tensile stress at 1 second and 10 seconds after intrusion. Waste gas pressure is 14 MPa prior to intrusion. Drilling wellbore pressure is set at the upper left corner of each plot to a constant value of 8 MPa. Contours are in MPa.
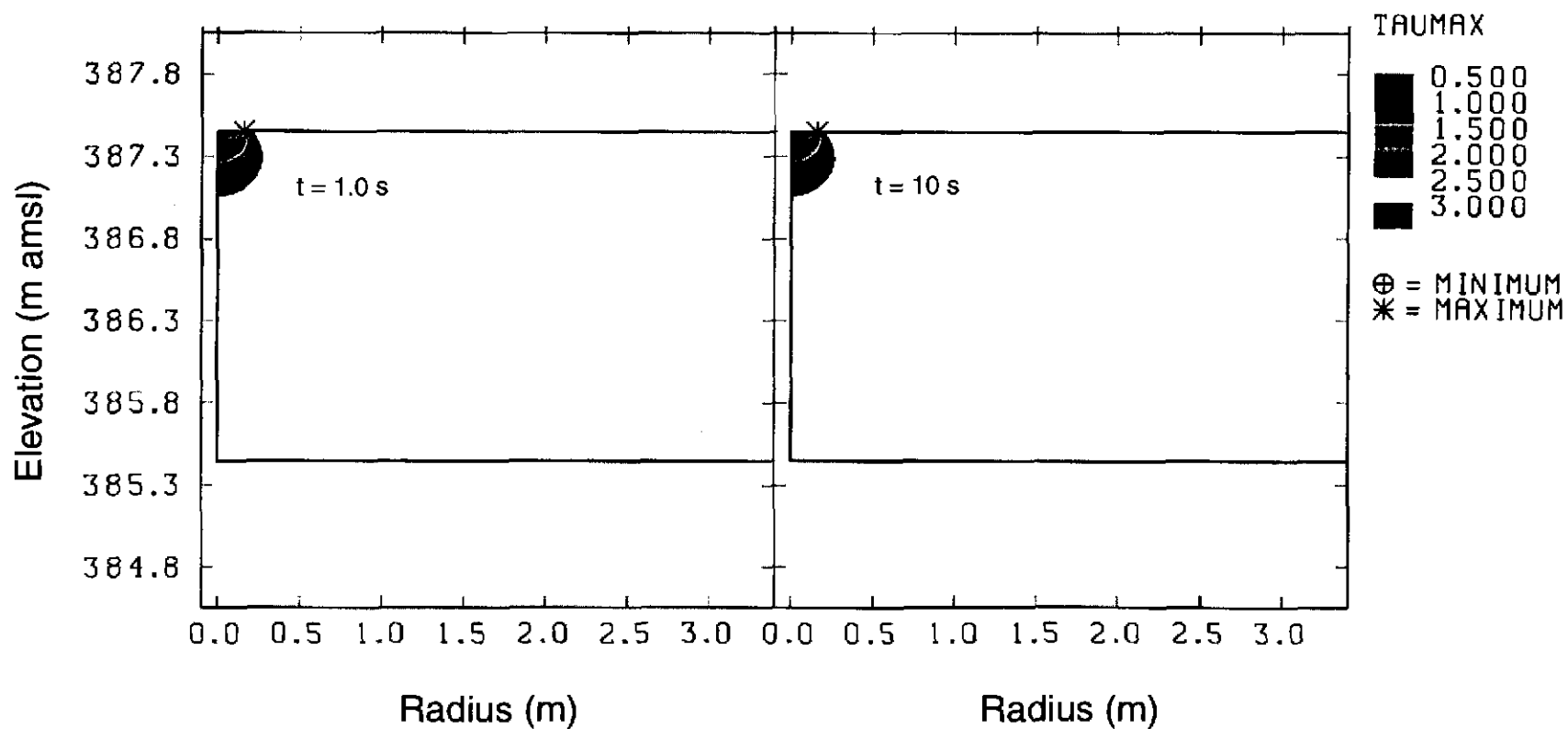
TRI-6121-418-0

Figure 4-8. Contours of maximum shear stress at 1 second and 10 seconds after intrusion. Waste gas pressure is 14 MPa prior to intrusion. Drilling wellbore pressure is set at the upper left corner of each plot to a constant value of 8 MPa. Contours are in MPa.
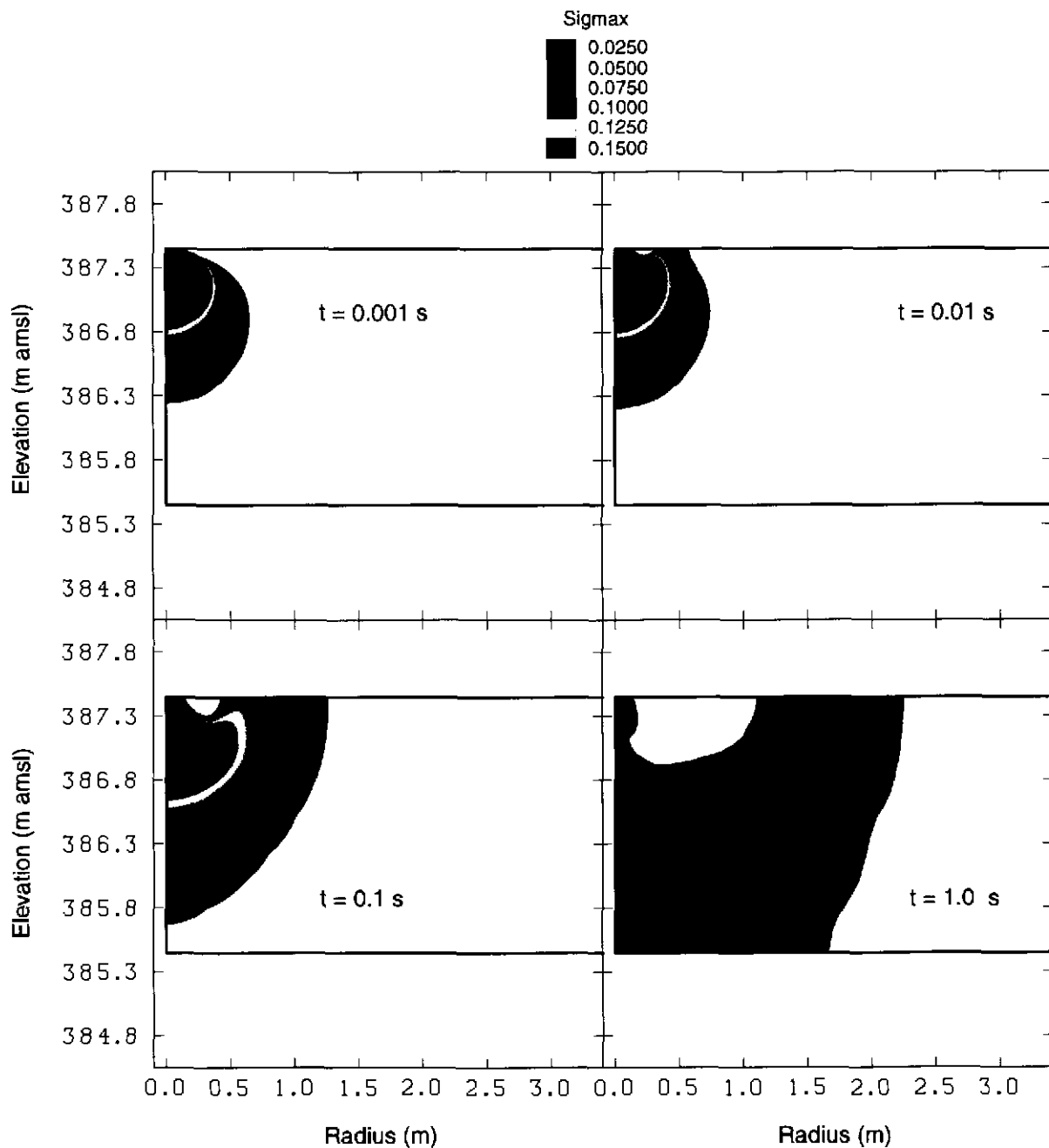
Figure 4-9. Contours of maximum tensile stress at 0.001, 0.01, 0.1, and 1 second after intrusion. Waste gas pressure is lithostatic (14.8 MPa) prior to intrusion. Drilling wellbore pressure is set at the upper left corner of each plot to a constant value of 8 MPa. Contours are in MPa.

4-16

The first point will be addressed in the remainder of this subsection. The influence of transient wellbore effects is presented in Section 4.1.7. Probable effects of waste heterogeneity are presented in Section 4.3.

4.1.6 Inelastic Deformation

Inelastic deformation after tensile failure at zero initial effective stress was addressed through a series of SPECTROM-32 calculations, which implemented the pore pressure fields presented for the IPNL data set (Figure 4-2). Application of a failure criterion resulting in inelastic deformation leads to redistribution of the stresses surrounding the material that has failed. In underground excavations, this stress redistribution (e.g., stress arching) results in the final stable configuration for the structure, even though a portion of the surrounding rock has experienced tensile failure, reducing the strength of the failed region. If stress redistribution cannot achieve a stable configuration, complete structural failure will occur, as opposed to local material failures. In the stress calculations presented in this subsection, the waste was assigned a finite tensile strength of 0.10 MPa (15 psi). Tensile stresses in the waste were limited to values less than this tensile strength by redistribution of the stresses following any tensile failure. Hence these SPECTROM-32 simulations are designated by the suffix "LT."

To track the propagation of material failure, an incremental loading approach must be used. In this approach, the transient change in forces acting on the waste are incrementally applied. As the incremental forces are applied, material failure is initiated in a portion of the material, reducing the load-bearing capacity of the failed region to zero. Strength of the failed region is simultaneously reduced to zero. Application of the load increments continues until the total load is reached. In the IPNL-LT simulations, the total load consists of a 6.8 MPa traction applied along the drilling intrusion elements. Sensitivity of the results to the number of load increments was assessed. It was found that variation of the results were minimal for more than 50 load increments.

Predictions of failure zones for incremental loading are presented in Figure 4-10. The largest zone of failure is predicted for the first pore pressure field, with only small increments resulting as the pressure decay propagates from the wellbore. The tensile zone extends less than 0.5 m below the intrusion point for the assumed boundary conditions. Regions of the waste that experience shear stresses greater than 0.5 MPa are entirely within the domain of the tensile zone. Comparison of the tensile stresses in Figure 4-10 with those in Figure 4-9 illustrate the substantial reduction in the potential zone of failure predicted using an inelastic material model.

4.1.7 Transient Boundary Condition Method

Because it is an extreme case, application of an instantaneous constant-pressure condition at the base of the borehole permits evaluation of the maximum extent of tensile stresses that might occur during the first fractions of a second following a blowout event. This method permits quantification of the maximum zone of influence of the initial intrusion event. A transient condition at the wellbore is also considered using two methods. The first method assumes that the pore pressure decay is gradual and that gradients will propagate without alteration during the first few seconds following intrusion. The second method assumes that the waste experiences fracturing as a result of the instantaneous intrusion. Fracture is assumed to result in a region of increased permeability.
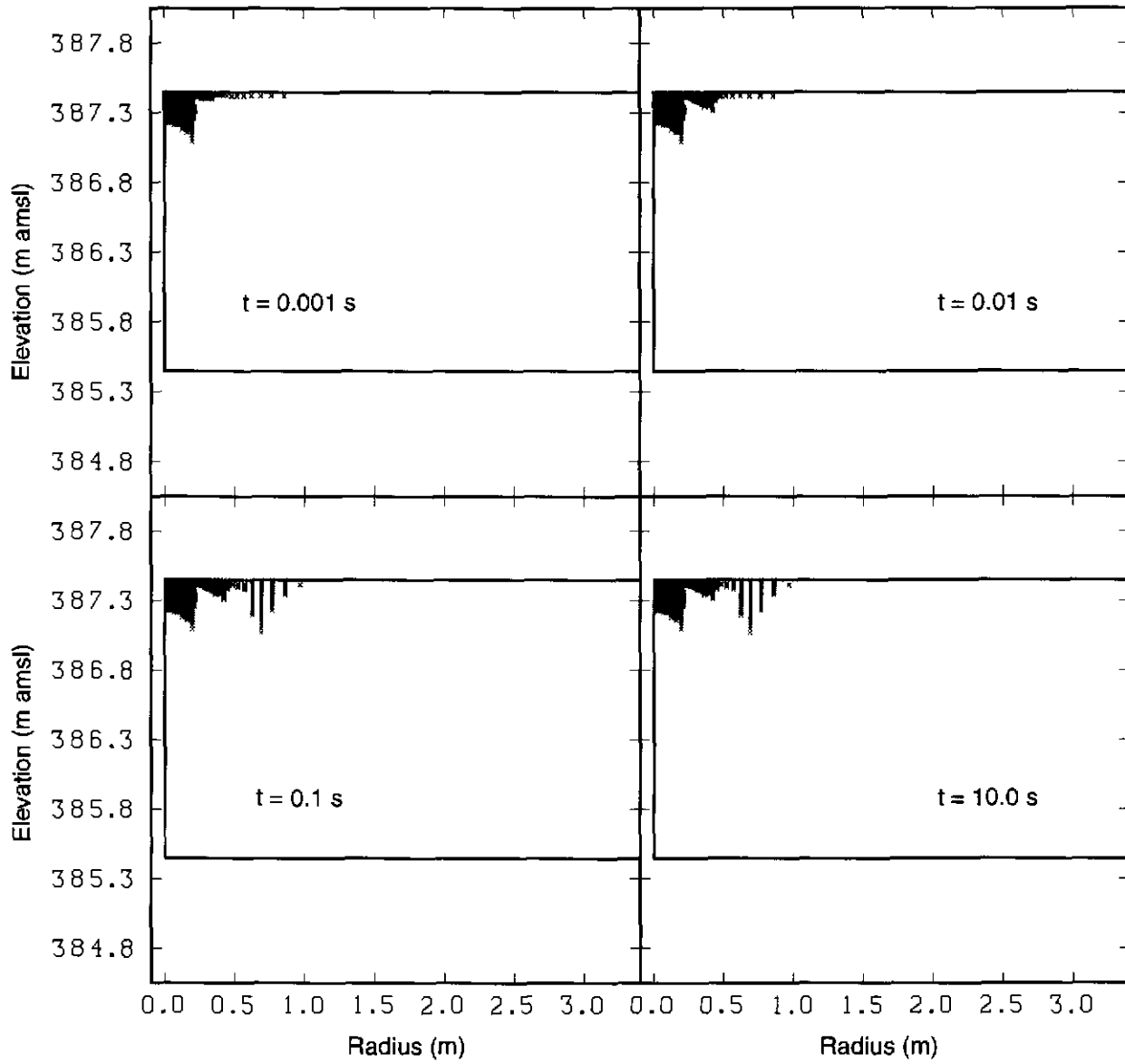
Figure 4-10. Tensile failure zones using incremental loading and a failure criterion of 15 psi.

Method One: Procedure

Initial formation pressures of 14.0 and 14.8 MPa are assumed for these calculations. The following changes were made to the mesh and initial conditions of the numerical model:

1. The volume of the elements associated with the drilling intrusion were reduced to facilitate the pressure drawdown. Several preliminary calculations were conducted to evaluate the response of the formation to the size of these elements.
2. Brine saturation in drilling and annular elements was set to zero.
3. A constant withdrawal rate of 0.80 kg/s was specified in the drilling element and each of the annular elements for a total withdrawal rate of 2.4 kg/s.

The final volumes and withdrawal rate were selected to achieve a pressure drawdown in the simulated wellbore that adequately matched that predicted by semi-analytic and numerical wellbore calculations (Sections 3 and 4.2). The withdrawal rate used in TOUGH28W calculations is greater than gas flow rates predicted using wellbore methods because of TOUGH28W limitations in this regime. The impact of the higher withdrawal rate is assessed in the presentation of results.

Method Two: Procedure

Tensile stresses predicted for the transient calculations at a formation gas pressure of 14.8 MPa indicate that material failure is likely to occur. This failure could result in fracturing of the waste material, thereby reducing its load-bearing capacity while increasing its permeability. To simulate this failure, a simple iterative procedure was developed.

Tensile failure criteria of both 3.75 and 7.5 psi were assumed. These values were selected to demonstrate the effects of fracturing on material response. Hence a very low tensile strength was selected. Tensile stresses predicted by SPECTROM-32 for the base case configuration and for a steady gas withdrawal rate were used to identify mesh elements that would experience failure. Tensions predicted at 0.01 s following initiation of the calculation were used for both configurations. Subsequent SPECTROM-32 calculations treat these elements as air, and tractions are applied at the surface of the "cavity." It is not assumed that these elements are removed, only that they have no strength. The corresponding TOUGH28W elements are treated as fractured media. Fracture of a porous medium results in a significant increase in permeability. The extent of this increase can be calculated using a number of models from the literature. For example, the fissure model (Bear, 1972) relates the fracture permeability, k_b, to the fracture aperture width (b) and fracture porosity (n) as follows:

$$k_b = \frac{nb^2}{12} \tag{1}$$

Fractures of 0.1 mm aperture resulting in a nominal porosity increase of 0.10 will have an equivalent permeability of approximately 10^{-10} m^2. For these calculations, it is assumed that the fractured zone will have a permeability 10^{-10} m^2. The respective TOUGH28W elements are assigned this permeability for the ensuing fluid flow calculations.

Because the step-function wellbore drawdown used in the base case configuration is overly conservative, a modified approach is taken for this simulation. The wellbore pressure was

reduced to 13.8 MPa and held at this value for one second. This approach permits evaluation of the effects of enhanced permeability while providing a less conservative approximation of the stress response of the waste formation.

The constant gas withdrawal calculation proceeded in a manner identical to that described for Method One, except for alteration in permeability of specified elements. Table 4-5 provides the calculation identifiers used in the transient wellbore pressure calculations.

Table 4-5. Transient Calculation Identifiers

Identifier	Comments
XPMP	Initial waste gas pressure of 14 MPa. Pore pressure and stress fields calculated for constant gas withdrawal rate of 2.4 kg/s.
IPMP	Initial waste gas pressure of 14.8 MPa. Pore pressure and stress fields calculated for constant gas withdrawal rate of 2.4 kg/s.
ITPNL	Initial waste gas pressure of 14.8 MPa. Fracturing assumed for zones failing in tension. Tensile failure criterion of 3.75 psi. Pore pressure and stress fields calculated after wellbore pressure is instantaneously reduced to 13.8 MPa.
ITPMP	Initial waste gas pressure of 14.8 MPa. Fracturing assumed for zones failing in tension. Tensile failure criterion of 7.5 psi. Pore pressure and stress fields calculated for constant gas withdrawal rate of 2.4 kg/s.

Results and Discussion

Comparison of the 14 MPa (XPMP) pore pressure fields (Figure 4-11) to those calculated using the constant (base case, Figure 4-3) boundary conditions shows that withdrawal of gas at this constant rate results in greater radial propagation of the pressure decay. This response results from the relatively high gas withdrawal rate. A tensile zone never develops for this simulation. This outcome is expected because the waste is in a compressive effective stress state at the time of penetration, and withdrawal of gas at a steady rate merely enhances this compressive state.

Pore pressure results for a waste gas pressure of 14.8 MPa (IPMP) are shown in Figure 4-12. Similar to the XPMP result, the pressure decay is more extensive for the case of steady gas efflux from the wellbore. Plots of the effective stress for the IPMP calculations (Figure 4-13) depict a response that is quite different from that predicted for the base case (IPNL) calculations discussed in Section 4.1.5. The only region showing tension at early times is in the immediate vicinity of the wellbore. Within 0.1 s after the calculation begins, a compressive zone develops, with a surrounding tensile zone. This effect results from the rapid reduction in gas pressure (hence an increase in effective stress) in the material near the wellbore. Tensile stresses exist outside this region because the gas pressure reduction is insufficient to overcome tensions caused by the pore pressure gradients (i.e., seepage forces).

The pore pressure response for a step-function reduction in wellbore pressure (ITPNL) is depicted in Figure 4-14. The extent of the fractured zone is readily apparent, as the wellbore pressure propagates outward to the edges of the region. The pressure gradient outside the fractured zone is not as steep as that seen for the IPNL calculation. This is a result of the difference in specification of wellbore pressure and also the increase in surface area. Most of the fractured zone is in a state of compression, as can be seen from Figure 4-15. Only a small region near the wellbore remains in tension. Magnitudes of tensile stresses outside the fractured zone are also reduced, compared to the IPNL calculation (Figure 4-9).
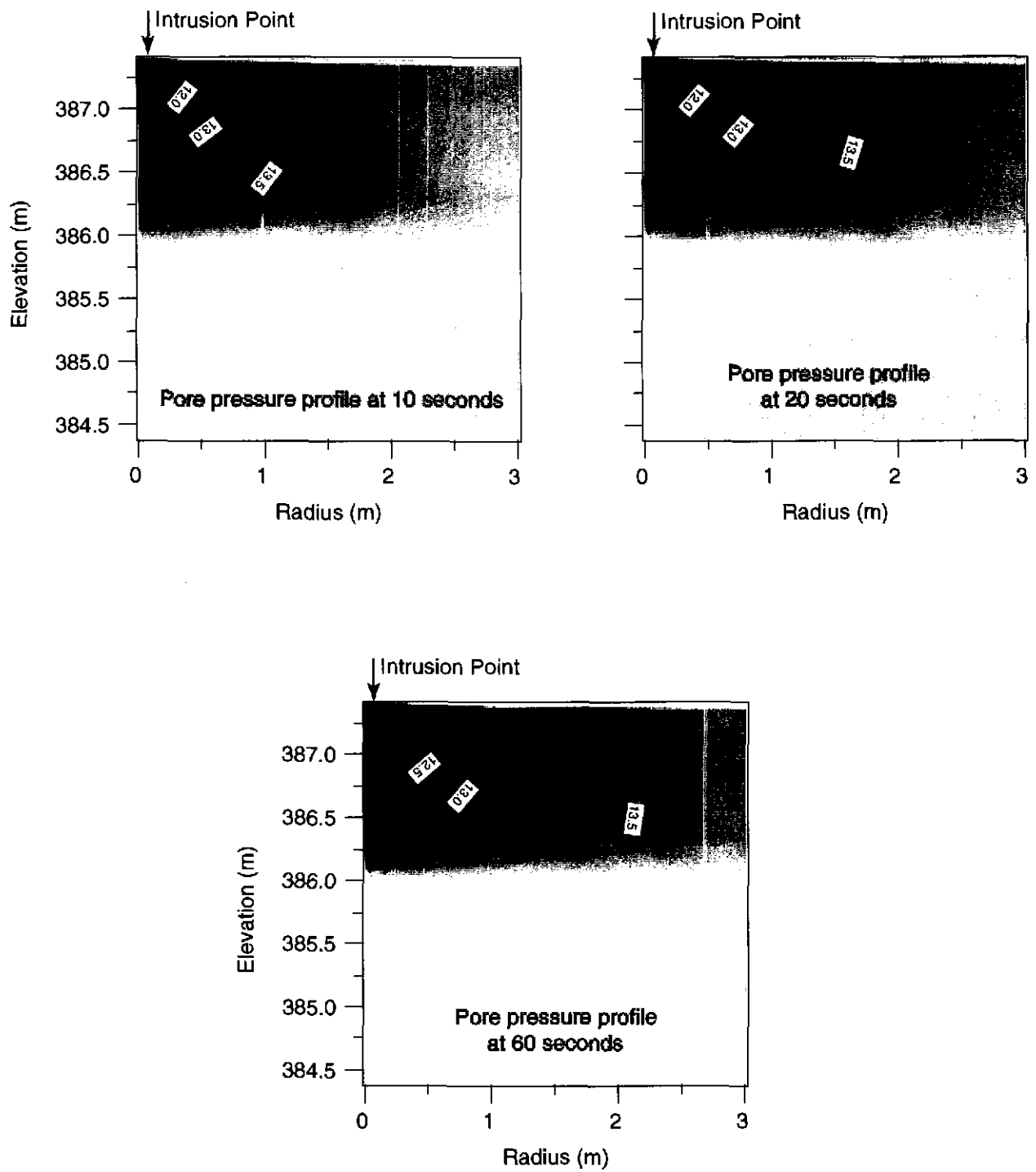
Figure 4-11. TOUGH28W pressure predictions for initial waste gas pressure of 14 MPa, constant gas withdrawal rate of 2.4 kg/s (XPMP) from the wellbore (upper left-hand corner of plots). Contours are in MPa.
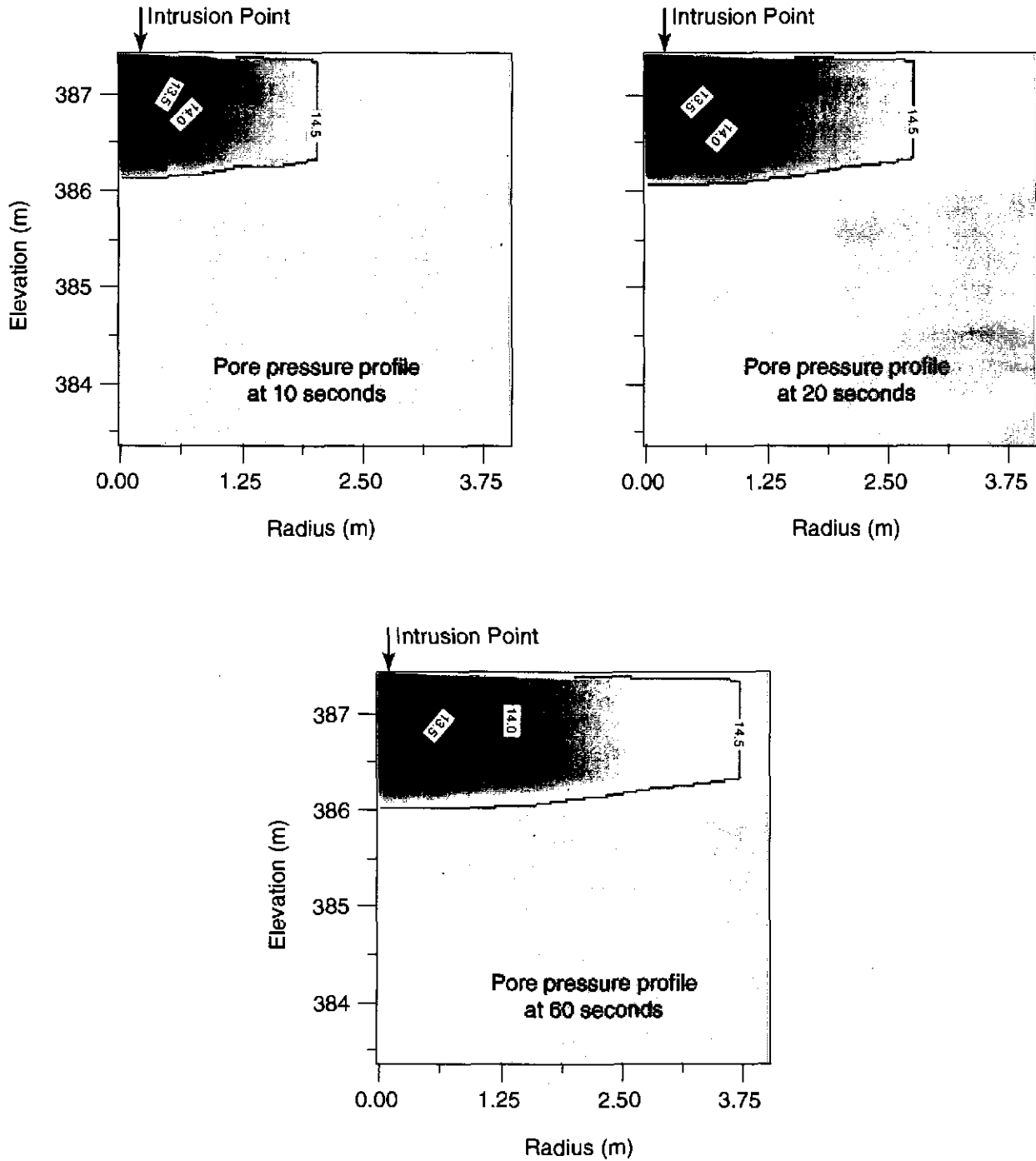
Figure 4-12. TOUGH28W pressure predictions for initial waste gas pressure of 14.8 MPa, constant gas withdrawal rate of 2.4 kg/s (IPMP) from wellbore (upper left-hand corner of plots). Contours are in MPa.

SPECTROM-32 results for IPMP calculations
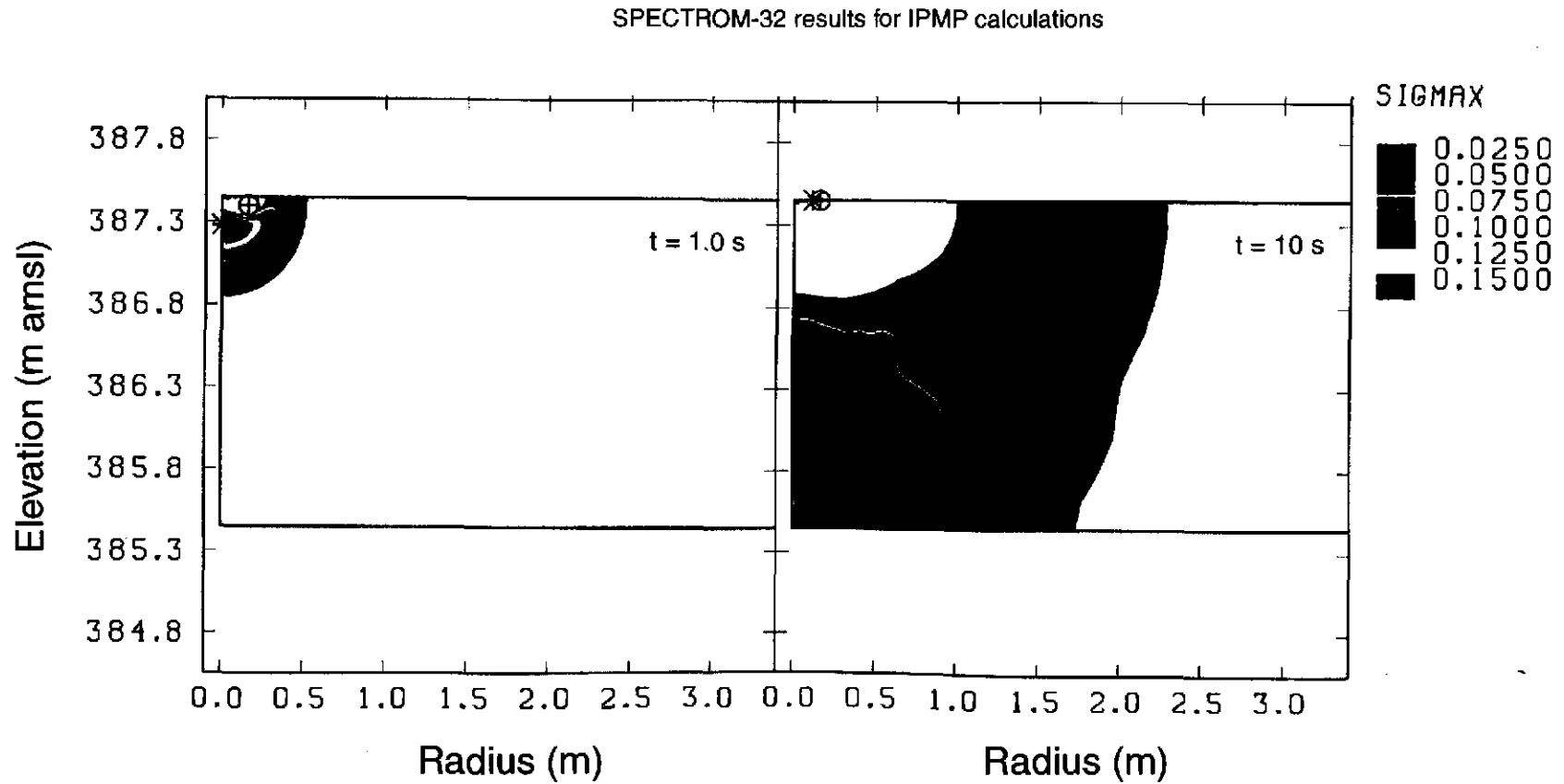
Figure 4-13. Contours of maximum tensile stress for an initial waste gas pressure of 14.8 MPa. Constant mass withdrawal rate of 2.4 kg/s specified at the wellbore (upperleft corner of plots). White zones are in compression. Contours are in MPa.
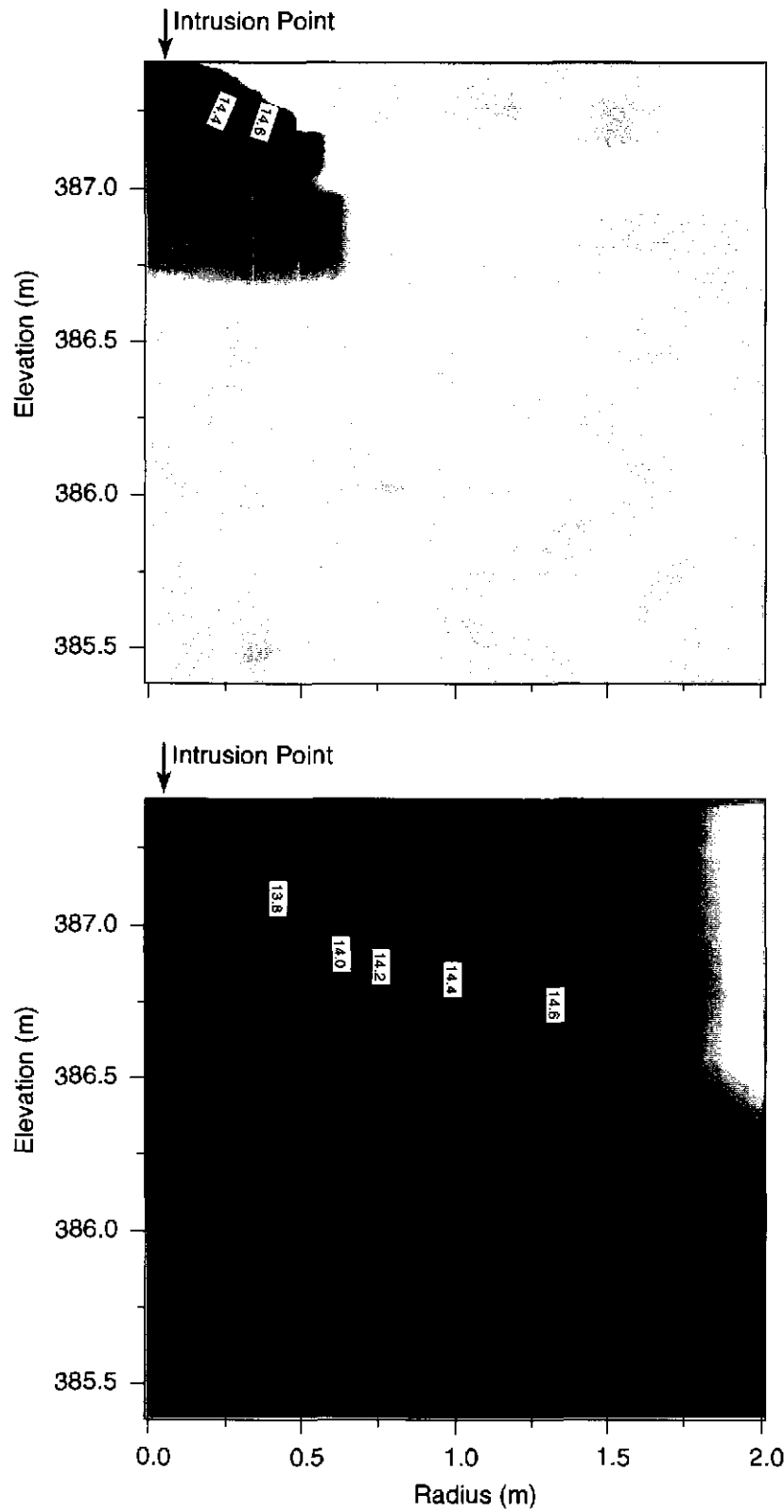
TRI-6121-421-0

Figure 4-14. TOUGH28W pressure predictions for waste gas pressure of 14.8 MPa (ITPNL), initial fractured zone determined using a tensile failure of 3.75 psi. Upper plot is for 0.001 s. Lower plot is for 1 s. Contours are in MPa.
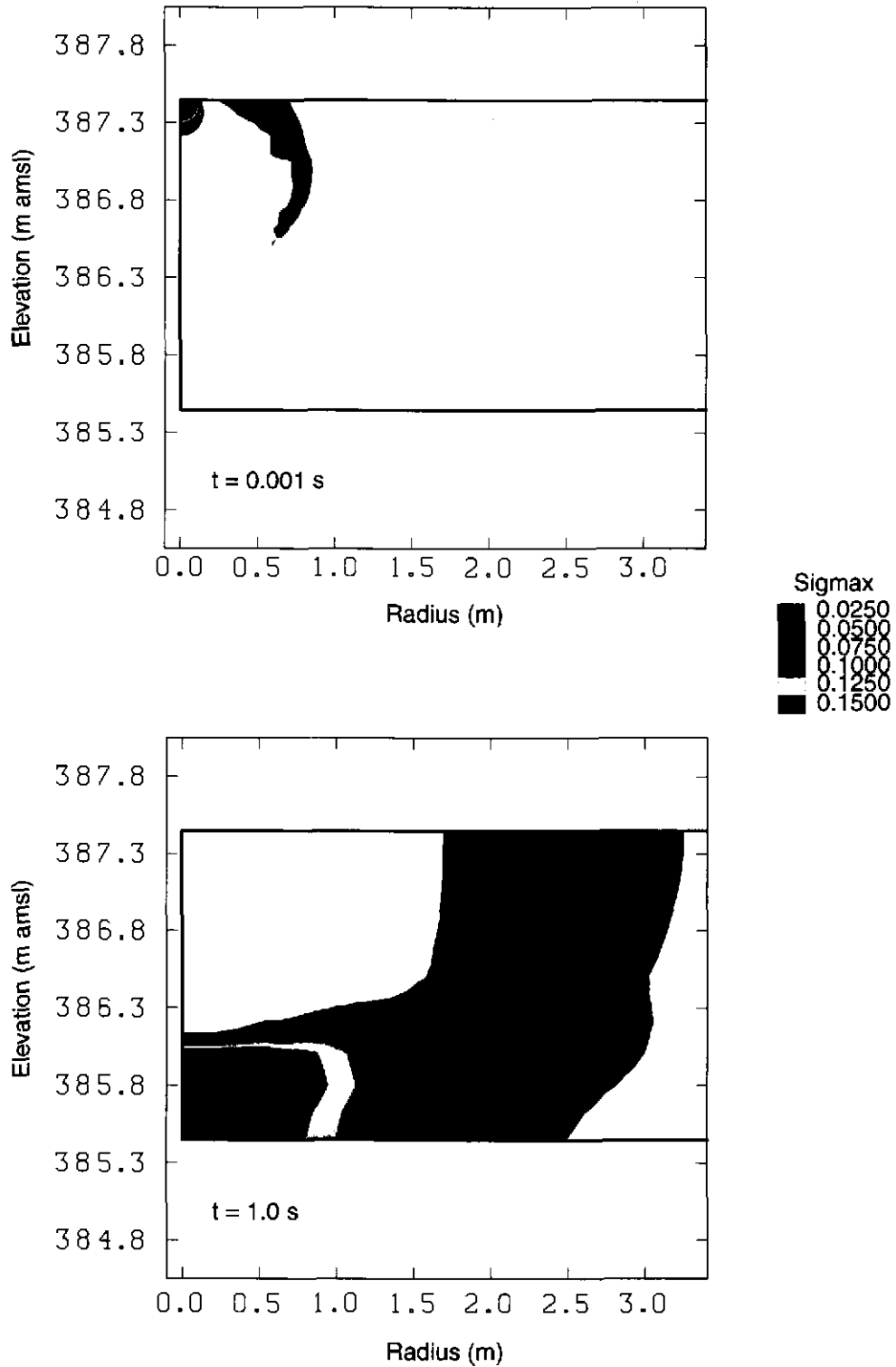
Figure 4-15. Contours of maximum tensile stress for 0.001 s (upper) and 1.0 s (lower) after wellbore pressure is reduced from 14.8 MPa to 13.8 MPa (ITPNL). Initial fractured zone determined from IPNL calculation. Contours are in MPa.

Predictions of pore pressure and tensile stresses for the constant gas-withdrawal calculation are shown in Figure 4-16. The general result is similar to that seen in the ITPNL calculations: wellbore pressure propagates to the edges of the fractured zone, which develops a compressive effective stress state. Tensile stresses outside the fractured zone are reduced, compared to the IPMP result.

4.2 Coupled Fluid Flow/Wellbore Hydraulics Calculations

This section describes a mathematical model that couples fluid flow, solids transport, and wellbore hydraulics. The mathematical technique uses TOUGH28W to produce an influence function capable of accurately describing cumulative gas flow from the waste room to the intrusion wellbore.

The objective of the coupled fluid flow/wellbore hydraulic calculations is to predict the bottomhole pressure throughout the mud ejection phase, including the effects of solids transport. The calculations also provide estimates of cumulative gas flow from the waste room to the intrusion borehole and provide insight into the rate and size of fragments that could be ejected from the borehole on intrusion.

4.2.1 Numerical Model

The borehole intrusion scenario assumes that a borehole filled with mud at 8 MPa bottomhole pressure will intersect a waste room containing gas at 14.8 MPa. This pressure differential will cause a fragmentation (spalling) of the waste, which may then be carried up the borehole to the surface by the gas flowing from the formation. There will be a short period during which a portion of the annular volume will contain an upward-moving mud column. After all the mud is ejected from the borehole, the borehole will contain only a flowing mixture of gas and solids. A schematic diagram illustrating this process, while the mud is still being displaced from the borehole, is shown in Figure 4-17.

A dynamic model of the processes described above should contain the following components:

1. a model for predicting gas influx from the waste room, subject to an imposed pressure at the bottomhole (the gas influx is a function of waste permeability),
2. a model for predicting pressure drop resulting from gas-solids transport between the bottom of the wellbore and the base of the mud column, and
3. a model for predicting pressure drop caused by the flow of mud up the borehole.

After all the mud is ejected from the borehole, the zone containing gas and suspended solids extends to ground surface (at atmospheric pressure), and only the first two components need to be evaluated. A brief description of each of these model components as implemented in the present analysis follows. Comparisons between this model and the semi-analytic model presented in Section 3 are discussed in Section 4.3.
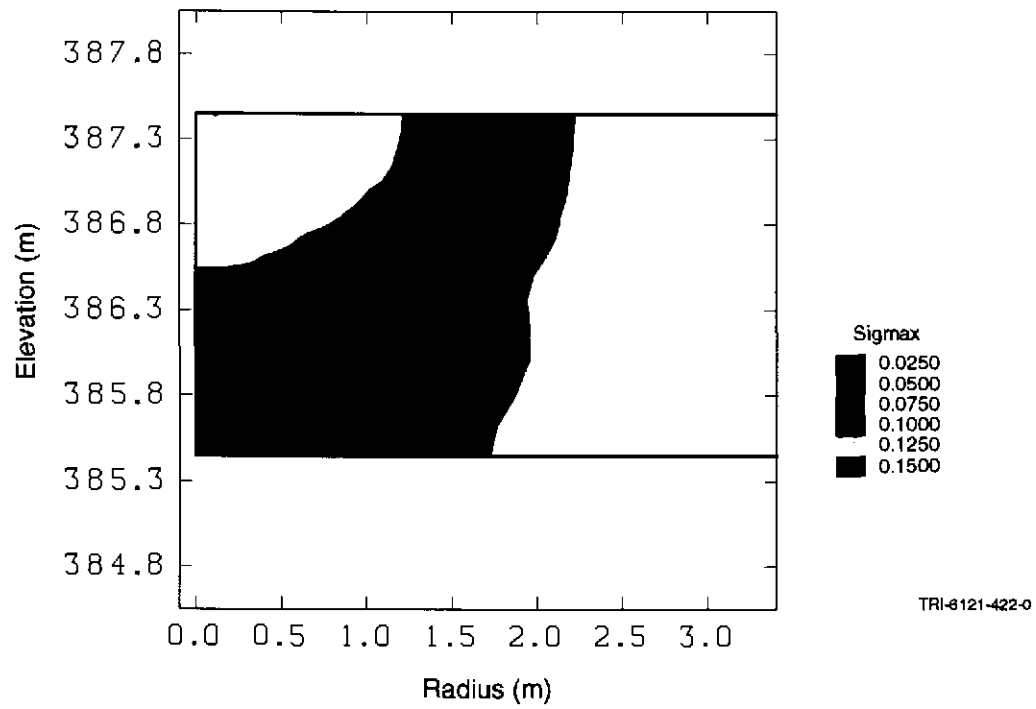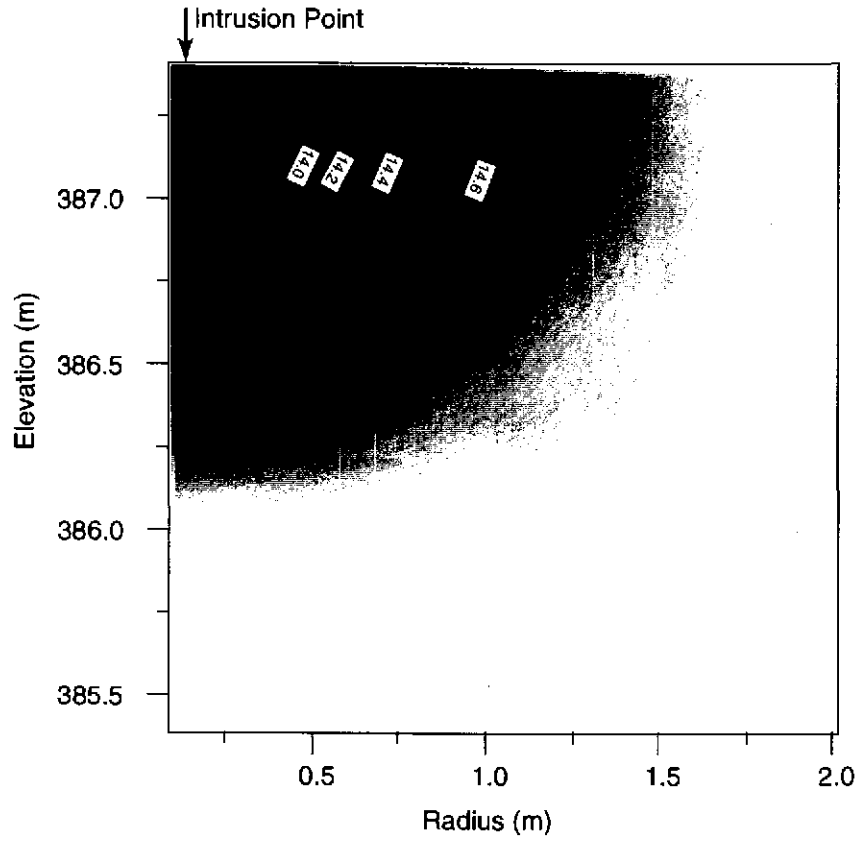
Figure 4-16. Contours of pore pressure and tensile stress for ITPMP calculation. Initial waste gas pressure is 14.8 MPa, at a simulated time of 1 second. Contours are in MPa.
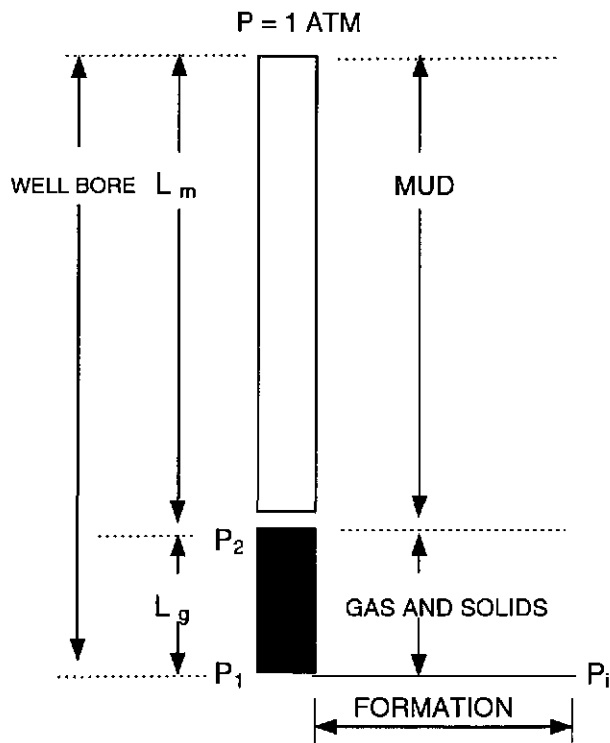
Figure 4-17. Schematic illustrating the repository breach scenario.

Gas-Influx Model

The "pseudo-pressure" concept of Al-Hussainy et al. (1966) is used to linearize the equations describing single-phase gas flow from the formation to the wellbore. When the bottomhole pressure is continuously varying, the principle of superposition gives:

$$Q(t_n) = \Sigma\left[m(p_{j-1}) - m(p_j)\right] I(t_n - t_{j-1}), j = 1,\ldots,n \qquad (2)$$

where:

Q	=	cumulative gas influx
$m(p)$	=	pseudo-pressure = 2 * Integral $(0, p)$ $[(p/\mu)\ dp]$
p	=	pressure
μ	=	viscosity
I	=	influence function, and
j	=	time index.

The influence function is defined as the cumulative gas influx per unit pseudo-pressure drop, and can be generated from a single TOUGH28W simulation with the bottomhole pressure kept fixed at some arbitrary value. For the problem at hand, the influence function was generated for a bottomhole pressure of 8 MPa, a waste-room pressure of 14.8 MPa, and a waste room permeability of 1.7×10^{-13} m^2. As discussed in Section 3, waste permeability significantly affects the gas influx to the wellbore. The porosity of the waste room is assumed to be 0.6 and the

borehole is assumed to be completed into the first 1 cm of the top of the room. Figure 4-18 presents a log-log plot of the influence function versus time in seconds. Incorporating the influence function into the wellbore submodel prevents an exterior iterative loop with TOUGH28W. This method was tested by comparing TOUGH28W results to those calculated using the influence function. The two solutions showed close agreement, verifying the influence function method.

Gas-Solids Flow Model

Based on a momentum balance, the pressure drop in the borehole can be expressed as the sum of friction, gravitation, and acceleration components. Following Machado and Ikoku (1981) the acceleration component due to changes in fluid velocity is assumed to be negligible. This leads to the following expression for the pressure drop, dp, over an incremental length, dL:

$$dp = \frac{\rho_m \, dL}{144} + \frac{f_m \rho_g v_g^2 \, dL}{72 \, g_c \, d_H} \tag{3}$$

where:

|		
ρ_m	=	volumetric-weighted suspension density
f_m	=	Fanning friction factor for the suspension
ρ_g	=	gas density
v_g	=	gas velocity
g_c	=	gravitational constant, and
d_H	=	effective diameter of the wellbore.
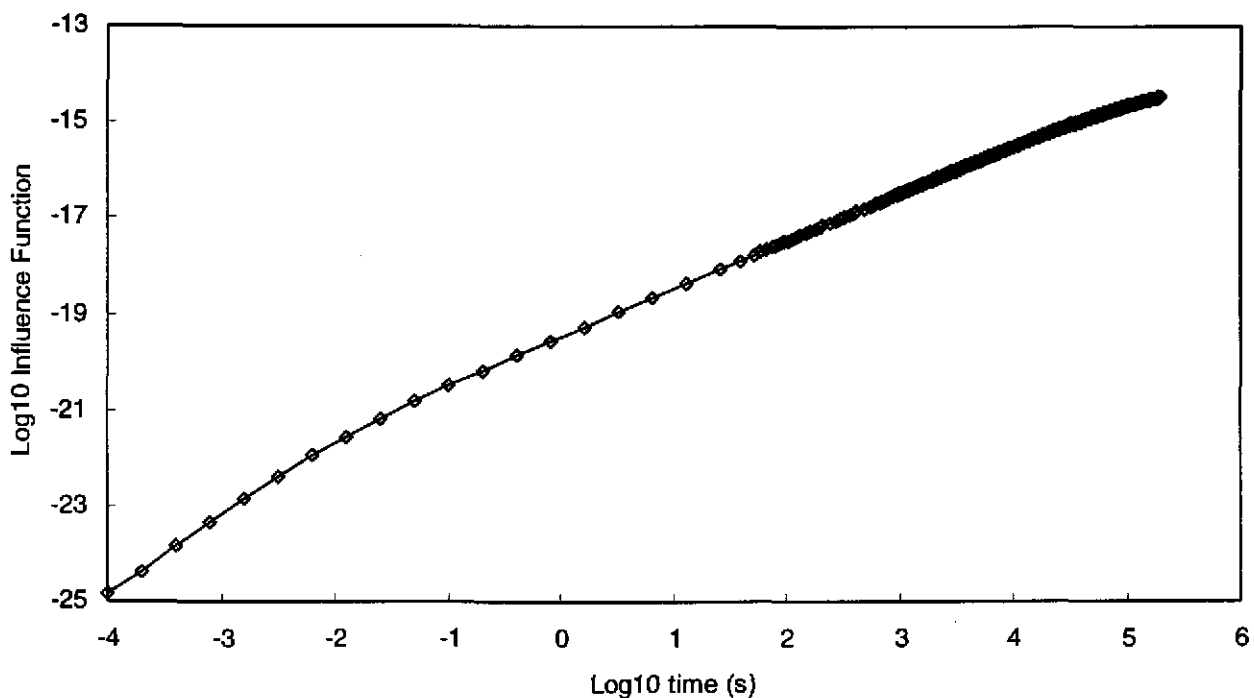
Figure 4-18. Influence function versus time.

The Fanning friction factor for the suspension is taken to be the sum of the gas and solid friction factors. The friction factor for gas is calculated from the Reynolds number using a closed-form version of the Colebrook equation provided by Jain (1976). The friction factor for solids is determined from an experimental relationship developed by Machado and Ikoku (1981), which requires a knowledge of the gas and solids mass flux rates, the gas velocity, and the average particle diameter. The current solids-transport model implementation assumes dilute phase transport of solids (solids-to-gas volume ratios greater than 4%). Higher solids loading would necessitate recalculation of friction factors and velocities within the wellbore.

Mud-Flow Model

Assuming the mud to be similar to brine in composition, the pressure drop resulting from the flow of mud along the borehole can be determined from the following expression for the pressure drop, ΔP, over time-step, Δt. In English engineering units:

$$\Delta P = \frac{\rho_{mud}}{144} \times L_{mud} + \frac{f_{mud}\,\rho_{mud}\,v_{mud}^2}{(4)(72 g_c d_H)} \times \frac{L_{mud} + \Delta L}{2} + \rho_{mud} \times \text{Vol}_{mud} \times \frac{a_{mud}}{g_c} / A / 144 \qquad (4)$$

where

ρ_{mud}	=	mud density
L_{mud}	=	length of the mud column at the end of the time-step
f_{mud}	=	Moody friction factor for the mud
v_{mud}	=	mud velocity
g_c	=	gravitational constant
d_H	=	effective diameter of the wellbore
ΔL	=	change in the length of the mud column for this time-step
Vol_{mud}	=	average volume of the mud column for this time-step
a_{mud}	=	acceleration of the mud ($\Delta v_{mud} / \Delta t$) for the time-step, and
A	=	area normal to flow.

Composite Model

The composite model for gas-solids transport is implemented using an iterative methodology, and the simulation period is broken into small time increments. The iterative implementation ensures that all models (gas influx, gas-solids flow model, mud-flow model) yield a self-consistent bottomhole pressure value for an atmospheric surface pressure and the chosen solids-to-gas ratio. This iterative procedure is shown as a flowchart in Figure 4-19.

Code

The code COMBO2.FOR, Version 2 incorporates the gas-influx model, the gas-solids flow model, and the mud-flow model into a single iterative package. Table 4-7 lists all subroutines with a brief description for each. The code was written in FORTRAN and was run on a DELL Dimension XPS P133c (pentium processor).

n=1

$P_1^n = 8$ MPa

$L_g = O$

$P_2^n = P_1^n$

Select Time Step
Δt_n

Calculate
Solids
Mass Flux

Set PR Drop
$= (P_i - P_1)$

Calculate
Gas
Mass Flux

Calculate Volume
Gas Influx at
$P = P_1^n - (P_1^n - P_2^n)/2$

Calculate L_g, L_m

Calculate P_2^n from
Head Loss and Friction Loss
Over L_m (Mud)

$P_1^n = 0.5 *$
$[P_1^n (NEW)+P_1^n]$

Calculate P_1^n (New) from
Head Loss and Friction Loss
Over L_g (Gas + Solids)

No

P_1^n (New) $- P_1^n$
$\leq \varepsilon$

Yes

Yes

Final Time
Reached

No

n = n+1

Stop

Figure 4-19. Flowchart showing the composite model for gas-solids transport.

Table 4-7. COMBO2 Subroutine Listing.

Subroutine	Description
COMBO.F	Main driver.
T2CLON.F	Gas-influx model.
LINTRP.F	Linear interpolation.
INPUT.F	Reads user input.
BHWMUD.F	Mud-flow and gas-solids flow models.
TEMP.F	Temperature as a function of depth.
VIS.F	Viscosity as a function of temperature.
DENS.F	Density as a function of pressure, gas gravity, temperature, and gas deviation factor (Machado and Ikoku, 1981).
VELS.F	Terminal and gas velocities (Machado and Ikoku, 1981).
FF2.F	Gas friction factor (Jain, 1976).
FFSOL.F	Solids friction factor (Machado and Ikoku, 1981).
MIXDEN.F	Gas-solids suspension density (Machado and Ikoku, 1981).
MASFLW.F	Gas and solids mass flow rates.
PRDROP.F	Pressure drop due to gas-solids suspension (Machado and Ikoku, 1981).
BHPDEF.F	List of variables. Printed when any print switch is set to 1.
GASVL.F	Gas volume generated by the gas-influx model.
VMUD.F	Velocity of the mud column for a given time-step.
FFMUD.F	Mud friction factor.
PRMUD.F	Pressure at the base of the mud column.

COMBO2 starts with an initial estimated bottomhole pressure, which the gas-influx model subroutine uses to generate a mass flow rate (see Figure 4-19). During mud expulsion, the gas mass flow rate from the gas-influx model subroutine is used to calculate a volume of gas that enters the borehole under the given pressure and temperature conditions. The pressure used to calculate gas volume is set to the bottomhole pressure less one half of the pressure drop across the gas column for the previous iteration. Temperature is set to the average temperature of the gas column.

The volume of gas entering the borehole is converted to a length of borehole based on the borehole annulus area. This change in the length of the gas column is used in conjunction with the time-step length to estimate the velocity of the mud column, its frictional pressure drop, and the acceleration of the mud column. The combination of the frictional pressure, inertial pressure, atmospheric pressure, and the pressure resulting from the weight of the mud column are then used to calculate a pressure at the base of the mud column. This pressure is used as the upper boundary pressure for the gas-solids flow model, which in turn provides an improved estimate of the bottomhole pressure.

After the mud column is expelled, the mud-flow model is bypassed and atmospheric pressure is used as the upper boundary pressure for the gas-solids flow model. The gas-solids flow model iteratively calculates a bottomhole pressure based on the upper pressure boundary. This bottomhole pressure is then compared with the initial estimated bottomhole pressure, and the simulation ends if the difference between the two bottomhole pressures is acceptable. If the difference is too large, a new bottomhole pressure based on the original estimated bottomhole pressure and the calculated bottomhole pressure is calculated, and the process is repeated. COMBO2 has several hard-coded parameters; these are listed in Table 4-8.

Table 4-8. Hard-coded Parameters in COMBO-2

Parameter	COMBO-2 Value
Temperature	Surface temperature of 60°F with a temperature gradient of 1°C / 80 ft.
Viscosity	Linear temperature dependence between the temperatures 0°C and 129.4°C. Values for these temperatures were taken from the *CRC Handbook of Chemistry and Physics* (1978). Viscosity is not pressure dependent.
Gas gravity	Molecular weight of H_2 / molecular weight of dry air = 2.016/28.97 = 0.06959 for H_2 (Bradley et al., 1989).
Gas deviation factor	1.0 for H_2, which was assumed to be an ideal gas.

Results and Discussion

To describe a well blowout, COMBO2 was used to predict the bottomhole pressure, cumulative gas flux, and time taken to expel 20 m^3 of spalled materials. This volume was selected for purposes of example only. This calculation assumes that the spalled material is of a uniform diameter of 150 microns (0.00015 m). Several other model input values assumed for the calculation are summarized in Table 4-9.

Table 4-9. Input Parameter Values for Coupled Fluid Flow/Wellbore Hydraulic Model

Parameter	Units	Value
Total Depth	meters	654.10
Collar Diameter	meters	0.2032
Collar Length	meters	182.88
Drillpipe Diameter	meters	0.1143
Drillpipe Length	meters	471.22
Drilled Diameter	meters	0.31115
Spalled Particle Diameter	meters	0.00015
Particle Specific Gravity	kg/m^3	2650
Waste Room Permeability	m^2	1.7×10^{-13}
Waste Room Porosity	m^3/m^3	0.6
Waste Room Initial Pressure	MPa	14.8

Figure 4-20 plots bottomhole pressure versus time for the case where the spalled waste particle size is assumed uniform and equal to a diameter of 150 microns. In this simulation it is assumed that 20 m^3 of spalled mass are available at time zero and that the delivery rate of solids to the borehole is limited by a 4% volumetric solids-to-gas ratio. The model predicts that the mud will be expelled from the borehole approximately 235 s after intrusion. The pressure falls from the initial room pressure of 14.8 MPa to approximately 8 MPa in the first 10 s after intrusion. Pressure fall-off then slows considerably except for short periods marking the removal of mud from the collar region of the annulus at 88 s and the expulsion of the mud from the annulus at 235 s. At 100 s, the bottomhole pressure is approximately 6 MPa. By mud expulsion, the bottomhole pressure has fallen to approximately 0.5 MPa, where it remains until all solids are expelled. After solids exhaustion, the bottomhole pressure falls to 0.16 MPa (approximately 1.5 atm) and slowly approaches atmospheric pressure. From this simulation one can see that the bottomhole pressure does not fall to pressures approaching atmospheric conditions for many minutes after intrusion. If

the particle size is increased, the predicted borehole pressure will be larger at a given time and the duration to mud expulsion will be lengthened.

Figure 4-21 plots the cumulative gas that is expelled through the borehole versus time after borehole intrusion. The cumulative gas curve suggests that the coupling of wellbore and gas-reservoir models yields a reasonably constant mass flow rate for the gas.

Figure 4-22 plots the maximum spalled particle diameter that could be expelled as a function of time for the gas velocities calculated in the simulation discussed above. These gas velocities are calculated assuming a uniform particle diameter of 150 microns, and particle size does effect gas velocity. Nevertheless, a sensitivity simulation has shown that neglecting this feedback loop only causes noticeable error at times close to the mud expulsion time. This plot shows that, prior to mud ejection, the maximum particle size that could be transported is less than 0.3 mm. Following mud ejection, particles of the order of centimeters can be transported.

4.3 Two-Phase Pressure Decay

The coupled calculations presented in Sections 4.1 and 4.2 assess the sensitivity of the modeled systems to material parameters, assumed boundary conditions, and coupling approaches. In response to CMPRP questions regarding waste heterogeneity, this section provides additional information regarding the fluid flow response of the waste for other configurations. Inferences regarding coupled responses could be made from these studies, but no SPECTROM-32 simulations were conducted for these models.
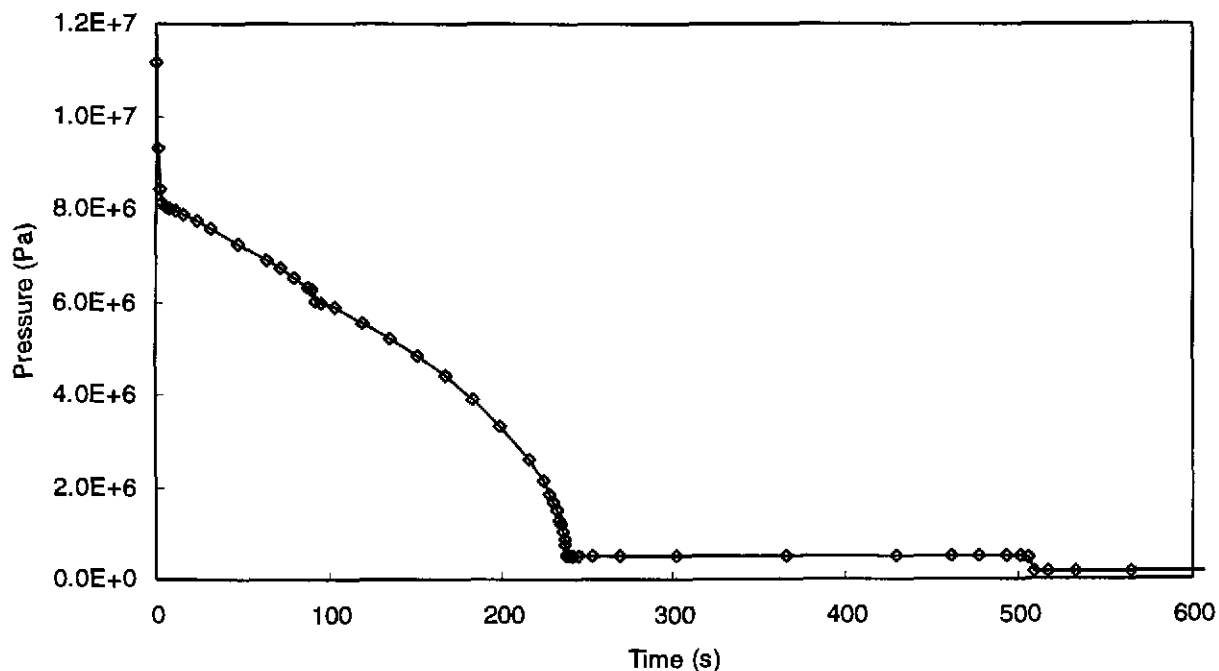
Figure 4-20. Bottomhole pressure versus time.

4-34
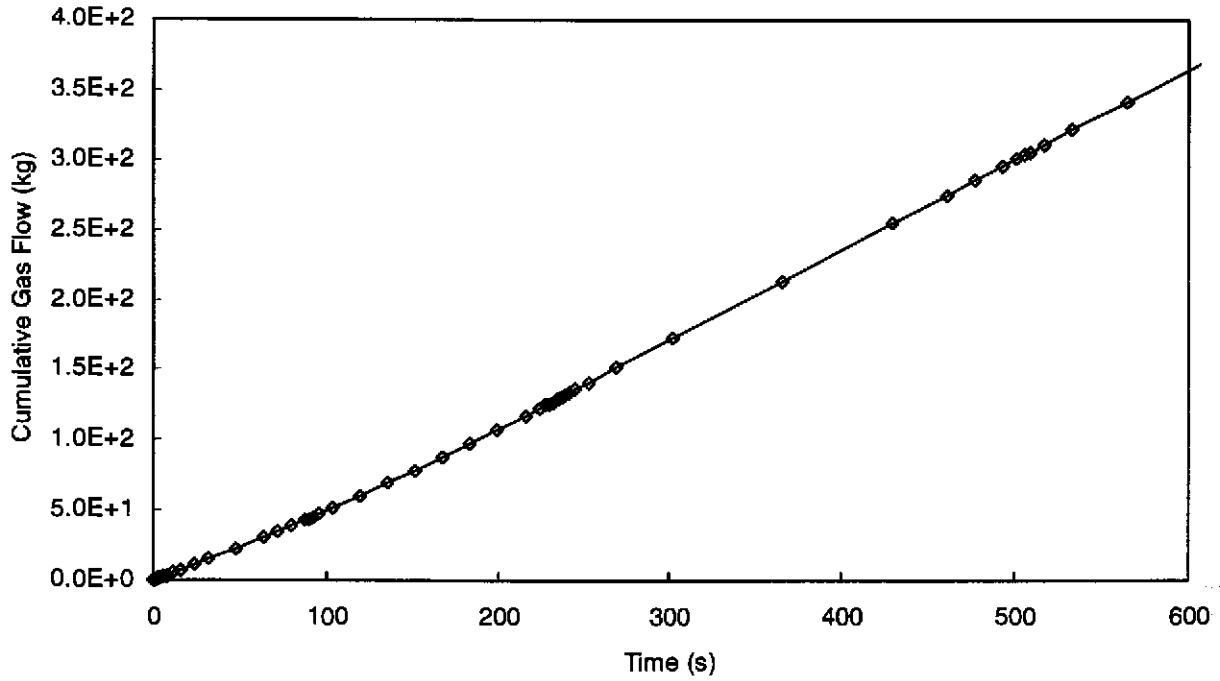
Figure 4-21. Cumulative gas flow versus time.
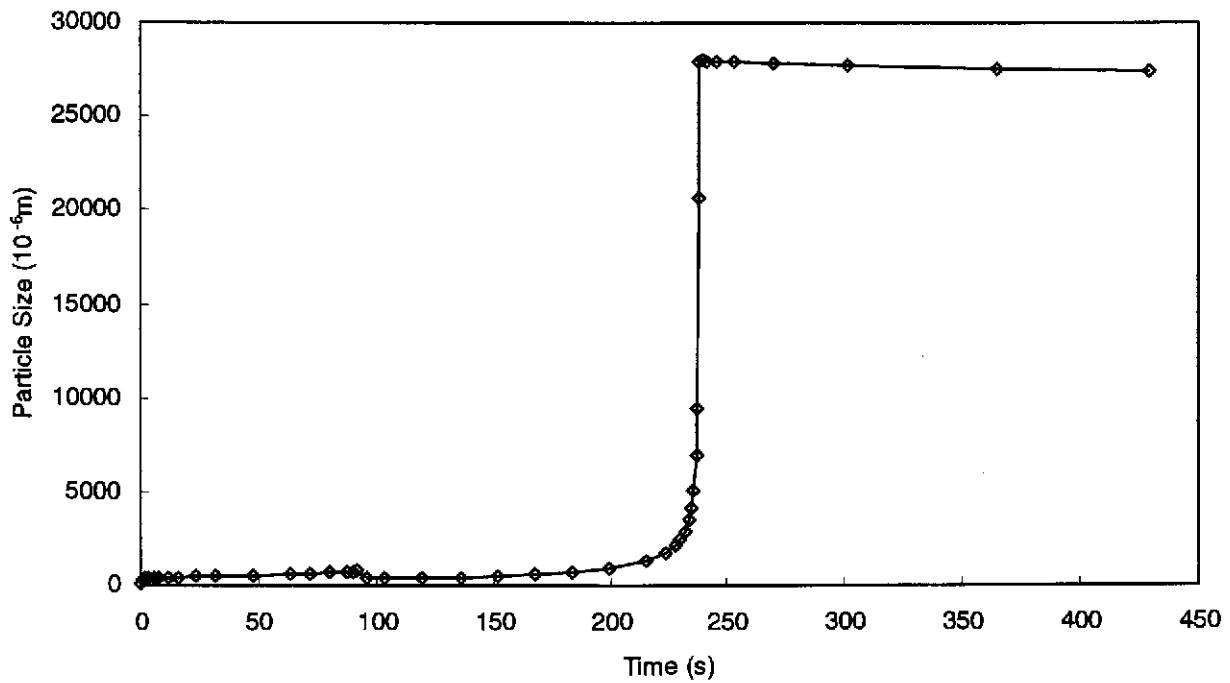
Figure 4-22. Maximum size of particles (diameter) expelled as a function of time.

As discussed in Section 2, the waste may exhibit a layered character. Degradation of the waste will not be uniform within a disposal room because of gravitational effects. This effect is clearly seen in the CCA predictions (Figures 4-23 and 4-24). A conceptual model of a layered waste panel was developed to assess the response of this configuration to a drilling intrusion. This model divided the waste into four regions, each with a different material porosity, brine saturation, and permeability. It is assumed that the upper regions consist largely of compressed, relatively undegraded drums and that the lowest region consists primarily of degradation products similar in character to the surrogate waste tested (Section 2). A schematic of the layered models is shown in Figure 4-25.

Because considerable uncertainty exists regarding the state of the waste at the time of a drilling intrusion, a random model was also developed. This model assumes that randomness can be captured through variation of waste permeability. Grid elements are randomly assigned a permeability ranging from 10^{-12} to 10^{-16} m^2. The model distribution of permeability is shown in Figure 4-26.

4.3.1 Effects of Waste Heterogeneity: Layered Model

Geometry

The uppermost layer was assumed to consist of crushed, relatively undegraded waste drums. It was assigned a thickness of 0.1 m. The next two layers were assumed to consist of partially degraded, compressed waste and were given thicknesses of 0.55 and 0.7 m. The lowest layer was assumed to consist of largely degraded waste material and byproducts. It was assigned a thickness of 0.65 m. The total thickness of the mesh was 2 m. Radial discretization differed slightly from that described in Section 4.1.1. This difference was evaluated and found to produce negligible effects on calculated results. The thickness of grid elements and associated material assignments are found in Table 4-10.

Table 4-10. Details of the Grid Layers

Layer	Δ Z	4 Layer Material Types	Elevation at Element Midpoint (m)
1	1	halite	388.6080
2	0.4	halite	387.9080
3	0.2	halite	387.6080
4	0.1	halite	387.4580
5	0.01	halite	387.4030
6	0.01	waste 1	387.3930
7	0.01	waste 1	387.3830
8	0.01	waste 1	387.3730
9	0.01	waste 1	387.3630
10	0.0105	waste 1	387.3528
11	0.011	waste 1	387.3420
12	0.012	waste 1	387.3305
13	0.013	waste 1	387.3180
14	0.014	waste 1	387.3045
15	0.015	waste 2	387.2900
16	0.0175	waste 2	387.2738
17	0.02	waste 2	387.2550
18	0.03	waste 2	387.2300
19	0.04	waste 2	387.1950
20	0.05	waste 2	387.1500
21	0.075	waste 2	387.0875
22	0.1	waste 2	387.0000

Table 4-10. Details of the Grid Layers

Layer	Δ Z	4 Layer Material Types	Elevation at Element Midpoint (m)
23	0.1	waste 2	386.9000
24	0.1	waste 2	386.8000
25	0.1	waste 3	386.7000
26	0.1	waste 3	386.6000
27	0.1	waste 3	386.5000
28	0.1	waste 3	386.4000
29	0.1	waste 3	386.3000
30	0.1	waste 3	386.2000
31	0.1	waste 3	386.1000
32	0.1	waste 4	386.0000
33	0.1	waste 4	385.9000
34	0.1	waste 4	385.8000
35	0.1	waste 4	385.7000
36	0.12	waste 4	385.5900
37	0.132	waste 4	385.4640
38	0.15	halite	385.3230
39	0.5	halite	384.9980
40	1	halite	384.2480

Material Properties

Properties for the layered waste material are presented in Table 4-11. Properties for the halite, drill string, and annulus were presented in Table 4-3.

Table 4-11. Waste Formation Properties - 4 Layer Model

| Parameter	Waste 1	Waste 2	Waste 3	Waste 4
Permeability (m^2)	1.0E-12	5.0E-13	5.0E-15	1.0E-16
Porosity	0.90	0.80	0.70	0.60
Density (kg/m^3)	1920	2963	2963	2963
Initial Brine Saturation	0.05	0.31	0.30	0.60
Brooks-Corey	2.89	2.89	2.89	2.89
Compressibility of Rock (1/Pa)	0	0	0	0
Threshold Pressure (Pa)	0	0	0	0
Residual Brine Saturation	0.075	0.075	0.075	0.075
Residual Gas Saturation	0	0	0	0
Relative Permeability Model	Brooks-Corey	Brooks-Corey	Brooks-Corey	Brooks-Corey
Capillary-Pressure Model	Brooks-Corey	Brooks-Corey	Brooks-Corey	Brooks-Corey

Results and Discussion

The influence of a thin layer consisting of the highest assumed values for permeability and porosity is minimal, as shown in Figure 4-27. A slight "bump" in pressure decay is seen at 0.001 s, but has disappeared by 0.1 s after the simulation begins. This result implies that a pressure wave cannot readily propagate along thin channels. The pressure front proceeds readily through Layer 2, as seen in Figure 4-28. Within 1 s following intrusion, the wave has reached the third layer, but does not extend more than 0.2 m into this lower permeability (5×10^{-15} m^2) region. Gas blowdown will continue for several days, provided that no effort is made by the driller to rectify the situation. Extended simulation times show that the pressure front will not reach the fourth layer for several hundred seconds.
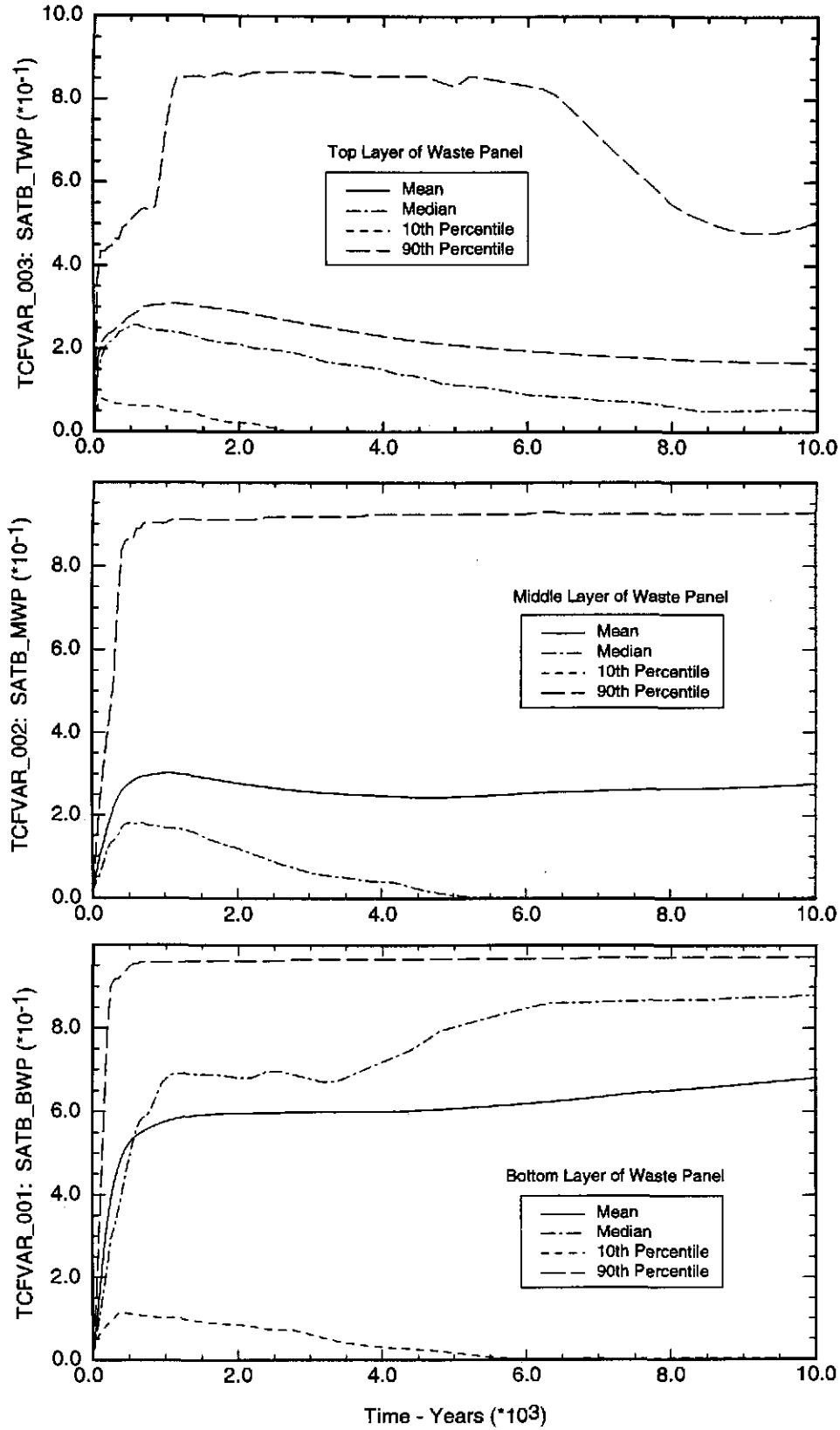
Figure 4-23. CCA predictions of volume averaged brine saturation in waste panels.
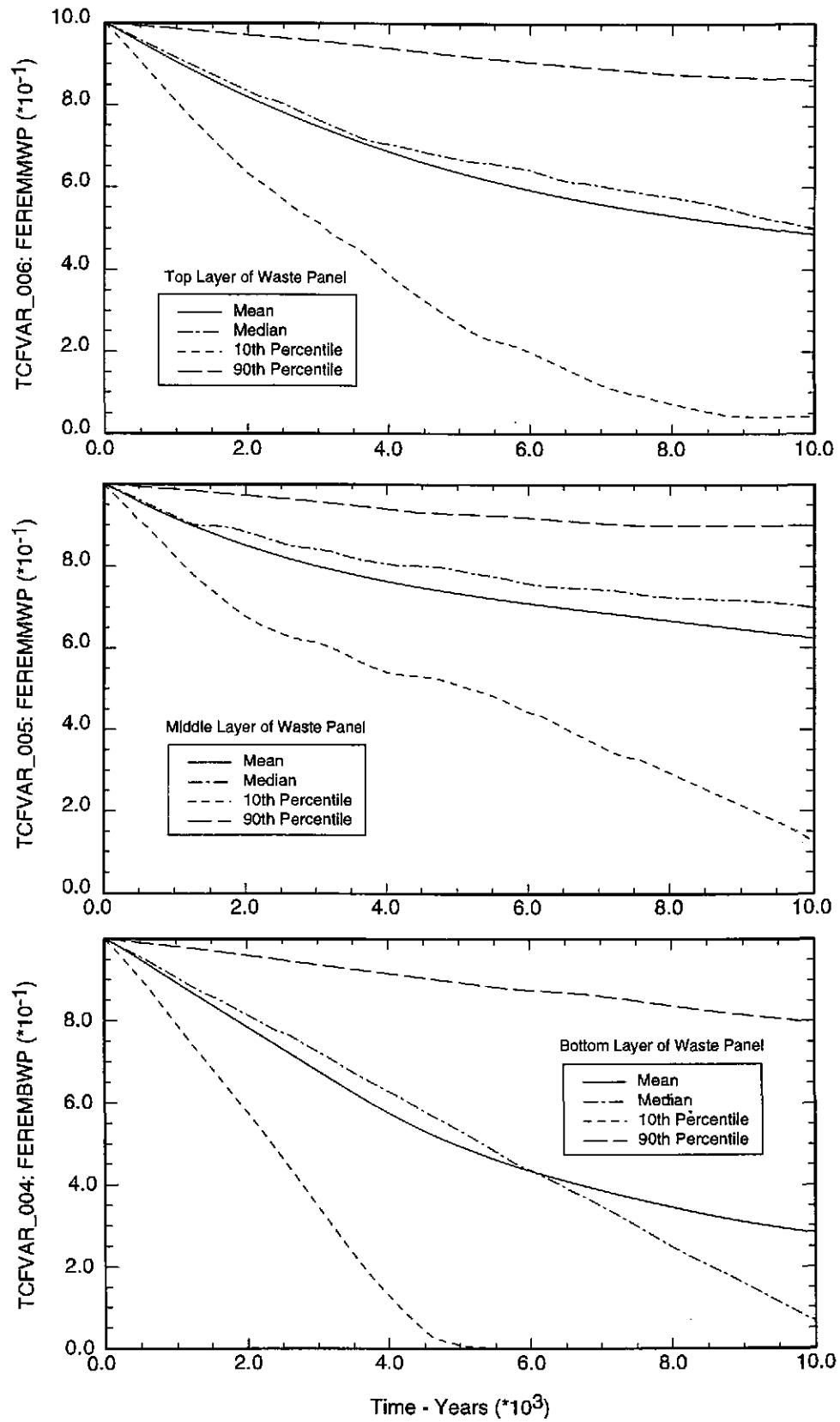
TRI-6121-434-0

Figure 4-24. CCA predictions of remaining fraction of steel in waste panels.
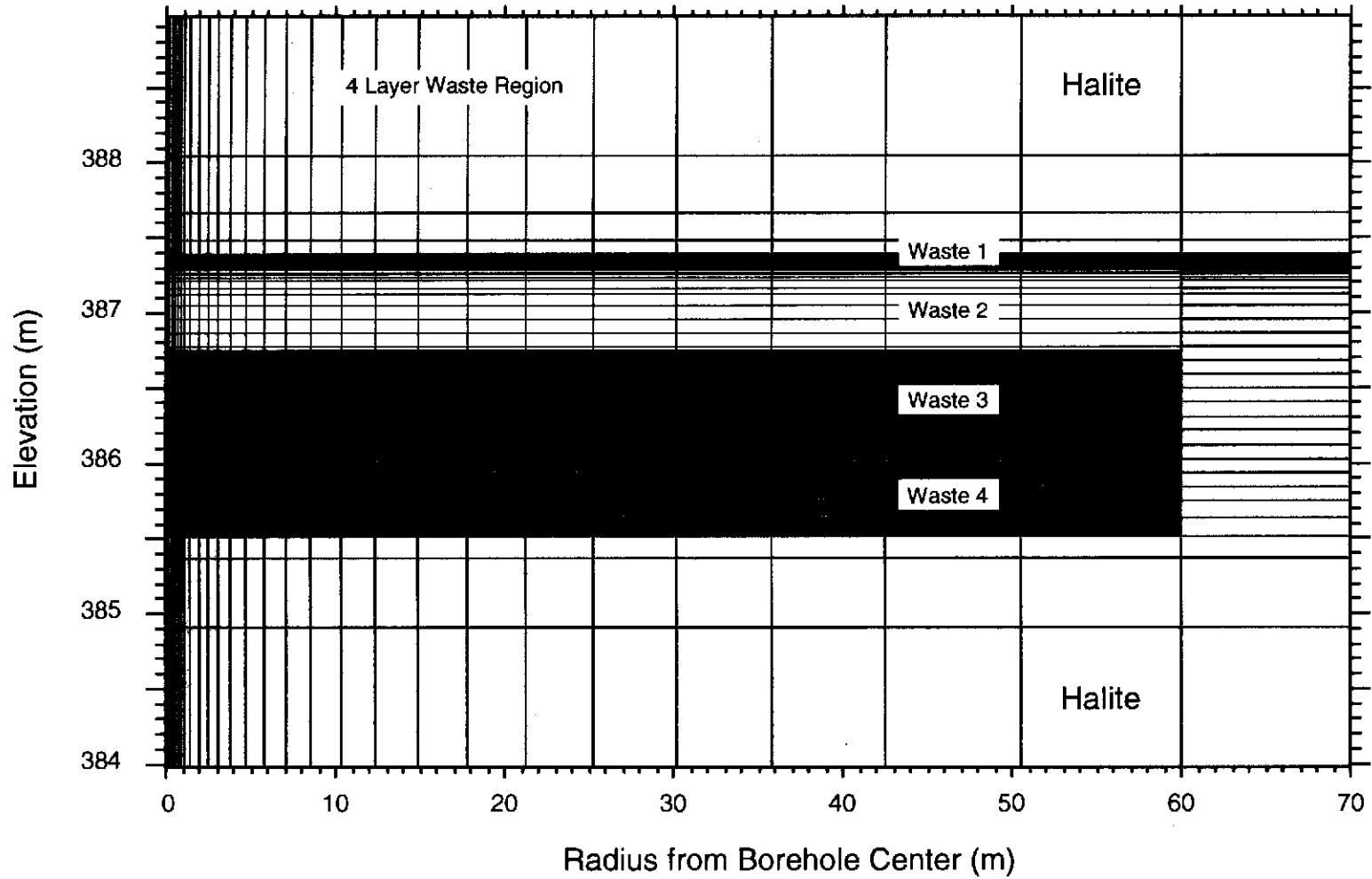
Figure 4-25. Schematic of the layered model.
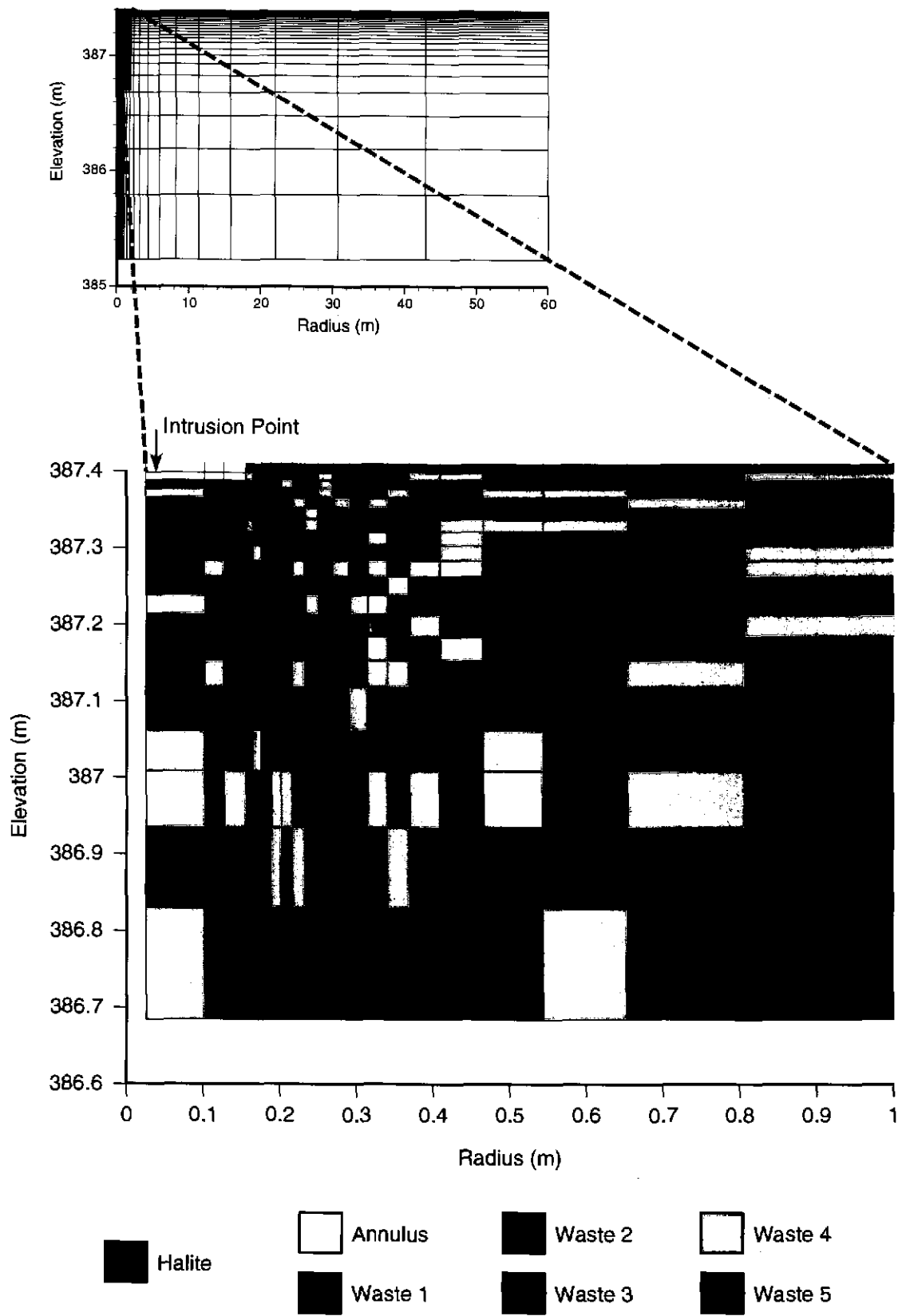
TRI-6121-427-0

Figure 4-26. Schematic of the random model.

TRI-6121-430-0

4-41
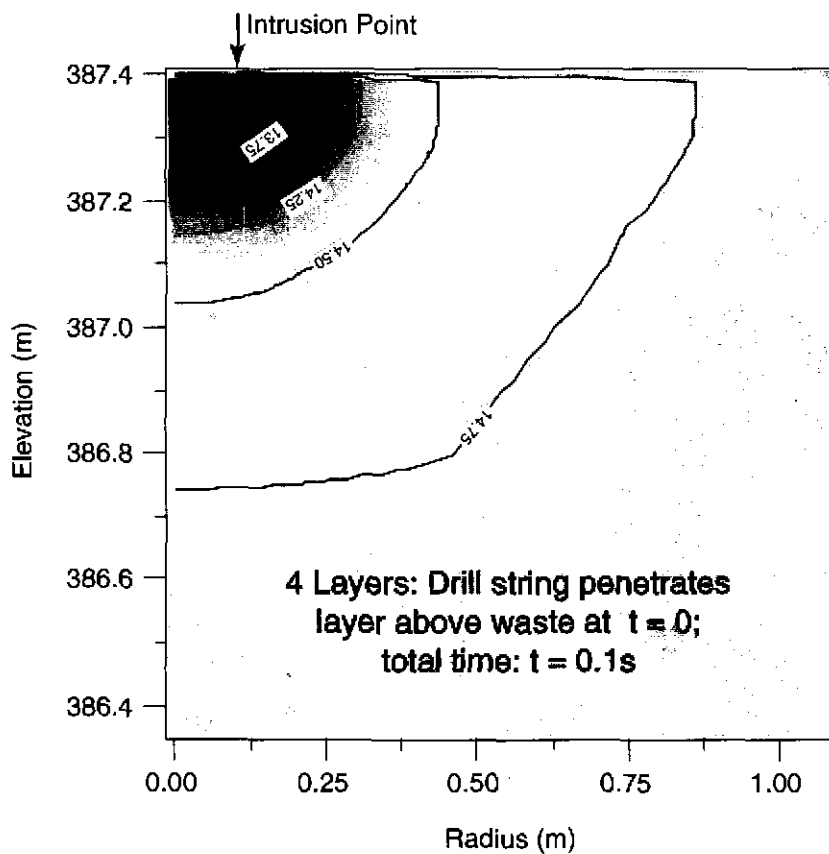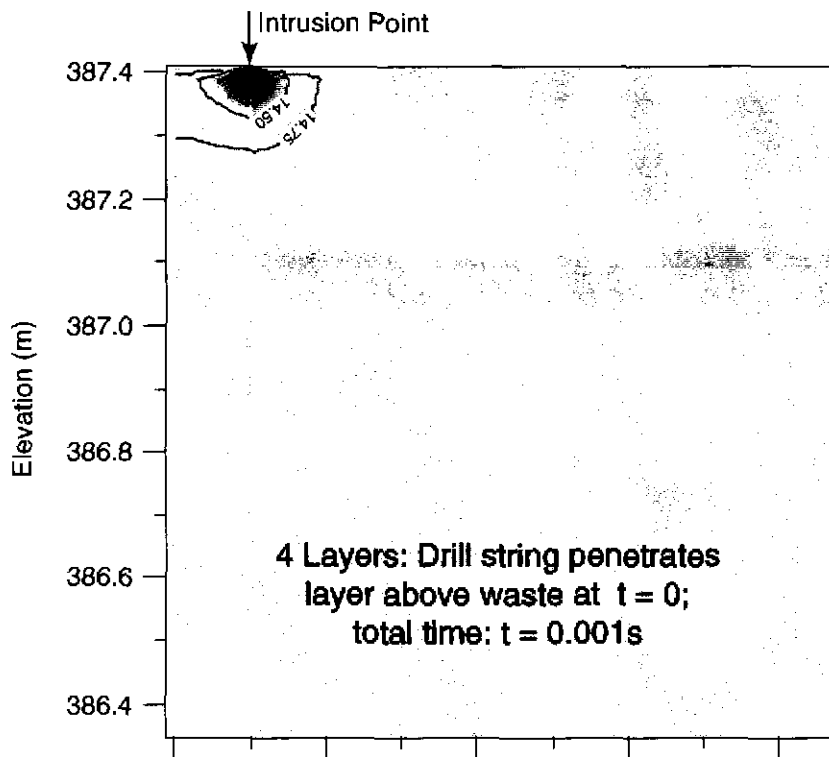
Figure 4-27. TOUGH28W results for 4 layer model at 0.001s and 0.1s following drilling intrusion. Initial waste gas is 14.8 MPa. Wellbore pressure is held constant at 8MPA . Contours are in MPa.

4-42
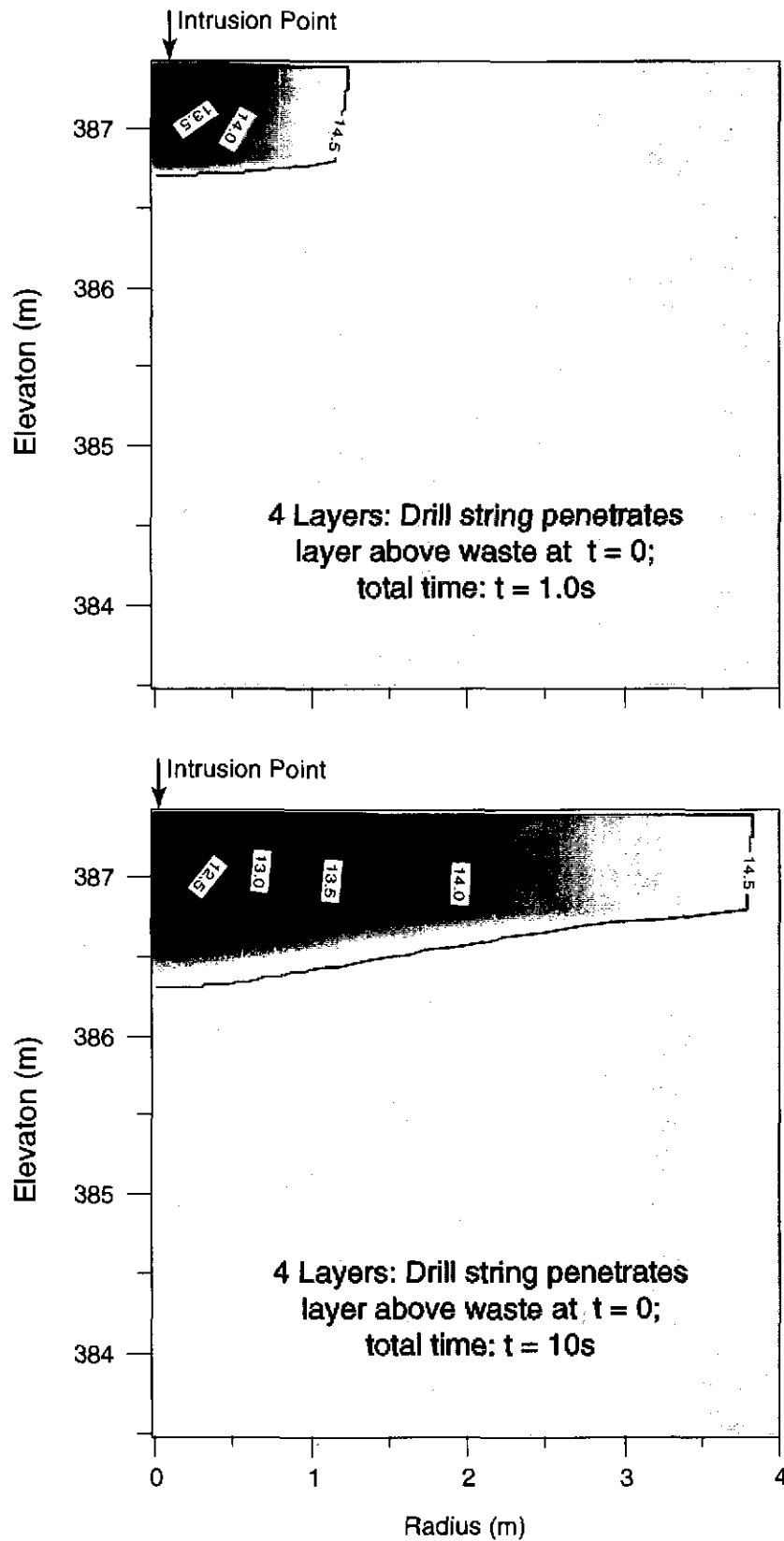
Figure 4-28. TOUGH28W results for 4 layer model, initial waste gas pressure of 14.8 MPa. Wellbore pressure is held at a constant value of 8 MPa. Contours are in MPa.

4-43

The layered model results strongly suggest that (1) seepage forces will not propagate along thin channels, and (2) lower permeability layers significantly slow the depressurization process. Both these effects of heterogeneity imply that a homogeneous model will produce a conservative result.

4.3.2 Effects of Waste Heterogeneity: Random Model

As demonstrated by the preceding layered model results, the geometry and properties of the waste significantly influence pore pressure gradients during depressurization. Because of considerable uncertainty with regard to the state of the waste at the time of a drilling intrusion, a fully random approach was also taken.

Geometry

Five material types were assumed to exist for the waste, each having a different permeability. Porosity was assumed constant throughout the waste region. A pre-processor assigned a material type to each element in the mesh used for the homogeneous model described in Section 4.1. The material type was picked by randomly selecting a number between 1 and 5, and assigning properties of that waste type to a particular element. Because the mesh is finely gridded in the immediate vicinity of the borehole, considerably greater variability exists within this region. This is considered appropriate because, as shown by previous pore pressure calculations, steep gradients only exist in the immediate vicinity of the drilling intrusion.

Material Properties

Permeability for the random waste types are listed in Table 4-12. All other properties were identical to base case properties shown in Table 4-3.

Table 4-12. Properties for Random Waste Material Types

Waste Type	Permeability (m^2)
waste 1	1.0E-12
waste 2	1.0E-13
waste 3	1.0E-14
waste 4	1.0E-15
waste 5	1.0E-16

Results and Discussion

Pore pressure results for the random model are shown in Figure 4-29. Gas does not flow readily in this model because of the absence of large connected zones of high permeability. This result is entirely consistent with that presented for the layered model. As seen in Figure 4-26, high permeability regions exist within the immediate vicinity of the wellbore. Although material failure and cavity growth could propagate the pressure front farther into the waste, it is reasonable to assume that the resultant pressure front will produce seepage forces only within a limited radius of the wellbore. The behavior of the random model is, in fact, similar to that of a low permeability medium. Shown in Figure 4-30 is the pressure decay for a homogeneous waste panel with a permeability of 10^{-15} m^2. From results presented in Section 3, it is known that the gas flow from the formation to the wellbore is insufficient to initiate a blowout. Results of both the layered and random models therefore indicate that waste heterogeneity will reduce any calculated spall volumes.
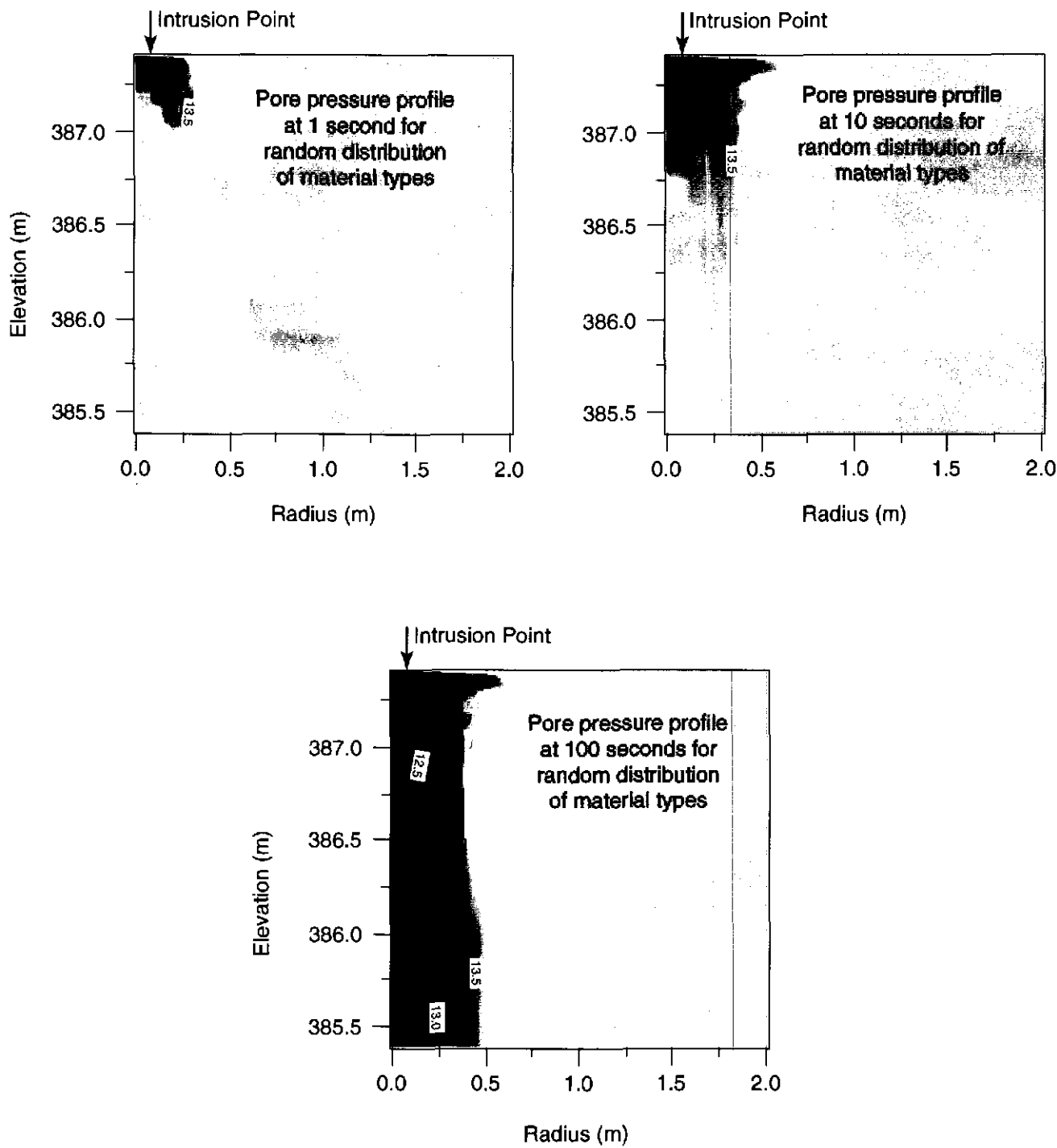
Figure 4-29. TOUGH28W results for random model, constant wellbore pressure of 8 MPa, gas pressure of 14 MPa. Contours are in MPa.

4-45
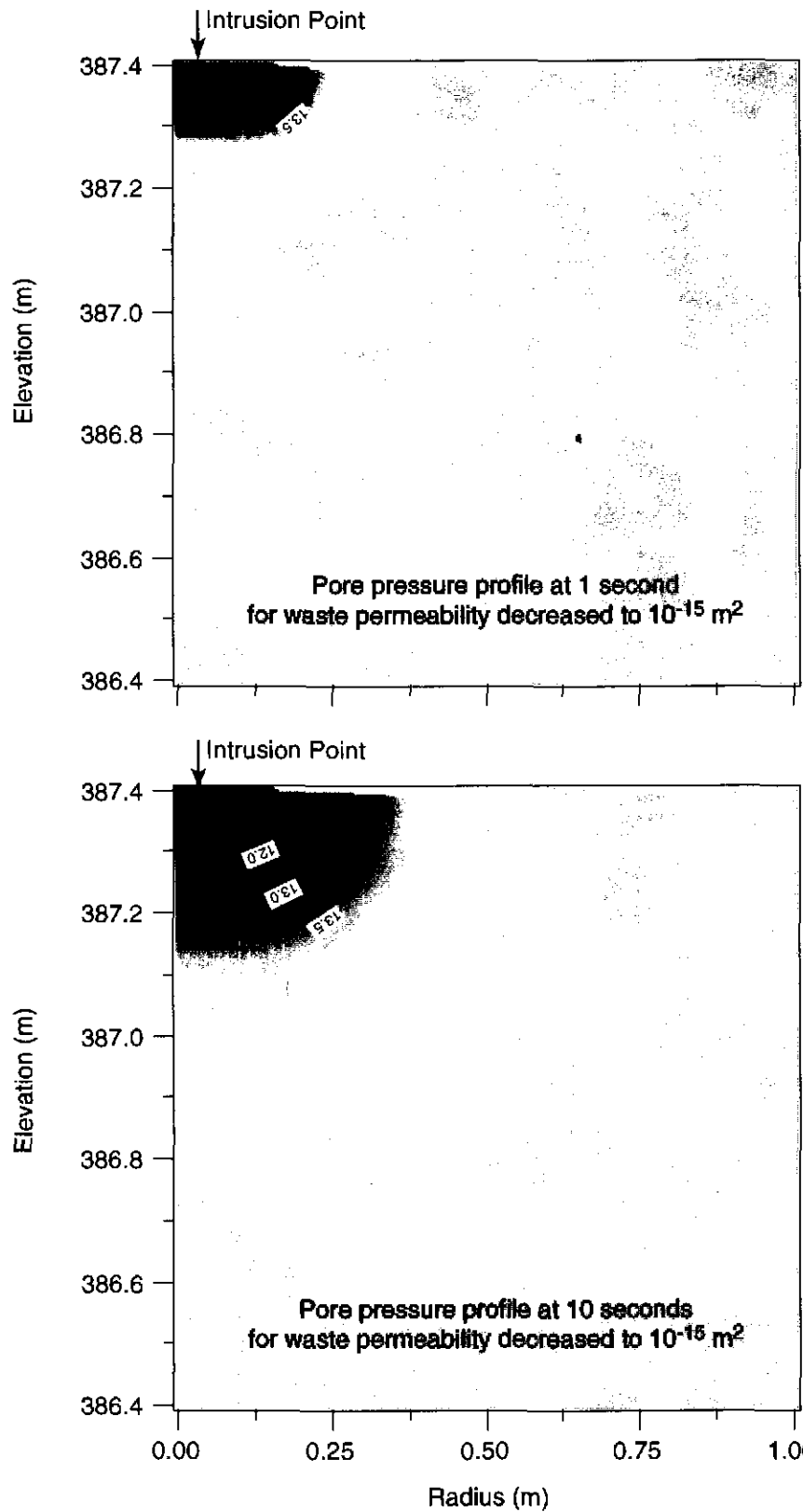
Figure 4-30. TOUGH28W results for homogeneous, low-permeability model, constant wellbore pressure of 8 MPa, gas pressure of 14 MPa. Contours are in MPa.

4-46

4.4 Comparison of the Numerical Results to Semi-analytic Calculations

In this section the semi-analytic results (quasi-static and cavity growth methods) are compared to the numerical calculation results, which were summarized in Section 4.1. Primary comparisons are made for two cases. The first compares TOUGH28W calculations of a constant mass from the repository. The mass flux was chosen to give similar bottomhole pressures to those calculated for the quasi-static method in the 14.8 MPa initial pressure case. The step-function pressure change in borehole from 14.8 to 8 MPa at time zero is compared in the second case. For both cases stresses have been calculated using the closed-form spherically symmetrical stress solutions with the TOUGH28W calculated pressure gradients; these are compared to the stresses from the quasi-static method, the cavity growth model, and the numerical TOUGH28W/SPECTROM-32 calculations.

The different approaches were taken to allow mutual verification and checking of results. In addition, the different levels of complexity of the various methods enabled them to be used for different purposes. The cavity growth method, which accounts for the effects of progressive spall in a simplified geometry, was used as the primary (base case) method for calculating spall volumes. The quasi-static method is the simplest to use for purposes of evaluation. As such, this method was used to examine the sensitivity to various parameters and as a verification of the more complex calculations. TOUGH28W calculations of pressure gradients were used to verify the pore pressures from the quasi-static models, and coupled TOUGH28W/SPECTROM-32 calculations were used to verify the stress calculations.

Note that for initial pressure conditions that are high (i.e., on the order of 14.8 MPa), the stresses, and thus the predicted volumes, are sensitive to the manner in which the borehole cavity pressure is allowed to decrease. Assumption of instantaneous wellbore pressure drop leads to more severe pressure gradients, and therefore greater tensile stresses than when the pressure decreases over time. The use of an instantaneous pressure drop is, in fact, an unrealistic assumption. As noted elsewhere, it will take some time for the bottomhole pressure to drop as the mud is ejected, and this delay impacts the pore pressure gradients during the critical first second of events. This case is only used for comparison because of the ease of calculation.

4.4.1 Verification of Flow Results

As noted above, the pore pressure results from the semi-analytic methods have been compared to those from TOUGH28W calculations under two sets of conditions: an instantaneous borehole pressure reduction from 14.8 to 8 MPa, and a continuous pressure reduction. The second of these comparisons uses a constant mass rate of gas withdrawal in TOUGH28W of 2.4 kg/s to simulate the borehole cavity pressure reduction calculated from the quasi-static wellbore model. This gas withdrawal rate is approximately twice as high as that predicted using wellbore hydraulics methods.

Figure 4-31 compares the borehole cavity pressures for the three methods. Comparative pore pressure distributions are shown in Figures 4-32 to 4-35. Results from the quasi-static and cavity growth methods differ from TOUGH28W most at early times, and consistently give steeper gradients. This occurs in spite of the more conservative boundary conditions applied in the TOUGH28W calculations. Because the primary tensile events are early in the process, and because steeper pressure gradients lead to more severe stresses, the quasi-static results lead to more severe predictions for the extent of any failed zone.
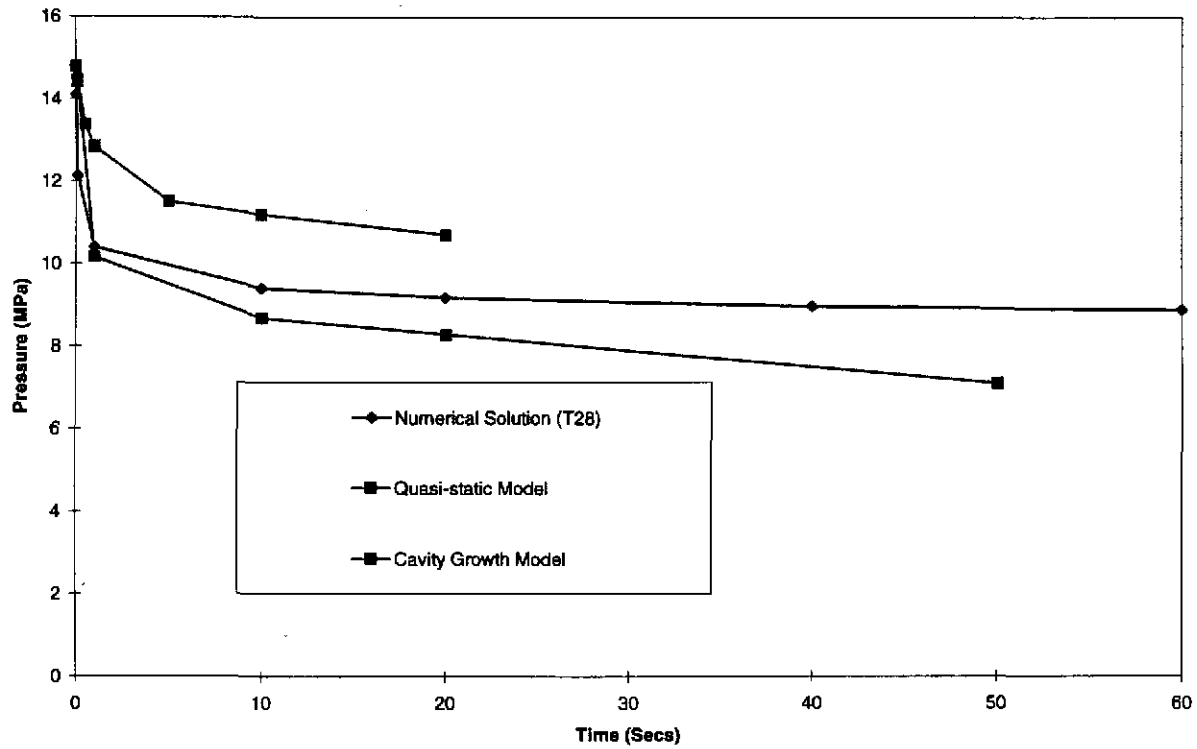
Figure 4-31.   Comparison of wellbore pressures predicted by the numerical (T28), quasi-static, and cavity growth models.
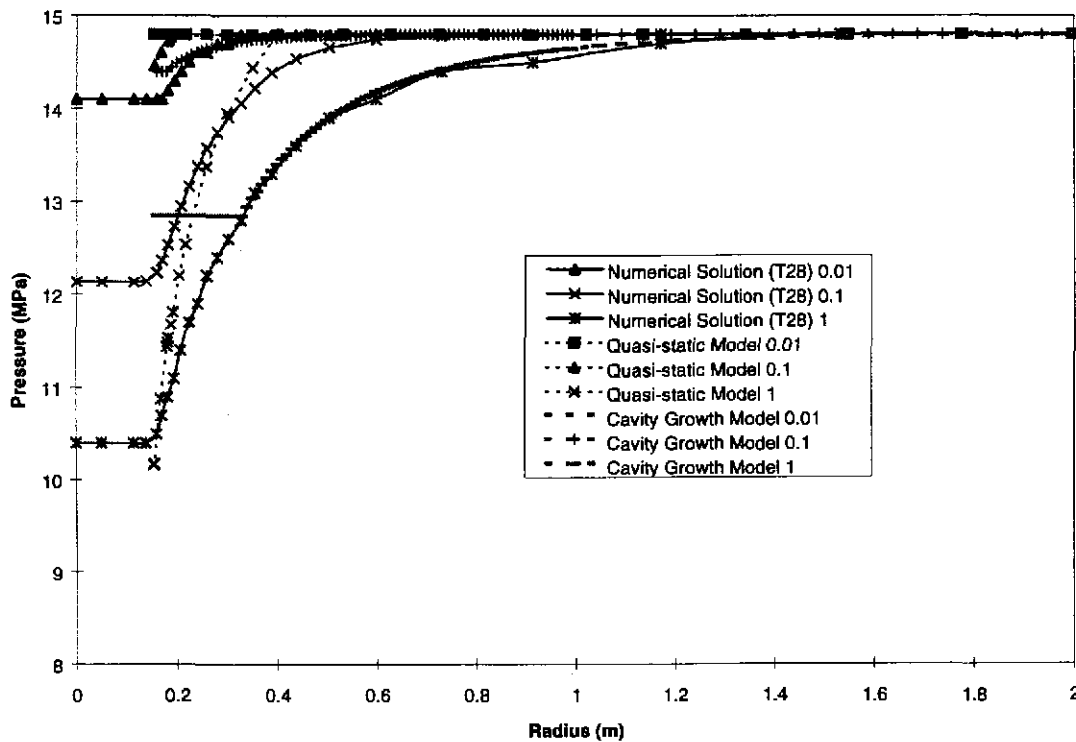

Figure 4-32.   Comparison of pressure distributions for numerical (T28), quasi-static, and cavity growth models for early times (<1 s) following drilling intrusion.
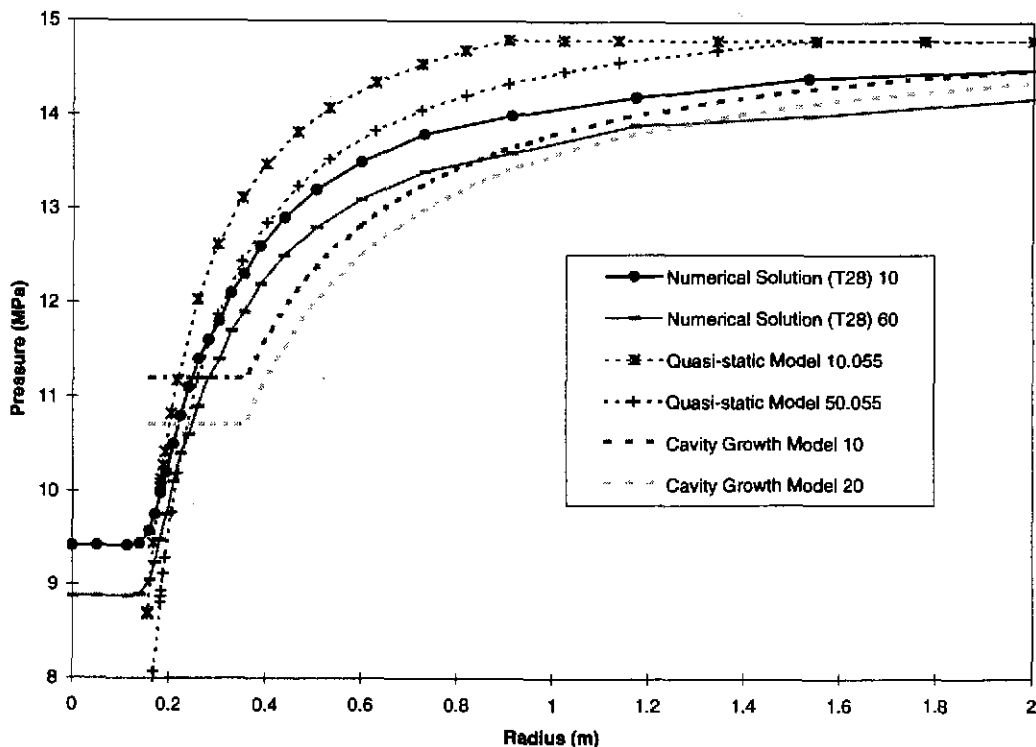
Figure 4-33. Comparison of pressure distributions for numerical (T28), quasi-static, and cavity growth models for later times (>1 s) following drilling intrusion.
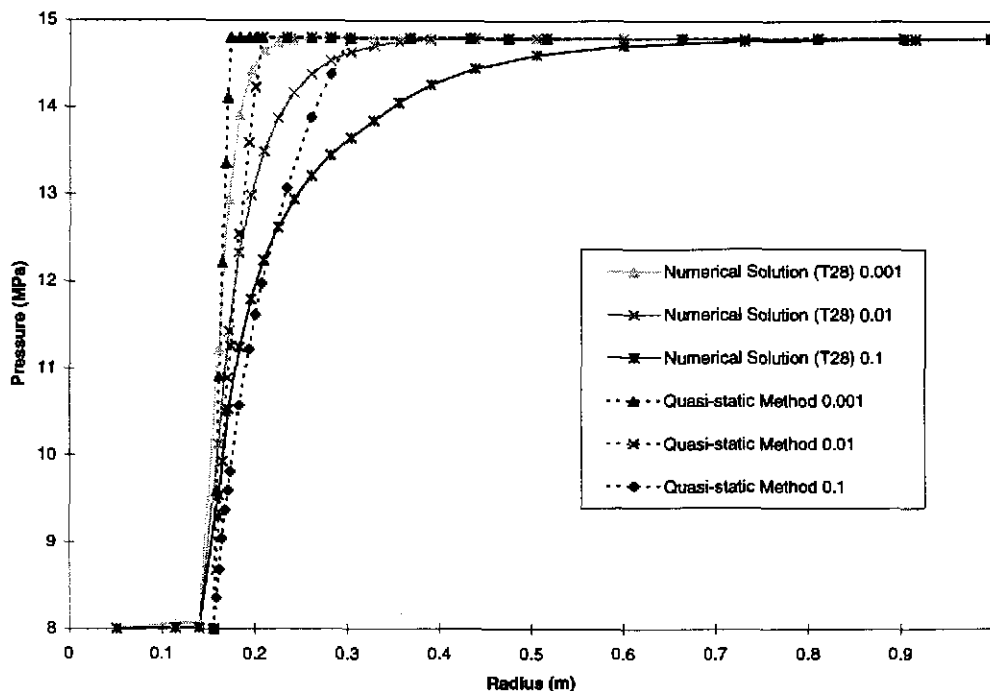

Figure 4-34. Comparison of pressure distributions for numerical (T28), quasi-static, and cavity growth models for early times (<1 s) following drilling intrusion for instantaneous wellbore depressurization.

4-49
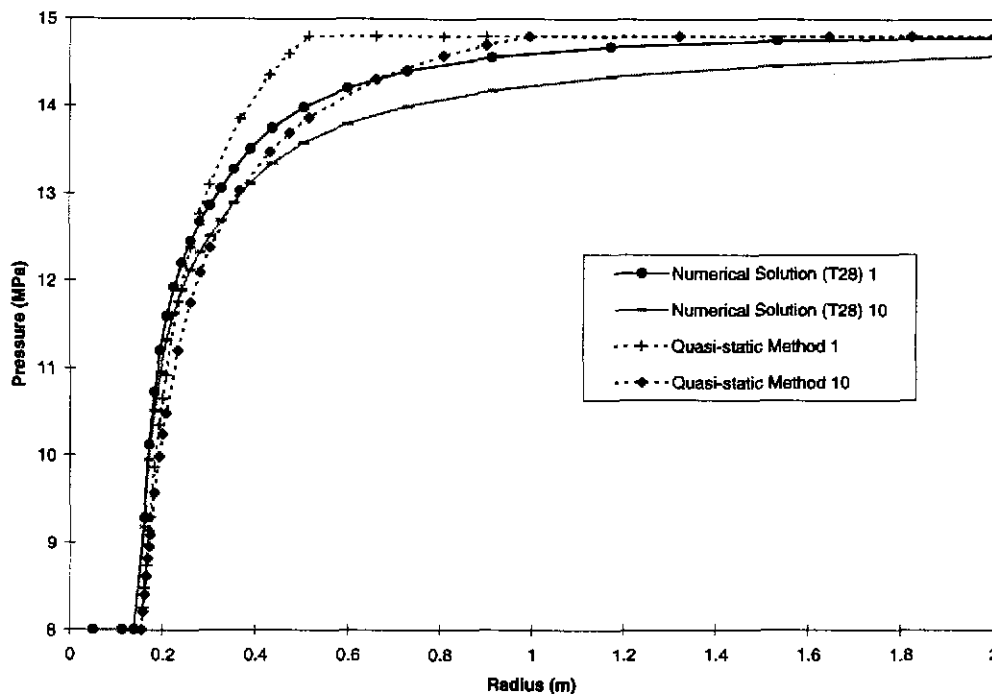
Figure 4-35. Comparison of pressure distributions for numerical (T28), quasi-static, and cavity growth models for later times (>1 s) following drilling intrusion, assuming instantaneous wellbore depressurization.

The mud flow results from COMBO2 have been compared quantitatively to TOUGH28W and qualitatively to the results from the quasi-static model results. The comparison with TOUGH28W ensures that the influence function was implemented correctly and that it provides an accurate gas flow rate given a specified wellbore pressure. Figure 4-36 plots the COMBO2 influence-function flow rate versus the flow rate predicted by TOUGH28W for the same transient wellbore pressure profile. As can be seen, COMBO2 results are virtually identical to those of TOUGH28W.

The quasi-static model approximates the response of the waste-panel reservoir through an approximate solution for a hemispherical reservoir. COMBO2 solves the transient solution of a reservoir defined by the flow dimensions of the waste panel. Figures 4-37 and 4-38 show that although predicted wellbore pressures show acceptable agreement, predicted flow rates are quite different. Quasi-static flow rates exceed those predicted by COMBO2 by more than a factor of two, causing a similar reduction in the mud expulsion time. The agreement between the COMBO2 flow solution and TOUGH28W, described above, indicates that the quasi-static flow rates would also exceed TOUGH28W flow rates by a similar margin. From the comparison of TOUGH28W to the quasi-static solution pressure profiles provided earlier, it can be seen that the quasi-static solution predicts higher pressure gradients surrounding the wellbore than TOUGH28W. Consistent with this observation, the quasi-static model predicts more than two times the gas production than does COMBO2 (i.e., coupled to TOUGH28W).
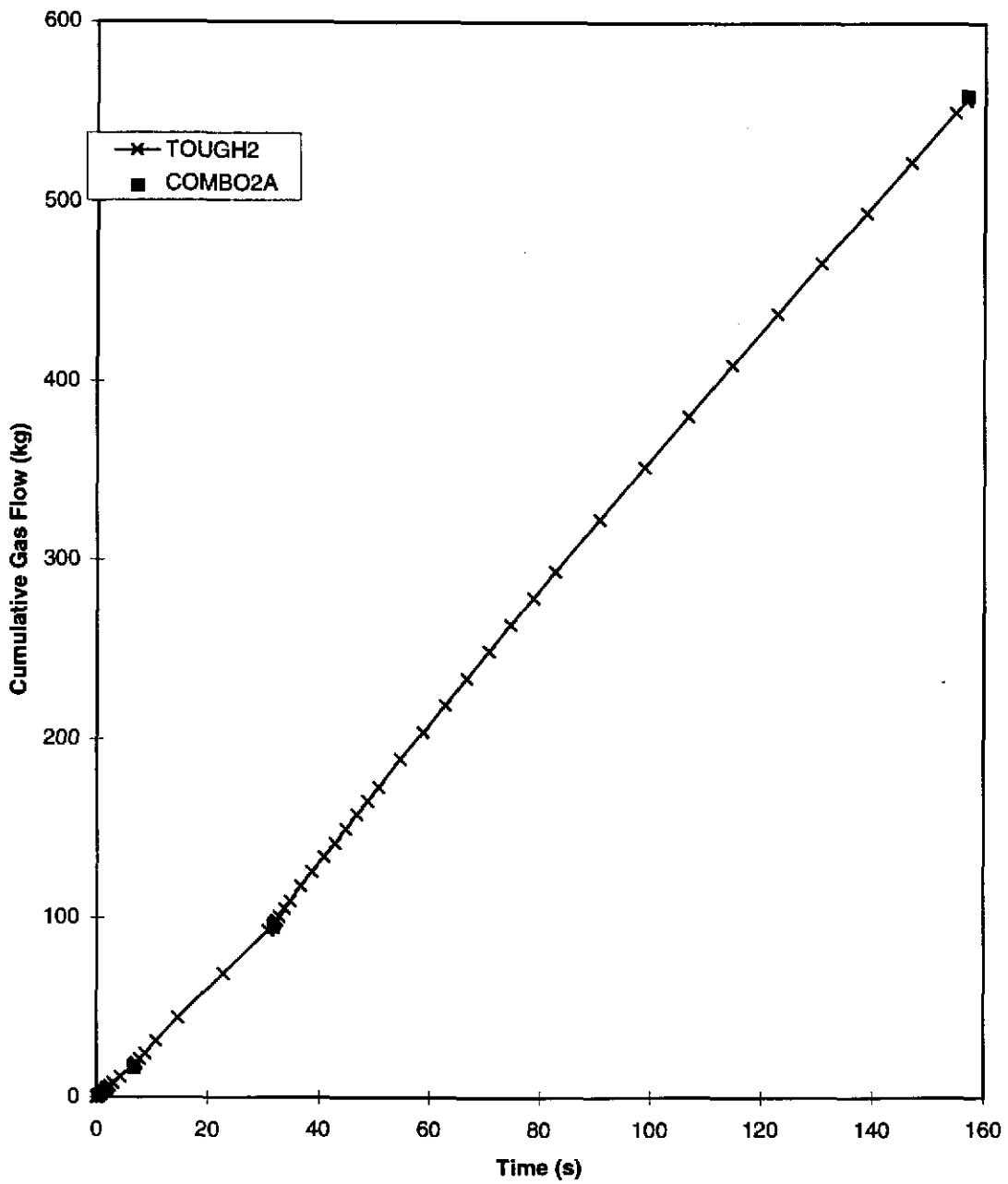
Figure 4-36. Comparison of gas flow rates for COMBO2 and TOUGH28W calculations.
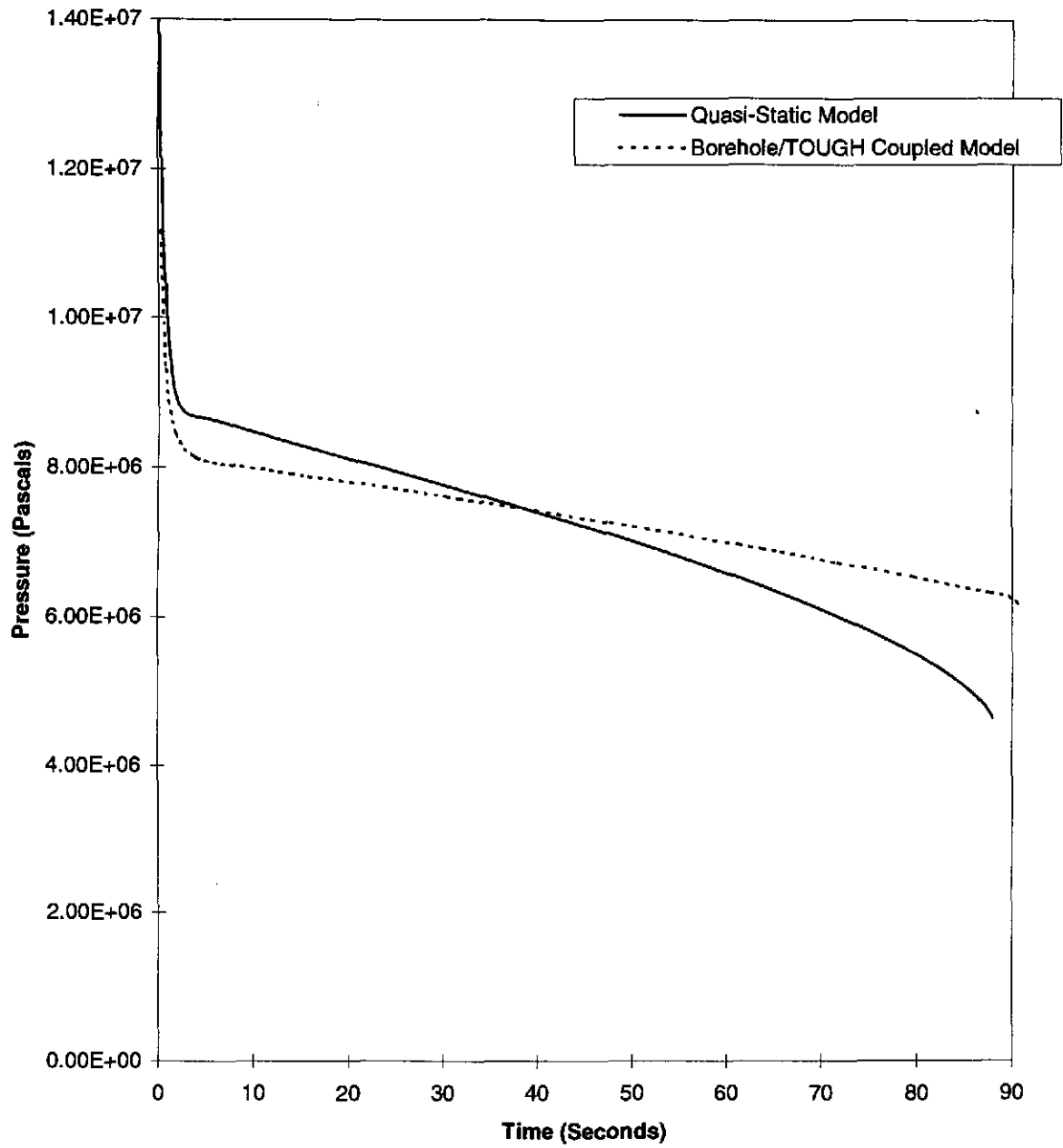
Figure 4-37. Comparison of wellbore pressures for the quasi-static and numerical models.
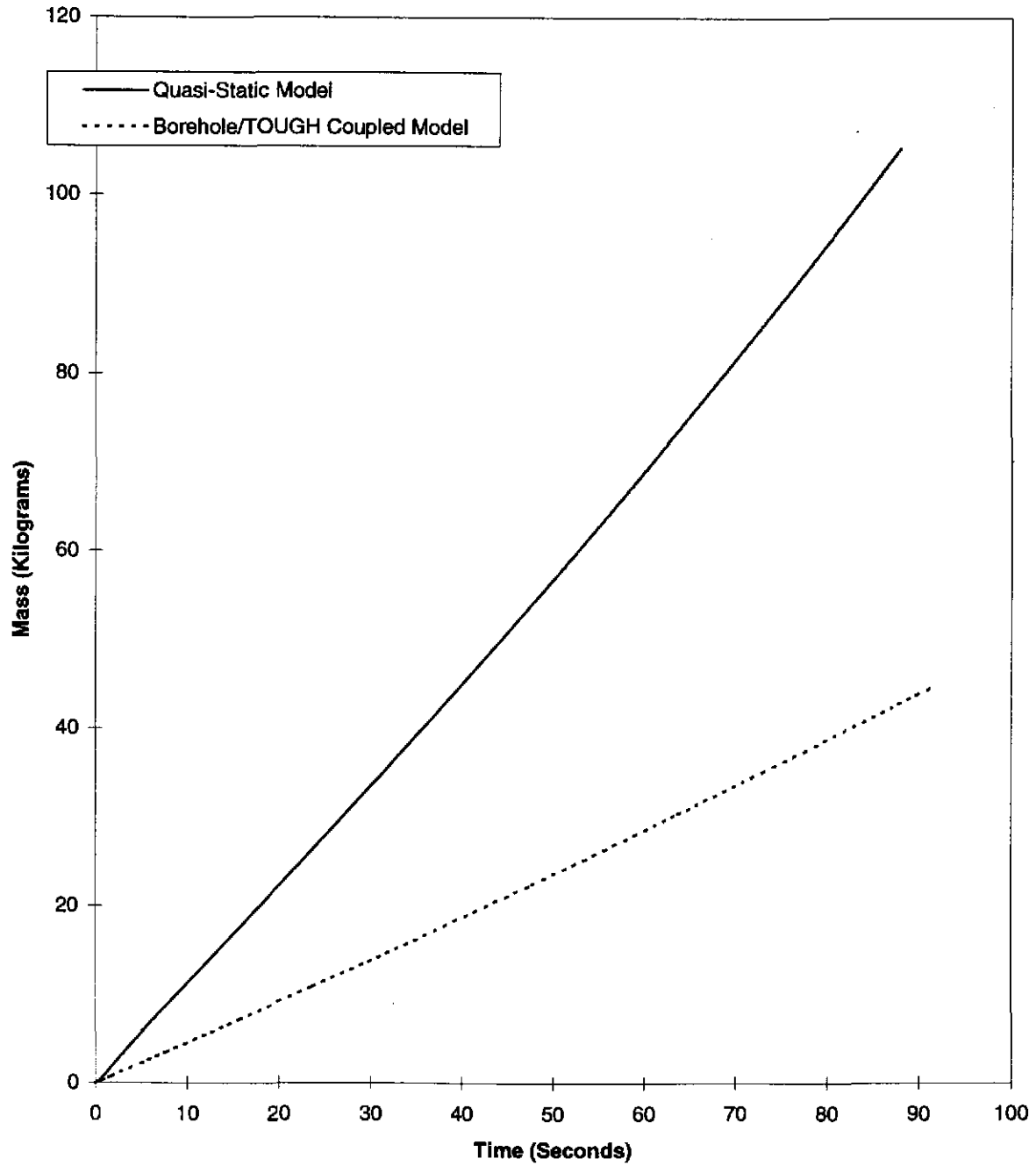
Figure 4-38. Comparison of cumulative gas volumes for the quasi-static and numerical models.

Parameter differences also exist between the COMBO2 and the quasi-static flow models. These differences include waste room porosity (0.6 versus 0.7), wellbore volume available for flow (39 m³ versus 28.5 m³), and penetration depth of the intrusion borehole into the waste room (0.01 m versus 0.15 m). A comparison of wellbore pressures and gas flow rates for the quasi-static and cavity growth models was considered in Section 3. It was shown that good agreement exists between these two semi-analytic models. The higher gas flow rates predicted by these models result in faster mud ejection and steeper pressure gradients in the waste. Therefore it can be concluded that tensile stresses predicted using these models will produce more conservative results than would the numerical model. The principal function of the numerical model is to demonstrate this conservatism, and also to verify that solids transport will be limited prior to mud ejection.

4.4.2 Verification of Stress Results

Radial effective stresses calculated for the two test cases (instantaneous 14.8 to 8 MPa, and continuos pressure drop) for the semi-analytic and TOUGH28W models are compared in Figures 4-39 to 4-42. The stresses are more severe for the quasi-static calculations than for the numerical results, as would be expected given the steeper pore pressure gradients. Thus the early time stresses (0 to 1 s) show more tension over a greater area for both cases (Figure 4-39), and for the continuous pressure drop case the SPECTROM-32 results consistently show a compressive zone adjacent to the borehole cavity before going into tension, which is not seen in the early time quasi-static results (Figure 4-41). At later times (>1 s) the quasi-static results are again more severe, with higher internal tension over a wider area, although at these greater times the tension zone is entirely internal, being separated from the borehole cavity by a compressive zone (Figures 4-40 and 4-42).

A number of additional observations may be made. First, the TOUGH28W/SPECTROM-32 results demonstrate that the assumption of spherical symmetry for the pore pressure and stress fields is reasonable, at least in the early times. Second, the general form of the stress distributions is similar between the SPECTROM-32 and semi-analytic results. At early times a zone of tension near the borehole cavity extends to a radius of about 0.5 m at 0.01 s. Inside this zone of tension is a small compressive zone that grows with time. SPECTROM-32 results show a compression zone at 0.01 s on the order of 0.1 m. In the TOUGH28W/quasi-static calculations it has a similar extent at 0.01 s, while it is not seen in the quasi-static calculations at early times because of the more severe pressure gradients in this case. The maximum tensions in the 0.01 to 0.1 s time frame are consistently of the order of 0.15 to 0.2 MPa.

A comparison of the quasi-static and cavity growth results in Figures 4-41 and 4-42 shows that the quasi-static method predicts a more severe tension early in the depressurization process. As might be expected, where these early tensions occurred in the cavity growth model, spalling occurred, reducing the tension in the surrounding regions and pushing compression peaks farther into the waste interior.

At greater times (1 s and higher) all calculations show qualitatively similar results, with the tensile zone being pushed further into the waste and a more extensive zone of quite high compressive stresses appearing close to the wellbore, shielding the tensile zone from the well. Again the quasi-static calculations show a more severe reaction, with higher tensile values and more delay in establishing the compressive zone around the borehole cavity.
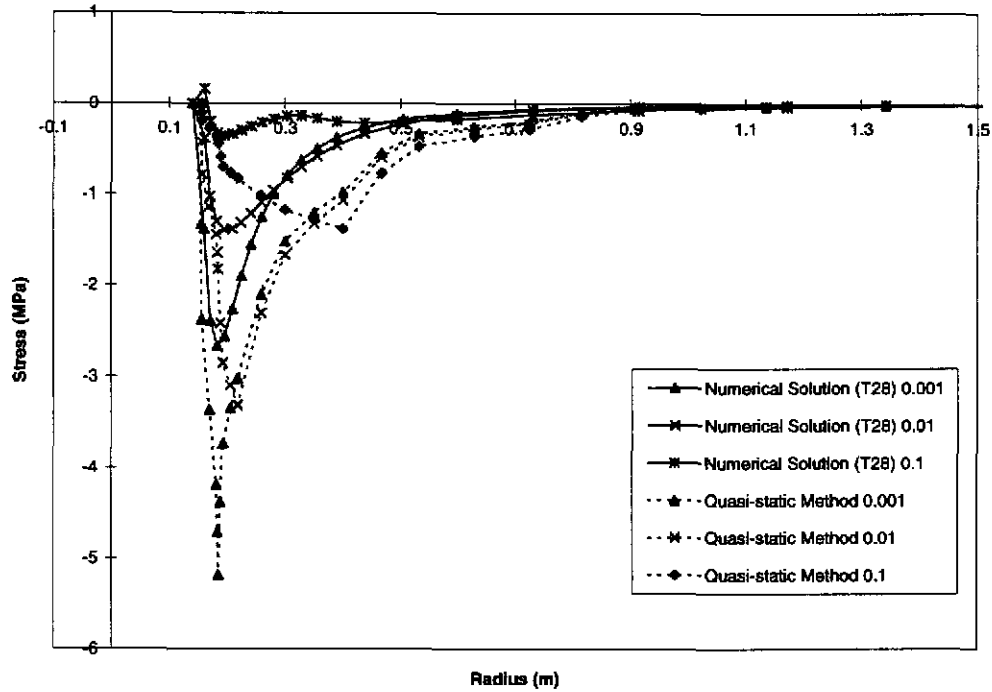
Figure 4-39. Comparison between numerical (T28) and quasi-static results for early (<1 s) times, assuming instantaneous wellbore depressurization.
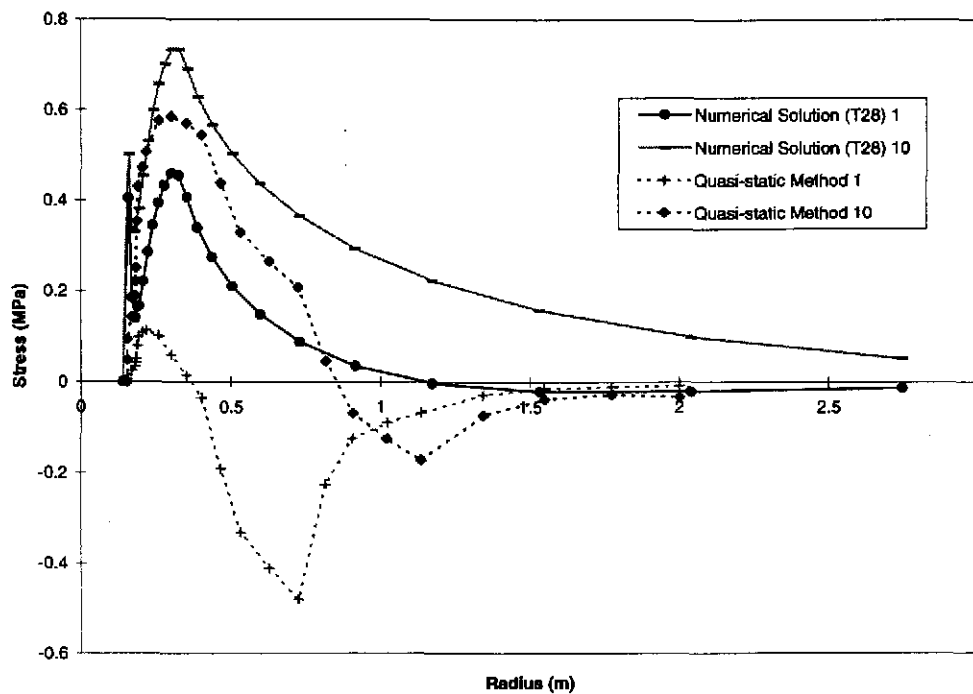

Figure 4-40. Comparison between numerical (T28) and quasi-static results for later (>1 s) times, assuming instantaneous wellbore depressurization.
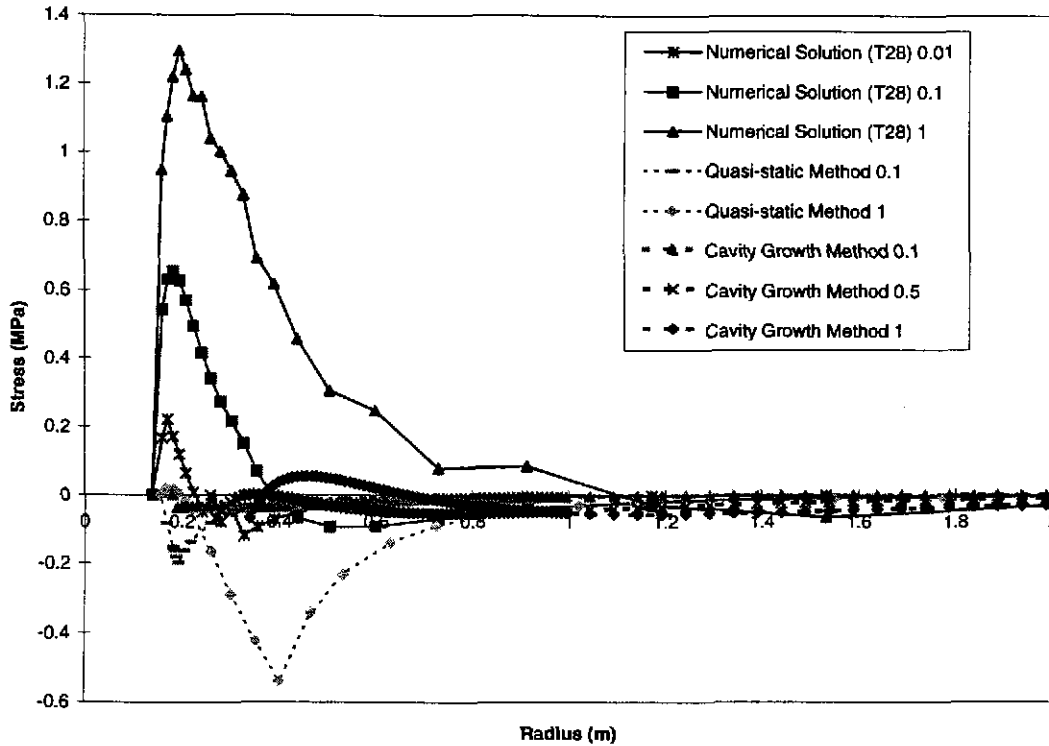
Figure 4-41. Comparison between numerical (T28), quasi-static, and cavity growth models for early times (<1 s), assuming continuous pressure drop in the wellbore.
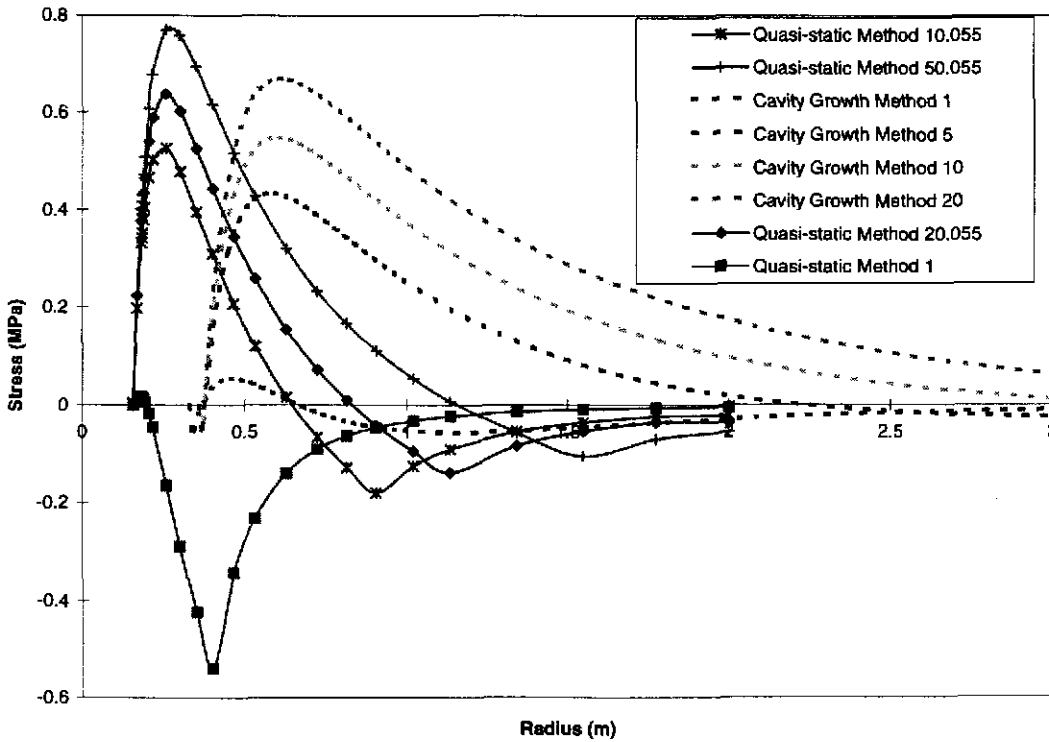

Figure 4-42. Comparison between numerical (T28), quasi-static, and cavity growth models for later times (<1 s), assuming continuous pressure drop in the wellbore.

Based on these comparisons it is apparent that the various computational methods are giving similar stress results and that where they differ it is a direct result of the various approximations. It is also apparent that the consequences (in terms of tensile failure) calculated from the quasi-static model will be more severe than predicted by the other methods.

4.5 Influence of Modeling Assumptions on Estimation of Volumetric Releases

Estimation of the volume of waste material transported to the surface during a drilling intrusion requires an understanding of the mechanisms that could lead to any such transport. The previous sections presented calculations of pore pressure decay, poromechanical response of the waste to the resultant pressure gradients, and calculations of the fluid and mass flux through the drilling annulus to the surface. It is clear that these processes are coupled during a spall event and that a fully coupled code for spalling would incorporate all the relevant mechanisms. In the absence of such a code, it is still possible to predict the volumes of material that could be available for transport to the surface. These predictions should include the relevant processes, with application of conservatism in those areas in which detailed information is lacking. However, predictions must not rely on overly conservative assumptions. For example, many of the calculations presented in Sections 4.1 and 4.3 assume a constant pressure boundary during the drilling intrusion. This very conservative assumption was necessary to provide a decoupled perspective on the pressure decay and poromechanical responses. Use of this boundary condition for volumetric predictions must be managed carefully. An additional conservatism inherent in the calculations presented in Sections 4.1 and 4.2 is that the waste is a homogeneous medium. As was demonstrated in Section 4.3, the effects of waste heterogeneity will limit the geometric extent of the propagation of high pressure gradients.

The numerical and semi-analytic models have shown that the only waste gas pressure leading to significant spall events is the case of zero effective stress at the time of a drilling intrusion. Volumetric estimates of spall cases of compressive effective stress are small, even using the overly conservative approximations discussed in the previous paragraph. Although it is possible to reduce the predicted volumes substantially by invoking more realistic (and less conservative) approximations of the repository state and response, it is more valuable to focus these discussions on the more significant case. This is because only very small failed volumes are predicted for all gas pressures below the extreme case of zero effective stress. It is therefore important to emphasize analysis of this limiting condition. The discussion that follows has been developed for the case of repository gas pressures of approximately lithostatic. It can be extended to the compressive effective stress states, but this will not be done within the current framework.

A final consideration with regard to any estimates of volumetric releases is the state of the waste. Although the geometry and flow properties (i.e., layering effects, porosity, and permeability) are important parameters, the tensile strength of the waste will govern the system response at zero effective stress. Characterization of the waste has focused on weaker configurations so that lower bounds on the strength can be made. However, it is important to recognize that the state of the repository with regard to geometry, saturation, and chemical processes dictates that the effective strength of the waste formation will be much higher than has been assumed for these calculations.

4.6 References

Al-Hussainy, R., H.J. Ramey, Jr., and P.B. Crawford, 1996. "The flow of real gases through porous media," *J. Pet. Tech.* (May), p. 624-636.

Bear, J. 1972. *Dynamics of Fluids in Porous Media.* Elsevier Publishing Co. p. 164.

Bradley, H.B. (Editor), 1989. *Petroleum Engineering Handbook.* Society of Petroleum Engineers, Richardson, TX.

Callahan, G.D. 1994. "SPECTROM-32: A Fnite Element Thermomechanical Stress Analysis Program, Version 4.06." Topical Report RSI-0531. Rapid City, SD: RE/SPEC, Inc. (Copy on file in SWCF as WPO#27178).

Jain, A.K., 1976. "An accurate explicit equation for friction factor," *J. Hydraulics Div. ASCE,* Vol. 102, No. HY5.

Machado, C.J. and C.U. Ikoku, 1981. "Experimental determination of solids friction factor and minimum volumetric requirements in air and gas drilling," SPE 9938, paper presented at the California Regional Meeting, Bakersfield, CA, March 25-26.

Pruess, K. 1991. *TOUGH2 – A Numerical Simulator for Pultiphase Fluid and Heat Flow.* LBL-29400. Berkeley CA: Earth Sciences Division, Lawrence Berkeley National Laboratory (Copy on file in SWCF).

Weast, R.C. (Editor), 1978. *CRC Handbook of Chemistry and Physics,* 59th Edition, 1978-1979. CRC Press, Inc., Boca Raton, FL.

5.0 ANALOG SITUATIONS

5.1 Summary of Analogous Situations

A number of analogous situations are encountered in geotechnical applications with a degree of similarity to what would occur with drilling intrusion into a pressurized repository at the WIPP. For an analog to be suitable for application to the WIPP site it must present quantifiable similarity in both the material being spalled and the process that causes spalling. Of the situations examined, the following do not meet these criteria.

- In civil engineering, there are seepage phenomena associated with flow under dams or liquefaction occurrences associated with earthquakes. However, most of the published civil engineering applications, with the exceptions of deep tunnels in South Africa and Japan, involve similar physical concepts. These occur at much lower stresses, pressures, and hydraulic gradients. Because of this, they will not be discussed in detail.

- Kimberlite pipes represent rapid vertical propagation. The geologic environment and the conditions of evolution and propagation are so complex and controversial that simple analogies are difficult to quantify.

In the petroleum industry numerous analogs are suitable for comparison to the WIPP site, including the following:

- Blowouts (LeBlanc and Lewis, 1973; Schurman and Bell, 1973) occurring when the drilling mud pressure is less than the pressure in the reservoir. The petroleum literature on well control (predicting, preventing, and handling blowouts) focuses on wellbore hydraulics. The physical principles used are similar to those adopted in forecasting the mud ejection and the flow of gas in the annulus (Sections 3.0 and 4.0). These hydraulics calculations do not address the potential for reservoir disaggregation as a consequence of stress and flow boundary conditions.

- Wellbore stability problems (Wang and Dusseault, 1991; and many others)

- Sand production during hydrocarbon production (this is the production of reservoir particulate matter through perforations in casing cemented into a reservoir or from an open hole)

- Proppant flowback in hydraulic fractures

- Cold production in the Alberta oil sands where sand is intentionally produced back with extremely viscous crude oil

- Dynamic openhole cavitation in coalbed methane wells where spalling is intentionally encouraged.

Various examples of analog situations in the petroleum industry are discussed in this section. *The cavitation of wellbores in coalbed methane reservoirs offers the strongest analog. The basis of this assertion is the similarity in the process of relatively rapid pressure drop as well as material properties comparable to those at the WIPP site. The material properties of coal in the San Juan Basin, New Mexico and Colorado, and the surrogate waste material for the WIPP site will be shown to be remarkably similar. Based on analog numerical modeling of cavitation operations in San Juan Basin coal, experience indicates that cavitation will not occur at the WIPP site.* Other analogs, primarily those concerned with wellbore stability and sand production, illustrate

the validity of the approaches used in the semi-analytic evaluations, and demonstrate the conservative nature of these evaluations.

Various analog situations will be presented in the following discussion, either illustrating quantifiable similarity or conceptual similarity when physical comparisons are not directly possible. Section 5.2 introduces the historical and rudimentary analytical protocols for evaluating whether a reservoir will be stable under a change in boundary conditions associated with drilling and production. Progressively more sophisticated analytical and numerical approaches to wellbore and reservoir stability are presented. Section 5.3 highlights the considerations in preventing proppant from being produced back into a wellbore from a hydraulic fracture. Section 5.4 presents comparative calculations for dynamic openhole cavitation in coal. The discussion of coalbed methane cavitation is the most dramatic and quantitative analog relative to the WIPP. Readers familiar with wellbore and perforation stability analysis may wish to refer immediately to Section 5.4.

5.2 Sand Production Case Studies

In this section, variations of the sand production analog from the petroleum industry will be examined. In this analog, the production of "sand" (reservoir particulate matter) occurs at various times during the production life of a reservoir, as the reservoir pressure is reduced during production of hydrocarbons and fluid flows towards the production wells.

5.2.1 Example 1 (A Spherical Cavity)

One of the concerns in hydrocarbon production is to prevent (or at least minimize) the production of reservoir particulates through perforations [an orifice through well casing and the cement sheath into the reservoir rock, created with a shaped charge]. These are often mathematically represented as arched, spherical cavities. The most basic evaluation of the potential for formation failure and collapse is based on analytical work published by Bratli et al. (1983). The poroelastic formulations presented by Bratli et al. (1983) for a penetrating wellbore (and earlier spherical solutions for a nonpenetrating wellbore) are simplifications of the semi-analytic modeling of the WIPP site, presented elsewhere in this report (based on gas flow solutions published by Chan et al., 1991). Example 1 is included because it demonstrates the approximate methodology adopted historically by the petroleum industry. It demonstrates simple, analytical modeling and shows the differences between forecasting from the WIPP site and for a typical coalbed methane scenario. It corroborates major changes occurring over a relatively small range and value of cohesion. Figure 5-1 is an example of representative WIPP site properties. The data shown in Figure 5-1 are summarized in Table 5-1. The formulation used was:

$$\frac{\mu q}{2\pi k r} = 2\frac{T+1}{T}C_o$$
$$T = 2(\tan\alpha - 1)$$
$$C_o = 2\,c'\tan\alpha$$
$$\alpha = \frac{\pi}{4} + \frac{\phi}{2}$$

where:

μ =   viscosity (Pa·s),

|		
q	=	flow rate (m^3/s/perforation),
k	=	permeability (m^2),
r	=	cavity radius (m),
C_o	=	unconfined compressive strength (Pa),
c'	=	effective cohesion (Mohr-Coulomb) (Pa), and
ϕ	=	angle of internal friction (radians).
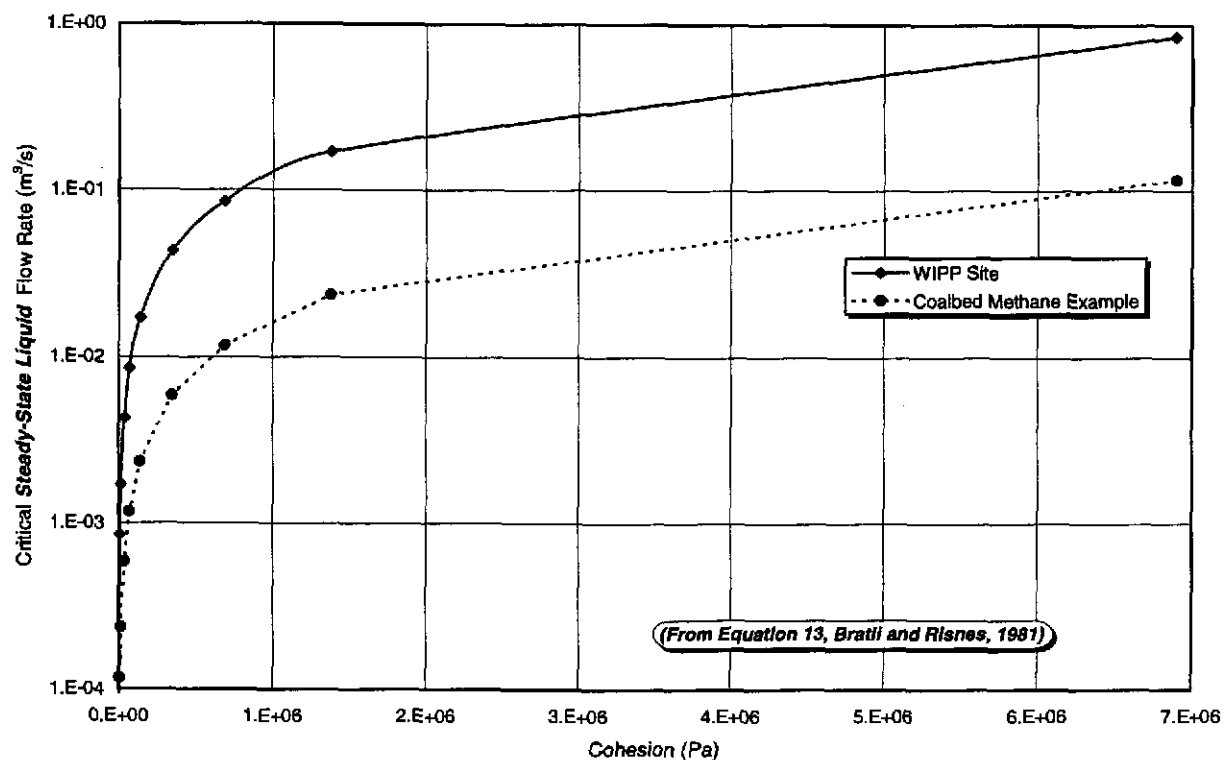
Figure 5-1. Critical liquid flow rates in simple analytical approximations (after Bratli et al., 1983); curves are for spherical cavity with steady-state liquid flow and only indicate the initiation of tensile failure. Estimates of plastic radius (extent of yielded zone) are approximate; cavity evolution is not possible. Curve for coal is shown because precise numerical calculations indicated this coal did not cavitate when cohesion was greater than 0.1 MPa. Predicted tolerable conditions using WIPP site data (also assuming liquid flow) are even greater than for coal shown (i.e., even more stable).

Table 5-1. Properties Used in Figure 5-1

Property	WIPP Site	Typical Coalbed Methane Reservoir
Viscosity (Pa·s)	9.32×10^{-6}	1×10^{-5}
Permeability (m^2)	5.2×10^{-14}	1×10^{-14}
Angle of Internal Friction (°)	47	27
Initial Height (m)	2	2
Initial Diameter (m)	0.3115	0.3115

These early approximations (i.e., Bratli et al., 1983) were for steady-state liquid flow. One exception (relaxing the assumption of incompressibility of the flowing phase) is the modification of the liquid criteria to accommodate gas, as in the analytical relationships derived by Perkins and Weingarten (1992):

$$\rho = \gamma_o \, p^m$$

$$m = \frac{\log(\rho_2 / \rho_1)}{\log(p_2 / p_1)}$$

where:

ρ	=	density (kg/m^3),
subscripts 1, 2	=	indicate different pressure and temperature environments,
γ_0	=	coefficient incorporating the density at STP, and
p	=	pressure (MPa).

The equations used to determine critical pressure conditions (no tensile stress) were:

$$\frac{4\sin\alpha}{1-\sin\alpha} - \frac{p'_w - p'_a}{(m+1)} p'_a{}^{-m/m+1} = 0$$

$$p'_a = \left[\frac{p_a \tan\alpha}{C_u}\right]^{m+1}$$

$$p'_w = \left[\frac{p_w \tan\alpha}{C_u}\right]^{m+1}$$

where:

α	=	angle of internal friction (degrees),
p'_w	=	normalized pressure in the vicinity of the wellbore,
p'_a	=	normalized pressure at the face of the cavity,
m	=	an exponent in the equation of state ($m = 1$ for an ideal gas and $m = 0$ for a liquid),
p_a	=	pressure at the face of the cavity (MPa),
p_w	=	pressure in the vicinity of the wellbore (MPa), and
C_u	=	cohesion (MPa).

This is a criterion for tensile failure for a spherical cavity. "When a fluid flows into a cavity, it is possible for tensile net stresses to be induced in the surrounding formation if the flow rate is sufficiently large. A conservative design criterion for cavity stability is to limit the drawdown [reduction in pressure] to those values which would not induce tensile net stresses ... Thus to avoid net tensile stresses near the cavity face, the largest permissible value of (p_w - p_a) [the drawdown] is that value which makes $d\sigma_r/dr$ [effective radial stress gradient] = 0 at r = a" (Perkins and Weingarten, 1992). Darcy flow of gas is assumed, as are steady state conditions.

5-4

Figure 5-2 shows calculations using the tensile failure criterion adopted by these authors (using properties relevant to the WIPP site). The WIPP properties assumed were:

$$\alpha = 44°$$
$$p'_w = 14.8\ \text{MPa}$$
$$m = 0\ \text{and}\ 1.$$

The calculations are summarized in Figure 5-2. This plot was derived by an approximate iterative solution, for $m = 1$ (gas) and using an explicit procedure for $m = 0$ (liquid). This figure highlights the fact that greater total drawdown (reduction in pressure) can be tolerated for a gas. This means that, for the properties used in the calculations, greater drawdown is tolerable if gas is the flowing medium before the effective radial stress gradient is negative (acting to produce solids into the well). Any semi-analytic liquid solutions will indicate lower tolerable drawdowns. Also note that this plot indicates conditions suitable for the start of spalling.
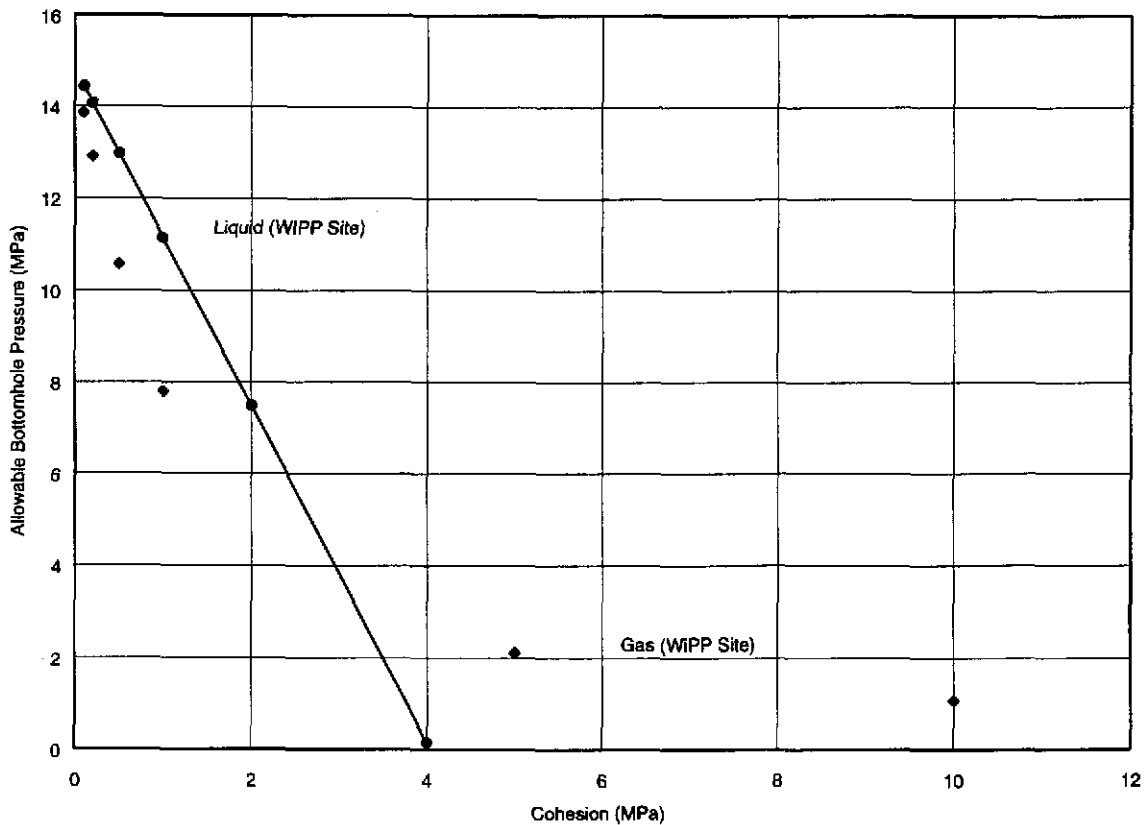

Figure 5-2.   The variation of allowable bottomhole pressure as a function of cohesion for a spherical cavity (after Weingarten and Perkins, 1992). These data were derived using WIPP site properties shown in Table 5-1 (but varying m; m = 0, 1).

5.2.2 Example 2: (A Spherical Cavity with An Intersecting Discontinuity)

This extension of the previous example demonstrates the stabilizing influence of intersecting discontinuities. In many situations where there are sand production problems, wells are hydraulically fractured to provide a highly conductive channel extending away from the wellbore. The purpose of this is to distribute the pressure drawdown near the wellbore along the fracture, thereby reducing the near wellbore pressure gradient. Fletcher et al. (1994) modified the equations (from Weingarten and Perkins, 1992, shown in Example 1), to incorporate the influence of the hydraulic fracture. These authors demonstrated that, contrary to what one might expect, the presence of a highly conductive discontinuity *will provide a stabilizing influence*. An example in the Gulf of Mexico was given. "For a given flow rate, the total allowable, sand-free drawdown, TDP, for a perforation [an orifice through well casing and the cement sheath into the reservoir rock, created with a shaped charge] is:

$$\frac{4\sin\alpha}{1-\sin\alpha} - \frac{p'_w - p'_a}{(m+1)}p'^{-m/m+1}_a = 0$$

$$TDP = dP_w + \Delta P(X_f)$$
$$\text{where } \Delta P(X_f) = P_{inf} - P_w(X_f)$$

where P_{inf} is the far-field reservoir pressure (at infinity) [and] dP_w is the perforation critical drawdown evaluated using P_w, the near-perforation reservoir pressure. For a given fluid rate, P_w is a function of the fracture half length (X_f). The pressure difference $\Delta P(X_f)$ quantifies the effect of the fracture on pore pressure near the perforation. Without the fracture, $\Delta P(X_f)$ is zero and, with a 2-wing hydraulic fracture, $\Delta P(X_f)$ is a function of frac half length ... Therefore, $\Delta P(X_f)$ is the additional allowable drawdown contributed by the hydraulic fracture."

Generation of the drawdown curves for discontinuities (i.e., hydraulic fractures, high permeability discontinuities, or dislocations) is accomplished using conventional reservoir engineering methods for production simulation. *The important concept is that an intersecting discontinuity can serve to be a stabilizing influence and will reduce spall.*

5.2.3 Example 3 (The Influence of Cohesion and Angle of Internal Friction)

The next level of sophistication in the approach to sand production problems was demonstrated by Wang and Dusseault (1991). These authors assumed an instantaneously strain-softening material, with subsequent behavior being ideally plastic. They published equations for an analytical solution of the active loading of a borehole, assuming plane strain. Active loading means that the radial stress (acting normal to the surface of a borehole) is less than the circumferential stress (acting tangential to the wellbore). This is a situation commonly encountered in drilling with a borehole pressure less than the tangential stress concentration caused by the presence of the wellbore. This would be the situation for WIPP site penetration. As stated by Wang and Dusseault (1991) and demonstrated by elastic stress concentrations around a wellbore (Equation 8 in Wang and Dusseault, 1991), "During drilling, σ_r is reduced at the borehole wall, [from the far-field total stress, to the wellbore pressure], and this corresponds to active loading." With penetration at the WIPP site, the total radial stress at the wellbore

boundary would reduce from 14.8 MPa to a smaller value (the bottomhole wellbore pressure), regulated by the hydraulic transport in the annulus.

These analyses are similar to earlier approaches, with the exception that the strain softening was incorporated, the horizontal stress field was not isotropic, and rudimentary stress path dependence was incorporated. Failure in shear and tension can be determined analytically for no flow situations. Plastic radii can be determined; that is, the extent of the zone that has undergone irreversible plastic deformation can be calculated. These same parameters can be predicted with a hybrid analytical numerical model for steady-state flow into the wellbore.

"Under active loading (during drilling), it is the pore pressure gradient magnitude rather than its absolute value that dominates borehole stability."[1] This is equally appropriate to the WIPP site, where it is the magnitude of the pressure gradient which affects the stability. This is consistent with other WIPP site analytical calculations which indicate that the most deleterious instability occurs at those times when the near-well reservoir pressure gradient is largest.

It is inappropriate to consider pressure drop from initial pressure to 0^+ MPa[2]. Not only is this precluded by the wellbore hydraulics, but it is not instantaneous, and stress and gradient conditions vary. This indicates that all analytical calculations which assume complete or instantaneous reduction in wellbore pressure will overestimate cavity growth.

Despite limitations of these analytical models, they do clearly demonstrate that cohesion is a dominant material parameter. A yielded zone will develop around an opening in weak material during excavation due to reduction of internal pressure. If the wellbore pressure decreases enough, a plastic zone develops. The plastic zone radius is affected by the magnitude of the *in-situ* stresses, the pore pressure, and the material strength constants, particularly cohesion. This is clearly shown in Figure 5-3.

It must be emphasized that even though yield has occurred to form this plastic zone, it retains significant load bearing capacity (the stress-strain curves for WIPP surrogate sample S14QS show almost no degradation in load bearing capacity: it is nearly an ideally plastic material) and it will only be removed if seepage forces are large enough.

The paper by Wang and Dusseault (1991) is particularly important because it shows the development of a plastic zone in which yield occurs and stresses are transferred away from the cavity. This has two consequences. The first is that there is a degree of hole stabilization because of the reduced stress concentrations. *Second, it is anticipated that as stresses are reduced in the plastic zone, its permeability will increase. If its permeability increases, the near wellbore flowing pressure gradients will be reduced and stability is dramatically improved.*

5.2.4 Example 4: (Field Examples)

Petroleum journals contain numerous examples of sand control problems from actual field situations. Veeken et al. (1991) provided summaries of characteristic data from wells where sand (or other reservoir particulates) have been produced. In many of these instances, even extremely small volumes of sand are disastrous because of the potential of erosion of wellhead components

---

[1] Wang and Dusseault, 1991.

[2] 0^+ indicates a small, non-zero, positive pressure.

on the seabed floor. Figure 5-4 is excerpted from this paper to schematically show the types of failure that were anticipated to occur in the reservoirs that were evaluated. The speculated mechanisms are similar to those being evaluated at the WIPP site. These include the following:

- *Extensile failure associated with drawdown* (called tensile failure in Figure 5-4). A tensile stress regime is developed and failure occurs when the tensile strength of the candidate reservoir is surpassed. This is characterized by the semi-analytic modeling presented in Section 4 of this document.

- *Compressional shear failure* of some level of complexity. This results when the shear stress increases as a consequence of reduction in wellbore pressure or changes in the effective stresses in the reservoir (as would happen during intrusion into a repository).

- *Erosional removal of particulate matter* as a consequence of flow into the wellbore. Erosional transport is discriminated from shear failure, indicating that shear failure does not imply production of particulate matter *a priori*.

Veeken et al. (1991) stated that "A reasonable consensus exists on how to model tensile failure. The stability criterion can be expressed in terms of the normalized drawdown gradient (g_{pn}) at the cavity wall [sic; the procedure is similar to that used for the WIPP site in Section 4 of this document] ... Note, that g_{pn} depends on the near-wellbore permeability (k) ...[It] is higher in [the] case of impairment ... (due to e.g. perforating, fluid invasion, fines movement) and lower in case of stimulation (due to e.g. acidizing or material dilation ...)." This is a critical concept.


TRI-6121-399-0
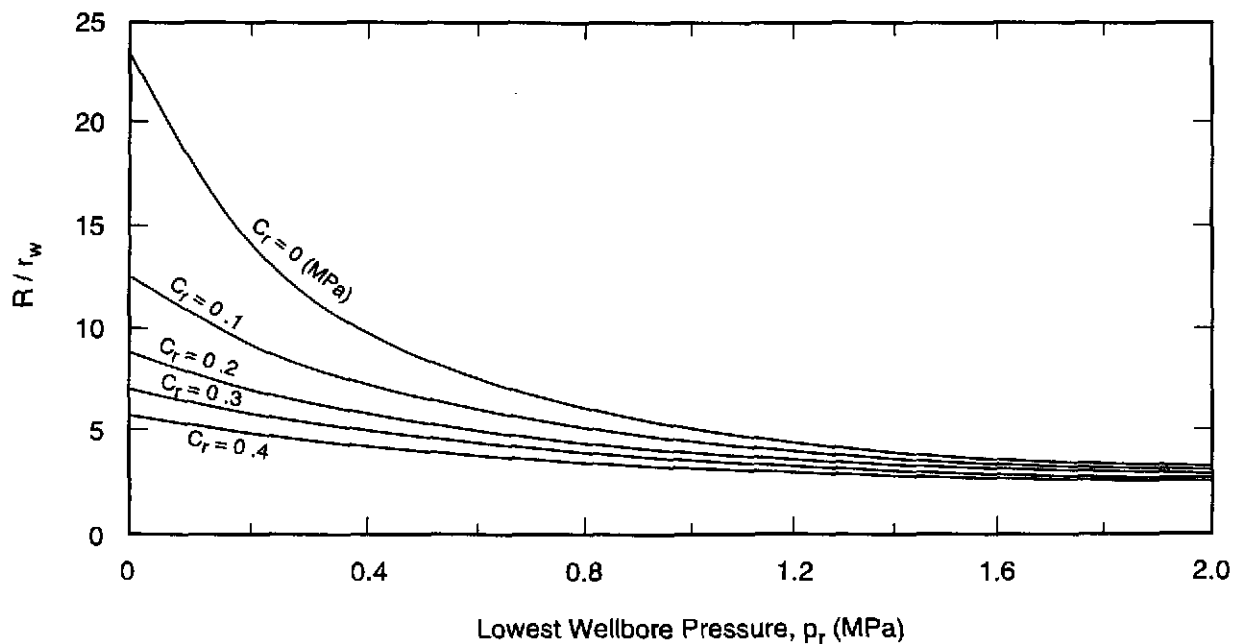
Figure 5-3. Plot of plastic zone radius, R, normalized by initial wellbore radius, r_w, versus the lowest possible wellbore pressure (after Wang and Dusseault, 1991). Residual cohesion is used in characterization of plastic zone dimensions because yielding has occurred. Importance of cohesion is shown. Evaluation of the stress-strain curves for WIPP surrogate sample S14QS indicates minimal strain softening, and it can be determined that the intact and residual cohesion are practically the same.
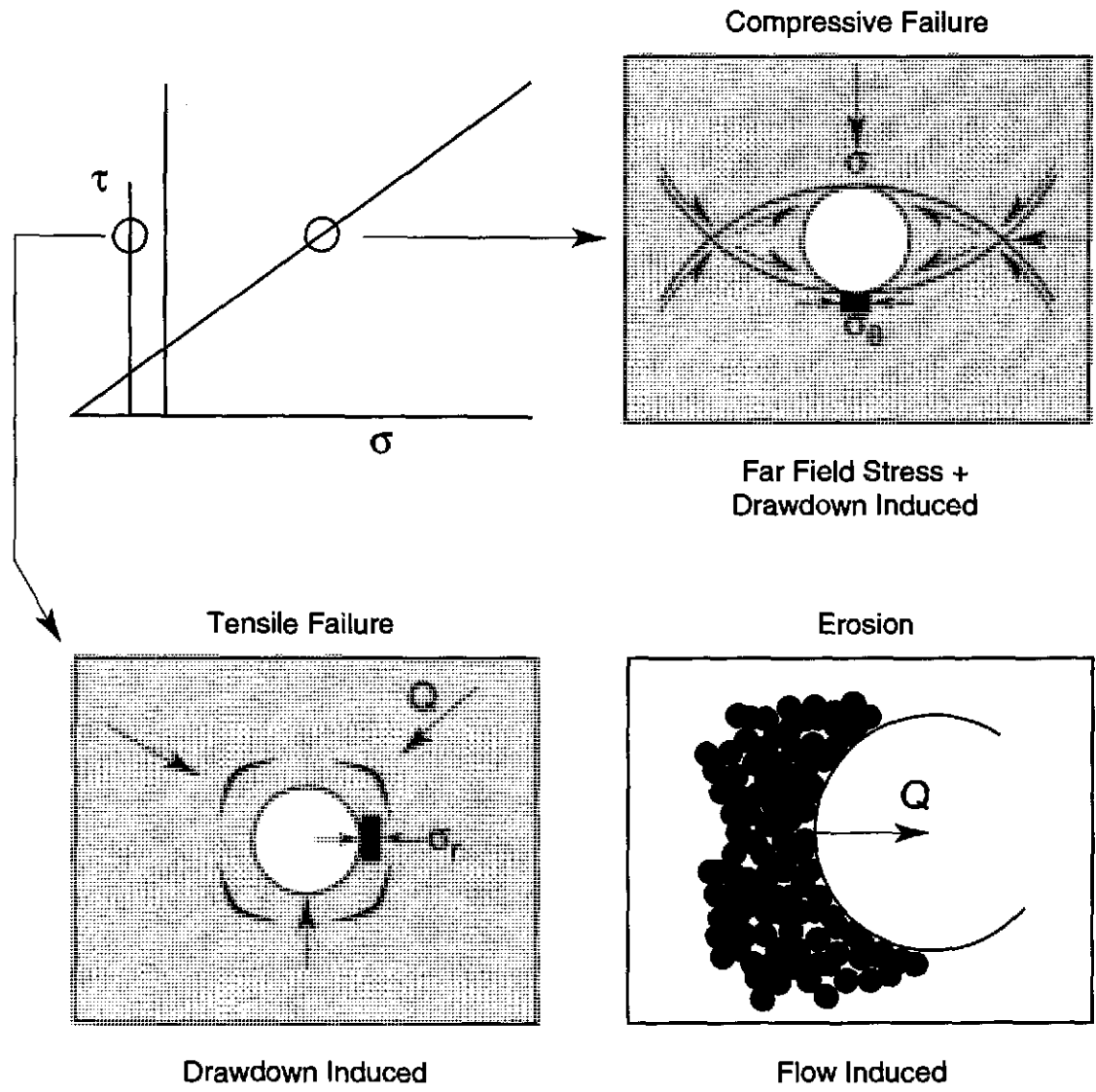
Figure 5-4.   Schematic representations of the mechanisms for particulate production into a wellbore, as well as a generic Mohr-Coulomb failure criterion (after Veeken et al., 1991).

Anticipated increases in permeability associated with reduction in the mean effective stresses in the near-cavity region at some time after the start of flow (and possibly with dilation) will likely cause a near-wellbore increase in permeability. This causes a reduction in the reservoir pressure gradient and increased stability.

Actual data from wells producing sand were provided. These data are shown in Figure 5-5, which indicates concentrations of sand as a function of drawdown pressure for a poorly consolidated formation. These data indicated that a criterion for sand production in a radial configuration was that the drawdown pressure should not exceed 50% of the unconfined compressive strength. This pressure value is quite restrictive and is probably associated with

supplementary stresses associated with the vertical principal stress and the stress concentrations and *damage associated with perforating a well.* Perforation damage in these petroleum examples is an important consideration. Note that the vertical scale in Figure 5-5 is liters per *1000 m³*. This is an extremely small volumetric rate. At the peak sand production in Figure 5-5, the rate of sand production has stabilized at approximately 6×10^{-4} m³ of solids per m³ of slurry (assuming a 40% porosity for the collected sand at the surface).

There is also a discussion of the stabilizing influence of a discontinuous water phase. This is an underlying consideration in most sand production publications; the onset of significant sand production is commonly associated with increasing produced volumes of formation water and an alleged reduction in strength due to capillarity. This contribution is incorporated in models only when specific laboratory measurements of capillary pressure as a function of saturation are made. Because of formation variability and wettability considerations, micromechanical quantification of these capillary effects is usually not attempted (i.e., empirical methods are used). Regardless, field evidence provides little dispute to the contribution of capillarity on a qualitative basis. This is shown in Figure 5-6, where significant sand production does not commence until the water cut (the amount of water produced in terms of the overall flow) increases to a level where a continuous water phase is evidenced (i.e., flow occurs). The important observation is that at the WIPP site, low levels of water saturation (existing under the most extreme pressure situations) will serve to stabilize (inhibit spalling by increasing cohesion) the repository. Capillary pressure-saturation relationships cannot be estimated *a priori.* Ignoring them in the semi-analytic and numerical calculations is a conservative assumption.

In terms of these flied data, the qualitative observation applied to the WIPP site evaluation emphasizes the potential of additional supplementary strength at the WIPP for saturations where there is a discontinuous phase. This will characteristically be largest at saturations close to the irreducible water saturation. These cohesive forces, associated with interfacial tension, are not included in WIPP spalling calculations.

5.2.5 Example 5 (Nonlinear Elasticity)

Even with certain assumptions of ideal plasticity and poroelasticity, basic analytical models from the petroleum industry still *commonly underestimate the integrity (i.e., would overestimate spall releases)* of drilled formations (Fairhurst, 1990). To overcome this, additional levels of sophistication have been added to available models. These have included more precise representation of the constitutive behavior (how stresses and strains interrelate, before and after yield; refer for example to Papanastasiou et al., 1994) and incorporating pressure-sensitive mechanical properties and pressure-sensitive permeability.

The influence of pressure-sensitive permeability has been discussed previously. In terms of pressure-sensitivity of moduli, there are many examples in the literature (e.g., Nawrocki and Dusseault, 1995; Nawrocki et al., 1995) of this stabilizing effect. The modulus of many geotechnical materials varies with the stress regime it is subjected to. For example, Lambe and Whitman (1969) stated:
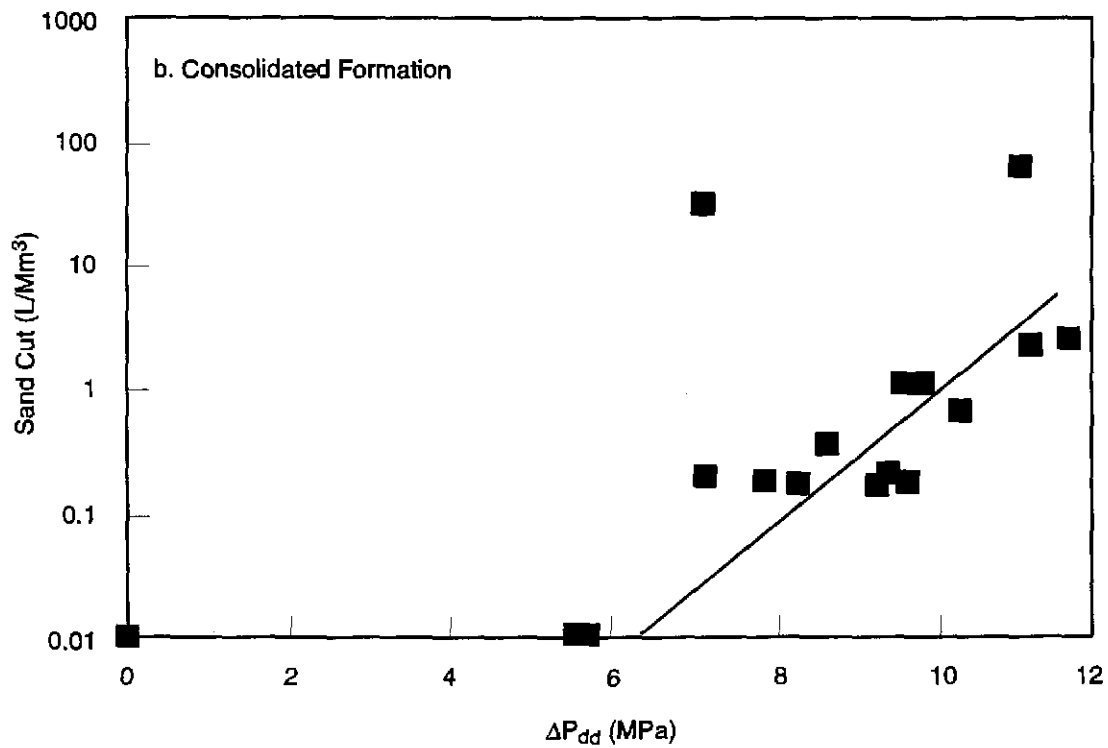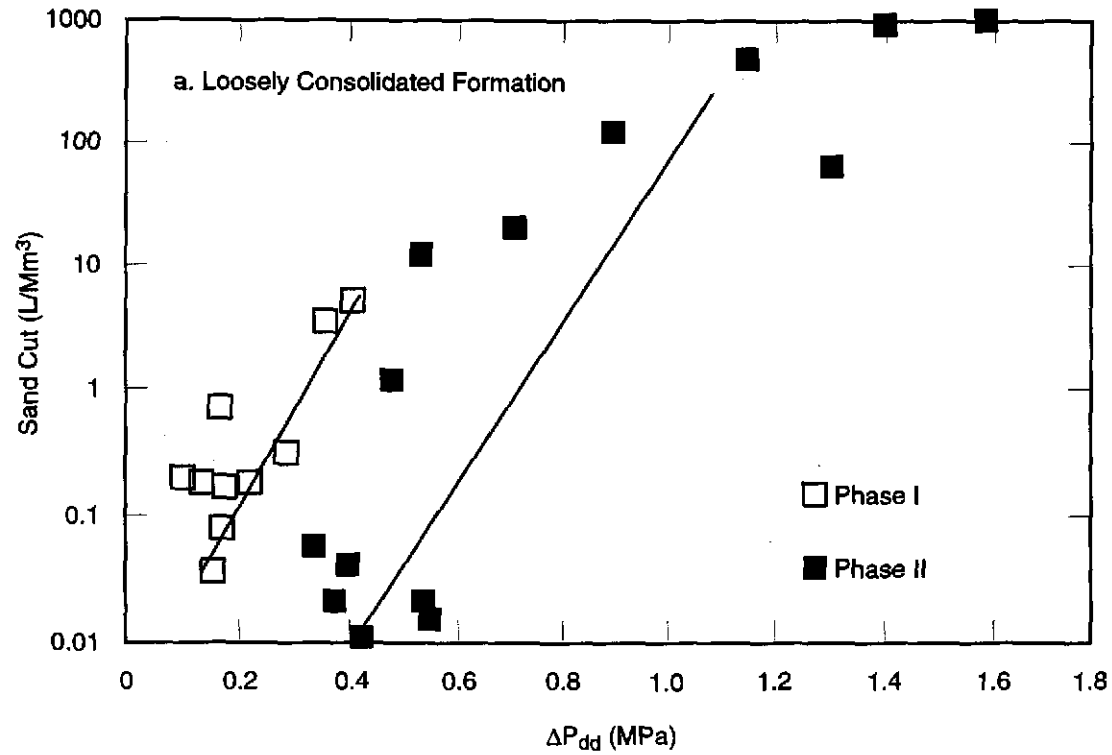
Figure 5-5.   Sand concentrations versus drawdown pressure (after Veeken et al., 1991).
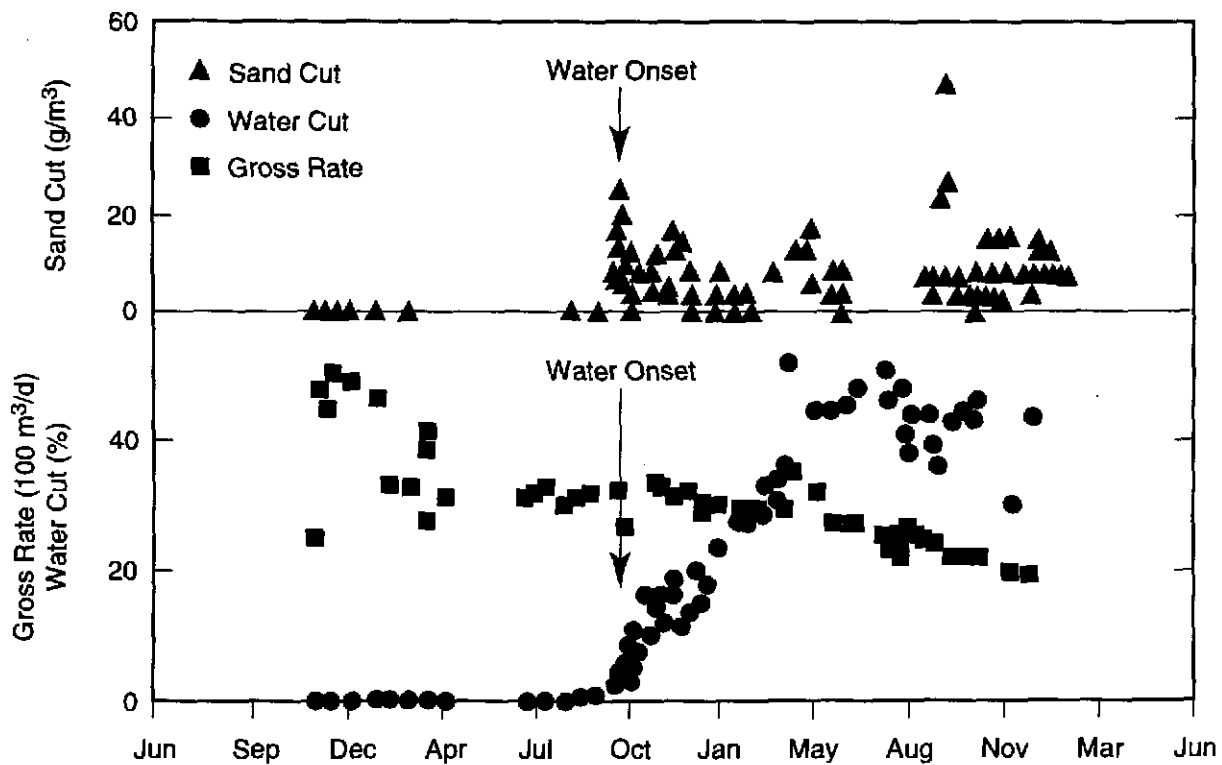
TRI-6121-401-0

Figure 5-6.   Field data showing the gross rate (all fluids produced), the water cut (the portion of
the total rate which is brine) and the surface sand production (mass per volume of
produced fluid) (after Veeken et al., 1991).

"As the confining stress increases, the modulus increases. For the case where the initial stress σ_0
is isotropic the modulus increases as σ_0^n where n varies from 0.4 to 1.0. A reasonable average
value is n = 0.5. The larger values of the exponent tend to apply to loose sands."

This stress dependency leads to a reduction in the tangential stress around the wellbore (similar
to what might happen for elastoplastic behavior; refer for example to Papanastasiou et al., 1994),
with a resulting improvement in shear stability. Also, after a period of time, a reduction in the
mean effective stress near the wellbore reduces the pressure gradient; this is a dominant factor in
reducing sand production and leads to cavity stabilization. There are reduced tangential stresses
and the difference between the tangential and radial stress (a shearing stress, which acts to cause
shear failure) is also reduced. This is not represented in most simple analytical models. This
effect is shown in Figure 5-7, taken from Nawrocki et al. (1995). The model used to develop this
representation included nonlinear elastic behavior by considering the elastic moduli as functions
of stress or strain (as shown for example in Figure 5-7). This figure indicates that the critical load
acting on the outside of a wellbore is significantly higher for situations where stress-dependent
moduli are incorporated (nonlinear situation). The data for the WIPP site surrogate material
indicate $E=367.5\sigma^{0.5441}$ (as the data were limited, this relationship can be considered as
illustrative only; it was based on tangent moduli for first reloading for Specimens S6, S14 and
S23). This dependency causes additional stability not represented in most analytical models.

Figure 5-7 shows numerical simulations of the external pressure required to fail a thick-walled cylinder. The ordinate in Figure 5-7 shows the pressure (applied on the outer radius of a thick-walled cylinder) required to collapse an inner concentric bore. This external pressure is analogous to a reduction in reservoir pressure (refer to the relationship for tangential total stress in Wang and Dusseault, 1991). Either increasing the far-field stress in a reservoir or reducing the wellbore pressure will increase the chance of shear failure in a wellbore. By analogy, Figure 5-7 demonstrates that incorporating nonlinearity will increase the cavity integrity (whether the cavity is the inner bore in a thick-walled cylinder in the laboratory or a wellbore, similar arguments can be made for spherical geometries).

Despite the limited data set used to infer a modulus confining pressure relationship ($E=367.5\sigma'^{0.5441}$), it can reasonably be expected that modulus will increase with effective confining pressure. Effective confining pressure will increase with reduction in repository pressure. There will be supplementary stabilizing effects due to the variation of modulus with stress level.
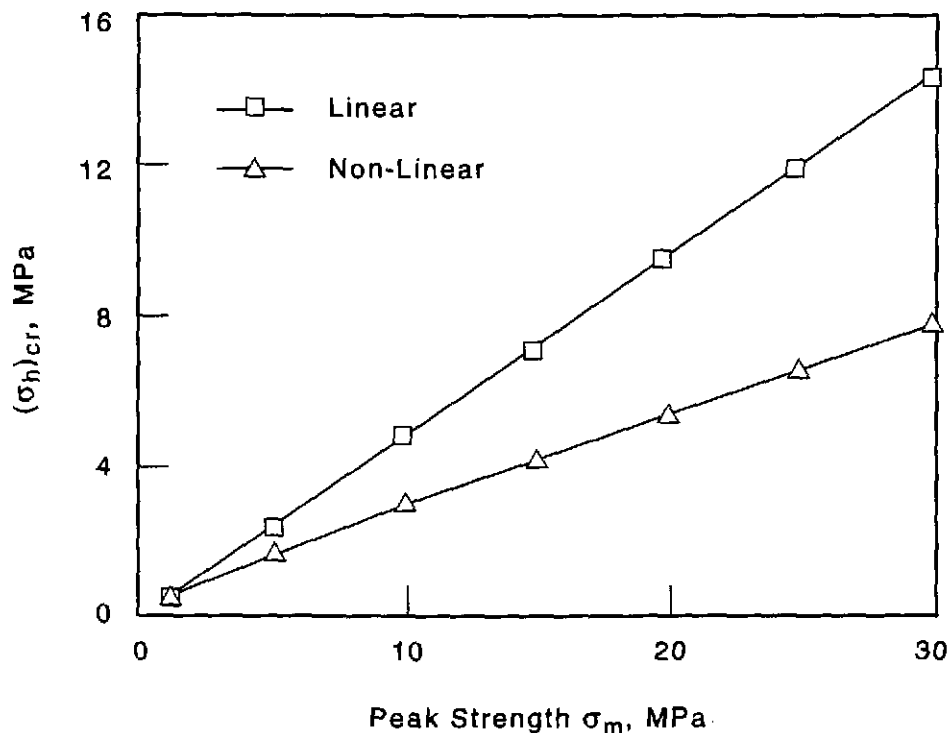

TRI-6121-403-0

Figure 5-7. The critical load on the outside of a hollow cylinder for a linear situation (no modulus dependence) and a nonlinear situation (modulus dependence) (after Nawrocki et al., 1995).

Example 5 indicates that many basic, elastic analytical models underestimate the integrity of formations. Two principal reasons for this are that Young's modulus can be an increasing

function of increasing effective stress and permeability can be an increasing function of decreasing effective stress. Either one of these factors will serve to stabilize a cavity.

5.2.6 Example 6 (Numerical Modeling)

This section introduces coupled and uncoupled numerical simulations of wellbore or perforation scenarios. The discussion introduces the coupled model used for coalbed methane calculations, emphasizes the influence of rate of loading, and provides citations that sand production problems are worsened if the pressure conditions in a reservoir are cycled (something that will not be the case at the WIPP site).

The next level of development for sand production prediction was uncoupled fluid flow and deformation finite element modeling. The classic references are Morita et al. (1987), Morita and Boyd (1991), and Morita (1994). Most of these analyses were directed to perforated completions which are similar to the single-point entry scenario at the WIPP site.

- Examples were given for sand production from poorly consolidated formations in Alaska. "The amount of sand produced from poorly consolidated formations is significant due to shear failure while tensile failure during perforation cleanup [this is where a well is flowed back to try and remove debris such as fractured rock and metal from perforations created when a shaped charge (perforator) has penetrated into the reservoir] is sporadic and generally low in magnitude."

- Morita and Boyd (1991) also discussed the critical importance of water breakthrough (start of water production from other parts of the reservoir).

  "The wells producing near the critical bottom hole flowing pressure induce shear failure. The shear failure zone around the perforation cavities remained intact at the cavity surface with sufficient capillary pressure prior to water breakthrough. These failed zones, although weak, can still support the cavity surface which prevents propagating the shear zone. However, after the loss of capillary bonding with water breakthrough, the failed zone is quickly washed away by the tensile failure due to flow friction. The loss of support by the failed shear zone causes an extension of the shear zone. The shear expansion alternating with tensile grain washing results in continuous sand problems.

  "The well producing near the critical bottom hole flowing pressure induces tensile failure due to unloading if the well is repeatedly shut-in." This means that sand production is exaggerated by pressure cycling. Unloading refers to the increase in pore pressure (and reduction in effective stress, the unloading) when a well is shut-in (valved off at the surface). Putting the well back on production can cause a spike of sand production before stabilization occurs. This cycling is common in petroleum applications and tends to bias sand production measurements used as analogs. At the WIPP site, cycling will not occur.

- A critical concept discussed by these authors is that the tensile strength in the plastic (shear failed zone) is commonly reduced. With a reduction in tensile strength, extensile removal of particulate is encouraged.

- "The cavity becomes more stable to tensile failure due to the larger cavity surface, the thinner damaged zone, and the more spherical cavity surface shape."

The next numerical improvement for modeling was initiated for characterizing oil sands in Alberta. Coupled, single-phase flow and deformation models were developed (refer for example to Vaziri and Byrne, 1990). While material properties were represented quite well, the flow was restricted to be single phase and laminar. Transient flow effects were however represented. Methodologies for representing the material properties in these models are summarized in Vaziri (1990).

"In most field problems, because of the transient nature of fluid flow, fluid-pressure gradients near the wellbore initially may be greatly in excess of the long-term steady-state values. This results in early instability which is not included in [analytical formulae]. As collapse of the surrounding material occurs, permeability in the collapsed zones will increase and, assuming no other changes, the pressure gradient will drop. When the pressure gradient is reduced to subcritical levels, sand production ceases. By the time steady-state conditions are reached, the formation properties may have changed substantially." The work of Vaziri and Byrne (1991) overcomes these limitations by incorporating *fully* coupled flow and deformation solutions. The model under comparable conditions was verified against closed form solutions for sample problems (compared to elastic, steady-state predictions based on the formulations of Risnes et al., 1983). A refinement of this model was used for simulating coalbed methane cavitation, certainly the closest WIPP site analog.

This numerical modeling allowed the cavity to grow in size with time. "Application of Risnes' theoretical solution for this purpose is inappropriate since the solution implies that once the critical flow rate is exceeded, the entire formation becomes unstable. Such a phenomenon is not observed within the site under consideration [i.e., in the analysis presented by Vaziri and Byrne]." The problem evaluated using this finite element model is summarized in Table 5-2.

The variation in stresses for the example (from Vaziri and Byrne, 1991) shown in Table 5-2 are shown in Figure 5-8. With the exception of the lower *in situ* stresses, this example is reasonably similar to the WIPP site scenario. It indicates (Figure 5-8) that, at the end of the simulation, the cavity had stabilized at a radial extent of approximately 1 meter. The physical extent of the cavity is the radial limit of the tensile zone. Note that the governing property in the simulation, cohesion, is approximately three times smaller than at the WIPP site. As will be seen in the following section, this small difference is important.

The rate at which pressure is reduced was also shown to be an important factor. "Based on a number of studies performed, but not presented here, it has been found that a major factor that influences the formation stability is the operational scheme adopted to reduce pressure inside the well-bore. The faster the pressure reduction process is carried out, the steeper will be the fluid pressure gradient at the well-face, and hence the greater are the chances of developing instability. Particularly, the flow rate during the early stages of pressure reduction in the well-bore has a profound influence on the extent of instability. A sudden initial surge of flow is likely to mobilize an appreciable quantity of sand, particularly within a region close to the well-face where the very high shear stresses have already brought the formation to a state of failure. A slow reduction of well-head pressure, on the other hand, provides an opportunity for the sand to consolidate without much disturbance from excessive seepage forces. An increase in the mean effective stress state caused by a gradual decrease in fluid pressure close to the well-bore helps to strengthen the formation in that region. Once such a support zone is fully developed, the formation can remain stable, even when the flow rate is further increased. This is because very

large seepage forces associated with very high rates of inflow would be required to dislodge the mass of material around the well-bore that has, by now, developed much higher strength or resistance characteristics compared with its previous failed condition." At the WIPP site, the relatively slow reduction in pressure, during early time as mud is expelled, is very advantageous for developing a stable cavity.

Table 5-2. Example Problem (Vaziri and Byrne, 1990)

Formation Properties	Initial Values (Vaziri and Byrne, 1990)	Inferred WIPP Site Properties (Initial Values)	Typical Values Computed After Well Depressurization		
			Nonlinear Elastic Zone	Plastic Zone	Tensile Zone
Effective Cohesion (MPa)	0.035	0.13	0.035	0.035	0.035
Effective Angle of Friction (°)	40	44	40	40	40
Young's Modulus (MPa)	1000	354	500-1000	0.5-1	0.001
Permeability (m^2)	2.5×10^{-12}	1.7×10^{-13}	$2.5\text{-}3.0 \times 10^{-12}$	$2.5\text{-}5.0 \times 10^{-12}$	2.0×10^{-11}
Viscosity (Pa-s)	$1.8 \times 10^{-6*}$	9.32×10^{-6}	$1.8 \times 10^{-6*}$	$1.8 \times 10^{-6*}$	$1.8 \times 10^{-6*}$
Porosity	0.3	0.4	0.3	0.3	0.3
Effective Radial Stress (MPa)	4.0	0	1.7-4.0	-0.04-1.7	-0.042
Effective Circumferential Stress (MPa)	4.0	0	6.2-4.0	-0.04-6.2	-0.042
Effective Vertical Stress (MPa)	7.5	0	7.5	-0.04-7.5	-0.042
Pore Pressure (MPa)	3.5	14.8	2.2-3.5	0.5-2.2	0.5

* Vaziri and Byrne (1990) reported viscosity units as MPa-s; they should be Pa-s.

5.2.7 Example 7 (Cold Production)

Cold production involves aggressively producing poorly consolidated reservoirs containing low gravity (highly viscous) crude oil. Extremely high drag forces result because of the high oil viscosity. It has been found that cavity creation tends to increase production. It has been argued that highly permeable channels, known as wormholes, are developed and afford improved access to the reservoir. The existence of wormholes has not been definitively proven. Experimental work by Tremblay et al.(1996) *showed* the generation of wormholes under laboratory conditions. Experimental work by Vaziri (1997), however, *did not show* wormholes at all. Both of these experimental programs are discussed below. This discussion is included to demonstrate opposing viewpoints on the potential for wormhole creation.
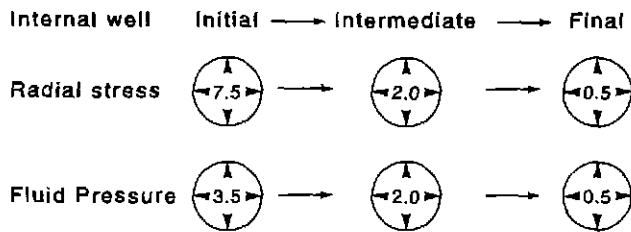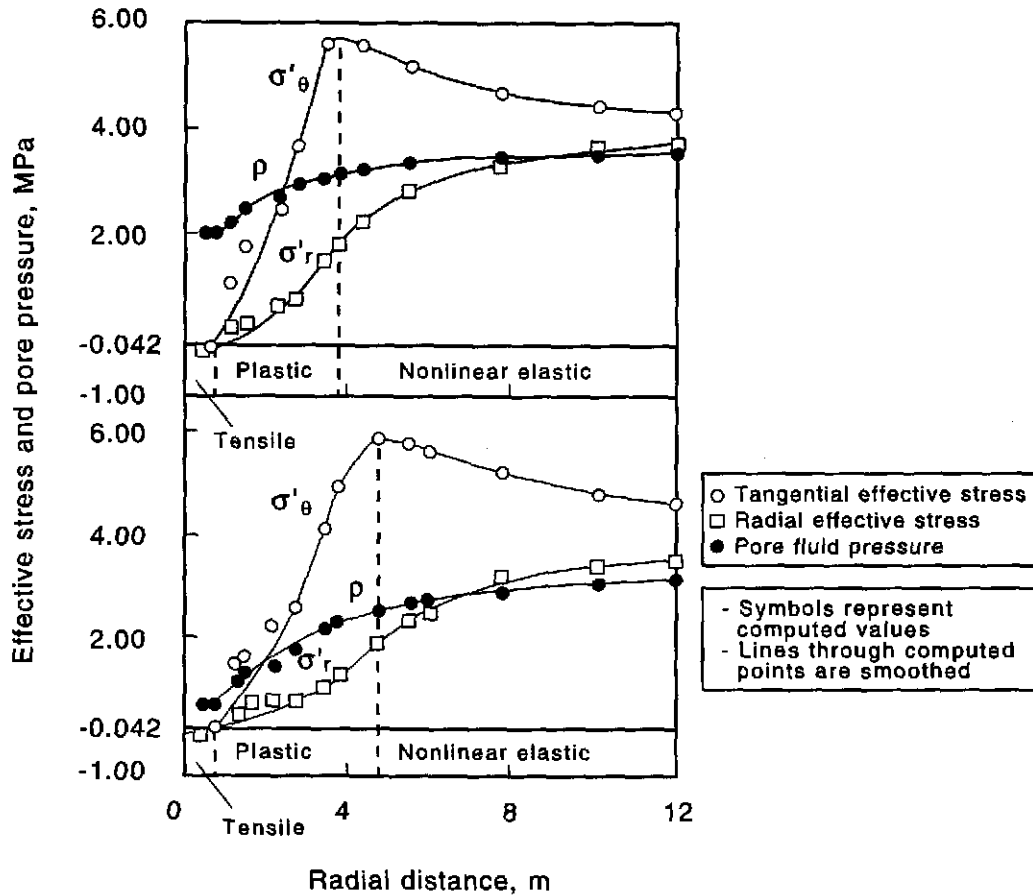
Figure 5-8.   Variation of effective stress and fluid pressure with radial distance at two stages, intermediate and final (after Vaziri and Byrne, 1990).

Tremblay et al., 1996

"Cold production is a nonthermal recovery process used in unconsolidated heavy oil reservoirs in which sand and oil are produced together. Production rates from wells that are on cold production can be up to 20 times larger than the rate predicted by Darcy flow. The drive mechanism is considered to be solution gas. Heavy oil producers recognized that producing large quantities of sand (typically 500 m^3) is necessary to enhance oil production significantly. All producers report high sand cuts (10% to 40%) at the start of the cold production process for approximately 1 month."

Tremblay et al (1996) performed laboratory flow measurements to establish whether high porosity channels (wormholes) could occur. The material used was angular and had an average grain size of 177 μm with 2.5 wt% of fines (diameter less than 37 μm). A cylindrical sand pack was created and saturated with oil with a viscosity of 21.5 Pa·s at 18.5°C. The pack was enclosed in an aluminum cylinder, 102 mm in diameter, with an exit orifice of 6.25 mm. Lifts of 20 mm were applied and compressed at a pressure of 27.2 MPa (porosity of approximately 32%). Water was pumped against the unconfined pack, pressures were measured, and the entire sample was CT scanned after the test. The pressure drop along the length of the laboratory sample was approximately 700 psi.

These authors stated that "another significant conclusion is that the wormhole developed in regions of higher porosity and therefore lower unconfined compressive strength. ... We did not observe a dilated region around the orifice. Instead, the wormhole diameter converged as the orifice was approached. The region outside the wormhole did not change porosity when the wormhole developed."

After CT scanning, "a dark, strikingly circular region of variable diameter" was visible in the tomographs, suggesting a wormhole-like feature. This was not a void per se, but actually a higher porosity zone.

There are three important considerations.

• The gradients involved (700 psi over 122 mm) are at least 39.57 MPa/m. Near the orifice, these gradients are possibly much larger than would occur at the WIPP site, and wormhole development may consequently not occur.

• Generation of the wormhole may have been associated with exit conditions through the small orifice, not occurring at the WIPP site.

• If wormholes could develop, they are quite possibly a stabilizing influence, like other highly conductive discontinuities discussed earlier.

Vaziri et al., 1997

Vaziri et al. (1997) undertook a physical modeling program to evaluate the mechanisms of cold production. "Centrifuge experiments were conducted to identify mode of failure following sand production (e.g., erosional channels or enlarged cavity) and to quantify impact of sand production on flowrate. Fifteen tests were performed, all indicating that sand production resulted in an enlarged cavity that was cone-shaped. The cone extended to the top surface of the sand with a slope angle of about 35°. Typically, the average cavity radius was ten times the initial well radius and the improvement in the steady state flowrate was ten-fold. In one test where the boundary conditions permitted formation of stable erosional channels [wormhole formation was physically encouraged], flowrate was improved by a factor of twenty. *The centrifuge tests neither captured the conditions resulting in formation of long erosional channels nor the several orders of magnitude improvement in production as inferred from some field projects in the Clearwater oil sand formation."*

However, results "based on injectivity tests conducted after six months of primary production at two Mobil Celtic pilot wells, ... suggested the existence of high permeability channels in the reservoir. Numerical simulation of the pressure build-up assuming linear flow into induced high permeability channels was found to be consistent with the measured data. Tracer experiments

between injection and production wells have been performed in the field by several operators to measure the tracer travel between wells after considerable sand production took place (Squires, 1993). In general, the travel time was at least an order of magnitude shorter than that normally predicted for unaltered formations. Such short communication times can be explained by the formation of wormholes (Tremblay et al., 1996)."

"In total 15 centrifuge and three 1-g tests were performed. The variables considered in these tests included: fluid saturation and viscosity, sand density, flowrate and centrifugal acceleration. In ten of these tests involving homogeneous sand, the mode of failure was an enlarged cavity that was cone shaped with no indications of wormhole initiation. In the subsequent 5 tests, special efforts were made to encourage and facilitate wormhole development." Oil and water saturation of the samples "resulted in adhesion between sand particles which is estimated to provide an equivalent cohesion of 5 kPa."

Results from two of these tests are shown in Figures 5-9 through 5-11. These figures clearly demonstrate stabilization in cavity growth because the mass of produced sand is seen to stabilize.

Vaziri et al. (1997) observed that gravity was an appreciable driving component in their experiments. "This is manifested by a conical-shaped cavity up to the cap; had gravity not been dominant, [the] zone of depletion would travel radially out in the plane of the slit resulting in channeling (wormholes). In fact, as was seen in Test 14 that involved supported sand channels, the gravitational effects still dominated resulting in a cone-shaped cavity."
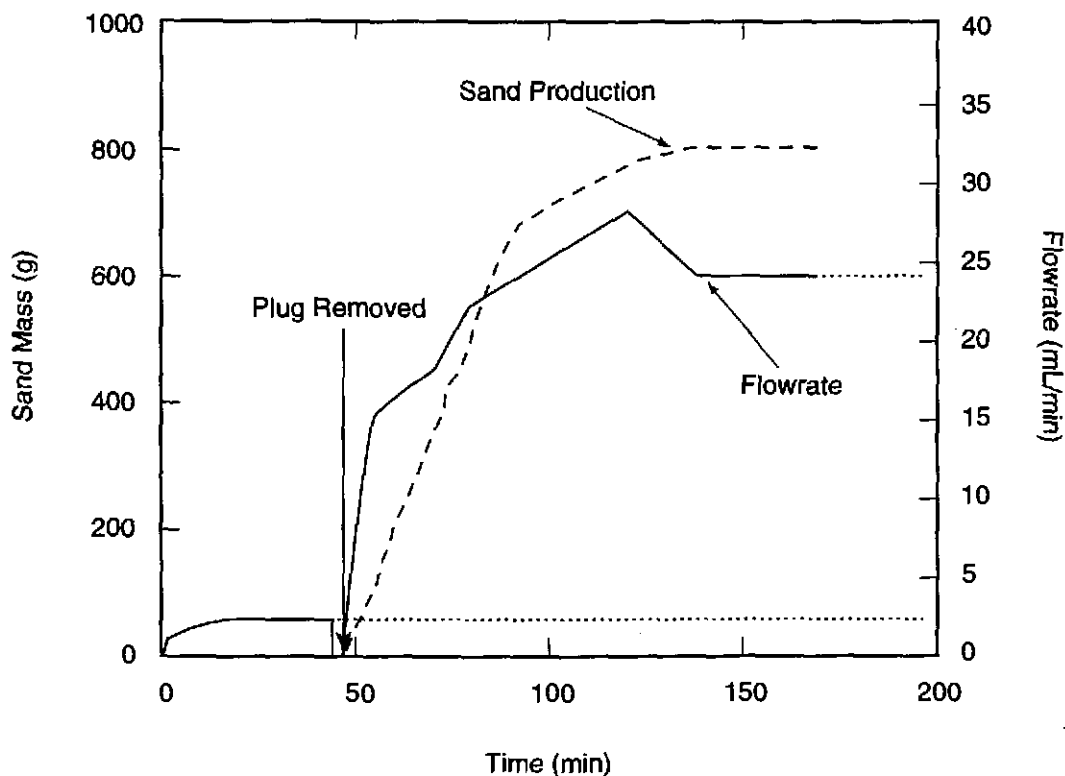
TRI-6121-408-0

Figure 5-9.   Flowrate and sand production response (cumulative mass of produced sand) for Test 15 (after Vaziri et al., 1997). Channel formation was not seen (possible indications at an acceleration of 24 g).
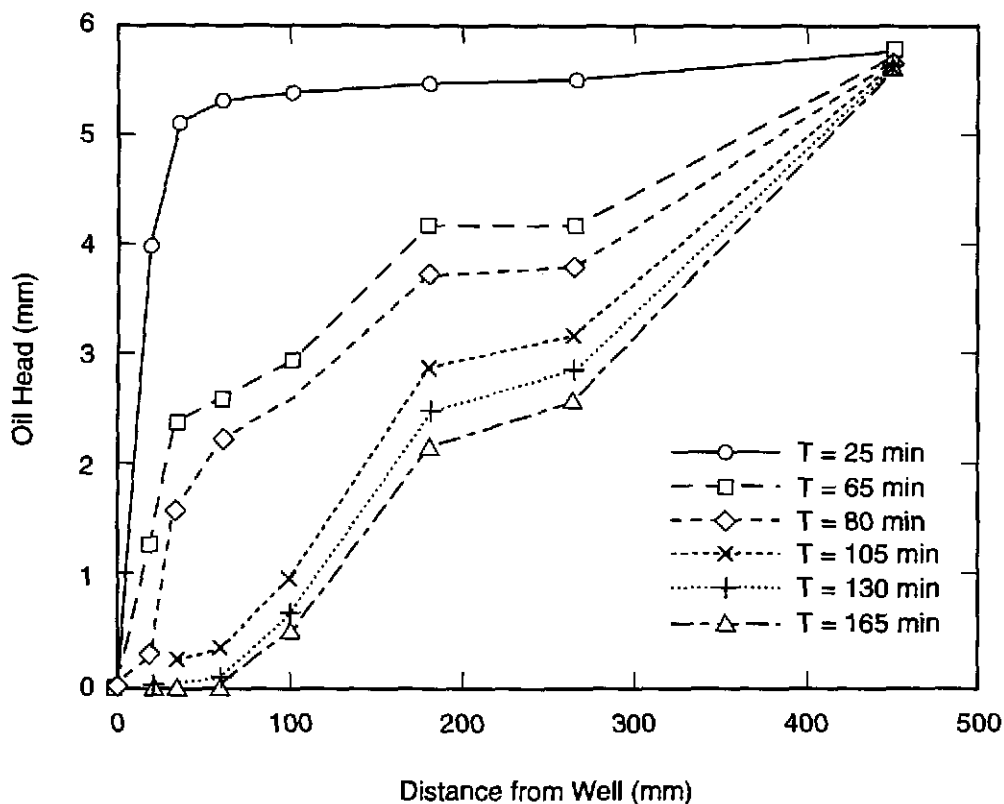
TRI-6121-407-0

Figure 5-10.   Pore pressure profile at various stages of Test 15 (after Vaziri et al., 1997).

Other observations by Vaziri et al. (1997) included the following:

- "Although not presented here, numerical analyses of the problem has shown that radius of the plastic zone is typically four times the cavity radius (the denser the sand, the smaller is the plastic radius)."

- "Using established geotechnical concepts that govern the mechanical response of sands, it is not possible to extend the stress effects associated with sand production around an opening of 0.1 m radius to distances further than 60 m from the well."

- "Initially, an enlarged cavity was formed to the top of the sand layer (beneath the shale cap) as spherically/cylindrical cavities forming around perforations coalesced. The strongest seepage path then started to form at the shale/oil sand interface. As the sand lens closest to the shale interface is in the region of the largest cavitation (due to the cone shaped nature of the cavity), it undergoes the greatest extent of yielding and hence the highest level of permeability enhancement. (Note that the sand is particularly susceptible to erosion as it has yielded and possibly strain-softened.) The diversion of stronger flow through this zone results in the erosion of sand. As the erosional process in the top sand lens continues, greater quantity of flow will be diverted through it thus facilitating its further extension. By this stage, it can be assumed that the critical flowrate has been reached. Critical flowrate is the rate sufficient to mobilize the flow of the sand particles. This pancake-shaped cavity grows as long as the source can provide the required volume of fluid. It can be noted that the cavity beneath the shale cap can also occur as a result of collapse of wormholes. Therefore, whether an enlarged cavity is initially formed or wormholes, erosion below the shale cap remains a viable scenario."
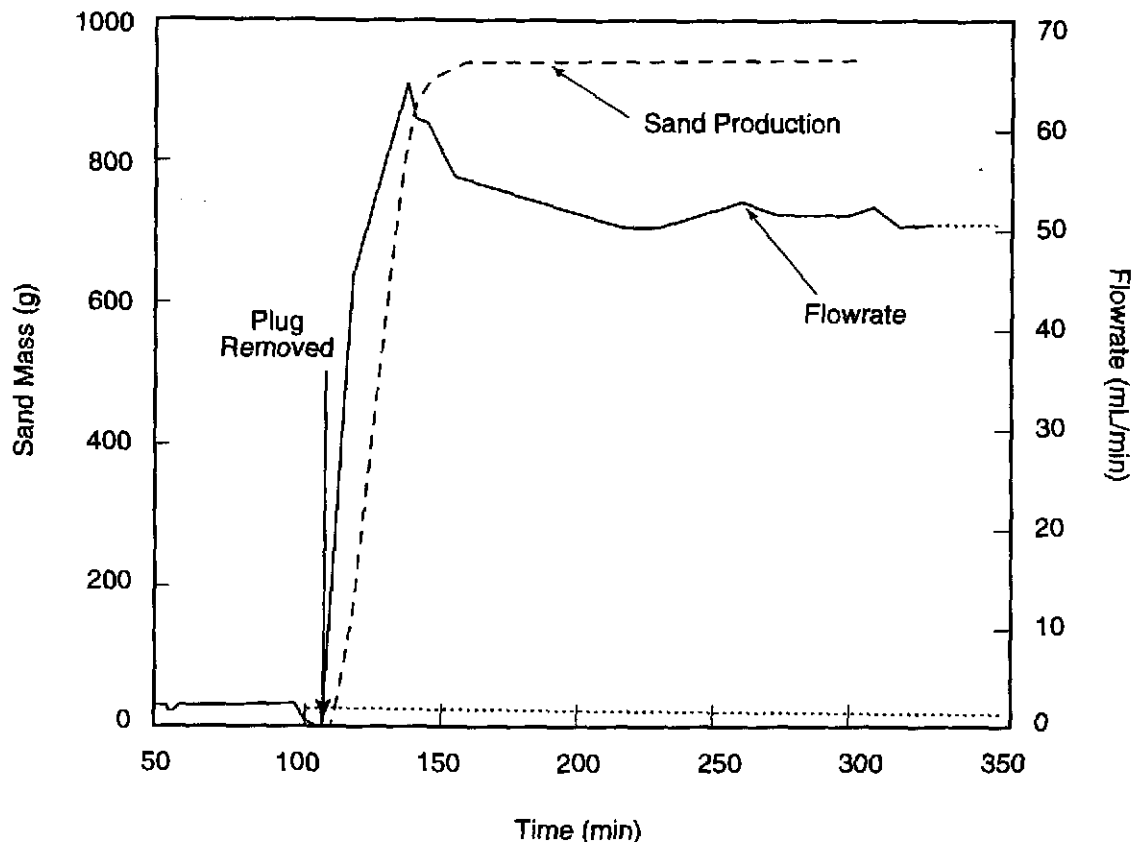
TRI-6121-408-0

Figure 5-11. Flowrate and sand production response (cumulative mass of produced sand) for Test 14 (after Vaziri et al., 1997). Boundary conditions were specifically adopted to attempt to create wormholes; sand production occurred faster and stopped sooner than in Test 15.

5.2.8 Summary

It cannot be clearly established, from analog data, if wormholes would form. If they do, the argument shown in Example 2, where there is an existing discontinuity, can be followed to imply that these structures may improve stability by offering more highly conductive channels. Tremblay et al. (1996) also showed that these channels were not voids. This implies that there will be some pressure drop along them, as flow occurs into a wellbore.

5.3 Proppant Backflow

Hydraulic fracturing is a commonly adopted methodology in the petroleum industry for increasing rate of deliverability to wells, usually performed in low or marginally permeable formations (hydraulic fracturing is also used in some high permeability formations). Viscous fluids are injected at pressures large enough to hydraulically create fractures and a highly conductive channel, with a large surface area in the reservoir. To maintain the conductivity of this fracture after pumping has stopped, proppant (commonly 20/40 Ottawa sand) is entrained in the viscous treatment fluid and remains in the created fracture after the pumping has terminated and the fracture closes. It is essential that conductivity (the product of the propped fracture width and the permeability of the proppant pack) is maintained to provide this highly conductive channel.

Erosional removal of proppant from hydraulic fractures (due to high rates of flow of gas, oil, and/or water into the wellbore during production) can occur (proppant flowback), and is a serious consideration in the petroleum industry. This analog provides some fundamental information which addresses the mobility of the proppant in seepage environments. Figure 5-12, from Asgian et al. (1994) schematically illustrates this problem.

Asgian et al. (1994) numerically modeled flowback in a simulated hydraulic fracture using the Distinct Element Method (DEM). The proppant pack was represented as an accumulation of interacting spherical solids, with Hertzian type contacts. Boundary friction against the fracture walls was incorporated as was flow through the proppant pack. The particles were a collection of elastic spheres. They were allowed to deform in shear and compression due to contact. The particles can also slide past one another when the shear stress exceeds the normal stress × the coefficient of friction (no cohesion).


TRI-6121-405-0
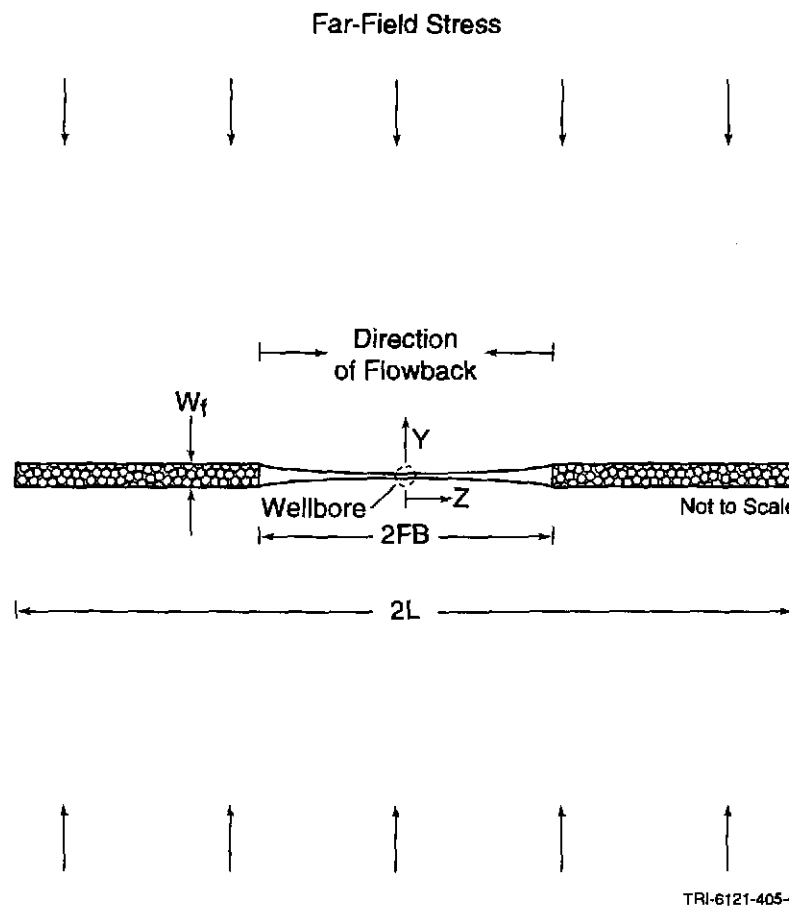
Figure 5-12. Schematic plan view of a hydraulic fracture, showing proppant packing and direction of flowback. The near-wellbore choked zone has a reduced conductivity and impairs future production. If the fracture closes completely on itself near the wellbore, conductivity reduction can occur (after Asgian et al., 1994).

Asgian et al. (1994) showed that drawdowns of 150 psi/ft were sufficient to mobilize particles in a fracture. "For a drawdown of 150 psi/ft ... , the average radial (compressive) grain-to-grain force is 0.478 lb, whereas the drag force is equal to 7.9×10^{-5} lb (0.016% of the average radial force)." This very small drag force was sufficient for destabilization. These authors found that the proppant pack in fractures propped with cohesionless, unbonded proppant is inherently unstable for fracture widths greater than 5.5 mean grain diameters. A radial or spherical configuration will possibly be more stable (this was for a linear feature with linear flow).

Proppant flowback seemed to offer some level of similarity to seepage situations in channels, if any, venting into the wellbore at the WIPP site. There were some approximate presentations of the gradients required to cause arch collapse and movement of the proppant to the sink. The analogy to the WIPP site is difficult to develop because the mechanics are dependent on geometric configuration, particle size, and particle size distribution, none of which are adequately known to develop meaningful conclusions.

5.4 Dynamic Openhole Cavitation

The closest analog to repository penetration is the procedure of dynamic openhole cavitation, adopted for stimulating coalbed methane reservoirs. It is not asserted that coal, *as a material*, is analogous to surrogate waste. When surrogate properties are compared to the coalbed methane properties that have been used in coupled numerical models, analogous behavior can be inferred. The models are based on implementation of stresses, cohesion, angle of internal friction, and permeability, properties that are available for WIPP site surrogate material. Methane recovery from coal is encouraged by deliberately increasing the wellbore diameter. In conjunction, the peripheral permeability also increases. Hole enlargement and permeability enhancement are accomplished by air injection (at pressures below those required to fracture the well), followed by rapid surging (blowdown) of the well. This operation is characteristically repeated many times a day for ten to fifteen days. According to Khodaverdian et al. (1995):

"Cavitation, or the creation of an enlarged openhole across the completion interval of a coalbed methane well, has produced spectacular results in the prolific "fairway" region of the San Juan Basin. Cavity completions in this region generally produce at rates several times greater than analogous, hydraulically fractured wells. Some produce 10 MMcfd from depths of 3000 feet and a gross coal thickness of only 40 feet. Outside of this fairway, however, cavity-completed wells have not been as effective as hydraulically fractured wells. Understanding the reason for this difference is an important objective for maximizing production from coalbed methane wells in the San Juan Basin and nationwide....

"Historically, coalbed methane reservoirs have been stimulated either by hydraulic fracturing or cavitation. Cavitation, sometimes called dynamic open-hole completion, employs a series of surging cycles to create a cavity across the completion interval and stimulate production. The typical post-drilling cavitation sequence of surging, clean-out, and production testing is carried out over a 10- to 15-day period.

"Two variations on the surging process are typically carried out: natural surging and injection surging. During natural surging, the well is shut-in before being abruptly opened up for blowdown. With injection surging, air is injected between blowdowns, sometimes combined with water, to help in the coal dislocation process.

"After the injection period, a surface valve is opened and the pressure is rapidly and violently released. Fluids, gas, air and coal [sic, if cavitation occurs] are produced to a pit. This procedure of injection and

surging is repeated until the wellbore becomes full of coal and shale and must be circulated clean. Typically, 20 to 30 injections are performed during the cavitation process."

During these blowdown operations, the stress concentrations around the wellbore commonly lead to plastic failure for a finite radius around the wellbore. Even though yield has occurred, the plastic zone retains some load-bearing capacity. However, because of its reduced ability to carry load, the *in situ* stresses are transmitted to stronger rock away from the wellbore (see Figure 5-13). The result of these injection-surge operations is a permanently deformed zone with a reduced capacity to carry load and to resist hydraulic drag forces. Depending on the radial position and the dilatant nature of the reservoir rock, permeability may or may not be increased. *The primary factor governing the extent of the plastically yielded zone is its cohesion.*
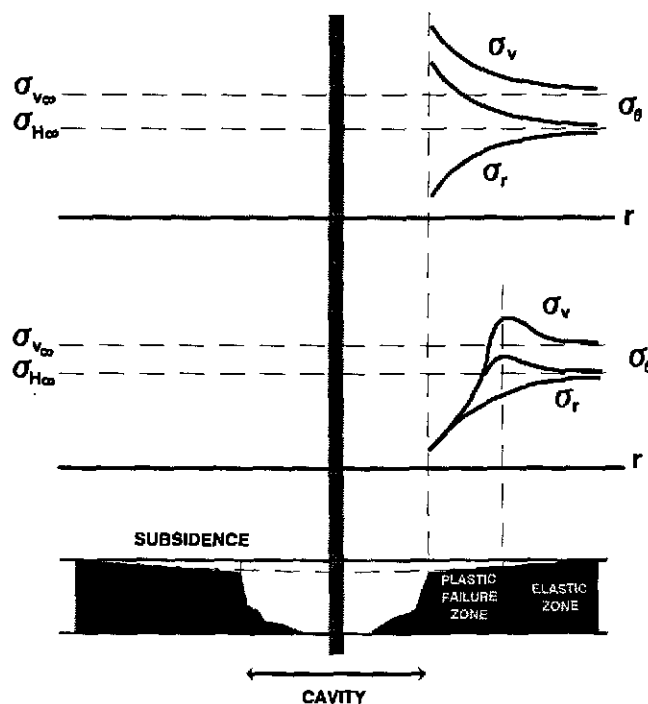

Figure 5-13. Schematic representation of reduced levels of stresses accompanying cavitation operations. Upper panel shows elastic solutions, indicating high stress levels near the wellbore. Middle panel shows reduced stress levels near the wellbore, caused by the reduced load-bearing capacity of the yielded formations. Stresses are transmitted away from the wellbore. Lower panel is a schematic of the near-wellbore region. Subsidence is not expected to be a factor at the WIPP site for spall releases.

The physical cavity occurs inside the plastic zone. Extensile stresses lead to cavity formation. The extent of cavity can be roughly approximated by some of the simpler equations shown previously (refer to Figure 5-13). However, the complexity of the environment has generally required numerical modeling. *Cavitation operations in coalbed methane wells have been very successfully modeled using finite element methodologies.* The computer program used is similar to that presented by Vaziri and Byrne (1990). Figure 5-14 is a comparison of the model

predictions against a closed-form solution (using Risnes et al., 1983). The model predictions have also been validated against cavity sizes in coalbed methane reservoirs determined by logging the wellbores with sonar calipers. Results are summarized in a number of publications (e.g., Khodaverdian, 1996). A good summary is presented by Palmer and Vaziri (1995). These authors stated:

"The numerical model that was employed for this study, called ENHANS, uses a finite-element technique to solve the fully coupled flow and stress formulations. This model was adapted from an unconsolidated sand model. Both compressible gas and liquid flow can be modeled, but not as a mixture. Flow is assumed to be single-phase. The model tracks changes in permeability due to changes in stress and/or volumetric strain, and allows for the development of cavitation when tensile failure occurs."

Palmer and Vaziri (1995) presented results for a *one-step* blowdown. Specifically, they modeled a coalbed methane reservoir, subjected to one instantaneous cycle of pressure reduction to zero. The reservoir parameters that were adopted are shown in Table 5-3. Comparative properties for the WIPP site are also shown in this table.
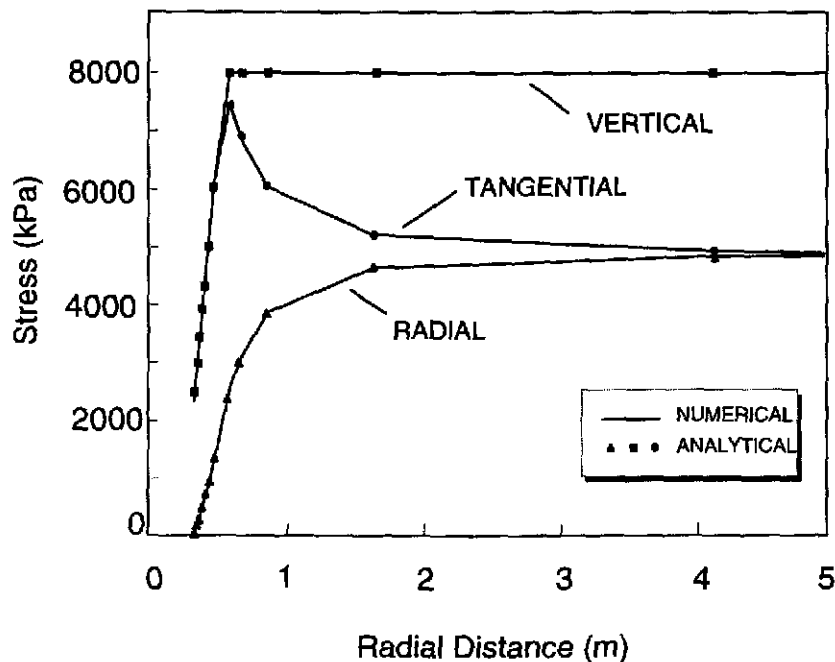

Figure 5-14. Comparison of the predictions of the numerical model ENHANS with a closed form solution.

Table 5-3. Properties of a Characteristic Coalbed Methane Reservoir Used in
Single Cycle Surge Modeling (after Palmer and Vaziri, 1991)

Parameter	Coalbed Methane Reservoir	WIPP Site	Comments
Depth (m)	762	655	Depths are relatively comparable.
Pore Pressure (MPa)	8.97	14.8	Under the most extreme circumstances, the initial reservoir pressure at the WIPP is higher than for that modeled in a representative coalbed methane scenario.
Total Vertical Stress Gradient (kPa/m)	22.6	22.5	Nominally identical.
Total Vertical Stress, Remote from the Wellbore (MPa)	17.2	14.8	The differences only reflect the differences in depth.
Initial Effective Vertical Stress, Remote from the Wellbore (MPa)	8.23	0	Effective stress is determined by subtracting pore pressure from total stress.
Total Horizontal Stress Gradient (kPa/m)	18.3	22.5	
Total Horizontal Stress, Remote from the Wellbore (MPa)	14.0	14.8	Coincidentally, the two values are nearly the same.
Initial Effective Horizontal Stress, Remote from the Wellbore (MPa)	5.03	0	Effective stress is determined by subtracting pore pressure from total stress.
Wellbore Radius (m)	0.3048	0.1556	The larger hole may be initially more stable. This is presuming a radial geometry, rather than a spherical geometry, more likely at the WIPP site. The spherical geometry will be more stable.
Bottomhole Pressure (MPa) (for simulation purposes at $t = 0^-$)	0	8	The 8 MPa value at the WIPP site changes as gas is discharged and mud is removed from the wellbore.
Pressure Drop at $t = 0^+$ (MPa).	8.97	6.8	Even though the effective stresses are lower at the WIPP site, the instantaneous pressure drop (and the accompanying gradients) are higher in the coal situation over the most critical short-time period of flow.
Distance to the outer boundary (m)	182.9	17.1	
Permeability (m^2)	1×10^{-14}	5.2×10^{-14}	Higher permeability at the WIPP site will afford greater stability.
Initial Gas Density (kg/m^3)	76.99 (at 8.97 MPa)	10.5894 (at 14.8 MPa)	Methane is substantially heavier. This will contribute to higher Reynolds numbers for the methane.
Gas Viscosity (Pa·s)	10×10^{-6}	9.32×10^{-6}	Viscosities are very similar.
Young's Modulus (MPa)	345	354	The values of modulus are almost identical.

Table 5-3. Properties of a Characteristic Coalbed Methane Reservoir Used in
Single Cycle Surge Modeling (after Palmer and Vaziri, 1991)

| Parameter	Coalbed Methane Reservoir	WIPP Site	Comments
Angle of Internal Friction (°)	27	44	The very high angle of internal friction makes the WIPP material more stable. This is shown (by analogy) in Figure 5-3.
Cohesion (MPa)	0.0010345 – 0.20689	0.13	Parametric analyses were done for the coal data. The WIPP data are bracketed by the analyses.

*The material properties of the coal used in the simulations and the surrogate waste at the WIPP
site are very similar.* This is shown in Figure 5-15, which is a common representation of the
potential for failure. If the shear stresses in a material fall on or above a failure locus in this type
of plot, failure will occur. The figure shows that, at higher normal stress levels, the surrogate
material is actually stronger than the coal used in the simulations performed by Palmer and Vaziri
(1995). At low effective stress levels, the similarities are remarkable. The major difference
between the two situations lies in the magnitudes of the initial effective stress conditions. After
initiation of flow (very quickly), this will not be an issue of great importance because:

- Depending on the pressure regime during mud expulsion, the pressure gradients controlling
  extensile failure will quite possibly be higher in the coalbed methane simulations. The
  gradient, not the magnitude of the reservoir pressure, controls failure.

- Permeability in the coalbed methane simulations was lower, leading to larger pressure
  gradients in the reservoir than would occur at the WIPP site for an equivalent pressure drop.

The numerical findings of Palmer and Vaziri (1995), with cohesion as a variable, are shown in
Table 5-4. Two scenarios are shown. The first involved no depressurization (i.e., what happens
to the wellbore if a hole is drilled but the pressure is not reduced below the original mud pressure
of 8.97 MPa). The second simulation involved instantaneous depressurization (instantaneous
reduction of the bottomhole pressure to zero). Pseudo-instantaneous flowrate is shown for the
fully depressurized case. This is a bottomhole production rate. Note that the original wellbore
radius is 0.3048 ft. Cavity growth is only forecast for radii larger than this value.

Table 5-4. Variation of Created Cavity Radius and Created Plastic Zone for No Depressurization
and for Full Depressurization (after Palmer and Vaziri, 1995)

Cohesion (MPa)	No Depressurization		Full Depressurization		
	Cavity Radius (m)	Plastic Zone Radius (m)	Cavity Radius (m)	Plastic Zone Radius (m)	Flowrate ($m^3/s/m$)
1.034×10^{-3}	0.6096	9.144	~1.524	15.09	0.0798
0.1034	0.3048	Not reported	0.3048	3.875	Not reported
0.207	0.3048	Not reported	0.3048	2.72	0.0093
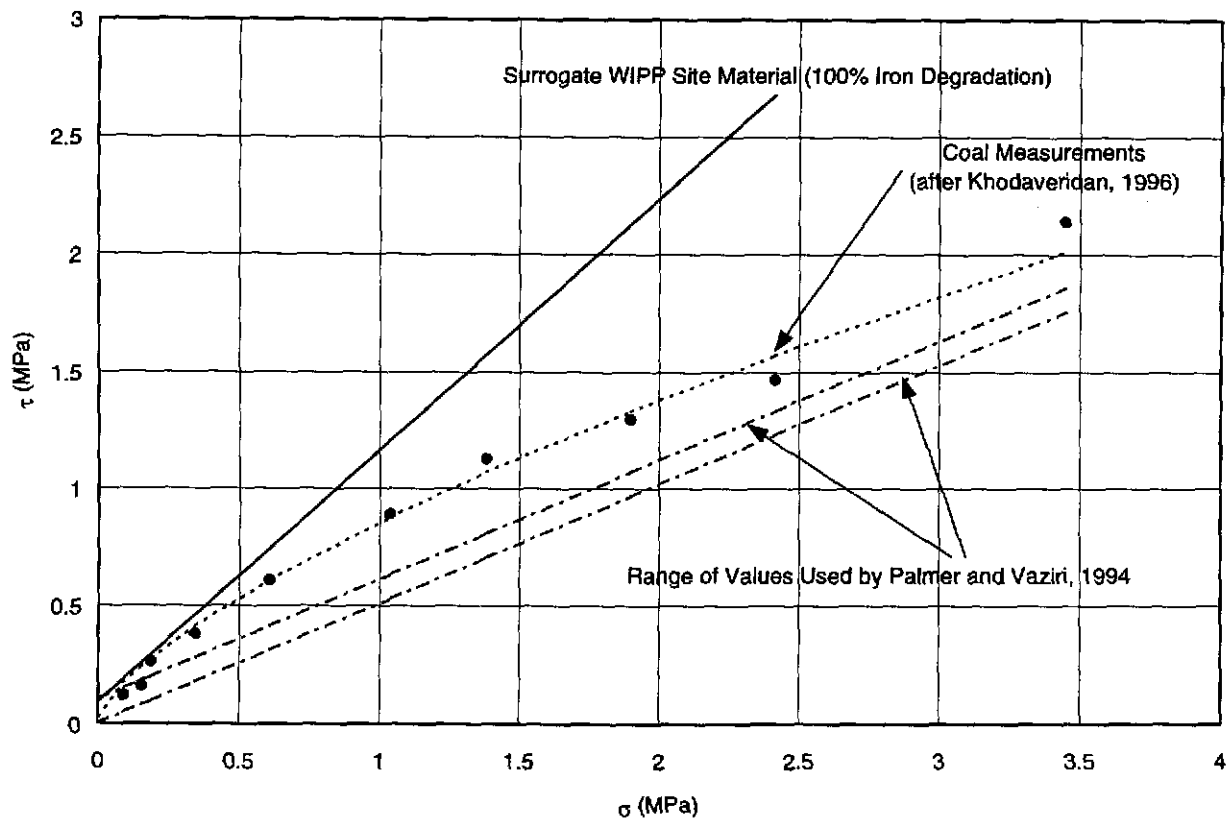
Figure 5-15. Mohr envelopes designating failure locii for coal and for a surrogate waste material. Coal data are from Khodaverdian, 1996. Coal cleating was considered in the development of the failure locus for coal. Shear testing, along face and butt cleat surfaces, was carried out to develop the envelope at low effective normal stresses.

- Table 5-4 shows that for sophisticated numerical simulations on a similar material (San Juan Basin coal), a penetrating wellbore, subjected to an instantaneous pressure drop of 8.97 MPa., did not increase beyond its original drilled radius of 0.3048 m, when the cohesion was 0.1034 MPa. WIPP site cohesion, based on linear regression on wet data for Recipes 2, 4, and 5, was found to be 0.13 MPa. This suggests that, with the cohesion at the WIPP site, cavitation will not occur.

- The model making these predictions was calibrated and validated against known solutions and against sonar caliper logs of actual cavities created in low cohesion seams.

- This model explicitly and intimately coupled flow, deformation, and failure.

- Most simple failure analyses only indicate the initiation of failure. This sophisticated modeling represents failure initiation and progressive cavity evolution. It clearly suggests that in a situation which is very similar to what would exist for unplanned intrusion into the repository, cavity growth will not occur for values of cohesion approximately equal to 0.1 MPa. The inferred cohesion of WIPP surrogate material is in the neighborhood of 0.13 MPa, at the very least. Note that the angle of internal friction used in these simulations was 27°. This is dramatically less than the value of 44° measured for the surrogate material.

- Much of the recorded field data reflect progressive cavity evolution as a result of multiple injection and surging cycles, where additional material is removed with each cycle. The simulations shown here represent a single cycle.

- The coalbed methane models have been calibrated against measured cavity dimensions, using sonar calipers. These measured dimensions were the consequence of multiple injection and blowdown cycles, with the exception of the data presented by Palmer and Vasiri (1994), which were numerical. The models have also been calibrated against closed form solutions. Note particularly that the large volumes in published literature are for multiple cycles and were matched for cohesions of approximately 3 psi, substantially less than what is indicated for saturated surrogate material. Production matching and pulse permeability (interference testing) were also used to verify the numerical model. Validation is documented in Khodaverdian (1996).

5.5 Summary

After evaluating published data from various engineering disciplines, several situations from the petroleum industry were selected for further evaluation as analogs to the spall of waste. These included wellbore stability during drilling, the production of formation particulates during depletion/production of the reservoir itself, the flowback of proppant from hydraulic fractures, and dynamic openhole cavitation of coalbed methane seams.

The cavitation of wellbores in coalbed methane reservoirs offers the strongest analog. The basis of this assertion is the similarity in the process of rapid pressure drop as well as material properties comparable to those at the WIPP site. The material properties of coal in the San Juan Basin of New Mexico and Colorado, where cavitation is most commonly attempted (it is successful only in parts of this basin because cohesion prevents cavity growth), and the surrogate waste material for the WIPP site are remarkably similar. Material properties of the surrogate waste material possess strength properties sufficient to preclude cavity development and growth based on analogous industrial experience.

Cavitation of coalbed methane reservoirs, sometimes called dynamic openhole cavitation, employs a series of surging cycles to create a cavity across the coal zone. Two variations on the surging process are typically carried out: natural surging and injection surging. During natural surging, the well is shut-in (a valve is closed at the surface), before being abruptly opened for blowdown. During this blowdown period, gas, air, and sometimes solids are violently ejected. This process is repeated numerous times over a ten to fifteen day period. This analog has direct relationship to the WIPP because of the similarity in the material properties of coal to those for the WIPP surrogate materials, as well as because of the similar pressure conditions and the fact that gas is the flowing fluid. Differences include the rapid, intentional depressurization of the coal seams compared to the somewhat slower depressurization expected at the WIPP because of mud blowout. Other differences include the fact that only one surging cycle is represented at the WIPP site, whereas multiple surging and shut-in cycles (and/or injection) are imposed in coalbed methane cavitation situations (typically 20 to 30 cycles).

Documented mechanical properties from coal are presented and compared with the WIPP site surrogate data. Public domain, numerical simulation data for single cycle (only one surge and instantaneous pressure reduction) are also presented. These published simulations were performed with one of the petroleum industry's most advanced, fully coupled flow and

deformation models (originally developed for modeling unconsolidated oil sands in Alberta). Single phase, transient gas flow was represented. The model tracked changes in permeability resulting from changes in stress and/or volumetric strain, and allowed for the development of cavitation when tensile failure occurred. The input data and boundary conditions for these coalbed simulations are compared with the WIPP site conditions.

The published results for this analogous coalbed methane situation indicated no increase in the original wellbore dimensions as a consequence of instantaneous pressure reduction, for cohesion greater than 0.1 MPa. The cohesion of the WIPP site surrogate material exceeds this limiting value. This analog strongly suggests that the cohesive strength of WIPP degraded waste will prevent cavity growth and will prevent the creation of spalled material with depressurization of the wellbore.

A consideration of analogs from evaluations of sand production and wellbore stability has shown that the methods used in the semi-analytic studies reported elsewhere are appropriate, and have highlighted the relevance of several parameters, including cohesion and the effects of capillary tension. In addition, these analogs have highlighted the essential conservatism of most analytic approaches based on continuum mechanics. As noted by Fairhurst (1990), these analytic models commonly underestimate the integrity of the formation, and thus will tend to overestimate spall releases. As shown by many other studies, this is especially true when linear elastic methods are used and nonlinear effects and plasticity are ignored. An evaluation of various analogs from petroleum engineering has allowed the semi-analytic methods used to be validated, and has enabled additional estimates of releases to be made. These estimates bound or are reasonable.

5.6 References

Asgian, M.I., Cundall, P.A. and Brady, B.H.G.: "The Mechanical Stability of Propped Hydraulic Fractures: A Numerical Study," paper SPE 28510 presented at the 1994 SPE Annual Technical Conference and Exhibition, New Orleans, September 25-28.

Bratli, R.K., Horsrud, P. and Risnes, R.: "Rock Mechanics Applied to the Region near a Wellbore," *Proc.* 5th Intl. Cong. Rock Mechanics (1983) F1-F17.

Bratli, R.K. and Risnes, R.: "Stability and Failure of Sand Arches," *SPEJ* (April 1981) 236-248.

Chan, D.Y.C., Hughes, B.D. and Paterson, L.: "Tensile Stresses Around Boreholes due to Transient Fluid Flow," (1991).

Fairhurst, C.: "General Report: Deformation, Yield, Rupture and Stability of Excavations at Depth in Rock," *Rock At Great Depth*, V. Maury and D. Fourmaintraux (eds.), Balkema, Rotterdam (1989) 1103-1114.

Fletcher, P.A., Montgomery, C.T., Ramos, G.G., Miller, M.E. and Rich, D.A.: "Using Fracturing as a Technique for Controlling Formation Failure," paper SPE 27899 presented at the 1994 SPE Western Regional Meeting, Long Beach, CA, March 23-25.

Khodaverdian, M.F.: "Cavity Completions for Enhanced Coalbed Methane Recovery," Final Report GRI-95/0432, Contract No. 5091-214-2220, Gas Research Institute, Chicago, IL (June 1996).

Khodaverdian, M., McLennan, J. Palmer, I. and Vaziri, H.: "Coalbed Cavity Completion Analysis Suggests Improvements," GasTIPS, Gas Research Institute, Chicago, IL (Winter 1995/1996).

LeBlanc, J.L. and Lewis, R.: "A Mathematical Model of a Gas Kick," *Drilling,* Reprint Series, SPE of AIME, Dallas, Texas (1973) **6a**, 78-88.

Morita, N., and Boyd, P.A.: "Typical Sand Production Problems: Case Studies and Strategies," paper SPE 22739 presented at the 1991 Annual Technical Conference and Exhibition, Dallas, TX, Ocotober 6-9.

Morita, N., Whitfill, D.L., Massie, I. And Knudsen, T.W.: "Realistic Sand Production Prediction: Numerical Approach," paper SPE 16989 presented at the 1987 Annual Technical Conference and Exhibition, Dallas, TX, September 27-30.

Morita, N.: "Field and Laboratory Verifications of Sand Production Prediction Models," paper SPE 27341 presented at the 1994 SPE International Symposium on Formation Damage Control, Lafayette, LA, February 7-10.

Nawrocki, P.A. and Dusseault, M.B.: "Modeling of Damaged Zone Around Openings Using Radius-Dependent Young's Modulus," *Rock Mechanics and Rock Engineering* (1995) 28 (4), 227-239.

Nawrocki, P.A., Dusseault, M.B. and Bratli, R.K.: "Addressing the Effects of Material Non-Linearities on Wellbore Stresses Using Stress-and Strain-dependent Elastic Moduli," *Rock Mechanics,* Daemane and Schultz (eds.), Balkema, Rotterdam (1995) 819-824.

Palmer, I.D. and Vaziri, H.H.: "Modeling of Openhole Cavity Completions in Coalbed Methane Wells," paper SPE 28580 presented at the 1994 Annual Technical Conference and Exhibition, New Orleans, LA, September 25-28.

Papanastasiou, P., Thiercelin, M., Cook, J. And Durban, D.: "Behavior and Stability Analysis of a Wellbore Embedded in an Elastoplastic Medium," *Rock Mechanics,* Nelson and Laubach (eds.), Balkema, Rotterdam (1994) 209-216.

Schurman, G.A. and Bell, D.A.: "An Improved Procedure for Handling a Threatened Blowout," *Drilling,* Reprint Series, SPE of AIME, Dallas, Texas (1973) **6a**, 89-96.

Tremblay, B., Sedgwick, G. and Forshner, K.: "Imaging of Sand Production in Horizontal Packs by X-ray Computed Tomography," *SPE Formation Evaluation* (June 1996) 94-98.

Vaziri, H.H., Phillips, R. and Hurley, S.: "Physical Modelling of Sand Production," Int. J. Rock Mech. & Min. Sci., **34:3-4**, Paper No. 323 (1997).

Vaziri, H.H. and Byrne, P.M: "Analysis of Stress, Flow and Stability Around Deep Wells," *Géotechnique* (1990) **40**, No. 1, 63-77.

Vaziri, H.H.: "Numerically-Derived Stress, Strain and Thermodynamic Properties of Athabasca Oil Sand," paper CIM/SPE 90-26 (preprint) presented at the 1990 CIM/SPE International Technical Meeting , Calgary, Canada, June 10-13.

Veeken, C.A.M., Davies, D.R., Kenter, C.J. and Kooijman, A.P.: "Sand Production Prediction Review: Developing an Integrated Approach," paper SPE 22792 presented at the 1991 SPE Annual Technical Conference and Exhibition, Dallas, TX, October 6-9.

Wang, Y. and Dusseault, M.B.: "Borehole Yield and Hydraulic Fracture Initiation in Poorly Consolidated Rock Strata - Part II. Permeable Media," *Int. J. Rock Mech. Min. Sci. & Geomech. Abstr.* (1991a) **28**, No. 4, 235-246.

Weingarten, J.S. and Perkins, T.K.: "Prediction of Sand Production in Gas Wells: Method and Gulf of Mexico Case Studies," paper SPE 24797 presented at the 1992 Annual Technical Conference and Exhibition, Washington, DC, October 4-7.

6.0 CONCLUDING REMARKS

The purpose of this study has been to develop a mechanistic conceptual model for the spalling process and to predict spall volumes under conditions that are relevant to the WIPP repository. The conceptual model is based on a detailed analysis of the relevant physical processes during a borehole intrusion, including the ejection of drilling mud immediately following the intrusion and the subsequent blowdown of high pressure gas from the repository. The spall volumes have been estimated with a semi-analytic methodology called the cavity growth model. The results from this model have been corroborated with numerical calculations based on the TOUGH28 and SPECTROM codes, with an analog to coalbed methane production, and with a quasi-static semi-analytic methodology. The range of values for the tensile strength and Poisson's ratio, which are key input parameters for all calculations, are based on experiments conducted on analogs of fully and partly degraded WIPP waste.

The predicted spalling volumes from the cavity growth model demonstrate that the spall volumes in the Compliance Certification Application (CCA) are conservative because:

- The maximum spalling volume from the cavity growth model is 0.25 m^3. This maximum value is at least a factor of two less than any spalling volume in the CCA, which ranges from 0.5 to 4.0 m^3.
- The frequency of nonzero spalling events is much smaller for the cavity growth model than for the CCA. The cavity growth model predicts zero spalling volume for repository pressures of 8 MPa to approximately 14 MPa, while the CCA model predicts at least 0.5 m^3 for all spalling events above 8 MPa repository pressure.

The conceptual model, mathematical model, and numerical implementations are based on many conservative assumptions, which are discussed below.

The preceding sections have described the results of idealized calculations that were made to evaluate the processes potentially leading to spall releases and to estimate bounding values for the volumes of these releases. Of necessity, these calculations included a number of assumptions made to simplify and make tractable the problem at hand. These assumptions are based on our best understanding of the nature of the relevant processes. To the extent possible these assumptions were chosen to maintain the realism of the description of the system: where the assumptions tend to deviate from realism they were chosen to overestimate the consequences of an intrusion.

The validity of the various assumptions varies with the nature of the calculations. This is particularly true when considering the calculations made at different pressures. Thus at relatively low gas pressures, where the initial effective stresses are compressive, the calculations are much less sensitive to the assumptions than at high initial pressures, where the effective stress is close to zero. Some of the most significant assumptions are discussed briefly below.

Constitutive Behavior of the Waste: The bulk of the calculations assume linear elastic material behavior for the waste, this assumption being made because of the simplicity of the resulting constitutive relationship and its amenability to application in closed form solutions. All the available information on the likely waste properties show that the

material will exhibit nonelastic behavior, which may be expected to reduce the severity of the stresses imposed by the wellbore intrusion. The assumption of elasticity, then, tends to overestimate the severity of induced stresses and thus to overestimate the potential spall volumes.

Failure Criterion/Mechanism: In the simplest cases (especially in the quasi-static cases) the simplifying assumption can be made that tensile failure of the waste leads inevitably to removal of material. However, this will not always be the case. Tensile failure of the waste will lead to the development of discrete failure planes. Near the wellbore these planes may join to form a fractured medium that can in fact be removed by gas flow out of the waste at elevated velocities. However, where these failure planes are internal to the waste, as they are calculated to be in many cases, they may not produce material that can be easily removed. In such a case, interior zones of fractured material may be sheltered from the borehole by zones of unfractured material where the tensile stresses are lower or the stress is compressive. Zones such as these will lead to a transfer of stress and a mitigation of the stress concentrations. This effect is well known in underground structures and is illustrated in the results of the limited tension cases reported in Section 4.

Waste Heterogeneity: Throughout most of the calculations reported here, the assumption is made that the waste is homogeneous, although this is unlikely to be the case. The effect of heterogeneity in terms of the pressure profiles was shown in Section 4.3 to result in strong modification of the geometry of the pressure field and/or modification of the values of pressure gradients. Waste heterogeneity will also significantly modify the response of the waste to imposed stresses. In particular, the waste will likely comprise blocky materials that will stabilize against movement of finer materials and also be difficult to transport if they are isolated by tensile failure planes.

Mechanical Properties of the Waste: Certain assumptions are made regarding the mechanical properties of the waste materials, in particular with respect to their strength and deformation properties. Throughout the calculations, 10 psi was taken as the "base" value for strength at lower pressures, and 15 psi was used for higher pressure, dry conditions. Both these values are based on laboratory testing of the surrogate materials. A strength of 10 psi was the mean value for saturated materials, while 15 psi is a low value for dry waste. Tensile strength of dry surrogate wastes was greater than 20 psi, and that of sand with precipitated salt was 50 psi. A strength of 10 psi is clearly a lower bound value under nearly dry conditions, while calculations indicate that strengths of the order of 20 psi will prevent failure.

The bounding release volumes predicted here are based on values calculated using the cavity growth method for implementation of the mechanical conceptual model. As discussed in Section 3, this implementation uses an elastic constitutive relationship with a tensile failure criterion, which accounts for the effects of a growing spall cavity. Experimental results indicate that the waste is nonelastic, and the use of a linear elastic constitutive relationship will lead to overestimation of cavity failure volumes. In summary, the spall volumes are conservative because of conservative simplifying assumptions made in the calculational method and the use of a bounding, weak waste strength.

Calculated volumes are included in the following table and in Figures 6-1 and 6-2.

Table 6-1. Cavity Radii and Release Volumes from the Cavity Growth Semi-Analytic Implementation of the New Conceptual Model for Spallings as a Function of Repository Pressure and Waste Strength

Initial Gas Pressure (MPa)	Tensile Strength (psi)	Tensile Radius (m)	Uncompacted Volume (m^3)
12		0.156	0
	10	0.156	0
	15	0.156	0
14	5	0.37	0.19
	10	0.21	0.02
	15	0.156	0
14.3	10	0.28	0.07
	15	0.20	0.02
	20	0.156	0
14.5	10	0.33	0.13
	15	0.23	0.03
	20	0.156	0
14.6	10	0.35	0.16
	15	0.24	0.04
	20	0.156	0
14.7	10	0.37	0.19
	15	0.26	0.06
	20	0.18	0.01
14.8	10	0.40	0.25
	15	0.27	0.07
	20	0.21	0.02

Figure 6-1. Decrease in potential spall volume resulting from strength increase (<14 MPa).
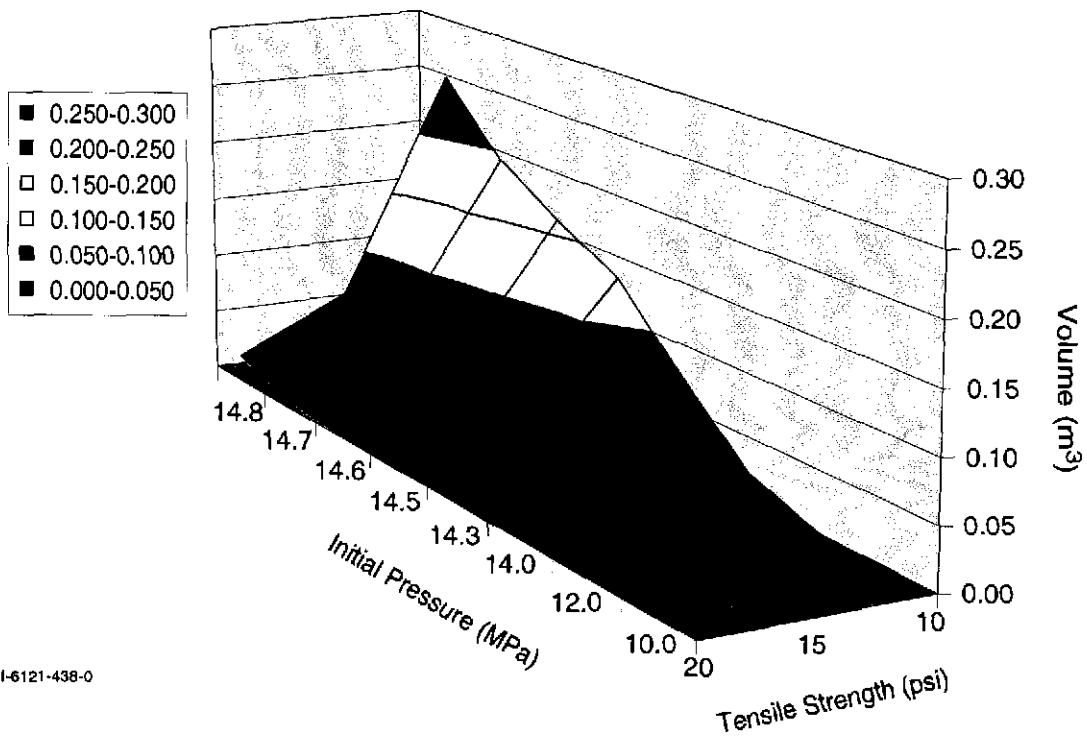

TRI-6121-438-0

Figure 6-2. Decrease in potential spall volume resulting from strength increase (>14 MPa).

6-4

Appendix A
Rationale for Waste-Surrogate Strength Experiments

date: 3 March 1997

to: Frank D. Hansen, MS 1322 (Org. 6121)
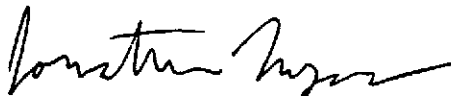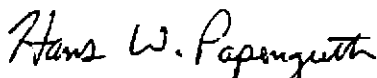
from: Hans W. Papenguth, MS 1320 (Org. 6832) and Jonathan Myers (IT Corporation)

subject: Rationale for Waste-Surrogate Strength Experiments

An important release path for the Waste Isolation Pilot Plant (WIPP) is spallings, which is actinide-bearing particulate material entrained in pressurized gas immediately following a drilling penetration, and transported up the intrusion borehole. The extent of spallings release is dependent on several repository-specific factors, particularly gas pressure and characteristics of the waste (e.g., strength and particle sizes). Gas pressures in the WIPP are produced by the evolution of hydrogen, and perhaps methane, as ferrous and some non-ferrous metals are corroded; and by microbial degradation of cellulosic, plastic, and rubber waste constituents.

Several processes combine to indurate the waste. First, is compression by inward creep of the Salado salt. Room closure during the operational period of some 35 years, plus 100 years of institutional control allow for significant room closure before the possibility of an inadvertent human intrusion. In addition, gas generation is a relatively slow process compared to closure by salt creep. Therefore, the waste will be compacted to a thickness of two meters or less prior to the first intrusion. Halite deformation enhanced by pressure solution, requiring only a small amount of moisture, will result in some encapsulation and cementation of some waste constituents near the edges of waste stacks. This is verified by experience and observations in old salt mine workings in which small objects are observed to be completely encapsulated after several hundred years. In addition to cementation caused by plastic and brine-aided deformation of surrounding WIPP salt, several chemical drivers exist for precipitation of halite and other evaporitic salts from Salado brine. The corrosion of iron and aluminum requires water as a reactant, and brine dewatering will result in precipitation of salts. Similarly, hydration of MgO-backfill material will result in salt precipitation.

This memorandum develops the linkage between waste inventory and physical and chemical processes necessary to quantify appropriate surrogate materials for degraded waste experiments supporting spall modeling. The constitutive behavior of the waste will determine the potential to fail and to transport waste to the wellbore. This memorandum describes the rationale for the construction of surrogate WIPP waste material appropriate for mechanical testing.

The basis for this memorandum was developed in a series of meetings held at Sandia, and represents the ideas of a large number of individuals. The work described herein is authorized through an Expedited CCA Activity Request initiated by Margaret Chu, dated 12/13/96, in accordance with Sandia WIPP Quality Assurance Procedure 9-6.

It is important to note that the surrogate waste being specified does not represent the expected average waste condition, but rather the extremes in waste conditions. The selection of extremes is based on demonstrable concepts: Wet waste is weaker; spall is increasingly likely as pressure increases; high pressure requires that microbial degradation occurs; brine inflow is required for high pressures to be attained; corrosion leads to smaller average particulate sizes; and salt precipitation is accompanied by corrosion and microbial degradation. In the remainder of this memorandum, we discuss the repository conditions likely to produce the greatest spallings release, materials to simulate degraded WIPP waste, and quantification of the amount of salts that would be chemically precipitated by corrosion and MgO-backfill hydration reactions to add to the surrogate waste.

1.0 Test Scenarios

The magnitude of a spallings release is greatest under conditions of high gas pressure and low waste strength. In this section, we discuss temporal changes in the repository and waste and define realistic test scenarios consistent with results of the Compliance Certification Application (CCA) performance assessment (PA) calculations.

1.1 Repository Gas Pressure

In the CCA PA calculations, many intrusion scenarios occur during the 10,000-year performance period of the repository. Analysis of the results of the CCA PA calculations shows that gas pressures at the first intrusion are much higher than subsequent intrusions. Once the first intrusion has occurred, subsequent gas tends to vent through the abandoned borehole. Because Rustler and Castile Formation brines can only enter the repository through intrusion boreholes, use of Salado Formation brine is the most relevant.

Gas will be produced in the repository by three processes: Corrosion of iron-bearing materials; microbial degradation of cellulosics; and microbial degradation of plastic and rubber. The probability that these processes will occur is a sampled parameter in the CCA PA calculations. In the calculations, situations exist in which only corrosion produces gas, corrosion and cellulosic degradation produce gas, and all three processes produce gas. The greatest gas pressure is generally associated with latter situation. Finally, corrosion and microbial degradation reactions are most active in subaqueous environments.

1.2 Mechanisms for Induration of Waste

Following closure of the WIPP repository, a host of physical and chemical processes will begin concurrently, leading to degradation and induration of the waste. Shortly after a waste panel is closed, plastic deformation of the Salado Formation host rock coupled with roof collapse and floor heave, reduces the repository porosity and introduces host rock (WIPP salt) into interstices at the edges of the waste stack. Halite is an easily deformed plastic material whose deformation is manifestly enhanced by grain-boundary pressure solution. The mobility of halite will lead to further occlusion of porosity, as well as cementation, in some regions of the repository. Salado brine will slowly be introduced to the repository through brine seeps. In the presence of water, chemical degradation of the waste will occur. The corrosion of iron-bearing metals, aluminum, copper, and lead, microbial-induced destruction of cellulosic materials, and breakdown of solidification media such as Portland cement and Envirostone ($CaSO_4$ with melamine formaldehyde binder) may lead to a decrease in the grain size of the initial waste constituents. The volume of metal-bearing solids in the repository will increase, however, as a result of corrosion reactions generating solid metal hydroxides, oxides, and carbonates.

The relative timing and rates of waste degradation and induration processes have not been fully developed. It is known, however, that salt creep, as well as hydration of MgO backfill, are relatively fast processes. Precipitation of halite is kinetically favored, and consequently, halite will precipitate concurrently with MgO hydration. Similarly, halite will precipitate concurrently with iron corrosion.

Analysis of the vectors comprising the CCA PA calculations shows that, in the undisturbed repository, corrosion of iron is limited by the availability of water. In undisturbed cases, corrosion consumes up to a maximum of approximately 60 weight percent of the iron present at the end of the 10,000-year performance period. In the disturbed repository cases, in which more water is available for reaction, corrosion could conceivably consume up to a maximum of 86 weight percent of the iron present, again, at the end of the 10,000-year performance period. The amounts of iron consumed at the time of the first spallings release is significantly less than 60 and 86 weight percent, for the undisturbed and disturbed cases, respectively. For the surrogate waste materials, we assume conservative extents of iron corrosion of 50 and 100 weight percent. This is conservative because corrosion adds significantly to decreased particle size and increased gas pressure, whereas salt precipitation increases strength slightly in a saturated state.

Four cases are proposed to represent two extents of waste degradation, with and without the effects of MgO backfill. For cases 1 and 3, one-half of the iron in the WIPP waste is assumed to be corroded; the precipitated salts stemming from that corrosion are included in the waste test matrix. For cases 2 and 4, all of the iron in the WIPP waste is assumed to be corroded. Similarly, for cases 1 and 3, one-half of the cellolusics, plastic, and rubber is assumed to be degraded. For cases 2 and 4, all of the cellulosics, plastic, and rubber is assumed to be degraded. MgO backfill may add significant strength to the waste as a result of MgO-hydration reactions producing cementitious materials, as well as inducing salt precipitation from MgO hydration.

Cases 1 and 2 represent scenarios in which MgO is not included as a backfill, and therefore, MgO-induced salt precipitation is ignored. For cases 3 and 4, appropriate concentrations of MgO are included. Primary emphasis is given to determination of the appropriate amount of precipitate derived from degradation processes. Salt aggregate, to simulate salt introduced from roof fall or floor heave, may be added to some of the surrogate waste forms.

Summarizing, the four cases represent the following conditions:

1. 50 wt% of iron is corroded; 50 wt% of cellulosics, plastics, rubber are degraded; corrosion-induced salt precipitates are included; (+ roof-fall salt in some samples)
2. all iron is corroded; all cellulosics, plastics, rubber are degraded; corrosion-induced salt precipitates are included; (+ roof-fall salt in some samples)
3. 50 wt% of iron is corroded; 50 wt% of cellulosics, plastics, rubber are degraded; corrosion-induced salt precipitates are included; MgO-induced salt precipitates are included; (+ roof-fall salt in some samples)
4. all iron is corroded; all cellulosics, plastics, rubber are degraded; corrosion-induced salt precipitates are included; MgO-induced salt precipitates are included; (+ roof-fall salt in some samples)

Calculations of the amounts of salt precipitated from iron corrosion are discussed later in this memorandum.

2.0 Initial Waste Forms and Quantities

The initial characteristics of the waste anticipated for the WIPP are described in the Transuranic (TRU) Waste Baseline Inventory Reports (BIR; US DOE, 1995; 1996). The following waste categories and descriptions are taken directly from the BIR, Rev. 2 (US DOE, 1995; Note that WMP is "waste material parameter"):

Table 1.—Waste Categories and Descriptions

- Iron-base metal/alloys — This designation is meant to include iron and steel alloys in the waste and does not include the waste container materials. This also includes an iron-base metallic phase associated with any vitrification process, if applicable.
- Aluminum-base metals/alloys — Aluminum or aluminum-base alloys in the waste materials.
- Other metals/alloys — All other metals found in the waste materials (e.g., copper, lead, zirconium, tantalum, etc.). The lead portion of lead rubber gloves/aprons is also included in this category.
- Other inorganic materials — Includes inorganic non-metal waste materials such as concrete, glass, firebrick, ceramics, graphite, sand, and inorganic sorbents.

- <u>Vitrified</u> — This refers to waste that has been melted or fused at high temperatures with glass forming additives such as soil or silica in appropriate proportions to result in a homogenous glass-like matrix. (Note that any unoxidized metallic phases, if present, are included in the "iron-base metal/alloys" WMP).

- <u>Cellulosics</u> — Includes those materials, generally derived from high polymer plant carbohydrates. Examples are paper, cardboard, Kimwipes, wood, cellophane, cloth, etc.

- <u>Rubber</u> — Includes natural or manmade elastic latex materials. Examples are Hypalon®, Neoprene, surgeons' gloves, leaded-rubber gloves (rubber part only), etc.

- <u>Plastics</u> — Includes generally manmade materials, often derived from petroleum feedstock. Examples are polyethylene, polyvinylchloride, Lucite®, Teflon, etc.

- <u>Solidified Inorganic Material</u> — Includes any homogeneous materials consisting of sludge or aqueous-base liquids that are solidified with cement, Envirostone®, or other solidification agents. Examples are wastewater treatment sludge, cemented aqueous liquids, and inorganic particulates, etc. If a TRU waste site has not reported cement used as part of the solidification process in the "cement (solidified)" WMP, the density of the cement is included in this field.

- <u>Solidified Organic Material</u> — Includes cemented organic resins, solidified organic liquids, and sludges.

- <u>Cement (solidified)</u> — Includes the cement used in solidifying liquids, particulates, and sludges. If for a solidified final waste form this field is left blank, it means that either cement is not the solidifying agent or that the cement is included in the "solidified inorganic material" WMP.

- <u>Soils</u> — Generally consists of naturally occurring soils that have been contaminated with inorganic radioactive waste materials.

The packaging materials for contact-handled (CH) waste are:

- <u>Steel</u> — The weight of the steel part of the packaging from container information provided by the TRU generator/storage sites. Any necessary overpacking is included in the weight.

- <u>Plastic</u> — The weight of any plastic packaging submitted by the TRU site. When weight of a rigid liner is not given a 90-mil HDPE (high-density polyethylene) liner is assumed.

The relative proportions of the CH-TRU waste constituents are compiled in the BIR, Rev. 3 (US DOE, 1996, first two columns below are from Table 2-2), and summarized below in Table 2:

Table 2.—Waste Concentrations

Waste Category	Inventory, average (kg/m^3)	Inventory without MgO backfill (weight %)	Inventory with MgO backfill (weight %)
iron-base metal, alloys	170	22%	14%
steel container material	139	18%	12%
aluminum-base metal, alloys	18	2%	1%
other metal, alloys	67	9%	6%
other inorganic materials	31	4%	3%
vitrified	55	7%	5%
cellulosics	54	7%	4%
rubber	10	1%	1%
plastics	34	4%	3%
plastic container/liner material	26	3%	2%
solidified inorganic material (including the cement)	54	7%	4%
solidified organic material (not including the cement)	5.6	1%	0%
solidification cement	50	7%	4%
soils	44	6%	4%
MgO backfill	451	0%	37%

The MgO backfill inventory was calculated assuming 83,150 tons of MgO will be emplaced (RCRA Part B Permit; equivalent to 1.9 x 10^9 moles), and a repository volume of 1.685 x 10^5 cubic meters (US DOE, 1996, page 2-1).

3.0 Surrogate Waste

In this section, the rationale for the formulation of waste surrogates is developed, based on the nature of the initial waste inventory described in section 2.0, the four cases described in section 1.2, and an assumed level of degradation of waste constituents. Greatest emphasis is placed on anticipating the physical nature of the degraded waste, which would affect the grain size and cohesion of the waste and the ability for precipitated salt to cement the grains. The chemical nature of the degraded waste is less important. The discussion follows the order of the BIR waste inventory list presented above (Tables 1 and 2).

The extent of corrosion of iron-bearing materials and steel waste containers is constrained by parameters used in the CCA PA calculations, captured in the four test cases described in section 1.2. It is likely that the extents of degradation of iron-bearing materials will be affected by their initial surface to volume ratio and the vertical position of the waste in the repository. The saturation of the repository is uncertain depending on position, time, and

the values of sampled parameters. The existence of a gas phase may limit the corrosion of the materials in the upper portions of the repository, but some down-slope areas of the repository tend to have higher brine saturations in the CCA PA calculations. The most active corrosion in steel drums probably occurs at creases developed as they are crushed. Massive objects, such as metal-working equipment, will be less susceptible to corrosion than objects with high surface to volume ratios, such as metal cuttings. Likewise, the porosity of the metal will affect the extents of corrosion. Cast iron is likely to be degraded more completely than annealed steel. Some of the stainless steels will not experience substantial degradation, because of their high chromium and nickel content (e.g., Hastalloy, which is almost exclusively nickel and chromium).

An additional consideration is the fact that the repository environment is very reducing, and the corrosion products will consist of ferrous iron and not the ferric iron observed under atmospheric conditions. In contrast to the surface films of rust seen under atmospheric conditions, experiments conducted at Pacific Northwest National Laboratory (PNNL) in support of the WIPP suggest that ferrous iron appears to migrate away from the corroding surface to form more granular crystals of $Fe(OH)_2$. In those experiments, coupons of steel with the composition of waste drums were suspended in brine in sealed containers under anoxic conditions.

As a surrogate for corroded iron, we recommend that a finely divided reagent iron-bearing powder not be used, because its fine grain size is not representative. Further, reagent-grade $Fe(OH)_2$ is not recommended because under atmospheric conditions, it will dehydrate the brine, possibly resulting in non-relevant precipitation of salt from the brine. In spite of the previous concerns of surface precipitation of ferrous iron under atmospheric conditions, we recommend using some rust scraped off rusted metal, such as rusted automobiles, engine mufflers, pipes, or boilers. The bulk of the material, however, can be emulated by using limonite- or goethite-rich rock samples, crushed to silt to sand size particles (1/32 to 2 mm, Wentworth scale). The non-corroded iron component (for test cases 1 and 3) should consist of iron with some surface texture to represent minor amounts of corrosion. Clean galvanized sheet metal and nails, for example, are probably not appropriate.

The relatively small quantities (compared to iron and steel) of aluminum-base metals and alloys, as well as copper and lead, are very corrodible. Consequently, we recommend representing those metals as corrosion products. The texture and grain size of the corroded material is likely to be similar to iron corrosion products, and is best represented by the same materials (i.e., crushed limonite and rust scrapings). The amount of non-corrodible metals in the "Other metals/alloys" BIR category, such as tantalum, zirconium, and platinum, is likely to be insignificant.

As iron corrodes to $Fe(OH)_2$, there is an increased volume, on a mole-per-mole Fe basis, of about 1.6. We assume the same volume expansion for aluminum-base metals and alloys, copper, and lead. We take into account that volume expansion in developing waste mass distributions below.

Many of the materials listed in the BIR categories "Other inorganic materials" and "Vitrified" (Tables 1 and 2) are essentially inert at 20-25°C, the WIPP repository temperature (e.g., graphite, ceramics, glass, firebrick, sand). The concrete component will be degraded by reaction with brine constituents, primarily Cl^-, SO_4^{2-}, and Mg^{2+}. The aggregate portion of the concrete will not be affected, however, as it generally consists of grains of crystalline rock. We recommend simulating the wastes in these two categories with broken bottles and glass. The concrete component is included in the solidified material categories.

In situations in the CCA PA calculations in which all of the carbon associated with cellulosics, plastics, and rubber was converted to $CO_2(g)$, it is likely that some of that material will be refractory and difficult for microbes to metabolize and will remain as a waste constituent. To be consistent with the CCA PA calculations, however, we recommend eliminating all cellulosics, plastics, and rubber in cases 2 and 4, where complete conversion to $CO_2(g)$ is assumed. In cases 1 and 3, where one-half of the material is degraded, we recommend simulating the one-half of the mass of the partially degraded material with a mixture of paper, plastic, rubber scraps which has been disaggregated as much as possible in an industrial blender or other comminution device. The remaining one-half should consist of peat, which is a naturally occurring microbially degraded cellulosic material. Degradation of cellulosics may be accompanied by the formation of humic materials. Peat is an appropriate surrogate.

The "Solidified Inorganic Material" and "Cement" categories (Tables 1 and 2) have solidification cements as a major constituent, and are combined here. Portland cement will be degraded by the brine constituents. In addition, Envirostone, a mixture of $CaSO_4$ and an organic binder, is likely to be degraded, although the gypsum component will be stable in Salado brine. We recommend pulverizing dried concrete, dried mortar, and gypsum board (sheet rock) to silt size (1/32 mm) up to about medium pebble size (16 mm; Wentworth scale) as a surrogate. We speculate that operators in the field would add an excess of cement to materials they were solidifying to assure complete isolation. We recommend not adding non-hydrated raw materials because the excess added is difficult to quantify and it is conservative to do so. The texture of sludge solidified in the case of the "Solidified Organic Material" category is captured by the finer-grained component of the pulverized concrete and gypsum board.

The "Solidified Organic Material" category does not include the solidification component. It is likely to consist of immiscible organics which impart little, if any, strength to the waste. We recommend disregarding that category.

Soils consist of disaggregated rocks with a small weight percent of organic materials. The rock component will not be degraded under the low temperatures of the WIPP and the absence of physical weathering phenomena. The organic portion is trivial. The soil component can accurately represented with natural soil.

On the basis of the discussion above, the masses of the constituents of the surrogate waste and the recommended surrogate materials are summarized in Tables 3 and 4, respectively. To aid the reader, Table 3a shows examples of the approach used in obtaining the percentages in Table 3b (cross reference the numbers to Table 1). In the next section, we calculate and add the masses of salts which would precipitate from the waste degradation reactions.

Table 3a.—Example Waste Surrogate Calculations (kg/m^3)

	Case 1	Case 4
iron, not corroded	= (170 + 139)/2	0
corroded iron and other metals	= 1.6(170 + 139)/2 + 1.6(18 + 67)	= 1.6(170 + 139) + 1.6(18 + 67)
glass	= 31 + 55	= 31 + 55
cellulosics + plastics + rubber	= (54 + 10 + 34 + 26)/2	= 0
solidification cements	= 54 + 50	= 54 + 50
soil	= 44	= 44
MgO backfill	= 0	= 451

Table 3b.—Waste Surrogate Constituents (weight %)

	Case 1	Case 2	Case 3	Case 4
iron, not corroded	19	0	12	0
corroded iron and other metals	46	73	30	48
glass	10	10	7	7
cellulosics + plastics + rubber	7	0	5	0
solidification cements	12	12	8	8
soil	5	5	3	3
MgO backfill	0	0	35	34

Table 4.—Waste Simulants

Waste Category	Example Waste Simulants
iron-base metal, alloys; steel container material	strips of steel sheet metal, small nails (cut-up), scraps of steel or iron
corroded iron-base metal, alloys; steel container material	scrapings from rusted steel or iron; supplement with Fe(III)O·OH (goethite or limonite rock samples) crushed sand- to silt-sized particles
corroded non-ferrous metal and alloys	as above for corroded iron-base metal, etc.
other inorganic materials; vitrified	broken labware, broken glassware
cellulosics + rubber; plastics; plastic container/liner material	equal masses of: (a) finely shredded paper, snipped cotton balls, sawdust, shredded plastic grocery bags, o-rings, rubber gloves, rubber bands, polyethylene sheet and bottles (all comminuted with a blender or other means) + (b) peat (no vermiculite)
solidification cement	broken hydrated concrete and mortar, crumbled sheet-rock
soils	natural soil
MgO backfill	commercial pellets

3.0 Quantification of Corrosion-Induced Salt Precipitation

Two key reactions that will cause the precipitation of minerals from the brine are the anoxic corrosion of metals and the reaction of brine with the MgO backfill. An ideal experiment would be to simply combine metal and brine (either with or without MgO), and directly measure the cementation effects of the brine precipitates, corrosion products, and cementing phases. However, the corrosion reactions are quite slow, especially in the anoxic repository environment. Tests will thus need to be performed with simulated corrosion products and brine precipitates. This section provides the ratios of the various materials that should be combined to simulate waste in varying states of degradation.

The two factors that affect the mass of precipitates that will form from Fe corrosion and MgO/brine reactions are the percentage of metals in the inventory that will corrode, and the extent that MgO/brine reactions are considered. The four experimental cases described in section 1.0 were configured to reflect those two factors. The most likely corrosion reaction is the formation of ferrous hydroxide [$Fe(OH)_2$] from the anoxic corrosion of steel drums, standard waste boxes, and metallic waste materials (tools, sheet metal, conduit, equipment, etc.). This reaction can be expressed as:

$$Fe + 2H_2O = Fe(OH)_2$$
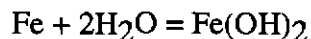
Note that this reaction consumes 2 moles of H_2O per mole of Fe corroded. The formation of 1 kg of $Fe(OH)_2$ from iron metal will consume 0.40 L of water. Since this water is in the form of a saturated brine, the removal of any amount of water from the brine will cause the immediate precipitation of minerals.

Chemical analyses of G-Seep brine (Brush, 1990, Table 2.1) provides the composition of a relevant Salado brine at the repository horizon. Geochemical reaction path model calculations conducted using EQ3/6 coupled with the Harvie-Møller-Weare brine database (Wolery, 1992; Wolery and Daveler, 1992), indicates that as evaporation of G-Seep brine occurs, anhydrite ($CaSO_4$), halite (NaCl), glauberite [$Na_2Ca(SO_4)_2$], polyhalite [$K_2CaMg(SO_4)_4 \cdot 2H_2O$], leonite [$K_2Mg(SO_4)_2 \cdot 4H_2O$], sylvite (KCl), kainite [$KMg(SO_4)Cl \cdot 3H_2O$], and carnallite ($KMgCl_3 \cdot 6H_2O$) precipitate. As evaporation progresses some minerals precipitate as others dissolve. Over the evaporation range corresponding to about 50 to 70 percent evaporation, halite and polyhalite are the dominant minerals present. At less and greater extents of evaporation, glauberite and leonite are present, respectively. The mineral assemblage resulting from complete precipitation is shown in Table 5.

Table 5.—Minerals Forming from Evaporation of 1 kg Water in Salado G-Seep Brine

Mineral	Formula	Moles	Mole Wt. (g/mole)	Mass (g)	Mass Ratio
halite	NaCl	4.67	58.4	273	0.74
carnallite	$KMgCl_3 \cdot 6H_2O$	0.064	277.9	18	0.05
kainite	$KMg(SO_4)Cl \cdot 3H_2O$	0.30	249.0	75	0.20
polyhalite	$K_2CaMg(SO_4)_4 \cdot 2H_2O$	0.0044	603.0	3	0.01
SUM				369	1.00

To convert the masses in Table 5 to units of masses per liter of initial G-seep brine, it is necessary to multiply the values by the amount of water in G-seep brine. To accomplish that, values for brine density and total dissolved solids taken from Brush (1990, Table 2.1) result in a factor of 0.875 liter water per liter of G-Seep brine.

Chemical interactions between Salado brine and the MgO backfill may also affect the strength of the waste/backfill composite material. Those interactions consume water from the brine and produce Mg-oxychloride [$Mg_2Cl(OH)_3 \cdot 4H_2O$] and brucite [$Mg(OH)_2$]. Similarly to corrosion-induced precipitation described above, removal of water from Salado brine by MgO reaction should result in precipitation of a significant volume of salt. Hydration of one kilogram of MgO will consume about 0.45 L of H_2O. For the experiments proposed herein, we recommend adding MgO-induced halite precipitate to the waste matrix.

The mass of metal, corrosion product, and brine precipitates that are predicted to form for each of the four cases are shown in Table 6. The mass of each material is normalized to 1 kg of corrosion product. The proportion of MgO to metal is based on 83,150 tons of MgO backfill, CH TRU iron and steel, and a 61 percent mass expansion as iron corrodes to form $Fe(OH)_2$.

Table 6.—Mass of Materials Normalized to 1 kg of $Fe(OH)_2$ Corrosion Product (g)

	Case 1	Case 2	Case 3	Case 4
	50% Fe corrosion	100% Fe corrosion	50% Fe corrosion + MgO backfill	100% Fe corrosion + MgO backfill
iron, not corroded	625	0	625	0
$Fe(OH)_2$	1000	1000	1000	1000
MgO	0	0	1812	906
Fe-corrosion induced salt precipitate	158	158	158	158
MgO-hydration induced salt precipitate	0	0	299	149

In Table 7, masses of waste materials from Table 6 are shown in terms of mass ratios. That format may be more convenient for scaling the materials to test specimens of differing sizes.

Table 7.—Mass Ratios of Precipitates (dimensionless)

	Case 1	Case 2	Case 3	Case 4
	50% Fe corrosion	100% Fe corrosion	50% Fe corrosion + MgO backfill	100% Fe corrosion + MgO backfill
iron, not corroded	0.35	0	0.16	0
$Fe(OH)_2$	0.56	0.86	0.26	0.45
MgO	0	0	0.47	0.41
Fe-corrosion induced salt precipitate	0.09	0.14	0.04	0.07
MgO-hydration induced salt precipitate	0	0	0.08	0.07
Sum	1	1	1	1

Rock salt from the WIPP can be used as a surrogate for the precipitates because it is dominantly halite but it includes minor amounts of polyhalite. Alternatively, reagent-grade NaCl or generic table salt may be used. The presence of kainite, and carnallite in the G-Seep precipitation sequence can be represented by halite.

Additional WIPP rock salt may be added to, or placed adjacent to, some waste surrogate materials in test vessels to simulate salt introduced by roof-fall, creep closure, and pressure dissolution processes in the repository.

4.0 Summary

Test cases representing four waste degradation and MgO backfill emplacement scenarios were described. The configurations of the four cases are:

1. 50 wt% of iron is corroded; 50 wt% of cellulosics, plastics, rubber are degraded; corrosion-induced salt precipitates are included; (+ roof-fall salt in some samples)
2. all iron is corroded; all cellulosics, plastics, rubber are degraded; corrosion-induced salt precipitates are included; (+ roof-fall salt in some samples)
3. 50 wt% of iron is corroded; 50 wt% of cellulosics, plastics, rubber are degraded; corrosion-induced salt precipitates are included; MgO-induced salt precipitates are included; (+ roof-fall salt in some samples)
4. all iron is corroded; all cellulosics, plastics, rubber are degraded; corrosion-induced salt precipitates are included; MgO-induced salt precipitates are included; (+ roof-fall salt in some samples)

Suggested formulas for approximately 10 kg batches of test specimens are summarized in the following table.

Table 8.—Mass of Material in Test Specimens (kg)

	Case 1	Case 2	Case 3	Case 4
iron, not corroded	1.9	0	1.2	0
corroded iron and other metals	4.6	7.3	3.0	4.8
glass	1.0	1.0	0.7	0.7
cellulosics + plastics + rubber	0.7	0	0.5	0
solidification cements	1.2	1.2	0.8	0.8
soil	0.5	0.5	0.3	0.3
MgO backfill	0	0	3.5	3.4
salt precipitate, corrosion-induced	0.47	0.90	0.30	0.60
salt precipitate, MgO-induced	0	0	0.57	0.57
Total batch size	10.4	10.9	10.9	11.2

5.0 References

Brush, L.H. 1990. *Test Plan for Laboratory and Modeling Studies of Repository and Radionuclide Chemistry for the Waste Isolation Pilot Plant.* SAND90-0266. Albuquerque, NM: Sandia National Laboratories.

US DOE (Department of Energy). 1995. *Waste Isolation Pilot Plant Transuranic Waste Baseline Inventory Report.* DOE/CAO-95-1121. Revision 2. December 1995. Carlsbad, NM: United States Department of Energy, Carlsbad Area Office.

US DOE (Department of Energy). 1996. *Waste Isolation Pilot Plant Transuranic Waste Baseline Inventory Report.* DOE/CAO-95-1121. Revision 3. June 1996. Carlsbad, NM: United States Department of Energy, Carlsbad Area Office.

Wolery T.J., 1992. EQ3NR. A Computer Program for Geochemical Aqueous Speciation-Solubility Calculations: Theoretical Manual, Users Guide, and Related Documentation (Version 7.0). Lawrence Livermore Laboratory, Livermore California.

Wolery T.J., and S.A. Daveler. 1992. EQ6, A Computer Program for Reaction Path Modeling of Aqueous Geochemical Systems: Theoretical Manual, Users Guide, and Related Documentation (Version 7.0). Lawrence Livermore Laboratory, Livermore California.

Distribution

MS 1320   R. V. Bynum (6831)
MS 1320   D. E. Hobart (6831)
MS 1320   E. J. Nowak (6831)
MS 1320   J. W. Kelly (6832)
MS 1320   D. A. Lucero (6832)
MS 1320   H. W. Papenguth (6832)
MS 1322   F. D. Hansen (6121)
MS 1322   M. K. Knowles (6121)
MS 1322   J. R. Tillerson (6121)
MS 1328   D. R. Anderson (6849)
MS 1328   J. W. Garner (6849)
MS 1335   M.S.Y. Chu (6801)
MS 1335   D. S. Coffey (6811)
MS 1335   N. Linarez-Royce (6811)
MS 1335   S. P. Miller (6811)
MS 1335   P. N. Swift (6801)
MS 1337   W. D. Weart (6800)
MS 1341   J. T. Holmes (6832)
MS 1341   K. W. Larson (6821)
MS 1341   Y. Wang (6832)
MS 1395   L. E. Shephard (6800)
MS 1395   M. G. Marietta (6821)

Don Galbraith, DOE/CAO
Dick Lark, DOE/CAO

D'Ann Bretzke, SAIC
Jonathan Myers, IT Corporation
Bill Thompson, CTAC

SWCF-A:1.2.01.5.3.1:CCA/CO:Spallings Model Position Paper; Waste-Surrogate Strength Experiments (WPO#43214)

A-18

Appendix B
Memorandum on
Review of the Excel Spreadsheet SPHERE.XLS

(R/S) **RE/SPEC Inc.**

External Memorandum

To: Sandia National Laboratories
Dr. Kathy Knowles
Mail Stop 1322
P.O. Box 5800
Albuquerque, NM 87185-5800

cc: Project Central File 325 — Task 19 — Category A

From: Dr. Gary D. Callahan
Vice President of Operations
RE/SPEC Inc.
P.O. Box 725
Rapid City, SD 57709

Date: March 26, 1997

Subject: Review of the Excel Spreadsheet SPHERE.XLS (Sandia National Laboratories Contract AG-4911, Task 19)

As you requested, I have reviewed the spreadsheet authored by Dr. T. W. Thompson. The purpose of the spreadsheet is to estimate the spall zone for a repository drilling intrusion scenario. The spreadsheet accomplishes this based on analytical solutions for a variety of spherical models. The spherical models include solutions to: (1) the steady-state compressible gas flow equation to determine pore pressure, (2) elastostatics equations to determine mechanical stresses, (3) thermal elastostatics equations to determine mechanical-induced stresses caused by pore pressure distributions, and (4) the Mohr-Coulomb criterion and a maximum tensile stress criterion to determine potential zones of failure. The spreadsheet generates 12 graphs of variables included in the spreadsheet, copies of which are included in Appendix A and hand labeled Figure 1 through 12 for reference.

In summary, I found some approximations that seemed unnecessary; however, their impact is believed to be negligible. Otherwise, I found the equations to be entered correctly and the solutions to be correct within the assumptions, limitations, boundary conditions, and approximations included in the analytical solutions. I did not, however, check sensitivity of results based on integration step sizes or material property variations. The remainder of this memorandum discusses the components of the spreadsheet reviewed. Keep in mind that compressive stress and pore pressure are assumed to be positive in the spreadsheet and in the development of the equations presented in this memorandum.

Pore Pressures

Pore pressure distributions are approximated using the compressible gas flow equation of an isothermal, ideal gas

$$\frac{\partial P}{\partial t} = \frac{k}{2\phi\eta} \nabla^2(P^2) \tag{1}$$

where P is pressure, t is time, k is permeability, ϕ is porosity, and η is viscosity. For the case of flow in a sphere with continuous, homogeneous boundary conditions, Equation 1 reduces to:

$$\frac{\partial P}{\partial t} = \frac{k}{2\phi\eta}\left(\frac{\partial^2 P^2}{\partial r^2} + \frac{2}{r}\frac{\partial P^2}{\partial r}\right) \tag{2}$$

For the steady-state case, Equation 2 may be written as:

$$\frac{d}{dr}\left(r^2 \frac{dP^2}{dr}\right) = 0 \tag{3}$$

which may be integrated directly to yield the general solution, viz:

$$P^2 = \frac{A}{r} + B \tag{4}$$

where A and B are constants to be determined from the boundary conditions. Spreadsheet SPHERE.XLS assumes a far-field pressure value of P_1, which applies from very far away from the inner boundary up to the edge of a zone of influence at $r = R$, and an internal pressure, P_0 in the hollow sphere of inner diameter $r = a$. Application of these boundary conditions produces:

$$P(r) = \sqrt{\frac{P_1^2\frac{R}{a} - P_0^2 - \frac{R}{r}\left(P_1^2 - P_0^2\right)}{\frac{R}{a} - 1}} \tag{5}$$

Equation 5 represents the equation included in spreadsheet SPHERE.XLS to compute pore pressures as a function of the spherical radius. The zone of influence defined by R was taken from another spreadsheet (BASECASE.XLS), which apparently computes the transient solution, zone of influence, and cavity pressure for the spherical problem. Thus, SPHERE.XLS imports nine values of time (i.e., times approximately equal to 0.1, 0.2, 0.5, 1.0, 2.0, 5.0, 10.375, 20.375, and 50.375 seconds), each with associated values of cavity pressure (P_0) and radius (R) of the zone of influence. The values for R and P_0 versus time are plotted in Figures 1 and 2, respectively. These values are shown in Appendix B on the sheet titled P0-R(n). The cavity pressure at time = 0.2 s shown on the sheet (P0(n)) seems incorrect since one would expect the cavity pressure to continually decay. These nine pore pressure fields are then used to compute

effective stresses. Figure 3 plots the pore pressure fields versus nondimensional radius (r/a) for various times; although, the abscissa is mislabeled *Time*. Appendix B includes pages printed from the spreadsheet showing the verification of Equation 5 for times 0.1 and 50.375 s and the transition of the equations for 21 points from $r = a$ (0.1555 m) to $r = 2$ m.

Mechanical Stresses

The elastostatic solution for a hollow sphere is given by Timoshenko and Goodier [1970]. In this problem, the inner surface at $r = a$ is subjected to a pressure (P_0) and the outer boundary of the sphere $(r = b)$ is subjected to the far-field pressure, P_1. The pressures in the sphere produce radial stresses (σ_r) and normal stresses in the tangential direction (σ_t). The stresses are given as:

$$\sigma_r = \frac{P_1 b^3(r^3 - a^3)}{r^3(b^3 - a^3)} + \frac{P_0 a^3(b^3 - r^3)}{r^3(b^3 - a^3)}$$

$$\sigma_t = \frac{P_1 b^3(2r^3 + a^3)}{2r^3(b^3 - a^3)} - \frac{P_0 a^3(2r^3 + b^3)}{2r^3(b^3 - a^3)}$$

(6)

where the signs have been reversed to account for compression being positive. If we assume that the outer boundary is far removed from the inner surface of the spherical cavity (i.e., $b >> a$), Equation 6 may be approximated by:

$$\sigma_r \approx P_1 - (P_1 - P_0)\frac{a^3}{r^3}$$

$$\sigma_t \approx P_1 + (P_1 - P_0)\frac{a^3}{2r^3}$$

(7)

Equation 7 is the equation included in spreadsheet SPHERE.XLS to compute the mechanical loading stresses in the sphere. Calculations are carried out for the same radii values as are the pore pressures, which range from $r = a$ to $r = 2$ m. Appendix C includes pages printed from the spreadsheet showing the verification of Equation 7 for times 0.1 and 50.375 s and the transition of the equations for points from $r = a$ (0.1555 m) to $r = 2$ m. Figures 4 and 7 plot the radial and tangential stress values versus nondimensional radius, respectively, computed from Equation 7.

Pore Pressure-Induced Stresses

Stagg and Zienkiewicz [1975] discuss stress analysis in terms of total stress when pore pressures are present. They show that the effect of pore pressure turns out to be analogous to the standard elasticity formulations for thermal problems. Thus, the effect of pore pressures is to add a homogeneous strain of thermal type to the usual definitions. Therefore, if α is an expansion coefficient and T is the temperature, the identical pore pressure problem can be solved by substituting:

$$\alpha T = P\left[\frac{1 - 2v}{E} - \frac{1}{3B_c}\right] \tag{8}$$

where B_c, E, and v are the average bulk modulus, elastic modulus, and Poisson's ratio of the solid phase. Also, note that:

$$\frac{1}{3B} = \frac{1 - 2v}{E} \tag{9}$$

where B is bulk modulus of the porous body. Thus, Equation 8 may be written as:

$$\alpha T = \frac{P}{3}\left[\frac{1}{B} - \frac{1}{B_c}\right] = \frac{P\beta}{3B} = \frac{P\beta(1 - 2v)}{E} \tag{10}$$

$$\beta = \left[1 - \frac{B}{B_c}\right], \quad \text{Biot's constant}$$

If the bulk modulus of the porous body (e.g., a porous material filled with gas) is much smaller than the bulk modulus of the solid phase, Biot's constant reduces to approximately one ($\beta = 1$), and Equation 10 may be written as:

$$\alpha T = \frac{P}{3B} = \frac{P(1 - 2v)}{E} \tag{11}$$

Therefore, to determine the total stresses when pore pressures are present, the thermoelastic solution is obtained and converted to the equivalent pore pressure solution using Equation 10. Timoshenko and Goodier [1970] provide the solution for thermal stresses in a hollow sphere with inner radius a and outer radius b under the condition that $\sigma_r = 0$ on the inner and outer boundaries. The solution is given as:

$$\sigma_r^t = \frac{2\alpha E}{1 - v}\left[\frac{r^3 - a^3}{r^3(a^3 - b^3)}\int_a^b Tr^2\,dr + \frac{1}{r^3}\int_a^r Tr^2\,dr\right]$$

$$\sigma_t^t = \frac{2\alpha E}{1 - v}\left[\frac{2r^3 + a^3}{2r^3(a^3 - b^3)}\int_a^b Tr^2\,dr - \frac{1}{2r^3}\int_a^r Tr^2\,dr + \frac{T}{2}\right] \tag{12}$$

where the signs have been reversed to account for compression positive and superscript t is used to denote the thermally-induced stresses. Substituting Equation 10 into Equation 12 produces the pore pressure-induced stresses:

$$\sigma_r^p = \frac{2\beta(1 - 2v)}{1 - v_*}\left[\frac{r^3 - a^3}{r^3(a^3 - b^3)}\int_a^b Pr^2 dr + \frac{1}{r^3}\int_a^r Pr^2 dr\right]$$

(13)

$$\sigma_t^p = \frac{\beta(1 - 2v)}{1 - v}\left[\frac{2r^3 + a^3}{r^3(a^3 - b^3)}\int_a^b Pr^2 dr - \frac{1}{r^3}\int_a^r Pr^2 dr + P\right]$$

Equation 13 provides the pore pressure-induced stresses. However, spreadsheet SPHERE.XLS has made a simplifying assumption regarding the first integrals appearing in Equation 13. The assumption is made that the outer boundary is far removed from the inner surface of the spherical cavity (i.e., $b \gg a$) and that the effect of the variation in the pressure field over a zone of influence (i.e., $a < R \ll b$) is negligible. In other words, the pressure field is assumed to be constant (P_γ). This enables the first integrals in Equation 13 to be approximated as:

$$\sigma_r^p \text{ first } \int \approx \frac{r^3 - a^3}{r^3(a^3 - b^3)}\int_a^b P_\gamma r^2 dr = -\frac{r^3 - a^3}{3r^3}P_\gamma = -\frac{P_\gamma}{r^3}\int_a^r r^2 dr$$

(14)

$$\sigma_t^p \text{ first } \int \approx \frac{2r^3 + a^3}{r^3(a^3 - b^3)}\int_a^b P_\gamma r^2 dr = -\frac{2r^3 + a^3}{3r^3}P_\gamma = \frac{P_\gamma}{r^3}\int_a^r r^2 dr - P_\gamma$$

On the surface, the effect of these integral approximations seems to be negligible, but their real impact is unknown. However, with the spreadsheet, the full integrals could be computed quite easily. This should probably be done. With these simplifying assumptions and defining $P' = P - P_\gamma$, Equation 13 becomes:

$$\sigma_r^p = \frac{2\beta(1 - 2v)}{r^3(1 - v)}\int_a^r P' r^2 dr$$

(15)

$$\sigma_t^p = -\frac{\beta(1 - 2v)}{(1 - v)}\left[\frac{1}{r^3}\int_a^r P' r^2 dr + P'\right]$$

Equation 15 is the equation included in spreadsheet SPHERE.XLS to compute the stresses caused by pore pressure distributions in the sphere. The integrals are approximated using the well known trapezoidal rule. Thus, the integral is approximated by:

$$\int_a^r P' r^2 dr \approx \sum_{i=1}^n I_i$$

(16)

where:

$$I_i = \int_{r_{i-1}}^{r_i} P'r^2\,dr \approx \frac{1}{2}\left(P'_{i-1}r_{i-1}^2 + P'_i r_i^2\right)(r_i - r_{i-1})$$

(17)

with $r_0 = a = 0.1555$ m and $r_n = 2$ m

Calculations are carried out for the same radii values as are the pore pressures, which range from $r = a$ to $r = 2$ m. The integral approximation given in Equation 16 is substituted into Equation 15 to compute the pore pressure-induced stresses. The material property values used in the calculations are $\beta = 1$ and $\nu = 0.35$. These property values are visible on mechanical stress sheets included in Appendix C. Appendix D includes sheets printed from the spreadsheet showing the verification of the integral approximation in Equation 16 and verification of Equation 15 for times 0.1 and 50.375 s and the transition of the equations for points from $r = a$ (0.1555 m) to $r = 2$ m. Figures 4 and 7 plot the pore pressure-induced radial and tangential stresses versus nondimensional radius, respectively.

TOTAL STRESSES

The complete solution for the total stresses in a hollow sphere subject to mechanical loading and pore pressure effects can be obtained by superposing the solutions for the mechanical loading (Equation 6) and the pore pressure effects (Equation 13), which gives:

$$\sigma_r = \frac{2\beta(1-2\nu)}{1-\nu}\left[\frac{r^3-a^3}{r^3(a^3-b^3)}\int_a^b Pr^2\,dr + \frac{1}{r^3}\int_a^r Pr^2\,dr\right]$$
$$+ \frac{P_1 b^3(r^3 - a^3)}{r^3(b^3 - a^3)} + \frac{P_0 a^3(b^3 - r^3)}{r^3(b^3 - a^3)}$$

(18)

$$\sigma_t = \frac{\beta(1-2\nu)}{1-\nu}\left[\frac{2r^3+a^3}{r^3(a^3-b^3)}\int_a^b Pr^2\,dr - \frac{1}{r^3}\int_a^r Pr^2\,dr + P\right]$$
$$+ \frac{P_1 b^3(2r^3 + a^3)}{2r^3(b^3 - a^3)} - \frac{P_0 a^3(2r^3 + b^3)}{2r^3(b^3 - a^3)}$$

Substituting the mechanical stress approximations in Equation 7 and the integral approximations given in Equation 14, Equation 18 becomes:

$$\sigma_r = \frac{2\beta(1-2\nu)}{r^3(1-\nu)} \int_a^r P' r^2 dr + P_1 - (P_1 - P_0)\frac{a^3}{r^3}$$

$$\tag{19}$$

$$\sigma_t = -\frac{\beta(1-2\nu)}{(1-\nu)}\left[\frac{1}{r^3} \int_a^r P' r^2 dr - P'\right] + P_1 + (P_1 - P_0)\frac{a^3}{2r^3}$$

Equation 19 is the equation included in spreadsheet SPHERE.XLS to compute the total stresses in the hollow sphere. Calculations are carried out for the same radii values as are the pore pressures and other stresses, which range from $r = a$ to $r = 2$ m. Appendix E includes sheets printed from the spreadsheet showing the verification of Equation 19 for times 0.1 and 50.375 s and the transition of the equations for points from $r = a$ (0.1555 m) to $r = 2$ m. Figures 5 and 8 plot the total radial and tangential stresses versus nondimensional radius, respectively, computed from Equation 19.

EFFECTIVE STRESSES

The effective stresses (σ'_{ij}) may be computed from the total stresses and the pore pressures by:

$$\sigma'_{ij} = \sigma_{ij} - \beta P \delta_{ij} \tag{20}$$

where compressive stresses and pore pressures are assumed to be positive quantities. Thus, the effective stresses in a hollow sphere subject to mechanical loading and pore pressure effects can be obtained by subtracting the pore pressures given in Equation 5 from the total stresses given in Equation 18, which yields:

$$\sigma'_r = \frac{2\beta(1-2\nu)}{1-\nu}\left[\frac{r^3-a^3}{r^3(a^3-b^3)} \int_a^b P r^2 dr + \frac{1}{r^3} \int_a^r P r^2 dr\right]$$

$$+ \frac{P_1 b^3(r^3 - a^3)}{r^3(b^3 - a^3)} + \frac{P_0 a^3(b^3 - r^3)}{r^3(b^3 - a^3)} - \beta P$$

$$\tag{21}$$

$$\sigma'_t = \frac{\beta(1-2\nu)}{1-\nu}\left[\frac{2r^3+a^3}{r^3(a^3-b^3)} \int_a^b P r^2 dr - \frac{1}{r^3} \int_a^r P r^2 dr + P\right]$$

$$+ \frac{P_1 b^3(2r^3 + a^3)}{2r^3(b^3 - a^3)} - \frac{P_0 a^3(2r^3 + b^3)}{2r^3(b^3 - a^3)} - \beta P$$

Substituting the mechanical stress approximations in Equation 7 and the integral approximations given in Equation 14, Equation 21 becomes:

$$\sigma_r' = \frac{2(1 - 2\bar{v})}{r^3(1 - v)} \int_a^r P'r^2 dr + P_1 - (P_1 - P_0)\frac{a^3}{r^3} - \beta P$$

$$\sigma_t' = -\frac{(1 - 2v)}{(1 - v)}\left[\frac{1}{r^3} \int_a^r P'r^2 dr - P'\right] + P_1 + (P_1 - P_0)\frac{a^3}{2r^3} - \beta P \tag{22}$$

Equation 22 is the equation included in spreadsheet SPHERE.XLS to compute the effective stresses in the hollow sphere. Calculations are carried out for the same radii values as are the pore pressures and other stresses, which range from $r = a$ to $r = 2$ m. Appendix F includes sheets printed from the spreadsheet showing the verification of Equation 22 for times 0.1 and 50.375 s and the transition of the equations for points from $r = a$ (0.1555 m) to $r = 2$ m. Figures 6 and 9 plot the effective radial and tangential stresses versus nondimensional radius, respectively, computed from Equation 22.

Failure Analysis

The spreadsheet contains two different estimates for the zone of failed material based on the effective stresses computed from Equation 22. The first estimate is a tensile failure evaluation; whereas, the second estimate is a shear failure evaluation based on the Mohr-Coulomb criterion.

Tensile Failure Zone

In the tensile failure criterion, the radial effective stresses are inspected to determine the radial vicinity that the stress is less than (recall tension is negative) a given tensile strength (T_0). Review of Figures 6 and 9 for the effective radial and tangential stresses, respectively, shows that the loading condition results in tangential effective stresses that are always compressive and that the radial effective stress has zones of compression and tension. Areas within the sphere that have radial effective stresses less than the tensile strength are actually interior regions that do not extend from the inner cavity surface. However, the computation in the spreadsheet assumes that the entire zone is failed from the cavity surface out to the edge of the region where the radial effective is less than the tensile strength. An approximate radial extent (r_f) of the region less than the tensile strength is interpolated from the computed radial effective stresses and their radial locations by:

$$r_f \approx r_{n-1} + \frac{r_n - r_{n-1}}{\sigma_r'(r_n) - \sigma_r'(r_{n-1})}\left[T_0 - \sigma_r'(r_{n-1})\right] \tag{23}$$

The volume of the tensile failure zone (V_t) is then computed from the radius of the identified region for a hemisphere of penetration from:

$$V_t = \frac{4\pi}{6}\left(r_f^3 - a^3\right) \tag{24}$$

Equations 23 and 24 are the equations included in spreadsheet SPHERE.XLS to compute a tensile failure region and a volume of failed material. The tensile strength is assumed to be −0.1 MPa. This value may be verified from the sheets included in Appendix C for the mechanical loading stress calculations; however, the tensile strength was entered as a positive quantity. Appendix G includes sheets printed from the spreadsheet showing the verification of Equations 23 and 24 at times = 0.1, 0.2, and 0.5 s. The computed effective radial stresses are also included in Appendix G and show the zone where the radial effective stress is less than the tensile strength. No tensile stresses are less than the tensile strength at times 0.1 and 0.2 s and the failure radius was set to $r_f = a$. No tensile failure zone exists at time = 50.375 s, and no tensile failure zones were computed for times = 10.375 and 20.375 s. The potential failure radius computed from Equation 23 is plotted in Figure 11, and the volume of the potential tensile failure zone is plotted in Figure 12. Figure 12 has several items mislabeled.

Shear Failure Zone

The Mohr-Coulomb failure criterion is:

$$|\tau| = S_0 + \tan\phi\,\sigma_n \qquad (25)$$

where τ is the shear stress on the failure plane, S_0 is the cohesion, ϕ is the angle of internal friction and σ_n is the normal stress on the failure plane. Equation 25 may also be stated as (e.g. see Jaeger and Cook [1969]):

$$\sigma_1 = 2S_0\tan\alpha + \sigma_3\tan^2\alpha = C_0 + \sigma_3\tan^2\alpha \qquad (26)$$

where:

$$C_0 = 2S_0\tan\alpha = \text{unconfined comnpressive strength}$$
$$\alpha = \frac{\pi}{4} + \frac{\phi}{2} \qquad (27)$$

Using Equations 26 and 27, a failure criterion (F) is written as:

$$F = \sigma_1 - \sigma_3\tan^2\alpha - C_0 \qquad (28)$$

For the spherical geometry being analyzed, both the radial and tangential stresses are principal stresses and Equation 28 may be written in terms of the effective stresses as:

$$F = \sigma_t' - \sigma_r'\tan^2\alpha - C_0 \qquad (29)$$

When $F > 0$, the potential for failure exists. Equation 29 is the equation included in the spreadsheet. Material property values used include $\phi = 45°$ and $C_0 = 0.7$ MPa. Appendix G

shows verification of Equation 29 at times = 0.1, 0.2, 0.5, and 1 s. Figure 10 plots the failure criterion versus nondimensional radius computed from Equation 29.

As an additional check of the shear failure zone, the Mohr-Coulomb criterion was written in an alternative form as:

$$\left| \frac{\sigma_t' - \sigma_r'}{2} \cos\phi \right| = S_0 + \left[\frac{\sigma_t' + \sigma_r'}{2} - \frac{\sigma_t' - \sigma_r'}{2} \sin\phi \right] \tan\phi \qquad (30)$$

and the failure condition was computed as:

$$f = \left| \frac{\sigma_t' - \sigma_r'}{2} \cos\phi \right| - S_0 - \left[\frac{\sigma_t' + \sigma_r'}{2} - \frac{\sigma_t' - \sigma_r'}{2} \sin\phi \right] \tan\phi \qquad (31)$$

When $f > 0$, the potential for failure exists. The computed values from Equations 29 and 31 are included in Appendix G and show that the failure zones computed by both equations are the same although their values are different. One can show that:

$$F = 2 f \tan\alpha \qquad (32)$$

References

Jaeger, J. C. and N. G. W. Cook, 1969. *Fundamental of Rock Mechanics*, Chapman and Hall Ltd., London, England.

Timoshenko, S. P. and J. N. Goodier, 1970. *Theory of Elasticity*, Third Edition, McGraw-Hill Book Company, New York, NY.

Stagg, K. G. and Zienkiewicz O. C. (ed.), 1975. *Rock Mechanics in Engineering Practice*, John Wiley & Sons, London, England.

GDC:krl

APPENDIX A

Excel Workbook SPHERE.XLS Figures

Figure No.	Workbook Page	Description
1	Outer radius	Effective outer radius (influence zone) vs time.
2	Po	Inner boundary (cavity surface) pressure vs time.
3	P Gradients	Pore pressure at various times vs nondimensional radius.
4	Radial	Radial mechanical loading stresses and pore pressure-induced radial stresses vs nondimensional radius.
5	Total R	Total radial stress vs nondimensional radius.
6	Effective R	Effective radial stress vs nondimensional radius.
7	Tangential	Tangential mechanical loading stresses and pore pressure-induced tangential stresses vs nondimensional radius.
8	Total T	Total tangential stress vs nondimensional radius.
9	Effective T	Effective tangential stress vs nondimensional radius.
10	Yield	Potential failure zones at various times vs nondimensional radius.
11	Failure	Extent of tensile stress zone radius vs time.
12	Failure (2)	Volume of tensile stress zone vs time.

Outer radius

Outer Radius
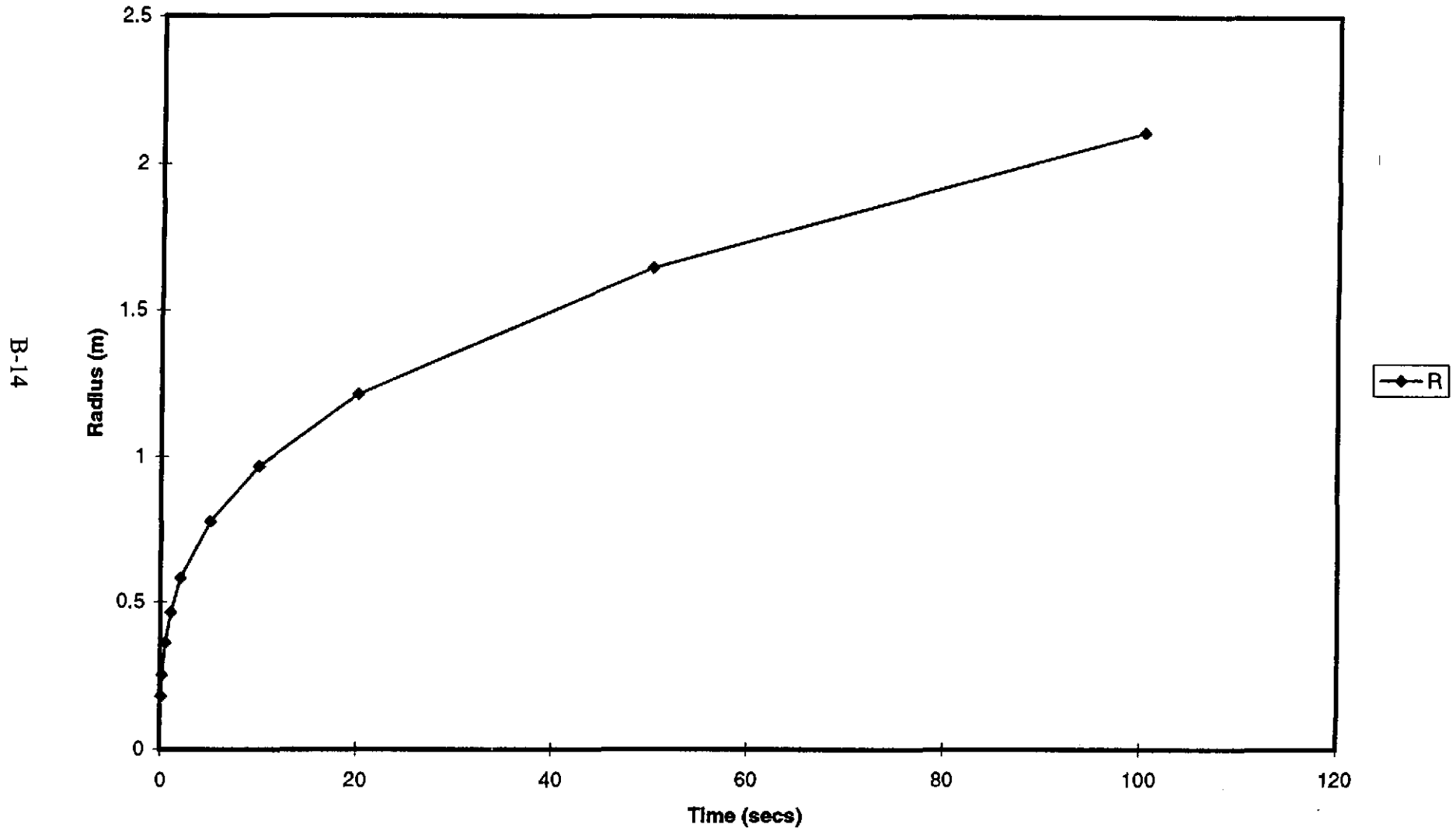
Figure 1.
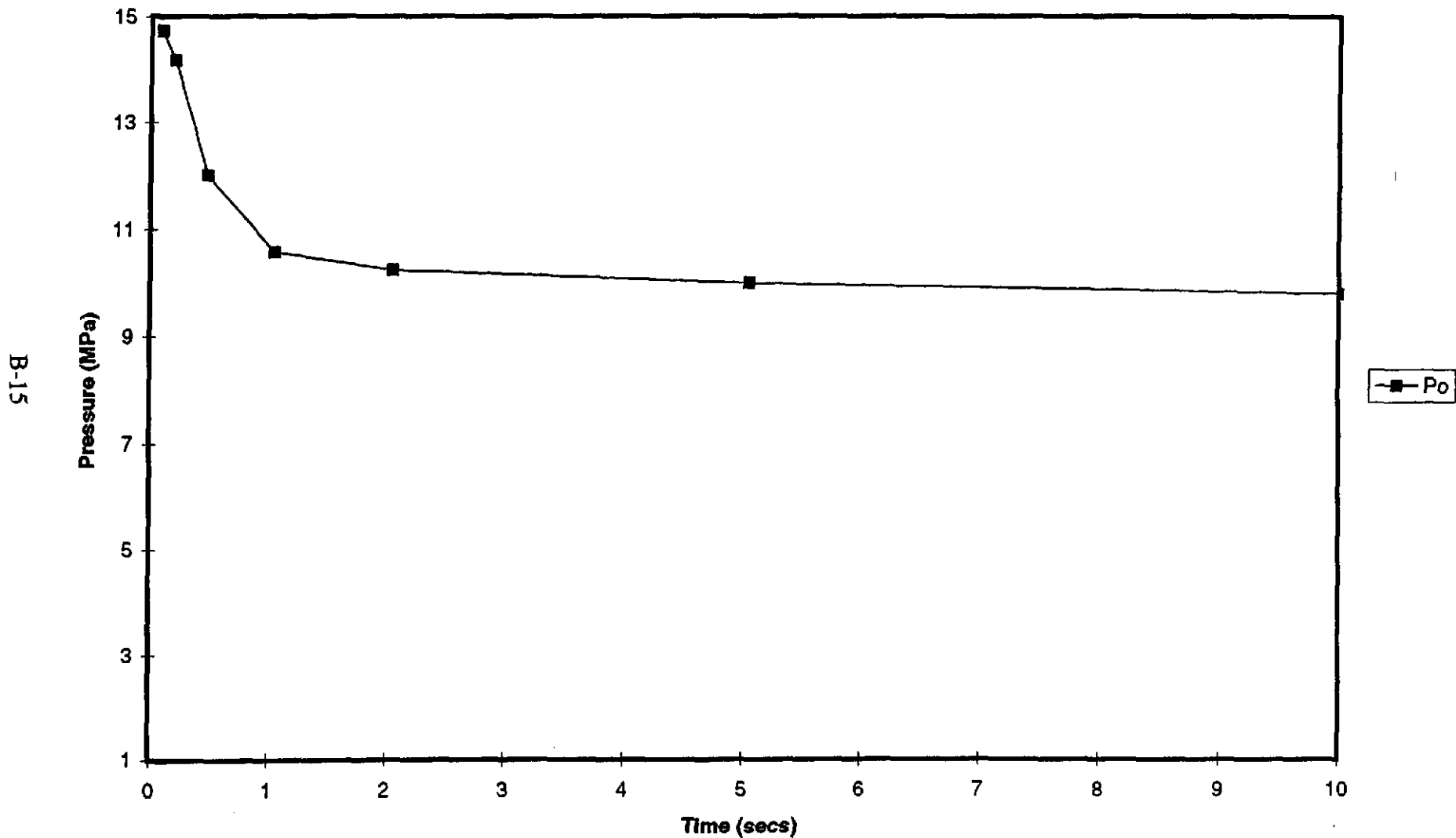
B-14

Cavity Pressure

Figure 2.

B-15

Pressure Gradients

Legend:
- 0.099
- 0.208
- 0.485
- 1.059
- 2.059
- 5.059
- 10.059
- 20.15
- 50.15
- 100.15

Axes: Pressure (MPa) vs Time (secs)

B-16

Mislabeled actually r/a
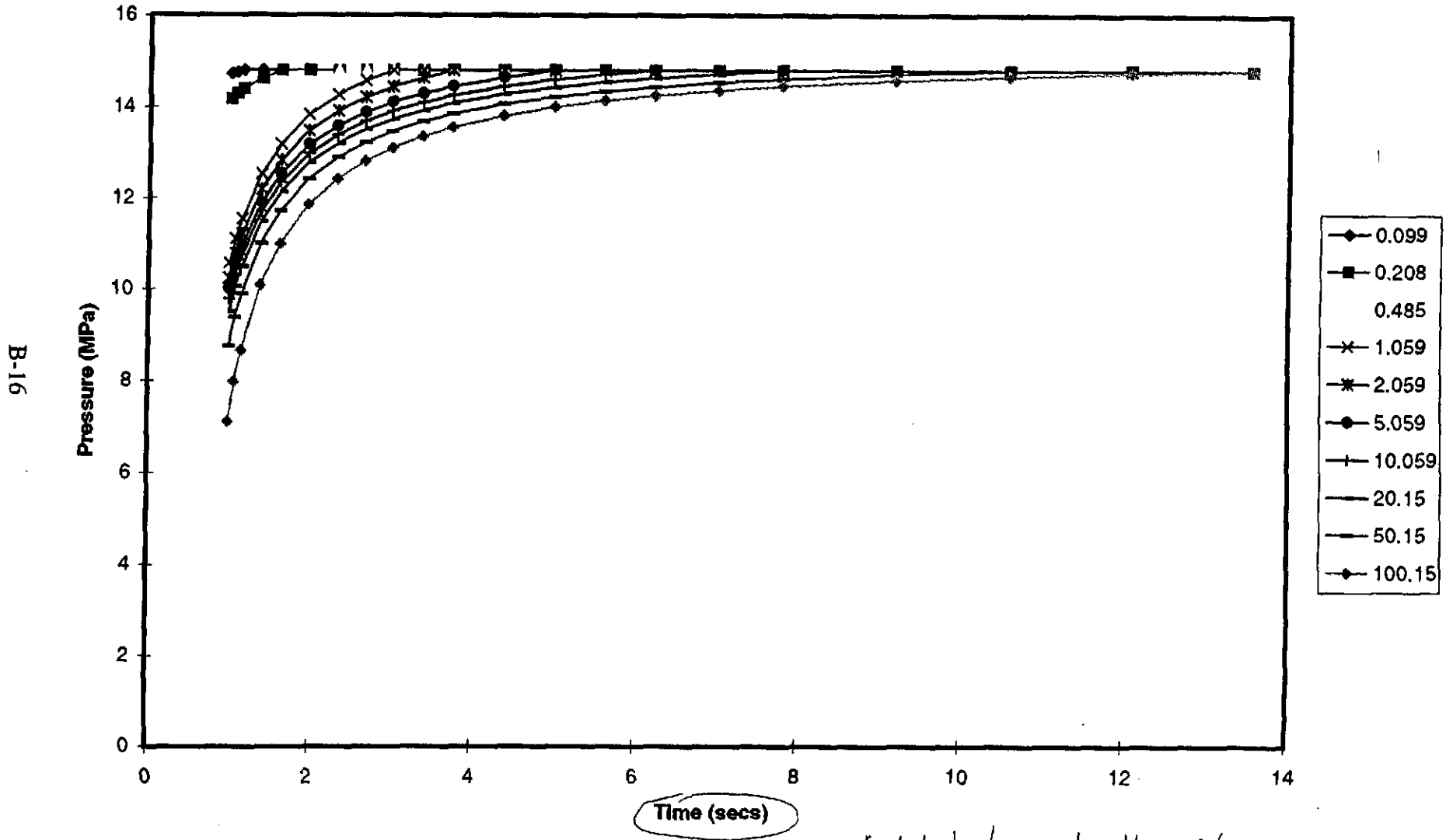
Figure 3.

Radial Stresses (No Pp and Pp)

B-17

Figure 4

Total Radial Stress

B-18

Figure 5
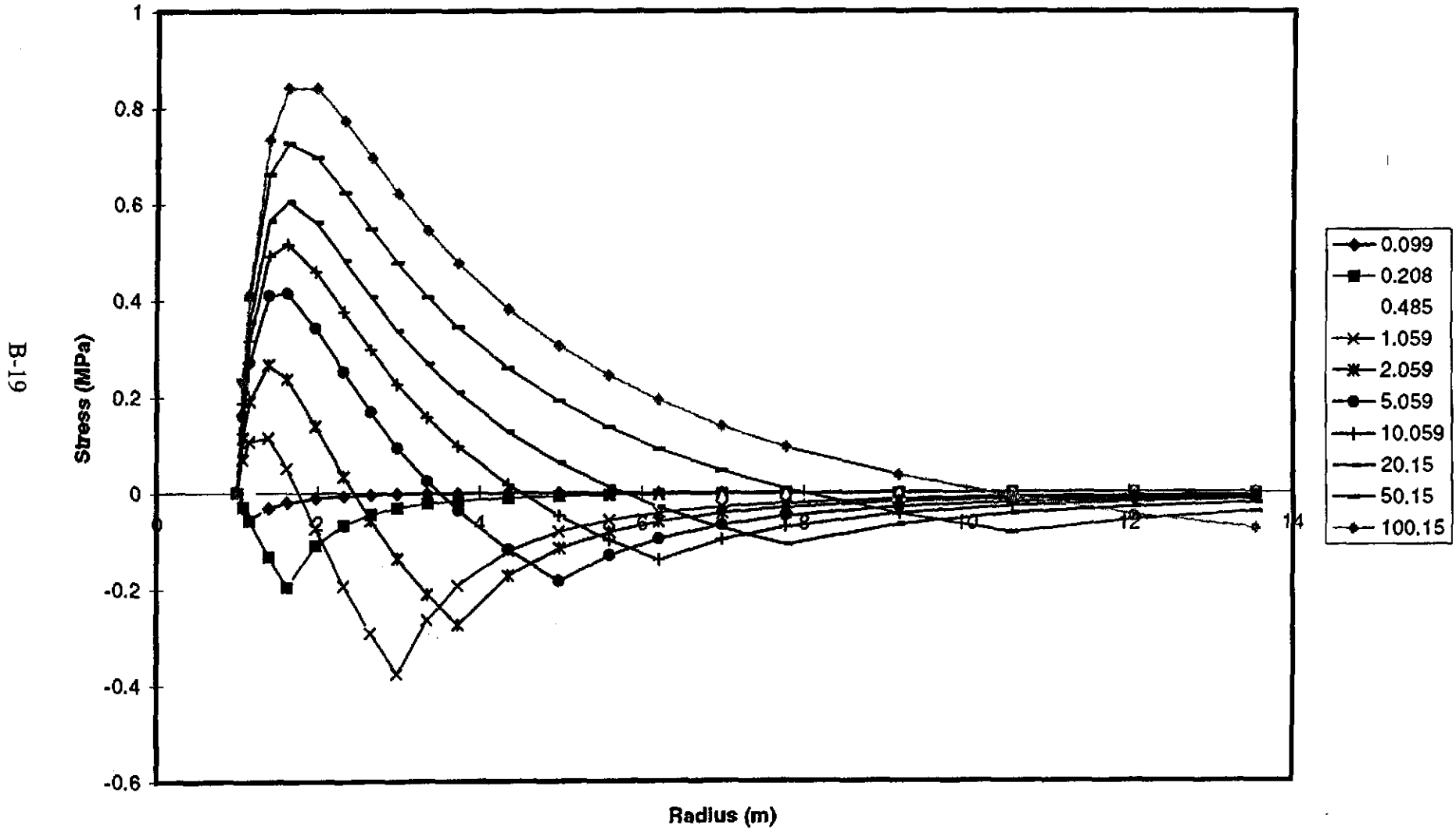
Effective R

Effective Radial Stress

Figure 6

Tangential Stresses (No Pp and Pp)

Figure 7

Total Tangential Stresses

Legend:
- 0.099
- 0.208
- 0.485
- 1.059
- 2.059
- 5.059
- 10.059
- 20.15
- 50.15
- 100.15

X-axis: Dimensionless Radius

Y-axis: Stress (MPa)

B-21

Figure 8

Effective Tangential

Figure 9.

B-22

Yield

Figure 10.

Tensile Failure Radius

Figure 11.

B-24

Tensile Failure (Radius) Volume
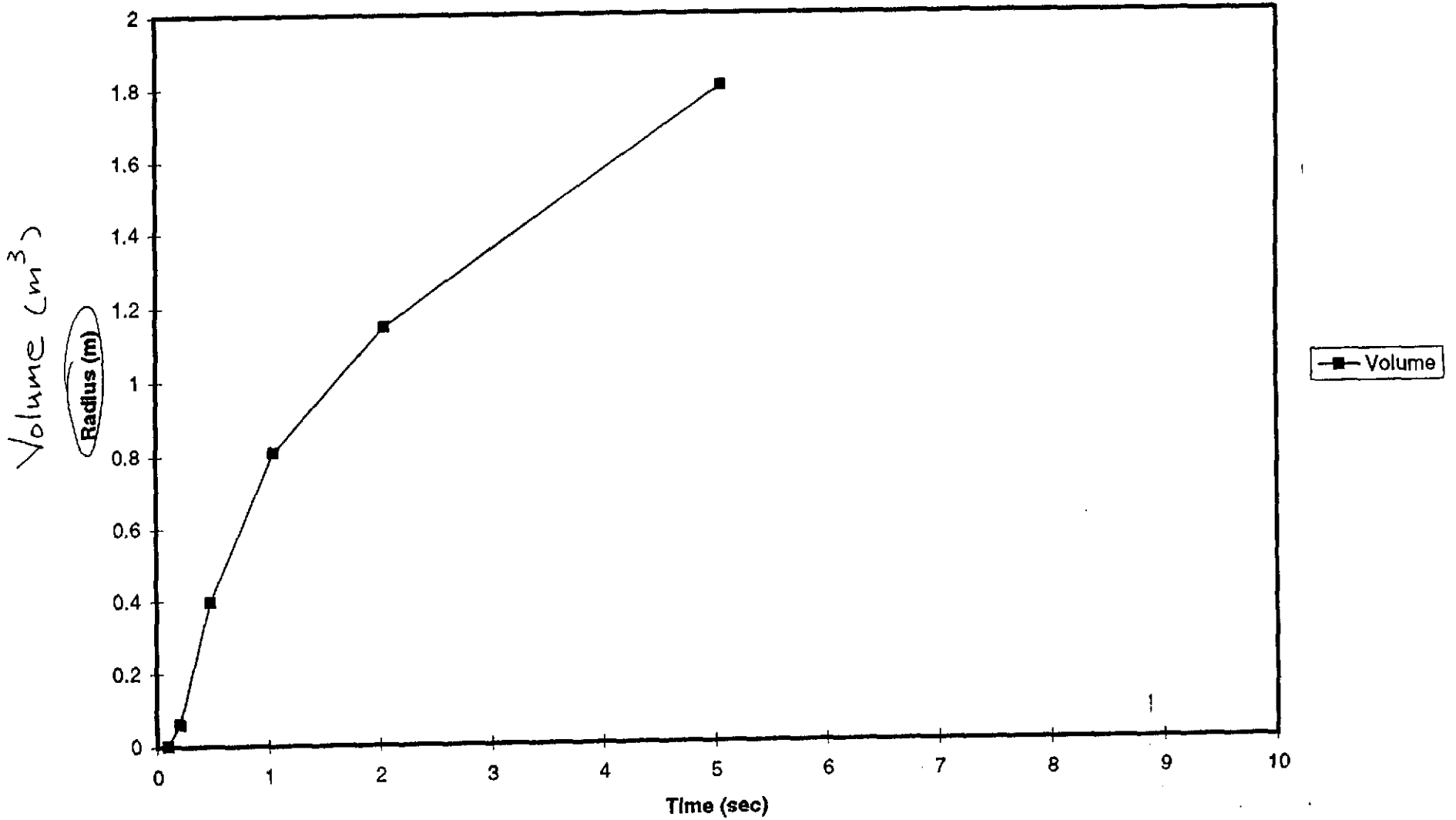
Figure 12.

APPENDIX B

Excel Workbook SPHERE.XLS (Page SHEET1)

Pore Pressure Calculations
(Memorandum Equation 5)

	A	B	C	D	E	F	G
1	Steady-state pressure data from MBG sheet: basecase.xls						
2	Time in secs, P0 is cavity pressure at time(n), R is SS outer radius at time (n)						
3							
4	Time (n)	P0(n)	R(n)				
5	0.1	14732655	0.175944				
6	0.2	14800000	0.288521				
7	0.5	11582624	0.394201				
8	1	10542592	0.494057				
9	2	10131730	0.615122				
10	5	9931655	0.817647				
11	10.37483	9737813	1.026873				
12	20.37483	9472377	1.271195				
13	50.37483	8746048	1.703142				

P0(n) seems incorrect !

	A	B	C
5	Pore Pressures (MPa)		
6	Far-Field P (P1)		14.8 P_1
7	Time (sec)		='[Sphere.xls]P0-R(n)'!A5 t
8	R (m) (see: P0-R(n))		='[Sphere.xls]P0-R(n)'!C5 R
9	R/a (a = well radius)		=C8/$A$13 R/a
10	Po (cavity pressure)		='[Sphere.xls]P0-R(n)'!B5/1000000 P_0 [MPa]
11	Time		=C7 ≈ 0.1s
12	r (m)	r/a	
13	0.1555	=A13/$A$13	=IF($A13<C$8,SQRT((($C$6^2*C$9-C$10^2)-C$8/$A13*($C$6^2-C$10^2))/(C$9-1)),$C$6)
14	=(A13+A15)/2	=A14/$A$13	=IF($A14<C$8,SQRT((($C$6^2*C$9-C$10^2)-C$8/$A14*($C$6^2-C$10^2))/(C$9-1)),$C$6)
15	=C8	=A15/$A$13	=IF($A15<C$8,SQRT((($C$6^2*C$9-C$10^2)-C$8/$A15*($C$6^2-C$10^2))/(C$9-1)),$C$6)
16	=(A15+A17)/2	=A16/$A$13	=IF($A16<C$8,SQRT((($C$6^2*C$9-C$10^2)-C$8/$A16*($C$6^2-C$10^2))/(C$9-1)),$C$6)
17	=D8	=A17/$A$13	=IF($A17<C$8,SQRT((($C$6^2*C$9-C$10^2)-C$8/$A17*($C$6^2-C$10^2))/(C$9-1)),$C$6)
18	=(A17+A19)/2	=A18/$A$13	=IF($A18<C$8,SQRT((($C$6^2*C$9-C$10^2)-C$8/$A18*($C$6^2-C$10^2))/(C$9-1)),$C$6)
19	=E8	=A19/$A$13	=IF($A19<C$8,SQRT((($C$6^2*C$9-C$10^2)-C$8/$A19*($C$6^2-C$10^2))/(C$9-1)),$C$6)
20	=(A19+A21)/2	=A20/$A$13	=IF($A20<C$8,SQRT((($C$6^2*C$9-C$10^2)-C$8/$A20*($C$6^2-C$10^2))/(C$9-1)),$C$6)
21	=F8	=A21/$A$13	=IF($A21<C$8,SQRT((($C$6^2*C$9-C$10^2)-C$8/$A21*($C$6^2-C$10^2))/(C$9-1)),$C$6)
22	=(A21+A23)/2	=A22/$A$13	=IF($A22<C$8,SQRT((($C$6^2*C$9-C$10^2)-C$8/$A22*($C$6^2-C$10^2))/(C$9-1)),$C$6)
23	=G8	=A23/$A$13	=IF($A23<C$8,SQRT((($C$6^2*C$9-C$10^2)-C$8/$A23*($C$6^2-C$10^2))/(C$9-1)),$C$6)
24	=(A23+A25)/2	=A24/$A$13	=IF($A24<C$8,SQRT((($C$6^2*C$9-C$10^2)-C$8/$A24*($C$6^2-C$10^2))/(C$9-1)),$C$6)
25	=H8	=A25/$A$13	=IF($A25<C$8,SQRT((($C$6^2*C$9-C$10^2)-C$8/$A25*($C$6^2-C$10^2))/(C$9-1)),$C$6)
26	=(A25+A27)/2	=A26/$A$13	=IF($A26<C$8,SQRT((($C$6^2*C$9-C$10^2)-C$8/$A26*($C$6^2-C$10^2))/(C$9-1)),$C$6)
27	=I8	=A27/$A$13	=IF($A27<C$8,SQRT((($C$6^2*C$9-C$10^2)-C$8/$A27*($C$6^2-C$10^2))/(C$9-1)),$C$6)
28	=(A27+A29)/2	=A28/$A$13	=IF($A28<C$8,SQRT((($C$6^2*C$9-C$10^2)-C$8/$A28*($C$6^2-C$10^2))/(C$9-1)),$C$6)
29	=J8	=A29/$A$13	=IF($A29<C$8,SQRT((($C$6^2*C$9-C$10^2)-C$8/$A29*($C$6^2-C$10^2))/(C$9-1)),$C$6)
30	=(A29+A31)/2	=A30/$A$13	=IF($A30<C$8,SQRT((($C$6^2*C$9-C$10^2)-C$8/$A30*($C$6^2-C$10^2))/(C$9-1)),$C$6)
31	=K8	=A31/$A$13	=IF($A31<C$8,SQRT((($C$6^2*C$9-C$10^2)-C$8/$A31*($C$6^2-C$10^2))/(C$9-1)),$C$6)
32	=(A31+A33)/2	=A32/$A$13	=IF($A32<C$8,SQRT((($C$6^2*C$9-C$10^2)-C$8/$A32*($C$6^2-C$10^2))/(C$9-1)),$C$6)
33	2	=A33/$A$13	=IF($A33<C$8,SQRT((($C$6^2*C$9-C$10^2)-C$8/$A33*($C$6^2-C$10^2))/(C$9-1)),$C$6)

Memorandum
Equation 5

$$IF\left(r<R, \quad P = \sqrt{\frac{P_1^2\left(\frac{R}{a}\right) - P_0^2 - \frac{R}{r}\left(P_1^2 - P_0^2\right)}{\frac{R}{a} - 1}}\right)$$

$$IF\left(r \geq R, \quad P = P_1\right)$$

Prepared by Bill Thompson 3/19/97

	K
5	PORE PRESSURE
6	
7	=ROUND('[Sphere.xls]P0-R(n)'!A13,3) t
8	='[Sphere.xls]P0-R(n)'!C13 R
9	=K8/$A$13 R/a
10	='[Sphere.xls]P0-R(n)'!B13/1000000 Po [MPa]
11	=K7 ≠ 50.375 s (time) t
12	✓ ✓ ✓ ✓ ✓ ✓ ✓ ✓ ✓ ✓ ✓ ✓
13	=IF($A13<K$8,SQRT((($C$6^2*K$9-K$10^2)-K$8/$A13*($C$6^2-K$10^2))/(K$9-1)),$C$6)
14	=IF($A14<K$8,SQRT((($C$6^2*K$9-K$10^2)-K$8/$A14*($C$6^2-K$10^2))/(K$9-1)),$C$6)
15	=IF($A15<K$8,SQRT((($C$6^2*K$9-K$10^2)-K$8/$A15*($C$6^2-K$10^2))/(K$9-1)),$C$6)
16	=IF($A16<K$8,SQRT((($C$6^2*K$9-K$10^2)-K$8/$A16*($C$6^2-K$10^2))/(K$9-1)),$C$6)
17	=IF($A17<K$8,SQRT((($C$6^2*K$9-K$10^2)-K$8/$A17*($C$6^2-K$10^2))/(K$9-1)),$C$6)
18	=IF($A18<K$8,SQRT((($C$6^2*K$9-K$10^2)-K$8/$A18*($C$6^2-K$10^2))/(K$9-1)),$C$6)
19	=IF($A19<K$8,SQRT((($C$6^2*K$9-K$10^2)-K$8/$A19*($C$6^2-K$10^2))/(K$9-1)),$C$6)
20	=IF($A20<K$8,SQRT((($C$6^2*K$9-K$10^2)-K$8/$A20*($C$6^2-K$10^2))/(K$9-1)),$C$6)
21	=IF($A21<K$8,SQRT((($C$6^2*K$9-K$10^2)-K$8/$A21*($C$6^2-K$10^2))/(K$9-1)),$C$6)
22	=IF($A22<K$8,SQRT((($C$6^2*K$9-K$10^2)-K$8/$A22*($C$6^2-K$10^2))/(K$9-1)),$C$6)
23	=IF($A23<K$8,SQRT((($C$6^2*K$9-K$10^2)-K$8/$A23*($C$6^2-K$10^2))/(K$9-1)),$C$6)
24	=IF($A24<K$8,SQRT((($C$6^2*K$9-K$10^2)-K$8/$A24*($C$6^2-K$10^2))/(K$9-1)),$C$6)
25	=IF($A25<K$8,SQRT((($C$6^2*K$9-K$10^2)-K$8/$A25*($C$6^2-K$10^2))/(K$9-1)),$C$6)
26	=IF($A26<K$8,SQRT((($C$6^2*K$9-K$10^2)-K$8/$A26*($C$6^2-K$10^2))/(K$9-1)),$C$6)
27	=IF($A27<K$8,SQRT((($C$6^2*K$9-K$10^2)-K$8/$A27*($C$6^2-K$10^2))/(K$9-1)),$C$6)
28	=IF($A28<K$8,SQRT((($C$6^2*K$9-K$10^2)-K$8/$A28*($C$6^2-K$10^2))/(K$9-1)),$C$6)
29	=IF($A29<K$8,SQRT((($C$6^2*K$9-K$10^2)-K$8/$A29*($C$6^2-K$10^2))/(K$9-1)),$C$6)
30	=IF($A30<K$8,SQRT((($C$6^2*K$9-K$10^2)-K$8/$A30*($C$6^2-K$10^2))/(K$9-1)),$C$6)
31	=IF($A31<K$8,SQRT((($C$6^2*K$9-K$10^2)-K$8/$A31*($C$6^2-K$10^2))/(K$9-1)),$C$6)
32	=IF($A32<K$8,SQRT((($C$6^2*K$9-K$10^2)-K$8/$A32*($C$6^2-K$10^2))/(K$9-1)),$C$6)
33	=IF($A33<K$8,SQRT((($C$6^2*K$9-K$10^2)-K$8/$A33*($C$6^2-K$10^2))/(K$9-1)),$C$6)

Memorandum Equation 5

Prepared by Bill Thompson 3/19/97

APPENDIX C

Excel Workbook SPHERE.XLS (Page SHEET1)

**Mechanical Stress Calculations
(Memorandum Equations 7)**

B-30

	A	B	C	D
35	Elastic Stresses			
36	Beta	1	=(1-cr/cb)	
37	nu	0.35	Pinf	14.8 P_1
38	(1-2v)/(1-v)	=(1-2*B37)/(1-B37)	To	0.1
39			$\sigma_r(r)$	
40	Radial: No Pp: Sr = Pinf - (Pinf - Pc)*(a/r)^3: Pc is cavity pressure f			
41	r	r/a	=C11 $t = 0.1 s$	=D11
42	=A13	=B13	=$D$37-($D$37-C$13)/$B42^3	=$D$37-($D$37-D$13
43	=A14	=B14	=$D$37-($D$37-C$13)/$B43^3	=$D$37-($D$37-D$13
44	=A15	=B15	=$D$37-($D$37-C$13)/$B44^3	=$D$37-($D$37-D$13
45	=A16	=B16	=$D$37-($D$37-C$13)/$B45^3	=$D$37-($D$37-D$13
46	=A17	=B17	=$D$37-($D$37-C$13)/$B46^3	=$D$37-($D$37-D$13
47	=A18	=B18	=$D$37-($D$37-C$13)/$B47^3	=$D$37-($D$37-D$13
48	=A19	=B19	=$D$37-($D$37-C$13)/$B48^3	=$D$37-($D$37-D$13
49	=A20	=B20	=$D$37-($D$37-C$13)/$B49^3	=$D$37-($D$37-D$13
50	=A21	=B21	=$D$37-($D$37-C$13)/$B50^3	=$D$37-($D$37-D$13
51	=A22	=B22	=$D$37-($D$37-C$13)/$B51^3	=$D$37-($D$37-D$13
52	=A23	=B23	=$D$37-($D$37-C$13)/$B52^3	=$D$37-($D$37-D$13
53	=A24	=B24	=$D$37-($D$37-C$13)/$B53^3	=$D$37-($D$37-D$13
54	=A25	=B25	=$D$37-($D$37-C$13)/$B54^3	=$D$37-($D$37-D$13
55	=A26	=B26	=$D$37-($D$37-C$13)/$B55^3	=$D$37-($D$37-D$13
56	=A27	=B27	=$D$37-($D$37-C$13)/$B56^3	=$D$37-($D$37-D$13
57	=A28	=B28	=$D$37-($D$37-C$13)/$B57^3	=$D$37-($D$37-D$13
58	=A29	=B29	=$D$37-($D$37-C$13)/$B58^3	=$D$37-($D$37-D$13
59	=A30	=B30	=$D$37-($D$37-C$13)/$B59^3	=$D$37-($D$37-D$13
60	=A31	=B31	=$D$37-($D$37-C$13)/$B60^3	=$D$37-($D$37-D$13
61	=A32	=B32	=$D$37-($D$37-C$13)/$B61^3	=$D$37-($D$37-D$13
62	=A33	=B33	=$D$37-($D$37-C$13)/$B62^3	=$D$37-($D$37-D$13

$< \$13 = P(a) = P_0$ @ $t = 0.1 s$

$$P_1 - (P_1 - P_0)\left(\frac{r}{a}\right)^3$$

Memorandum Equations 7

Prepared by Bill Thompson 3/19/97

	K
35	
36	
37	
38	
39	$\sigma_r(r)$
40	
41	=K11 $t = 50.375$ s
42	=$D$37-($D$37-K$13)/$B42^3
43	=$D$37-($D$37-K$13)/$B43^3
44	=$D$37-($D$37-K$13)/$B44^3
45	=$D$37-($D$37-K$13)/$B45^3
46	=$D$37-($D$37-K$13)/$B46^3
47	=$D$37-($D$37-K$13)/$B47^3
48	=$D$37-($D$37-K$13)/$B48^3
49	=$D$37-($D$37-K$13)/$B49^3
50	=$D$37-($D$37-K$13)/$B50^3
51	=$D$37-($D$37-K$13)/$B51^3
52	=$D$37-($D$37-K$13)/$B52^3
53	=$D$37-($D$37-K$13)/$B53^3
54	=$D$37-($D$37-K$13)/$B54^3
55	=$D$37-($D$37-K$13)/$B55^3
56	=$D$37-($D$37-K$13)/$B56^3
57	=$D$37-($D$37-K$13)/$B57^3
58	=$D$37-($D$37-K$13)/$B58^3
59	=$D$37-($D$37-K$13)/$B59^3
60	=$D$37-($D$37-K$13)/$B60^3
61	=$D$37-($D$37-K$13)/$B61^3
62	=$D$37-($D$37-K$13)/$B62^3

B-32

$$P_1 - (P_1 - P_0)\left(\frac{r}{a}\right)^3$$

Memorandum Equations 7

$$K\$13 = P(a) = P_0 \quad @ \quad t = 50.375\,s$$

Prepared by Bill Thompson 3/19/97

	A	B	C	D
67	Beta	=B36		
68	nu	=B37		
69	(1-2v)/(1-v)	=(1-2*B68)/(1-B68)		
70	Tangential: No Pp: Sr = Pinf + (Pinf - Pc)*(a/r)^3/2: Pc is cavity pres		$\sigma_t(r)$	
71		Pc	=C10	=D10
72	r	r/a	=C41 $t = 0.1 s$	=D41
73	=A42	=B42	=$D$37+($D$37-C$13)/$B73^3/2	=$D$37+($D$37-D$13
74	=A43	=B43	=$D$37+($D$37-C$13)/$B74^3/2	=$D$37+($D$37-D$13
75	=A44	=B44	=$D$37+($D$37-C$13)/$B75^3/2	=$D$37+($D$37-D$13
76	=A45	=B45	=$D$37+($D$37-C$13)/$B76^3/2	=$D$37+($D$37-D$13
77	=A46	=B46	=$D$37+($D$37-C$13)/$B77^3/2	=$D$37+($D$37-D$13
78	=A47	=B47	=$D$37+($D$37-C$13)/$B78^3/2	=$D$37+($D$37-D$13
79	=A48	=B48	=$D$37+($D$37-C$13)/$B79^3/2	=$D$37+($D$37-D$13
80	=A49	=B49	=$D$37+($D$37-C$13)/$B80^3/2	=$D$37+($D$37-D$13
81	=A50	=B50	=$D$37+($D$37-C$13)/$B81^3/2	=$D$37+($D$37-D$13
82	=A51	=B51	=$D$37+($D$37-C$13)/$B82^3/2	=$D$37+($D$37-D$13
83	=A52	=B52	=$D$37+($D$37-C$13)/$B83^3/2	=$D$37+($D$37-D$13
84	=A53	=B53	=$D$37+($D$37-C$13)/$B84^3/2	=$D$37+($D$37-D$13
85	=A54	=B54	=$D$37+($D$37-C$13)/$B85^3/2	=$D$37+($D$37-D$13
86	=A55	=B55	=$D$37+($D$37-C$13)/$B86^3/2	=$D$37+($D$37-D$13
87	=A56	=B56	=$D$37+($D$37-C$13)/$B87^3/2	=$D$37+($D$37-D$13
88	=A57	=B57	=$D$37+($D$37-C$13)/$B88^3/2	=$D$37+($D$37-D$13
89	=A58	=B58	=$D$37+($D$37-C$13)/$B89^3/2	=$D$37+($D$37-D$13
90	=A59	=B59	=$D$37+($D$37-C$13)/$B90^3/2	=$D$37+($D$37-D$13
91	=A60	=B60	=$D$37+($D$37-C$13)/$B91^3/2	=$D$37+($D$37-D$13
92	=A61	=B61	=$D$37+($D$37-C$13)/$B92^3/2	=$D$37+($D$37-D$13
93	=A62	=B62	=$D$37+($D$37-C$13)/$B93^3/2	=$D$37+($D$37-D$13

$$C\$13 = P(a) = P_0 @ t = 0.1s$$

$$P_1 + (P_1 - P_0)\left(\frac{r}{a}\right)^3$$

Memorandum Equations 7

Prepared by Bill Thompson 3/19/97

	K
67	
68	
69	
70	$\sigma_t(r)$
71	=K10
72	=K41 $t = 50.375\ S$
73	=$D$37+($D$37-K$13)/$B73^3/2
74	=$D$37+($D$37-K$13)/$B74^3/2
75	=$D$37+($D$37-K$13)/$B75^3/2
76	=$D$37+($D$37-K$13)/$B76^3/2
77	=$D$37+($D$37-K$13)/$B77^3/2
78	=$D$37+($D$37-K$13)/$B78^3/2
79	=$D$37+($D$37-K$13)/$B79^3/2
80	=$D$37+($D$37-K$13)/$B80^3/2
81	=$D$37+($D$37-K$13)/$B81^3/2
82	=$D$37+($D$37-K$13)/$B82^3/2
83	=$D$37+($D$37-K$13)/$B83^3/2
84	=$D$37+($D$37-K$13)/$B84^3/2
85	=$D$37+($D$37-K$13)/$B85^3/2
86	=$D$37+($D$37-K$13)/$B86^3/2
87	=$D$37+($D$37-K$13)/$B87^3/2
88	=$D$37+($D$37-K$13)/$B88^3/2
89	=$D$37+($D$37-K$13)/$B89^3/2
90	=$D$37+($D$37-K$13)/$B90^3/2
91	=$D$37+($D$37-K$13)/$B91^3/2
92	=$D$37+($D$37-K$13)/$B92^3/2
93	=$D$37+($D$37-K$13)/$B93^3/2

$$P_1 + (P_1 - P_0)\left(\frac{r}{a}\right)^3$$

Memorandum Equations 7

$$K\$13 = P(a) = P_0 \ @ \ t = 50.375\ s$$

B-34

APPENDIX D

Excel Workbook SPHERE.XLS (Page SHEET1)

Pore Pressure Induced Stress Calculations
(Memorandum Equations 15 and 16)

B-35

	M
8	Integral
9	This is Intgl{p'r^2dr} from r to a: needed for seepage stresses.
10	p' is Pp - P1
11	=C11 C=0.1
12	
13	0
14	=((C13-$C$6)*$A13^2+(C14-$C$6)*$A14^2)/2*($A14-$A13)+M13
15	=((C14-$C$6)*$A14^2+(C15-$C$6)*$A15^2)/2*($A15-$A14)+M14
16	=((C15-$C$6)*$A15^2+(C16-$C$6)*$A16^2)/2*($A16-$A15)+M15
17	=((C16-$C$6)*$A16^2+(C17-$C$6)*$A17^2)/2*($A17-$A16)+M16
18	=((C17-$C$6)*$A17^2+(C18-$C$6)*$A18^2)/2*($A18-$A17)+M17
19	=((C18-$C$6)*$A18^2+(C19-$C$6)*$A19^2)/2*($A19-$A18)+M18
20	=((C19-$C$6)*$A19^2+(C20-$C$6)*$A20^2)/2*($A20-$A19)+M19
21	=((C20-$C$6)*$A20^2+(C21-$C$6)*$A21^2)/2*($A21-$A20)+M20
22	=((C21-$C$6)*$A21^2+(C22-$C$6)*$A22^2)/2*($A22-$A21)+M21
23	=((C22-$C$6)*$A22^2+(C23-$C$6)*$A23^2)/2*($A23-$A22)+M22
24	=((C23-$C$6)*$A23^2+(C24-$C$6)*$A24^2)/2*($A24-$A23)+M23
25	=((C24-$C$6)*$A24^2+(C25-$C$6)*$A25^2)/2*($A25-$A24)+M24
26	=((C25-$C$6)*$A25^2+(C26-$C$6)*$A26^2)/2*($A26-$A25)+M25
27	=((C26-$C$6)*$A26^2+(C27-$C$6)*$A27^2)/2*($A27-$A26)+M26
28	=((C27-$C$6)*$A27^2+(C28-$C$6)*$A28^2)/2*($A28-$A27)+M27
29	=((C28-$C$6)*$A28^2+(C29-$C$6)*$A29^2)/2*($A29-$A28)+M28
30	=((C29-$C$6)*$A29^2+(C30-$C$6)*$A30^2)/2*($A30-$A29)+M29
31	=((C30-$C$6)*$A30^2+(C31-$C$6)*$A31^2)/2*($A31-$A30)+M30
32	=((C31-$C$6)*$A31^2+(C32-$C$6)*$A32^2)/2*($A32-$A31)+M31
33	=((C32-$C$6)*$A32^2+(C33-$C$6)*$A33^2)/2*($A33-$A32)+M32

Pore Pressure

Integral approximation

Memorandum Equation 16

exact $\int_a^a f(x)\,dx = 0$

$$: \frac{1}{2}\left[(P_{(r_{n-1})} - P_\gamma)\, r_{n-1}^2 + (P_{(r_n)} - P_\gamma)\, r_n^2 \right](r_n - r_{n-1}) + I_{n-1}$$

B-36

	U
8	
9	
10	
11	=K11 $t = 50.375$ S
12	
13	0
14	=((K13-$C$6)*$A13^2+(K14-$C$6)*$A14^2)/2*($A14-$A13)+U13
15	=((K14-$C$6)*$A14^2+(K15-$C$6)*$A15^2)/2*($A15-$A14)+U14
16	=((K15-$C$6)*$A15^2+(K16-$C$6)*$A16^2)/2*($A16-$A15)+U15
17	=((K16-$C$6)*$A16^2+(K17-$C$6)*$A17^2)/2*($A17-$A16)+U16
18	=((K17-$C$6)*$A17^2+(K18-$C$6)*$A18^2)/2*($A18-$A17)+U17
19	=((K18-$C$6)*$A18^2+(K19-$C$6)*$A19^2)/2*($A19-$A18)+U18
20	=((K19-$C$6)*$A19^2+(K20-$C$6)*$A20^2)/2*($A20-$A19)+U19
21	=((K20-$C$6)*$A20^2+(K21-$C$6)*$A21^2)/2*($A21-$A20)+U20
22	=((K21-$C$6)*$A21^2+(K22-$C$6)*$A22^2)/2*($A22-$A21)+U21
23	=((K22-$C$6)*$A22^2+(K23-$C$6)*$A23^2)/2*($A23-$A22)+U22
24	=((K23-$C$6)*$A23^2+(K24-$C$6)*$A24^2)/2*($A24-$A23)+U23
25	=((K24-$C$6)*$A24^2+(K25-$C$6)*$A25^2)/2*($A25-$A24)+U24
26	=((K25-$C$6)*$A25^2+(K26-$C$6)*$A26^2)/2*($A26-$A25)+U25
27	=((K26-$C$6)*$A26^2+(K27-$C$6)*$A27^2)/2*($A27-$A26)+U26
28	=((K27-$C$6)*$A27^2+(K28-$C$6)*$A28^2)/2*($A28-$A27)+U27
29	=((K28-$C$6)*$A28^2+(K29-$C$6)*$A29^2)/2*($A29-$A28)+U28
30	=((K29-$C$6)*$A29^2+(K30-$C$6)*$A30^2)/2*($A30-$A29)+U29
31	=((K30-$C$6)*$A30^2+(K31-$C$6)*$A31^2)/2*($A31-$A30)+U30
32	=((K31-$C$6)*$A31^2+(K32-$C$6)*$A32^2)/2*($A32-$A31)+U31
33	=((K32-$C$6)*$A32^2+(K33-$C$6)*$A33^2)/2*($A33-$A32)+U32

Handwritten annotations:

$\int_{a}^{a} f(x)\,dx = 0$ exact

Pore Pressure

Integral approximation

Memorandum Equation 16

$$= \frac{1}{2}\left[\left(P(r_{n-1}) - P_\gamma \right) r_{n-1}^2 + \left(P(r_n) - P_\gamma \right) r_n^2 \right] (r_n - r_{n-1}) + I_{n-1}'$$

B-37

$$\sigma_r^{\,p}$$

	M
40	Radial: Pp stresses: S'r = 2Beta*(1-2n)/(1-n)*intgl/r^3
41	=C41 $t = 0.1$
42	=M13/$A42^3*2*$B$36*$B$38
43	=M14/$A43^3*2*$B$36*$B$38
44	=M15/$A44^3*2*$B$36*$B$38
45	=M16/$A45^3*2*$B$36*$B$38
46	=M17/$A46^3*2*$B$36*$B$38
47	=M18/$A47^3*2*$B$36*$B$38
48	=M19/$A48^3*2*$B$36*$B$38
49	=M20/$A49^3*2*$B$36*$B$38
50	=M21/$A50^3*2*$B$36*$B$38
51	=M22/$A51^3*2*$B$36*$B$38
52	=M23/$A52^3*2*$B$36*$B$38
53	=M24/$A53^3*2*$B$36*$B$38
54	=M25/$A54^3*2*$B$36*$B$38
55	=M26/$A55^3*2*$B$36*$B$38
56	=M27/$A56^3*2*$B$36*$B$38
57	=M28/$A57^3*2*$B$36*$B$38
58	=M29/$A58^3*2*$B$36*$B$38
59	=M30/$A59^3*2*$B$36*$B$38
60	=M31/$A60^3*2*$B$36*$B$38
61	=M32/$A61^3*2*$B$36*$B$38
62	=M33/$A62^3*2*$B$36*$B$38

PORE PRESSURE (time = 0.1)
INDUCED STRESS $\sigma_r^{\,p}$
Memorandum Equation 15

$\beta = 1$

$\nu = 0.35$

$$\frac{I_n}{r_n^{3}}\, 2\beta \left[\frac{1-2\nu}{1-\nu}\right] = \frac{2\beta}{r_n^{3}}\left[\frac{1-2\nu}{1-\nu}\right]\int_a^{r_n} P\, r^{2}\, dr$$

Prepared by Bill Thompson 3/20/97

σ_r^P

	U
40	
41	=K41 $t = 50.375$
42	=U13/$A42^3*2*$B$36*$B$38
43	=U14/$A43^3*2*$B$36*$B$38
44	=U15/$A44^3*2*$B$36*$B$38
45	=U16/$A45^3*2*$B$36*$B$38
46	=U17/$A46^3*2*$B$36*$B$38
47	=U18/$A47^3*2*$B$36*$B$38
48	=U19/$A48^3*2*$B$36*$B$38
49	=U20/$A49^3*2*$B$36*$B$38
50	=U21/$A50^3*2*$B$36*$B$38
51	=U22/$A51^3*2*$B$36*$B$38
52	=U23/$A52^3*2*$B$36*$B$38
53	=U24/$A53^3*2*$B$36*$B$38
54	=U25/$A54^3*2*$B$36*$B$38
55	=U26/$A55^3*2*$B$36*$B$38
56	=U27/$A56^3*2*$B$36*$B$38
57	=U28/$A57^3*2*$B$36*$B$38
58	=U29/$A58^3*2*$B$36*$B$38
59	=U30/$A59^3*2*$B$36*$B$38
60	=U31/$A60^3*2*$B$36*$B$38
61	=U32/$A61^3*2*$B$36*$B$38
62	=U33/$A62^3*2*$B$36*$B$38

B-39

PORE PRESSURE (time = 50.375
INDUCED STRESS σ_r^P
Memorandum Equation

$\beta = 1$
$\gamma = 0.35$

$$\frac{I_n}{r_n^3} \, 2\beta \left[\frac{1-2\nu}{1-\nu}\right] = \frac{2\beta}{r_n^3}\left[\frac{1-2\nu}{1-\nu}\right] \int_a^{r_n} P' r^2 dr$$

σ_t^P

	M
70	Tangential: Pp stresses: S't = -Beta*(1-2n)/(1-n)*{Intgl/r^3-p'}
71	
72	=C72 c = 0.1 s
73	=-$B$36*$B$38*(M13/$A73^3-(C13-$C$6))
74	=-$B$36*$B$38*(M14/$A74^3-(C14-$C$6))
75	=-$B$36*$B$38*(M15/$A75^3-(C15-$C$6))
76	=-$B$36*$B$38*(M16/$A76^3-(C16-$C$6))
77	=-$B$36*$B$38*(M17/$A77^3-(C17-$C$6))
78	=-$B$36*$B$38*(M18/$A78^3-(C18-$C$6))
79	=-$B$36*$B$38*(M19/$A79^3-(C19-$C$6))
80	=-$B$36*$B$38*(M20/$A80^3-(C20-$C$6))
81	=-$B$36*$B$38*(M21/$A81^3-(C21-$C$6))
82	=-$B$36*$B$38*(M22/$A82^3-(C22-$C$6))
83	=-$B$36*$B$38*(M23/$A83^3-(C23-$C$6))
84	=-$B$36*$B$38*(M24/$A84^3-(C24-$C$6))
85	=-$B$36*$B$38*(M25/$A85^3-(C25-$C$6))
86	=-$B$36*$B$38*(M26/$A86^3-(C26-$C$6))
87	=-$B$36*$B$38*(M27/$A87^3-(C27-$C$6))
88	=-$B$36*$B$38*(M28/$A88^3-(C28-$C$6))
89	=-$B$36*$B$38*(M29/$A89^3-(C29-$C$6))
90	=-$B$36*$B$38*(M30/$A90^3-(C30-$C$6))
91	=-$B$36*$B$38*(M31/$A91^3-(C31-$C$6))
92	=-$B$36*$B$38*(M32/$A92^3-(C32-$C$6))
93	=-$B$36*$B$38*(M33/$A93^3-(C33-$C$6))

PORE PRESSURE (time = 0.1 s
INDUCED STRESS σ_t^P

Memorandum Equation 15

$\beta = 1$

$\nu = 0.35$

$$-\beta \left[\frac{1-2\nu}{1-\nu} \right] \left[\frac{I_n}{r_n^3} - (P_n - P_\gamma) \right] = -\beta \left[\frac{1-2\nu}{1-\nu} \right] \left\{ \frac{1}{r_n^3} \int_a^{r_n} P' r^2 dr - P' \right\}$$

σ_t^P

	U
71	
72	=K72 $t = 50.375\ s$
73	=-$B$36*$B$38*(U13/$A73^3-(K13-$C$6))
74	=-$B$36*$B$38*(U14/$A74^3-(K14-$C$6))
75	=-$B$36*$B$38*(U15/$A75^3-(K15-$C$6))
76	=-$B$36*$B$38*(U16/$A76^3-(K16-$C$6))
77	=-$B$36*$B$38*(U17/$A77^3-(K17-$C$6))
78	=-$B$36*$B$38*(U18/$A78^3-(K18-$C$6))
79	=-$B$36*$B$38*(U19/$A79^3-(K19-$C$6))
80	=-$B$36*$B$38*(U20/$A80^3-(K20-$C$6))
81	=-$B$36*$B$38*(U21/$A81^3-(K21-$C$6))
82	=-$B$36*$B$38*(U22/$A82^3-(K22-$C$6))
83	=-$B$36*$B$38*(U23/$A83^3-(K23-$C$6))
84	=-$B$36*$B$38*(U24/$A84^3-(K24-$C$6))
85	=-$B$36*$B$38*(U25/$A85^3-(K25-$C$6))
86	=-$B$36*$B$38*(U26/$A86^3-(K26-$C$6))
87	=-$B$36*$B$38*(U27/$A87^3-(K27-$C$6))
88	=-$B$36*$B$38*(U28/$A88^3-(K28-$C$6))
89	=-$B$36*$B$38*(U29/$A89^3-(K29-$C$6))
90	=-$B$36*$B$38*(U30/$A90^3-(K30-$C$6))
91	=-$B$36*$B$38*(U31/$A91^3-(K31-$C$6))
92	=-$B$36*$B$38*(U32/$A92^3-(K32-$C$6))
93	=-$B$36*$B$38*(U33/$A93^3-(K33-$C$6))

PORE PRESSURE (time =50.375)
INDUCED STRESS σ_t^P

Memorandum Equation 15

$$-\beta\left[\frac{1-2\nu}{1-\nu}\right]\left[\frac{I_n}{r_n^3} - (P_n - P_\gamma)\right] = -\beta\left[\frac{1-2\nu}{1-\nu}\right]\left\{\frac{1}{r_n^3}\int_a^{r_n} P' r^2 dr - P'\right\}$$

B-41

Prepared by Bill Thompson 3/20/97

APPENDIX E

Excel Workbook SPHERE.XLS (Page SHEET1)

Total Stress Calculations
(Memorandum Equations 19)

Radial Stress (handwritten)

	W	X
40	Total Radial Stress = Non Pp + Pp stresse	
41	*r*	=M41 *t=0.1S*
42	=B42	=C42+M42
43	=B43	=C43+M43
44	=B44	=C44+M44
45	=B45	=C45+M45
46	=B46	=C46+M46
47	=B47	=C47+M47
48	=B48	=C48+M48
49	=B49	=C49+M49
50	=B50	=C50+M50
51	=B51	=C51+M51
52	=B52	=C52+M52
53	=B53	=C53+M53
54	=B54	=C54+M54
55	=B55	=C55+M55
56	=B56	=C56+M56
57	=B57	=C57+M57
58	=B58	=C58+M58
59	=B59	=C59+M59
60	=B60	=C60+M60
61	=B61	=C61+M61
62	=B62	=C62+M62

Mech. Loading + Pore Pressure Induced Stresses (handwritten)

Memorandum Equations 19 σ_r (handwritten)

B-43 (left margin, rotated)

Radial Stress

	AF
40	
41	=U41
42	=K42+U42
43	=K43+U43
44	=K44+U44
45	=K45+U45
46	=K46+U46
47	=K47+U47
48	=K48+U48
49	=K49+U49
50	=K50+U50
51	=K51+U51
52	=K52+U52
53	=K53+U53
54	=K54+U54
55	=K55+U55
56	=K56+U56
57	=K57+U57
58	=K58+U58
59	=K59+U59
60	=K60+U60
61	=K61+U61
62	=K62+U62

$t = 50.375$ S

Mech Loading + Pore Pressure Induced Stresses

Memorandum Equation 19 σ_r

B-44

Sheet1

	W	X
70	Total Tangential Stress = Non Pp + Pp str	
71		
72		=M72
73	=B73	=C73+M73
74	=B74	=C74+M74
75	=B75	=C75+M75
76	=B76	=C76+M76
77	=B77	=C77+M77
78	=B78	=C78+M78
79	=B79	=C79+M79
80	=B80	=C80+M80
81	=B81	=C81+M81
82	=B82	=C82+M82
83	=B83	=C83+M83
84	=B84	=C84+M84
85	=B85	=C85+M85
86	=B86	=C86+M86
87	=B87	=C87+M87
88	=B88	=C88+M88
89	=B89	=C89+M89
90	=B90	=C90+M90
91	=B91	=C91+M91
92	=B92	=C92+M92
93	=B93	=C93+M93

B-45

Mech. Loading Stress + Pore Pressure Induced Stress

Memorandum Equations 19, σ_t

Tangential Stress

	AF
71	
72	=U72
73	=K73+U73
74	=K74+U74
75	=K75+U75
76	=K76+U76
77	=K77+U77
78	=K78+U78
79	=K79+U79
80	=K80+U80
81	=K81+U81
82	=K82+U82
83	=K83+U83
84	=K84+U84
85	=K85+U85
86	=K86+U86
87	=K87+U87
88	=K88+U88
89	=K89+U89
90	=K90+U90
91	=K91+U91
92	=K92+U92
93	=K93+U93

B-46

Mech. Loading Stress + Pore Pressure Induced Stress

Memorandum Equations 19, σ_t

APPENDIX F

Excel Workbook SPHERE.XLS (Page SHEET1)

Effective Stress Calculations
(Memorandum Equations 24)

B-47

	AH	AI
40	Effective Radial Stress = Total Stress - Pp	
41	r/a	=X41 $t = 0.1s$
42	=B42	=X42-C13
43	=B43	=X43-C14
44	=B44	=X44-C15
45	=B45	=X45-C16
46	=B46	=X46-C17
47	=B47	=X47-C18
48	=B48	=X48-C19
49	=B49	=X49-C20
50	=B50	=X50-C21
51	=B51	=X51-C22
52	=B52	=X52-C23
53	=B53	=X53-C24
54	=B54	=X54-C25
55	=B55	=X55-C26
56	=B56	=X56-C27
57	=B57	=X57-C28
58	=B58	=X58-C29
59	=B59	=X59-C30
60	=B60	=X60-C31
61	=B61	=X61-C32
62	=B62	=X62-C33

B-48

EFFECTIVE STRESS

Memorandum Equation 23

Total Stress

Pore Pressure

$$\sigma_r' = \sigma_r - P$$

Prepared by Bill Thompson 3/25/97

Information Only

	AQ
40	
41	=AF41
42	=AF42-K13
43	=AF43-K14
44	=AF44-K15
45	=AF45-K16
46	=AF46-K17
47	=AF47-K18
48	=AF48-K19
49	=AF49-K20
50	=AF50-K21
51	=AF51-K22
52	=AF52-K23
53	=AF53-K24
54	=AF54-K25
55	=AF55-K26
56	=AF56-K27
57	=AF57-K28
58	=AF58-K29
59	=AF59-K30
60	=AF60-K31
61	=AF61-K32
62	=AF62-K33

$t = 50.375 s$

EFFECTIVE STRESS

Memorandum Equation 23

Total Stress   Pore Pressure

$$\sigma_r' = \sigma_r - P$$

B-49

Prepared by Bill Thompson 3/25/97

	AH	AI
70	Effective Tangential Stress = Total Stress - Pr	
71		
72	r/a	=X72 t=0.1s
73	=B73	=X73-C13
74	=B74	=X74-C14
75	=B75	=X75-C15
76	=B76	=X76-C16
77	=B77	=X77-C17
78	=B78	=X78-C18
79	=B79	=X79-C19
80	=B80	=X80-C20
81	=B81	=X81-C21
82	=B82	=X82-C22
83	=B83	=X83-C23
84	=B84	=X84-C24
85	=B85	=X85-C25
86	=B86	=X86-C26
87	=B87	=X87-C27
88	=B88	=X88-C28
89	=B89	=X89-C29
90	=B90	=X90-C30
91	=B91	=X91-C31
92	=B92	=X92-C32
93	=B93	=X93-C33

EFFECTIVE STRESS

Memorandum Equation 2.3

Total Stress

PORE PRESSURE

$$\sigma_t' = \sigma_t - P$$

Prepared by Bill Thompson 3/25/97

	AQ
70	
71	
72	=AF72 t=50.375 s
73	=AF73-K13
74	=AF74-K14
75	=AF75-K15
76	=AF76-K16
77	=AF77-K17
78	=AF78-K18
79	=AF79-K19
80	=AF80-K20
81	=AF81-K21
82	=AF82-K22
83	=AF83-K23
84	=AF84-K24
85	=AF85-K25
86	=AF86-K26
87	=AF87-K27
88	=AF88-K28
89	=AF89-K29
90	=AF90-K30
91	=AF91-K31
92	=AF92-K32
93	=AF93-K33

B-51

EFFECTIVE STRESS

MEMORANDUM Equation 23

Total Stress

Pore Pressure

$$\sigma_t' = \sigma_t - P$$

APPENDIX G

Excel Workbook SPHERE.XLS (Page SHEET1)

Failure Analysis Calculations
(Memorandum Equations 25, 26, and 31)

	AG	AH	AI	AJ	AK
63	Failure Zone Calcula				
64	Time		=AI41 $t=0.1\ s$	=AJ41 $t=0.2\ s$	=AK41 $t=0.5\ s$
65	Row		0	43	48
66	Failure Radius		=A42	=AI66	=$A$52+($A$53-$A$52)/(AK53-AK52)*(-$D$38-AK52)
67	Volume		=4/3*PI()*(AI66^3-$A$42^3)/2	=4/3*PI()*(AJ66^3-$A$42^3)/2	=4/3*PI()*(AK66^3-$A$42^3)/2
68					

$$\frac{4\pi}{3}\left(a^3-a^3\right)\frac{1}{2} \qquad \frac{4\pi}{3}\left(a^3-a^3\right)\frac{1}{2}$$

$A42 = a = 0.1555\,m$

$\$A52 = r_{n-1} = 0.6151211794$

$\$A53 = r_n = 0.7163884293$

$AK53 = \sigma_r'(r_n) = -0.10327738$

$AK52 = \sigma_r'(r_{n-1}) = -0.065380829$

$\$D\$38 = T_0 = 0.1\ MPa$

$$AK66 = r_{n-1} + \frac{r_n - r_{n-1}}{\sigma_r'(r_n) - \sigma_r'(r_{n-1})}\left[-T_0 - \sigma_r'(r_{n-1})\right]$$

Negative sign because compression (+ and T_0 entered as (+)

Prepared by Bill Thompson 3/21/97

	AG	AH	AI	AJ	AK	AL	AM	AN	AO	AP	AQ
40		Effective Radial Stress = Total Stress - Pp									
41		r/a	0.1	0.2	0.5	1	2	5	10.375	20.375	50.375
42		1	0	0	0	0	0	0	0	0	0
43		1.065735124	-0.026665262	0	0.030190289	0.074189954	0.111397837	0.147238942	0.168972554	0.186267859	0.207068539
44		1.131470249	-0.049403784	0	0.042329773	0.121624747	0.188553969	0.252552561	0.291559781	0.322976652	0.363010127
45		1.493455662	-0.021483876	-1.77636E-15	-0.033306994	0.144216664	0.298547653	0.445139825	0.535013397	0.608649291	0.712326177
46		1.855441076	-0.011203356	0	-0.171613843	0.033288186	0.220637233	0.400587762	0.510252753	0.599357427	0.725123025
47		2.195249114	-0.006764539	0	-0.291374206	-0.081250789	0.120268623	0.316328513	0.434936487	0.53013094	0.662189522
48		2.535057151	-0.004392648	0	-0.392404651	-0.183976133	0.024924645	0.230637573	0.354216735	0.452180688	0.58510869
49		2.856137304	-0.003071513	0	-0.274384874	-0.267557986	-0.054691163	0.157069791	0.283532785	0.382706038	0.514418387
50		3.177217456	-0.002231253	0	-0.199322622	-0.339103812	-0.123836187	0.092231829	0.220599848	0.320294905	0.449997754
51		3.566492311	-0.001577487	0	-0.140920292	-0.239745031	-0.195223206	0.024612455	0.154514792	0.254364446	0.381289254
52		3.955767166	-0.001156106	0	-0.103277388	-0.17570387	-0.255401805	-0.032782843	0.098160671	0.197913374	0.322068348
53		4.606972942	-0.000731885	0	-0.065380829	-0.11123117	-0.161684781	-0.11051286	0.021498076	0.120823348	0.24070605
54		5.258178719	-0.000492248	0	-0.043973535	-0.074811345	-0.1087452	-0.171514411	-0.038828043	0.060014502	0.17625838
55		5.930931733	-0.000343021	0	-0.030642813	-0.05213204	-0.075778735	-0.119519253	-0.088674646	0.009688676	0.122773336
56		6.603684747	-0.000248502	0	-0.022199256	-0.037767174	-0.054898077	-0.086585994	-0.129188324	-0.031257993	0.079174374
57		7.389287095	-0.000177371	0	-0.01584491	-0.026956647	-0.039183976	-0.061801501	-0.092209282	-0.070237503	0.037602531
58		8.174889444	-0.000130992	0	-0.011701775	-0.019908009	-0.02893813	-0.045641613	-0.068098351	-0.102135884	0.003547028
59		9.563785946	-8.18088E-05	0	-0.007308157	-0.012433229	-0.018072848	-0.028504741	-0.042529739	-0.063787337	-0.043426092
60		10.95268245	-5.44663E-05	0	-0.004865595	-0.008277744	-0.012032466	-0.018977769	-0.028315274	-0.04246807	-0.078950419
61		11.90720939	-4.23896E-05	0	-0.003786757	-0.006442338	-0.009364534	-0.01476987	-0.022036991	-0.033051718	-0.061444916
62		12.86173633	-3.3635E-05	0	-0.003004683	-0.00511181	-0.007430488	-0.011719466	-0.017485717	-0.026225586	-0.048754771
63	Failure Zone Calculations: Fall If Sr(eff) < -To										
64	Time		0.1	0.2	0.5	1	2	5	10.375	20.375	50.375
65	Row		0	43	48	49	50	51			
66	Failure Radius		0.1555	0.1555	0.623879226	0.74761169	0.845398096	0.984263145			
67	Volume		0	0	0.500706079	0.867283815	1.257567495	1.989190403			

$|\sigma_r'| < |T_0|$ $|\sigma_r'| < |T_0|$ $\sigma_r' < T_0$

between

$r/a = 3.9576\ldots$

&

$r/a = 4.6069\ldots$

$T_0 = -0.1\ MPa$

Computed radial effective stresses

Prepared by Bill Thompson 3/25/97

	A	B	C	D	E
95	Shear Failure Potential (Yield>0)				
96	Uses Mohr-Coulomb: St(eff) - Sr(eff)*tan^2(alp)-2So*tan(alp)=0				
97	Co	0.7 MPa		=Uniaxial Compressive Strength	
98	phi	45 deg		=Angle of Internal Friction	
99	alpha	=45+B98/2 deg		tan(alp)	=TAN(B99/180*PI())
100	So	=B97/2/E99		= Cohesion = Co/2tan(alp)	
101					
102	r	r/a	=C72 t = 0.1	=D72 t = 0.2	=E72 t = 0.5
103	=A73	=B73	=AI73-AI42*$E$99^2-2*$B$100*$E$99	=AJ73-AJ42*$E$99^2-2*$B$100*$E$99	=AK73-AK42*$E$99^2-2*$B$100*$E$99
104	=A74	=B74	=AI74-AI43*$E$99^2-2*$B$100*$E$99	=AJ74-AJ43*$E$99^2-2*$B$100*$E$99	=AK74-AK43*$E$99^2-2*$B$100*$E$99
105	=A75	=B75	=AI75-AI44*$E$99^2-2*$B$100*$E$99	=AJ75-AJ44*$E$99^2-2*$B$100*$E$99	=AK75-AK44*$E$99^2-2*$B$100*$E$99
106	=A76	=B76	=AI76-AI45*$E$99^2-2*$B$100*$E$99	=AJ76-AJ45*$E$99^2-2*$B$100*$E$99	=AK76-AK45*$E$99^2-2*$B$100*$E$99
107	=A77	=B77	=AI77-AI46*$E$99^2-2*$B$100*$E$99	=AJ77-AJ46*$E$99^2-2*$B$100*$E$99	=AK77-AK46*$E$99^2-2*$B$100*$E$99
108	=A78	=B78	=AI78-AI47*$E$99^2-2*$B$100*$E$99	=AJ78-AJ47*$E$99^2-2*$B$100*$E$99	=AK78-AK47*$E$99^2-2*$B$100*$E$99
109	=A79	=B79	=AI79-AI48*$E$99^2-2*$B$100*$E$99	=AJ79-AJ48*$E$99^2-2*$B$100*$E$99	=AK79-AK48*$E$99^2-2*$B$100*$E$99
110	=A80	=B80	=AI80-AI49*$E$99^2-2*$B$100*$E$99	=AJ80-AJ49*$E$99^2-2*$B$100*$E$99	=AK80-AK49*$E$99^2-2*$B$100*$E$99
111	=A81	=B81	=AI81-AI50*$E$99^2-2*$B$100*$E$99	=AJ81-AJ50*$E$99^2-2*$B$100*$E$99	=AK81-AK50*$E$99^2-2*$B$100*$E$99
112	=A82	=B82	=AI82-AI51*$E$99^2-2*$B$100*$E$99	=AJ82-AJ51*$E$99^2-2*$B$100*$E$99	=AK82-AK51*$E$99^2-2*$B$100*$E$99
113	=A83	=B83	=AI83-AI52*$E$99^2-2*$B$100*$E$99	=AJ83-AJ52*$E$99^2-2*$B$100*$E$99	=AK83-AK52*$E$99^2-2*$B$100*$E$99
114	=A84	=B84	=AI84-AI53*$E$99^2-2*$B$100*$E$99	=AJ84-AJ53*$E$99^2-2*$B$100*$E$99	=AK84-AK53*$E$99^2-2*$B$100*$E$99
115	=A85	=B85	=AI85-AI54*$E$99^2-2*$B$100*$E$99	=AJ85-AJ54*$E$99^2-2*$B$100*$E$99	=AK85-AK54*$E$99^2-2*$B$100*$E$99
116	=A86	=B86	=AI86-AI55*$E$99^2-2*$B$100*$E$99	=AJ86-AJ55*$E$99^2-2*$B$100*$E$99	=AK86-AK55*$E$99^2-2*$B$100*$E$99
117	=A87	=B87	=AI87-AI56*$E$99^2-2*$B$100*$E$99	=AJ87-AJ56*$E$99^2-2*$B$100*$E$99	=AK87-AK56*$E$99^2-2*$B$100*$E$99
118	=A88	=B88	=AI88-AI57*$E$99^2-2*$B$100*$E$99	=AJ88-AJ57*$E$99^2-2*$B$100*$E$99	=AK88-AK57*$E$99^2-2*$B$100*$E$99
119	=A89	=B89	=AI89-AI58*$E$99^2-2*$B$100*$E$99	=AJ89-AJ58*$E$99^2-2*$B$100*$E$99	=AK89-AK58*$E$99^2-2*$B$100*$E$99
120	=A90	=B90	=AI90-AI59*$E$99^2-2*$B$100*$E$99	=AJ90-AJ59*$E$99^2-2*$B$100*$E$99	=AK90-AK59*$E$99^2-2*$B$100*$E$99
121	=A91	=B91	=AI91-AI60*$E$99^2-2*$B$100*$E$99	=AJ91-AJ60*$E$99^2-2*$B$100*$E$99	=AK91-AK60*$E$99^2-2*$B$100*$E$99
122	=A92	=B92	=AI92-AI61*$E$99^2-2*$B$100*$E$99	=AJ92-AJ61*$E$99^2-2*$B$100*$E$99	=AK92-AK61*$E$99^2-2*$B$100*$E$99
123	=A93	=B93	=AI93-AI62*$E$99^2-2*$B$100*$E$99	=AJ93-AJ62*$E$99^2-2*$B$100*$E$99	=AK93-AK62*$E$99^2-2*$B$100*$E$99

time (s) $\sigma'_r (r_1 .. r_n)$ $\sigma'_t (r_1 .. r_n)$

t 0.1   AI 42 .. AI 62   AI 73 .. AI 93

    0.2   AJ 42 .. AJ 62   AJ 73 .. AJ 93

    0.5   AK 42 .. AK 62   AK 73 .. AK 93

$$B99 = \alpha = \frac{\pi}{4} + \frac{\phi}{2}$$

$$E99 = \tan\alpha = \tan\left[\frac{B99 * \pi}{180}\right]$$

$$B100 = S_o = \frac{Co}{2\tan\alpha}$$

$$F = \sigma'_t - \sigma'_r \tan^2\alpha - 2\,\frac{Co}{2\tan\alpha}\,\tan\alpha$$

Memorandum Equation

Prepared by Bill Thompson 3/25/97

	L	M	N	O	P	Q	R	S	T	U
95										
96										
97										
98										
99		GDC check calcs								
100		F = abs((s1-s3)*.5)*cos(phi) - S0 - [(s1+s3)*.5 - (s1-s3)*.5*sin(phi)]*tan(phi)								
101		F>0 Potential Failure								
102	0.1	0.2	0.5	1	2	5	10.375	20.375	50.375	r/a
103	-0.13049	-0.144974747	0.546994	0.770676	0.859041	0.902072	0.943762	1.00085	1.157063	1
104	-0.10324	-0.144974747	0.428403	0.576453	0.613343	0.612003	0.624856	0.656033	0.770241	1.065735124
105	-0.08022	-0.144974747	0.344623	0.431764	0.427607	0.391552	0.381539	0.391663	0.469132	1.131470249
106	-0.11682	-0.144974747	0.192455	0.10179	-0.0232	-0.1597	-0.23674	-0.2899	-0.33187	1.493455662
107	-0.13029	-0.144974747	0.230687	0.079165	-0.09188	-0.26782	-0.37074	-0.44792	-0.53597	1.855441076
108	-0.13611	-0.144974747	0.29973	0.126878	-0.06423	-0.2587	-0.37324	-0.46049	-0.56642	2.195249114
109	-0.13922	-0.144974747	0.369334	0.188711	-0.01304	-0.21834	-0.33929	-0.43157	-0.54518	2.535057151
110	-0.14095	-0.144974747	0.214651	0.246442	0.038835	-0.17309	-0.29774	-0.39257	-0.50909	2.856137304
111	-0.14205	-0.144974747	0.116269	0.299475	0.08823	-0.12833	-0.25539	-0.35165	-0.469	3.177217456
112	-0.14291	-0.144974747	0.039724	0.16925	0.142279	-0.07824	-0.20724	-0.30439	-0.42136	3.566492311
113	-0.14346	-0.144974747	-0.00961	0.085313	0.18977	-0.03363	-0.16393	-0.26149	-0.37737	3.955767166
114	-0.14402	-0.144974747	-0.05928	0.000812	0.066939	0.029044	-0.10256	-0.20024	-0.31373	4.606972942
115	-0.14433	-0.144974747	-0.08734	-0.04692	-0.00245	0.079822	-0.0526	-0.15014	-0.26122	5.258178719
116	-0.14453	-0.144974747	-0.10481	-0.07665	-0.04565	0.011674	-0.01043	-0.10773	-0.21652	5.930931733
117	-0.14465	-0.144974747	-0.11588	-0.09547	-0.07302	-0.03149	0.024347	-0.07269	-0.17946	6.603684747
118	-0.14474	-0.144974747	-0.12421	-0.10964	-0.09362	-0.06397	-0.02412	-0.03896	-0.14367	7.389287095
119	-0.1448	-0.144974747	-0.12964	-0.11888	-0.10705	-0.08515	-0.05572	-0.01111	-0.11406	8.174889444
120	-0.14487	-0.144974747	-0.1354	-0.12868	-0.12129	-0.10761	-0.08923	-0.06137	-0.07291	9.563785946
121	-0.1449	-0.144974747	-0.1386	-0.13413	-0.1292	-0.1201	-0.10786	-0.08931	-0.0415	10.95268245
122	-0.14492	-0.144974747	-0.14001	-0.13653	-0.1327	-0.12562	-0.11609	-0.10166	-0.06444	11.90720939
123	-0.14493	-0.144974747	-0.14104	-0.13827	-0.13524	-0.12961	-0.12206	-0.1106	-0.08107	12.86173633

Values of f

Memorandum Equation 32

Prepared by Bill Thompson 3/24/97

B-56

Appendix C
GasOut Code Listing

```
{
Program GasOut          --

-- written by John Schatz, John F. Schatz Research & Consulting, Inc.

GasOut calculates non-steady radial isothermal gas gas flow in a pre-pressurized
cylindrical porous, permeable volume of material with a vertical axis coincident
with a  wellbore.  The basic concepts of Chan et al. (1991), are followed, and
the previous Chan et al. (1991) calculations are used for approximate validation.
The outer boundary is assumed to be no flow.  The inner (wellbore) boundary is
either constant pressure, or mud flow is calculated up the wellbore as caused by
pressurization of the hole from the porous volume.  (Wellbore flow is not
included in Chan et al.)  In this case, the gas pressure in the well and
pressure at the hole boundary of the porous volume are approximately coupled and
mud flow is modeled ballistically.  If all mud is removed from the wellbore, the
flow up the well is instead calculated by a standard gas pipe flow equation.

The main calculation is by implicit finite differences with the main independent
variable being pressure.  In the porous volume, a tri-diagonal matrix inversion
is used to find coefficients for time stepping.  Some guidance in numerical
methodology is obtained from Press and Teukolsky (1989)

All computational units are SI, according to SPE (1984).

Chronology of physics-related features:

1. 02/27/97 -- Started development.
2. 02/28/97 -- Impicit differencing and tridiagonal inversion for porous flow
               entered.  Began testing.  Constant pressure boundaries work.
               No flow outer boundary works.
3. 03/01/97 -- Began effort on gas/mud interaction at face and in well.
4. 03/02/97 -- Completed gas/mud interaction.  Added stress calculation.
5. 03/03/97 -- Added tensile failure material removal.
6. 03/04/97 -- Tested all subroutines.  Made simple validation calculations
               (using Chan et al.).  Looks good.
7. 03/10/97 -- Added seepage stresses, following suggestion of T.W. Thompson.
               Greatly increases tendency to create internal tensile failure.
               Calculations are also slowed down to to required integrations.
8. 03/15/97- Various modifications to correct difference scheme, increase
               timestep, and add interior failed zone
   04/17/97

{-----------------------------------------------------------------------------}

unit Calc;

interface

uses
  Math, Forms, Controls;

procedure Start;

var
  {gas pressure array}
  pressure: array[0..10000] of Double;
  {waste geometry arrays}
  radius: array[0..10000] of Double;
  index : array[0..10000] of Integer;
  tensileFailed, contiguousTensileFailed, shearFailed: array[0..10000] of Boolean;
  {waste property arrays}
  porosity, permeability: array[0..10000] of Double;
  {stress arrays}
  radEffStress, tanEffStress, shearStress: array[0..10000] of Double;

  {time}
```

```
    time, deltaTime, maxDeltaTime, maxTime, minDeltaTime: Double;
    {initial values}
    initialPressure, initialPorosity, initialPermeability: Double;
    initialCellLength: Double;
    {vertical geometry variables}
    surfaceElevation, baseElevation, baseHeight: Double;
    {horizontal geometry variables}
    wellboreDiameter, pipeDiameter, annulusArea: Double;
    zoneLength, wellboreRadius, outerRadius: Double;
    numZones: Integer;
    {isothermal ideal gas properties}
    gasBaseDensity, gasViscosity: Double;

    {inhole properties}
    mudDensity, mudFrictionFactor, mudBottom, mudVelocity: Double;
    initialMudBottom, workingVolume, workingMass, gasFrictionFactor: Double;
    contiguousTensileFailedTotalVolume, tensileFailedTotalVolume,
      contiguousTensileFailedSolidVolume, tensileFailedSolidVolume: Double;
    mudAcceleration, gasFlowRate: Double;

    {stress-related}
    farfieldStress, farFieldPorePressure, verticalStress: Double;
    poissonsRatio, biotBeta: Double;
    tensileStrengthSI, cohesionSI, frictionAngleSI: Double;
    tensileStrength, cohesion, frictionAngle: Double;
    tensileFailureVelocity, tensileFailureTimeZero: Double;
    maxContiguousTensileFailedIndex, maxTensileFailedIndex,
      minInteriorTensileFailedIndex, maxShearFailedIndex, firstIntactZone: Integer;

    {geometry}
    geomExponent: Integer;

    {calculational control}
    ejectMud, noFlowOuterBoundary, timeStepOK, spherical, allowMaterialRemoval,
      permFromPorosity: Boolean;
    screenSaveTime, radialSaveTime: array[0..200] of double;
    timeSaveTime: array[0..2000] of double;
    runIndex, screenSaveIndex, radialSaveIndex, timeSaveIndex: Integer;
    runComment: String;

const
  AtmosphericPressure=101300.0;
  Gravity=9.8067;
{------------------------------------------------------------------------------}

implementation

uses
  Main;
{------------------------------------------------------------------------------}

procedure CalculateStresses;
var
  i, j: Integer;
  temp1, temp2, temp3, tensileCommLength, shearStrength, meanEffStress: Double;
  radElasticStress, tanElasticStress, radSeepageStress, tanSeepageStress: Double;
  radTotStress, tanTotStress: Double;
  mu, S0, preFactor, integral1, integral2: Double;
  numberOfCellsNewlyTensileFailed: Integer;
  rN, rIN, rWN, pPrime: Double;

begin
  {seepage force constant}
  preFactor:=biotBeta*(1.0-2.0*poissonsRatio)/(1.0-poissonsRatio);
  {failure constants}
  mu:=Tan(frictionAngleSI);
  S0:=0.5*cohesionSI/(mu+Sqrt(Sqr(mu)+1.0));
  tensileCommLength:=tensileFailureVelocity*(time-tensileFailureTimeZero);
```

C-4

```
        numberOfCellsNewlyTensileFailed:=0;
        temp3:=geomExponent-1;

     for i:= firstIntactZone to numZones do begin
        if maxContiguousTensileFailedIndex=maxTensileFailedIndex then begin
           {contiguous failed volume only}
           {elastic}
           temp1:=power((radius[firstIntactZone]-0.5*zoneLength)/radius[i],
geomExponent);
           radElasticStress:=(pressure[0]-farfieldStress)*temp1+farfieldStress;
           tanElasticStress:=-(pressure[0]-farfieldStress)*temp1/temp3+farfieldStress;
           {seepage stresses}
           integral1:=0.0;
           for j:=firstIntactZone to i do begin
             pPrime:=pressure[j]-farFieldPorePressure;
             integral1:=integral1+pPrime*power(radius[j], geomExponent-1)*zoneLength;
           end;
           radSeepageStress:=(geomExponent-1)
             *preFactor*integral1/Power(radius[i], geomExponent);
           pPrime:=pressure[i]-farFieldPorePressure;
           tanSeepageStress:=-preFactor*(integral1/Power(radius[i], geomExponent)-
pPrime);
           {total stresses}
           radTotStress:=radElasticStress+radSeepageStress;
           tanTotStress:=tanElasticStress+tanSeepageStress;
           {effective stresses}
           radEffStress[i]:=radTotStress-pressure[i];
           tanEffStress[i]:=tanTotStress-pressure[i];
           shearStress[i]:=0.5*Abs(radEffStress[i]-tanEffStress[i]);
           meanEffStress:=(radEffStress[i]+(geomExponent-
1)*tanEffStress[i])/geomExponent;
        end
        else begin
           {contiguous plus inner failed volume}
           {elastic near cavity}
           if i<minInteriorTensileFailedIndex then begin
             rN:=power(radius[i], geomExponent);
             rIN:=power((radius[minInteriorTensileFailedIndex]-0.5*zoneLength),
geomExponent);
             rWN:=power((radius[firstIntactZone]-0.5*zoneLength), geomExponent);
             temp1:=(rN-rWN)/(rIN-rWN);
             temp2:=((geomExponent-1)*rN+rWN)/(rIN-rWN);
             radElasticStress:=(pressure[0]-pressure[minInteriorTensileFailedIndex])
               *temp1+pressure[minInteriorTensileFailedIndex];
             tanElasticStress:=-(pressure[0]-pressure[minInteriorTensileFailedIndex])
               *temp2/temp3+pressure[minInteriorTensileFailedIndex];
             {seepage stresses}
             integral1:=0.0;
             for j:=firstIntactZone to (minInteriorTensileFailedIndex-1) do begin
               pPrime:=pressure[j]-pressure[minInteriorTensileFailedIndex];
               integral1:=integral1+pPrime*power(radius[j], geomExponent-1)*zoneLength;
             end;
             integral2:=0.0;
             for j:=firstIntactZone to i do begin
               pPrime:=pressure[j]-pressure[minInteriorTensileFailedIndex];
               integral2:=integral2+pPrime*power(radius[j], geomExponent-1)*zoneLength;
             end;


             radSeepageStress:=2.0*preFactor
               *(-(temp1/Power(radius[i],geomExponent))*integral1
               +(1.0/Power(radius[i],geomExponent))*integral2);

             pPrime:=pressure[i]-pressure[minInteriorTensileFailedIndex];
             tanSeepageStress:=-(2.0*preFactor/(geomExponent-1))
               *((temp2/Power(radius[i],geomExponent))*integral1
               +(1.0/Power(radius[i],geomExponent))*integral2-pPrime);
```

C-5

```
        {total stresses}
        radTotStress:=radElasticStress+radSeepageStress;
        tanTotStress:=tanElasticStress+tanSeepageStress;
        {effective stresses}
        radEffStress[i]:=radTotStress-pressure[i];
        tanEffStress[i]:=tanTotStress-pressure[i];
        shearStress[i]:=0.5*Abs(radEffStress[i]-tanEffStress[i]);
        meanEffStress:=(radEffStress[i]+(geomExponent-
1)*tanEffStress[i])/geomExponent;
      end;
    {tensile failed interior}
    if ((i>=minInteriorTensileFailedIndex) and (i<=maxTensileFailedIndex)) then
begin
        radEffStress[i]:=0.0;
        tanEffStress[i]:=0.0;
        shearStress[i]:=0.0;
        meanEffStress:=0.0;
      end;
    {elastic outer}
    if i>maxTensileFailedIndex then begin
        temp1:=power((radius[maxTensileFailedIndex]+0.5*zoneLength)/radius[i],
          geomExponent);
        radElasticStress:=(pressure[maxTensileFailedIndex]-farfieldStress)
          *temp1+farfieldStress;
        tanElasticStress:=-(pressure[maxTensileFailedIndex]-farfieldStress)
          *temp1/temp3+farfieldStress;
        {seepage stresses}
        integral1:=0.0;
        for j:=(maxTensileFailedIndex+1) to i do begin
          pPrime:=pressure[j]-farFieldPorePressure;
          integral1:=integral1+pPrime*power(radius[j], geomExponent-1)*zoneLength;
        end;
        radSeepageStress:=(geomExponent-1)
          *preFactor*integral1/Power(radius[i], geomExponent);
        pPrime:=pressure[i]-farFieldPorePressure;
        tanSeepageStress:=-preFactor*(integral1/Power(radius[i], geomExponent)-
pPrime);
        {total stresses}
        radTotStress:=radElasticStress+radSeepageStress;
        tanTotStress:=tanElasticStress+tanSeepageStress;
        {effective stresses}
        radEffStress[i]:=radTotStress-pressure[i];
        tanEffStress[i]:=tanTotStress-pressure[i];
        shearStress[i]:=0.5*Abs(radEffStress[i]-tanEffStress[i]);
        meanEffStress:=(radEffStress[i]+(geomExponent-
1)*tanEffStress[i])/geomExponent;
      end;
    end;
  {tensile failure}
  if ((-radEffStress[i]>tensileStrengthSI) and
    ((tensileCommLength+radius[firstIntactZone])>radius[i])) then begin
      if tensileFailed[i]=False then
        numberOfCellsNewlyTensileFailed:=numberOfCellsNewlyTensileFailed+1;
      tensileFailed[i]:=True;
    end;
  {shear failure}
  shearStrength:=S0+meanEffStress*Tan(frictionAngleSI);
  if (shearStress[i]>shearStrength) then
    shearFailed[i]:=True;
  Application.ProcessMessages;
  end;
  if ((maxContiguousTensileFailedIndex+2)=(minInteriorTensileFailedIndex)) then
begin
    tensileFailed[minInteriorTensileFailedIndex-1]:=True;
    numberOfCellsNewlyTensileFailed:=numberOfCellsNewlyTensileFailed+1;
  end;
  if ((numberOfCellsNewlyTensileFailed<3) or (deltaTime<2.0*minDeltaTime)) then
```

C-6

```
      timeStepOk:=True
    else
      timeStepOK:=False; _

  end; {procedure CalculateStresses}
  {~--------------------------------------------------------------------------}

  procedure SetupRun;
  var
    i: integer;

  begin
    tensileStrengthSI:=tensileStrength*6895.0;
    cohesionSI:=cohesion*6895.0;
    frictionAngleSI:=frictionAngle*2.0*Pi/360.0;
    if spherical=True then
      geomExponent:=3
    else
      geomExponent:=2;
    initialCellLength:=0.01;
    maxDeltaTime:=1.0;
    deltaTime:=0.00001;
    minDeltaTime:=0.00001;
    time:=0.0;
    runIndex:=0;
    mudVelocity:=0.0;
    mudBottom:=baseElevation+baseHeight;
    initialMudBottom:=mudBottom;
    tensileFailedTotalVolume:=0.0;
    contiguousTensileFailedTotalVolume:=0.0;
    tensileFailedSolidVolume:=0.0;
    contiguousTensileFailedSolidVolume:=0.0;
    maxTensileFailedIndex:=0;
    maxContiguousTensileFailedIndex:=0;
    minInteriorTensileFailedIndex:=0;
    maxShearFailedIndex:=0;
    tensileFailureTimeZero:=0.0;
    radEffStress[0]:=0.0;
    tanEffStress[0]:=0.0;
    firstIntactZone:=1;
    if permFromPorosity=True then
      initialPermeability:=(3.0E-13)*Power(initialPorosity,3.441);
    {cell count}
    numZones:=Round(outerRadius/initialCellLength);
    {lengths and positions}
    wellboreRadius:=0.5*wellboreDiameter;
    annulusArea:=Pi*(Sqr(wellboreRadius)-Sqr(0.5*pipeDiameter));
    zoneLength:=(outerRadius-wellboreRadius)/numZones;
    radius[0]:=0.0;
    for i:=1 to numZones do
      radius[i]:=wellboreRadius+zoneLength*(i-0.5);
    {other array variables}
    for i:=1 to numZones do begin
      pressure[i]:=initialPressure;
      porosity[i]:=initialPorosity;
      permeability[i]:=initialPermeability;
      tensileFailed[i]:=False;
      shearFailed[i]:=False;
    end;
    tensileFailed[0]:=True;
    {initial mud pressure and wellbore mass}
    {pressure[0]:=mudDensity*Gravity*(surfaceElevation-mudBottom);}
    pressure[0]:=initialPressure;
    gasFlowRate:=0.0;
    if ejectMud=True then begin
      {arbitrarily set the wellbore initial volume to be 100% of the pore volume of
the
      first zone}
```

```pascal
      workingVolume:=1.0*porosity[1];
      if spherical=True then
        workingVolume:=workingVolume*2.0*Pi*Sqr(radius[1])*zoneLength
      else
        workingVolume:=workingVolume*2.0*Pi*radius[1]*zoneLength*baseHeight;
      workingMass:=(pressure[0]/AtmosphericPressure)*gasBaseDensity*workingVolume;
      mudBottom:=mudBottom+workingVolume/annulusArea;
    end;
    time:=0.0;
    CalculateStresses;
    WriteHeadersToFiles;
    WriteToPressureFile;
    WriteToRadEffStressFile;
    WriteToTanEffStressFile;
    WriteToTimeFile;
    ResetTimeGraphs;
    WriteRadialGraphicsToScreen;
    WriteTimeGraphicsToScreen;
    WriteInfoToScreen;
    screenSaveIndex:=1;
    radialSaveIndex:=1;
    timeSaveIndex:=1;

end; {procedure SetupRun}
{------------------------------------------------------------------------------}

procedure CalculateWellbore;
var
    dragAcceleration, tempInitialMudBottom, flowingGasDen, gasVelocity,
      gasFlux, intrinsicGasFlowIntoWell, intrinsicGasFlowRate: Double;

begin
  {move mass in/out of working volume}
  if pressure[firstIntactZone]>pressure[0] then
    flowingGasDen:=(pressure[firstIntactZone]/AtmosphericPressure)*gasBaseDensity
  else
    flowingGasDen:=(pressure[0]/AtmosphericPressure)*gasBaseDensity;
  gasFlux:=flowingGasDen*((pressure[firstIntactZone]-pressure[0])/(0.5*zoneLength))
      *permeability[firstIntactZone]/gasViscosity;
  if spherical=True then
    intrinsicGasFlowRate:=gasFlux*2.0*Pi*Sqr(radius[firstIntactZone]-
0.5*zoneLength)
  else
    intrinsicGasFlowRate:=gasFlux*baseHeight*2.0*Pi*(radius[firstIntactZone]
        -0.5*zoneLength);
  intrinsicGasFlowIntoWell:=intrinsicGasFlowRate*deltaTime;
  {mud removal}
  if mudBottom<surfaceElevation then begin
    {restrict working mass change to 2% for any time step}
    if ((Abs(intrinsicGasFlowIntoWell)<=0.02*workingMass) or
      (deltaTime<2.0*minDeltaTime)) then begin
      timeStepOK:=True;
      gasFlowRate:=intrinsicGasFlowRate;
      {new working mass and pressure}
      workingMass:=workingMass+gasFlowRate*deltaTime;
      {motion}
      {drag}
      dragAcceleration:=0.5*mudFrictionFactor*Sqr(mudVelocity)/
        (wellboreRadius-0.5*pipeDiameter);
      if mudVelocity<0.0 then
        dragAcceleration:=-dragAcceleration;
      {acceleration (positive upward)}
      mudAcceleration:=(pressure[0]-AtmosphericPressure)/
        (mudDensity*(surfaceElevation-mudBottom))
        -Gravity-dragAcceleration;
      {velocity}
      mudVelocity:=mudVelocity+mudAcceleration*deltaTime;
      {motion}
```

```
                mudBottom:=mudBottom+mudVelocity*deltaTime;
                {new working volume}
                workingVolume:=(mudBottom-initialMudBottom)*annulusArea;
                if allowMaterialRemoval=True then
                   workingVolume:=workingVolume+contiguousTensileFailedTotalVolume
                      -contiguousTensileFailedSolidVolume;
                {new working pressure}

      pressure[0]:=((workingMass/workingVolume)/gasBaseDensity)*AtmosphericPressure;
            end else
               timeStepOK:=False;
         {gas flow only}
         end else begin
            {**this has not been fixed for material removal}
            {gasFlowRate:=gasFlowIntoWell/deltaTime;}
            {gasVelocity:=gasFlowIntoWell/(gasBaseDensity*deltaTime*annulusArea);
            {pressure[0]:=AtmosphericPressure+gasFrictionFactor*gasBaseDensity*
               Sqr(gasVelocity)/(2.0*(wellboreRadius-0.5*pipeDiameter));}
         end;

      end; {procedure CalculateWellbore}
      {--------------------------------------------------------------------------------}

      procedure RunLoop;
      var
         i, j, oldMaxContiguousTensileFailedIndex, oldMaxTensileFailedIndex: Integer;
         a, b, c, r: array[0..10000] of Double;
         dPrime, alpha1, alpha2, beta: Double;
         bet, deltaFailedVolume: Double;
         gam, savedPressure: array[0..10000] of Double;
         savedTensileFailed, savedShearFailed: array[0..10000] of Boolean;
         contiguousCheck, innerCheck: Boolean;
         savedFirstIntactZone: Integer;

      begin
         while time<maxTime do begin
            deltaTime:=deltaTime*1.1;
            if ((time<10.0) and (deltaTime>0.1)) then
               deltaTime:=0.1
            else if ((time<1.0) and (deltaTime>0.01)) then
               deltaTime:=0.01
            else if ((time<0.01) and (deltaTime>0.001)) then
               deltaTime:=0.001
            else if ((time<0.001) and (deltaTime>0.0001)) then
               deltaTime:=0.0001
            else if deltaTime>maxDeltaTime then
               deltaTime:=maxDeltaTime;
            for i:=firstIntactZone to numZones do begin
               savedPressure[i]:=pressure[i];
               savedTensileFailed[i]:=tensileFailed[i];
               savedShearFailed[i]:=shearFailed[i];
            end;
            savedFirstIntactZone:=firstIntactZone;
            repeat
               {march time}
               time:=time+deltaTime;

               {set up coefficients for tridiagonal inversion}
               {interior zones}
               for i:=(firstIntactZone+1) to (numZones-1) do begin
                  dPrime:=permeability[i]/(2.0*porosity[i]*gasViscosity);
                  alpha1:=1.0/Sqr(zoneLength)-0.5*(geomExponent-1)/(radius[i]*zoneLength);
                  alpha2:=1.0/Sqr(zoneLength)+0.5*(geomExponent-1)/(radius[i]*zoneLength);
                  beta:=1.0/(2.0*dPrime*deltaTime);
                  a[i]:=-alpha1;
                  b[i]:=alpha1+alpha2+beta/pressure[i];
                  c[i]:=-alpha2;
                  r[i]:=beta;
```

C-9

```
        end;
        {first zone}

dPrime:=permeability[firstIntactZone]/(2.0*porosity[firstIntactZone]*gasViscosity);
        alpha1:=1.0/Sqr(zoneLength)-0.5*(geomExponent-
1)/(radius[firstIntactZone]*zoneLength);
        alpha2:=1.0/Sqr(zoneLength)+0.5*(geomExponent-
1)/(radius[firstIntactZone]*zoneLength);
        beta:=1.0/(2.0*dPrime*deltaTime);
        b[firstIntactZone]:=alpha1+alpha2+beta/pressure[firstIntactZone];
        c[firstIntactZone]:=-alpha2;
        r[firstIntactZone]:=beta+alpha1*pressure[0];

        {last zone}
        dPrime:=permeability[numZones]/(2.0*porosity[numZones]*gasViscosity);
        alpha1:=1.0/Sqr(zoneLength)-0.5*(geomExponent-
1)/(radius[numZones]*zoneLength);
        alpha2:=1.0/Sqr(zoneLength)+0.5*(geomExponent-
1)/(radius[numZones]*zoneLength);
        beta:=1.0/(2.0*dPrime*deltaTime);
        a[numZones]:=-alpha1;

        if noFlowOuterBoundary=True then
          b[numZones]:=alpha1+beta/pressure[numZones]
        else
          b[numZones]:=alpha1+alpha2+beta/pressure[numZones];
        r[numZones]:=beta;

        {tridiagonal inversion}
        bet:=b[firstIntactZone];
        pressure[firstIntactZone]:=r[firstIntactZone]/bet;
        for i:=(firstIntactZone+1) to (numZones) do begin
          gam[i]:=c[i-1]/bet;
          bet:=b[i]-a[i]*gam[i];
          pressure[i]:=(r[i]-a[i]*pressure[i-1])/bet;
        end;
        if noFlowOuterBoundary=False then
          pressure[numZones]:=initialPressure;
        for i:=(numZones-1) downto firstIntactZone do
          pressure[i]:=pressure[i]-gam[i+1]*pressure[i+1];
        {wellbore}
        if ejectMud=True then
          CalculateWellbore
        else
          timeStepOK:=True;
        if timeStepOK=True then
          CalculateStresses;
        {step check}
        if timeStepOK=False then begin
          for i:=firstIntactZone to numZones do begin
            pressure[i]:=savedPressure[i];
            tensileFailed[i]:=savedTensileFailed[i];
            shearFailed[i]:=savedShearFailed[i];
            firstIntactZone:=savedFirstIntactZone;
          end;
          time:=time-deltaTime;
          deltaTime:=0.5*deltaTime;
        end;
      until timeStepOK=True;
      runIndex:=runIndex+1;
      {failure indices}
      oldMaxContiguousTensileFailedIndex:=maxContiguousTensileFailedIndex;
      oldMaxTensileFailedIndex:=maxTensileFailedIndex;
      for i:= firstIntactZone to numZones do begin
        if (tensileFailed[i]=True) then begin
          maxTensileFailedIndex:=i;
        end;
      end;
```

```
        contiguousCheck:=True;
        for i:= firstIntactZone to numZones do begin
            if ((tensileFailed[i]=True) and (tensileFailed[i-1]=True) and
    (contiguousCheck=True)) then
                maxContiguousTensileFailedIndex:=i
            else
                contiguousCheck:=False;
        end;
        innerCheck:=True;
        for i:= (maxContiguousTensileFailedIndex+2) to numZones do begin
            if ((tensileFailed[i]=True) and (innerCheck=True)) then begin
                if (tensileFailed[i-1]=False) then
                    minInteriorTensileFailedIndex:=i
                else
                    innerCheck:=False;
            end;
        end;
        for i:= firstIntactZone to numZones do begin
            if ((shearFailed[i]=True) and (i>maxShearFailedIndex)) then
                maxShearFailedIndex:=i;
        end;
        {advance first cell if material removal allowed}
        if (allowMaterialRemoval=True) and (ejectMud=True) then
            firstIntactZone:=maxContiguousTensileFailedIndex+1;
        {contiguous material removal}
        if maxContiguousTensileFailedIndex>oldMaxContiguousTensileFailedIndex then
begin
            for i:=(oldMaxContiguousTensileFailedIndex+1) to
              maxContiguousTensileFailedIndex do begin
                deltaFailedVolume:=(2.0/geomExponent)*Pi
                 *(Power(radius[i]+0.5*zoneLength, geomExponent)
                 -Power(radius[i]-0.5*zoneLength, geomExponent));
                if spherical=False then
                    deltaFailedVolume:=deltaFailedVolume*baseHeight;
                contiguousTensileFailedSolidVolume:=contiguousTensileFailedSolidVolume
                 +deltaFailedVolume
                 *(1.0-porosity[i]);
                if allowMaterialRemoval=True then begin
                    tensileFailureTimeZero:=time;
                    radEffStress[i]:=0.0;
                    tanEffStress[i]:=0.0;
                    workingMass:=workingMass+deltaFailedVolume*porosity[i]*
                        gasBaseDensity*(pressure[i]/AtmosphericPressure);
                end;
            end;
        end;
        if maxContiguousTensileFailedIndex>0 then
            contiguousTensileFailedTotalVolume:=(2.0/geomExponent)*Pi
             *(Power(radius[maxContiguousTensileFailedIndex]+0.5*zoneLength,
geomExponent)
             -Power(radius[1]-0.5*zoneLength, geomExponent));
        if spherical=False then

contiguousTensileFailedTotalVolume:=contiguousTensileFailedTotalVolume*baseHeight;
        if maxTensileFailedIndex>0 then
            tensileFailedTotalVolume:=(2.0/geomExponent)*Pi
             *(Power(radius[maxTensileFailedIndex]+0.5*zoneLength, geomExponent)
             -Power(radius[1]-0.5*zoneLength, geomExponent));
        if spherical=False then
            tensileFailedTotalVolume:=TensileFailedTotalVolume*baseHeight;
        {write screen and save files}
        if time>=screenSaveTime[screenSaveIndex] then begin
            WriteRadialGraphicsToScreen;
            j:=0;
            repeat
                j:=j+1;
            until screenSaveTime[j]>=time;
            screenSaveIndex:=j;
```

```pascal
      end;
      if time>=radialSaveTime[radialSaveIndex] then begin
        WriteToPressureFile;
        WriteToRadEffStressFile;
        WriteToTanEffStressFile;
        j:=0;
        repeat
          j:=j+1;
        until radialSaveTime[j]>=time;
        radialSaveIndex:=j;
      end;
      if time>=timeSaveTime[timeSaveIndex] then begin
        WriteToTimeFile;
        j:=0;
        repeat
          j:=j+1;
        until timeSaveTime[j]>=time;
        timeSaveIndex:=j;
      end;
      WriteInfoToScreen;
      WriteTimeGraphicsToScreen;
      Application.ProcessMessages;
    end;

end; {procedure RunLoop}
{---------------------------------------------------------------------------}

procedure Start;

begin
  if pressureFileName='noFile' then
    MainForm.SaveDialog.FileName:='*.hdr';
    MainForm.FileSaveAsItem.Click;
  if pressureFileName<>'noFile' then begin
    Screen.Cursor:=crHourglass;
    AssignFile(fileE, headerFileName);
    Rewrite(fileE);
    AssignFile(fileF, pressureFileName);
    Rewrite(fileF);
    AssignFile(fileG, radEffStressFileName);
    Rewrite(fileG);
     AssignFile(fileH, tanEffStressFileName);
    Rewrite(fileH);
    AssignFile(fileI, timeFileName);
    Rewrite(fileI);
    SetupRun;
    RunLoop;
    CloseFile(fileE);
    CloseFile(fileF);
    CloseFile(fileG);
    CloseFile(fileH);
    CloseFile(fileI);
    Screen.Cursor:=crDefault;
  end;

end; {procedure Start}
{---------------------------------------------------------------------------}

end.
```

Appendix D
Memorandum on
Typical Repository Conditions Indicated by the
CCA Performance Assessment Calculations

D-2

date: April 7, 1997

to: Frank Hansen   MS 1322 (Org. 6121)
    Kathy Knowles   MS 1322 (Org. 6121)
    Hans Papenguth   MS 1322 (Org. 6832)

from: Kurt Larson   MS 1341 (Org. 6821)
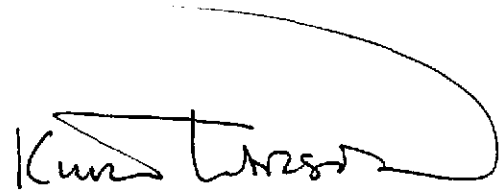
subject: Typical repository conditions indicated by the CCA performance assessment calculations

Introduction

Inadvertent intrusion into the WIPP repository may be associated with a spall release if pressures are greater than 8 MPa. The quantity of material released by a spall event depends in part on the material properties of the waste at the time of intrusion. These material properties are influenced by both the original composition of the waste, and by processes that occur after waste placement. The original composition of the waste is provided in the Transuranic Waste Baseline Inventory Report and Database (TWBIR and TWBID) (see Papenguth, 1997, for a summary of relevant information). Subsequent to emplacement, processes and conditions that affect the material properties of the waste at time of spall include compaction, liquid saturation, pressure, degradation by gas-generating reactions, and salt precipitation. Performance assessment modeling indicates variability in the state of these processes and conditions at the time of an inadvertent human intrusion. Since the times of occurrence and numbers of inadvertent intrusion are uncertain, several possible sequences of inadvertent intrusion types (scenarios) need to be considered.

Several discussions have occurred in the past several months on topics included in this memorandum in which the compositions of suitable waste surrogataes were determined for use in strength experiments related to the new spall model. The basis and specification of waste surrogates is provided in Papenguth and Myers (1997). This memorandum documents results from performance assessment that Papenguth and Myers (1997) considered in developing waste surrogates.

The times and sequences of intrusions

The EPA in 40 CFR 194 has specified the methods through which future human actions shall be incorporated in the WIPP performance assessment. For the spall model, the relevant actions are inadvertent penetration by deep drilling associated

with oil and gas exploration and production. The methods prescribed by the EPA for deep drilling lead to the following model for deep drilling:

1. deep drilling occurs randomly in space and time
2. the times it occurs can be described with a Poisson model with in which the rate of intrusion is divided into three time periods
3. the first time period is Active Institutional Control (AIC), which last for 100 years has a rate of drilling intrusion equal to zero.
4. the second time period is Passive Institutional Control, which follows AIC and lasts 600 years. The rate of intrusion for this time is 0.468 boreholes/km^2/10,000 years.
5. the third time period is uncontrolled, follows PIC, and has a rate of intrusion of 46.8 boreholes/km^2/10,000 years.
6. technologies used should be assumed to be the same as those used in current practice

The time periods and rates described in points 2-5 above are shown in Table 1.

Table 1. Time periods and rates of intrusion during the regulatory period.

Period Name	Time period (years)	Intrusion Rate (boreholes/km^2/10,000 years)
Active Institutional Control (AIC)	0-100	0.0
Passive Institutional Control (PIC)	100-600	0.468
Uncontrolled	700-10,000	46.8

Using the time periods and rates shown in Table 1 in the Poisson model (CCA 6.4.12), the probability that a single intrusion has occurred by a specified time can be derived. Jay Johnson derived the probabilities of intrusion occurring by a specified time shown in Table 2.

Table 2 indicates that it is extremely likely that a first intrusion will occur (p = 0.997). The time period up to 4000 years is associated with a probability of 0.869. Thus, first intrusion will most likely occur by 4000 years.

Intrusions subsequent to the first are very likely given the drilling rate specified by the EPA. As discussed in CCA Section 6.4.12.2, The most likely number of intrusions into the repository is 5, occurring with a probability of 0.1715; the average number of intrusions is 7. The maximum number of intrusions that can occur with a probability greater than 10^{-4} is 15.

Table 2. Probabilities of first intrusion occurring by a specified time during the regulatory period.

Time (years)	Probability first intrusion has occurred by specified time
500	0.00246
1000	0.172
1500	0.391
2000	0.552
2500	0.671
3000	0.758
3500	0.822
4000	0.869
4500	0.904
5000	0.929
5500	0.948
6000	0.962
6500	0.972
7000	0.979
7500	0.985
8000	0.989
8500	0.992
9000	0.994
9500	0.996
10,000	0.997

Inadvertent intrusion boreholes can be of two types, E1 and E2, with probabilities of occurrence of 0.08 and 0.92 respectively. When abandoned, intrusion boreholes are assumed to plugged with one of three possible plug configurations (CCA 6.4.7.2; 6.4.12.7). Boreholes abandoned with a continuous concrete plug have negligible effect on subsequent repository conditions, but only 2% of the boreholes are abandoned with this plug configuration. From the perspective of the repository, the other plug patterns provide a mechanisms for generally increasing brine saturation in the repository and decreasing repository pressure.

Compaction

The process of creep closure of disposal rooms is incorporated in BRAGFLO. The BRAGFLO results of coupled creep closure, brine inflow, gas generation, and brine outflow indicate that the disposal room will compact in about 100 years from their initial height to an end height, and further variations are very small. Although closure is not explicitly calculated by BRAGFLO, indications of the end-state height are obtained by interpreting the porosity changes as height changes. With an initial porosity of 84.8 and constant height of 4 meters, the end state height of disposal rooms indicated by BRAGFLO end-state porosities of 0.08 to 0.2 (Figure 1), is 0.9 m to 1.5 m. The first inadvertent intrusion generally allows noticeable but negligible further consolidation of the waste, due to pressure drop in the repository (Figure 2). These predictions are consistent with other modeling predictions. Compaction of waste will exceed 2 m for all intrusions.

Liquid Saturation

Brine saturation at the time of intrusion is variable. In undisturbed performance, the waste panel saturation is generally greater than the rest of repository saturation (Figures 3 and 4), since the waste panel is located down-dip. For all times and pressures of first intrusion, the volume-average brine saturation varies from 0.00 to 0.95. Low pressure conditions are generally wetter, with minimum saturations of ˜0.35 up to pressures of 5 MPa at 4,000 years. High-pressure conditions are generally drier, with saturations not exceeding 0.20 for pressures greater than 14 MPa at 4,000 years. At 1,000 years, the volume-average brine saturation of the panel is 0.00 to ˜0.50 percent for pressures greater than 8 MPa (Figure 5). At 4,000 years, the volume-average brine saturation of the panel is 0 to 0.95 for pressures exceeding 8 MPa at this time (Figure 6).

Brine saturations generally increase after intrusion, especially in the intersected panel, since in an E1 case the reservoir provides a source of brine from below and in both the E1 and E2 cases failure of the Rustler-Salado bridge plug at 200 years allows the possibility of downward flow into the intruded panel if its pressure is less than about 7.5 MPa and it is not already saturated. With an E1 intrusion at 1,000 years, at 2,000 years the intruded panel typically has saturations at or near maximum (Figure 7), whereas the rest of the repository has much lower and more variability in brine saturations (Figure 8). By 4,000 years, the intruded panel is still near maximum saturation (Figure 9), but the rest of the repository has dried out completely in many vectors (Figure 10). BRAGFLO results with an E2 intrusion at 1,000 years show similar trends, although with generally lower saturation and slightly lower pressures because the Culebra source of brine is not as effective in saturating the intruded panel as the brine reservoir, and can only contribute brine to the repository when the repository pressure is below hydrostatic pressure (Figures 11-14). In Figures 7-14, it is apparent that pressures greater than 8 MPa are associated with generally drier conditions than

lower pressure, except in the case of an E1 intrusion in the intruded waste panel. The post-intrusion plots of saturation suggest that intrusions subsequent to the first will penetrate a repository that has much variability in saturation conditions, but if pressures are greater than 8 MPa, the average saturation will likely be below 50%.

It is expected that there will be heterogeneity of brine saturation in the waste. As discussed in the next section, brine enters the repository early mostly by drainage of the upper DRZ. However, after about 100 years this source is depleted and further brine inflow is caused by drainage of interbeds. Most of the interbed contribution comes from below (from Marker Bed 139). Intrusion boreholes provide a brine source that flows laterally across the floor of the intruded panel, rising and filling porosity from below. Dip and gravity tend to force brine toward the floor and lower portions of the repository, but capillary forces and brine sources at the top of the rooms oppose complete drying of waste at the top of rooms. Thus, the location of sources of brine to the repository are time-dependent. It is clear the average saturation in a vector is not likely the same as the range of local brine saturations in the repository. For example, in down-dip regions near the floor, fully-brine saturated conditions might be encountered even in a very dry repository. Even taking into account the heterogeneities, as the repository rises in pressure, it becomes systematically drier. This makes sense physically, since high pressures eliminate some mechanisms of brine inflow.

Brine Fluxes

Brine fluxes can be split into two general categories - sources and sinks. These categories are discussed separately.

Brine sources

The sources of brine to the repository, in addition to the small initial free liquid content of the waste, are otehr materials in the disposal system containing brine. This brine may enter the repository as inflow from the disturbed rock zone (DRZ), interbeds, and boreholes.

DRZ inflow

The DRZ contribution of brine to the repository is brief and of variable magnitude. From several hundred to about 23,000 m^3 brine flows out of the DRZ into the repository in the first hundred years or so (Figure 15). Most of this brine enters the repository from above, and this source is distributed fairly uniformly over the waste. Long-term fluxes to the repository from the DRZ do not occur unless flow from the interbeds to the DRZ occurs. In other words, the long-term flow from the DRZ to the repository is actually long-term flow from interbeds to the repository that necessarily crosses the DRZ.

Interbed inflow

Interbeds connect to the DRZ rather than the repository. The long-term flux from interbeds to the repository passes through the DRZ. Thus, the flow from interbeds directly to the DRZ is a measure of how much inflow occurs due to long-term interbed drainage.

Figures 16, 17, and 18 show the flux of brine from anhydrite interbeds into the DRZ for undisturbed performance. Marker Bed 138 contributes up to 4,400 m^3 brine, but only 9 of 100 vectors exceed 200 m^3 contribution. Anhydrite A and B contributes up to 21,000 m^3, and only 7 of 100 vectors exceed 3,000 m^3. The fluxes from Marker Bed 138 and Anhydrite A and B enter the repository from above. Marker Bed 139 contributes up to 45,000 m^3 of brine to the repository, with 8 of 100 vectors exceeding 6,000 m^3 contribution.

The same factors, primarily interbed permeability, halite permeability, and repository pressure, control the quantity of brine contributed to the repository from each interbed. Thus, the fraction of total interbed inflow from each interbed is similar in all vectors. Marker Bed 139 contributes ˜ 64%, Anhydrite A and B contributes ˜ 30%, and Marker Bed 138 contributes ˜ 6%. In summary, after initial DRZ drainage, in which most brine seeps down from above the waste, approximately 1/3 of brine inflow seeps into the waste from the upper DRZ, and approximately 2/3 wells up from the lower DRZ.

Following an intrusion, the rate of brine inflow from the interbeds to the repository generally increases, by a factor approaching 2 in some vectors. This is caused by the depressurization of the repository occurring after plug degradation, and the inability of the repository to repressurize and resist further inflow due to the presence of the degraded borehole. The total quantity of interbed inflow is similar for both E1 and E2 intrusions.

Borehole inflow

With an E1 intrusion at 1,000 years, up to 50,000 m^3 brine flows out of the brine reservoir into the lower DRZ (Figure 19). Figure 20, the total brine inflow into the waste panel, shows that while the brine reservoir contribution is large in many vectors, interbed inflow can be of comparable or larger magnitude.

With an E2 intrusion at 1,000 years, up to ˜ 45,000 m^3 brine flowed down the borehole from the Culebra into the waste panel (Figure 20). Approximately one-quarter of the vectors show flow down the borehole. In those vectors with down-borehole flow, flow reversals occur after the waste panel is saturated since the far-field Salado hydraulic potential is greater than that of the Culebra. As with the E1 intrusion, interbed inflow is of comparable or larger magnitude in many vectors.

The brine contributed from the borehole likely flows along the floor of the intruded panel and rises from below into void spaces as saturation increases.

Brine sinks

There are three major sinks of brine in the repository: anoxic corrosion, interbed outflow, and borehole outflow. Note that two of these, interbeds and boreholes, may also serve as sources of brine. These materials may serve as sources when the hydraulic gradient along them favors flow to the repository; they may serve as sinks when the hydraulic gradient along them favors outflow. Whether flow actually occurs to or from the repository along these materials depends on other factors, such as the two-phase properties along the materials or in the repository. In many vectors, flow reversals are observed to occur in these materials during the regulatory period as the repository pressure or saturation changes.

Brine consumption

Brine consumption by anoxic corrosion is a significant mechanism for removal of brine from the repository. In all scenarios, the quantity of brine consumed is less than the potential brine consumption given the iron inventory (see Degradation, below). The extent of anoxic corrosion is limited by the ability of brine to reach uncorroded iron, which is influenced by the quantity and location of sources of brine to the repository and by the effects of gravity in the repository. In undisturbed performance, an average of 80%-90% of total brine inflow is consumed by anoxic corrosion by 10,000 years. In disturbed performance scenarios, although more brine is consumed, a smaller fraction of the total brine inflow is consumed since a significant portion of the inflow is concentrated in the panel, where the iron inventory can be more depleted locally leaving brine unconsumed. The consumption of brine stimulates the precipitation of salt, which may affect the strength of the waste when inadvertent intrusion occurs.

Interbed outflow

Significant interbed outflow occurs only in undisturbed performance since intrusion boreholes vent the repository and reverse the gradients for flow. In undisturbed performance, interbed outflow is a minor brine sink compared to anoxic corrosion. In undisturbed performance, many vectors had outflow through Marker Bed 139, with up to 3,700 m^3 total Marker Bed 139 outflow (Figure 21). Up to 850 m^3 outflow (but usually less than 50 m^3) occurred through Marker Bed 138, and less than 1 m^3 outflow occurred through Anhydrite A and B.

In disturbed performance for either an E1 or E2 intrusion at 1,000 years, up to 660 m^3 brine flowed out Marker Bed 139 prior to intrusion (Figure 22). The flow reversal occurring after intrusion typically contributes more brine than this back into the repository.

Borehole outflow

From the perspective of the repository, the up to ˜ 40 m³ brine outflow up an intrusion borehole as direct brine release during drilling is negligible. This outflow mechanism is neglected in long-term BRAGFLO simulations.

Long-term outflow from the intruded panel up the degraded intrusion borehole and into the Culebra occurs in ˜20% of E1 intrusion vectors. If this outflow occurs, the quantity of brine removed from the repository can be large and comparable in magnitude to the quantity consumed by anoxic corrosion. For an E1 at 1,000 years, up to 35,000 m³ brine flowed up the intrusion borehole, but in only 3 vectors was this particular cumulative flux greater than 10,000 m³ (Figure 23). For an E2 at 1,000 years, upward flow occurs in ˜5% of vectors, with an even distribution between a few hundred m³ to 36,000 m³ cumulative outflow (Figure 24).

Borehole outflow from the intruded panel occurs only if the saturation in the panel is at or very near the maximum liquid saturation (1 - residual gas saturation). In other words, the pore space in the intruded panel is fully saturated before flow up the borehole becomes possible. All materials emplaced in a waste panel will be saturated with free, mobile liquid prior to a release to the Culebra.

Degradation

The progress of gas generation reactions is important in developing pressure in the repository, and impacts other characteristics of the waste. Anoxic corrosion occurs in all vectors. In undisturbed performance, between 2% and 60% of the steel in the repository is degraded by 10,000 years (Figure 25). For both E1 and E2 intrusions at 1,000 years, between 2% and ˜85% of the steel inventory is degraded by 10,000 years (Figure 26). Partial degradation of steel by anoxic corrosion is the expected future state of the repository. If microbial degradation occurs, all consumables in the repository will be exhausted within about 2000 years (Figure 27). Anoxic corrosion consumes brine and stimulates precipitation of salt, which may affect the strength of waste at time of intrusion. The quantity of brine consumed by anoxic corrosion is discussed above in the section on *Brine Sinks*, Anoxic Corrosion.

The extent to which anoxic corrosion has degraded waste is likely to be heterogeneous within the repository, because brine will tend to move toward the base of waste stacks and the lower portions of the repository due to gravity. Because microbial degradation consumes all microbial substrates rapidly, the composition of cellulosics, and of plastics and rubbers, will be homogeneous throughout the repository (either not degraded at all, or fully degraded).

Pressure

Repository pressure affects, and is affected by, all of the repository properties and characteristics discussed previously in this memorandum. Gas generation is the principal cause of repository pressure increase. Interbed and borehole inflow will cause repository pressure to increase; interbed and borehole outflow will cause repository pressure to decrease or stabilize.

The pressure in the repository for undisturbed performance is shown in Figure 28, and for disturbed performance in Figures 29-32.

For 200 years following the first intrusion, a plug is assumed to exist at the Salado-Rustler contact, and similar pressure is maintained while the plug persists. An inadvertent intrusion occurring during these 200 years would have a spall release occur with similar pressure conditions as the first intrusion.

The Salado-Rustler plug is assumed to degrade at 200 years, leaving a borehole filled with granular materials through which gas usually vents from the repository, depending on the sampled permeability of the borehole. With venting, some vectors remain at pressures greater than 8 MPa.

Surrogate Waste Forms in Strength Experiments

Papenguth and Myers (1997) state on page 2 of their memorandum:

> "It is important to note that the surrogate waste being specified does not represent the expected average waste condition, but rather the extremes in waste conditions. The selection of extremes is based on demonstrable concepts: (1) Wet waste is weaker; (2) spall is increasingly likely as pressure increases; (3) high pressure requires that microbial degradation occurs; (4) brine inflow is required for high pressures to be attained; (5) corrosion leads to smaller average particulate sizes; and (6) salt precipitation is accompanied by corrosion and microbial degradation." {Numbers added}

Three of Papenguth and Myers (1997) six concepts are demonstrable from the figures and discussion presented in this memorandum: that high pressures only occur with microbial degradation (Figure 33); that inflow is required for high pressures (inflow occurs for all vectors, Figure 15); and that anoxic corrosion consumes brine that would lead to salt precipitation (Figures 25 and 26). Two other concepts presented by Papenguth and Myers (1997) -- waste strength and pressure-dependent spall -- are consistent with the new spallings model experimental and numerical modeling work. The concept that corrosion leads to smaller particulate sizes is consistent with observations made during anoxic corrosion experiments.

D-11

Conclusions

Times and sequences of intrusion

Multiple intrusions are the norm. Undisturbed performance is very important because it determines the conditions in the repository at the unknown time of first intrusion.

Compaction

The waste will be compacted > 2 m for all intrusions.

Brine Saturation

Large variability if all times and pressures are considered. Waste at pressures greater than 10 MPa is noticeably drier, and waste at pressures greater than 14 MPa is considerably drier than lower pressures. Pressures lower than 5 or 6 MPa are generally wetter. Although repository-average saturations are useful for indicating overall conditions, brine saturation is expected to be heterogeneous in the repository due to the effects of gravity and locations and timing of brine sources and sinks.

Brine Sources

There are three stages of inflow: (1) DRZ inflow from above the repository during the first 100 years or so; (2) long-term interbed inflow, occurring unless pressures in the repository rise above far-field Salado pressure; and (3) borehole inflow, which usually occurs if the borehole is E1 and occurs about 25% of the time if the borehole is E2. Across the suite of vectors and scenarios, each of these three inflows spans the range of relative importance, accounting for from a small portion to the majority of total inflow.

The sources of brine suggest that in the first 100 years, DRZ brine will drip or seep into the repository from above and trickle through waste before collecting on the floor, making the materials in the disposal rooms wet but perhaps only those near the floor completely saturated. Long-term interbed inflow comes 1/3 from above the waste and 2/3 from below the waste. If it is of large magnitude, the interbed inflow from above the waste may keep waste wet; otherwise, the waste near the top of the rooms will tend to dry out because only the brief DRZ inflow and long-term interbed inflow provide brine at the top of waste stacks (capillary forces can make waste near the tops of stacks wet as well). Marker Bed 139 inflow rises from the floor, filling pore space as it displaces gas. Borehole inflow moves laterally along the floor of the intruded panel and rises through waste from the base of waste stacks. Borehole inflow has little effect on saturations in the rest of the repository.

Brine Sinks

The major sinks of brine in the repository are anoxic corrosion, which always occurs, and borehole outflow, which occurs occasionally. Significant interbed outflow occurs only for undisturbed performance. In undisturbed performance, anoxic corrosion consumes 80% - 90% of brine inflow. Anoxic corrosion and borehole outflow can be of similar magnitude. Borehole outflow only occurs if the intruded panel is saturated to maximum extent with liquid.

Degradation

Anoxic corrosion occurs in all vectors and consumes from 2% to about 85% of the initial steel inventory for all scenarios. Anoxic corrosion in undisturbed performance consumes 80% - 90% of brine inflow; generally less for disturbed performance. The distribution of corroded steel in the repository is likely to be heterogeneous since brine saturation is heterogeneous.

Microbial degradation occurs so rapidly that it is fair to assume that the distribution of non-degradable and degraded (depending on sampling) cellulosics, plastics, and rubbers will be homogeneous.

Pressure

Waste pressure is variable at the time of intrusion, ranging from approximately 3 MPa to 16 MPa, and depends on sampled parameter values and interrelated processes. After intrusion and Salado-Rustler plug degradation, waste pressures tend to stabilize at hydrostatic, but still vary from approximately 3 MPa to 10 MPa.
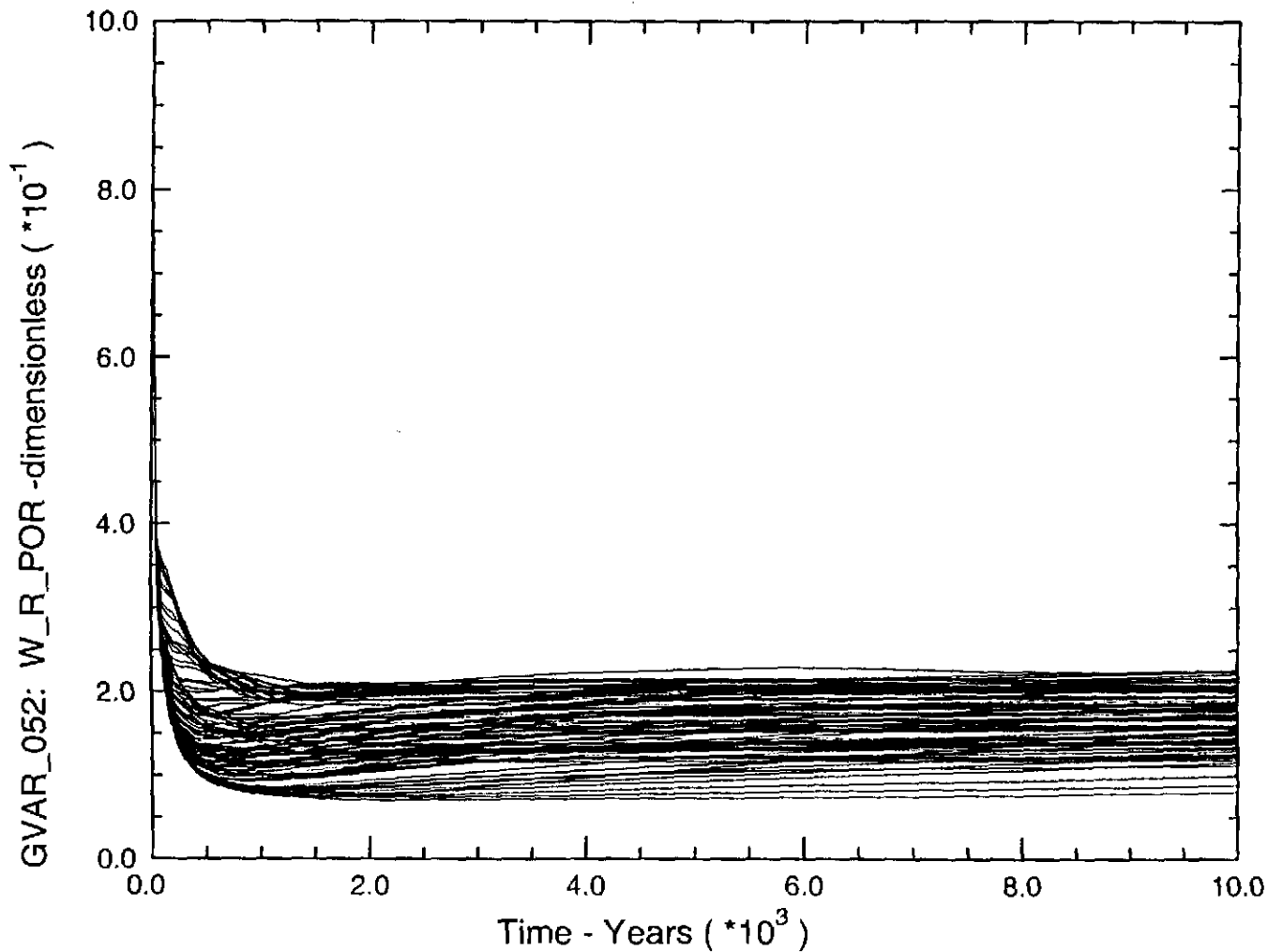
Figure 1.   Porosity in the waste disposal areas during the regulatory period for undisturbed performance from CCA Replicate 1.
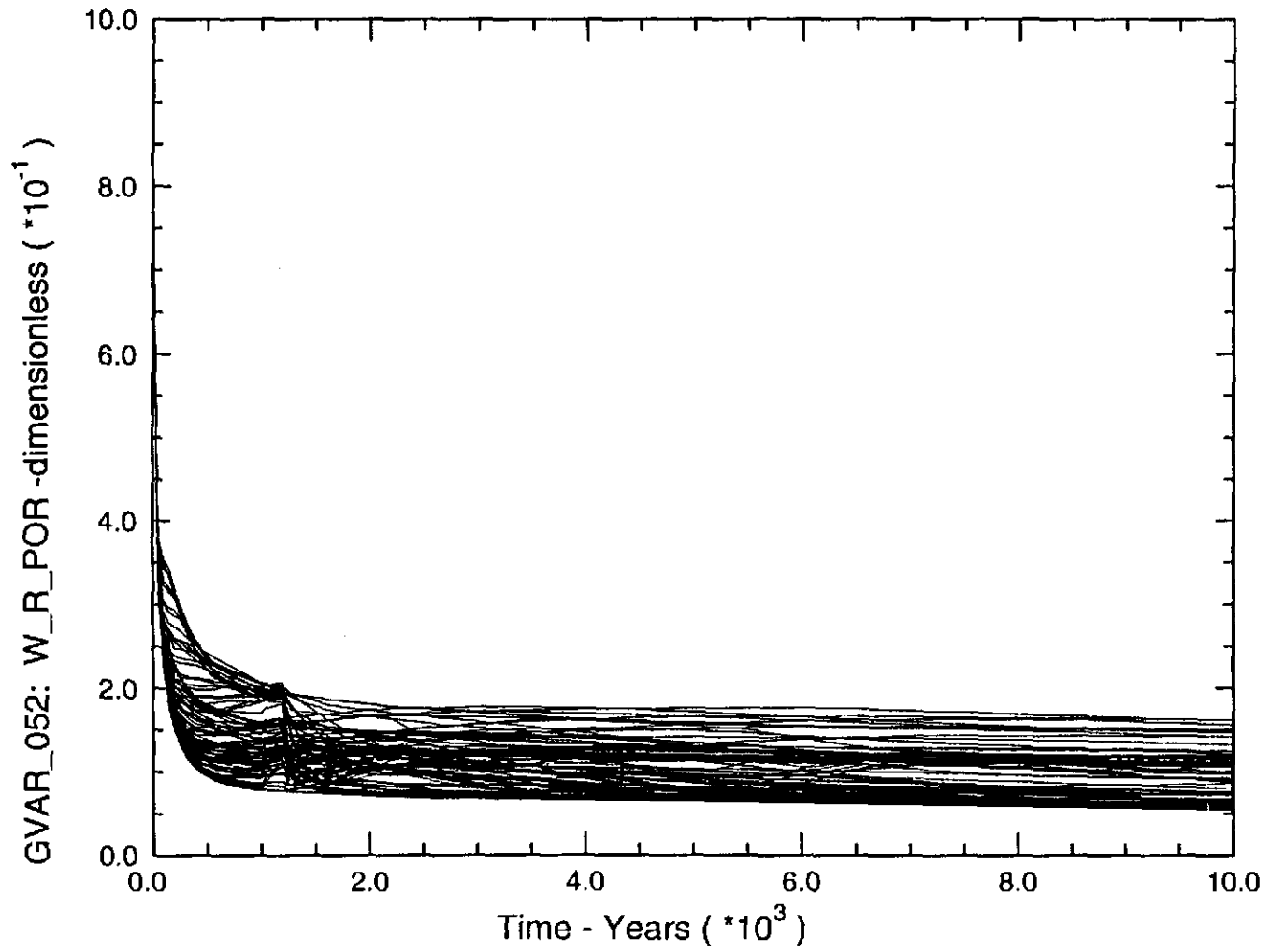
Figure 2.   Porosity in the waste disposal areas during the regulatory period for an E1 intrusion at 1000 years from CCA Replicate 1.
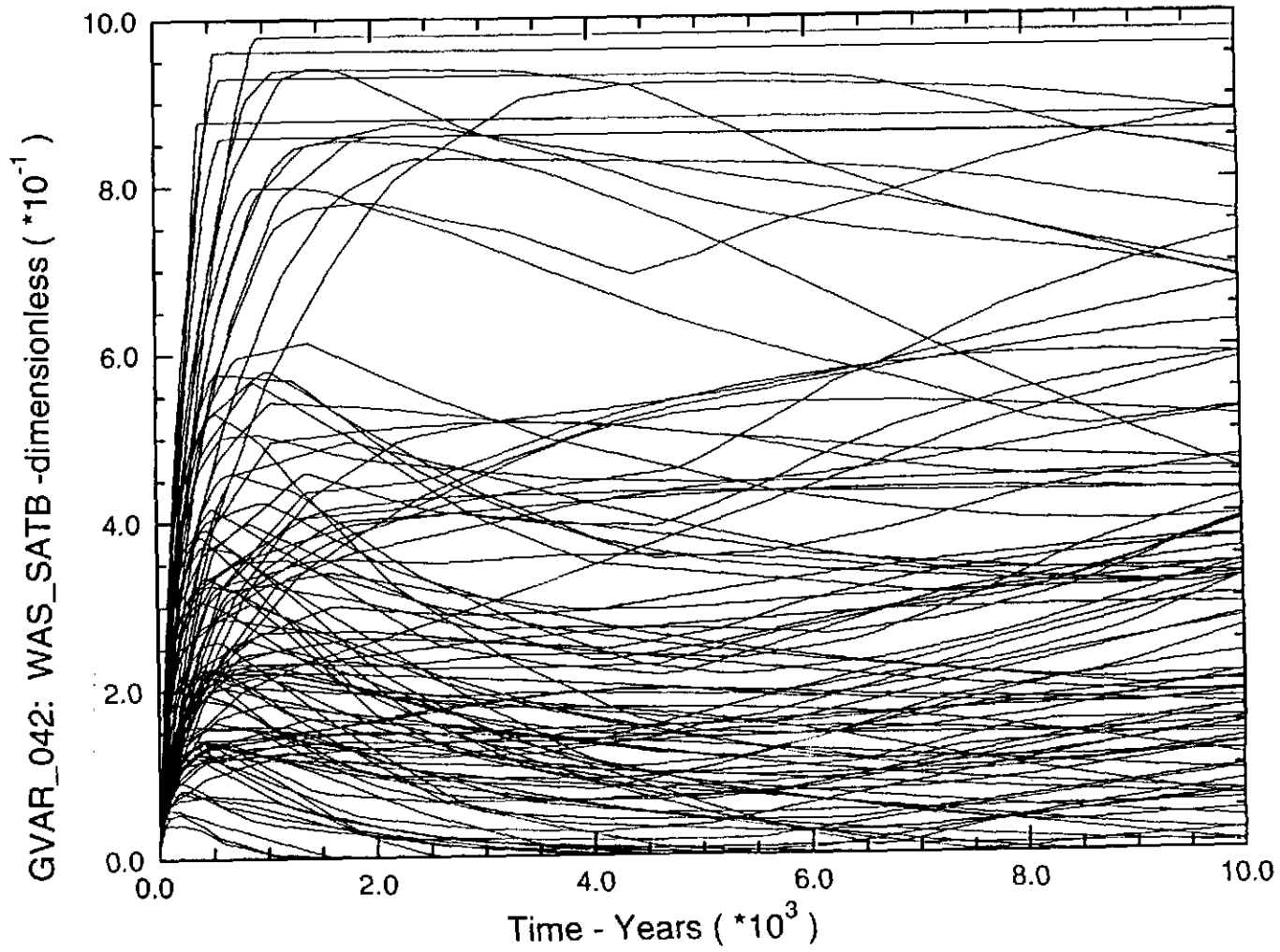
Figure 3.   Volume-average brine saturation in the waste panel for undisturbed performance from CCA Replicate 1.
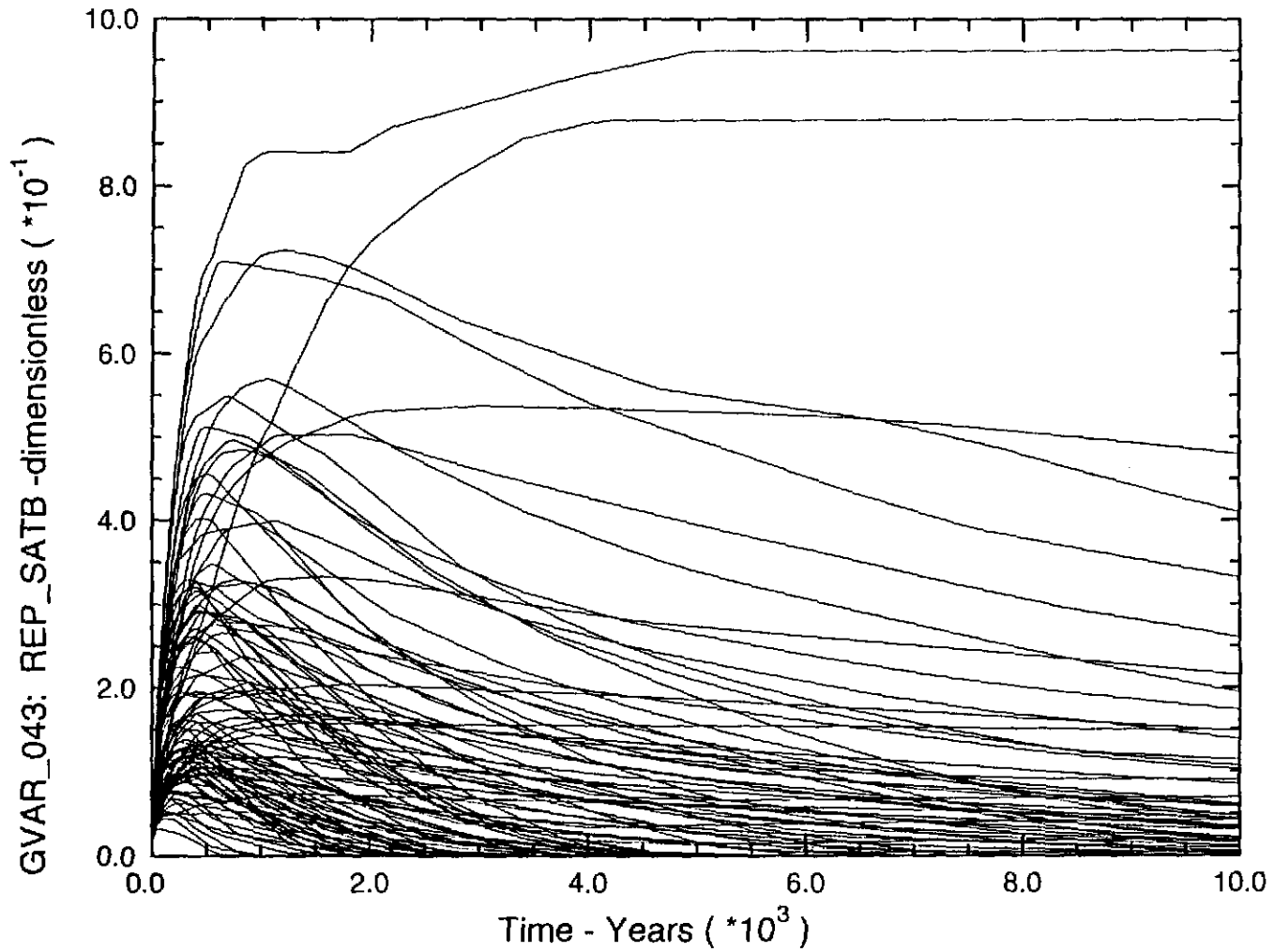
Figure 4. Volume-average brine saturation in the rest of the repository for undisturbed performance from CCA Replicate 1.
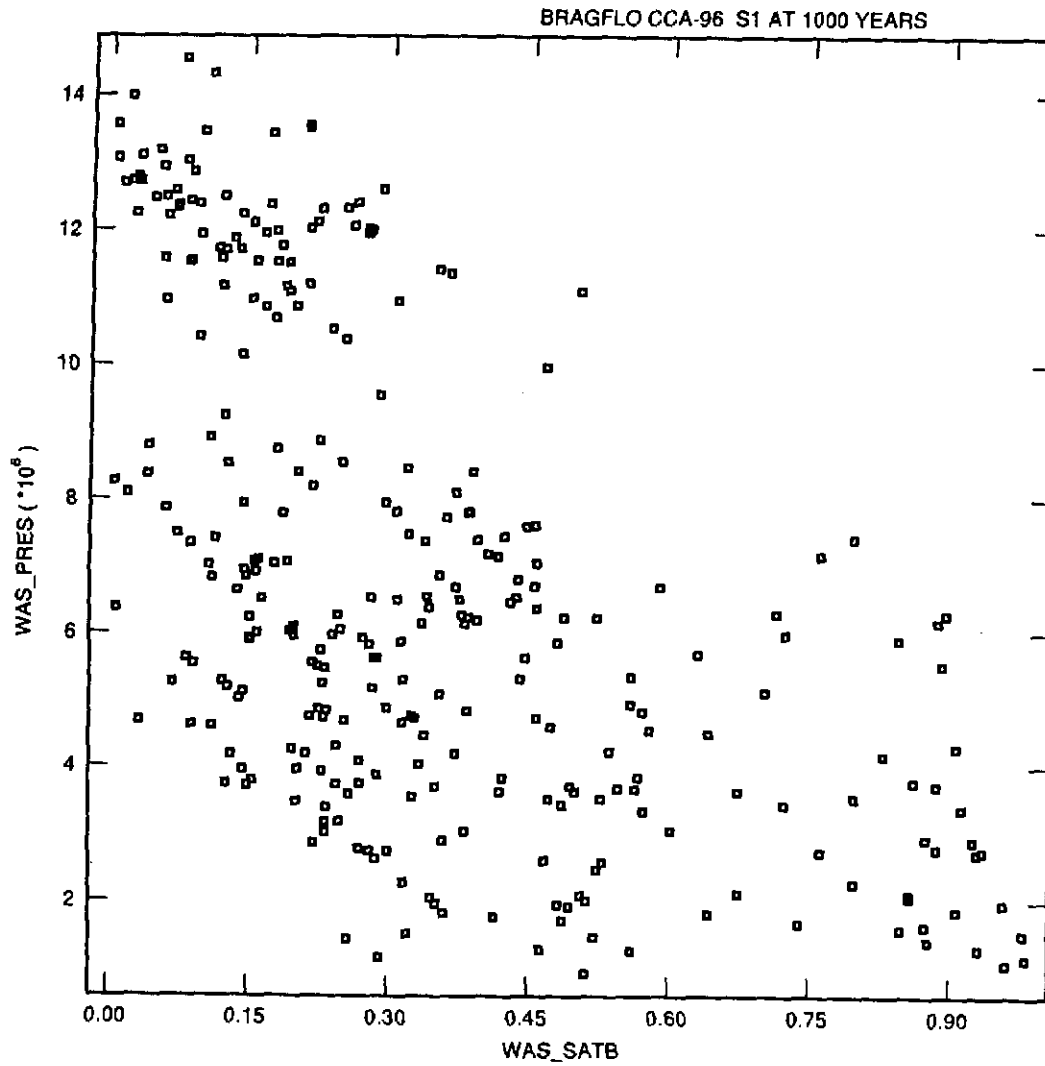
Figure 5.   Volume-average brine saturation in the panel versus pressure at 1,000 years for undisturbed performance from all three CCA Replicates.
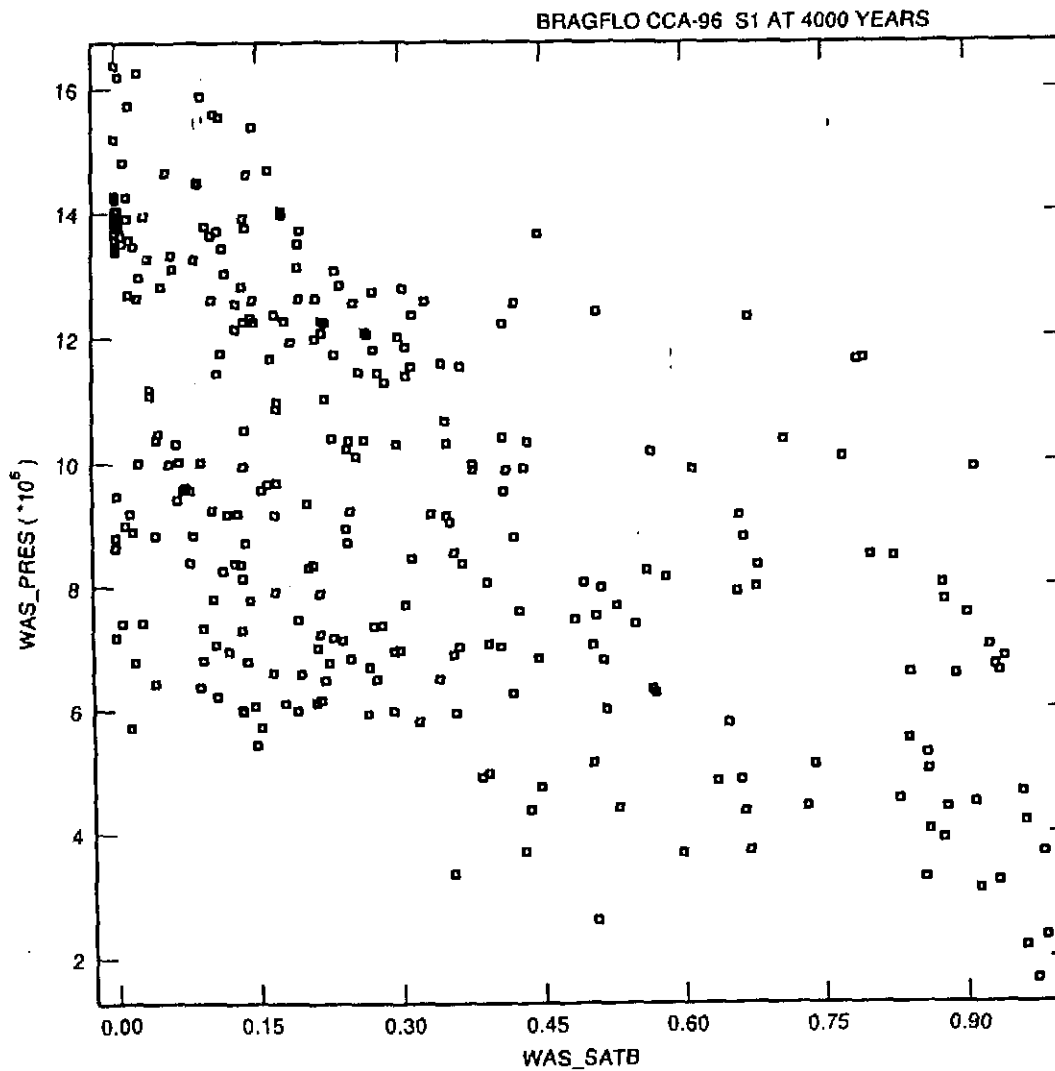
Figure 6. Volume-average brine saturation in the panel versus pressure at 4,000 years for undisturbed performance from all three CCA Replicates.
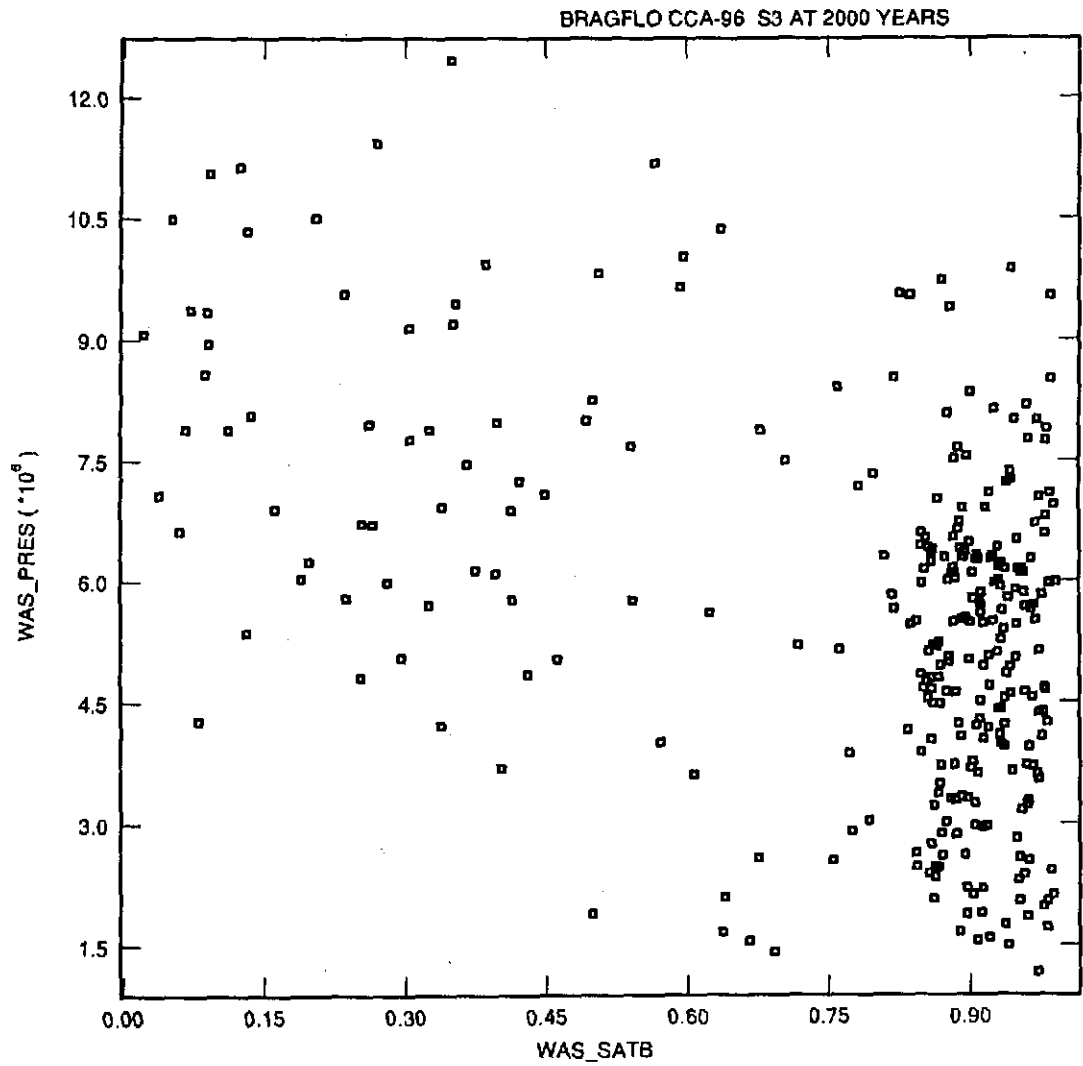
Figure 7.   Volume-average brine saturation in the intruded panel versus pressure at 2,000 years for an E1
             intrusion at 1,000 years from all three CCA replicates.
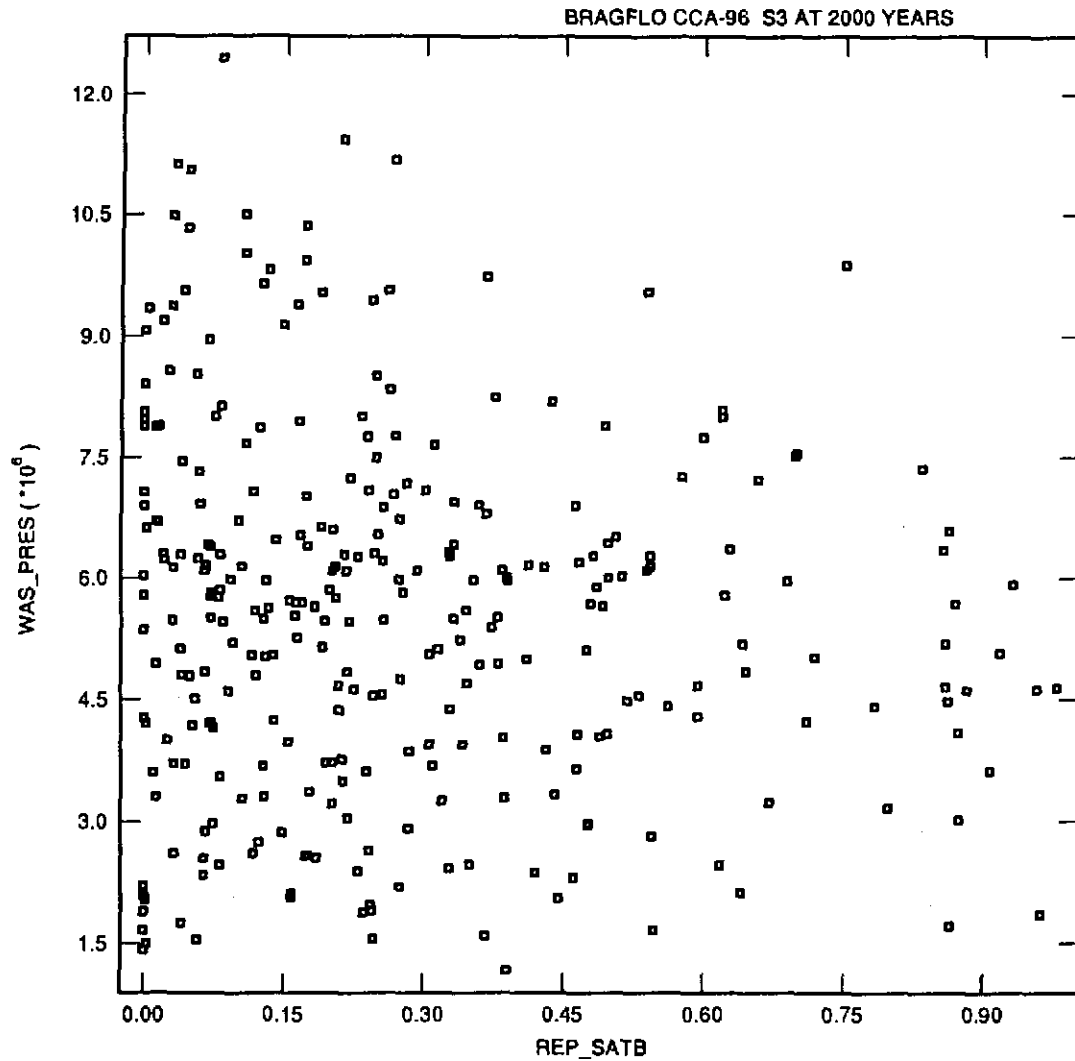
Figure 8.   Volume-average brine saturation in the rest of repository versus pressure at 2,000 years for an E1 intrusion at 1,000 years from all three CCA replicates.
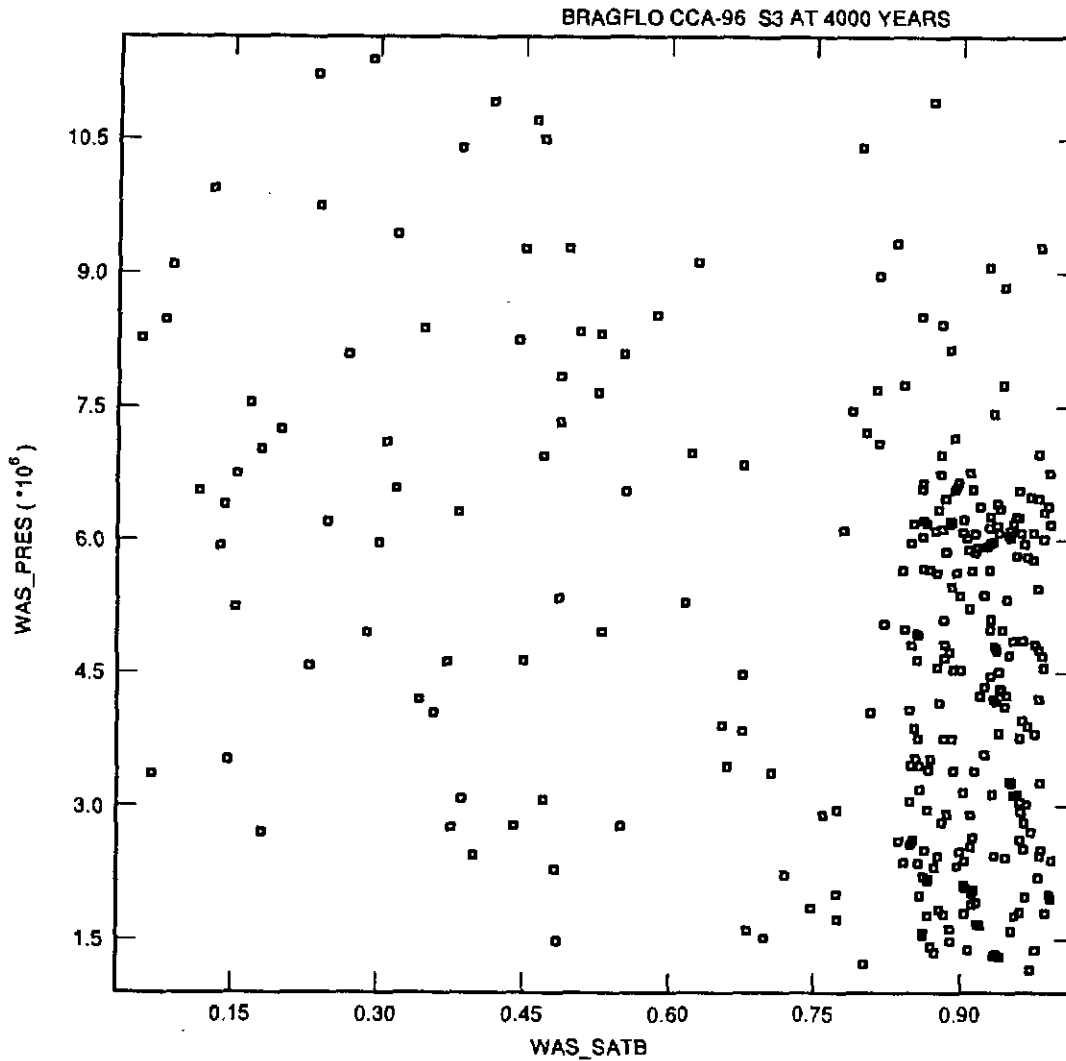
Figure 9. Volume-average brine saturation in the intruded panel versus pressure at 4,000 years for an E1 intrusion at 1,000 years from all three CCA replicates.
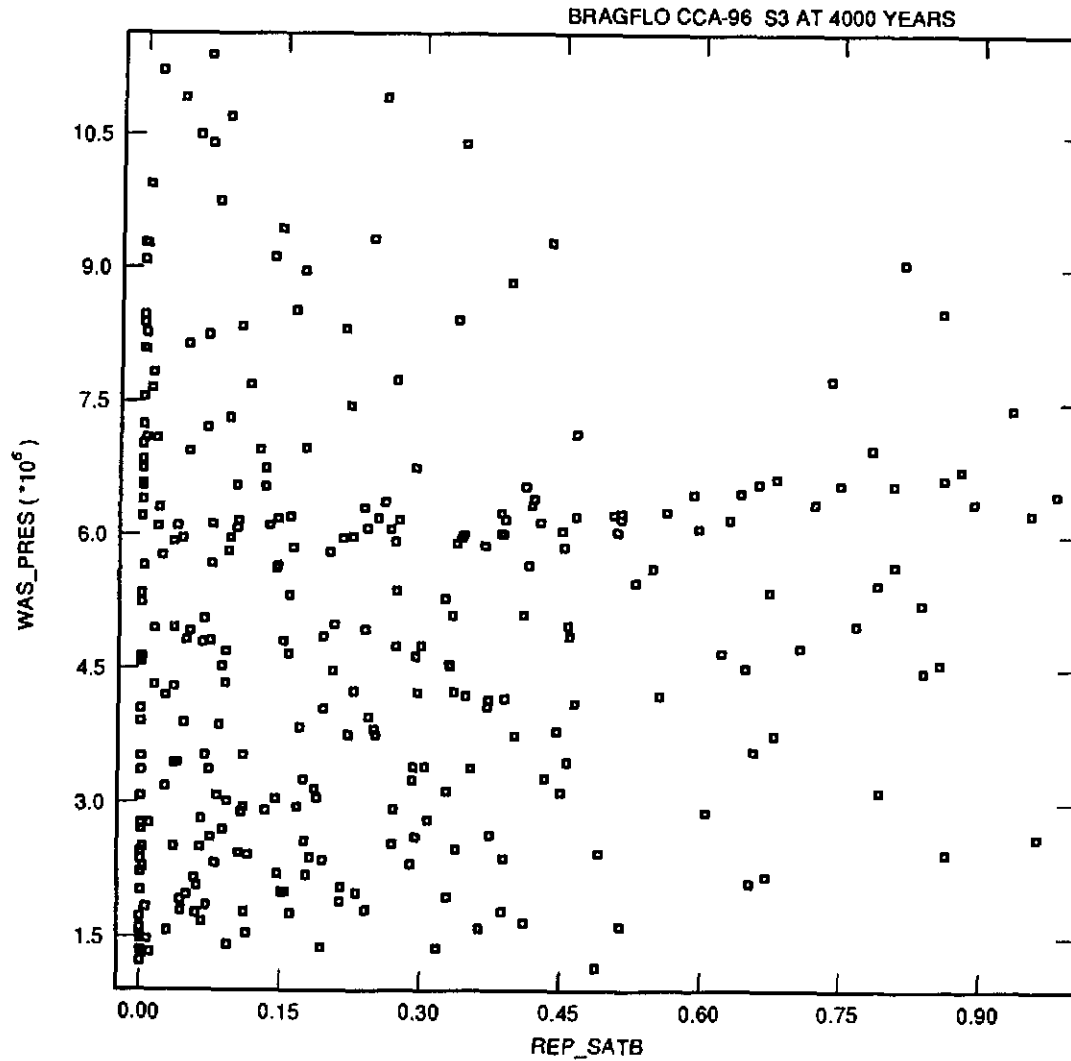
Figure 10.   Volume-average brine saturation in the rest of repository versus pressure at 4,000 years for an E1 intrusion at 1,000 years from all three CCA replicates.
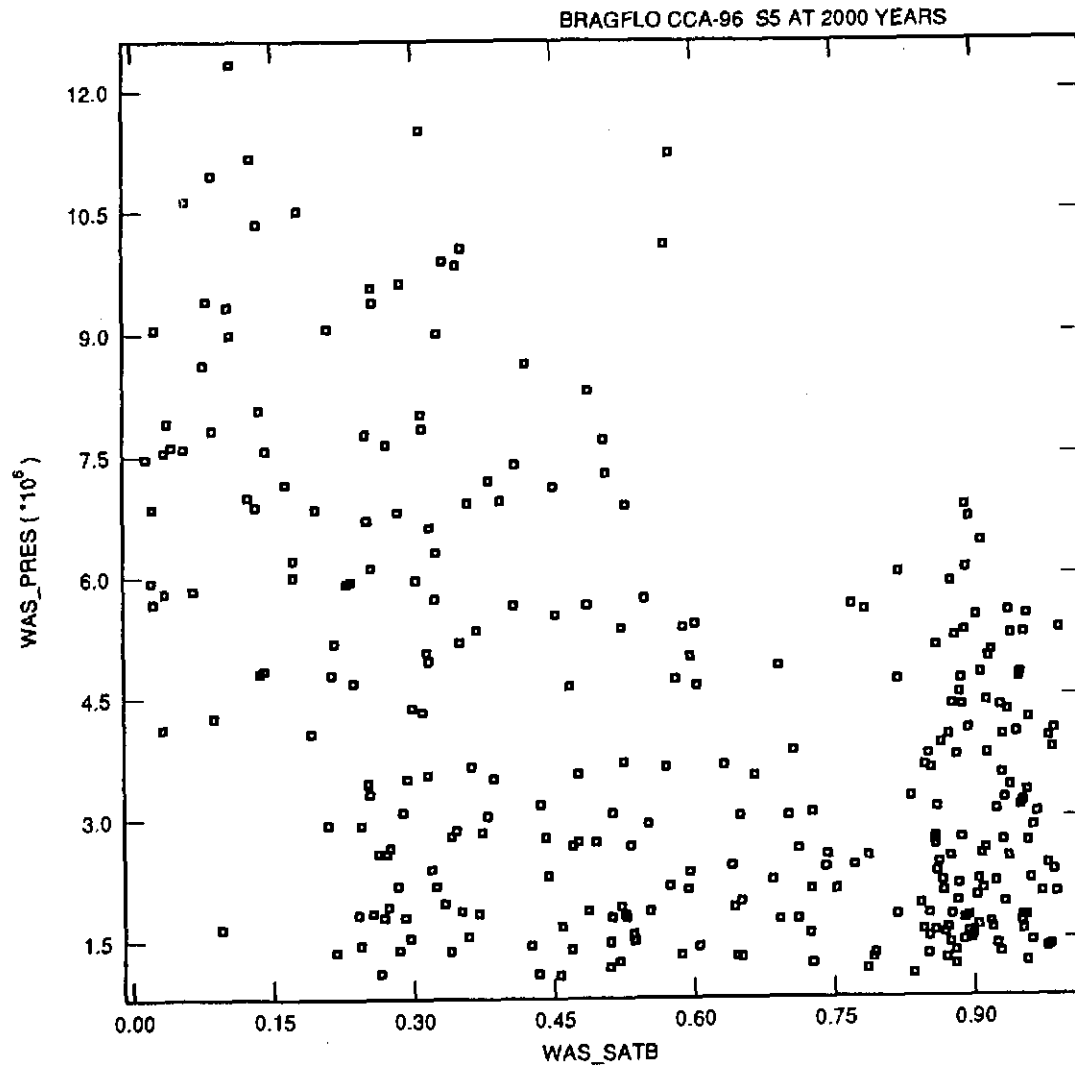
Figure 11.   Volume-average brine saturation in the intruded panel versus pressure at 2,000 years for an E2 intrusion at 1,000 years from all three CCA replicates.
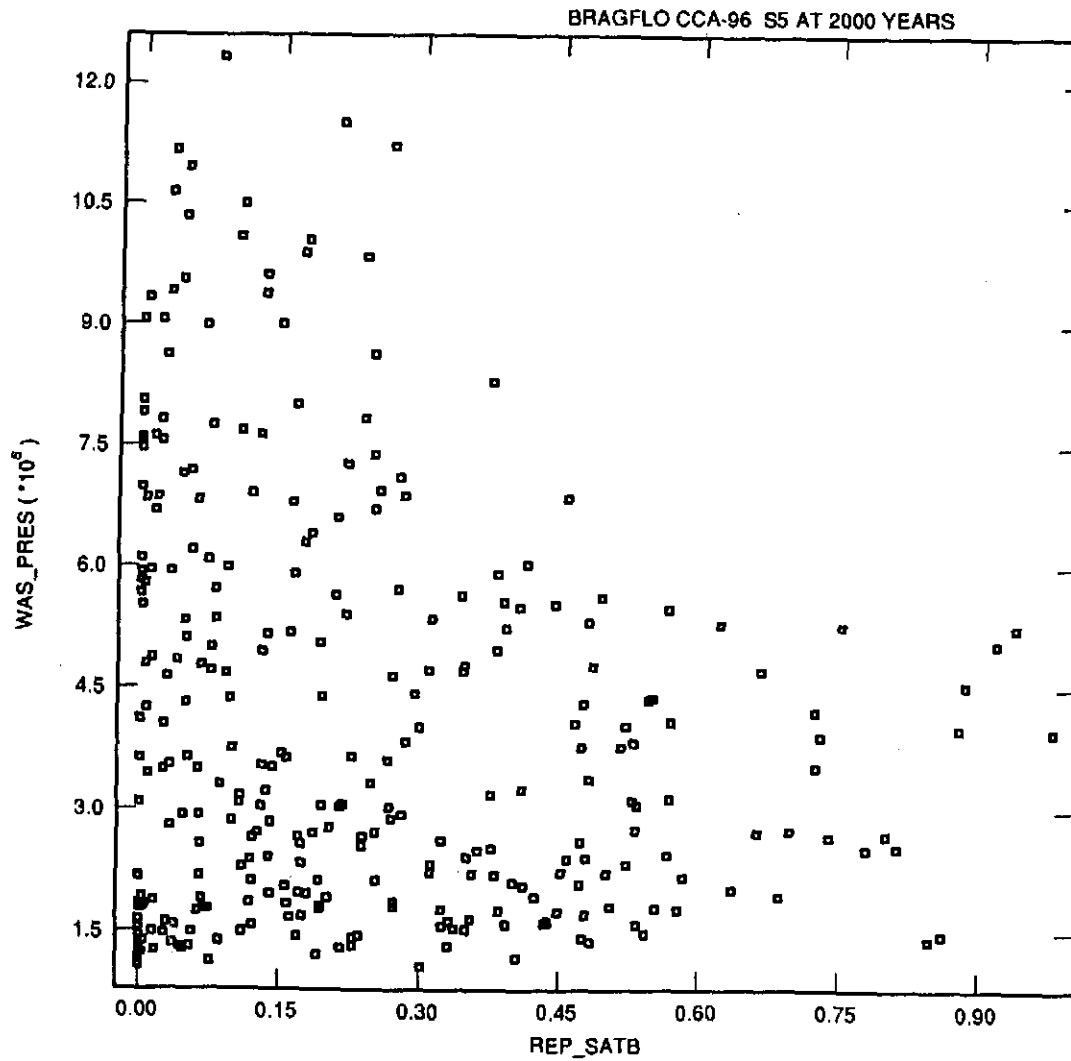
Figure 12.　Volume-average brine saturation in the rest of repository versus pressure at 2,000 years for an E2 intrusion at 1,000 years from all three CCA replicates.

Information Only
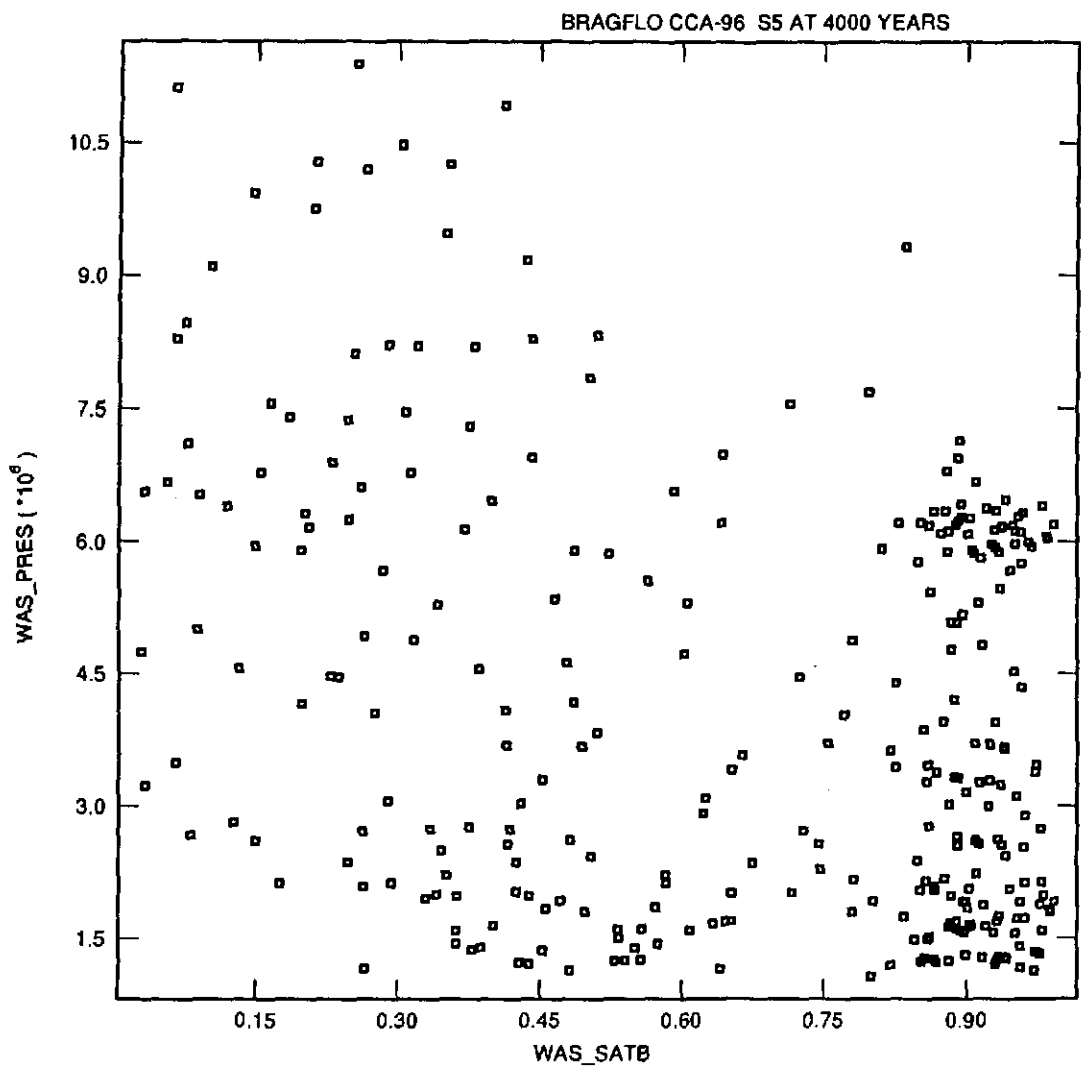
Figure 13. Volume-average brine saturation in the intruded panel versus pressure at 4,000 years for an E2 intrusion at 1,000 years from all three CCA replicates.
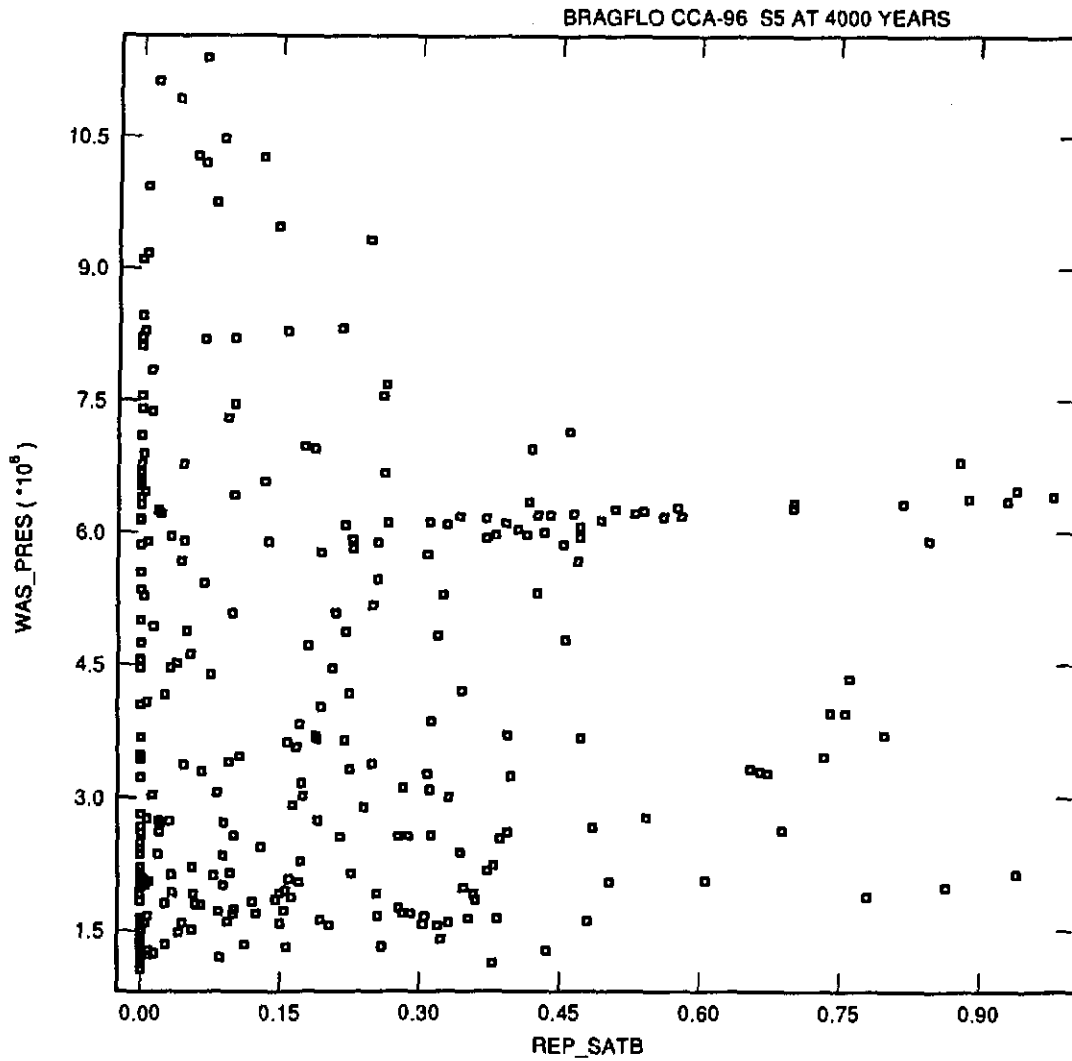
Figure 14. Volume-average brine saturation in the rest of repository versus pressure at 4,000 years for an E2 intrusion at 1,000 years from all three CCA replicates.
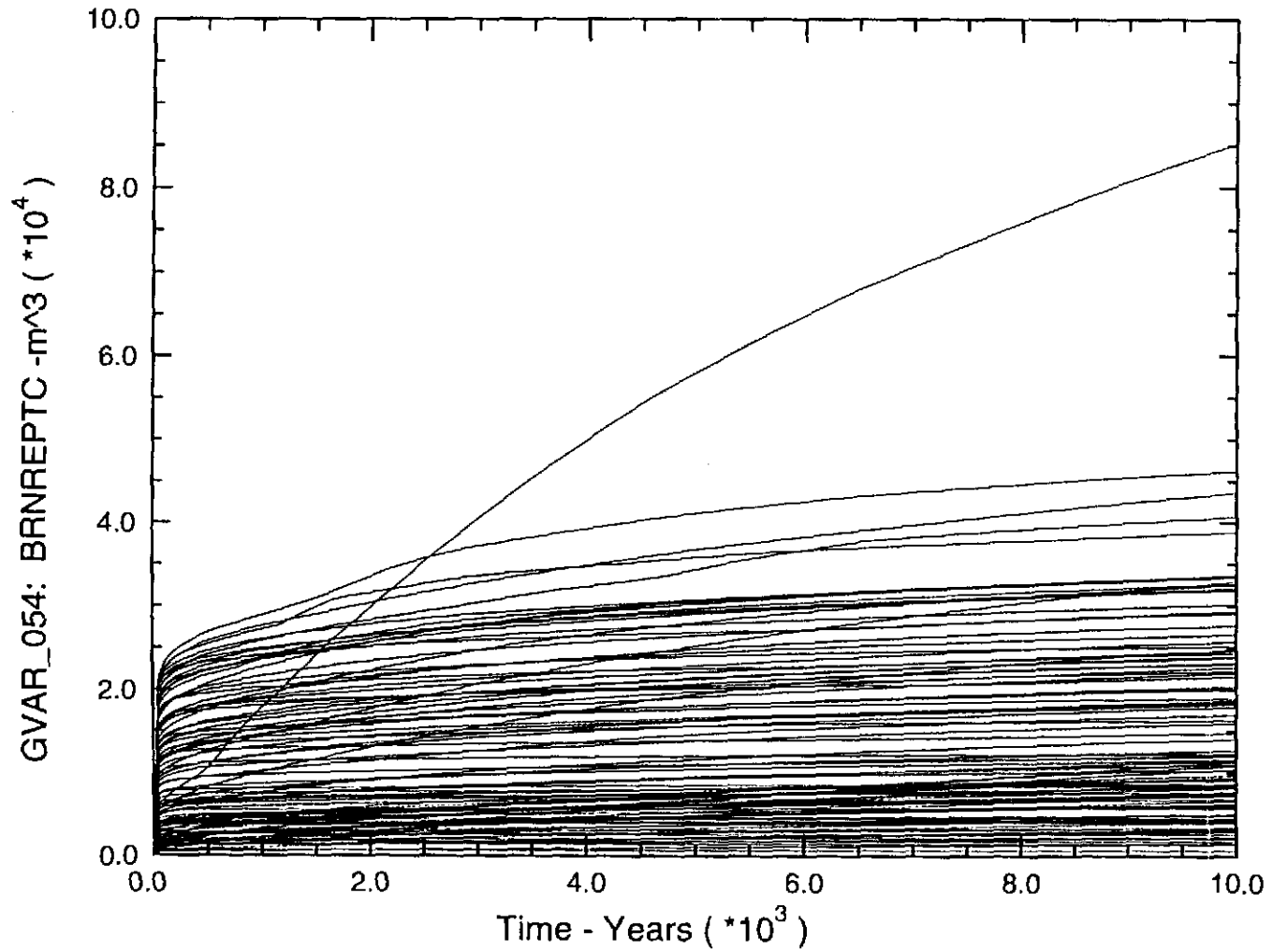
Figure 15.   Cumulative brine inflow into the repository during the regulatory period for undisturbed performance, showing the DRZ contribution during the first hundred years or so and the long-term interbed drainage contribution, from CCA Replicate 1.
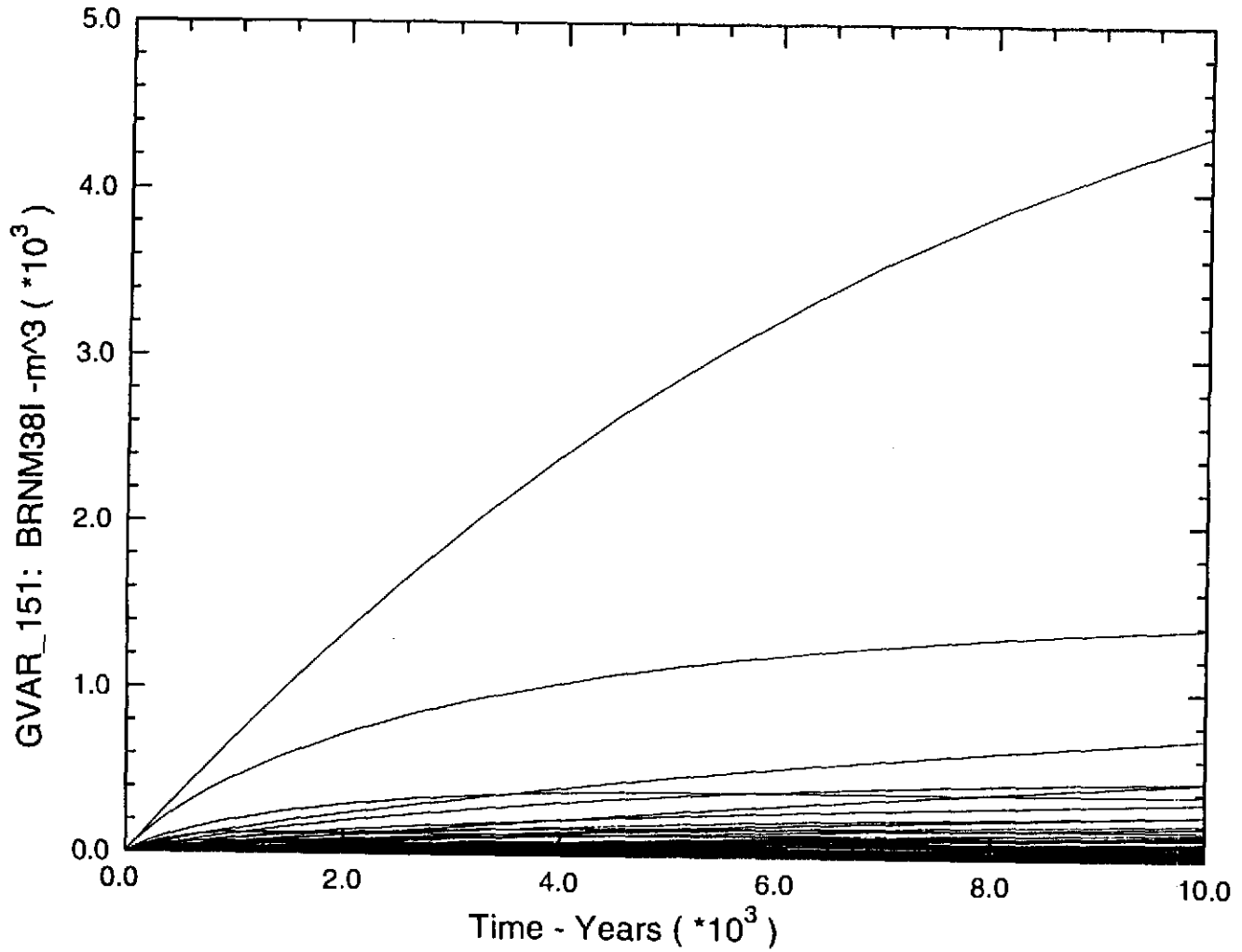
Figure 16.   Cumulative inflow from Marker Bed 138 to the DRZ during undisturbed performance, from CCA Replicate 1.
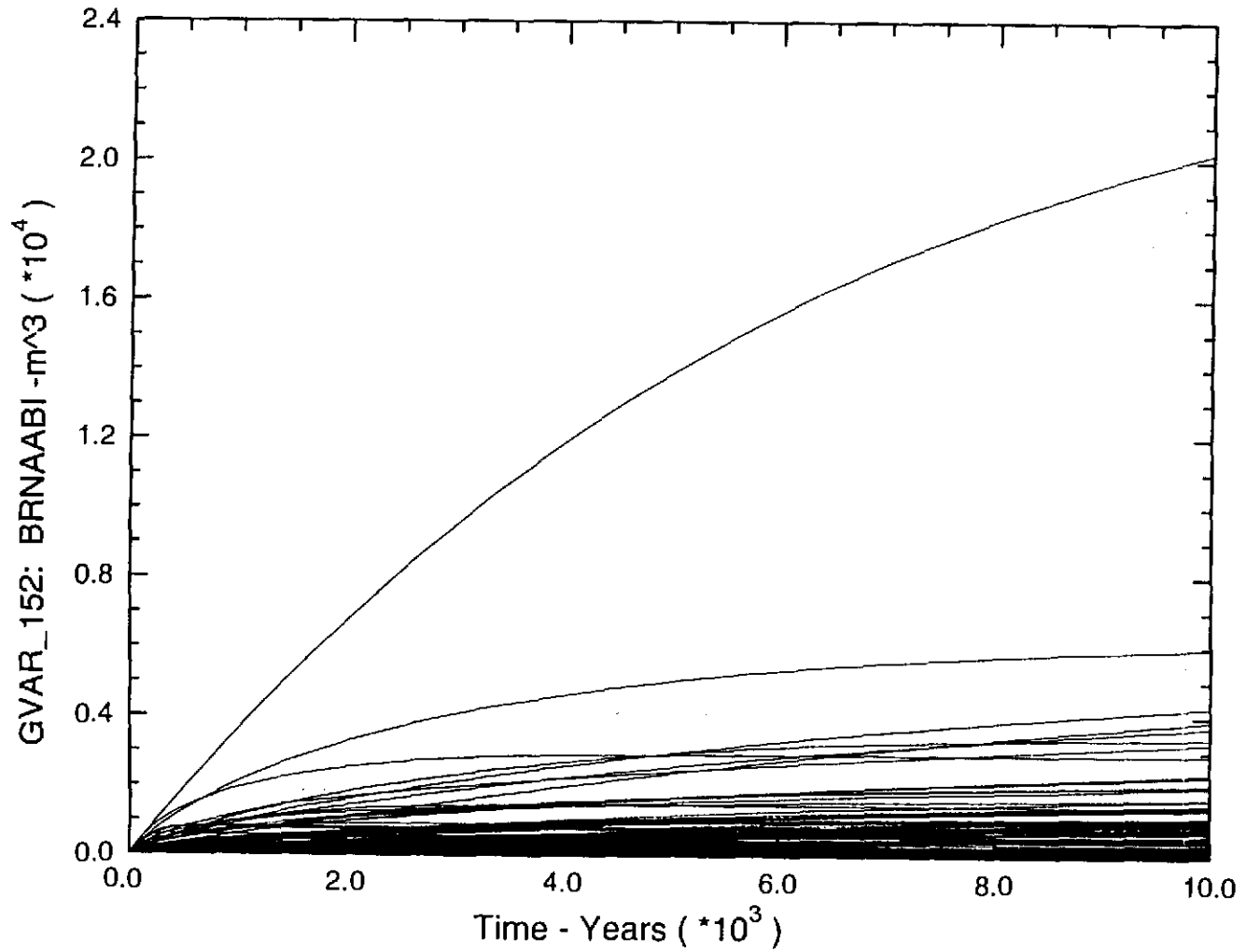
Figure 17.   Cumulative inflow from Anhydrite A and B to the DRZ during undisturbed performance, from CCA Replicate 1.
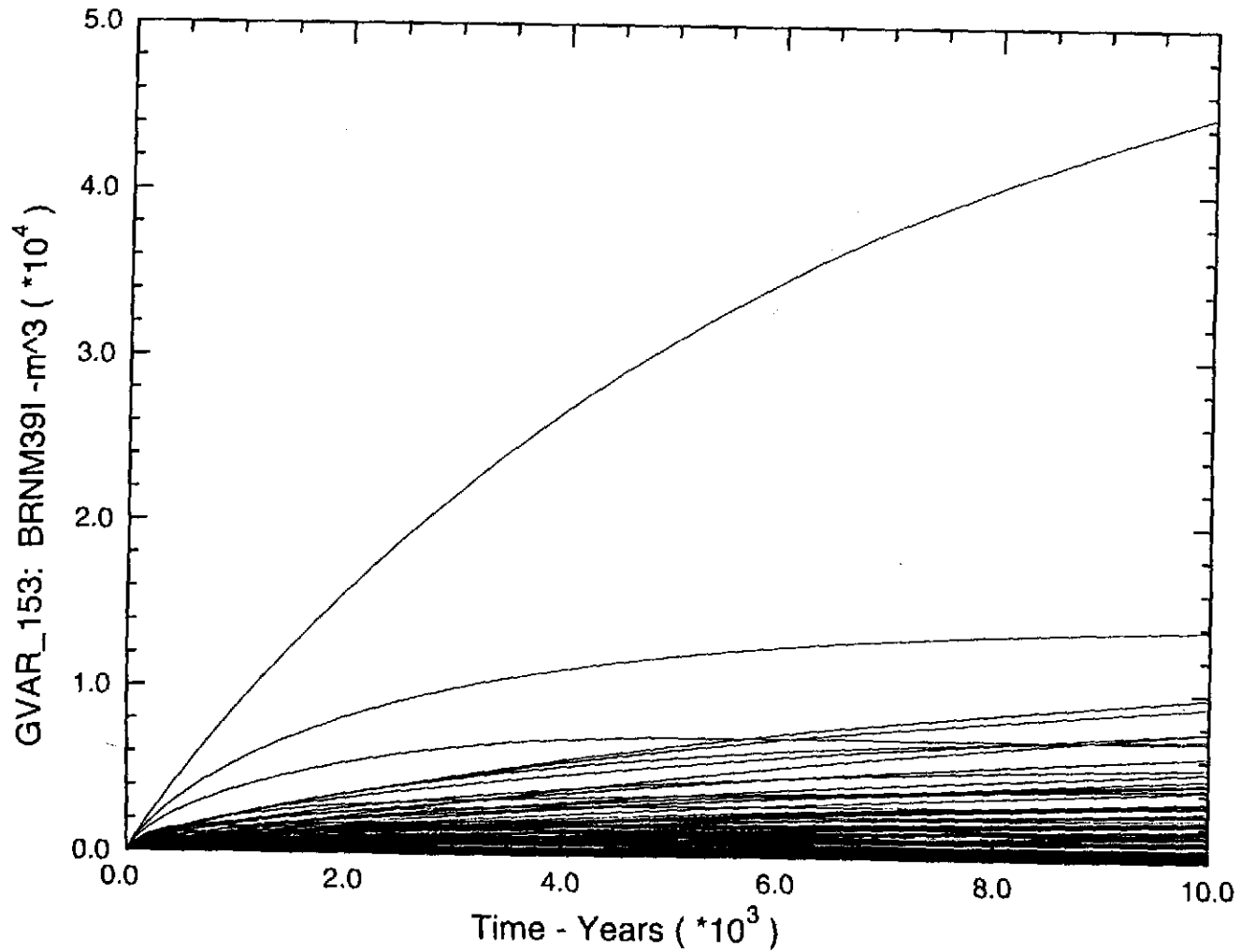
Figure 18.   Cumulative inflow from Marker Bed 139 to the DRZ during undisturbed performance, from CCA Replicate 1.
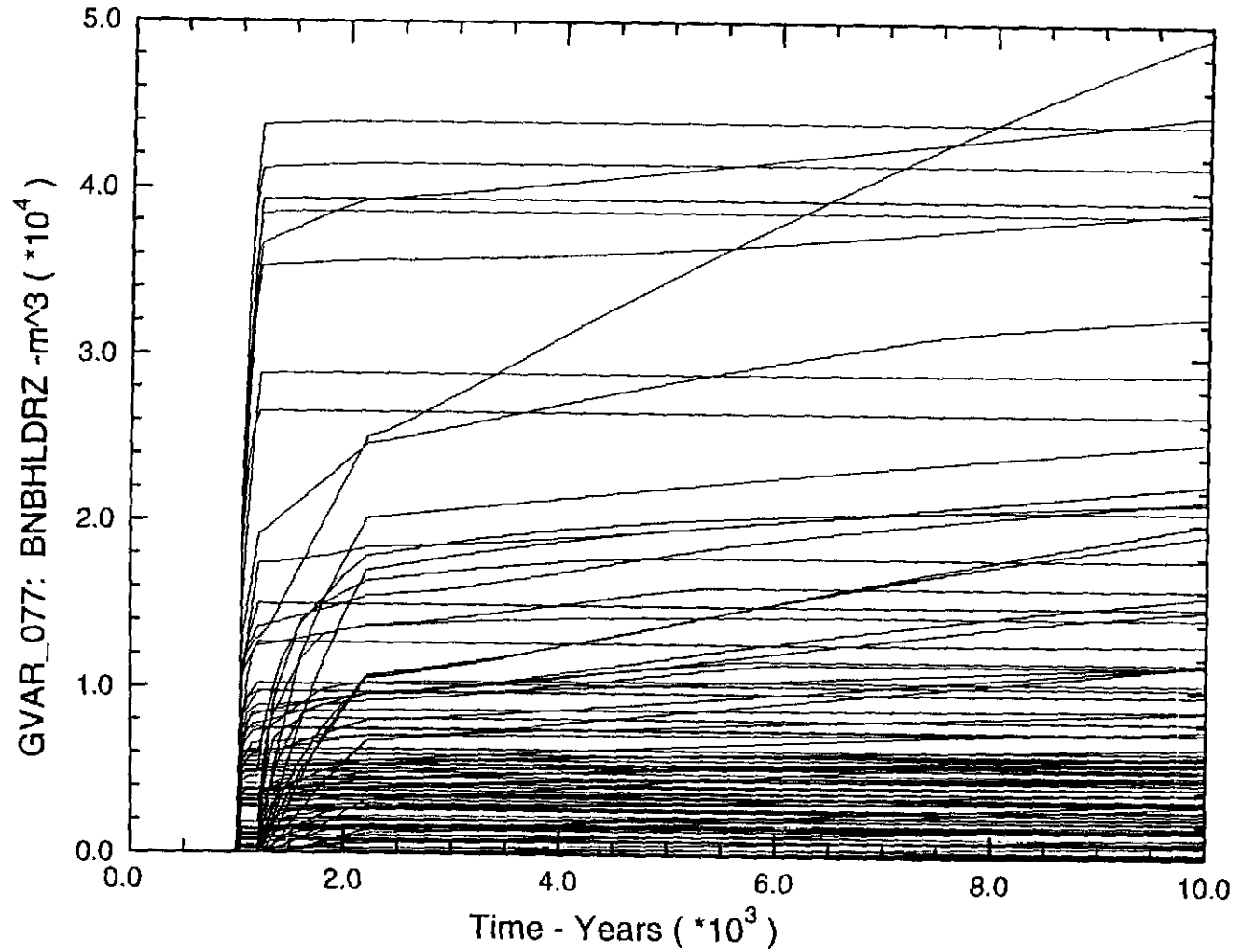
Figure 19.   Cumulative inflow from the brine reservoir to the intruded waste panel, E1 intrusion at 1,000 years, from CCA Replicate 1.
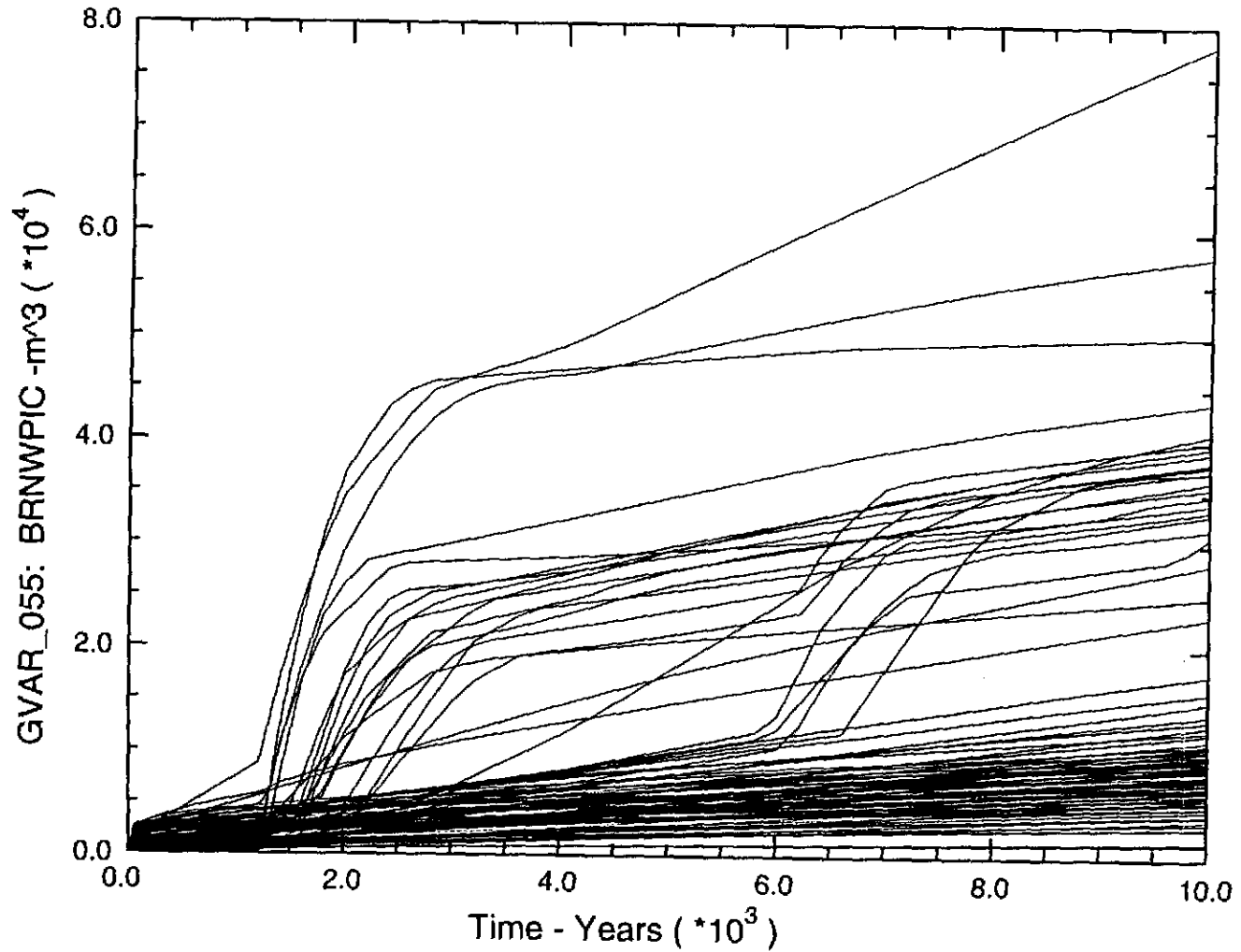
Figure 20.   Cumulative inflow to the intruded waste panel showing contribution of DRZ, interbeds, and down-borehole flow for an E2 intrusion at 1,000 years, from CCA Replicate 1.
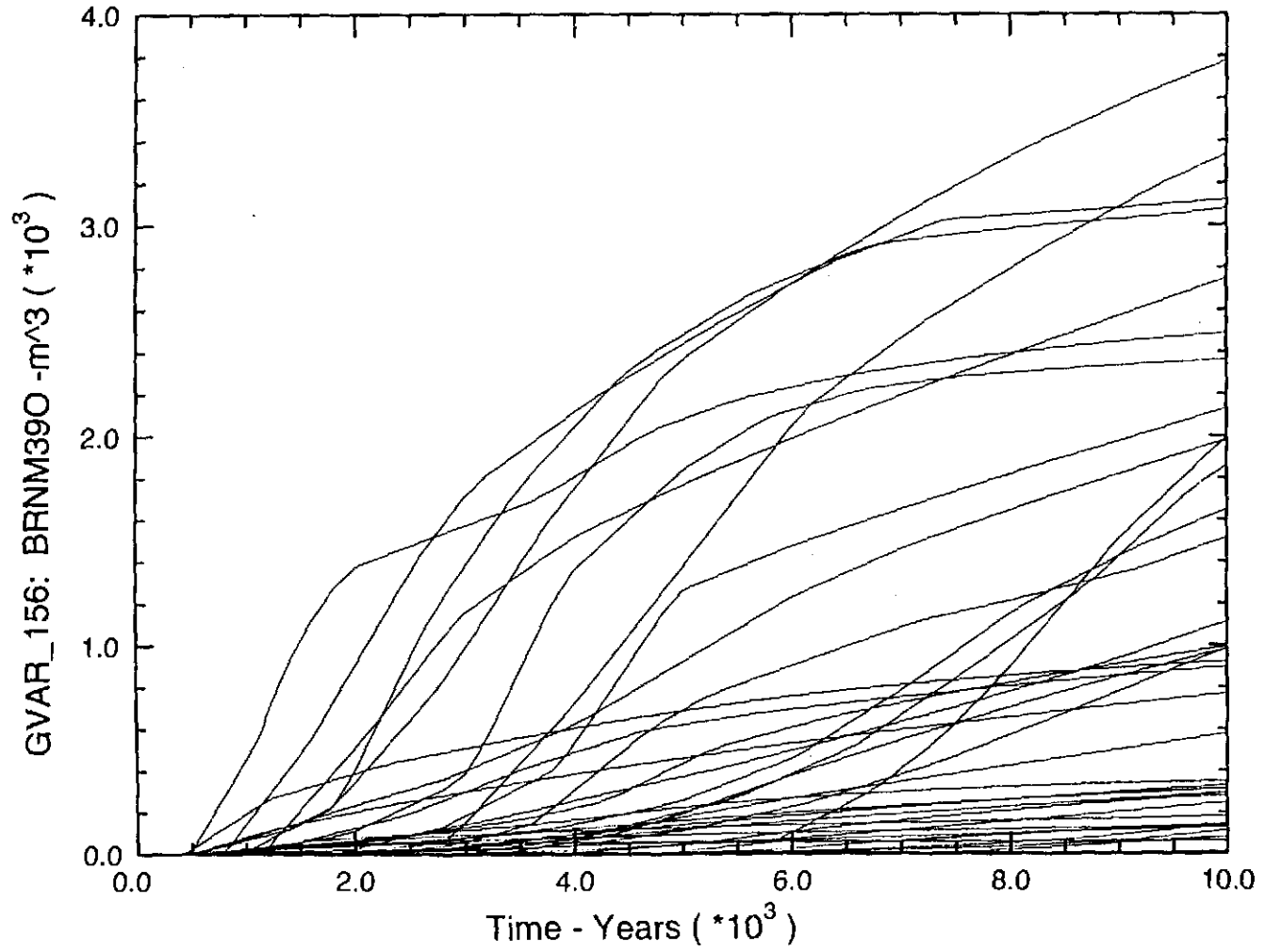
Figure 21.   Cumulative outflow through Marker Bed 139 for undisturbed performance from CCA Replicate 1.
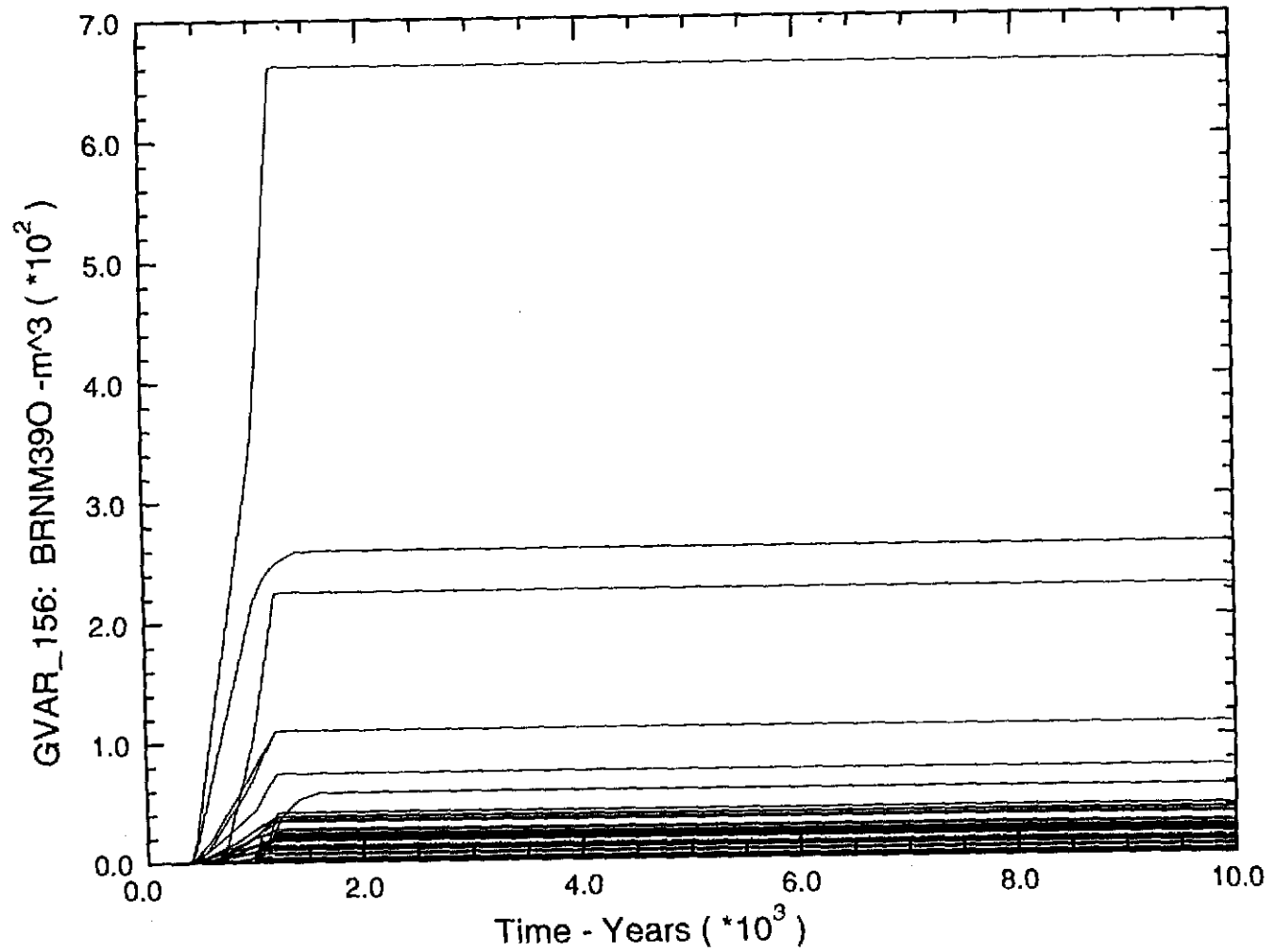
Figure 22.   Cumulative outflow through Marker Bed 139 for an E1 intrusion at 1,000 years from CCA Replicate 1.

Information Only
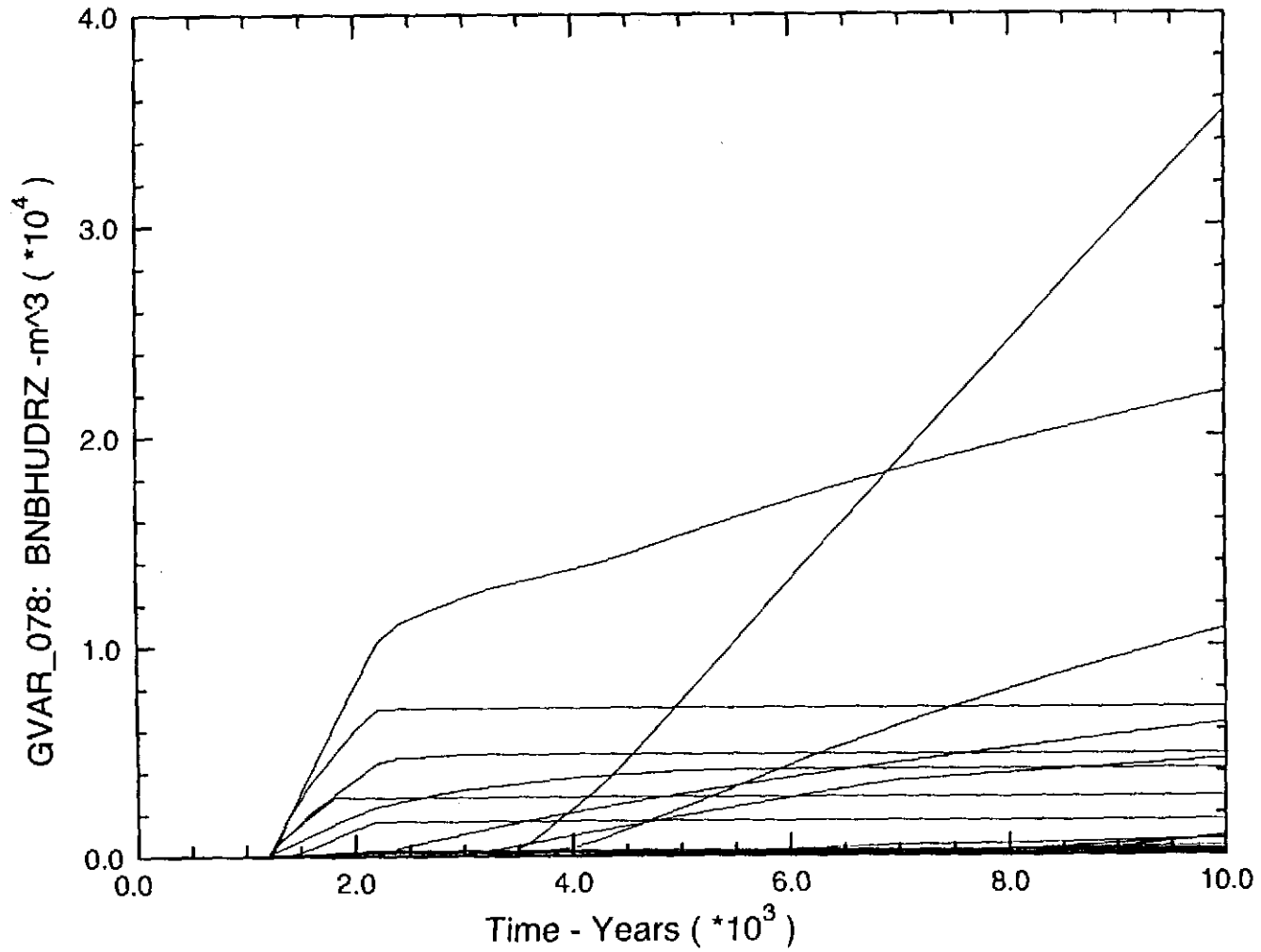
Figure 23.   Cumulative outflow up the intrusion borehole for an E1 intrusion at 1,000 years from CCA Replicate 1.

D-37
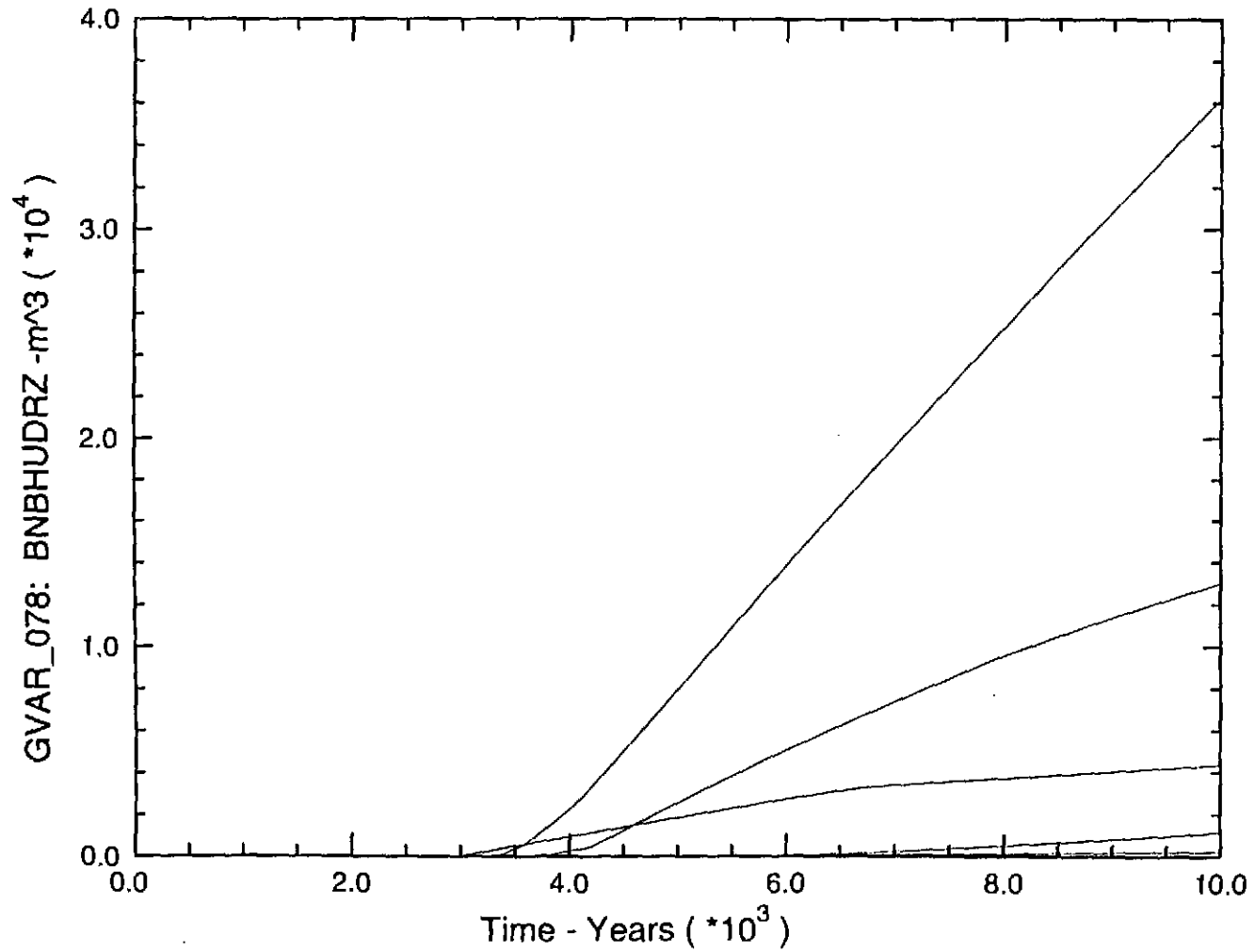
Figure 24. Cumulative outflow up the intrusion borehole for an E2 intrusion at 1,000 years from CCA Replicate 1.
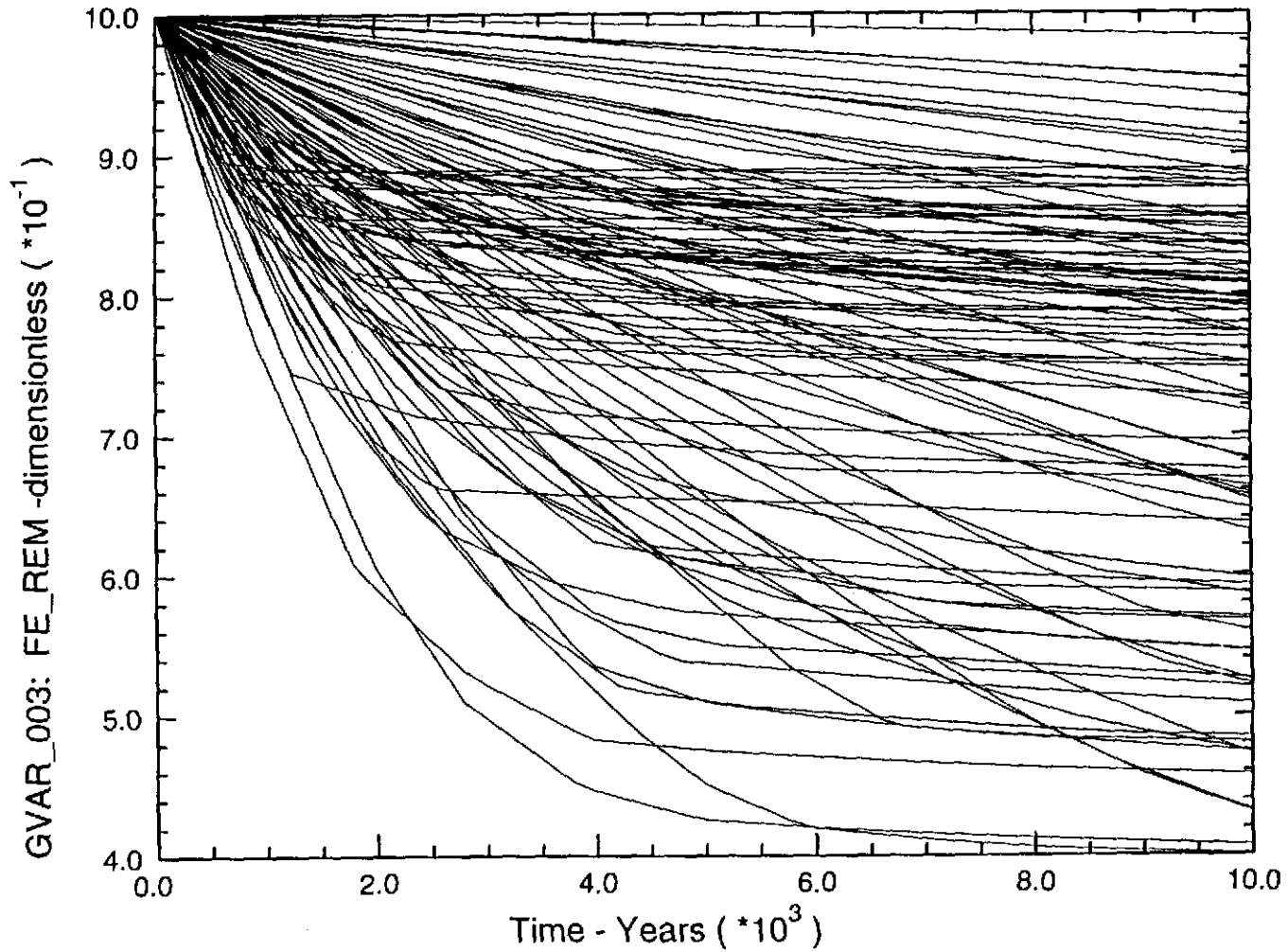
Figure 25. Fraction of initial steel inventory remaining in undegraded state during the regulatory period for undisturbed performance from CCA Replicate 1.
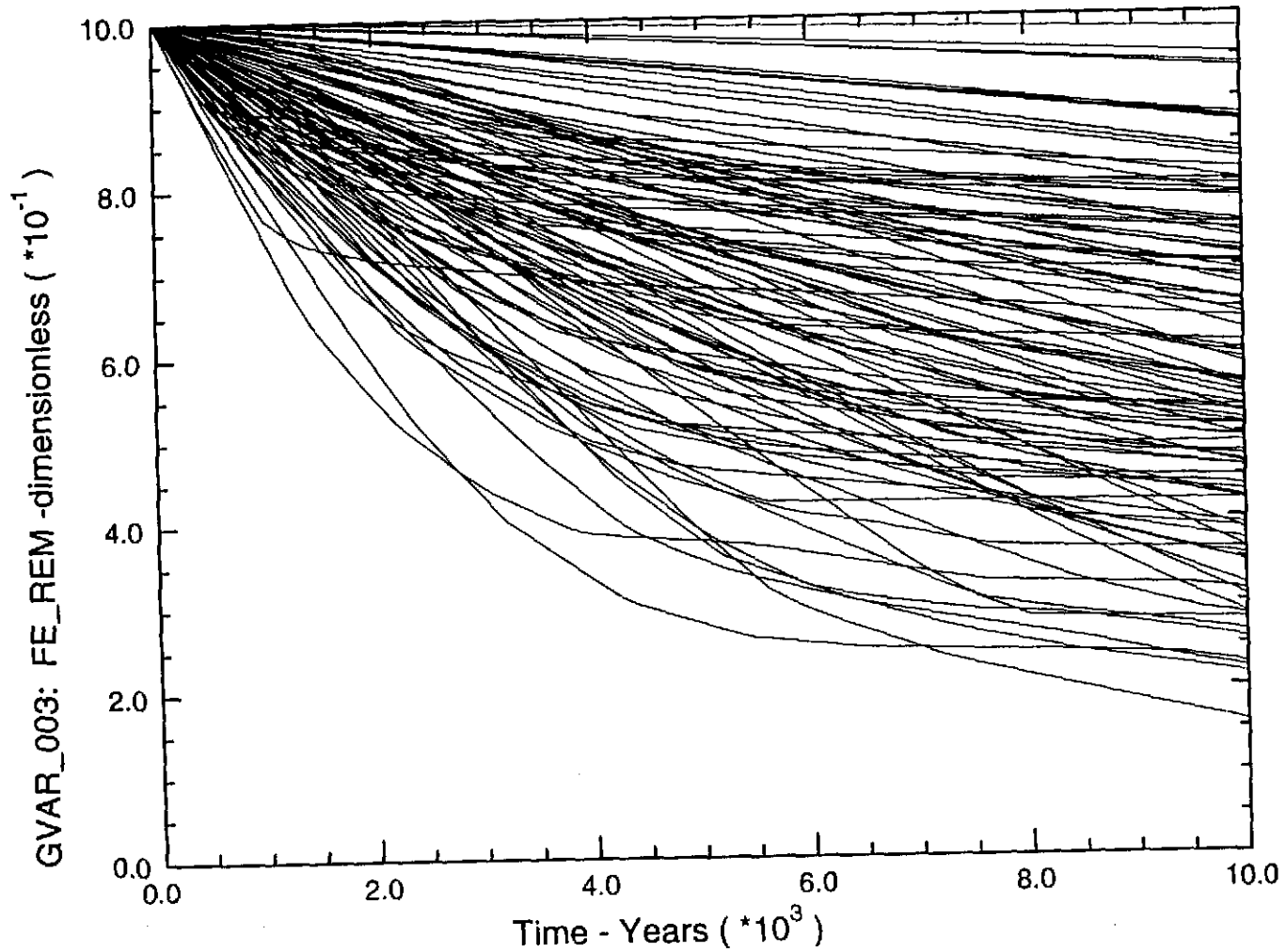
Figure 26.   Fraction of initial steel inventory remaining in uncorroded state during the regulatory period for an E1 intrusion at 1,000 years from CCA Replicate 1.
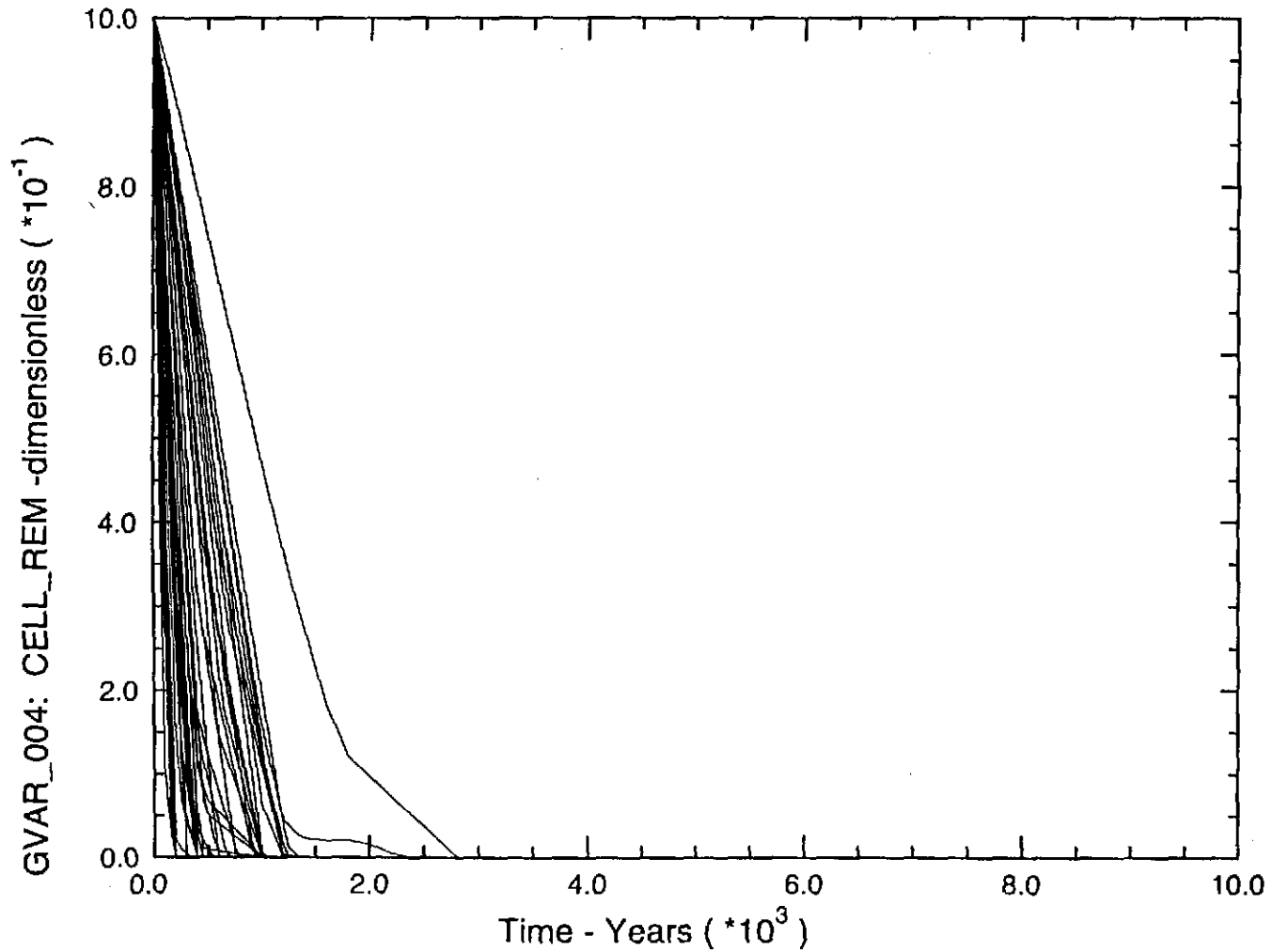
Figure 27.   Fraction of the degradable inventory of cellulosics, plastics, and rubbers remaining during the regulatory period from CCA Replicate 1.
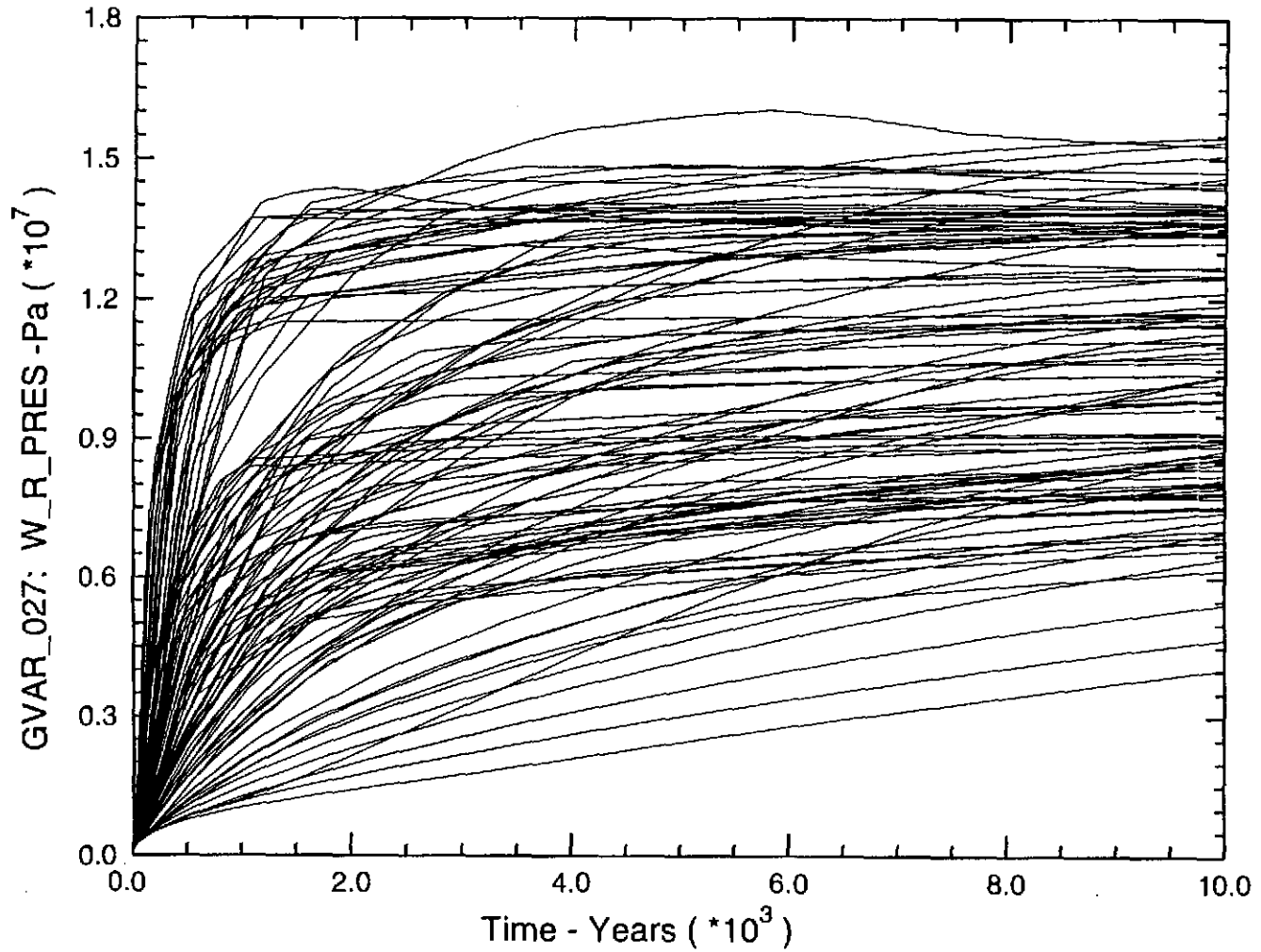
Figure 28.   Pressure in the waste disposal area during the regulatory period for undisturbed performance from CCA Replicate 1.
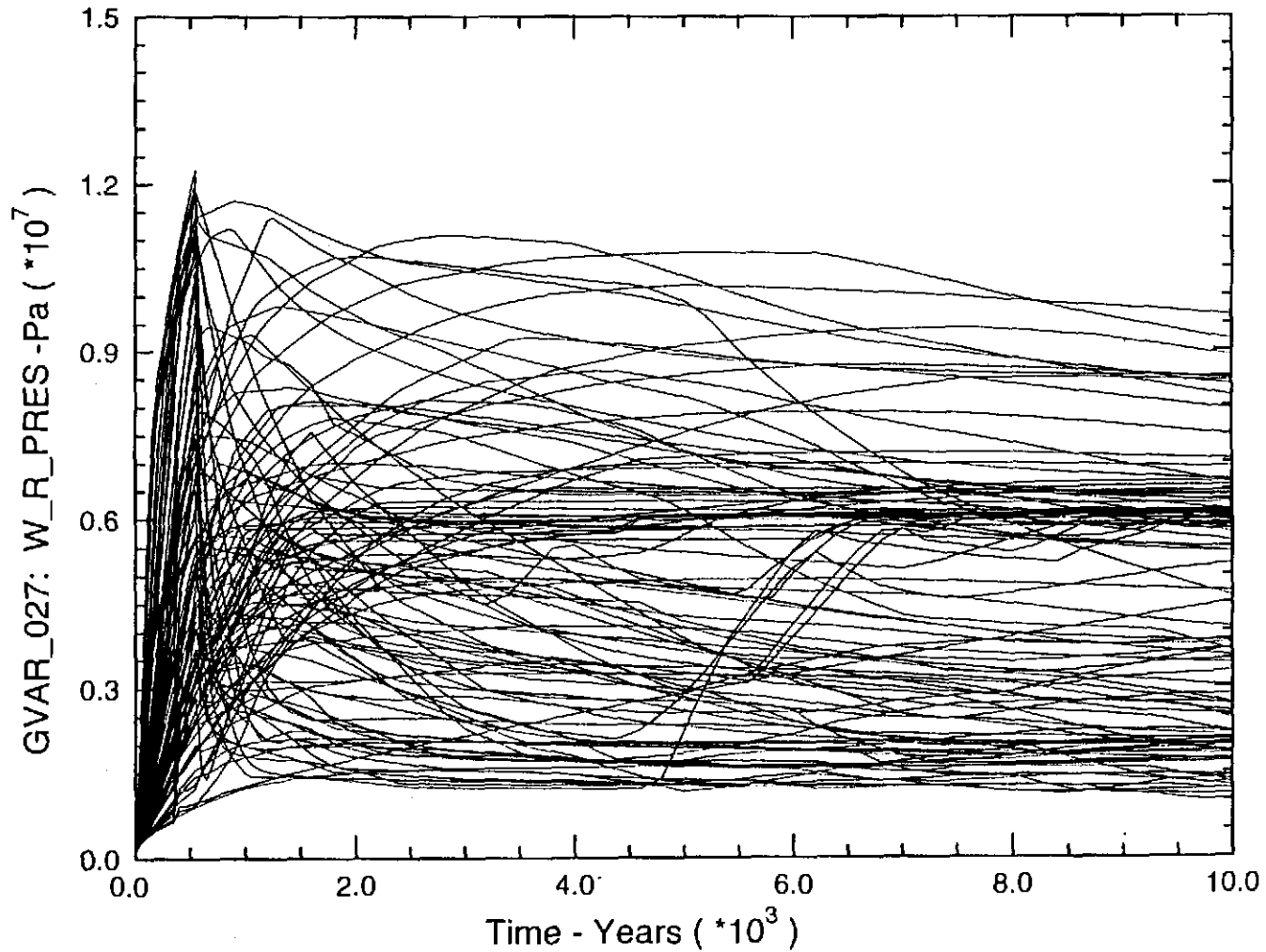
Figure 29.   Pressure in the waste disposal area during the regulatory period for an E1 intrusion occurring at 350
years from CCA Replicate 1.
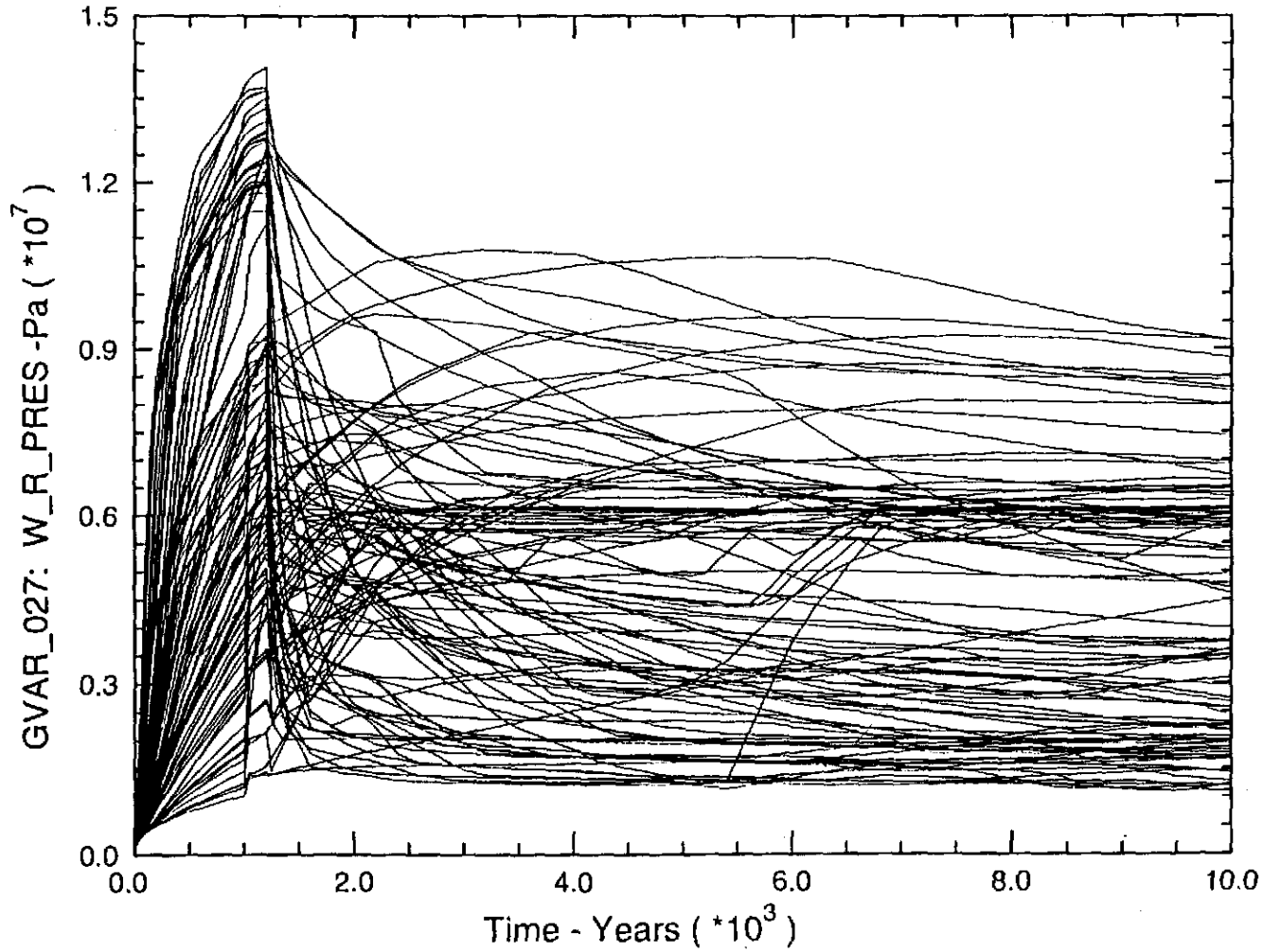
Figure 30. Pressure in the waste disposal area during the regulatory period for an E1 intrusion occurring at 1,000 years from CCA Replicate 1.
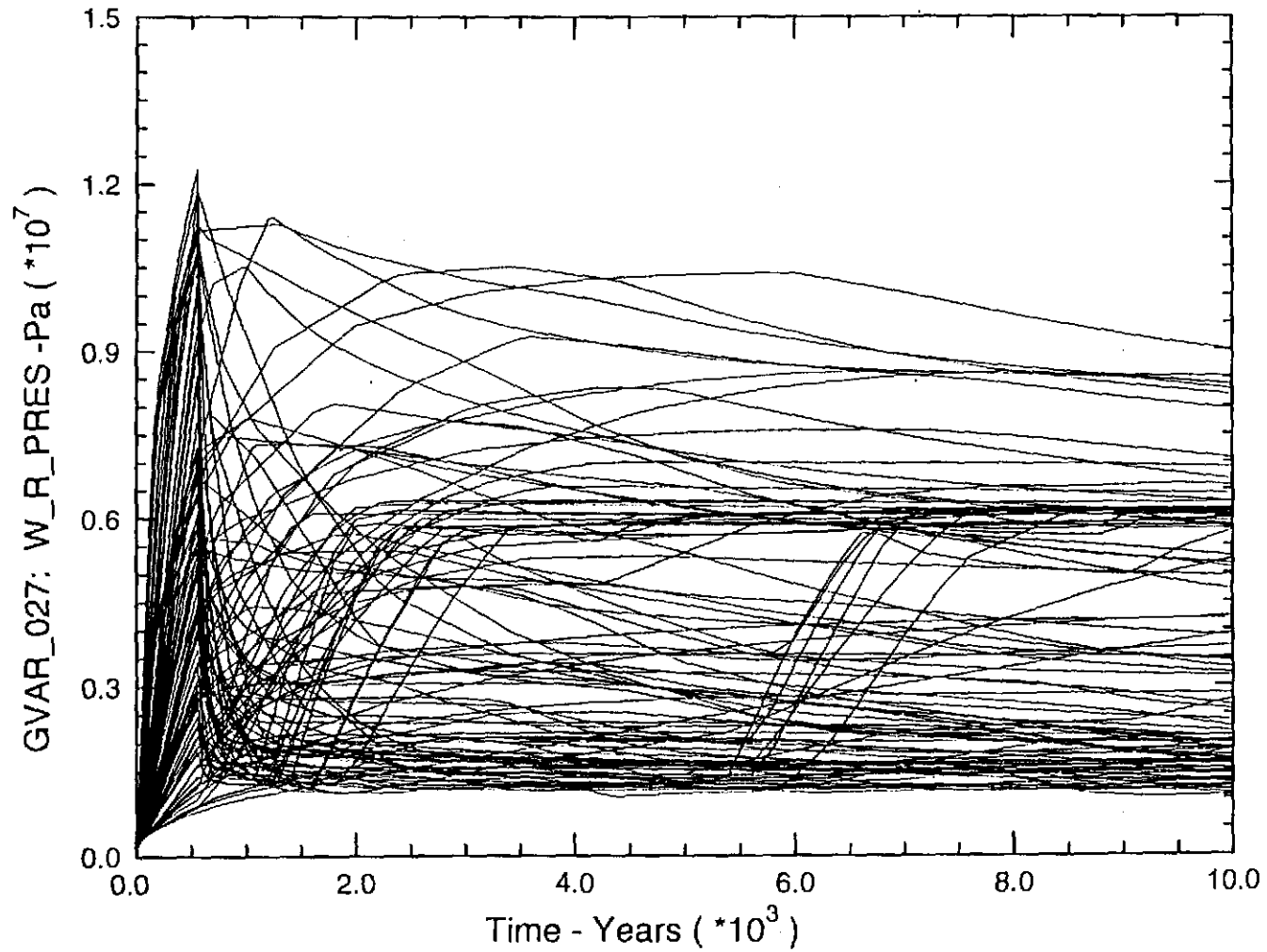
Figure 31.   Pressure in the waste disposal area during the regulatory period for an E2 intrusion occurring at 350 years from CCA Replicate 1.
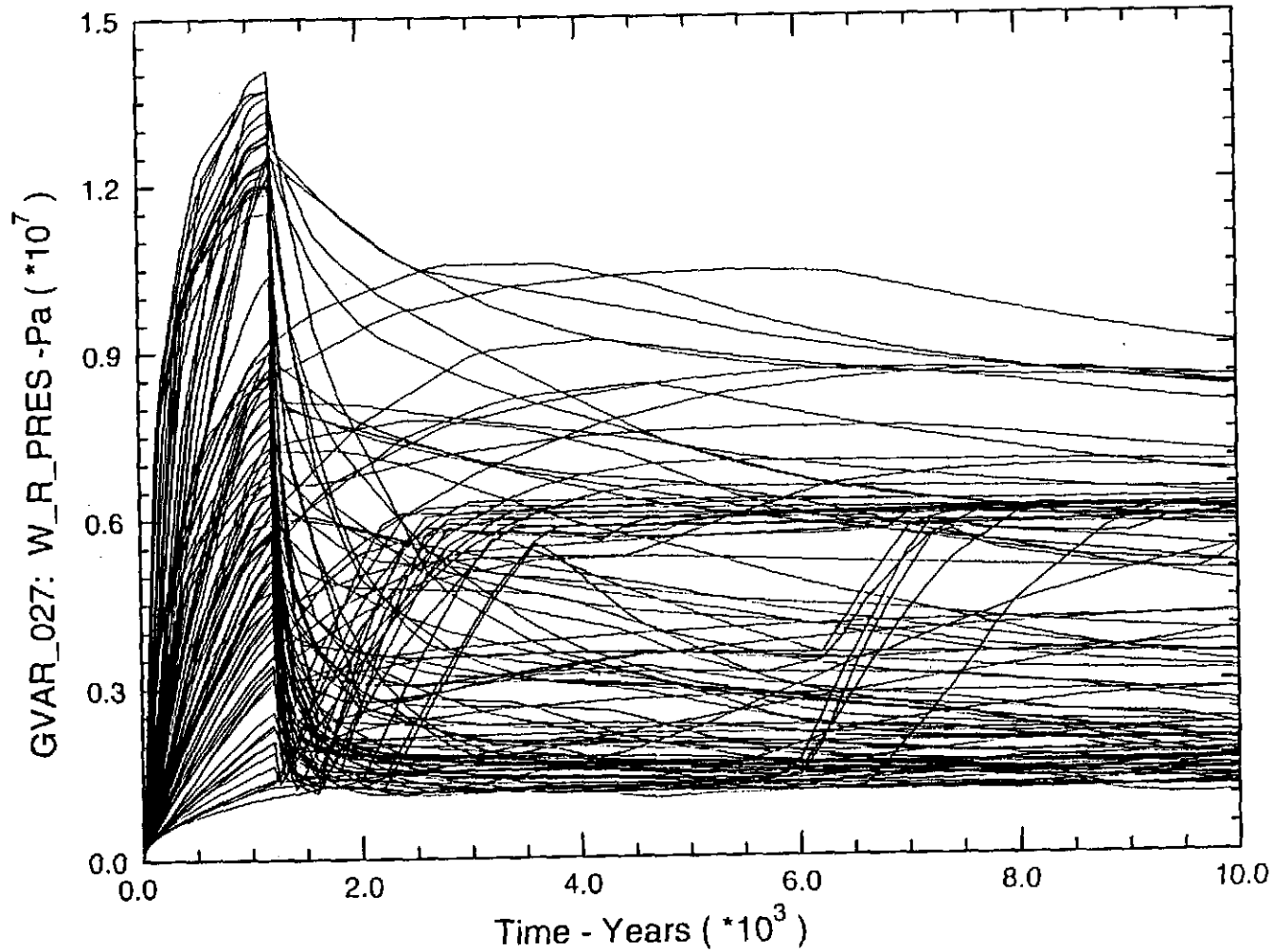
Figure 32.   Pressure in the waste disposal area during the regulatory period for an E2 intrusion occurring at 1,000 years from CCA Replicate 1.

References

Papenguth, H.W., and J. Myers, 1997. Rationale for Waste-Surrogate Strength Experiments. Unpublished memorandum to Frank D. Hansen, March 3, 1997. Albuquerque, NM: Sandia National Laboratories.

Copy to:

M.S.Y. Chu	1335
M.G. Marietta	1395
J.R. Tillerson	1322
E.J. Nowak	1320
R.V. Bynum	1320
P.N. Swift	1341
J. Johnson	1328
J. Helton	1328
P. Vaughn	1328
R. Thompson	CTAC/1322
M. Gross	CTAC/1322

SWCF-A:WBS 1.2.01.5.3.1: CCA/CO:NQ:Peer Reviews:Spallings

Appendix E
Memorandum on
Conditions in a Low Effective Stress Repository

E-2

Sandia National Laboratories

date: March 20, 1997

to: Frank Hansen, 6121, MS 1322
Kathy Knowles, 6121, MS 1322

from: Kurt Larson, 6821, MS 1341
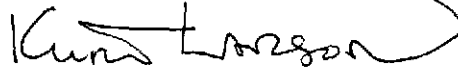
subject: Conditions in a low effective stress repository, and its probability

Introduction

Due to the realistic modeling of spall processes in the new spallings model, a higher level of consistency between model assumptions and the physical characteristics of the repository at the time of penetration is needed than for the spall releases used in the CCA. For example, whereas in the CCA spall releases were dependent on pressure mainly in the sense of whether they occur or not, in the new spallings model the quantity of release is highly sensitive to pressure. Furthermore, the volume released by spall is largest when the waste effective stress is below 0.3 MPa, which is an extreme case (discussed below). Over the past several months as the new spall model has been developed, indications of the physical conditions in the repository from the CCA performance assessment have been discussed several times. This memorandum provides a formal description of the processes that must occur for the effective stress on waste to be less than 0.3 MPa, the range of conditions that may result from these processes, and the probabilities that these conditions exist for first and subsequent intrusions.

The calculations from the CCA performance assessment relevant to this issue are BRAGFLO calculations of repository performance and CCDF_GF calculations of the times first and subsequent penetrations occur. BRAGFLO calculations were performed for six scenarios: undisturbed performance (S1); E1 at 350 years (S2); E1 at 1,000 years (S3); E2 at 350 years (S4); E2 at 1,000 years (S5); and an E1E2 scenario (S6). The conditions of the undisturbed performance scenario (S1) are most relevant to the new spallings model. There are several repository conditions indicated by the BRAGFLO modeling that are relevant to the new spall model, including pressure, brine and gas saturation, microbial degradation, and corrosion of steel. Prior to describing these specific properties, however, the probability and times of intrusion and the prediction of effective stresses from the BRAGFLO model results will be described.

The new spallings model fits into the context of a probabilistic performance assessment in which the limits of the future performance of the WIPP disposal system are quantified by the application of models incorporating the uncertainties about the processes and properties of the WIPP disposal system and the uncertainties in future human actions. The uncertainties in processes and properties of the disposal system lead to variation in the predicted physical characteristics of waste as it is penetrated. The uncertainties in future human actions lead to different time-sequences of inadvertent intrusions.

Probability and time of first intrusions

The EPA in 40 CFR 194 has specified the methods through which future human actions shall be incorporated in the WIPP performance assessment. For the spall model, the relevant actions are inadvertent penetration by deep drilling associated with oil and gas exploration and production. The methods prescribed by the EPA for deep drilling lead to the following model for deep drilling:

1. deep drilling occurs randomly in space and time
2. the times it occurs can be described with a Poisson model with in which the rate of intrusion is divided into three time periods
3. the first time period is Active Institutional Control (AIC), which last for 100 years has a rate of drilling intrusion equal to zero.
4. the second time period is Passive Institutional Control (PIC), which follows AIC and lasts 600 years. The rate of intrusion for this time is 0.468 boreholes/km^2/10,000 years.
5. the third time period is uncontrolled, follows PIC, and has a rate of intrusion of 46.8 boreholes/km^2/10,000 years.
6. technologies used should be assumed to be the same as those used in current practice

The time periods and rates described in points 2-5 above are shown in Table 1.

Using these time periods and rates in the Poisson model (CCA 6.4.12), the probability that a single intrusion has occurred by a specified time can be derived. Jay Johnson derived the probabilities of first intrusion occurring by a specified time that are shown in Table 2.

Table 2 indicates that it is extremely likely that a first intrusion will occur (p = 0.997). The time period up to 4,000 years is associated with a probability of 0.869. Thus, first intrusion will most likely occur by 4,000 years.

Table 1. Time periods and rates of intrusion during the regulatory period.

Period Name	Time period (years)	Intrusion Rate (boreholes/km^2/10,000 years)
Active Institutional Control (AIC)	0-100	0.0
Passive Institutional Control (PIC)	100-600	0.468
Uncontrolled	700-10,000	46.8

Interpreting effective stress from BRAGFLO results

For the new spalling model, the effective stress at the time of intrusion is the most important waste condition indicated by BRAGFLO results. Effective stress is defined as the difference between the total stress acting on a plane and the opposing fluid pressure in pores intersecting the plane. Effective stress is the portion of the total

Table 2. Probabilities of first intrusion occurring by a specified time during the regulatory period.

Time (years)	Probability first intrusion has occurred by specified time
500	0.00246
1000	0.172
1500	0.391
2000	0.552
2500	0.671
3000	0.758
3500	0.822
4000	0.869
4500	0.904
5000	0.929
5500	0.948
6000	0.962
6500	0.972
7000	0.979
7500	0.985
8000	0.989
8500	0.992
9000	0.994
9500	0.996
10,000	0.997

stress that is borne by the solid particles intersected by the plane of interest. In situations where the thickness of overburden above a particular horizon is constant, the total vertical stress at a point underground is generally assumed to be constant. In this case, variation in effective stress is caused entirely by variation in fluid pressure. As fluid pressure rises, the effective stress decreases. As fluid pressure decreases, effective stress increases.

The BRAGFLO model calculates fluid pressure in all regions of the disposal system. Seemingly, then, determining effective stress should be simple, by subtracting repository pressure from total stress. However, the BRAGFLO model does not know what the total stress at any point in the system is. Like most fluid flow codes, BRAGFLO does not model the solid phase, and its compressibility equations are formulated so it is not necessary. Total stress is a concept foreign to BRAGFLO's governing equations. Complicating this issue is gas generation and the dilation and

fracturing of interbeds. Experimental evidence indicates that anhydrite interbeds in the Salado will dilate as effective stresses decrease (Beauheim et al., 1994), and fracture when effective stress becomes zero or slightly negative (Beauheim et al., 1993).

To incorporate the effects of dilation and fracturing at low effective stresses, a set of equations was incorporated into BRAGFLO that allow porosity and permeability to increase as a function of pressure (Appendix BRAGFLO). These equations were parameterized so that the BRAGFLO model would behave similarly to the pressure-dependent behavior observed in the experiments mentioned in the preceding paragraph. With these equations and the proper selection of parameters, pressures in BRAGFLO do not exceed 15 MPa very often (realistic), and when they do 15 MPa is not exceeded by much. However, even with these equations the BRAGFLO model does not incorporate the concept of total stress, but rather the possible effects on fluid-flow properties of rocks as they are deformed. BRAGFLO was never designed to predict effective stress. Thus, using BRAGFLO to predict effective stress is not straightforward.

From the preceding discussion, it is plain that any algorithm attempting to derive quantitative estimates of effective stress from BRAGFLO results would be speculative and uncertain. In this case, a simplifying conservative assumption is useful. The BRAGFLO results can be split into two regimes: one in which effective stress is considered high, and one in which it is considered low. In the context of the new spallings model, effective stresses of less than 0.3 MPa are considered low. This would indicate that a condition of low effective stress would not occur until repository pressures exceed 14.5 MPa. Thus, one possibility would be to assume that conditions of low effective stress do not occur unless BRAGFLO pressures are above 14.5 MPa. To allow some conservatism, it will be assumed that conditions of low effective stress (0.3 to 0 MPa) exist in the repository whenever BRAGFLO pressures are above 14 MPa. As discussed in the next section, the selection of exactly 14 MPa as the indicator value turns out to be unimportant in the overall context of the performance assessment.

Pressure in the repository

The pressure in the repository predicted by BRAGFLO for the regulatory period for the 100 vectors in the first replicate is shown in Figure 1. The probability of intrusions occurring by a specified time (the information in Table 2) is shown across the top axis of the figure. This figure shows that in many vectors, 14 MPa is not attained, and conditions of low effective stress would therefore not be possible for a first intrusion at any time. Figure 2 shows the statistical comparison of the three replicates and indicates stability of the pressure predictions.

In evaluating the effect of predicted pressure-dependent releases from the new spallings model, it is necessary to predict the probabilities of intrusions occurring at different conditions of effective stress. Figure 3 shows a complementary cumulative distribution function (CCDF) for the pressure at time of first intrusion for the 100 vectors of the first replicate. This figure was constructed by sampling 10,000 times of first intrusion by the methods used in the CCA for each of the vectors shown in Figure 1. At each time of first intrusion, the corresponding pressure was noted. After 10,000
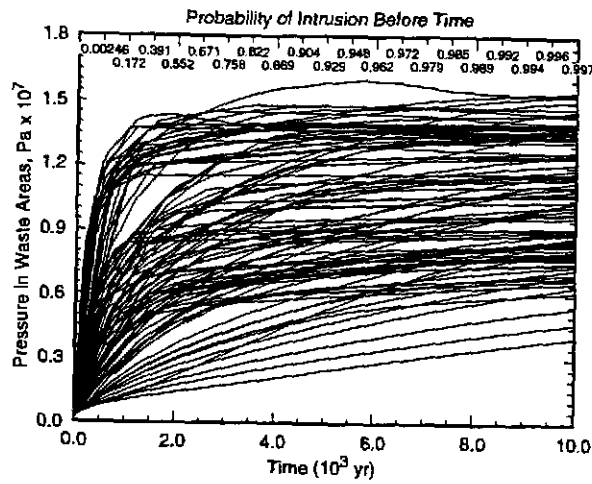
Figure 1. Pressure in the waste disposal area during the regulatory period for undisturbed performance, CCA Replicate 1. Across the top axis are the probabilities of first intrusion occurring by the time indicated along the bottom axis (from Table 2).
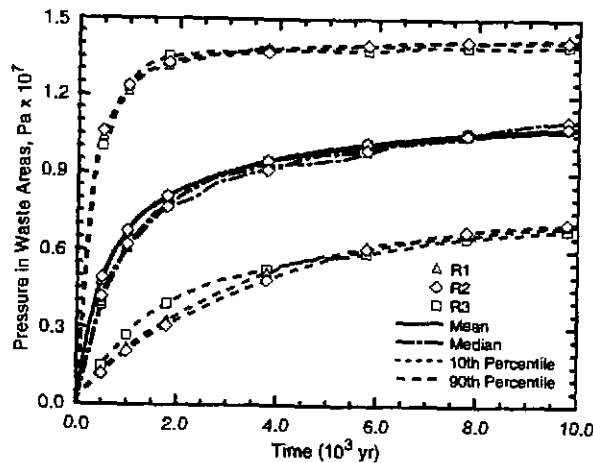

Figure 2. Statistical summary of the three CCA replicates for pressure in the waste disposal region, indicating stability of pressure predictions.

samplings, the CCDF could be constructed. Figure 3 shows that only 6 vectors, of 100, have a probability exceeding 10^{-4} of attaining pressures greater than 14 MPa by the time of first intrusion.

For WIPP, specific regulatory requirements dictate that the appropriate indicator of behavior of the disposal system is the arithmetic average of exceedance probabilities for a given value. Thus, the probability of low effective stresses (pressures greater than

CCDF of Pressure at First Intrusion, R1 S1
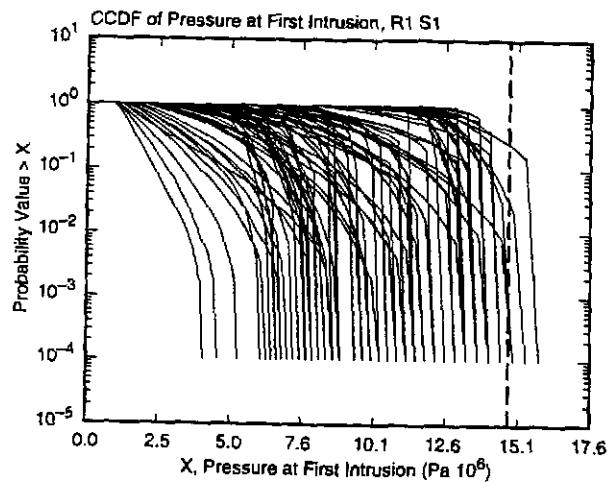
TRI-6342-5214-0

Figure 3. Family of CCDFs for pressure at the time of first intrusion for CCA Replicate 1. The CCDFs show variability due to uncertainty in future repository pressures, which depends on many sampled parameters, and uncertainty in the time of first intrusion. The vertical dashed line indicates 14.8 MPa for reference.

14 MPa) in any particular vector is not really important. Rather, it is the average or mean CCDF of pressure at first intrusion that indicates how the probabilities of low effective stress should be developed. The mean CCDF for the family of CCDFs for pressure at the time of first intrusion is shown in Figure 4.

It is vital to understand the information in Figure 4 to understand the relationship of the new spallings model release volumes to release volumes used in the CCA. Because new spall model release volumes are a function of pressure, the probability of exceeding a release of a given magnitude in the first intrusion can be directly estimated from the probability of exceeding the pressure at which the release occurs. Figure 4 shows that the probability of exceeding 8 MPa (the threshold for spall) is approximately 0.5, the probability of exceeding 10 MPa is approximately 0.35, the probability of exceeding 13 MPa is approximately 0.1, and the probability of exceeding 14 MPa (the threshold of low effective stress) is about 0.01. Figure 4 shows that the probability of low effective stresses is low, but not low enough that they are unimportant with respect to compliance, which would occur at probabilities less than 0.001. Calling low effective stresses an extreme case is considered consistent with it having an exceedance probability of 0.01 or less.

From Figure 4, it can be seen that a comparison to compliance measures would not be sensitive to the choice of 14 MPa pressure as indicating the onset of low effective stresses in BRAGFLO. In other words, choosing another value in the neighborhood of 14 MPa would not make the probabilities move significantly toward the region of increased sensitivity (above the 0.1 probability, 1.0 EPA normalized release compliance point), or towards the region of no importance (below the 0.001 probability, 10 EPA normalized release point).

E-8
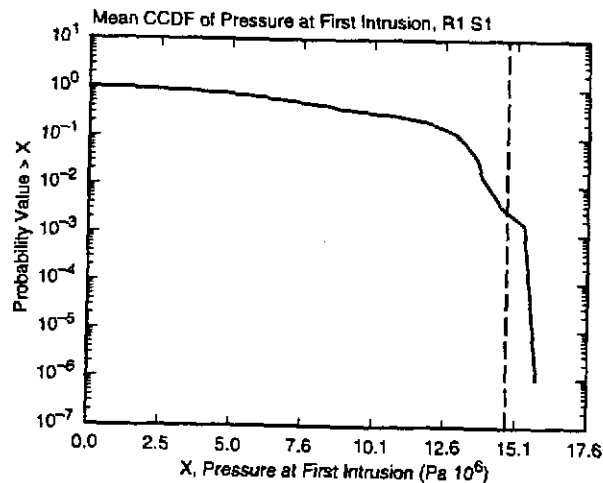
Figure 4. The arithmetic mean CCDF for pressure at the time of first intrusion, CCA Replicate 1. This is the mean of the family of CCDFs shown in Figure 3. The vertical dashed line indicates 14.8 MPa for reference.

Up to 15 intrusions were modeled in the performance assessment, and spall could potentially occur during any of the intrusions subsequent to the first. Figures 5, 6, 7, and 8 show pressure in the repository following E1 and E2 intrusions at 350 and 1000 years. It is obvious from these four plots that the probability of a second or subsequent intrusion encountering conditions of low effective stress are low, because pressures in excess of 14 MPa at the time of first intrusion do not remain above 14 MPa for very long.

When any intrusion penetrates the repository, a decline in repository pressure might be expected due to spallings and direct brine release processes. However, this possible pressure change is assumed to be negligible for long-term performance and it is neglected in long-term BRAGFLO calculations.

For 200 years following the first intrusion, a plug is assumed to exist at the Salado-Rustler contact, which generally prevents decreases in pressure for 200 years following the first intrusion. An inadvertent intrusion occurring during these 200 years would have a spall release occur with the similar pressure conditions as the first intrusion. Using the Poisson model equations presented in CCA 6.4.12.2 with a rate constant of 5.9×10^{-4} intrusions/year (4.68×10^{-3} boreholes/km^2/yr X 0.126 km^2/repository), the probability of a single intrusion occurring before the Culebra plug degrades 200 years after the first intrusion is about 0.10. The probability of two intrusions in these 200 years is much lower, about 0.006, and the probability of additional intrusions is lower yet.
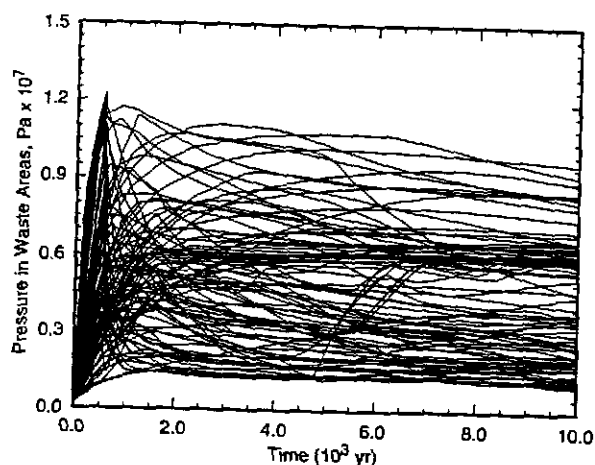
TRI-6342-5216-0

Figure 5. Pressure in the waste disposal area during the regulatory period for an E1 intrusion occurring at 350 years, CCA Replicate 1.
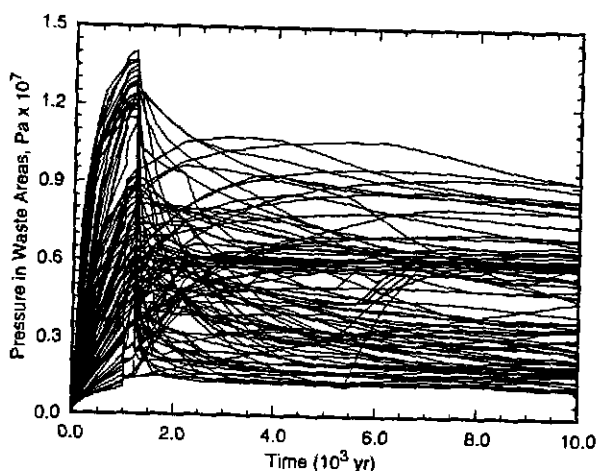

TRI-6342-5217-0

Figure 6. Pressure in the waste disposal area during the regulatory period for an E1 intrusion occurring at 1,000 years, CCA Replicate 1.

The Salado-Culebra plug is assumed to degrade at 200 years, leaving a borehole filled with granular materials through which gas usually vents from the repository, depending on the sampled permeability of the borehole. With venting, some vectors remain at pressures high enough for a spall event to occur, but no vectors in any scenario remain high enough for a low effective stress spall event to occur (see Figures 5 - 8).

E-10
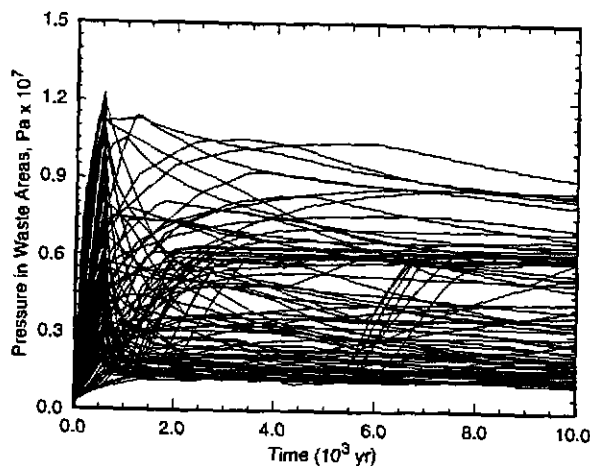
TRI-6342-5218-0

Figure 7. Pressure in the waste disposal area during the regulatory period for an E2 intrusion occurring at 350 years, CCA Replicate 1.
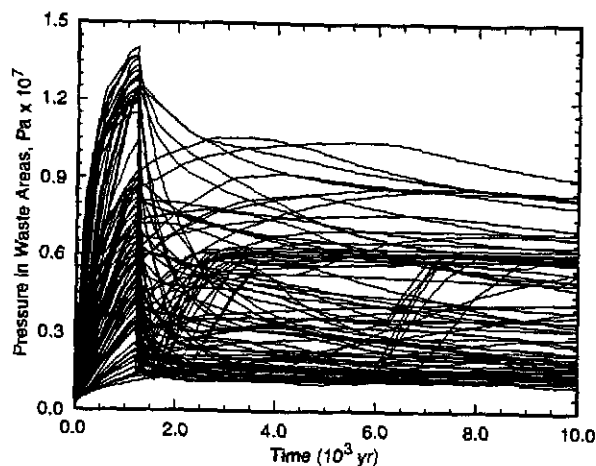
TRI-6342-5219-0

Figure 8. Pressure in the waste disposal area during the regulatory period for an E2 intrusion occurring at 1,000 years, CCA Replicate 1.

In summary, the probability of the first intrusion occurring at low effective stress is ~0.01. Multiplying the probabilities of subsequent intrusions occurring while the Culebra plug remains and pressure conditions are similar, the probability of two low effective stress intrusions occurring is ~0.001, and the probability of three or more low effective stress spall events occurring is less than 10^{-4}. Thus, as a result of the venting phenomenon and the probabilities of intrusions while the plug remains, only two low effective stress, maximum-volume spall events can happen at probabilities greater than

E-11

10^{-4}. Table 3 presents an important summary of the estimated probabilities of various types and sequences of intrusions occurring.

Compaction of waste

The process of creep closure of disposal rooms is incorporated in BRAGFLO. The BRAGFLO results of coupled creep closure, brine inflow, gas generation, and brine outflow indicate that the disposal room will compact in about 100 years from their initial height to an end height, and further variations are very small. Although closure is not explicitly calculated by BRAGFLO, indications of the end-state height are obtained by interpreting the porosity changes as height changes. With an initial porosity of 84.8 and constant height of 4 meters, the end state height of disposal rooms indicated by BRAGFLO end-state porosities of 0.08 to 0.2 (Figure 9), is 0.9 m to 1.5 m. These predictions are consistent with other modeling predictions. Compaction of waste will exceed 2 m for all intrusions.

Gas generation leading to low effective stress

The progress of gas generation reactions is important in developing pressure in the repository, and also impacts other characteristics of the waste. For pressures above 14 MPa to occur in the first 4,000 years, with few exceptions the three processes of gas generation must occur: anoxic corrosion of steel, microbial degradation of cellulosics, and microbial degradation of plastics and rubber (Figure 10). If microbial degradation occurs, performance assessment results indicate that all degradable cellulosics, plastics, and rubbers in the repository will be exhausted within about 2,000 years (Figure 11). Most to all of the cellulosics, plastics, and rubbers will be degraded to its end state prior to the time of a first intrusion in which pressure exceeds 14 MPa.

Table 3. Spalling pressures and associated probabilities of occurrence.

Pressure Event	Associated Probability
First intrusion P > 8 MPa	~ 0.5[1]
First intrusion P > 10 MPa	~ 0.35[2]
First intrusion P > 14 MPa	~ 0.01
Two or more intrusions P > 8 MPa	~ 0.25[1] (very approximate, estimated from Figures 5-8)
Two intrusions P > 14 MPa	~ 0.001 (~0.01 1st X ~0.10 2nd)
Three intrusions P > 14 MPa	< 0.0001 (~0.01 1st X ~0.006 2nd + 3rd)

P is pressure in the repository at time of intrusion.
[1] includes probability of P > 10 MPa and P > 14 MPa.
[2] includes probability of P > 14 MPa.
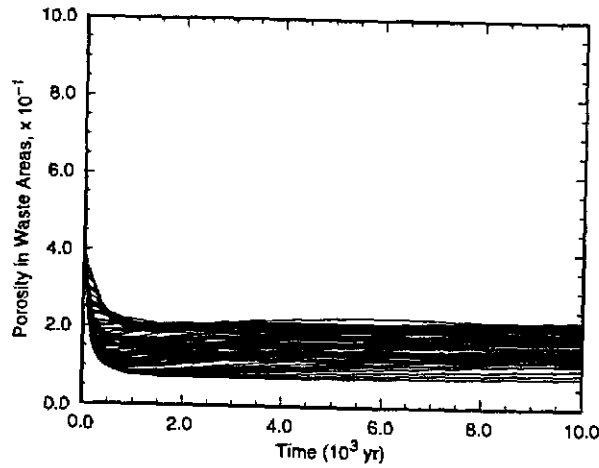
TRI-6342-5220-0

Figure 9. Porosity in the waste disposal areas during the regulatory period, CCA Replicate 1.
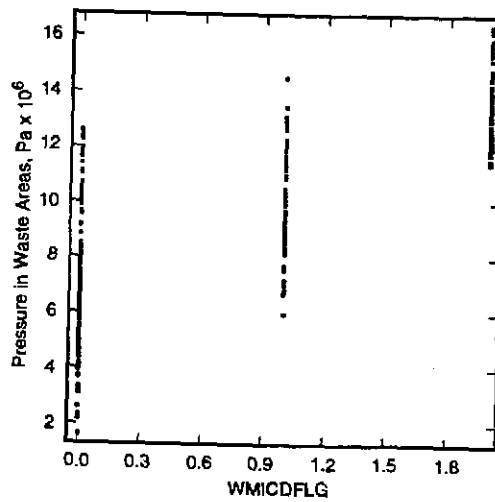

TRI-6342-5221-0

Figure 10. Pressure at 4,000 years in the waste disposal area for undisturbed performance as a function of gas generation processes active. Along the x-axis, 0 indicates only anoxic corrosion, 1 indicates anoxic corrosion and cellulosics degradation only, and 2 indicates anoxic corrosion with microbial degradation of cellulosics, plastics, and rubbers. Results from all 3 replicates indicated.

Anoxic corrosion occurs in all BRAGFLO simulations. Anoxic corrosion consumes brine and stimulates precipitation of salt, which may affect the strength of waste at time of intrusion. In vectors exceeding 14 MPa by 1,000 years, 12,000 cubic meters of brine had been consumed by anoxic corrosion (Figure 12). In vectors exceeding 14 MPa by
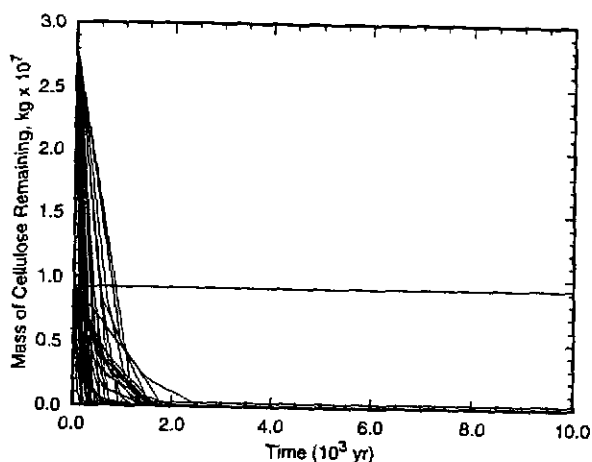
TRI-6342-5222-0

Figure 11. Mass of cellulose remaining during the regulatory period for undisturbed performance. The horizontal line has the value of 0.96×10^7 kg indicating no cellulose is consumed when anoxic corrosion is the only gas generation process.
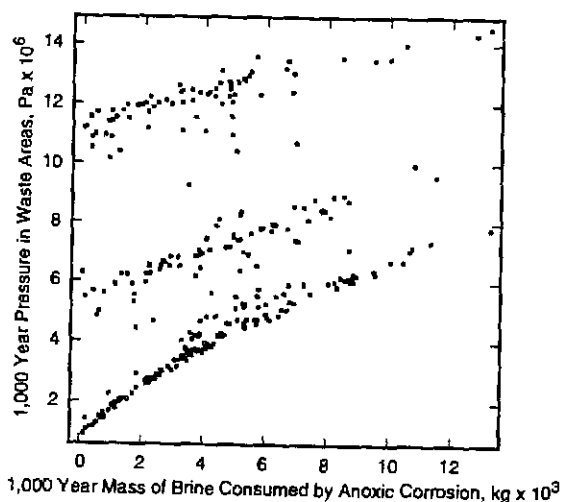

TRI-6342-5223-0

Figure 12. Cumulative brine consumed at 1,000 years by the anoxic corrosion process, all three CCA Replicates.

4,000 years, between 7,000 and 29,000 cubic meters of brine had been consumed by anoxic corrosion (Figure 13).

The extent to which anoxic corrosion has degraded waste is likely to be heterogeneous within the repository, because brine will tend to move toward the base of waste stacks and the lower portions of the repository due to gravity. Because microbial degradation consumes all materials that are assumed to be consumable, the composition of
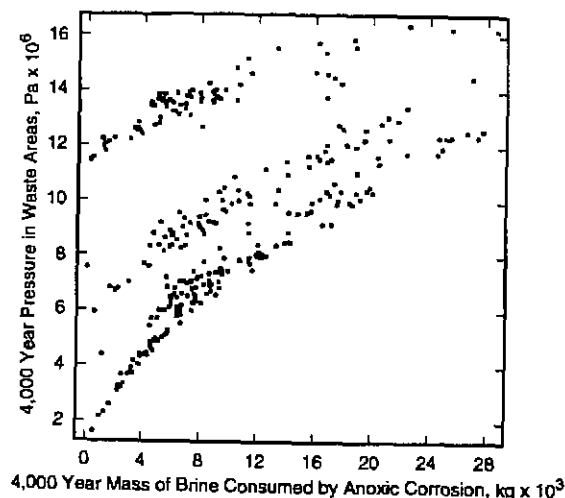
TRI-6342-5224-0

Figure 13. Cumulative brine consumed at 4,000 years by the anoxic corrosion process, all three CCA Replicates.

cellulosics, plastics, and rubbers will be homogeneous throughout the repository (either not degraded at all, or fully degraded).

Waste saturation at low effective stress

Vectors in which pressures exceed 14 MPa have repository brine saturations significantly lower than in lower pressure vectors. At 1,000 years, the volume-average brine saturation of the waste regions for vectors exceeding 14 MPa is 0.0 to 0.12 percent, compared to 0 to 0.95 percent for all pressures at this time (Figure 14). At 4,000 years, the volume-average brine saturation of the waste regions for all vectors exceeding 14 MPa is 0.0 to 0.20, compared to 0 to 0.95 for all pressures at this time (Figure 15).

It is expected that there will be some heterogeneity of brine saturation in the waste. Early, brine enters the repository mostly by drainage of the upper DRZ. However, after about 200 years this source has been depleted and further brine inflow is caused by drainage of marker beds. Most of the marker bed contribution comes from Marker Bed 139. Thus, the location of sources of brine to the repository are time-dependent. As well, dip contributes to higher saturations in the lower panels and lower saturations in the upper panels. Thus, the range of average conditions stated above is not likely the same as the range of local brine saturations in the repository. For example, in down-dip regions near the floor, fully-brine saturated conditions might be expected even in a very dry repository. Even taking into account the heterogeneities, it is reasonable to conclude that a repository at pressures greater than 14 MPa is quite a bit drier than a lower pressure repository.
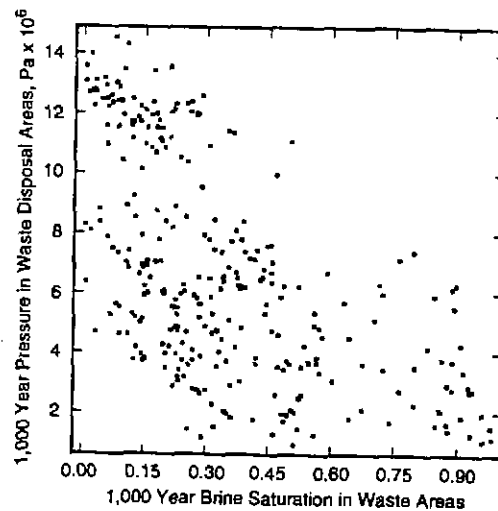
TRI-6342-5225-0

Figure 14. Volume-average brine saturation in the waste disposal areas at 1,000 years, all three CCA Replicates.
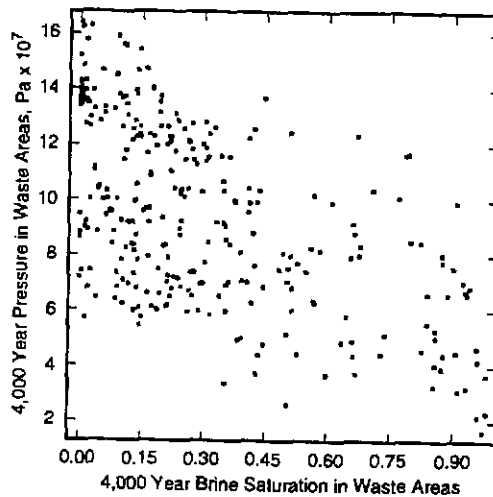
TRI-6342-5226-0

Figure 15. Volume-average brine saturation in the waste disposal areas at 4,000 years, all three CCA Replicates.

Quality Assurance

This memorandum was prepared and reviewed in accordance with QAP 9-5, "Quality assurance procedures for routine calculations." Peter Swift was the technical reviewer.

Acknowledgments

References

Beauheim, R.L., W.R. Wawersik, and R.M. Roberts. 1993. Coupled Permeability and Hydrofracture Tests to Assess the Waste-Containment Properties of Fractured Anhydrite. *Int. J. Rock Mech. Min. Sci. & Geomech. Abstr. Vol. 30, No. 7.* Great Britain: Pergamon Press. SAND93-06395.

Beauheim, R.L., S.M. Howarth, P. Vaughn, S.W. Webb, and K.W. Larson. 1994. Integrated Modeling and Experimental Programs to Predict Brine and Gas Flow at the Waste Isolation Pilot Plant. *in* GEOVAL `94, Validation Through Model Testing, OECD-NEA Proceedings, 11-14 October 1994. SAND94-05996.

Distribution

M.S.Y. Chu	1335
M.G. Marietta	1395
H.W. Papenguth	1341
P.N. Swift	1341
J. Johnson	1328
J. Helton	1328
P. Vaughn	1328
R. Thompson	CTAC/1322
M. Gross	CTAC/1322

SWCF-A:WBS 1.2.01.5.3.1: CCA/CO:QA:9-5:Peer Reviews:Spallings

E-18